University of São Paulo
São Carlos School of Engineering
Mechanical Engineering Department
Mechanical Engineering Graduate Program – Aircraft

Luiz Otávio Furtado Ferreira

Experimental investigations of stability and aerodynamic interference effects of an x-tail conventional airship

São Carlos

2018

Universidade de São Paulo
Escola de Engenharia de São Carlos
Departamento de Engenharia Mecânica
Programa de Pós-Graduação em Engenharia Mecânica – Aeronaves

Luiz Otávio Furtado Ferreira

Investigações experimentais de estabilidade e efeitos de interferência aerodinâmica de um dirigível convencional com cauda em x

Versão Corrigida

(Versão original encontra-se na unidade que aloja o Programa de Pós-Graduação)

Dissertação apresentada à Escola de Engenharia de São Carlos, Universidade de São Paulo, como requisito parcial para a obtenção do título de Mestre em Engenharia Mecânica.

Área de Concentração: Aeronaves

Orientador: Prof. Tit. Fernando Martini Catalano

São Carlos
2018

Ferreira, Luiz Otávio Furtado
F383e Experimental investigations of stability and Aerodynamic interference effects of an x-tail conventional airship / Luiz Otávio Furtado Ferreira; advisor Fernando Martini Catalano. São Carlos, 2018.

Master (Thesis) - Graduate Program in Mechanical Engineering and Subject area in Aircraft -- São Carlos School of Engineering, at University of São Paulo, 2018. Corrected version.

1. Airship. 2. Aerodynamic interference effects. 3. Airship stability. 4. Wind tunnel testing. I. Title.

FOLHA DE JULGAMENTO

Candidato: Engenheiro **LUIZ OTÁVIO FURTADO FERREIRA.**

Título da dissertação: "Investigações experimentais de estabilidade e efeitos de interferência aerodinâmica de um dirigível convencional com cauda em X".

Data da defesa: 16/04/2018.

Comissão Julgadora: **Resultado:**

Prof. Titular **Fernando Martini Catalano** **(Orientador)** APROVADO
(Escola de Engenharia de São Carlos/EESC)

Prof. Dr. **Thorsten Lutz** APROVADO
(University Stuttgart)

Dr. **Sergio Bittencourt Varella Gomes** Aprovado
(Banco Nacional de Desenvolvimento Econômico e Social/BNDS)

Coordenador do Programa de Pós-Graduação em Engenharia Mecânica:
Prof. Associado **Gherhardt Ribatski**

Presidente da Comissão de Pós-Graduação:
Prof. Associado **Luís Fernando Costa Alberto**

Fondly, to my family: Luiz Carlos, Marilde and Rodolfo.

ACKNOWLEDGEMENTS

I would like to register my sincere “thank you” to the following people, ones that I admire for the knowledge and the human beings they are:

Luiz Carlos Ferreira and Marilde Furtado Ferreira, my parents, and Rodolfo, my brother, indescribably essential and important in my life, to whom I owe all knowledge and achievements I will ever have, and incentivized me to complete and give my best to this work.

Fernando Martini Catalano, more than my professor and supervisor, an outstanding friend, who taught me a lot, and supported me during the most difficult phases of this work, guiding me throughout this challenging step in life.

Leandro Falcão Loureiro Rego, a very good friend I regret getting closer so late, to whom I owe memorable and funny moments, a remarkable engineer and researcher, who advised and helped me along this work.

Osnan Faria, the LAE technician, an artist, responsible for the high quality model used in this work, despite the geometrical complexity and tools limitations.

Lourenço Tércio Lima Pereira, a great friend, with whom I shared a lot of memorable moments at the Aerodesign Team, and to whom I specially thank for patience and contribution on the data acquisition systems.

Isaac Heras Cebolla, someone that I did not meet personally, but worked at AdB before me, and helped me a lot by providing his model for modifications, and also guided me through the very early literature review.

Caroline Camatari, André Nascimento and Guilherme Sinoara, college and work colleagues, but mainly great friends, with whom I shared the most part of my life time while at AdB, and to whom I owe laughs and unforgettable moments.

Elena Luzia Palloni Gonçalves, the EESC-USP librarian, who helped formatting and properly (formally) providing the information in this work.

Gisele Poppi Lavadeci, the secretary of the aeronautical engineering department and a friend, who always supported me on the university procedures.

I would also like to thank Airship do Brasil for all support and time provided to conduct and complete this work, without what I would not have had conditions of reconciling work and studies.

“[…] since airship design draws on the whole domain of aerodynamics and since special airship aerodynamics should contain as its most notable problem the full analysis of airship drag, it seems quite possible that from airship theory may some day come forward such fundamental progress as shall revolutionize our technique of air travel.” (Max M. Munk in Durand, 1936, p. 32).

ABSTRACT

FERREIRA, Luiz Otávio Furtado. *Experimental investigations of stability and aerodynamic interference effects of an x-tail conventional airship*. 2018. 383 p. Dissertation (Master of Science) – São Carlos School of Engineering, University of São Paulo, São Carlos, 2018.

Supporting the rising LTA industry, this works focus on investigating the general aerodynamics of a conventional X-tail airship, identifying the most relevant aerodynamic interference effects, besides developing a new method for initial tail design with simple but objective parameters (Tail Volume Coefficient – TVC). A 1:116 scale wind tunnel model of ADB-3-30 airship, under development at Airship do Brasil, was used. Firstly, through a similitude analysis, model and tunnel parameters were adjusted so the aerodynamics could be considered valid for full scale. The test campaigns were divided in two phases; Phase I comprised the steady investigations, obtaining standard aerodynamic polars and trimming curves, besides visualizing and explaining interference effects. During Phase II, oscillation damping tests were conducted in order to evaluate the proposed TVC, assessing the damping of yawing oscillations for different tail arrangements. The flow is strongly three-dimensional, with main interference effects of hull on tail, dominated by longitudinal eddy structures. The behavior at small and large incidences is very different regarding interferences, compromising the X-tail efficiency. The oscillation tests demonstrated a preferential sequence for tail arrangement efficiency, where X-tail figures at the last place; ADB-3-30 was found static and dynamically unstable. Unfortunately, no simple direct law, like TVC, which measures with confidence the degree of stability, was found. Nevertheless, a lower threshold law was determined for directional stability (TVC_Y-*ARb*). As a whole, despite all the complexity involved on testing airship models in wind tunnels (geometric scale, flow similitude, manufacturing, positioning, etc.), the objectives were fulfilled, enriching the study field with new aerodynamic and stability information, also showing that properly predicting airship stability is no simple task. The results are useful for academy and industry, and may help detailing and support further researches by presenting new information on a specific configuration.

Keywords: Airship, Aerodynamic interference effects, Airship stability, Wind tunnel testing

RESUMO

FERREIRA, Luiz Otávio Furtado. *Investigações experimentais de estabilidade e efeitos de interferência aerodinâmica de um dirigível convencional com cauda em x*. 2018. 383 p. Dissertação (Mestrado em Ciências) – Escola de Engenharia de São Carlos, Universidade de São Paulo, São Carlos, 2018.

Apoiando a crescente indústria LTA, este trabalho foca na investigação da aerodinâmica de um dirigível convencional com cauda em X, e seus principais efeitos de interferência, além de desenvolver um novo método para projeto inicial de cauda por parâmetros simples e objetivos (Coeficiente de Volume de Cauda – TVC). Um modelo de túnel de vento em escala 1:116 do dirigível ADB-3-30 (Airship do Brasil) foi utilizado. Inicialmente, através de análises de similaridade, modelo e túnel foram ajustados para que sua aerodinâmica refletisse a escala real. As campanhas foram divididas em duas fases. A Fase I compreendeu testes estáticos, obtendo polares e curvas de trimagem, além de visualizações do escoamento. Na Fase II, testes dinâmicos avaliaram a teoria de estabilidade proposta, através do amortecimento de oscilações para diferentes arranjos de cauda. O escoamento é extremamente tridimensional, com efeitos principais do envelope na cauda, dominado por vórtices longitudinais, havendo grandes diferenças entre baixas e elevadas incidências, e comprometimento da eficiência da cauda em X. Os testes dinâmicos demonstraram a existência de uma sequência preferencial quanto ao arranjo de cauda, sendo X o pior; o ADB-3-30 mostrou-se estática e dinamicamente instável. Infelizmente nenhuma regra simples como o TVC, que meça com confiança o grau de estabilidade, foi encontrada. No entanto, um limite mínimo foi identificado para estabilidade direcional (TVC_Y-ARb). Apesar da complexidade do ensaio de dirigíveis em túnel de vento (escala geométrica, similaridade, fabricação, posicionamento e etc.), os objetivos como um todo foram alcançados. Novas informações de aerodinâmica e estabilidade enriqueceram o campo de estudo, e mostraram que determinar a estabilidade de dirigíveis não é simples. Os resultados são úteis à academia e indústria, ajudando no detalhamento e suporte de pesquisas futuras, trazendo também novas informações sobre uma configuração específica.

Palavras-chave: Dirigível, Interferências aerodinâmicas, Estabilidade de dirigíveis, Ensaios em túnel de vento.

LIST OF FIGURES

LIST OF TABLES

LIST OF EQUATIONS

LIST OF ABBREVIATIONS AND ACRONYMS

AdB	Airship do Brasil
ADC	Airship Design Criteria
AIRSHIP	Model hull with tail installed
ARC	Aeronautical Research Committee
BARE HULL	Model bare hull
BUBLLEWRAP	Model bubble wrap cover
COLLANT	Model collant type stocking
CPF	Corrected Projection Factor
DCO*	Drag carry-over (defined in this work)
EESC	São Carlos School of Engineering
FAF	Full Attenuation Factor
FIN	Model tail fin
FPF	Full Projection Factor
FISHNET	Model fishnet type stocking
GWT	Gust Wind Tunnel
HEXNET	Model hexagonal net cover
HTA	Heavier than air
HULL	Model hull
ISA	International Standard Atmosphere
LAE	Laboratory of Aerodynamics – EESC-USP
LCO (LCO*)	Lift carry-over (Lift carry-over as defined in this work)
LFLS	*Lufttüchtigkeitsforderungen für Luftschiffe der Kategorie Normal und Zubringer*
LL	Lower left FIN
LR	Lower right FIN
LTA	Lighter than air
LTAV	Lighter than air vehicles
LWT	Large Water Tunnel
MHP	Multi Holes Probe
MWT	Medium Wind Tunnel
PAF	Projected Attenuation Factor
PIO	Pilot Induced Oscillation
RAS	Rotary Axis Support
RCF	Response to control factor
ROM	Rough Order of Magnitude
Stbd.	Starboard side
TAR	Transport Airship Requirements
TRIP	Model tripping band
TVC	Tail Volume Coefficient
TVC_Y	Tail Volume Coefficient for Yawing
TVC_Y–*ARb*	Tail Volume Coefficient for Yawing considering *ARb*
UL	Upper left FIN
UR	Upper right FIN
USP	University of São Paulo
“X”	X-like tail arrangement
“+”	Cruciform tail arrangement
“-Y”	Inverted Y-like tail arrangement

LIST OF SYMBOLS

A	Amplitude
A	Horizontal or vertical tail planform area (BURGESS, 2004)
A	State matrix
a	Speed of sound
AC	Aerodynamic center
Ah	Horizontal tail area according to Burgess (2004)
AoA	Angle of attack
AR	Aspect Ratio (Slenderness or fineness Ratio in the case of airship hulls)
ARb	Aspect Ratio (Fineness Ratio) proposed by Burgess (2004)
Av	Vertical tail area according to Burgess (2004)
B	Wind tunnel blockage factor or Control matrix
b	Span
b	Logarithmic decrement
C	Longitudinal distance between CB and tail AC/CG (area)
CB	Center of Buoyancy
C_D	Drag Coefficient
C_{Di}	Induced drag Coefficient
C_f	Skin friction Coefficient
CG	Center of Gravity
CHT, C_{HT}	Airship Horizontal Tail Volume Coefficient (CARICHNER and NICOLAI, 2013)
C_L	Lift Coefficient
C_M	Moment Coefficient
C_n	Yawing moment Coefficient
C_P	Pressure Coefficient
CP	Center of Pressure
CVT, C_{VT}	Airship Vertical Tail Volume Coefficient (CARICHNER and NICOLAI, 2013)
D	Drag
d	General dimension
$\mathbf{D_{máx}}$	Maximum hull diameter
DoF	Degree of freedom
d_x	Diameter at x
E	Identity matrix
e	Oswald factor
e	Exponential
Eu	Euler number
Fh	Horizontal tail reference coefficient (BURGESS,2004)
Fr	Froude Number
Fv	Vertical tail reference coefficient (BURGESS,2004)
F-Se	Blakemore’s criterion for airship elevator area
F-Sh	Blakemore’s criterion for airship horizontal tail area
F-Sh’	Blakemore’s criterion for airship horizontal tail area with **C**
F-Sr	Blakemore’s criterion for airship rudder area
F-St	Blakemore’s criterion for airship total tail area
F-Sv	Blakemore’s criterion for airship vertical tail area.

F-Sv'	Blakemore's criterion for airship vertical tail area with **C**
$\mathbf{F_0}$	All external forces acting on body
H	Boundary layer shape factor
H	Control vector
$\mathbf{I_0}$	Inertia matrix taken about the origin of the body frame
$\mathbf{I_0}'$	Added inertia matrix
L	Lift
L	Airship Length
L_H, L_{HT}	Longitudinal distance from horizontal tail AC to the aircraft CG
L_V, L_{VT}	Longitudinal distance from vertical tail AC to the aircraft CG
L_{CB-CA}	Longitudinal distance between aircraft CB and the geometrical center of the projected vertical tail
L_{Gen}	Generatrix length
M	Moment
m	Airship mass
Ma	Mach Number
$\mathbf{M'}$	Added mass matrix
MAC	Mean aerodynamic chord
M_q	Damping moment derivative with angular pitching velocity
M_θ	Disturbing moment derivative with pitch angle
M_θ'	Model damping moment derivative with pitch angle
P	Local pressure
P_∞	Pressure of reference (atmospheric)
Pe	Peclet number
Pr	Prandtl number
P_T	Total pressure
q	Dynamic pressure
R	Radius of turning circle
r	Transversal position along hull radius
Re	Reynolds Number within maximum length
Re_v	Reynolds Number within volumetric length
$\mathbf{r_G}$	Position vector
$\mathbf{r_{máx}}$	Maximum hull radius
$\mathbf{r_G^x}$	Skew symmetric matrix of the position vector
$R_{specific}$	Ideal gas constant
S	General area
s	Model scale factor
Se	Elevator area
Sh, S_H, S_{HT}	Horizontal tail area
S_{hull}	Hull surface area
Sr	Rudder area
St, S_{Tail}	Total tail area
St	Strouhal Number
Sv, S_V, S_{VT}	Vertical tail area
$S_{VT-Proj}$	Projected vertical tail area on longitudinal plane
S_W	Wing planform area
T	Temperature or distance between CB and tail AC
t	Time
Tu	Turbulence level

$\mathbf{T}$	All external torques acting on body
u	Local velocity
U_∞	Free stream velocity
V	Hull volume
ϑ	General velocity
V_H	Horizontal tail volume coefficient for fixed wing aircraft
V_V	Vertical tail volume coefficient for fixed wing aircraft
$V^{\frac{1}{3}}$	Volumetric length
$V^{\frac{2}{3}}$	Volumetric area
x	Longitudinal position along hull length
$\boldsymbol{x}$	State vector
xCP	Longitudinal position of the Center of Pressure
x_M	Longitudinal position of $\mathbf{D}_{\mathbf{máx}}$
$\mathbf{X}_0$	an eigenvector of a system
$\bar{x}_F$	Longitudinal distance between CB and tail CP
y	Vertical distance above wall
$\bar{Z}_G$	Vertical distance (parallel to hull radius) between CB and CG
α	Womersley number
β	Side slip angle
δ	Control surface deflection angle
δ_1	Boundary layer displacement thickness
δ_2	Boundary layer momentum thickness
δ_3	Boundary layer energy thickness
δ_{99}	Boundary layer thickness
ε	Roughness size
$\boldsymbol{\zeta}$	Damping factor/coefficient
λ	an eigenvalue of a system
μ	Fluid dynamic viscosity or coefficient of damping moment in pitch for the model (ZAHM, 1926)
$\boldsymbol{\nu_0}$	Linear velocity
ρ	Air Density
τ	Wall shear stress per unit area
Γ	Circulation
φ	Phase angle
ψ	Yawing angle
ω	Angular velocity or damped frequency (clarified along text)
$\boldsymbol{\omega}$	Angular velocity of the body-fixed frame
ω_0	Natural frequency
$_{\alpha}, \frac{\partial}{\partial \alpha}$	Indicates derivative with AoA
$_{\beta}$	Indicates derivative with β
$\frac{\partial}{\partial x}$	Partial derivative with x
$\frac{\partial}{\partial y}$	Partial derivative with y
$\dot{}$	Derivative with time
$_{máx}$	Indicates maximum
$_{min}$	Indicates minimum
$_{Y}$	Indicates yawing moment

LIST OF UNITS

J	Joule
kg	Kilogram
m, m^2, m^3	Meter (squared and cubic)
mm	Millimeter
K	Kelvin
°	Degree (angle)
°C	Degree Celsius
rad	Radian
Hz	Hertz
Pa	Pascal
ft, ft^2, ft^3	Foot (squared and cubic)
in, in^2, in^3	Inch (squared and cubic)
N	Newton
Nm	Newton-meter
lb	Pound
lb-ft	Pound-feet
s	Second
m/s	Meters per second
inWG	Inches of water gauge
Psi	Pounds per in^2
Psid	Differential Psi
mph	Miles per hour

TABLE OF CONTENTS

1 INTRODUCTION

1 INTRODUCTION

It is not going to be easy finding someone who have or had professional contact with airships; it is going to be also difficult to find people who simply saw an airship once or twice in their lives. The airships were much more common in the first decades of the last century, very well represented by the German aircraft, the famous so-called Zeppelins (in reference to the company name, derived from the founder's surname), or during 1980s and 1990s, carrying the Goodyear logo, floating over stadiums and crowded events, recording and broadcasting.

The lighter-than-air (LTA) industry has never received enough funding in order to establish itself as a strong branch of the market. Although the LTA vehicles (LTAV) were very well succeed in the anti-submarine warfare and convoy protection until early 1960s, the lack of knowing about this (and other usages) summed to the very negative public perception of people after the disasters during the 1920s and 1930s conducted this industry to almost vanishing (THE AIRSHIP ASSOCIATION, 2016).

However, in the last decades some interest has been shown for a sort of rebirth of this technology. This kind of aircraft, which is classified as an "aerostat" (Figure 1), is very different from what we see typically flying in the skies, the "aerodynes", represented by common airplanes and helicopters.

Figure 1 - Classification of aircraft.

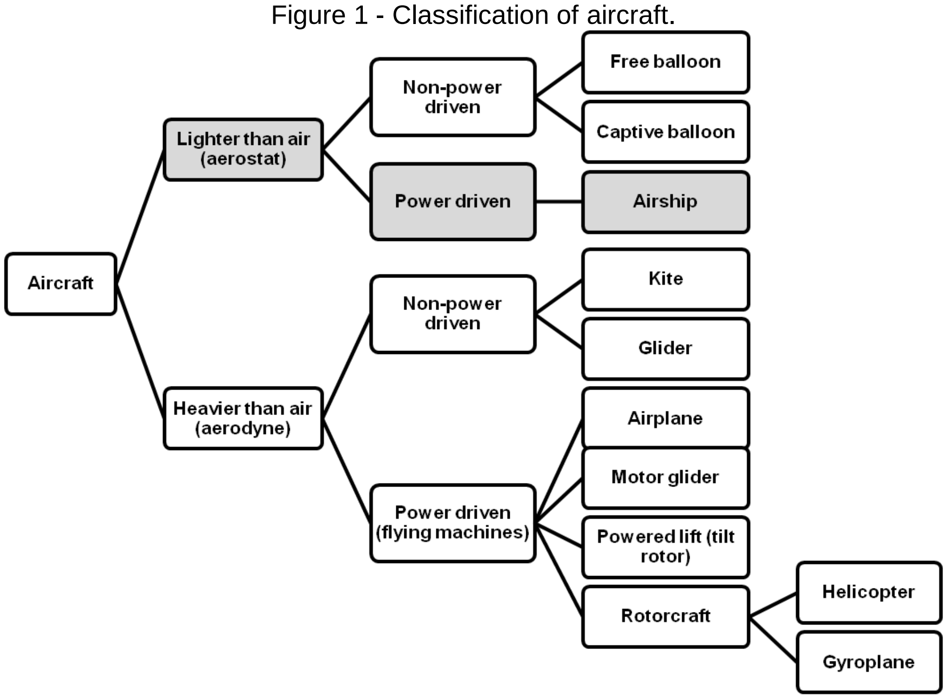

Source: adapted from The Air Navigation (Jersey) Order (2008).

Airships are much bigger and slower, but they are also very elegant and propitiate a very comfortable and pleasant flight. This characteristic was indeed explored by companies that used to offer sightseeing flights aboard of airships – or even by the transoceanic Zeppelins, being still in voga for some, and considered as a niche in the market by others.

1.1 BRIEF HISTORY

The origin of the lighter-than-air (LTA) technologies dates back to the spring of 1783, in Annonay, France, when the Montgolfier brothers were able to first fly a practical hot air balloon. The investigation and trials involving balloons continued until the French engineer Henri Giffard, in 1852, using a steam-powered engine and a huge propeller, crossed 17 miles in the skies at incredible 5 mph, flying on a steerable balloon: the very first dirigible (airship).

After him, the studies increased, and many others started looking at airships. The Brazilian Alberto Santos=Dumont became famous in the LTA field for his balloon Nr. 06, claimed to be the first practical airship. With it, he was able to win, in 1901, the *Deutsch de la Muerthe* Prize for managing to complete a mission circuit in a determined time, without ground support, demonstrating that controllable flight was possible. In 1908, following the airship technology development, the American inventor Thomas Baldwin was responsible for delivering the first US Army's powered aircraft, the SC-1.

Figure 2 - Santos=Dumont Nr.06, winner of the Deutsch Prize.

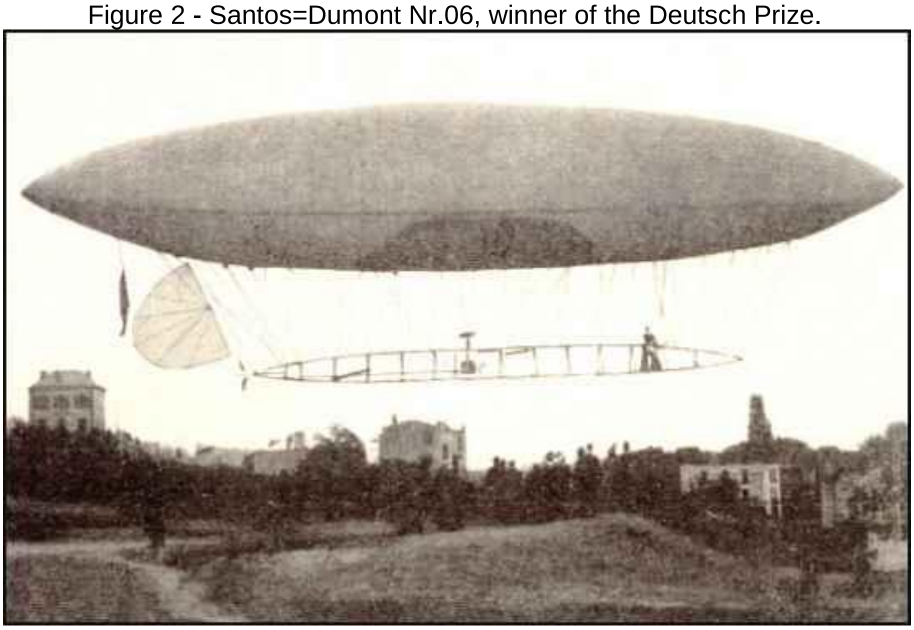

Source: Balloon No. 6 […] (2016).

The evolution did not stop, concomitant, the most famous name in LTA was also working. The Count Ferdinand von Zeppelin (Graf Ferdinand Adolf Heinrich August von Zeppelin), after the failure with the LZ-1 in 1900, was able to found the *Luftschiffbau Zeppelin GmbH* company, in Friedrischshafen, Germany, in 1908, when he already had LZ-2, 3 and 4 built. The company grew, and 119 models were developed, some of them (LZ-20 to LZ-112) were applied in military purposes during the I World War. The company did not give up, even after the founder's death in 1917, and the giants of the air were born: LZ-126 (ZR-3 "U. S. S. Los Angeles"), LZ-127 (Graf Zeppelin), the bigger brothers LZ-129 (the famous Hindenburg) and LZ-130, among others.

Unfortunately, the biggest aircraft ever built and flown, the LZ-129, was, despite its magnificence and elegance, also a tragic mark in the LTA history. On May 6^{th}, 1937, in New York, a tragic accident involving the huge LZ-129 "Hindenburg" put people's confidence on airships to a very low level.

Maybe due to it, little – at least to the humanity eyes – has been developed in the field of lighter-than-air technology aimed at large airships. However, digging deeper, it is undeniable that airships are back to the aviation horizon, or have never left it. In more recent times, a worldwide revival of the airship alternative, owing to the exceptional low fuel consumption, occurred due to the oil crises of '73 and '79. Even Brazil, still today a developing country, by that time commissioned studies in order to evaluate the use of airships for transportation in hinterland (GOMES, 1997). Many are the companies over the last decades around the world that have been researching and looking at airships for a wide variety of applications, both civil and military purposes.

The key aspect that contributed to the rising interest – besides the comfortable and safe flight – is the totally different operational system involved: easier hovering capacity; possibility of enduring days without refueling; lower power requirements and consequently lower fuel consumption, making it more economic and less aggressive to the environment (reduce both the energy cost and the consumption of natural resources); solution for carrying large indivisible loads; lower dependence on ground support and preparation compared to airports and long runways built in inhospitable regions; discrete and silent flight, with very low vibration (interesting for military and surveillance purposes, reducing also electronics malfunction); more secure logistics when dealing with high value added cargo, like electronics and medicines, among other applications.

From a qualitative comparison (Table 1) between airships and direct competitors as air transports (airplanes and helicopters), for a monitoring task, for example, it is possible to conclude that LTAV are far ahead. The probable reason for that is they do not require much energy for maintaining themselves in the air, only to cruise and compensate for wind and gusts drift.

Table 1 - Comparative efficiency of airship against competitors for a monitoring task.

Project requirement	Grade*		
	Airplane	**Helicopter**	**Airship**
Low operation cost	2	1	3
Long endurance	2	1	3
Hovering capability	1	3	3
Payload to weight ratio	2	1	3
High maneuverability	2	3	1
Low noise and turbulence	1	1	3
Vertical take-off and landing	1	3	3
Low fuel consumption	2	1	3
Low vibration	2	1	3

*1 = high, 2 = medium and 3 = low

Source: Adapted from Elfes (1998).

For this logistics purpose, a good benchmarking case can be made taking Brazil as the scenario. Considering a cargo load located in the southeastern Brazil, in São Paulo, delivered to Manaus, in the state of Amazonas, in the heart of Amazonia, the Rainforest. In order to get to Manaus, this cargo load travels five days by truck to Belém, in the state of Pará, and from there on it goes by barge or ferry, on the Amazonas River, for three more days. Usually these are the numbers, and the total time takes eight days, with nonstop journey and considering that no problems occurred. An alternate trip, with the same cargo, travelling at 80 km/h with an airship would take no more than two days nonstop and clear sky flight. Depending on the weight carried, the cost would be the same per kilometer-tonne (km.tonne) as it is for the truck plus barge (WATERHOUSE, 2011). Besides delivering it faster, economically the company would not be badly affected, even increasing its profit.

Prentice and Adaman (2017) published a very interesting work on an airship application very different of what would be expected: food transportation. The study explores the possibility of supplying food to Canada northern region, which possesses 70% of its landmass lacking all-season road infrastructure (PRENTICE and ADAMAN, 2017). This region ends up depending on very high-cost, unreliable and season dependent services. The study evaluates the potentials of a 50-tonne cargo airship against to ice road trucking and small airplanes, which are the most used options to supply food to these regions nowadays. Despite the detailed work developed for trip modelling and operating cost estimates, which do not apply for this work in deep, the overall conclusions are very promising, describing a multi-modal proposal. The results point great economic advantages of airships in delivering the goods to these almost inhospitable regions in northern Canada, making it possible to reduce more than 30% of direct freight transportation costs.

From this scenario, it is clear that the LTAV are not to be considered a replacement for conventional aircraft and ships, but a complementary solution, acting on specific niches, reducing the economic cost mainly of transport – and indeed in some cases making it feasible – in poorly prepared areas (THE AIRSHIP ASSOCIATION, 2016). By means of the correct tools, leading to an appropriate design, the combination of all of those aspects into a single aircraft would result in a multirole platform capable of catering different markets with small adaptations and better operating in very complicated regions, delivering quicker solutions at lower costs.

Until 2003, around 25 companies were active manufacturers with flying airships, whilst other 12 companies were in the design and construction phase, apart from other 13 that were already inactive by that time (THE AIRSHIP ASSOCIATION, 2016). Of course these numbers have changed since then. Some companies went bankrupt; others just gave up on studying airships due to costs and time schedule, which are as high as those for common light aviation; and fortunately some others were established in the mean time.

Nowadays, there are 18 constructors that have designed, built and certified LTAV under their own brand (ESCHER, 2016). Besides that, more 7 other companies are known to be involved in Research & Development (R&D) and prototyping of these aircraft. It is curious to notice that, for example, the company "Aeros" (AEROS, 2016), from the USA, known for the giant Aeroscraft, a hybrid cargo airship under development, and for the Aeros 40B, a fly-by-wire blimp, is not listed. This maybe means that not even this worldwide association registers the companies as fast as they start developing.

One can then infer, mainly for R&D, that other companies may exist and work on LTA technologies. This is the case of another missing name in the list mentioned above: the Brazilian company *Airship do Brasil* (AdB)[1]. With its origins in an SPE (Specific Purpose Entity) among logistic, transport and engineering companies, AdB was officially born in 2004 after the signing of a Letter of Understanding between the SPE and the Brazilian Army (AIRSHIP DO BRASIL, 2016), which had interest in airships for logistics in inhospitable regions like the Amazonia (Rainforest). Since then, the company has been working on LTA R&D, working on small technology demonstrators, radio-controlled small airships, aerostats and small-medium non-rigid airships. The following of such a very smart strategy, a learning curve, is made in other to consolidate the necessary knowledge for the achievement of its great objective: a family of large cargo airships. The first in the family is supposed to carry 30 tonnes of payload, named ADB 3-30.

These two examples, among others, show that the world is really looking at airships as an alternative for the traditional ways of transportation – by ground or air – introducing a new transportation mode. In spite of the promising scenario, there is a lot of prejudice involved. These aircraft, claimed to be outdated machines, poor in performance and effectiveness, and feared given the accident (great fire) with the Hindenburg, are being completely redesigned and reshaped. Innovative solutions and applications are going to bring people a new perspective about LTA Vehicles (LTAV), and consequently create and revolutionize the way of thinking about logistics, surveillance, searching, rescue and so on.

New concepts have also risen, such as the hybrid vehicles and the unmanned stratospheric airships. In the same way these concepts are completely new, so are the technologies and solutions involved in the classical airships studies as well. Despite the common ellipsoidal bodies and the similarity to the old models, these new generation aircraft are totally renewed by the present technology and safety resources (certification basis). This makes them very efficient and versatile vehicles, and, at the same time, much safer than in the past - the machines under development at AdB, in Brazil, are a good example. The company counts on several different kinds of computational methods, since simple shape optimization, up to very detailed structural, aerodynamic and flight dynamics models. Working with virtual prototypes allows quicker improvements, saving money and assuring safety.

[1] The author worked at AdB, from 2014 to 2018, as Aeronautical Engineer, leading the Engineering Team, besides contributing directly to the Conceptual Design Board, as an active member for the company's projects.

1.2 MOTIVATION

Lots of advantages and differentials of LTAV are then obvious. Being however a promising solution for specific problems and a potential vector of improvement for typical operations as a complementary platform does not mean that every particular characteristic of airships are known.

The airships were born before the airplanes could be imagined, and were purely a consequence of the need to control the classical hot-air balloons. With such a solution, the pilots would be able to guide and propel the aircraft regardless of the wind. Nevertheless, the winds still act on airships, and are extremely relevant during design. Since airships are vehicles very sensitive to atmosphere, gusts have powerful influence over their behavior, statically and dynamically.

Much of the principles are very well understood and dominated by specialists around the world, but some substantial design questions - maybe due to the empirical history involving airship design – persist, mainly on the flight mechanics field. What are the real aerodynamic characteristics of an airship, including the aerodynamic interference effects? How stable and steerable an airship can be, and what does it depend on? What is the best tail arrangement considering not only stability, but handling qualities, weight, systems simplification, etc? Is there any parameter on which one could rely for designing the aircraft tail?

These are common questions heard at an engineering office when designing a completely new airship from a blank sheet of paper. There is no running away, they must be answered, or at least after design checked. The main point is that the prototyping phase is a ticking time bomb: nobody wants to spend more time than expected, not even find out problems at this stage, otherwise cost and/or schedule are going to blow up. So it is much better if a good understanding of these questions already exists during the conceptual phase.

In this way, motivated by the recent Brazilian ascension to the LTA society as a potential maker (AdB), considering the author's self involvement with this cause as well, and aiming at contributing to the airship community and improving the existing knowledge, this work has the purpose of better understanding the stability and aerodynamics of conventional airships, propitiating a better comprehension of its specificities, and delivering useful technical information.

In order to achieve this in a more tangible way, the proposal is to use a scale model of an AdB's representative airship prototype under study, the ADB-3-30, on which the author worked, and run several wind tunnel tests, collecting quantitative and qualitative data, interpreting and converting it to knowledge and foundation for subsequent studies.

1.3 OBJECTIVES

The ultimate goal of this work is to better understand what the aerodynamic interference effects on a conventional airship are, and how they affect the vehicle stability. This allows understanding the flow dynamics around the hull and its effects on the tail, providing better guidance for similar aircraft design and development, apart from the academic contribution to the LTA community. The specific X-tail aircraft is the focus, but will be compared to other typical configurations.

Notwithstanding the importance of the main objective, many other secondary, but equally important, objectives must be accomplished. These secondary objectives are the main steps in order to effectively achieve the proposed goal; their fulfillment characterizes the needed knowledge and technology. The presentation of the secondary objectives of this work is made here in order to bring the reader the author's "mental milestones schedule", which describes the path for the aimed success. The following list contains the most relevant, with a brief explanation of each one:

a) Research review: review the available papers and studies on aerodynamic and stability modeling of airships, selecting the most relevant for this work.

b) Theoretical reference: review the theory involving mainly flight dynamics and stability of airships, besides the basic aerodynamic theory, in order to build a suitable theoretical framework to be applied along this work.

c) Parameters introduction: propose some parameters for measurement of airships stability.

d) Problem comprehension: to understand how the flow over the airship hull behaves, what are the main aerodynamic structures, and how they affect the tail incoming flow, so their effect on stability can be better understood as well.

e) Wind tunnel similitude proposal: based on the available knowledge and on the author’s previous experience, develop a procedure for simulating efficiently large Reynolds Number (*Re* > 1.0E+08) wind tunnel tests, considering the scalability problems and the need for similarity assurance.

f) Experimental analysis: run a series of wind tunnel tests (static and dynamic), gathering quantitative and qualitative data in order to evaluate the airship characteristics.

g) Discussion: present the obtained results, and discuss the package of information, describing the main aerodynamic characteristics and their interference effects on airship stability.

h) Continued study: to list and suggest possible future studies and investigations based on the results of this work.

2 LITERATURE REVIEW

2 LITERATURE REVIEW

This work has as main proposal to contribute to the evolution of the knowledge of the LTA technologies. In order to achieve this objective, and propitiate advances in this field, it is advisable, and also useful, to firstly know what is already known and researched by other people (VIANNA, 2001). This way, this review chapter is considered indispensable for knowing and trimming the boundaries around the investigated question, providing the real contribution that can be given by the results of this work to the LTA community. Knowing the current scenario of the studied issue supports the development of new theories, and allows one to identify what were well succeeded approaches during research of a specific topic, and the most important: identify topics not investigated or well understood yet. This last information is very precious, and leads to works like this, which aim to introduce new ideas and concepts, looking for technology improvements. So, before really starting this work, related topics were reviewed, looking for the necessary information to technically guide its development. The main subjects and themes were studied using mainly reference books and papers. Some graduation works were also investigated, which added lots of information to the repository. This review has the main objective of gathering information about what is already known, and done. This accelerates the learning curve, providing consolidated information; guide the work towards new investigations, since the previous path is known. This also leads to a more innovative investigation, looking at new aspects, avoiding *reinventing the wheel*.

2.1 AIRSHIP TECHNOLOGY: AN INTRODUCTION

It would be no surprise to hear that airships are old fashion machines, not really efficient, making them not compatible with the increasing need for highly rentable craft for different applications. However, this is a fallacy; indeed airships have been discussed and investigated in the recent years for a wide variety of jobs. A clear proof of that is the rising number of companies around the world investigating LTA technologies for logistics, defense, surveillance, etc. The new technologies available in materials, propulsion, energy storage and design itself, put the LTA vehicles back on the table for discussion. Also as a booster for this rebirth, the search for “greener solutions” in transportation, which airships can easily provide, is a strong motive for the new airships. These can be designed really optimized and in a shorter time when compared to other periods (STOCKBRIDGE, CERUTI and MARZOCCA, 2012), making them even more profitable. Besides their history, which has already been briefly discussed in section 1.1, it is necessary to better understand how airships do operate, what are the main characteristics and traditional constructions.

2.1.1 Aerostatics

As mentioned above, the airships are classed as aerostats, and common airplanes are aerodynes, and as such (LTAV) the main difference is the means of producing lift. While the common fixed- or rotary-wing aircraft generate lift using aerodynamic surfaces combined with inflow velocity, the LTA aircraft count on their volume, and the consequent buoyancy force generated by the surrounding fluid.

Everything, also everyone, immersed in a fluid receives the action of an upward force equal to the weight of the dislocated volume (the volume of the immersed body) – this is the famous Archimedes' Principle. The great differential here is that, while a common airplane, filled with common air, has a greater density than the atmospheric air, and not a large volume, the airships are filled with thousands cubic meters of lifting gases, whose density is lower than air. This generates a net force, the airship lift.

As the net buoyancy force is generated, the airship lift is equal to its weight; the airship stays "floating". This means that LTAVs generate their lift (or the greatest amount) from aerostatics, and not from aerodynamic principles. This way, since it is not required velocity in other to sustain the aircraft in the air, the required power is much smaller, and must only provide forward thrust for navigation. Aside from consuming less fuel, smaller engines produce less noise, vibration and turbulence to the flight and to the structure itself. This way of operating is one of the advantages that conventional airships have over common cargo aircraft: huge engines are not needed; they keep themselves "floating" in air. The required power and fuel are a consequence of cruising velocity and performance parameters related to operation. Usually conventional airships have an ellipsoidal axisymmetric shape, aiming at lowering the drag profile during the cruise, leading to even smaller engines.

Theoretically, this is achievable only in a very specific moment of the flight, and this one of the LTAV peculiarities. During operation, the airship, for example, burns fuel, which reduces its weight, while the buoyancy is still the same. This unbalanced condition is called *lightness*, and requires the generation of lift downwards for *equilibrium*. For this reason, when there is no technology in order to control the lift (recovering weight techniques), the airship would be better to start its operation in *heaviness*. In this condition, the aircraft has more weight than it can generate from aerostatic lift (its actual weight is above the static buoyancy), and must operate similarly to an aerodyne, producing aerodynamic lift, running and pulling the nose up, or vectoring thrusters upwards. The heaviness value is usually the total fuel weight, making it possible to land back in equilibrium or with a slight heaviness. At the end of the mission the aircraft may enter the opposite condition called lightness, when the buoyancy lift is greater than the total weight, and an additional force must be generated downwards.

Despite the usual small *lightness-heaviness* range, it is claimed that airships are not purely aerostats, but from essence a hybrid vehicle – this justifies the look for the hybrid concepts[2], an even redundant classification (KHOURY, 2012). Some new technology airships, the so called unconventional airships, base their operations on this lightness/heaviness question, generating enough buoyancy (via hull volume) for the empty weight and counting on aerodynamic lift (via hull shape) for the cargo weight. A deeper analysis of conventional and unconventional concepts peculiarities are not going to be discussed, since these are operational aspects which are not related to the main study proposal of this work. Although they have a completely different shape, the boundary layer influence over the tail – crucial for understanding the stability – is considered to have the same kind of nature, and for simplicity, this question is going to be investigated using a simple ellipsoidal body.

However, airships are still more economic and “greener” than aerodynes during operation, and the quoted advantages are still true. The available technology can help, as stated before, and the new structural alternatives for envelope and composites for rigid structures can become, among others, key contributors to increase the payload-weight ratio.

[2] The hybrid airships are a recent approach with the concept based on aerostatic and aerodynamic principles; an iconic item is the *Airlander*, designed by Hybrid Air Vehicles Ltd. (WESTCOTT, 2014). They combine three different sources of lift: buoyancy, aerodynamic lift and thrusters. Usually nearly half of the lift comes from aerodynamics, the self weight is supposed to be carried by the aerostatics, and hovering, landing and lift-off are assisted by the vectored thrusters (KORNIENKO, 2006).

2.1.2 Structural concepts

It is classical to divide the concepts in three different categories, classifying the hull structure as: non-rigid (blimp), semi-rigid or rigid. The choice is strategic, and must be made considering the “big picture”, and not only the structural design challenges, looking, for example, at the hull material price, availability and capacity (state-of-the-art) based on the expected loads.

The non-rigid airships, a.k.a. blimps, have usually a hull made of seamed and welded fabric gores, filled with gas at a higher pressure than atmospheric. The minimum permissible (operational) difference between the pressures is called *base pressure*, and is a key aspect during design. This value is responsible for maintaining the envelope shape and also contributes to its stiffness and integrity. Inside the envelope smaller fabric bags, called ballonets, are used in order to regulate the internal pressure due to temperature and external pressure (altitude changes) variation. The ballonets are filled with air, and some control valves are used either for inflating or deflating them. The rigid airships have internal structural frames (like the fuselage of a common airplane) which provide stiffness and shape to the envelope, besides withstanding the loads during flight, while out cover is only an aerodynamic matter. This was the traditional concept used on the Zeppelins. Internally, the gases are usually held inside multiple gasbags or fabric cells.

An intermediate concept is the semi-rigid; it does not have a framework that fully withstands the loads, but it does not rely only on the hull fabric. The most common construction is the combination of a basic inflated hull with higher pressure to which a long (slender) keel is attached, usually on the belly. This structure is going to be stressed by flying loads (transmitted by fins and envelope), relieving the envelope of the greater amount. The shape is maintained by the internal pressure against the stagnation pressure on the envelope, and the loads and the integrity are provided mainly by the keel stiffness in combination with the envelope also, for some load profiles. But not all semi-rigid are like this; a good example is the successor to the famous Goodyear airship GZ-20, the Zeppelin LZ N07-101, developed and built by Zeppelin with some Goodyear modifications (GOODYEAR BLIMP […], 2016). This airship, a semi-rigid concept, has a structure which is a combination of the overpressured envelope and three internal longerons connected by a sequence of triangular frames – internal frameworks. This internal rigid structure works just like the keels, withstanding the greatest amount of the loads but not providing the shape, and this is the main reason why it can be considered a semi-rigid concept as well. This technology makes this airship the most modern semi-rigid concept, and maybe among all other flying airships.

2.2 AIRSHIP TECHNOLOGY: SPECIFIC TOPICS

Nevertheless, besides the need for knowing the basics of airship operations, it is even more important to know about themes which directly affect the studied problem. The question of stability of aircraft in general is related to aerodynamics and, of course, to dynamics of flight. These are the main topics to be experimentally addressed in this work, and consequently to be researched previously. The main idea, however, does not involve designing a specific vehicle for an application, but evaluate its capability, its performance, and the main effects and behaviors in normal cruise flight, using a representative model. Therefore specific design techniques and procedures are not to be stressed. The only exception is the introduction to a new theory related to stability that is going to be proposed by this work, section 3.2.2.3.

The most relevant amount of papers on airships technical investigations are technical reports from the National Advisory Committee for Aeronautics (NACA) and the Royal Aeronautical Society (RAeS), dating back to early 1900s, 1920s and 1930s mostly (STOCKBRIDGE, CERUTI and MARZOCCA, 2012). Although old, they are very useful and instructive; massive information is provided on empirical and semi-empirical methods for weight estimates, structural design and aerodynamics as well. Apart from that, there is an abundance of experimental data on wind tunnels and also from full scale models tests.

Some more recent papers, dating from the 1990s until nowadays, provide some complementary information on aerodynamics and dynamics of flight. Some personal documents obtained by the author along the years at AdB, and from specialists with whom he had professional contact, also compose the studied and reviewed material. This guaranteed the necessary theoretical basis for guiding this work, as the main topics, aerodynamics and stability, were well covered.

2.3 AERODYNAMICS

The aerodynamic investigations were most focused on representative airship models and specific characteristics, instead of developing and providing modeling techniques. The wealth of empirical data on conventional airships – classical ellipsoidal, axisymmetric bodies of revolution – led the author to choose this type of airship for this work too. With more information available on it, there are also more data and methods to rely on and guide the development of new techniques.

2.3.1 Aerodynamic estimate models for airships

Even though the main objective here is not to design or develop the best aerodynamic shape for a classical airship, simplified aerodynamic models are considered to be very useful, providing boundary layer and forces estimates, for example. In this way, the relevant works – described below – were studied to a certain extent, and are better developed in the Theoretical Framework (Chapter 3).

Looking at the available researches, maybe the very first ones applied the simplest theory for aerodynamics, the potential flow (STOCKBRIDGE, CERUTI and MARZOCCA, 2012). Munk (1924) investigated the Navy's ZR-1, and derived the normal aerodynamic force distribution over the hull, modeling the body using the slender body assumption, adding factors of mass for ellipsoids based on the work conducted by Lamb (1918). One of the most important conclusions was that the airship hull has an unstable pitching moment when out of zero angle of attack reference. His work was used as a basis for further developments made by Allen and Perkins (1951), and by Hopkins (1951). Both proposed methods in order to get more precise results, trying to take in account the cross flow drag, and calculate the transverse forces along the hull. But the most famous aerodynamic model related to airships was developed by Jones and DeLaurier (1983), based on a semi-empirical approach, dividing the airship into two aerodynamic regions: hull (from the nose to the point where the fins first intersect the envelope) and the tail (fins and envelope are evaluated together). Although it was a foundation for others, since the method of Jones and DeLaurier (1983) does not provide useful information for this work, it is not going to be scrutinized.

More recently, in 2009, a series of studies conducted inside the Shangai Jiatong University aiming at the modeling of Stratosphere Airship proposed a combined approach for airship aerodynamics prediction (WANG, 2009). The model divides the airship in body and fins, very similar to the Jones and DeLaurier (1983) first approach, and for each of them composes the final aerodynamics by combining linear and nonlinear models. For the hull, Munk's airship theory (linear) is applied together with Allen's viscous crossflow theory (nonlinear). In the case of the fins, the linear aerodynamics is calculated based on a common panel methods complemented by the Polhamus-Lamar's suction analogy method (nonlinear) (WANG, 2009). Interference effects are taken into account by modeling the vortexes of the airship hull. The model was shown to be very useful and could efficiently estimate the aerodynamics of airships when compared to experimental results, using as reference the geometry of the LOTTE airship, a reference slender body of revolution and the U.S.S. "Akron" airship. These results showed that it is possible to estimate/predict with certain accuracy the aerodynamics of a conventional airship shape, even considering the tail in the calculations. However, the unique interference effect considered is a theoretically generated vortex coming from the hull, and not the boundary layer influence, as this work proposes.

As previously stated, there was not much development on aerodynamic modeling for airships, and this is one of the main reasons why the experimental approach was chosen for this work (Chapter 4). However, usually, for the very first approach some model is necessary. Besides some analytical technique (Chapter 3), another strategy for these estimates is the usage of computational fluid dynamics techniques. Simulating the aerodynamics of airships using softwares, such as ANSYS Fluent™, Star-CCM™ and others, was also theme of investigation. This strategy can save time and money when compared to experimental approaches. An effort was then also put on computational methods for predicting the aerodynamics of airships, and specially the boundary layer development.

The great questions are the challenges involved in correctly modeling the flow turbulence and what is the most advisable model to be used. The nature of the airship flow is supposed to be well modeled by LES (Large Eddy Simulation), which effectively removes the small-scale structures from the numerical solution, decreasing computational time by averaging some regions (SAGAUT, 2005). It is supposed that really small scales are not really relevant for airships investigations due the large Reynolds number, the unusual thick boundary layer and the simple lifting surfaces. Good results in terms of the qualitative structures – primary and secondary vortices in the aft region – expected to be found were obtained using *Large Eddy Simulation*, but with a multivariational approach. This was proven by El

Omari (2004) when three different LES turbulence models were compared, and all could predict the longitudinal vortex shedding expected for the wake, and one of them, the Variational Multiscale LES, could predict the vertical flow structure observed in experiments as well. A closer approach to the author's need and reality is the usage of one of the commercial packages cited above. The application of CFD was also proven to be useful for estimates about the resultant virtual mass for airships (WANG, 2009).

2.3.2 Wind tunnel experiments

There are three main technical approaches for engineering design: analytical, experimental, and given the new technologies of the last decades, the computational has also powerfully risen. Generally, the analytical way does not model precisely the systems, since it cannot deal with very complex problems, and usually leads to overestimated designs due to the needed simplifications. The computational approach, on the other hand, manages to design and analyze very complex and complete systems, providing deeply detailed information and opportunities of improvement. However, it costs a little more than the analytical, and requires a specific knowledge of the softwares employed in order to set them up correctly, and model the problems according to reality. It means that commonly some numbers and coefficients are *pulled out of a hat*, usually coming from what is claimed to be experience or good practices. The experimental approach is maybe the most expensive one, but probably the most correct also, having the capacity of providing precise information on the approximations made through the analytical approach.

In aeronautics, the most common experiments are flight tests campaigns, scale prototypes flight, wind tunnel experiments, drop tests, iron birds, etc. Each of them has a particular objective, and therefore is usually applied in a determined moment of the design cycle, and has an associated cost. When discussing about aerodynamic evaluations during the design, up to the preliminary phase, the most common approach is wind tunnel testing. In this phase, shape and proportions are already known – also proposals of change for comparison – and can be analyzed through simulating inside a wind tunnel the possible environmental and operational conditions. By means of such a test, valuable information can be obtained: overall lift, drag, moments, control forces and moments, trimming curves, stability characteristics, pressure distributions, wake characteristics, among others.

With the rise of airships in the beginning of the 1900s, an understanding and comprehension of the phenomena involved in their operation and the expected behaviors were crucial for the development of the technology. In this sense, many studies and research works on airships aerodynamics were conducted. There was a need for interpreting correctly the available data on full scale tests, mainly due to drag prediction. It was also necessary to lower the costs by means of cheaper and more versatile ways of studying them – for example, wind tunnel experiments – since the available theories were not precise. Even the classical boundary layer theory and the Reynolds studies date back to early 1900s, some years before the golden days of the Zeppelins.

After that, and taking advantage of the developed instrumentation, for full scale tests too, it was possible to gather some data on the topic. Though there were several limitations, wind tunnel experiments provided much useful information on airships and their characteristics, also considering the appendages and other protuberances – impossible to model without specific studies or the nowadays popular CFD techniques. A key player in this field was the National Advisory Committee for Aeronautics (NACA) form the USA, which led several tests on famous aircraft like ZRS-4 U.S.S. Akron and XZS2G-1. The main topics were overall forces (mainly drag), pressure distribution over the hull and tail, and boundary layer investigations (profile, development, transition, etc) as well.

There is extensive work on British airships regarding aerodynamic investigation. Pannel with other researchers published some important results on full scale tests on the R-26 (PANNEL and FRAZER, 1920), R-29 (PANNEL and BELL, 1920) and R-33 (PANNEL and FRAZER, 1919), looking for the relation between turn radius and rudder deflection, also providing drag forces. The results were not precise, because of the limited available technology at that time. More recently, during the 1980s, some similar studies were made using the Skyship-500 (JEX and GELHAUSEN, 1987), providing more accurate results. The models R-101 (JONES and BELL, 1926), R-29 (JONES, WILLIAMS and BELL, 1920) and L33 (PANNEL and JONES, 1917), a German model, were studied by Jones at the Aeronautical Research Committee (ARC). Their results and methods yielded reference papers on aerodynamics of airships, very precious to this work.

Some remarkable works on airships were carried out in the 1930s by Abbott and Freeman, who completely investigated the 1/40 scale model of U.S.S. Akron airship, obtaining lift, drag, pitching moment coefficients, besides some more elaborated studies on boundary layer (development, transition sensitiveness, profile). Freeman studied and measured lots of different aerodynamic characteristics, from normal forces acting on the model (FREEMAN, 1932a), going into smaller structures, investigating the flow inside the boundary layer (FREEMAN, 1932b), up to the specific investigation of the pressure distribution along the hull and the fins (FREEMAN, 1936). These publications meet perfectly the basics of the experimental procedures needed to evaluate the effects to be addressed by this work.

Complementarily, McHugh (1937) expanded the range of Freeman's work, providing even more information on the pressure distribution on the fins, investigating its behavior at large angles of attack, which can mean, for example, intense cross gusts. It is interesting to note that the aerodynamic studies, besides always looking at drag characteristics due to power and fuel consumption requirements, were also concerned, like this work is, about the flow influence on the dynamics, stability and controllability of airships. This is proven by the interest of investigating the tail pressure distribution, large angle of attack situations, and also the maneuverability that the fins can provide, represented by the achievable turn rate, as mentioned above. A great contribution came also from Gomes (1990); for his PhD thesis, besides the classical static studies, he made dynamic and response to turbulence tests with his models – a light weight model was manufactured for this purpose.

The attractiveness of the boundary layer studies was strong because of its key influence on the drag results – the most valuable results obtained from wind tunnels. Cerreta (1957) was responsible for proposing a means of reducing drag by a boundary layer controlled airship, which would suck the boundary layer on the aft portion of the hull, reducing the drag. The studies could provide an experimental verification of the theoretical expected drag reduction. Several different tail cones were tested, with different gaps –size and shape – and suction rates. The main result pointed to the existence of a *Re* thereupon suction to attach the flow on the model upstream flow is necessary in order to decrease drag. Beneath the determined value, no suction was necessary for the attachment, and therefore no advantage was guaranteed. Another conclusion led to the fact that the greater the *Re*, the greater the suction rate and the gap size should be in order to reduce drag.

Another relevant work was also related to this same field of study. Using a 1/20 scale airship model (inverted Y tail arrangement), McLemore (1962) conducted tests at the Langley Research Center, in the full-scale tunnel, to determine the characteristics of stern-mounted propellers on the airship. Airship forces and moments were also measured, besides the relevant study on propeller efficiency. Complementarily, hull boundary layer and wake characteristics were measured. The results showed that the assembly was more efficient than conventional options, having a small effect on the model aerodynamics. Most interesting for this work were the boundary layer measurements, captured by rakes, addressed in section 3.1.1.1.

More was done regarding airships. Concerning new configurations, Andreson and Flikinger Jr. tested different tail cones (C, X, Y and H types) analyzing longitudinal stability, longitudinal control and also hinge moments (ANDERSON and FLICKINGER, 1954). All configurations provided almost the same stability level for the pitch range (-15° to +15°) investigated. All of them were also capable of trimming the aircraft model neglecting moments due to thrust and buoyancy center (BC) and center of gravity (CG) misalignment – the H-tail required a 20° deflection, while the Y required only half, 10°. Regarding drag, the H-tail had around 35% more drag than the other for zero yaw. Rizzo (1924) also developed important work on configurations, analyzing L-33 airship characteristics changes due to modified tail arrangements. His tests were carried out at 40 mph. in the wind tunnel of the Massachusetts Institute of Technology, on a 1/153 scale model with changeable tails. Some of the results were very useful for this work in preparing the tests proposals, and are technically explained in section 3.2.2.2.

Another interesting aerodynamic study was conducted by Zahm, Smith and HILL (1923), when they investigated the influence on drag of adding straight middle bodies (cylinders) to a bare hull, varying their length from zero up to 9.5 diameters. This was very interesting because usually, during design phases, some increase in volume is necessary to compensate for an increase in weight or wrong weight estimates, but there is no budget or time for manufacturing a whole scaled up envelope again. So, knowing the consequences of inserting such cylindrical parts in the middle of the envelope contributes to work with this solution. According to Zahm, Smith and HILL (1923):

> Increasing the middle body from 1 up to 3 diameters increases the drag linearly, and is very near to what would be expected by only increasing the skin friction drag due to the increase in area. Beyond 3 diameters, the rate of drag increasing decreases, with two possible causes: the lessening of skin

friction with length and the changes in the pressure distribution at the stern. The insertion of a very short middle body would benefit more the aircraft by increasing its volume than it would spoil it by increasing the resistance.

2.3.2.1 Most recent and relevant works

More recently, the research group FOGL, founded in 1997, based at the University of Stuttgart, Germany, conducted several experimental investigations on the remotely controlled solar powered airship LOTTE, chosen as a reference configuration to perform scientific investigations in the fields of aerodynamics, flight mechanics and control, aeroelasticity, structural design and solar propulsion systems. The aircraft is 16 meters long, displacing 109 m^3 of air, being able to carry up to 15 kg of payload.

Inside the Institute for Aerodynamics and Gas Dynamics, wind tunnel and water tunnel tests were performed with different models of the airship. The group applied specific technologies for building and investigating, even in-flight experiments – intended to verify extrapolation of small scale wind-tunnel tests to full-size Reynolds number (LUTZ et al, 2002). The main objectives of the wind tunnel experiments comprised investigating in detail the three-dimensional boundary layer development, especially the shear layer separation line. Some probing was also carried out regarding hull-fin interference, and pressure distribution, followed by integral forces and moments measurements.

In 2009, with the purpose of verifying core technologies of stratosphere airships, a remote and autonomous controlled fuel-cell-powered airship, the ZHIYUAN-1, was manufactures at the School of Aeronautics and Astronautics of Shanghai Jiao Tong University, in China (WANG, 2009). The airship, a classical shape with “+” fins arrangement, served as reference configuration for theoretical investigations and as a flying testbed. It was possible to conduct studies on aerodynamics, flight mechanics and control, aeroelasticity and structures, besides propulsion technology as well. As already stated, for the aerodynamic configuration, the study of the interfaces is primordial. Another motivation was the need for validating CFD and panel-methods results and settings for such low speed, but high Reynolds number, the inherent flow condition of airships.

2.4 FLIGHT MECHANICS

Although detailed flight mechanics and stability are not the main focus of this work, some research was conducted in this sense. This provided information on relevant works, approaches and techniques for assessing stability. With such knowledge there would be a good guidance base for, in a simplified manner, develop a way of predicting airship stability in a qualitative manner.

Alongside with aerodynamics investigations, many studies were conducted on airship flight dynamics, mainly focused on static stability evaluation. It is very difficult to dissociate works from section 2.3 from those relevant for this section. The great majority was based on simplified theoretical approaches, similar to those applied for regular fixed-wing aircraft, or wind tunnel testing. It is interesting to highlight that litlle has been found regarding dynamic tests. For static stability, the most common approach was based on pitching and yawing moments results from steady wind tunnel tests. For dynamic stability, linearized and simplified equations were the main tools for investigation, using the derivatives obtained from testing. More recently, with the technological increasing trends, researchers all over the world are working on flight control system for autonomous airships, mainly for stratospherical types. Nevertheless, these are topics that, despite the high value, do not apply to this work, and are not going to be evaluated.

2.4.1 Flight dynamics: stability analyzes

All the already mentioned works regarding wind tunnel testing were also relevant on airships stability development. Despite the main objective of providing information on drag and general aerodynamics, even indirectly those works provided lots of information on real airships (using models) static stability. Iconic works on force and moment measurements, such as those with the AKRON 1/40 scale model conducted by Freeman (1932a and 1932b) and Abbott (1931) provided relevant data on C_M and aerodynamic derivatives, which are essential inputs for any flight mechanics evaluation. Higgins (1927) also contributed with forces and moment measurements, helping to build a static stability database for airships. Supporting very initial works on dynamics, reference works like the determination of the inertia factor for ellipsoids, made by Tuckerman (1926) and Lamb (1928), and the pitching estimates by Hopkins (1951) also deserve attention.

More related to studies that affect stability directly, the campaigns conducted by Anderson and Flickinger Jr. (1954), as already cited, showed airship stability behaviors for different tail arrangements. Also Rizzo (1924) may be classified as a very influent and relevant in the stability area. After presenting a series of theoretical evaluation of airships static stability, particularly assessing longitudinal and directional stabilities, but also critical speed and reversal of controls problem, Rizzo addressed, through wind tunnel tests of a 1/153 scale model of the L-33, the effects of tail area, aspect ratio, planform and thickness on the final airship characteristics. Through his works, he showed that, as expected, increase in area is advantageous, but specially for horizontal stabilizers. Also, he found that increase in tail aspect ratio was recommended, and that a rectangular planform would provide much better results than the original long streamlined tails. Similarly, he also showed that thinner airfoil sections provided better results, at least regarding aerodynamic effects.

In the topic of static stability, and fins influence on final characteristics, the works carried out at the IAG, mainly those performed by Lutz et al (1998, 2002, 2005), are also relevant. Based on a real airship design, the LOTTE, by means of different approaches, making sure the obtained results were adequate, the studies confirmed unstable regions for small AoAs, like expected, and were able to quantify them.

Another invaluable work in the area of airship stability, but this time as a whole, and maybe to be considered the “bible” on airship stability and control is the work conducted by Gomes (1990), also mentioned above for aerodynamics. Continuously referenced when the topic is airship flight dynamics, this work goes from simple aerodynamic characterizations, up to derivatives determination and application on equations of motion, defining the stability modes for longitudinal and lateral stability. His works on the dynamic stability of the YEZ-2A airship of the U.S. Navy provided such a great density of reliable data, that they are still used as references for validation of new approaches and proposals on the topic. A good example is a recent work carried out in 2001 in Korea, at the KARI (Korea Aerospace Research Center). In this work, Lee (2001) evaluates static and dynamic stability through CFD and linearized equations of motion for two fins configurations, different in *AR*, of a 4000 m^3 airship. The results are compared to those published by Gomes (1990) in order to assess their reliability. In a similar manner, Cook, Lipscombe and Goineau (2000), one year before, also basing his works on Gomes (1990) for some items, described and compared different analyses techniques that led to approximate models for non-rigid airships stability modes. In his work, he compared the approximate results for the modes with the actual airship modes.

These and other works are punctually mentioned and used along section 3.2, according to the need. As explained above, several works on this topic could be here mentioned, but the stability question in general is used in a very restrict manner in this work, and therefore is not worth going further.

3 THEORETICAL FRAMEWORK

3 THEORETICAL FRAMEWORK

In this chapter a more technical literature review is made, introducing some topics considered to be essential for the work evolution and conclusion. This chapter has a lower historical track importance than the previous (Literature Review), and addresses theoretical and practical aspects of aerodynamics and flight dynamics.

The main objective is to provide a technical basement for the whole work process, since the wind tunnel test campaign planning (types of tests, “where to look at”, expected flow structures, etc.) and model manufacturing and preparation, up to the data evaluation and the technical solid knowledge necessary to state conclusions and even propose next steps for further research.

Here are presented the basics of airship aerodynamics and some estimate techniques, flow patterns and trends expected for conventional types. Moreover the whole wind tunnel process is discussed based on previous works, discussing model manufacturing techniques, the similitude question, and the means of aerodynamic investigations using wind tunnels. Besides that the basics of airships flight dynamics is presented and the peculiarities are discussed. The work also contributes to the introduction, in this chapter, of some new theoretical approaches for stability evaluation of LTAV.

3.1 AERODYNAMICS OF AIRSHIPS

Airships in general are very slow when compared to fixed- and rotary-wing aircraft. The fastest ones fly around 0.1 of Mach Number (*Ma*), which means approximately 30-34 m/s, 100-120 km/h (KHOURY, 2012). This is really valuable information, as speed is one of the most important characteristics while studying aerodynamics, since there are very specific aerodynamic characteristics for each kind of flow.

The airship velocity range is a very interesting and accessible one; for being at a very low Mach number regime, effects like shock and expansion waves do not figurate, and the aerodynamic logic of the flow is easily understandable. Most flow behaviors are well known and the experiments do not require very sophisticated equipment. However, there is another equally important parameter in aerodynamic investigations, the Reynolds number (*Re*). Just like the *Ma*, *Re* is essential in order to understand the flow, and brings some trends to the overall behavior, like turbulence level, separation characteristics and special elements, like bubbles and boundary layer reattachments.

For *Re*, airships belong to a quite singular class of aircraft; while fast aircraft like commercial jets have *Re* in the order of 1.0E+06, airships can go easily up to 1.0E+08. This occurs specifically due to their size; given the need for a large air displacement, which means more buoyancy force, the dimensions also rise, increasing the *Re*, and changing the flow characteristics. In such a large *Re*, airships essentially develop almost fully turbulent boundary layers, and on normal cruise flight develop most of their drag as skin friction drag, a result of the enormous hull wetted area. For turbulent boundary layer development it is expected to have the flow attached up to the tail when considering an axial incoming flow (LUTZ et al, 1998). Although it is not expected for full scale bodies, some laminar regions probably will appear for typical airship hull as the *Re* decreases. The smaller the *Re*, the greater the dead-air separation region in the stern portion of the aircraft, which of course leads to additional pressure drag.

3.1.1 The basics of conventional airship aerodynamics

Similarly to the aerodynamic studies for aerodynes, it is usual to study aerodynamic forces and moments in airships by means of non-dimensional numbers, which allow easier comparison between different concepts and shapes. There is however a slight difference for aerostats in general. The so called reference area can be chosen from different sorts of values: the envelope surface area (less usual), the aircraft maximum longitudinal cross-section or related to the aircraft displacement volume (the most common approach) (BURGESS, 2004). Indeed, the reference area can be whatever number one wants, it is only required to check and be sure that all calculations use the same reference; the volumetric area – (Displaced Volume)$^{2/3}$ – is the most used, as the greater amount of lift generated by conventional airships is static lift, i.e. buoyancy force, proportional to the volume of atmospheric air displaced. In this way, the aerodynamic coefficients (lift, drag and pitching moment) are the following:

$$C_L = \frac{L}{\frac{1}{2} \cdot \rho \cdot \vartheta^2 \cdot V^{\frac{2}{3}}}$$

Equation 1 – Lift coefficient with volumetric area.

$$C_D = \frac{D}{\frac{1}{2} \cdot \rho \cdot \vartheta^2 \cdot V^{\frac{2}{3}}}$$

Equation 2 – Drag coefficient with volumetric area.

$$C_M = \frac{M}{\frac{1}{2} \cdot \rho \cdot \vartheta^2 \cdot V^{\frac{2}{3}} \cdot \mathbf{L}}$$

Equation 3 – Moment coefficient with volumetric area.

The most important aerodynamic characteristic for airships is drag. Given their large size, and the huge wetted area, the drag is an issue – not a privilege of airships – to which attention must be paid. A small increase in drag reduces endurance and range, or increases the needed fuel volume, reducing the available useful load (sum of payload, ballast, fuel, passengers, among others, besides bare structures and systems – that means literally the available weight to be used). Drag also influences directly on the required power, which limits once again several weight characteristics and affects the performance. In this sense, usually a lot of effort is put on studying airship drag, or it has to be simply overestimated, what leads to a less efficient aircraft.

Crucial for predicting drag is the understanding of boundary layer development. Studying the boundary layer requires an investigation of the pressure distribution over the body, and also a look at the external regime and at the surface roughness level. Normally, as for forces and moments, the pressure is investigated in comparison to a pressure of reference – usually the atmospheric pressure, also leading to a non-dimensional number, the well known pressure coefficient, C_P:

$$C_P = \frac{P - P_\infty}{\frac{1}{2} \cdot \rho \cdot \vartheta^2}$$

Equation 4 – Pressure coefficient.

To better understand the pressure distribution, one must know that the hulls of conventional airships are ellipsoidal or compounded curvatures (ellipsoidal, parabolic and hyperbolical curves) bodies of revolution. Usually in a range of slenderness ratio (Equation 5) of 3.5 to 8 (KHOURY, 2012), their geometry, and consequently their aerodynamic behavior, is very similar among all types.

$$AR = \frac{\mathbf{L}}{\mathbf{D_{max}}}$$

Equation 5 – Aspect (fineness or slenderness) ratio definition.

In other words, their length is 3.5 to 8 times their maximum diameter – for typical non-rigid aircraft, the case of this work, the *AR* is around 4, which is claimed to be the shape for lowest drag (BURGESS, 2004). For these ellipsoidal bodies, the pressure has a very steep distribution after the bow, reaching the atmospheric pressure around 3% to 5% of the hull's total length (BURGESS, 2004).

After this front region, the gradient tends to decrease, varying very little, staying around zero up to a region near to the stern. Along this section in between, some pressure increase is usually seen when long regions of straight/constant section exist. However, up to about 90% of the hull's total length the pressure is below the atmospheric. After that, at the stern, it tends once to again to increase, becoming sometimes higher than the atmospheric, which means a positive pressure coefficient (BURGESS, 2004).

In spite of this behavior, however, the boundary layer over airships is known to be turbulent. The main reasons for that are linked to the inherent turbulence of atmospheric air, as airships usually fly too close to ground, and therefore within the Earth's boundary layer, and the operational *Re*, which is rather large, inducing turbulent flow to exist. In addition, as discussed in the following sections, the hull surface roughness and the appendages at the bow region also force the boundary layer to transition from laminar to turbulent. Usually for ellipsoidal bodies, such as airships hulls, these flow and geometrical characteristics induce the flow to transition from laminar to turbulent, and the area where the boundary layer can be laminar is then restricted to somewhere around the nose, not further than that range.

As an example, the results of the investigations made with a model of R-33, and curve showing the typical distribution of pressure and velocity over the hull of a conventional airship with $AR \approx 5$ are illustrated in Figure 3.

Figure 3 - Pressure distributions over the R33 Airship hull (left) and the hull of typical conventional airship with $AR \approx 5$ (right).

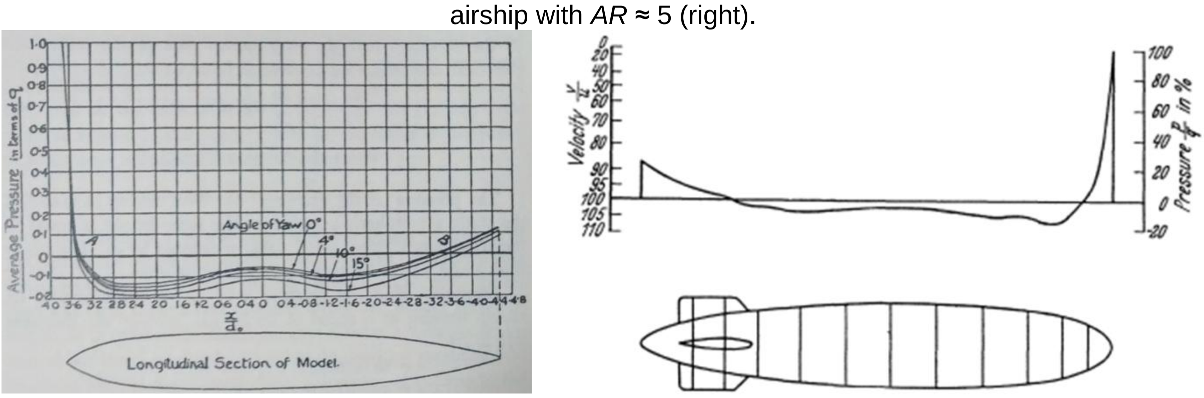

Source: Burgess (2004). Source: Durand (1936).

Nevertheless, after adding gondola and empennage to the bare hull, the expected pressure distribution changes. The presence of the gondola tends to increase the pressure ahead (upstream) of it (Figure 4), increasing however a little the velocity after it in comparison with the bare hull (GOMES[3], 1989 apud KHOURY, 2012). This generates a very small pressure difference between upper and lower side of the body, generating lift, but also increasing drag, as obviously expected. A good example of that was verified in using the Sentinel 5000 airship prototype scale experiments in a wind tunnel (KHOURY, 2012).

Figure 4 - Pressure distribution variation related to the gondola for Sentinel 5000 airship.

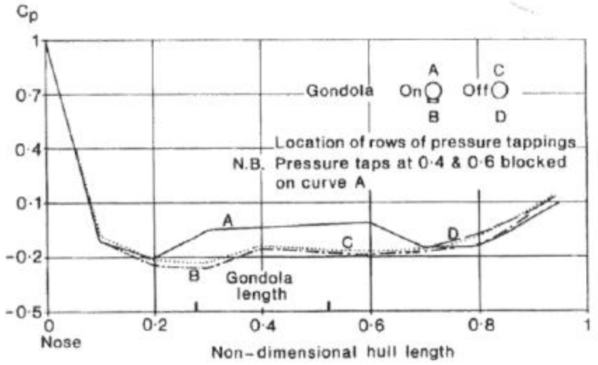

Source: Khoury (2012).

It is important to highlight that, in Figure 4, the graphical representation is mistaken: "A" refers to the pressure line along the hull lower side, whereas B is the top side, according to Khoury (2012). Still according to Khoury (2012), the two static tappings nearest to the gondola were blocked, and therefore the pressure over it is not precisely known.

In Figure 4, two configurations are shown: with and without the gondola. It is interesting to see that along the gondola length, just like for straight middle bodies in the hull, the pressure distribution is almost straight and a bit higher, but after that it becomes smaller than it is for the configuration without the gondola. Another interesting observation is the good agreement among the curves up to 70% of the total length, a little after the end of the gondola.

These effects are quite similar for the conventional shapes with gondolas, but without the tail. When the tail is added to the set, the pressure distribution is disturbed. This effect is more relevant around the stern, despite affecting the whole flow field. It is expected that also upstream of the tail the flow trend should change since for airships the flow is subsonic, and the information can be spread in all directions in time (aerodynamic elliptical problem). The presence of the fins increases the velocity over the hull, increasing the suction (negative pressure) in comparison

[3] GOMES, S.B.V. *Task 2 Report: Measurement of forces and moments, pressure distribution and hinge moments on a 1/75 scale model of the Sentinel 5000 airship*. Cranfield Instutute of Technology. CoA Report No. 8903,

with the configuration without them, increasing obviously the lift and drag forces as well. Once again, Gomes (1989 apud Khoury, 2012) presented some measured data comparing the configurations with and without the fins placed, showing that the expected behavior does occur, by means of monitoring the pressure distribution over the hull along pressure lines in between the fins.

3.1.1.1 Boundary layer estimates for airships

As already stated, the study of boundary layer growth along the longitudinal axis, and its effective thickness at the stern region, around the fins, are very important for the evolution, and consequent success of this work, by analyzing the aerodynamic interference effects between hull and tail. The boundary layer is a proportionally thin layer of fluid attached to a body immersed in the same fluid. This layer is strongly dominated by viscous effects, such as friction and vorticity. The velocity inside the boundary layer grows asymptotically from zero at the wall station up to the outer flow velocity. The extent perpendicular to the body wall along which the fluid layer velocities increase up to the outer flow velocity is called boundary layer thickness. This dimension, however, is very difficult to be clearly defined, especially because of this asymptotical characteristic.

The boundary layer thickness, according to Schlichting and Gersten (2006), is then usually defined as distance across the boundary layer velocity profile, normal to the wall, where the boundary layer velocity *u* is $0.99U_\infty$ (local outer edge flow velocity). Therefore, it is represented by δ_{99}, once it is impossible to precisely define the point where the boundary layer becomes free stream flow. Nevertheless, considering aerodynamic modeling, this thickness definition is not very useful, because it is not precise in terms of flow. Other measures, similar to thickness, were then defined in order to support flow studies.

The displacement thickness, called δ_1, is the distance perpendicular to the wall necessary to move the surface outwards in order to have the same original mass flow rate considering local free stream by means of inviscid flow calculations. In practical terms, this is the geometrical modification (thickening) to be applied to the body shape so the inviscid solution is capable of reproducing the real solution (viscid). This definition simplifies a lot some flow prediction, and therefore is vastly applied, in place of δ_{99}. Another useful definition is the momentum thickness (δ_2). Similarly defined to δ_1, this is the distance by which the body surface in an inviscid flow must be displaced normal to it in order to experience the same reduction in momentum flux caused by the boundary layer presence in a real fluid. Directly translating it from German would lead to “Momentum loss thickness”; this is exactly what it measures: the amount of momentum lost by the flow due to the boundary layer presence. A third definition exists, the energy thickness, δ_3, which is very similar to δ_2, but refers to energy.

Knowing those measures is important to interpret changes in flow in terms of boundary layer changes. Since they are directly dependent on the boundary layer typical profile, and the boundary layer nature has strong influence on the velocity distribution above the wall, it is possible to guide evaluations based on them. The ratio between δ_1 and δ_2 is called shape factor and is represented by *H*. A quick rule shows that the stronger the adverse pressure gradient along a surface, the greater the value of *H* will be. This is relevant information, because it helps assessing and predicting boundary layer transition into turbulent flow. Complementarily, since the boundary layer is a region around the body where flow velocity is smaller than the outer velocity, flow momentum flux is lost and friction occurs, everything that is contained inside this region is also subject to these reductions, both velocity and momentum.

Such physical phenomenon was very well captured in a wind tunnel, although for different purposes, by McLemore (1962). He was able by means of rakes to measure the boundary layer profile development from 90%**L** up to 104%**L** (wake). As predicted, he proved by physical observation that the layer thickness is really relevant dimension-wise: approximately 4%**L** @ 90%**L**, and increasing. The tests were conducted for 11.9E+06 < *Re* < 17.5E+06, an order of magnitude above the one achieved in this present work, which in theory reduces thickness.

Figure 5 - Variation of the boundary layer and wake flow characteristics at α = -0.5° with and without propeller 1 operating.

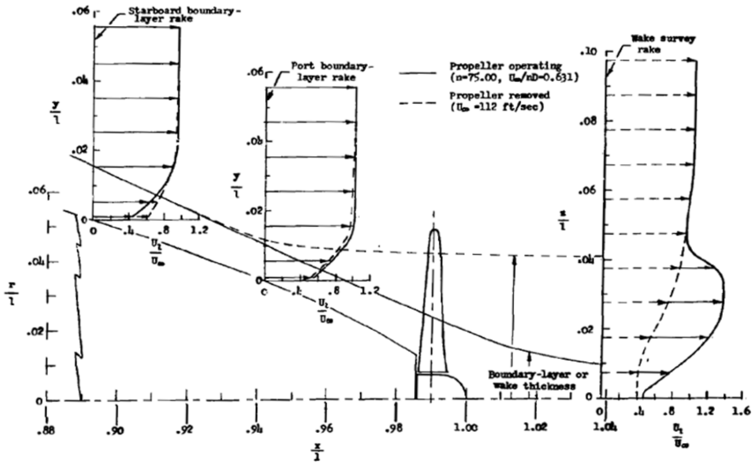

Source: McLemore (1962).

An extraordinary work conducted for the Office of Naval Research, led by Cornish, III and Boatwright (1960), provided extraordinary information on boundary layer development on airships. By means of flying an instrumented ZS2G-1 Airship, a report was published presenting analyses of the drag and boundary layer characteristics in full-scale. This work served as a reference for various subsequent contributions. It provided very good information for this work, and complements the above mentioned facts about fins immersed in low speed regions. The work also proposed some extrapolation for the wake development based on the measured boundary layers.

Figure 6 - Separation region on ZS2G-1 Airship straight and level flight.

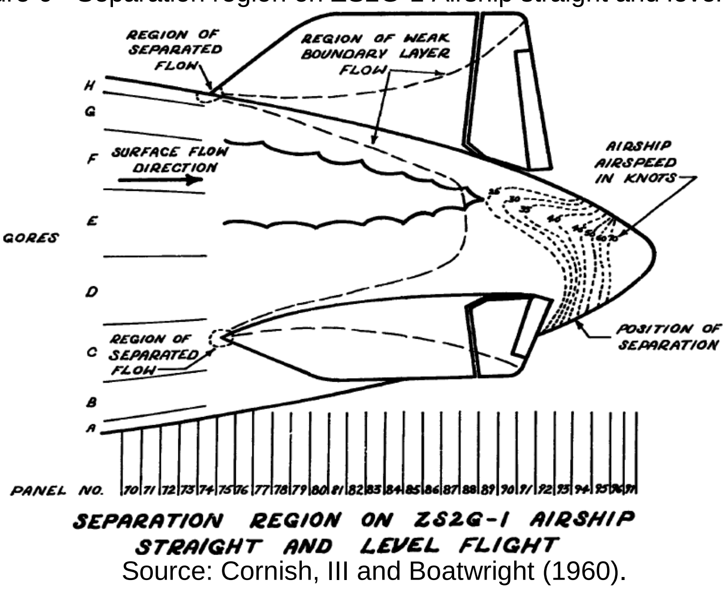

Source: Cornish, III and Boatwright (1960).

As can be seen, although for straight and level flight separation occurs far downstream on the hull surface, the fins leading edges induce flow separations, as also highlighted by Lutz and Funk (2005). Also the hull boundary layer is affected by such flow characteristics, and can locally increase.

Figure 7 - Momentum thickness in inches for the vertical fin of ZS2G-1 Airship @ 70 mph, and displacement thickness of hull boundary layer.

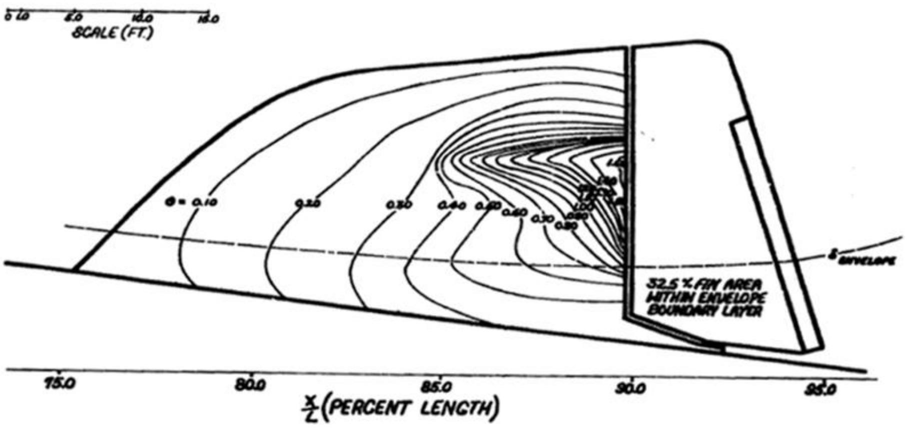

Source: Cornish, III and Boatwright (1960).

From the conducted investigations, Cornish, III and Boatwright (1960) concluded that more than 30% of the fin area was contained inside the hull boundary layer.

Figure 8 - Wake of ZS2G-1 extrapolated from boundary layer measurements.

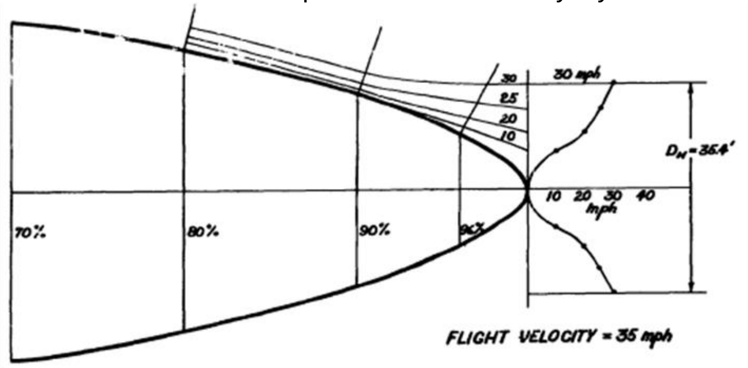

Source: Cornish, III and Boatwright (1960).

With this in mind, and given that the generated forces on an aerodynamic surface are proportional to the flow velocity (Equation 6), if the surface is totally, or even partially, contained in a region with lower air speeds, the generated force is consequently lower as well.

$$F = \frac{\rho \cdot \vartheta^2}{2} \cdot S \cdot C$$

Equation 6 - General aerodynamic force definition.

, where

F = aerodynamic force, [N]
ρ = fluid density, [kg/m³]
ϑ = flow velocity, [m/s]
S = reference area, [m²]
C = dimensionless coefficient, [-]

Imagining the fins flowfield, the fact of having a smaller force actuating for the stabilization and control of the airship, even if the flight speed is the expected one, makes it necessary to enlarge the surface. This occurs for the reason that the surface area out of the boundary layer must be bigger in order to be in the higher velocity fields, generating a higher force, guaranteeing the control and stabilization.

However, bigger surfaces result in more empty weight for the aircraft, which decreases the available weight for payload, and even affects the structural and aerodynamic designs in order to consider and adapt them to new and larger surfaces. Moreover, larger stabilizers have consequently larger control surfaces, which demand more powerful actuators, mainly when talking about airships, which have usually huge tailplanes.

Due to all of these reasons, it is expected that, in order to better understand the boundary layer thickness development and influence over the tail, one must know its natural behavior for a studied model. With the natural growth characteristics, a concept can be studied and investigated to solve this issue, providing useful information for the development of means of improving the controllability and stabilization of airships.

As quoted before, the understanding of boundary layer development is essential therefore to predict the pressure distribution and extract such information like it was done in the above paragraphs. An analytical boundary layer model was proposed by Hoerner (1965) considering the airship a body of revolution and based on the bare hull shape at zero angle of incidence to the flow. The model is very simple and considers two different equations – one before the maximum diameter and other after it – based on the distance from the bow and on the ratio between the local diameter and the maximum.

$$\mathrm{\delta_{99}(x)} = \begin{cases} 0.02 \cdot \mathrm{x}, & x < \mathrm{x_M} \\ 0.02 \cdot \mathrm{x} \cdot \dfrac{\mathbf{D_{máx}}}{\mathrm{d_x}}, & x \geq \mathrm{x_M} \end{cases}$$

Equation 7 – Boundary layer thickness estimate for ellipsoidal bodies at zero AoA. Adapted from Hoerner (1965).

, where

$\mathbf{x}$	= position measured along the longitudinal axis of the hull from the nose, [m]
$\mathrm{x_M}$	= position x of the maximum diameter, [m]
$\mathrm{\delta_{99}(x)}$	= boundary layer thickness at position x, [m]
$\frac{\mathrm{D_{max}}}{\mathrm{d_x}}$	= ratio between the maximum diameter and the diameter at position x, [-]

Although this model shows an increase in boundary layer past maximum diameter of bodies like airplane fuselages, it was applied to the airship hull model of this work. An illustration of the predicted boundary layer follows:

Figure 9 - Boundary layer based on Hoerner (1965) over the normalized ADB-3-30 model.

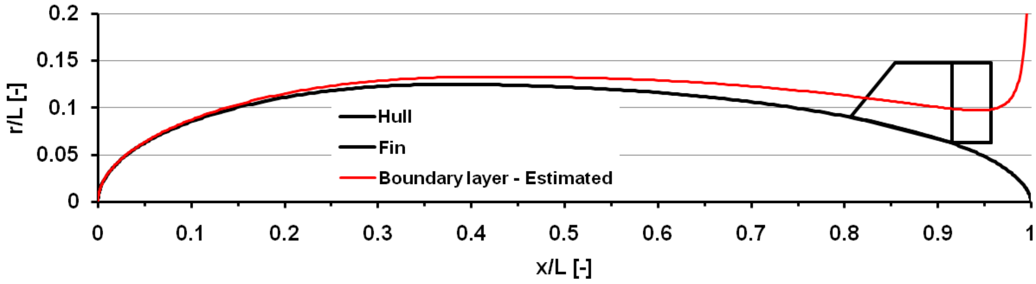

Source: Author (2018).

Figure 10 - Estimated boundary layer thickness along the normalized length of ADB-3-30 model based on Hoerner (1965).

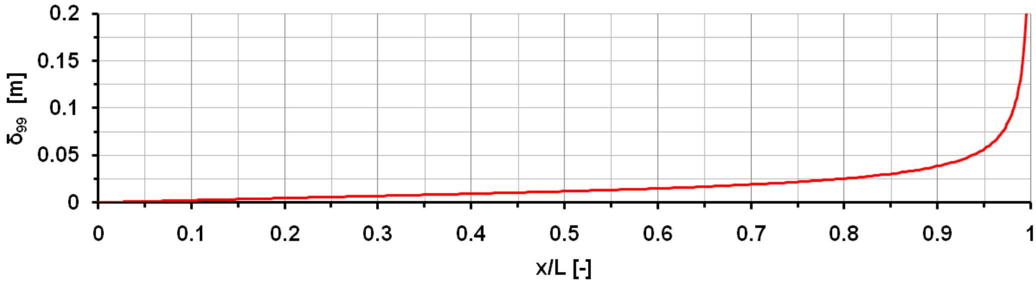

Source: Author (2018).

The developed boundary layer is supposed to be also axisymmetric, consequently of an annular form. This model however has some disadvantages since it does not predict the layer thickness for non-zero AoAs, and it does not consider the boundary layer detachment (boundary layer separation). Besides that, since it depends on the ratio between the diameters (local and maximum), at the stern region the thickness growth becomes exponential. Nevertheless, it is interesting to compare such a simple model with results observed during flow visualization (section 5.2.3.4).

Despite the fact that this prediction does not take into account the presence of the fins, assuming that it develops the way is shown in Figure 9, by a rough estimate one may say that the predicted boundary layer at AoA = 0° would shade approximately 48% and 60% of S0 and S1 FINs (section 5.2.4), respectively. Even though these are greater values, it is not far from what was observed by Cornish, III and Boatwright (1960), equivalent to 32.5% in area. Also, assuming that the exponential increase in thickness would not be held in a real fluid flow, it can be assumed that separation would occur nearly to that longitudinal station, which is around x = 95%**L**, right downstream from the FINs trailing edges.

It is important to emphasize that the aerodynamic behavior of an airship, as will be better addressed along this work, is highly dependent on three-dimensional vortical structures, strongly influenced by crossflow and mutual interferences of lifting surfaces (fins) on the lifting body (hull), and vice-versa. It is then extremely difficult to precisely describe all effects, and quantify them. Boundary layer development is already by itself a very complex mechanism even when evaluating simple well-behaved aerodynamic surfaces, such as flat plates. In this case the complexity level rises indeterminately.

Atmani, Brima and Askovic (2009) investigated the boundary and separation lines on a flattened spheroid (6:3:1), presenting very interesting results, which illustrate the crossflow present on such blunt bodies. During their work, they compared calculated and experimentally determined separation line predictions.

Figure 11 - Streamlines on the flattened ellipsoid (6:3:1) at 6° of incidence.

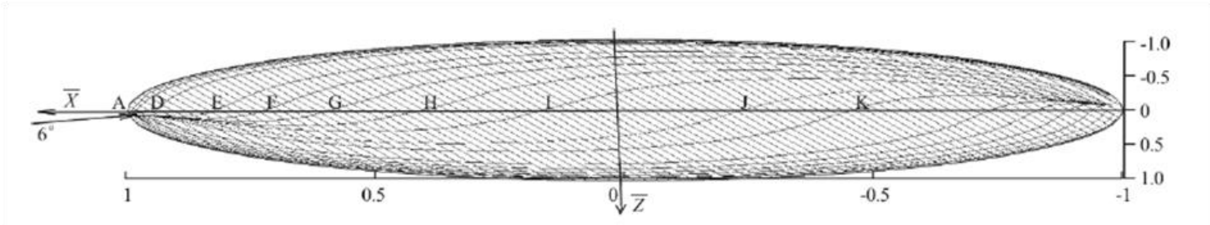

Source: Atmani, Brima and Askovic (2009).

They predicted a very characteristic streamlining distribution (Figure 11), which was similarly obtained in this work through oil flow visualization (section 5.2.2). Also, they detected that the separation would be of the closed type (bubble) appearing at the very end of the body for low incidences (AoA = 6°). Crossflow and meridional velocities were also plotted for some cases, considering the “J” line of Figure 11, demonstrating very clearly the existence of crossflow, changing in magnitude and direction along the streamlines path.

Figure 12 - Meridional (left) and crossflow (right) velocity profiles of the boundary layer for different positions along Line J.

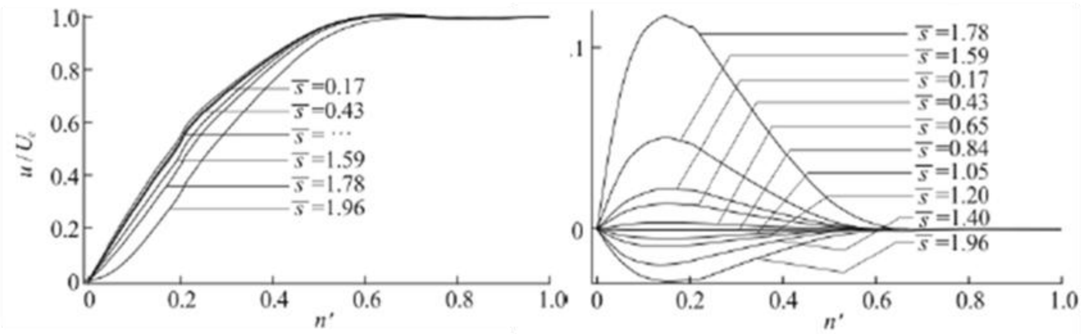

Source: Atmani, Brima and Askovic (2009).

Such results prove the complex flow about ellipsoids, similar in shape to conventional airship hulls, and anticipate some flow characteristics expected to be obtained along the results evaluation in this work.

3.1.2 Drag prediction: Bare hull

All models and approaches always aim at obtaining a good boundary layer model in order to predict drag with accuracy for the reasons discussed. It is common to breakdown drag in several different categories based on source. There are however two main branches: skin friction and pressure. The first one is correlated to the shear produced between consecutive fluid layers and how this shear is transferred to the surface of a immersed body (Equation 8); the second is more variable, and can come from all sorts of pressure acting such as shock waves, aircraft trimming, induced by lift, form or shape, among others. Analyzing Equation 8, one may easily see that it is intimately linked to the boundary layer development and nature. Once it depends on the velocity profile derivative at the contact point (wall), skin friction drag is determined by boundary layer nature.

$$\tau = \mu \cdot \frac{\partial \vartheta}{\partial y}_{y=0}$$

Equation 8 – Wall shear stress.

, where

τ	= wall shear stress per unit area, [Pa]
μ	= fluid dynamic viscosity, [kg.s-1.m-1]
$\frac{\partial \vartheta}{\partial y}_{y=0}$	= local shear velocity derivative with vertical position at wall, [s-1]

The key point is to understand the behavior of the low speed flow of airships, and identify which factors of those are the most important and investigate them. Firstly, it is obvious that at such low speeds like described in 3.1, shock waves are not going to appear, and compressibility effects are not relevant. Regarding the drag due to trimming (trim drag), it is acting when a heading or pitch correction is necessary, which means usually constant winds or occasional gusts acting along cruise flight. Its importance is not to be underestimated because it influences directly the airship performance, and must be taken into account during the dimensioning process. Besides that, when discussing correlation of theoretical and experimental results, trim drag is usually the key to understand full scale drag measurements data. This drag classification is a combination of shape and induced drag, discussed later in this work.

Usually induced drag is associated with wing tip vortices. However, this sort of pressure drag is generated by all finite lifting bodies or surfaces, and is related to a pressure difference between the acting surfaces (lower and upper), that leads to the formation of trailing vortices. For regular lifting surfaces, the induced drag coefficient (C_{Di}) is defined by the following equation:

$$C_{Di} = \frac{C_L^2}{\pi \cdot AR \cdot e}$$ Equation 9 - Induced drag coefficient definition.

, where

π = number pi (≈3.1415)
e = Oswald coefficient (related to the wing planform), [-]

For airships specifically, when generating aerodynamic lift by means of inclining the hull (or deflecting control surfaces, although this can ascribed to trim drag) the induced drag is a part of the drag breakdown. A huge three dimensional aerodynamic structure of vortices appear around the hull, producing a complex shed vortex wake, inducing also crossflow over the hull surface. These structures are further discussed in Sections 3.1.5 and 3.1.6.

Even though these last two sorts of pressure drag seem to be very relevant, they are much less significant than shape and skin friction drag for airships. In an ideal incompressible and inviscid fluid, the vector sum of the pressure vectors acting on the surface along the flow direction would result in zero, which means no counter force to the movement. However, in spite of the extremely low viscosity of air (17.2E−06 Pa.s at 0°C), there is shear between the fluid layers which is transferred to the body surface, generating a force against the desired movement, named skin friction drag. Besides that, the same viscosity leads to other effects like an adverse pressure gradient and boundary layer separations; these cause the balanced force distribution to break, the forward and rearward force in the flow direction are not anymore the same, generating the shape or form drag (a kind of pressure drag), named this way since it is directly dependent on the body shape.

Differently from common airplanes, for example, the ratio between form and skin friction drag is smaller. For airships, which are usually big aircraft, the surface area in contact with the fluid (wetted area) is much bigger, and so becomes the friction proportion of drag. Equation 8, which models the skin friction, takes into account how quickly the velocity of the layers varies in the normal direction of the surface from zero velocity (on the surface) to the first layer right after that. And here is an important reason why the boundary layer must be known: each type of boundary layer has a different velocity profile, which means different derivatives of velocity, and consequently different amounts of drag. In other words, the laminar boundary layers usually have much thinner velocity profiles (smaller derivatives in wall normal direction) than the turbulent, producing less skin friction drag, as a consequence.

Figure 13 - Normalized boundary layer typical profiles: Laminar (left) and Turbulent (right).

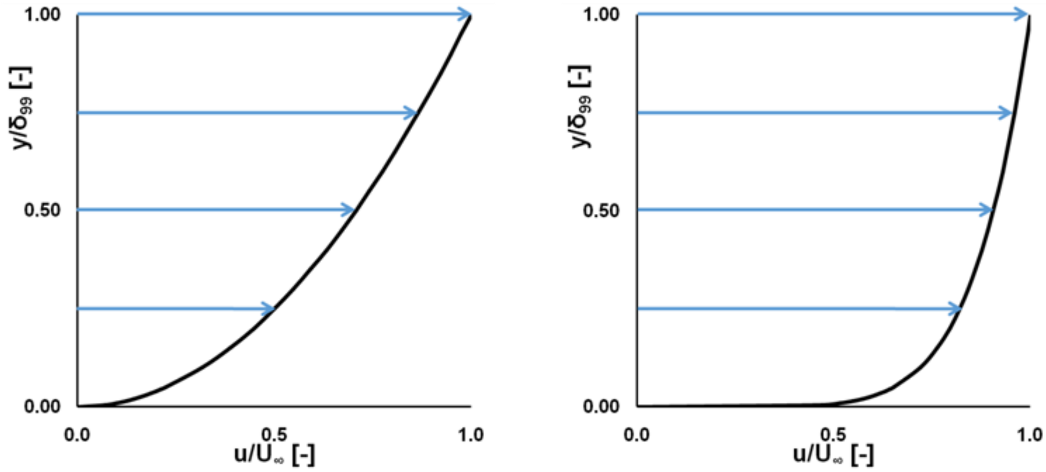

Source: Author (2018).

The transition from laminar to turbulent, specially ruled by *Re* and shape – pressure gradient, is then a key aspect to be understood and investigated. The variation of the transition point along the length can lead to considerable variations of skin friction drag, well illustrated by Gomes (1990). On the other hand, the development of a turbulent boundary layer improves the layer attachment and flow stability, postponing separation, and consequently reduces drag for greater incidences.

Purely in terms of skin friction drag, it would be interesting to have the lowest surface area for a given volume, which means having a spherical envelope, since the *Re* influence on any shape would be almost the same. However, this is a big issue when considering pressure drag and also some non-stationary aerodynamic effects, like vortex shedding – von Kármán Vortices. The solution for this question must come from some intermediate shape, which led to the conventional ellipsoidal bodies, guiding the design to different streamline curvatures and slenderness ratio (*AR*) bodies. This shape has some performance advantages in terms of drag, but must be well designed – and the appendages as well – in order to avoid stability and dynamic problems during maneuvering, landing and taking-off, ground handling and even cruise flight due to oscillatory movements.

Some theoretical considerations affirm that form drag varies with L^2, while skin friction drag, with $L^{1.86}$, where L is a linear dimension for geometrically similar forms at same speed (BURGESS, 2004). Other studies, considering different *AR* bodies with same volume, like Young[4] (1939 apud Khoury, 2012, p. 26-29) showed that, based on total drag, skin friction and form drags are directly and inversely proportional to *AR*, respectively (Figure 14).

Figure 14 - Drag components dependence on the *AR*.

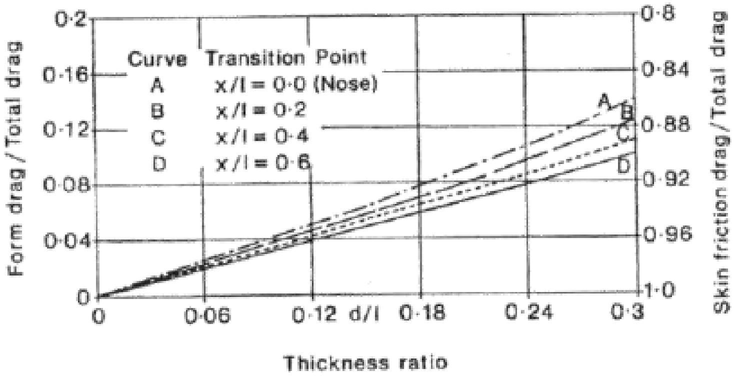

Source: Khoury (2012), p. 29.

Based on those results, and since he had already noticed that the ratio between skin friction and total drag varied little with changing the transition point, Young (1939 apud Khoury, 2012, p. 27) suggested the following equations as an approximation to the mean values for initial estimates:

$$\frac{\text{Skin friction drag}}{\text{Total drag}} = \frac{0.6}{AR}$$

Equation 10 – Ratio between friction and total drag. Source: Khoury (2012).

$$\frac{\text{Form drag}}{\text{Total drag}} = 1 - \frac{0.6}{AR}$$

Equation 11 – Ratio between form and total drag. Source: Khoury (2012).

It is possible to conclude, as expected, that the more slender the body, the larger the skin friction is, and the lower the form drag is. A similar rule applies for the transition point, linked to the boundary layer nature over the body: the farther away the transition is from the nose, the lower will be the friction drag for the same *AR*.

Also useful for estimating the drag of airships are some studies made by Hoerner (1965) on bodies of revolution. With a semi-empirical approach an expression for friction drag was proposed related only to *Re* (Equation 12).

$$\mathrm{C_f} = \frac{0.043}{Re^{1/6}}$$

Equation 12 – Friction coefficient based on *Re*. Source: Hoerner (1965).

Based on this expression, Hoerner (1965) proposed an estimate for the total drag coefficient based on the buoyant volume – volumetric area (Equation 13).

$$\mathrm{C_D} = \mathrm{C_f}\left[4 \cdot AR^{1/3} + 6 \cdot \frac{1}{AR}^{1.2} + 24 \cdot \frac{1}{AR}^{2.7}\right]$$

Equation 13 – Total drag coefficient estimate. Source: Hoerner (1965).

[4] YOUNG, A.D. *The calculations of the total and skin friction drags of bodies of revolution at zero incidence.* London, HMSO: ARC R&M, 1939.

In a similar manner, another expression for friction drag was proposed by Burgess (2004), relating the flow properties (density and viscosity) and the surface area of the body (Equation 14).

$$C_f = 0.0035 \cdot \rho \cdot S^{0.93} \cdot \vartheta^{1.86}$$

Equation 14 – Skin friction coefficient based on surface are and velocity. Source: Burgess (2004).

Cornish, III and Boatwright (1960) demonstrated from their full scale tests that envelope drag was mainly due to skin friction rather than pressure drag. Their model had *AR* around 4, being within the margins studied by Young (1939).

3.1.3 Drag prediction: appendages

Although the great highlight for airships is given to the envelope, all appendages must be investigated. All the described investigations so far considered drag for the bare hull aligned with the flow. Obviously this is not enough, and airships do have some key appendages such as cars, the tail surfaces, ground handling attachments, equipments, etc. These additional structures must be studied connected to the bodies/hulls since they are affected by aerodynamic interference effects, like the fuselage of airplanes acts on the wing root for example. The most discussed are gondola, power plant and tailplane.

Studies were conducted on airship drag breakdown by means of parametric studies, wind tunnel tests and more recently Computational Fluid Dynamics (CFD). It has been shown that the bare hull contributes to approximately 50% of the total drag (DURAND, 1936), and this is probably the reason – together with the simplicity – why so many studies are made for minimizing the drag of the hull. Complementarily, based on the full scale tests with the ZS2G-1 Airship, Cornish, III and Boatwright (1960) also showed that drag is almost evenly divided between airship envelope and the rest of the aircraft.

However, the ultimate goal here is to reduce the total drag as a whole, which encouraged many investigations on the aerodynamic interactions between different parts of an airship.

As already described, the presence of the gondola changes the standalone pressure distribution, contributing to lift, but also to drag generation. Something similar occurs for the propulsion units; despite the needed power and thrust generation, they also produce drag, and given the new capabilities of thrust vectoring, this drag is even greater under certain conditions. Another interesting observation is that, when some appendages are put ahead of the maximum diameter, hull drag increases more than when the same structures are put after it (BURGESS, 2004). This can be explained by the already discussed nature of the boundary layer. Before the maximum diameter, there is a region of laminar flow, or at least a small level of turbulence, which when perturbed by the appendage, transitions or increases the boundary layer turbulence, and increases skin friction drag as well.

Despite all those accessories, the leading topic when discussing aerodynamic interference is the tailplane. Vital for maintaining the heading of the airship, trimming and controlling it, there are plenty of possible configurations ("+", "X", "-Y[5]", "H", …); some of them were compared through wind tunnel testing, evaluating aerodynamic and performance characteristics (ANDERSON and FLICKINGER Jr., 1954). The stability aspects involved are discussed further on, but the correct dimensioning of the tail surfaces is crucial for avoiding multidisciplinary problems during design and operation.

It was also shown that the interference of the hull on the fins is considerable and must be take into account (CURTISS JR., HAZEN and PUTMAN, 1976[6] apud CEBOLLA, 2013, p. 27). By means of a quantitative study based on seven different airships (R 29, R 32, R 33, R 38, Bodensee, U.S.S. Los Angeles and U.S.S. Akron) aiming at comparing tail to bare hull drag, Curtiss Jr., Hazen and Putman (1976 apud Cebolla, 2013) found that in most cases the boundary layer at the stern is detached or is at least rather thick, causing a big piece of the fins to operate in a very turbulent and low velocity region, decreasing their efficiency. With the results, it was possible to produce a table containing the parametric results for each airship configuration (Table 2).

---

[5] This configuration refers to inverted "Y"-like, which means one top rudder, and two lower ruddervators.

[6] CURTISS JR., H.C.; HAZEN, D.C.; PUTMAN, W.F. LTA Aerodynamic Data Revisited. *Journal of Aircraft*, v.13, n.11, p.835-844, 1976.

Table 2 - Tail and hull drag comparison.

Airship	Bodensee	R29	R32	R33	R38	USS LA	Akron
AR	6.7	10.2	8.2	8.2	8.2	6.90	5.92
$\frac{S_{wet}^{T}}{S_{wet}^{H}}$	≈0.1	0.08	0.06	0.06	0.07	0.07	0.11
$\frac{Drag^{T}}{Drag^{H}}$	0.27	0.18	0.07	0.12	0.07	0.22	0.24
$\frac{Drag^{\frac{T}{H}}}{S_{wet}^{\frac{T}{H}}}$	≈2.7	2.2	1.2	2.0	1.0	3.1	2.2

Source: Adapted from Cebolla (2013), p. 27.

From this data a relation between the desired drags was inferred:

$$\frac{\text{Tail drag}}{\text{Hull drag}} = 3.56 - 0.195 \cdot AR$$

Equation 15 – Ratio between tail and hull drag per unit area. Source: Cebolla (2013), p. 27.

Investigating the airships Bodensee, U.S.S. Los Angeles and U.S.S. Macon, Durand (1936) tried to get a global view of the drag breakdown, listing some accessories and gathering the information (Table 3).

Table 3 - Drag area breakdown for airships.

Estimated drag area breakdown [m²]	Bodensee	U.S.S. Los Angeles	U.S.S. Macon
Bare Hull	9.4	21.8	39.0
Fins and Rudders	2.5	4.9	14.0
Wing Power Cars and their Misc.	2.8	6.8	10.7
Rear Power Car and Misc.	2.4	2.2	-
Control Car and Misc.	2.4	4.5	2.8
Misc. Protrusions (mooring eqpt. and etc.)	0.5	0.8	1.8
Total	20.0	41.0	68.3
$V^{\frac{2}{3}}$ [m³]	790	1845	3528
C_D [-]	0.025	0.022	0.019

Source: Adapted from Durand (1936).

Cornish, III and Boatwright (1960) also concluded that by suitable fairings and modifications to the nose structures of the ZS2G-1 airship, the skin friction drag of the envelope could be reduced by more than 20%. This shows that all structures exert strong aerodynamic influence over each other, mainly due to effects on boundary layer development characteristics. Besides this, they also showed in full scale that the pressure drag coefficient, as well as the skin friction coefficient, decreases with increasing *Re*.

3.1.4 Lift and moment prediction

The study of transversal forces, and also moments – yawing and pitching, requires special attention to non-linear effects, which are similar for other lifting bodies and surfaces as well. When the angle of attack (AoA) is increased, the nonlinearities show up, influencing the curves of force and moment. For the bare hull, it is proposed a division around AoA = 5°: low angles (< 5°) and high angles (> 5°) (CURTISS JR., HAZEN and PUTMAN, 1976[7] apud CEBOLLA, 2013, p. 28-29).

Below AoA = 5°, the previously discussed pressure distributions of the bare hull are quite correct, mainly near the bow, and the flowfield around the body is quite similar, in good agreement even with the inviscid theory. Nevertheless, as the angle increases, since the crossflow is strongly dependent on *Re* and AoA, the three-dimensional effects become stronger, generating lateral upwards vortices rolls (LUTZ et al, 1998).The influence of such nonlinear aerodynamic structures increases with the increase of AoA, and the organized wake vortices become dominant, resulting in a stronger relationship between force generation and AoA, decreasing the *Re* influence.

Figure 15 - Typical increase of dynamic lift for airships.

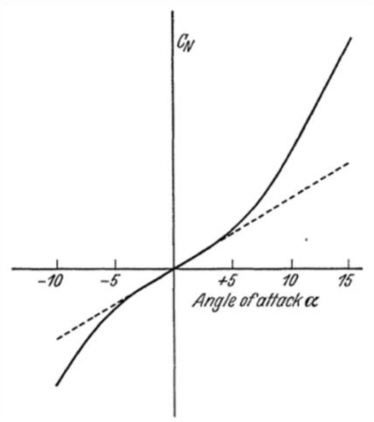

Source: Durand (1936).

According to DURAND (1936), for higher angles, it seems that the phenomenon of detaching vortices on the lee side (leeward or downstream the body) is controlled by some “sensitive mechanism, and the upstream area subject to it expands with increasing AoA”. It is very difficult to precisely predict the location of such structures, but it is highly dependent on the body shape and *Re*. An interesting observation is that, when appendages are added to the bare hull, the lift slope increases while the central linear region tends to zero width (Figure 15). This proves that the airship as a whole is a complex aerodynamic body, highly non-linear, and care must be taken when approximations are inferred using only the hull.

Regarding aerodynamic moments, since they are strongly influenced by the forces generated at the tail, it is rather more complex to study them. Since the

[7] CURTISS JR., H.C.; HAZEN, D.C.; PUTMAN, W.F. LTA Aerodynamic Data Revisited. *Journal of Aircraft*, v.13, n.11, p.835-844, 1976.

flowfield at the stern is more turbulent and not well predicted by simple theories (like inviscid potential flow) because of the boundary layer development – and consequent effects, this becomes a challenging task. After some studies, Abbott (1931) suggested a typical value of 70% of the predicted moment as the actual one. In this way, both moments, pitching and yawing, become less sensitive to *Re* since they are based on pressure distributions better predicted for the forward part of the hull, given the good agreement with inviscid theory.

This does not solve the issues around the tail. The aerodynamics of airships is dominated by significant interference effects among the flows around the different vehicle components. The viscous and complex flowfield in the vicinity of the fins makes it very difficult to predict fins effectiveness and loading. The tail surfaces are affected by lower velocity regions, lateral upwards rolling vortices and, since they usually have a very low aspect ratio, their aerodynamic efficiency is naturally lower. Besides that, these surfaces, which are usually also swept, tend to generate leading edge vortices, that together with the other vortices and turbulence, tend to produce non-stationary and complex loads.

3.1.5 Interference effects

The evident non-linear aerodynamic behavior of airships must come from the flowfield. A complex interaction among all “flows” over the different parts of the aircraft tends to make it challenging to determine and quantify the aerodynamic results.

A widely known formation is the separating free shear layers from the hull at AoA or β different from zero. Maneuvers or gusty situations are the main cases when this angle increase is clear, affecting the 3D boundary layer development, that due to the naturally crosswise pressure gradient, tends to have the internal flow directions changed. The streamlines converge into an envelope (3D separation line) from where a vortex sheet detaches, rapidly rolling up into a distinct vortex (LUTZ et al, 1998). Obviously this affects the original pressure distribution, and consequently the lift and drag forces. It is from that strong interaction between hull and wake that the aerodynamic forces are dependent. Moreover, given the fact that the separation line length varies with respect to the AoA, a non-linear behavior can be visualized (LUTZ and FUNK, 2005). It is possible to visualize the mentioned vortex, and even track its variation with the AoA by different means. Figure 16 contains results obtained using a Seven-Hole Probe mapping the flowfield past the hull of the LOTTE airship (FUNK et al, 1998).

Figure 16 - Development of the crossflow velocity components on plane x/L = 1.4 at AoA =10°, 20° and 30°. The reference vector magnitude is 5 m/s.

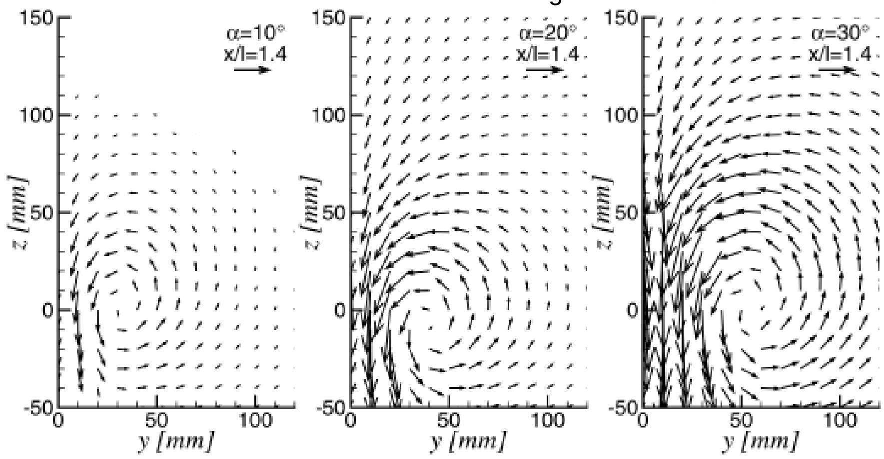

Source: Funk et al (1998).

A very comprehensive research on the description of the flow about an inclined spheroid was published by Han and Patel (1979). They highlighted that, for three-dimensional steady flow the term separation is not as precise as it is for two-dimensional cases. Usually, in cases like airship hulls (or the studied spheroids) flow detachment is not directly determined by near-surface characteristics like vanishing of wall shear stress; indeed, this amount tends to remain constant, being even large in some cases. They also proposed that separation lines for three-dimensional flows may be lines on which some component of wall shear stress vanishes, limiting streamlines converging to singular points, the envelope of limiting streamlines, lines dividing flow coming from different regions and even a combination of one or more of these characteristics.

Han and Patel (1979) conducted experiments on wind tunnels using wool tufts, but mainly using a low Reynolds hydraulic flume, visualizing the flow using coloured dye. Although the study focused on the location of laminar separation, not representing very well the full turbulent flow of airships, the results are very elucidative regarding surface and outer flow patterns. Using a 4.3:1 prolate spheroid at *Re* = 8.0e+04, expecting a full laminar boundary layer, they assessed the flow patterns at different incidences: axisymmetric (AoA = 0°), low incidence (AoA = +5°), moderate incidence (AoA = +10°) and high incidence (AoA = +20°, +30° and +40°).

Axisymmetry was observed for AoA = 0°, and a very well defined separation around x = 80%**L**. Increasing AoA, at low incidence, reversed flow appears near the tail, a little downstream from the earlier separation. Laterally, on the flank side, the streamlines converge from windward to leeward, but from the middle onwards they acquire a downward deflection. Similarly, a convergence-divergence trend is observed on the leeward side, and reversed flow is encountered at approximately x = 94%**L**.

Figure 17 - Top view of the flow about a 4.3:1 prolate spheroid at AoA= 0° and Re = 8.0e+04.

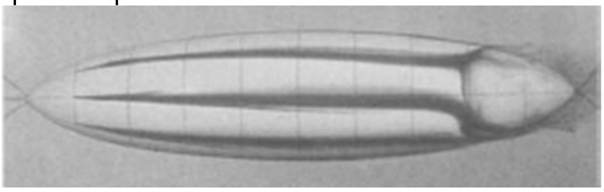

Source: Han and Patel (1979).

Figure 18 - Side view of the flow about a 4.3:1 prolate spheroid at AoA= +5° and Re = 8.0e+04.

Source: Han and Patel (1979).

For moderate incidence, windward and leeward streamlines increase the diverging tendency from their origins, tending to merge laterally forming a very well defined line. Some flow visualization showed a tendency for the boundary layer to roll up into a longitudinal vortex along this line. In addition, flow reversal increased in the tail region, mainly on the flank side.

Figure 19 - Top view of the flow about a 4.3:1 prolate spheroid at AoA= +10° and Re = 8.0e+04.

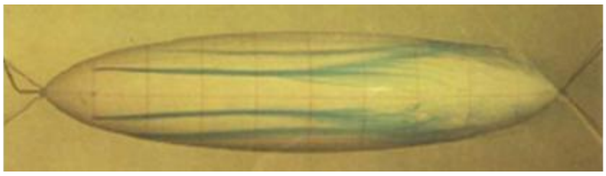

Source: Han and Patel (1979).

Figure 20 - Side view of the flow about a 4.3:1 prolate spheroid at AoA= +10° and Re = 8.0e+04.

Source: Han and Patel (1979).

For higher incidences, a new phenomenon was observed by them: a secondary separation and a reattachment between upper and lower separation lines. Those separation lines are classified as open separation, according to Wang[8] (1972 apud Han and Patel, 1979), once limiting streamlines converge from both sides into a single 3D separation line (Figure 21).

Figure 21 - 3D open separation leading to a vortex free layer.

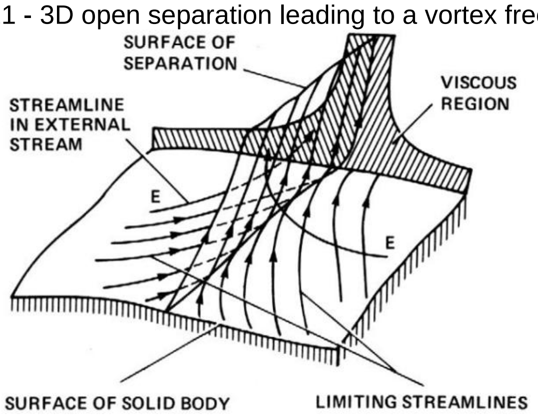

Source: Funk et al (1998).

[8] WANG, K.C. Separation Patterns of Boundary Layer over an Inclined Body of Revolution. *AIAA Journal*. August, 1972, Vol. 10. p. 1044-1050.

If the lines converged only from one side into a singularity separation line, it would be classified as a close separation. Similarly, once the reattachment line has lines emanating from it in both directions, it is an open reattachment line. By observations, Han and Patel (1979) showed that two pairs of longitudinal vortices emanate from the lateral open separation lines, eventually detaching from the surface.

Figure 22 -Side view of the flow about a 4.3:1 prolate spheroid at AoA= +30° and Re = 8.0e+04.

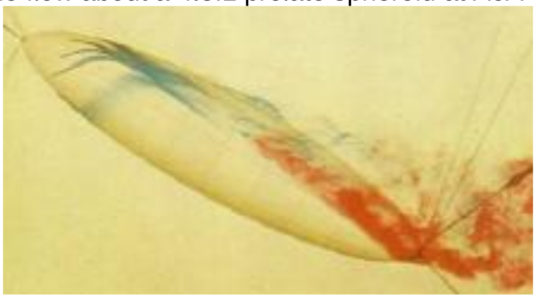

Source: Han and Patel (1979).

Basically, with increasing incidence, Han and Patel (1979) demonstrated that vortices and reverse flow appear along the spheroid, mainly longitudinal vortices for higher incidences, and a very complex and separation dominated flow is created. It is interesting to highlight that some previous observations had already been made, and presented (THWAITES, 1960), being cited by Han and Patel (1979). In his schematics, Thwaites (1960) shows the flow changing behavior and dominance with increasing AoAs. For low incidence, Thwaites (1960) presents Nonweiler's theoretical prediction of the limiting streamlines past a body of revolution at low incidence. The limiting streamlines (dashed lines in Figure 23) are the limit of the streamlines as the body surface is reached, and are tangential to the shear stress direction on it.

Figure 23 - Schematic representation of Nonweiller's theoretical prediction of the flow past a body of revolution at low incidence. (a) Side view of surface flow. (b) Three-quarter view from below suggesting vortex formation.

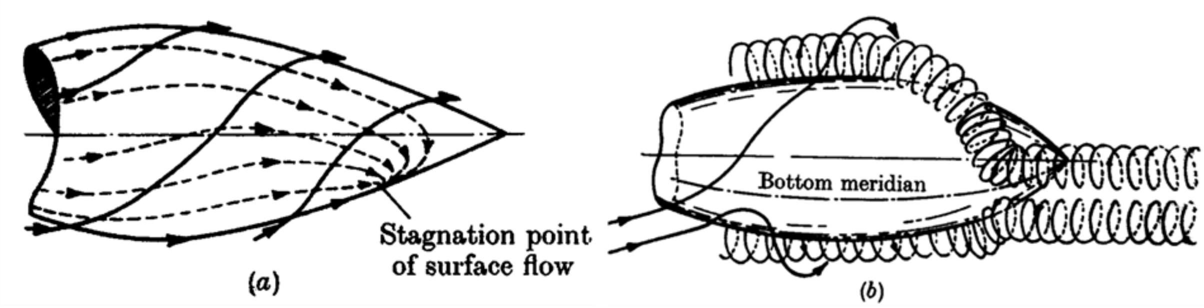

Source: Thwaites (1960), p. 412.

As depicted in Figure 23, it is possible to see the formation of a pair of lateral longitudinal vortices tubes along a line resulting from converging streamlines, just like shown by Han and Patel (1979). The separation occurs on a singularity like a stagnation point, constituting an open separation line. Nonweiller's prediction also shows that the outer flow (solid black lines in Figure 23) behaves very differently from the limiting streamlines, once external flow streamlines go over the lateral vortices, converging over the leeward side.

Based on the same experiments, Thwaites (1960) also presents some schematic interpreting experimental data, describing the flow past a body of revolution at moderate incidence (AoA = +20°). The pattern is basically similar to what would be seen afterwards by Han and Patel (1979), being comprised of two pair of longitudinal vortices, with a reattachment region in between. Han and Patel (1979), despite the similarity, highlighted that the primary vortices observed by them (lower) seemed to be larger than those shown by Thwaites (1960). It is worth observing that Thwaites (1960) showed results for *Re* = 1E+06, while for Han and Patel (1979) it was 8E+04.

Figure 24 - Schematic interpretation of experimental data on the flow past a body of revolution at moderate incidence (AoA = +20°, and *Re* = 1.0E+06).

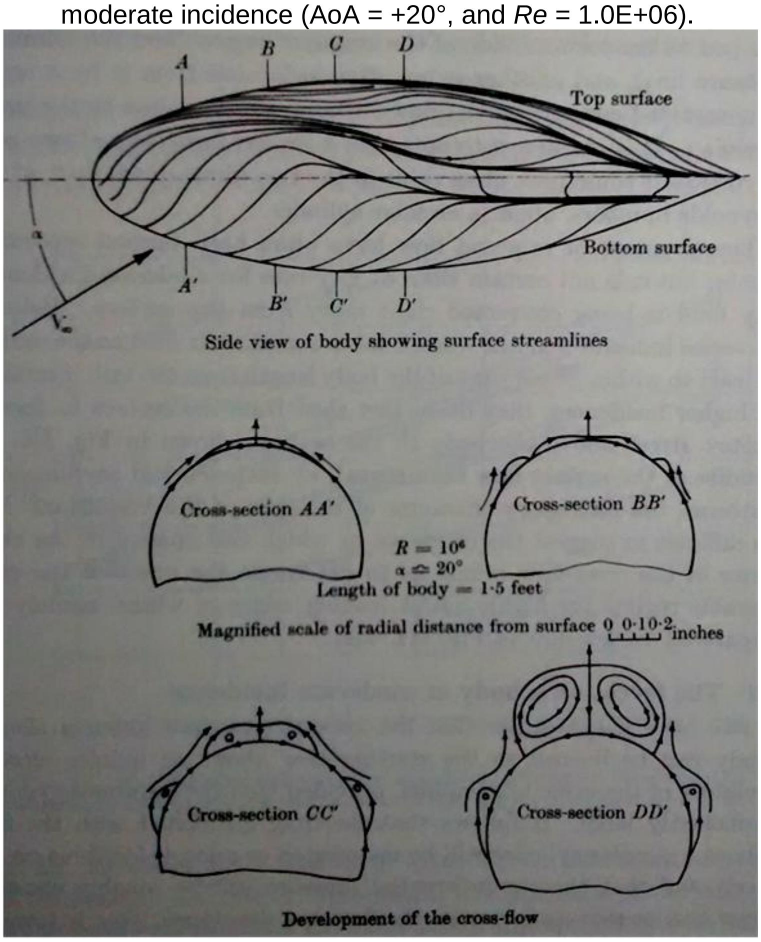

Source: Thwaites (1960), p. 413.

In order to assess the results sensitivity to *Re*, Han and Patel (1979) increased the *Re* up to 7.0E+05 using a wind tunnel, and visualizing the results using wool tufts. They basically observed that there was an abrupt change in flow while increasing *Re*, which was already stabilized at the final value. They considered the boundary layer to be predominantly turbulent over the body surface. This is really questionable, and will be shown along the results of this work, once the used *Re* is still very small for a full turbulent boundary layer development. Anyway, once no precise information about the wind tunnel is provided, it is difficult to evaluate it precisely. As a general conclusion, they say that the separation travelled significantly downstream, being around 95%**L** for AoA = 0°, and that at high incidences, even with the poor tufting mesh used, an open type separation line was identified laterally. This line moved upstream as the incidence increased, and some closed separation was observed near the tail. The secondary separation was not identified with the tufts. However, once again, from the published pictures, it is clear that the tufting technique was not properly applied, since rather long strings were used, and their density at the surface was far too low (Figure 25).

Figure 25 - Wind tunnel flow about a 4.3:1 prolate spheroid visualization using tufts at AoA = +40° and *Re* = 7E+05.

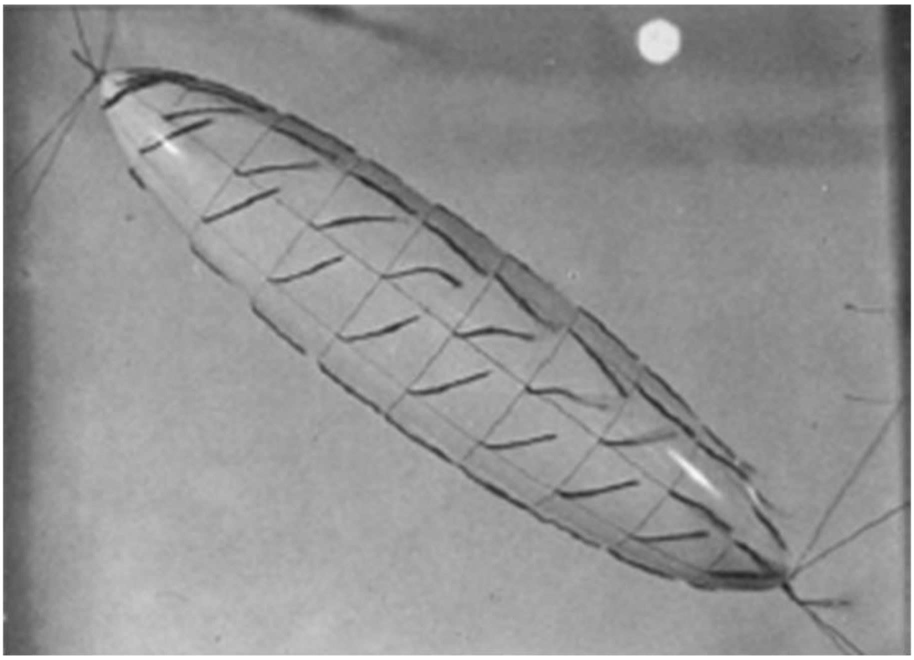

Source: Han and Patel (1979).

Contemporary of Han and Patel (1979), another very interesting work, and also geometrically close to what is investigated in this work, was published by Fairlie (1980). Using a wooden 4:1 prolate spheroid (the same *AR* of the ADB-3-30 hull), at approximately *Re* = 6.0E+06, he evaluated the separated flow patterns using a transonic wind tunnel at *Ma* = 0.55, with no shock waves detected. At this *Ma*, he could use the Schlieren technique[9] in order to visualize vortex shedding in the flow separations; for the limiting streamlines traditional oil flow techniques were applied, using titanium dioxide in silicone oil. Differently of Han and Patel (1979), Fairlie (1980) used a band of fine carborundum particles, fixing transition to turbulent flow very close to nose.

The results for zero incidence were quite similar to those obtained by Han and Patel (1979) using the wind tunnel, as separation occurred around 96%**L**. For AoA = +5°, Fairlie (1980) identified two counter-rotating spiral nodes at the stern region on the flank side. With increasing AoA, the extent of these stable foci nodes enlarged, and the distortion grew as well.

Figure 26 - Side view of rear portion limiting streamlines of a 4:1 prolate spheroid at AoA = +5° and Re = 6.0E+06. Left: oif flow visualization. Right: Streamlines schematic.

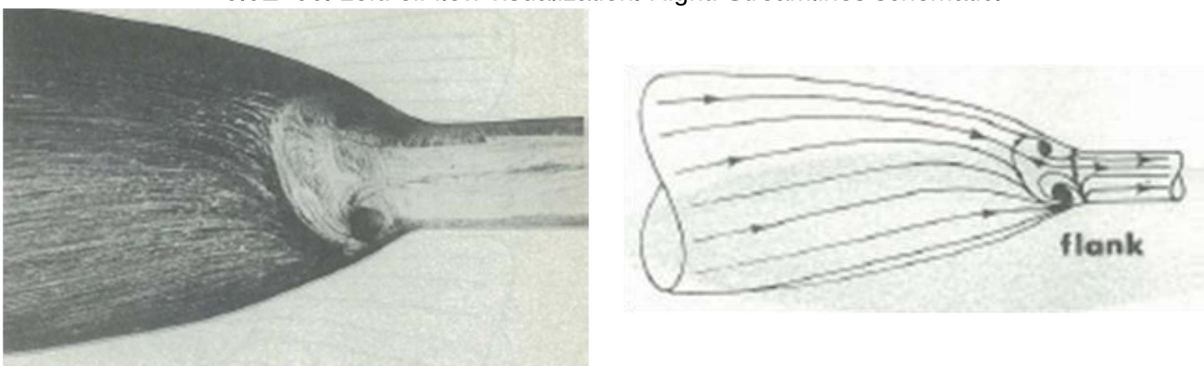

Source: Fairlie (1980).

The model was supported by the rear portion by a 25 mm diameter sting, with the body contour being faired smoothly into the sting. It is possible to see by closely inspecting the streamlines representations of Fairlie (1980) that the formation of those spiral nodes, or at least their size, may be related to flow reversal induced by the sting. This is not commented by Fairlie (1980), and constitutes a personal evaluation of the author. This structure was named “owl”, and was also identified on the leeward side of a second model, hemisphere-cylinder, at AoA = +25°.

Regarding the limiting streamlines, the same structures identified by Han and Patel (1979), and shown by Thwaites (1960), were observed as well. For moderate incidence, the lateral free vortex separation layer (MASKELL, 1955) or open separation line was observed, forming the same described longitudinal vortex. For larger AoAs (30°), the rear portion suffers from greater distortion (very difficult to

[9] This a visualization technique used to photograph the flow of fluids of varying density. It was invented by the German physicist August Toepler in 1864 to study supersonic motion, and is commonly used in aeronautical engineering to photograph the flow of air around objects.

precisely describe, but similar to the low incidences pattern), and the second open separation line is also identified.

Figure 27 - Side view of rear portion limiting streamlines of a 4:1 prolate spheroid at AoA = +15° (left) and AoA = +30°, both at Re = 6.0E+06.

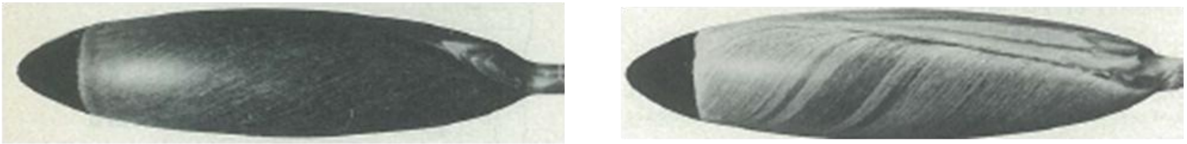

Source: Fairlie (1980).

Finally, Fairlie (1980) depicts two possible representations of the crossflow streamlines patterns, illustrating the lateral longitudinal vortices, and a pair of counter-rotating vortices over the leeward side. The patterns are very similar to those depicted by Thwaites (1960), and very similar to each other. According to Fairlie (1980), both are topologically correct, and no distinction can be made on topological grounds, considering both rather similar.

Figure 28 - Possible crossflow streamlines patterns proposed by Fairlie (1980).

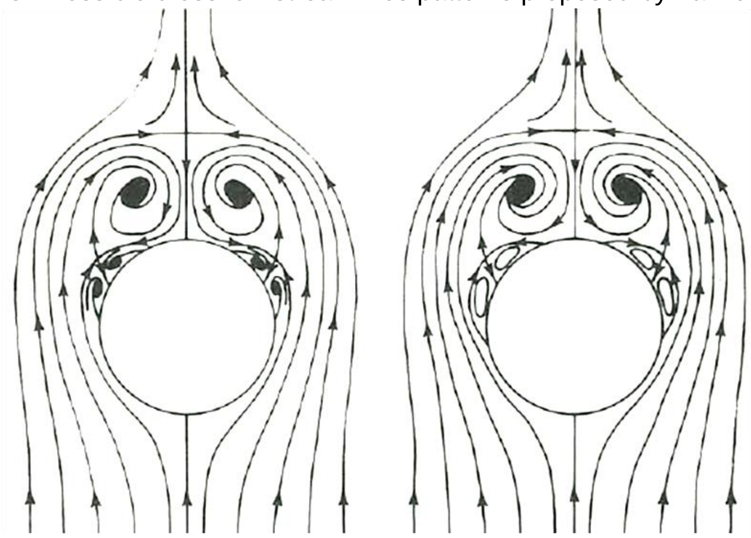

Source: Fairlie (1980).

In 1993, a very relevant work on three-dimensional flow separation was published by Patel (1993), showing numerical results on the laminar flow prediction past a 6:1 prolate spheroid. The same “owl” structure was predicted on the flank side of the spheroids near to the trailing edge. With increasing AoA, their area increased, and the structure travelled upstream, stretching itself. It was identified as constituted of spiral nodes, which were probably leaving the surface as tornado-like vortices. The crossflow topology predicted by him was also very similar to that presented by Fairlie (1980), demonstrating an indeed complex vortical structure around the body.

It is possible to conclude that the flow past the hull alone is very challenging to be predicted and understood. Nevertheless, adding the tail creates a novel complex flow region, which is comprised by the interaction between fins and hull. In this case, it is possible to study the problem considering viscid and inviscid effects. Firstly for the viscous dominated problems, from the interaction between the hull and fins boundary layers, secondary flow effects occur. Due to the stagnation effect of the fins, the hull boundary layer decelerates, probably separating. This leads to one or more corner vortices detaching from the hull surface (LUTZ and FUNK, 2005). Looking at the fin surface, a vortex structure appears very near to the junction between fin and hull, generating a low pressure region. This low pressure sucks the flow towards the envelope surface, diminishing in strength as the streamline is more distant from the hull. A clear division line is possible to be observed over the fin surface: at the inner side, the flow goes to the hull, while at the outer, the streamlines go towards the surface tip (Figure 29).

Figure 29 - Typical flow over the tail fins (wind tunnel visualization).

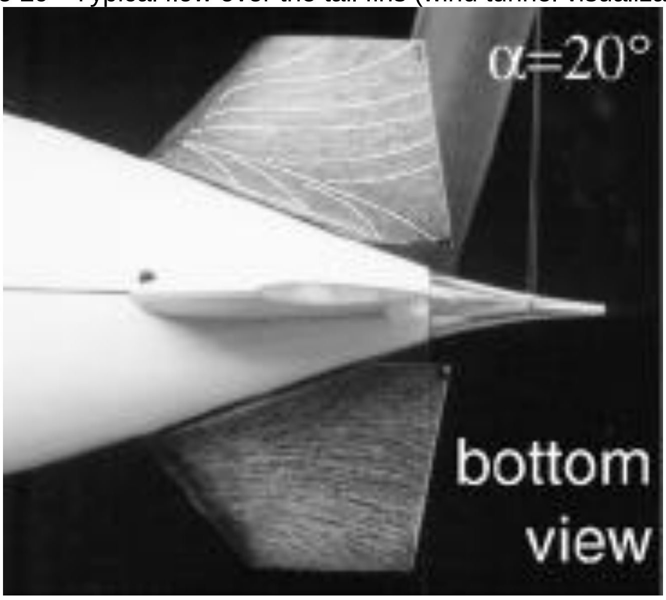

Source: Lutz and Funk (2005).

Looking at the flow over the hull, what really happens is the inevitable separation of the incoming turbulent boundary layer when reaching the stagnation region of the tail surfaces. This occurs mainly because the boundary layer is not able to overcome the intense adverse pressure gradient, developing vortices near the junction to the pressure side of the surface. A very interesting observation made through CFD analysis by Lutz and Funk (2005) showed that the fins low pressure regions tend to suck in some vortex rolls that eventually find a way out and roll up downstream together with the fin tip vortices. This kind of interaction shows that flow over airships is really complex and interference dependent, justifying many studies – even this one – and evaluations on this topic, so as to make it possible to better know the vehicle characteristics for design and safe operation support. Very similar observations were made by Cornish, III and Boatwright (1960) during the full scale investigation of the ZS2G-1 airship (Figure 6).

In his work on three-dimensional flow separation of 1993, Patel (1993) also reviews some results from flow visualization for low *AR* wings intersecting a plane. This is very similar to the fins region on an airship, as the fins constitute low *AR* lifting surface intersecting the hull. The reviewed work was published by Johnson[10] (1991 apud Patel, 1993), based on wind tunnel and water channel results of a one-half 12:6:1 triaxial ellipsoid mounted on a flat wall, subject to *Re* = 2.5E+05.

Despite the low effect of root boundary layer, which is much larger for the fins positioned very close to the hull trailing edge, the results are very interesting. For zero incidence, a very symmetric topology was observed, and the separation line was very clear, perpendicular to the flow direction. Near the root, two pairs of counter rotating spiral nodes are formed on the surface trailing edge, and from the separation lines, on the plate surface another pair of counter rotating vortices takes place. This allows the buildup of reversal flow on the surface, directed to the trailing edge.

With increasing incidence, as expected the stagnation point moves to the pressure side, and the pair of surface trailing vortices becomes a single vortex, detaching from the suction side. The separated region on the wing trailing edge becomes asymmetric, and the nearer to the wall, the quicker it converges to the trailing edge. On the pressure side the separation line extent is decreased going to the root. On the suction side, apparently, given the interaction between base plate and trailing edge flows, a spiral node is formed on the trailing edge, sucking the streamlines to it, until they reach the trailing edge vortex separation. This constitutes an open separation line as defined above.

Figure 30 - Skin friction topology of an ellipsoidal wing intersecting a surface at AoA = 0° (left) and AoA = +5° (right).

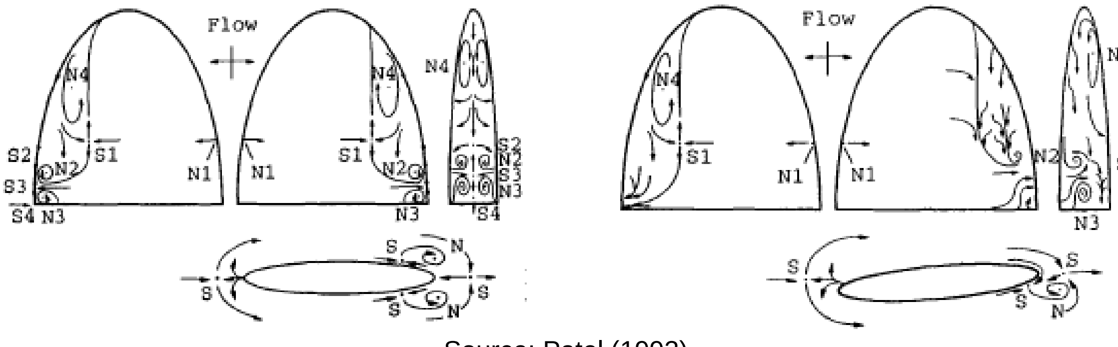

Source: Patel (1993).

[10]JOHNSON, T.A. *Visualization of Topology of Separated Flow over a Semi-elliptic Wing at Incidence Intersecting a Plane Wall*. Iowa city : University of Iowa. 1991. Master's Thesis.

For greater incidences, the trailing vortex increases in strength, and steadily travels upstream and away from the wall, enlarging the separated region on the surface. On the wing surface flow reversal increases drastically, mainly for high incidence, and near-to wall vortices form on the suction side. In this last case, a clear bifurcation is seen on the suction side. As the reversed flow reaches the separation line, a great portion of it redirects to the wing tip, whereas the other generate the near-to-wall vortex. In addition, recirculating flow is observed on the trailing edge itself, along the spanwise direction.

Figure 31 - Skin friction topology of ellipsoidal wing intersecting surface at AoA = +15° (left) and AoA = +25° (right).

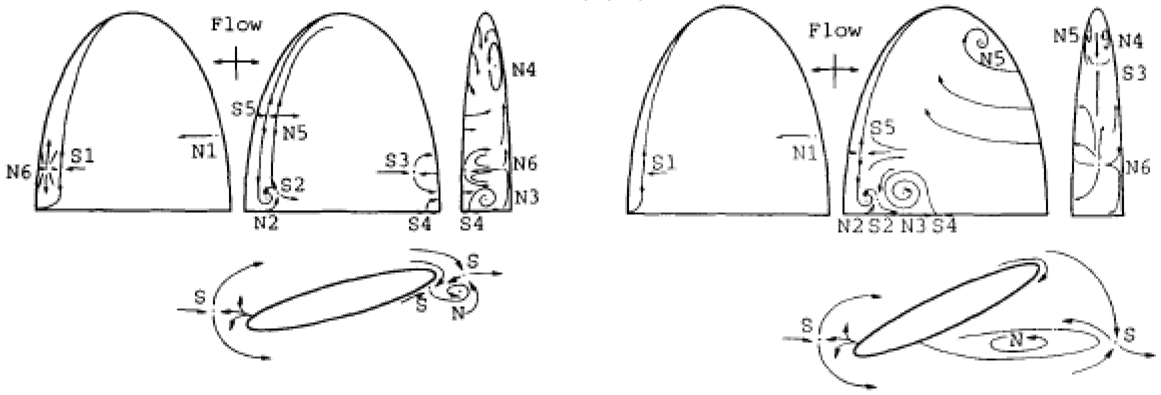

Source: Patel (1993).

It is then clear that the viscous interference, mainly near the hull, is expected to be quite strong and relevant. Complementarily, as stated above, also some inviscid effects do appear from this hull-fins interaction, and they can be investigated by looking at the pressure distribution along the hull. Adding stabilizers usually affects the pressure at a region considerably upstream from them. For some investigations made on a LOTTE airship model (LUTZ and FUNK, 2005), the distribution was affected some 15% ahead of the fins-hull intersection. The presence of the fins leads to deceleration over the lower region (surface high pressure) and acceleration over the upper region (surface lower pressure), which increases the net lift in the tail region. This increasing effect given the tail is known as “Lift Carry Over” - LCO. The LCO significantly contributes to the lift increase of the hull-fin configuration (LUTZ and FUNK, 2005).

Figure 32 - Measured LCO for LOTTE (AoA = +20°, Re_V=3.9E+05, fully turbulent).

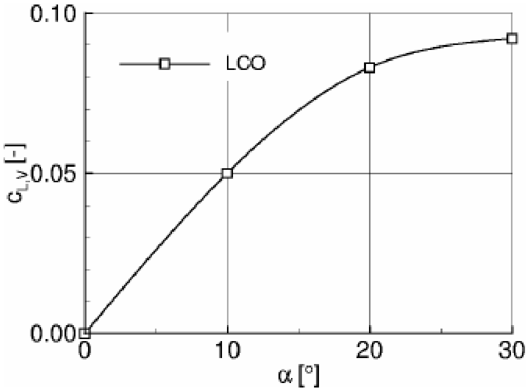

Source: Lutz et at (1998).

Another topic related and important to airships is the ground effect, more important to be examined during landing and when masted, since the clearance to the ground is small. Like for any other aircraft, the smaller the height, the stronger the influence, and for this reason it must also be studied when dealing with operational issues. However, this work does not aim at this last topic, but at regular, steady cruise flight operations only. Other effects are likely to occur but are not specific from classical airship bodies, such as propulsion efficiency variation, and are not going to be studied in this work.

3.1.6 Wind tunnel experiments

The main objective usually associated with wind tunnel testing is to obtain the real characteristics of the studied body, ensuring that the estimates made beforehand are correct, and that the design is converging to the desired aircraft. Besides that, it is usual also to use wind tunnel tests for investigating problems after design, or examine strange behaviors detected during operation. In all cases, it is necessary to plan the campaign, preparing an experiment master table, identifying the planned tests, and organizing them in specific sets according to the kind of study: purely aerodynamic evaluations, stability characterization, investigation of new concepts and configurations, among others.

Usually investigations aimed at the determination of general forces and coefficients are divided in two main phases: drag-*Re* and stability evaluation. In the first one, the main objective is to obtain accurately the model drag, and for that, various *Re* are used and usually the roughness is also changed before repeating runs until the correct correlation setting is found. The second phase is usually conducted at constant *Re*, investigating the transversal forces and moments, also the trimming forces if relevant, and when possible investigating even dynamic responses.

Besides all technical aspects regarding the techniques and the tests characteristics, it is essential to build the model. Knowing how previous models have already been manufactured provides a foundation for discussing new building techniques, mitigating problems already observed and manufacture the model according to the expected campaigns. Therefore this has to be a topic of technical review as follows.

3.1.6.1 Model manufacturing

The most common construction technique observed was wooden hollow models (e.g. pine, mahogany), counting on some specific parts made of aluminum, like the nose and tail, probably due to the necessary precision. An interesting observation is that the very first models did not have cylindrical cross sections; instead of that, the cross section was a polygon. Good examples are Abbott (1931) and Freeman (1932a), whose models had 24 and 36 sides respectively. An interesting set of models was developed for the Higgins (1927) studies, when cast of aluminum machined in a lathe was the chosen technique, aiming to obtain specified ordinates measured on original models that were being used as reference for building two new “N.P.L.” models. These models had obviously to be connected somehow to a means of measuring the acting forces. Among various ways of attaching the model to the wind tunnel, using struts along the models or the classical system of cables and pulleys were the most used.

Given the need for internal space (in order to insert pressure taps, smoke hose or any other recording or test equipment), it was common to divide the models at least in two parts, some were divided in three so as to accommodate interchangeable tails (ANDERSON and FLICKINGER JR., 1954). However, a recurrent issue was the hard work for obtaining good fitting parts; their bad construction led to mistaken measurements, mainly due the interference effects and incompatible geometry. Usually, the surface finishing was very detailed and handmade. The raw model was fine sanded, varnished, painted and sanded once again, according to the expected roughness.

Nevertheless, according to Catalano (2016)[11], with the new techniques based on composite laminates, it would be possible to obtain much better geometrically coherent models. Using such approach, the models would be much lighter and easier to manufacture – requiring less time and experience, with the same stiffness and integrity of the wooden models. This would even make it easier to install and inspect the pressure taps and fixation structure. Various aircraft composite models from LAE had very fine and precise surface finishing. The same technique could be applied to the airship model. Using a sequence of fast drying compound layers combined with sanding and lacquering before painting, grants well finished surface. For the fixation it would possible to use a unique strut, easily assembled to the model and balance, and with enough strength. The simplicity of the fixation would also make it easier to reproduce it afterwards in order to extract its aerodynamics characteristics, aiming at taring the final results. This was very useful information, which contributed to the manufacture of the model used in this work (Appendix A).

3.1.6.2 Similitude

Usually, along with model definitions, the wind tunnel is also selected– size and desired analyzes are planned. The main motivation for that is the key aspect of wind tunnel testing: the similitude – similarity – of flow characteristics. When running a wind tunnel test, the challenge is to reproduce the same properties and characteristics of a full scale model flight using a smaller prototype in a controlled environment. In order to ensure that, it is typical to evaluate the fluid mechanics by means of analyzing the Navier-Stokes[12] (NS) equations.

The full set of Navier-Stokes equations, however, is very complex, what makes it unrealistic and unrevealing to work with for general solutions. Therefore, it is valid to look for approximations aiming at certain specific circumstances, supposed to be much more useful. The approximations depend upon the discernment of what is small and what is not (relevant or not for the specific case). The standard way of doing this is to first find the scales relevant to the problem, normalizing the terms by these scales, leading to dimensionless parameters which represent the relative

[11] Information obtained during discussions about the possible methods of manufacturing airship models, at LAE, considering previous works and experience acquired along years of experimental aerodynamics.

[12] Indeed, the Navier-Stokes equations are only the momentum equations, but it is accepted by some authors that the set of momentum, continuity and energy equations for fluid mechanics are the Navier-Stokes equations.

importance of various parts of the full equations (or the physical relative importance of each property) (MEI, 2016). The obtained magnitudes provide suitable approximations which can lead to the essence of the problem.

Before this, however, the scales of motion must be defined, even though some are not obvious, and they can be derived from physical considerations. For example the height of a mountain susceptible to air flow or the length of a sailing ship, is the length scale *L*. The time from the start of the wind or from the start of the ship motion can be the time scale *T* (or the inverse of a characteristic frequency - $\frac{1}{f}$). The speed of incoming wind, or the ship velocity, is the natural scales for the velocity *U*. If gravity is expected to be important, the gravitational acceleration *g* can be used as the scale of body force per unit mass (MEI, 2016). This idea must be applied to all characteristic properties present on the investigated condition.

With these terms determined, it is then possible to introduce dimensionless variables, which change the NS equations to a more comprehensible, and friendly form: the dimensionless form. The usual terms to appear, considering the full set of NS equations follow:

Figure 33 - Typical dimensionless variables for fluid mechanics.

Reynolds number	$Re = \frac{\rho v_0 L_0}{\mu}$	$\frac{\text{inertia}}{\text{viscosity}}$	Mach number	$M = \frac{\lvert \mathbf{v} \rvert}{c}$
Froude number	$Fr = \frac{v_0}{\sqrt{L_0 g}}$	$\frac{\text{inertia}}{\text{gravity}}$	Strouhal number	$St = \frac{L_0}{v_0 t_0}$
Peclet number	$Pe = \frac{v_0 L_0}{\kappa}$	$\frac{\text{convection}}{\text{diffusion}}$	Prandtl number	$Pr = \frac{\mu}{\rho \kappa}$

Source: Kuzmin (2016).

Since there is no predicted compressibility, nor heat transfer effects, the heat equation can be neglected, and terms like the Prandtl number – *Pr* and Peclet number – *Pe* are not considered. Knowing that the flow can be considered incompressible (constant density) for this work, this procedure would lead to normalized momentum equations as follows:

Figure 34 - Nondimensional form of NS momentum equations, with special numbers (coefficients) highlighted.

$$\boxed{\frac{fL}{V}}\frac{\partial \vec{V}^*}{\partial t^*} + \left(\vec{V}^* \cdot \vec{\nabla}^*\right)\vec{V}^* = -\boxed{\frac{P_0 - P_\infty}{\rho V^2}}\vec{\nabla}^* P^* + \boxed{\frac{gL}{V^2}}\vec{g}^* + \boxed{\frac{\mu}{\rho V L}}\nabla^{*2}\vec{V}^*$$

Strouhal number, where $\mathrm{St} = \frac{fL}{V}$

Euler number, where $\mathrm{Eu} = \frac{P_0 - P_\infty}{\rho V^2}$

Inverse of Froude number squared, where $\mathrm{Fr} = \frac{V}{\sqrt{gL}}$

Inverse of Reynolds number, where $\mathrm{Re} = \frac{\rho V L}{\mu}$

Source: Cimbala (2016).

The normalized equations facilitate the scale-up of obtained results to real flow conditions, avoid round-off due to manipulations with large/small numbers and show the relative importance of terms in the model equations, as expected (KUZMIN, 2016). Each of the highlighted ratios in Figure 34 measures the magnitude of the term it multiplies.

For similitude applications on incompressible flows, *Re* and pressure terms are the most relevant; when considering boundary layer thickness similitude, it is important to look at dynamic similarity, represented by *Re* and Womersley number (α) (KLINE,1986). This last coefficient is inserted in the first term in relation with *Re*, since the *St* (Strouhal number) is the ratio between α^2 and *Re*. By analyzing the terms, considering that the *Re* >> 1, and a steady flow (the time scale is large compared to L/U), the dominant terms are dependent on pressure, and the *St* could then be neglected.

For dynamic tests, looking at *St* and *Fr* is considered to be important. Analyzing the tests described in section 4.4.2, the external force (gravitational field) may be neglected, once the model is supported, and the simulated situation is a near equilibrium (neutral buoyancy). For this reason, *Fr* is not required to be equivalent.

Regarding *St*, it is known that this coefficient describes oscillating flow mechanisms, and for aircraft it may describe oscillation damping characteristics, for example those investigated along Phase II (section 4.4.2). For large numbers, the dynamics is dominated by viscous effects, whereas for small it is the high-speed portion of the motion that dominates the oscillation. The inertias of model and full scale are not going to match because a key aspect is missing: added mass. Then, it is expected that the model is going to present a lower *St* in comparison to the full scale aircraft, whose oscillations are known to be, in general, of a very low frequency (personal information)[13]. In this sense, the model would answer much more by test velocity, whereas the ship in fact would be more viscous dominated. However, in the case of this work, the dynamic tests are only for comparative purposes, in order to assess different tail configurations, and are not going to be extrapolated to full scale oscillation parameters. Moreover, inspecting the *St* term in Figure 34, it is possible to see that it multiplies the variation of velocity in time. Once again, the dynamic tests are conducted under steady air flow velocity, and this derivative may be assumed as null. This also supports the proposal of eliminating the need for correlating *St*.

[13] These are informal data gathered along the work on LTA field, by analyzing and discussing with experienced people (engineers, mechanics, pilots and etc.) about airship behavior.

In this way, only Mach number *Ma* and Reynolds number *Re* still need to be investigated and checked for similarity:

$$Re = \frac{\text{Inertial forces}}{\text{Viscous forces}} = \frac{\rho \vartheta L}{\mu}$$ Equation 16 – Reynolds number.

$$Ma = \frac{\text{Inertial forces}}{\text{Elastic forces}} = \frac{\vartheta}{\mathbf{a}}$$ Equation 17 – Mach number.

$\boldsymbol{a}$ is the speed of sound on the medium at the studied conditions.

For the stationary studies, *Re* and *Ma* are the most relevant similarity parameters. Ideally, both should match when considering model and full scale, guaranteeing that forces and moments coefficients would be the same. Considering the airship case, as stated before by the incompressible flow characteristic, *Ma* is not a challenge, and can also be neglected since model and full scale are below 0.3, and can be considered in the same low subsonic region (KHOURY, 2012).

This scenario is not the same for *Re*. Although subsonic wind tunnels in general use air at atmospheric pressure and temperature – so density (ρ) and dynamic viscosity (μ) are the same as full scale – the relation length-velocity is not preserved due to the model scale. The relation to be then fulfilled is:

$$\vartheta_{\text{model}} \cdot L_{\text{model}} = \vartheta_{\text{real}} \cdot L_{\text{real}}$$ Equation 18 – Simplified similarity for low *Ma*.

Here is stated the greatest challenge for airship wind tunnel testing: achieving the *Re* similarity. Given the large size, the length values are rather large, while the velocities are quite the same as for small airplanes. So, if the model is in a very small scale – due to the facilities or costs – the velocity must be enormous, causing usually the *Ma* similarity to fail, and of course the wind tunnel capacity as well. For example, the work presented by Gomes (1990) showed the need for 2300 m/s of wind tunnel velocity in order to preserve the *Re*, because the Skyship 600 model was 1/75 scale (also a relatively large model – around one meter long). Gomes (1990), however, affirmed that the scale factor reached (35 times smaller than full scale for *Re*) was “considered to be quite an acceptable figure for airship model testing”.

Obviously, the velocity was impracticable, and typically the researchers look for solutions; the most common, enlarging the model. However, this has a limit, mainly because of the relation between the test section and the model cross section (blockage and buoyancy effects – section 4.3.2). The wind tunnel must simulate free flight conditions, which means having the same pressure distribution over the model. If the model has a large size relative to the working section the blockage phenomenon occurs, increasing velocity around the model and decreasing pressure, besides some other effects due to the tunnel walls proximity – e.g. ground effect (BARLOW, RAE and POPE, 1999) and additional drag (longitudinal buoyancy). The point is, if the model is too small, the *Re* is not achieved, and the measurements will be also wrong because the flow characteristics are not the same. The velocity drift due to the model size can be measured by the ratio between the front model area and the wind tunnel working cross section area – blockage factor.

The *Re* correlation as can be inferred is the greatest challenge concerning wind tunnel testing, affecting the correct estimate of drag. The usual values for airplanes in general have a rough order of magnitude (ROM) of 10^6 (1.0E+06), while airships can easily reach 10^8 (1.0E+08) depending on the *AR*, volume, velocity and other factors. The ADB-3-30, for example, is expected to fly at *Re* around 3.0E+08 when at top speed. According to Curtiss, Hazen and Putman (1976 apud Cebolla, 2013, p. 34), wind tunnel tests are usually two orders of magnitude below the full scale condition, in a region called transition regime (Figure 35).

Figure 35 - Drag variation with *Re* for bodies of revolution with AR > 5.

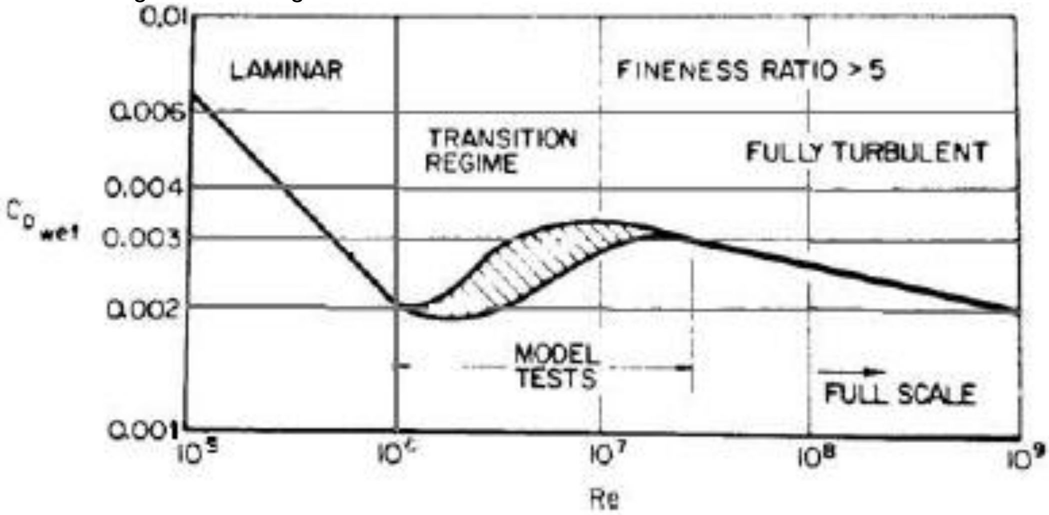

Source: Curtiss, Hazen and Putman (1976 apud Cebolla, 2013, p. 34).

A very interesting and similar chart is worth analyzing. Carichner and Nicolai (2013) plotted the skin friction coefficient (C_f) for some airships against full scale *Re* using the skin friction on a flat plate as the background. The values for the airships fell very well within the famous Schoenherr-von Kármán relationship curve. The good placement of the full scale airships C_f on this curve shows that one may assume that their behavior for this coefficient may be indeed very similar to that calculated for flat plates, regarding skin friction drag. Extrapolating it then to lower *Re* shows a similar trend as presented in Figure 35 which means it can then be used in wind tunnel models.

Figure 36 - Flat plate skin friction drag varying with *Re*.

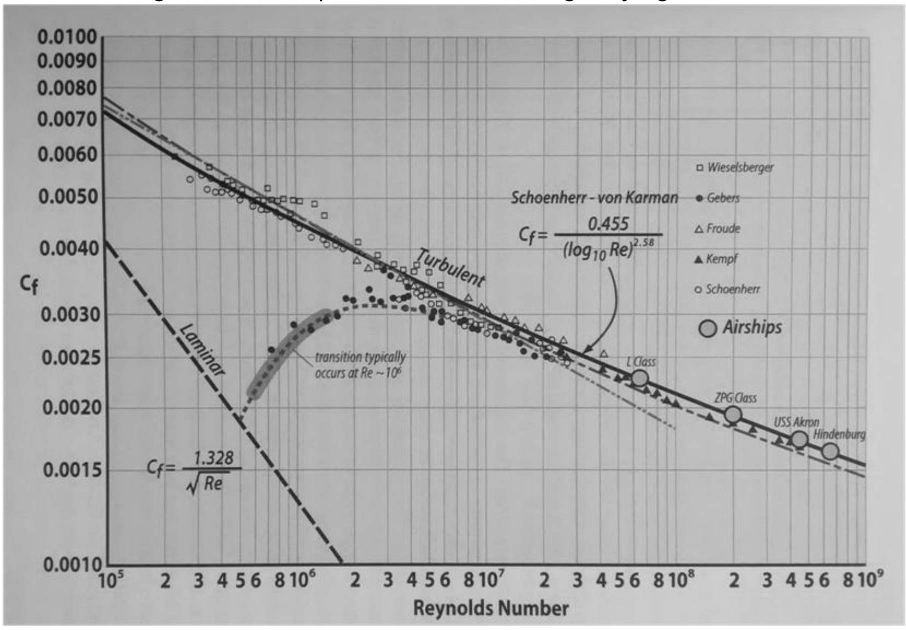

Source: Carichner and Nicolai (2013).

Anyhow, the problem of matching *Re* still persists despite being better known, at least in trend. This problem motivated many researchers to look for alternatives, more expensive and elaborate solutions – not possible for this work, but which are also feasible, such as variable density wind tunnel or towing tanks. A proposed solution was using a transonic wind tunnel at David Taylor Model Basin, increasing velocity in a medium size model (1.5 m long), making it possible to achieve *Re* = 4-12E+06 (CERRETA, 1957). Another approach, as already stated, was simply enlarging the model size to really big dimensions (5.98 m long and 1.012 m diameter) testing it at up to 100 mph, making it possible to achieve *Re* = 13-17E+06. This attempt was conducted by Freeman (1932a, 1932b and 1936) with the famous 1/40 scale model of the U.S.S. Akron.

Probably, in terms of *Re*, the best achievement was accomplished by Abbott (1931), who reproduced up to *Re* = 40E+06, by means of a variable density wind tunnel, applying 20 times the normal atmospheric pressure. During the investigations, it was found that the addition of fins and cars to airship models increased the drag by some 15% to 20% at zero pitch, at large *Re*; for smaller values, the increase can be greater. Besides that, according to Abbott (1931), for Goodyear-Zeppelin shapes, the drag had little variation between 4.8 and 7.2 fineness ratio (length to maximum diameter ratio). Nevertheless, once again in the conclusions, it is suggested that the initial degree of turbulence and the model surface roughness have a strong effect on the results, and may lead to erroneous conclusions regarding wind tunnel testing of airships.

Using the same variable density wind tunnel of the National Advisory Committee for Aeronautics, Higgins (1927) analyzed two airship models, known as the “N.P.L. Standardization models”, varying the *Re* between 110000 and 5E+06. The main objective was determining the resistance at the angle of zero pitch for both models, and for that, the velocity was set at 50 mph, varying the density from ½ atm up to 20 atm. It was possible to obtain a regular curve for the resistance coefficient, which decreased in value as the “scale” (*Re*) increased, approaching an apparent minimum at the upper limit. An interesting conclusion was that, even though the “flow scale” was 1/10 of the full scale, the nature of the curves indicated that extrapolation to determine a full-scale value for the resistance coefficient could be rather unreliable.

Nevertheless, as already cited, it is not only about reaching *Re*; it is much more because of the quest to obtain the same flowfield and boundary layer development and behavior that the *Re* is tried to be kept within the full-scale values. If the transition does not occur at the same region, the drag measurements are going to be completely wrong. As already discussed, the *Re* influences the nature of the boundary layer, and usually if it is small, it can be laminar. In the case of a scale model, this means that it can maintain a longer laminar region than would be possible in reality, decreasing, for example, the drag measured. Besides that, if the development is not the same, the thickness and velocities are not going to be the same as well (or at least scale with them), which affects directly the measurements and observation of interference effects. It is usual then to force the transition by means of trip wires or bands; their size and position are also unknown, and some parameters must be used in order to ensure that they are correct.

Though, it is necessary to ensure that the boundary layer is transitioned form laminar to turbulent flow, which is made by forcing transition. The effectiveness of such process is dependent on the employed techniques for the wind tunnel experiments. The usual solution is to change the model surface roughness, maintaining the boundary layer turbulent (GOMES, 1990). Once again, the roughness size and density have to be investigated, given the marked increase in drag due to excessive roughness. Aiming at this solution, before testing the YEZ-2A 1/75 scale model, Gomes (1990) studied the aerodynamic coefficients sensitivity to different sorts of roughness. The strategy comprised comparing the results using different surface finishing for the same airship model. The Skyship 600 airship model was very a smooth wooden model, tested with four surface roughness configurations: No stocking (the standard smooth wooden hull), Fine mesh (model covered with a fine mesh type stocking), Fishnet (model covered with a fishnet type stocking) and Nose band (the standard model with a trip nose band at the prow).

Figure 37 - Drag polars for Skyship 600 model with varying surface roughness.

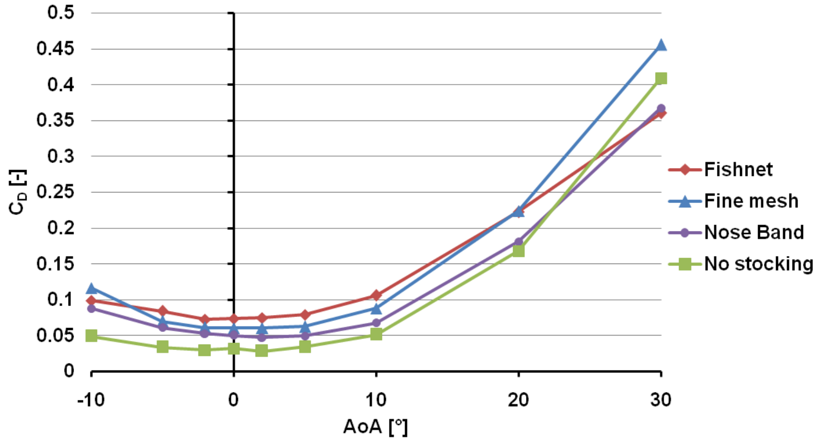

Source: Elaborated from Gomes (1990), p. 14.

The comparison among the four experiments and with previous wind tunnel tests and some flight test data showed interesting results. The lift and moment coefficients had a good agreement, indicating that the roughness had low influence on them. For drag (Figure 37), the scenario was different: with increasing roughness level, the drag also continued increasing, as expected – and predicted before, since drag is, to a considerable extent, skin friction drag. Comparing to the flight tests data, Gomes (1990) described the bare hull result as optimistic (below full scale), and the fine mesh stocking result as pessimistic, 60% greater. This led to the conclusion that the minimum degree of roughness was necessary for the subsequent airship wind tunnel testing, being noted that drag results would require some fine tuning before they could be said as really reliable. This approach limits the drag results to an acceptable range, assuring that the boundary layer is turbulent, although the *Re* is different from the full scale range.

According to Abbott (1931), it is known that the laminar boundary layer occurs only at small *Re* which is not applicable to large airships. As the *Re* is increased, the flow in the boundary layer becomes eddying (turbulent and swirling in due proportion) on the surface downstream, and the transition line progresses upstream. Usually, in wind tunnel tests, *Re* are so that the flow is a combination of laminar and turbulent, leading to the existence of a critical Reynolds Number (Re_{cr}), when the transition takes place. In many cases the drag forces of some of the models were predominantly skin-friction drag, the source being the model surface, since pressure drag was comparatively small. It could thus be shown that the drag curves resembled the curves for skin friction on flat plates.

Assuring that the wind tunnel in fact represents the reality is the main concern. The results of airship tests from wind tunnel campaigns can thus be rather inaccurate due to similitude issues, which must be previously considered during the tests planning. According to Durand (1936), there are six major phenomena that can compromise good comparative tests:

i. Pressure gradient ($\frac{\partial p}{\partial x}$) along the working section: can lead to an axial buoyancy over the model, that must be taken into account, mainly if the model is large, since its order of magnitude can be the same as the minimum measurable drag.

ii. Measurement of effective velocity head of the test: effects like solid blockage in the working section can generate velocity head variations over the surroundings of the model, accelerating the flow, and also changing the pressure distribution.

iii. Drag and flow interference: usually caused by the connecting system between model and balance, these forces are small and difficult to be determined, or even subtracted from the results.

iv. Small *Re*: leads to a larger extent of a laminar boundary layer, changing the flow characteristics, influencing mainly the drag, and thus detracting from the full scale turbulent flow that prevails throughout the body.

v. Inherent wind tunnel turbulence: it has a major influence on the boundary layer turbulence level, and for the same *Re* it may lead either to laminar or turbulent (high or low in intensity) layers. For airship models, it is suggested to artificially convert the flow to turbulent.

vi. Surface roughness[14]: some researchers have found large drag variations with varied surface finishing, while others found none. These results might be linked to the previous topic (wind tunnel turbulence) affecting the results. Nevertheless, the differences of surface finish can have a very impacting effect over the flowfield and flow characteristics, completely changing the expected similarity, and therefore this must be assessed.

Some of these effects can be predicted by means of analytical and theoretical models, such as buoyancy and blockage. Others can be evaluated in a preliminary campaign, like the influence of surface finishing and working section pressure gradient, and even the boundary layer characterization by turbulence inducers like trip wires, bands and etc. Nevertheless, some are really difficult to be evaluated without full scale tests results in order to compare and calibrate the model and wind tunnel features, such as the *Re* and turbulence level. These last ones are the challenges, and must be monitored as far as possible during the tests.

Abbott (1931) also describes at least four effects that mainly interfere on the balance measurements and must be tared. They are:

i. Forces on the model due to airstream convergence.

ii. Forces on the supports to the model.

iii. Forces due to mutual interference between model and supports.

iv. Forces due to windage on parts of the balance located outside the air stream.

These items were closely related to the applied methods for his experiments, but are worth investigating regardless of the particular tunnel and experiment. Complementarily, other aspects that deserve attention are mentioned: model vibration (unsteady flow or structure vibration) and changes in surface roughness between runs. These points are also important, because they influence directly the results, changing the accuracy level.

---

[14] As an informative note, Durand (1936) reveals that some researchers classified that, for full size airships, “both metal and well doped or rubberized fabric covered airships can probably be considered as aerodynamically “Smooth””. However, he also cites that other studies showed that to be “smooth the hull of airships should not have roughness exceeding 0.03 to 0.04 mm […], the very bow being the most sensitive”.

3.1.6.3 Recent works on airship wind tunnel testing

It is very useful comparing the pioneering research works with the more recent ones, so as to confront not only the techniques and methods available, but also the main changes in topics of interest.

The research group FOGL used three facilities during wind tunnel investigations of the LOTTE airship: the Medium Wind Tunnel (MWT), the Gust Wind Tunnel (GWT) and the Large Water Tunnel (LWT). For each of them a specific model was used based on physical and theoretical limitations. In the case of MWT, a "*Göttinger*" type wind tunnel (circular cross section and open measuring section), a nozzle of 1.75 m diameter and 24 m/s freestream velocity were employed. Complementarily, a lattice was mounted right downstream from the nozzle, increasing turbulence level from Tu = 0.01 to Tu = 0.06, ensuring such turbulence level in order to simulate the full scale patterns (LUTZ et al, 2002). This is an alternative strategy to the surface roughness method already mentioned. The model employed was 1:20 scale, made of fiberglass, laminated over two negative semi-moulds, constructed based on a CNC machined master model, guaranteeing a stable, true to contour body with fine finish (LUTZ et al, 2002). In this experiment, forces and moments on the hull were measured using a six-component balance above the working section, suspending the model with wires. The experiments were performed at the maximum flow velocity of the tunnel, reaching *Re* = 1.3E+06. The conclusions pointed to a non-linear lift curve, a high drag coefficient, due to the high turbulence level. As expected, the hull was found to be statically instable (Figure 38).

Figure 38 - Volumetric lift, drag and pitching moment coefficients for the hull of LOTTE Airship (*Re* = 1.3E+06 and Tu = 0.06).

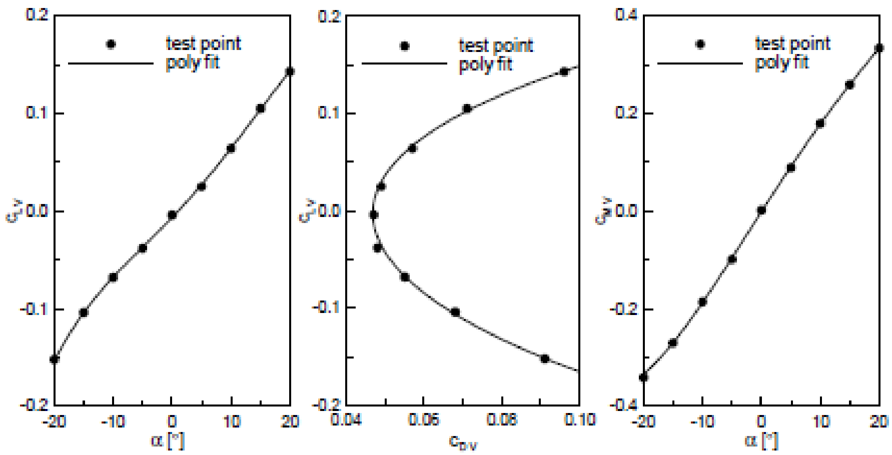

Source: Lutz et al (1998).

For the same model and wind tunnel a set of 15 single tests were carried out using a seven-hole probe in order to track and describe the vortices resulting from the lateral shear layer separations (FUNK, 1998). It was possible to confirm plausible and, in principle, matching results to the theoretical calculations. Besides that, also axial locations, position and strength of the vortex structures were determined, locating the core with extreme accuracy using this Multi Holes Probe (MHP) technique. Another interesting result was that no vortex breakdown was observed, even for the highest AoA, which was 30° (Figure 16).

Figure 39 - Lateral vortex structure along LOTTE airship model for x/**L** = 0.6, 0.8 and 1.0.

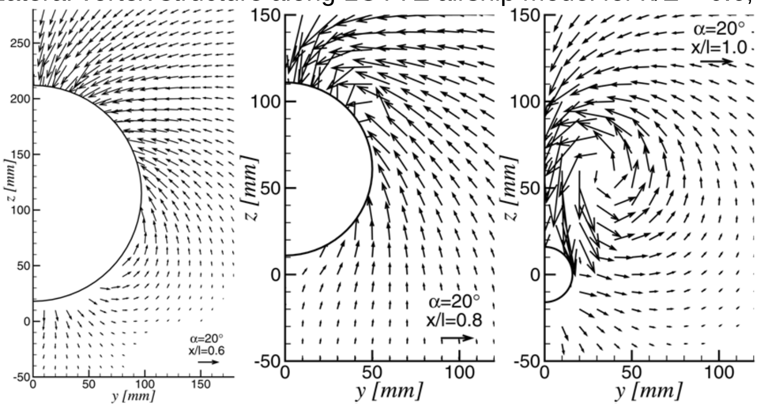

Source: Funk et al (1998).

It is very interesting to see that this mapping depicts a somewhat different pattern from what was proposed by Fairlie (1980), and was shown by Thwaites (1960). This might be so given the hull shape of LOTTE airship, which is rather different, with maximum diameter further downstream, in an attempt to decrease the adverse pressure gradient, and therefore the drag.

After the bare hull was investigated, the tail fins were added, and for several different deflection angles, the AoA was varied from -30° to 30°, in steps of 2.5°, obtaining trimming curves (Figure 40).

Figure 40 - Volumetric lift, drag and pitching moment coefficients for the LOTTE Airship with different rudder deflections (Re_V = 3.9E+05 and fully turbulent flow).

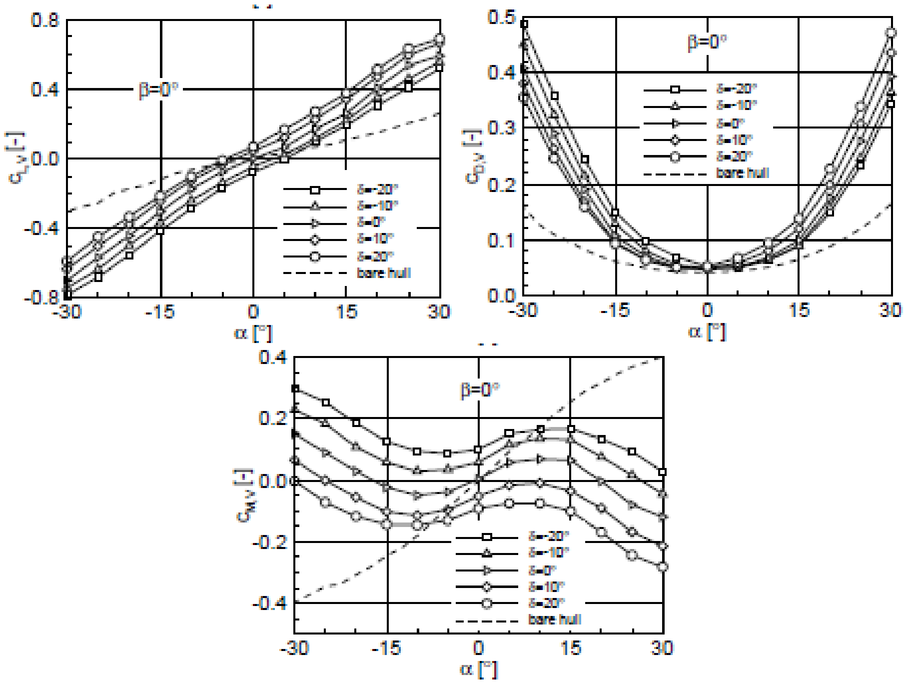

Source: Lutz et al (2002).

For all deflections, the drag curve was always parabolic, shifting towards negative AoA as the deflection increased. In spite of the shift, the ordinate was nearly independent of δ, and the axis-symmetry was found to be excellent. Regarding the lift slope, it was found that over the AoA range the coefficient varied slightly non-linearly, mainly in the central region of the curve (around zero degree). However, with increasing δ, the lift curve shifts in a positive direction with respect to the base line (δ = 0°). This means the rudder efficiency appears to be the same for small and large AoA. For the moment coefficient, the shift in magnitude was the opposite as δ increased, but again independent of the AoA value. It is interesting to notice that while -10° < AoA < 10° the configuration is unstable; out of this region, the derivative changes to negative, and the model is stable, at least around its center of volume, which was the moment reference chosen by Lutz et al (2002).

Also some flow visualization techniques were employed using MWT in order to capture some flow patterns. The limiting streamlines were visualized by means of the petroleum-soot method, providing a time-averaged picture of the real flow. All streamlines converge into specific regions: the three dimensional separation lines. From each line a vortex layer detaches, rolling up into a single vortex similar to a tip vortex type. This effect occurs for all *Re* range, affecting the pressure distribution over the hull, mainly at the suction side, generating some dynamic lift and induced drag as well. The length of this separation line depends on the AoA, causing a non-linear behavior to occur for resulting forces and moments. Besides the bare hull, some investigations were conducted on the tail region. The airship fins are usually very low aspect ratio surfaces, with large sweep angles. These characteristics lead to side edge and leading separation respectively. Besides that there is also a very strong interference between the fins and the hull, leading to a very complex flow pattern (Figure 42), making it complicated to calculate and estimate the flow field, and consequently the aircraft aerodynamic characteristics.

Figure 41 - Flow pattern of an inclined airship hull (Re = 1.5E+05 and AoA = 30°).

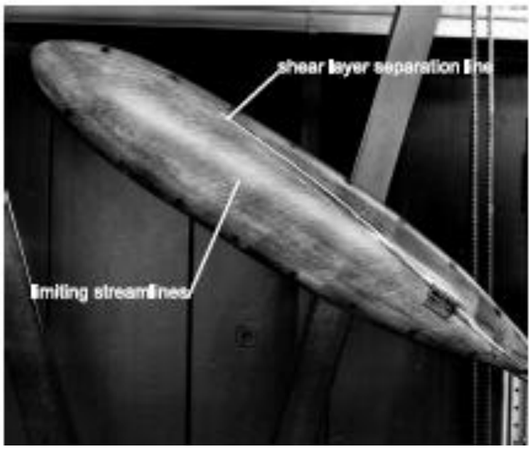

Source: Lutz et al (1998).

Figure 42 - Limiting streamlines on the suction side of a hull-fin combination (Re = 1.5E+05 and AoA = 20°).

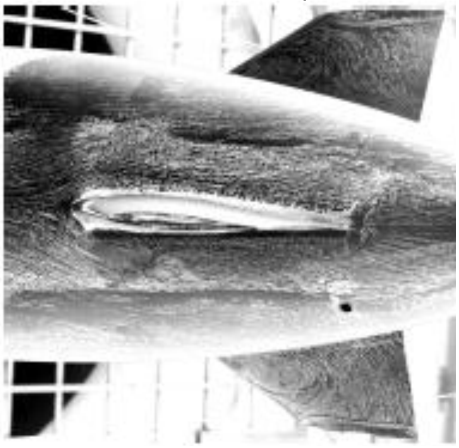

Source: Lutz et al (1998).

The GWT was used to investigate a stern-mounted model of 1/8 scale, being 2 m long. The main objective was, by adding the tail fins to the model to investigate the fins surface pressure distribution.

Considering only the airship hull, another test campaign was conducted, but in the LWT, aiming mainly at flow patterns visualization. The reason for that is that, since water has a 15 times lower kinematic viscosity when compared to air, assuming equal overall Reynolds and dimensions, the events are 15 times slower in water, being often pursued with unaided eyes (FUNK, 1998). The model was 0.60 m long, CNC machined and stern-supported. Due to the cross section (1.52 m wide and 0.76 m high), the model could not be larger because of blockage effects. The experiments were made at *Re* = 1.0E+06, forcing transition at x/**L** = 0.05. The most interesting results show the flow separation patterns (Figure 43).

Figure 43 - Surface flow patterns over the LOTTE airship hull (*Re* = 1.0E+06).

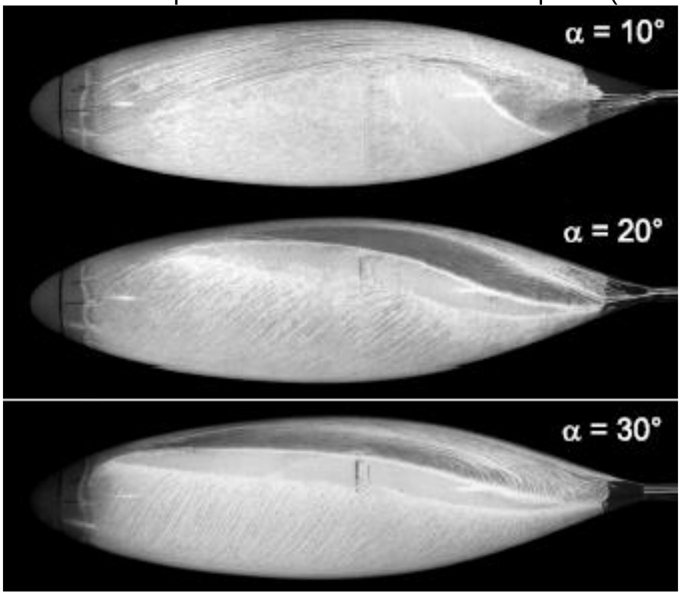

Source: Lutz et al (1998).

As the angle of attack increases, the separation region (BLACK) extends towards the body nose and downwards, establishing a clear division between a very low skin friction surface (WHITE region), and the separated region. Besides this surface investigation by means of a coating (paraffin oil, oleic acid and titanium white), another technique was used based on hydrogen bubbles visualization (LUTZ et al, 1998). This is a much more complex technique and requires smaller Reynolds numbers and also slightly turbulent flows. That is why *Re* = 0.3E+06 was achieved and the transition was natural (LUTZ et al, 1998). Using this method, it was possible to clearly see a dead air region at the stern region of the hull, attesting the longitudinal separation tendency as the hull cross section decreases (Figure 44).

Figure 44 - Flow separation over the hull surface of the LOTTE airship hull (*Re* = 0.3E+06).

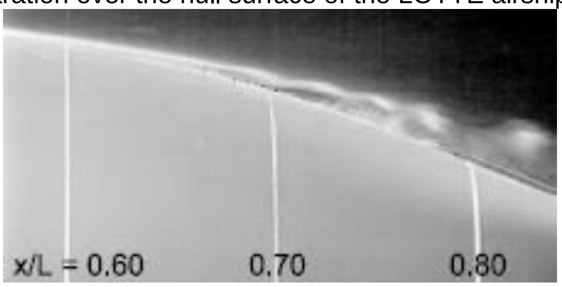

Source: Lutz et al (1998).

Another recent and very relevant research team worked on the ZHIYUAN-1 airship (WANG, 2010). The team conducted wind tunnel tests on a 1:13.7 scale fiberglass model of the airship, using a 3.2 m diameter wind tunnel with a 5 m long open test section, at 60.39 m/s speed, reaching a *Re* = 2.58E+06 (inside the real airship range, that is 1.8-9.3E+06) at a Tu = 0.1%. The model was 1.83 m long, supported by a stern bar, rigged by crossing wires, mitigating the bar vibration. The overall forces and moments were measured by means of a six-component strain balance, varying AoA from -30° to +30°, and β from -25° to +25°, at 25°C.

The experiments analyzed free and forced transition configurations. For the last one, strips were applied to the fore, middle and aft model hull surface, in order to avoid some kind of relaminarization. Comparing the results for free and forced transitions just with the hull, it was clear that drag is widely affected by the flow nature, increasing from 0.00692 to 0.0146 at AoA = 0°, respectively (WANG, 2010). As already known, for airships, the skin friction drag can represent up to 90% of the total drag (KHOURY, 2012); this means that, in a turbulent flow, since the skin friction increases, the same occurs with the final drag, almost at the some order of magnitude as the friction. However, as also expected, pitching moment and lift force were fairly affected, since they are related to the pressure distribution, which changes little due to flow nature only.

When studying the hull-fins configuration, there is a little increase in lift (the already mentioned LCO) and in static stability, as expected. However, adding the gondola to the model brings, in practical terms, no change to pitching moment and lift when compared to the just hull-fins configuration, but with an obvious increase in drag. The drag-lift curve showed a very good agreement with parabolic shapes, indicating that the theoretical approach of an almost constant friction drag plus an increasing quadratically drag-due-to-lift fits well for classical airships.

3.2 FLIGHT DYNAMICS AND STABILITY

Some researchers also dedicated time and effort to airship flight dynamics, mainly looking at stability and controllability. It is quite interesting how these topics recently raised too, probably given the new technologies regarding control systems (fly-by-wire, fly-by-light, etc) and embedded systems. The aim of this work is not, however, strongly tied to this area of knowledge, but only to some specific peculiarities, involving the tail and its efficiency variation due to interference effects. In spite of that, this investigation requires a minimum evaluation of key points and aspects, providing the foundation for discussing mostly stability variations. In this section, the most relevant works cited in section 2.4 are examined in detail, extracting information which is specifically useful for this work.

3.2.1 Dynamics foundation

As blunt and usually huge, slow vehicles, airships have a similar, but very peculiar, behavior when compared to common aerodynes, such as fixed-wing aircraft: their response time is much slower. When discussing about dynamics of any type of body, it is necessary to have relevant information, in order to characterize the body. The inertia-coefficients are maybe one of the most important parameters when studying the dynamics of a vehicle. In 1918, a reference report was published by Lamb (1918) discussing the inertia-coefficients of an ellipsoid moving in a fluid, and presenting an analytical estimate of them. This report was very useful, and many authors have since then cited its results or used them in order to produce new theories and studies. After a while, Tuckerman (1926) also studied inertia factors and aerodynamic forces on airship hulls (TUCKERMAN, 1923), providing complementary information and material in order to guide a more precise structural design as well.

Nevertheless, for all of them it was important to incorporate a specific parameter for the study of the dynamics of airships in general: the added mass – a.k.a. virtual mass (STOCKBRIDGE, CERUTI and MARZOCCA, 2012). Regarding the dynamics of an airship, it is essential to introduce the added (virtual) mass term. This term refers to the environmental (fluid) mass displaced and carried along with the body when it is accelerated. In fact, all bodies moving inside a fluid have an added mass related to it, but its magnitude is only relevant when the body grows to huge proportions, and the mass of dislocated fluid has the same order of magnitude of the aircraft mass. For buoyant aircraft the body density and the fluid density are very close, and added mass is important.

When an object accelerates, it will cause the surrounding fluid to move as well, leading to the generation of inertial loads (added masses, and consequently added inertia) that strongly affect the aircraft flight dynamics. However, so far, the methods for estimating the added mass are very poor. Usually, it is possible to assume that the added mass is equivalent to the dislocated fluid mass, using potential flow estimates (KHOURY, 2012). Munk (1924) developed a method to modify the body mass by means of inertia coefficients in order to account for added mass. For three-dimensional bodies in motion, he proposed two different methods: sum of 2D slices parallel to the incident flow and fitting the body with an ellipsoid of the same *AR* using potential flow estimates. With this, he showed that the axial motion added much less inertia to the body, than transverse motion and rotation (yawing). Hence, for the last two, the inertia factors could reach up to 96% and 89%

(*AR* = 10) against 50% for axial motion (*AR* = 1). In 2009, a numerical method was proposed for obtaining the added mass of an airship combining an aerodynamic inviscid model with a meshing technique called “Dynamic Mesh”, inside the commercial CFD code Fluent™ (WANG, 2009). According to this method, the accelerated motion of the body can be calculated, and using force balancing equations, the added mass can be determined. The results thus obtained were in good agreement with other methods, and the method demonstrated to have high efficiency and precision.

From a general point of view, an airship flying can be dynamically modeled as depicted in Figure 45. It is important to highlight that, besides the well-known CG (Center of Gravity) and AC (Aerodynamic Center), airships have another important reference point called the Center of Buoyancy (CB). Basically, this is the point where the resultant buoyant force is applied. Although it may be very complex to be precisely determined, since it is necessary to calculate the resulting buoyancy for the whole body, it is usual to neglect all appendages, and calculate the CB for the hull only. According to the United States War Department (1941), the CB is the center of gravity of the ascensional force of the gas contained in the envelope.

Since buoyancy is a force generated given the displacement of fluid, for evenly weight distributed (constant density) bodies, the CB would concur with the geometrical Center of Volume of the displaced fluid. Nevertheless, since the lifting gas (helium, for example) is lighter than air, it tends to have a higher concentration (density) in the upper portion of the envelope. In this way, since a resultant force exists even if there is a difference between air and helium densities and only the hull is considered, the CB and the CV will not be exactly the same. Nevertheless, it is usual to neglect this difference, and approximate the CB to the CV position.

Figure 45 - Static moment equilibrium condition for a conventional airship.

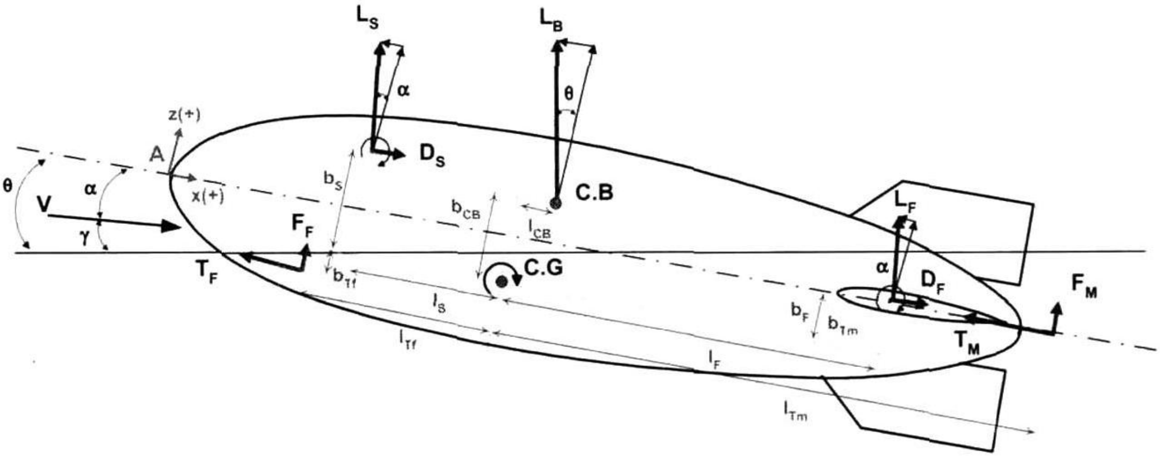

Source: Lee (2001).

With these peculiar differences in mind, the rest of the theory for airship stability and dynamics analysis is not that different from other common aircraft. It can be even claimed that they are supposed to be simpler regarding the modeling (when ignoring the aeroelastic effects – dismissed in this work). Usually the airship is modeled as a rigid body with six DoF, three translational and three rotational, resulting – like for airplanes – in six nonlinear equations that represent its motion (STOCKBRIDGE, CERUTI and MARZOCCA, 2012).

$$\begin{bmatrix} \mathrm{m}\mathbf{E} + [\mathbf{M}'] & -\mathrm{m}\mathbf{r}_{\mathbf{G}}^{\mathrm{x}} \\ \mathrm{m}\mathbf{r}_{\mathbf{G}}^{\mathrm{x}} & \mathbf{I_0} + [\mathbf{I_0}'] \end{bmatrix} \begin{bmatrix} \dot{\mathbf{v}}_{\mathbf{0}} \\ \dot{\boldsymbol{\omega}} \end{bmatrix} + \begin{bmatrix} \mathrm{m}(\boldsymbol{\omega} \times \mathbf{v_0} + \boldsymbol{\omega} \times (\omega \times \mathbf{r_G})) \\ \boldsymbol{\omega} \times ([\mathbf{I_0}]\boldsymbol{\omega}) + \mathrm{m}\mathbf{r_G} \times (\boldsymbol{\omega} \times \mathbf{v_0}) \end{bmatrix} = \begin{bmatrix} \mathbf{F_0} \\ \mathbf{T} \end{bmatrix}$$

Equation 19 - The airship motion equations. Source: Stockbridge, Ceruti and Marzocca (2012).

The clear differences are the added mass and added inertia matrices (designated by the apostrophe). The forces matrix, as usual, contains weight, aerodynamic forces and moments, propulsive forces and all the other natural external forces, considering, in the case of airships, the buoyancy force obviously. Lee (2001) reinforces these differences treating them as unique features. According to him, airship flight characteristics are similar to fixed-wing aircraft, but the theory is not as mature as for airplanes. Unique features as the cited virtual mass, virtual inertia, buoyancy and others which are usually disregarded, must be considered in this case.

These equations can be linearized and decoupled into two independent systems of equations that represent the longitudinal and lateral modes of the vehicle. The linearization procedure is based on the trim conditions for equilibrium flight (neutral buoyancy (LEE, 2001)), while the velocity components are treated as perturbations about the trim velocity (STOCKBRIDGE, CERUTI and MARZOCCA, 2012). This can be then represented in a state space form that comprises the state and the control matrices, besides their respective vectors.

$$\dot{\boldsymbol{x}} = \boldsymbol{A} \cdot \boldsymbol{x} + \boldsymbol{B} \cdot \boldsymbol{\eta}$$ Equation 20 - Space state representation.

A and *B* are the state and control matrices, while *x* and *η* are the state and control vectors. The longitudinal state components consist of the pitch rate, axial velocity and normal velocity, which are respectively affected by throttle, propeller pitch angle and symmetric elevator deflection, from the control vector. For the lateral state, yaw rate, roll rate and lateral velocity are affected by symmetric rudder deflection and differential elevator and rudder deflection (STOCKBRIDGE, CERUTI and MARZOCCA, 2012).

3.2.2 Stability and control

Specifically speaking about stability, the most widely known feature about airships is that, as determined by Munk (1924), the body has an unstable pitching moment due to the added mass terms, causing also the yaw rotations to destabilize. However, there are ways of stabilizing it, for example, using the viscous effects on the stern portion to which are added the empennage effects, counterbalancing the divergence effect, stabilizing the vehicle along with other aerodynamic forces (STOCKBRIDGE, CERUTI and MARZOCCA, 2012). This shows that, even though the dominant amount of lift in an airship comes from the buoyancy force, aerodynamic effects are the leading features for stability determination. To differentiate static from dynamic stability is very important, since airships are intrinsically statically unstable for a certain range of incidences, despite the possibility of ensuring dynamic stability characteristics (LEE, 2001). While static stability is assessed by investigating $C_{M\alpha}$ and $C_{n\beta}$ (negative values mean stable configurations), dynamic stability is related to the eigenvalues obtained from the solutions of Equation 20.

In 2000, a very relevant work regarding airship stability presented the main longitudinal and lateral-directional modes for airships (COOK, LIMPSCOMBE and GOINEAU, 2000), deriving and expressing approximate models of each mode in terms of simple aerodynamic stability derivatives. The neutrally buoyant airship is concluded to be always stable in all modes from hover over to the whole speed envelope. However, during hover all modes are nearly neutrally stable. Complementarily, it is stated that during hover, the aerodynamic effects over the stability modes are very small – not necessarily negligible, being dominated by the added mass and inertia. Another important conclusion, which directly influences this work, is that there is a transition velocity (around 10-15 m/s) where the longitudinal stability modes start to change appreciably and quite abruptly. This resembles one of the proposed aspects of the study from Crema and Catellani (1983), where it is stated that there is a need for more studies and development on the controllability at low speeds for airships.

According to Cook, Limpscombe and Goineau, 2000, the longitudinal modes are comprised of:

- Surge mode: caused by axial aerodynamic drag.
- Heave-pitch subsidence mode: caused by normal aerodynamic drag.
- Oscillatory pitch-incidence mode: caused by the relative position between center of gravity and center o buoyancy.

, and the lateral-directional modes are comprised of:

- Sideslip subsidence mode.
- Yaw subsidence mode.
- Oscillatory roll pendulum mode.

Lee (2001), almost at the same time, developed a very interesting applied investigation on static and dynamic stability of a 50 m long, 4000 m^3 non-rigid airship. Along his work, he compared the results for two different *AR* NACA 0006 fins: KA002Y (*AR* = 1.5) and KA003Y (*AR* = 1.7). He was able to conclude that the airships were statically unstable for small AoA ranges, up to 12°, but dynamically stable. For the first evaluation, using CFD estimates, he compared his results to those obtained by Freeman (1932a) on the 1/40 scale model of the AKRON, by means of analyzing C_{M0} and C_{α}. According to his work, the obtained instability range is the major difference of airships when compared to fixed-wing aircraft. For the second assessment, the dynamic, based on Gomes (1990), he derived linear and nonlinear dynamic equations of motion, fed them with the applicable derivatives

In 2003 a work presenting a series of flight tests using a full scale blimp conducted by Yamasaki and Goto (2003[15] apud Stockbridge, Ceruti and Marzocca, 2012) was published. The airship was equipped with feedback systems for stabilizing yawing and pitching motions. By means of a sensor system, the motion and control outputs were successfully compared to estimated analytical values, analyzing even the added mass effects and the stability derivatives. Some years later, some investigations on controllability and stability of airships were carried out using the LOTTE airship, of which the basic dynamic characteristics were determined from flight data records (KORNIENKO, 2006). The investigation aimed at gathering information under different flight and configuration conditions considering a linear model.

3.2.2.1 Stability of uncontrolled motion

In general, when flying, aircraft are always subject to momentary disturbances, mainly coming from atmospheric changes, such as gusts, density variation and so on. As such, it is clear that this is also relevant for LTA aircraft, especially airships, which strongly depend on atmospheric conditions. It is then vital to guarantee that the aircraft responds adequately to such perturbations to steady flight. Adequately means it must be safe, controllable and the least sensitive to the medium as possible. In other words, it is expected that the aircraft can deal, in some manner, with such external disturbances, and present a good behavior after their cessation, damping any remaining oscillations, and finally returning to the previously steady flight path.

Such characteristics describe what is called a statically and dynamically stable aircraft. Without control inputs, the aircraft keeps the disturbances to an acceptable level, even damping them, helping either a human (pilot) or some sort of automatic control system to bring the aircraft back to its original track quickly, if so desired. The stability of uncontrolled motion is exactly how the aircraft by itself – with no control input – behaves after the perturbations. For conventional airships, the natural oscillatory modes, which are the possible airship behaviors due to external perturbations, were already listed in section 3.2.2.

[15]YAMASAKI, T. and GOTO, N. Identification of blimp dynamics via flight tests. In: Transactions of the Japan Society for Aeronautical and Space Sciences, Vol. 46, No. 153, 2003, p.195-295.

During the design phases, it is necessary to predict the aircraft behavior, designing it so it behaves as expected, keeping the disturbances to acceptable levels. This is typically made through the application of small-disturbance models. According to Etkin and Reid (1996), the small-disturbance model is actually valid even for disturbance levels considered quite violent to occupants in general, meaning that it is more than sufficient for the purposes discussed here.

The basis for the small-disturbance model is the matrix equation (Equation 19). In the case of uncontrolled stability investigation, η (control vector) of Equation 20 is zero, resulting in:

$$\dot{\mathbf{x}} = \mathbf{A} \cdot \mathbf{x}$$[16]

Equation 21 - Space state representation of uncontrolled motion. Source: Etkin and Reid (1996).

Such first-order differential equations have well-known solutions of the form:

$$\mathbf{x}(\mathrm{t}) = \mathbf{X}_0 \cdot \mathrm{e}^{\lambda \mathrm{t}}$$

Equation 22 - Uncontrolled motion generalized solution. Source: Etkin and Reid (1996).

, where

$\mathbf{X}_0$ = an eigenvector of the system
λ = an eigenvalue of the system

Substituting the general solution into the equation, it leads to a system of *N*[17] homogenous equations, whose determinant must be equaled to zero so there is a nonzero solution for $\mathbf{X}_0$. This conditions leads to the characteristic equation of the system, which is of the N^{th} degree. This equation has, in general, *N* roots λ_i, some real and some conjugate complex pairs. Corresponding to each of these λ_i, there is an eigenvector (in the case of the complex pairs, there is also a complex pair of eigenvectors). Each of those solutions is the so-called natural mode (section 3.2.2), and the aircraft response is a linear sum of all corresponding individual solutions:

$$\mathbf{x}(\mathrm{t}) = \sum_{\mathrm{i}} \mathbf{X}_0 \cdot \mathrm{e}^{\lambda_{\mathrm{i}} \mathrm{t}}$$

Equation 23 - Most general solution for uncontrolled motion. Source: Etkin and Reid (1996).

Based on this, and the work presented by Cook, Limpscombe and Goineau, 2000, and by Etkin and Reid (1996), depending if λ_i is real or complex, the mode can be either steady or oscillatory, respectively. Besides that, depending on the sign of the real part of λ_i, the mode may grow or decay. The obtained solution determines whether the external disturbance will increase (instability) or decrease (stability) with time, in a manner that is steady (static) or oscillating (dynamic). Although it does not

[16] Bold symbols mean vector or matrix variables.
[17] *N* means any number of a determined quantity.

provide information on handling qualities, for a simple evaluation of aircraft stability, checking the sign of Re(λ_i)[18] should be enough.

For oscillatory modes[19], it is usual to expand the λ_i complex terms in order to convert them into real observable motion. Through this expansion, a linear combination of trigonometric functions, sine and cosine, is obtained. Assuming $\lambda_i = n \pm i\omega$, as proposed by Etkin and Reid (1996), one may reach:

$$\begin{aligned} x(t) &= a_1 \cdot e^{(n+i\omega)t} + a_2 \cdot e^{(n-i\omega)t} \\ &= e^{nt} \cdot (A_1 \cdot \cos\omega t + A_2 \cdot \sin\omega t) \end{aligned}$$

Equation 24 - Oscillatory mode generalization.

This generalized solution for an oscillatory mode can still be simplified further. Combining sine and cosine, and knowing that their functions are out of phase by $\frac{\pi}{2}$ rad, it is possible to combine both into a single function, adding a phase term φ.

$$x(t) = A \cdot e^{\boldsymbol{b}t} \cdot \cos(\omega t + \varphi)$$

Equation 25 - Oscillatory mode generalization simplification.

, where

A	= amplitude, [m]
$\boldsymbol{b}$[20]	= logarithmic decrement, [rad.s^{-1}]
ω	= damped natural frequency, [rad.s^{-1}]
φ	= phase, [rad]

Each term of Equation 25 has a specific physical meaning when looking at the oscillatory motion, as their meanings imply this being the harmonic oscillator position equation (FITZPATRICK, 2018). However, it is interesting to focus on the logarithmic decrement, ***b***. This exponent is a reference for how quick the oscillation damps out or diverges, if it is positive. The plot of $e^{\boldsymbol{b}t}$ is called the decay envelope, and constitutes the curve that connects all wave peaks, and represents very well the way the solution behaves over time, regarding the amplitude of the motion.

Figure 46 - Typical damped oscillation representation.

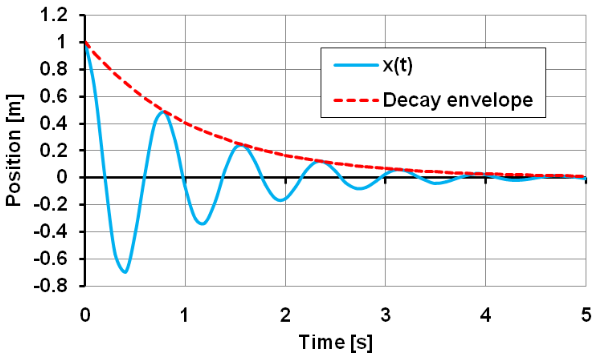

Source: Author (2018).

[18] Term denotes real part of λ_i).
[19] An oscillatory mode will be assessed through wind tunnel testing, and therefore its solution will be further detailed here in order to support the evaluation of the results.
[20] ***b*** and **ζ** are integers despite the fact of being in bold.

Besides that, the damped natural frequency is determined in terms of two other terms: natural frequency, ω_0, and damping ratio, $\boldsymbol{\zeta}$, through the following equation:

$$\omega = \omega_0 \cdot \sqrt{1 - \boldsymbol{\zeta}^2}$$

Equation 26 - Damped natural frequency definition.

The logarithmic decrement, ***b**,* is related to the same terms, but in a different way:

$$\boldsymbol{b} = \omega_0 \cdot \boldsymbol{\zeta}$$

Equation 27 - Logarithmic decrement definition.

The damping ratio value defines how quick the motion reaches the equilibrium position. If $0 < \boldsymbol{\zeta} < 1$, the oscillation is called underdamped, and it takes full oscillations in order to reach equilibrium, with subsequent decreasing overshoots. For $\boldsymbol{\zeta} = 1$, the system is called critically damped, and this is the threshold between oscillatory and steady motion. Finally, $\boldsymbol{\zeta} > 1$ defines an overdamped system, and no oscillation is observed at alll. The main difference is that critically damped systems require the minimum amount of time to reach equilibrium. The oscillatory modes for aircraft are well modeled as underdamped systems, although some modes, as explained above, show a steady behavior, converging or diverging, being critically or overdamped.

Based on this, it is possible to qualitatively evaluate how the exponential term, ***b***, essentially determined by the damping ratio $\boldsymbol{\zeta}$ and the natural frequency ω_0, affects aircraft flight in general. The larger the damping ratio, the quicker the system damps out to zero, and the better the configuration is regarding stability. However, if the damping happens to be very aggressive, controllability is strongly affected, and maneuvering the airship may be rather difficult. This is explained by the fact that if the aircraft tends to come too quickly to an equilibrium position, it also means that steering it to another direction, entering a curve for example, is going to be also very difficult. This is true because the control input is going to be physically sensed exactly as an external perturbation. So, as soon as the aircraft leaves the equilibrium position, it is going to tend to damp the input, offering an opposition to the desired change in motion. Besides that, it also means that the aerodynamic loads are very high, requiring an excessive weight during structural design. On the other hand, if the aircraft tends to oscillate for a long period before reaching the equilibrium position, it is clear that the stability is poor, although present. It is then going to be difficult to keep the aircraft in a desired attitude if any perturbation affects it during flight, even with pilot input. Truly, it is even going to be much more sensitive to inputs, characterizing a potential danger to the system in cases like Pilot Induced Oscillation (PIO), better explained in section 3.2.2.2.

Defining the adequate level of stability is very dependent on the required aircraft mission. For example, for transport category aircraft, stability is mandatory, since the main purpose of the aircraft is to carry people from one place to another safely, without harm, and in a comfortable manner. However, if it is required to pursue enemy aircraft and protect national borders, avoiding incoming artillery in flight, a high degree of maneuverability is desired. This means in other words that stability must but put apart in favor of controllability. It also requires more efficient and active means of controlling of the aircraft, either by human or more sophisticated automatic systems, depending on the stability level desired.

Airships are much more linked to normal and transport categories, as can be seen from the available certification bases (FAA P8110 Airship Design Criteria - ADC, Transport Airship Regulations - TAR and *Lufttüchtigkeitsforderungen für Luftschiffe der Kategorie Normal und Zubringer* - LFLS). In this way, a good degree of stability is desired, so passengers of sightseeing tours are not going to feel dizzy or miss the opportunity of seeing the views because of flight oscillations. For the ADB-3-30, which will aim to carry large amounts of cargo, stability is crucial, ensuring track steadiness, low disturbances and reduced pilot efforts for long journeys, and also eliminating the need for very complex automatic control systems. These considerations are crucial for design definitions at the very early stages.

3.2.2.2 Tail fins: stability and controllability

In spite of a considerable number of experiments and efforts carried out analyzing and estimating the stability and dynamics of airships, little has been done so far regarding tail fins design reflecting airship characteristics. The surfaces are known to be based on symmetric airfoils, low aspect ratios and positive sweeps, but only a few researchers and designers come out with a design methodology for that, focused on stability and control.

This may be so due to the limited number of successful airships which made history, which makes the available database rather poor for employing parametric design methodology, for example. Rizzo (1924) conducted one of the most interesting works regarding airship tail fins evaluation, and design guidance. In his works he evaluated three different fin areas: standard, 75% and 150% of the original area. In addition, keeping the same area, he varied the *AR* to 75% and 150% of original value, besides testing three different planforms: original, rectangular and balance rudder types. His last evaluation comprised analyzing the surface thickness influence on the airship characteristics, testing the original thickness and another two: 50% and 12.5% of the original. Summarizing the results, he reached expected conclusions such as larger areas provide better stability, increasing tail lift but also drag, proportionally to the area. For the specific airship, the increase also showed to be more advantageous for horizontal tail. It was demonstrated that a higher *AR* was recommended in that case, improving moment generation and lift. However, a higher *AR* also increased overall drag. It was perhaps caused by having a larger spanwise surface exposed to high velocities (outside the boundary layer). The rectangular shaped tail was the best among the tested options, improving moment generation and lift, and followed very closely by the rudder balance configuration, which surpassed the lift generation of the rectangular shape for AoA > 12°. Finally, despite the fact that the lowest thickness resulted in the highest drag, it provided the best results for lift and moment generation. All those results help, by means of observable results related to physical changes, to get a better understanding tail fins effects on stability.

Figure 47 - Tail modifications tested for the 1/153 scale model of the L-33 airship.

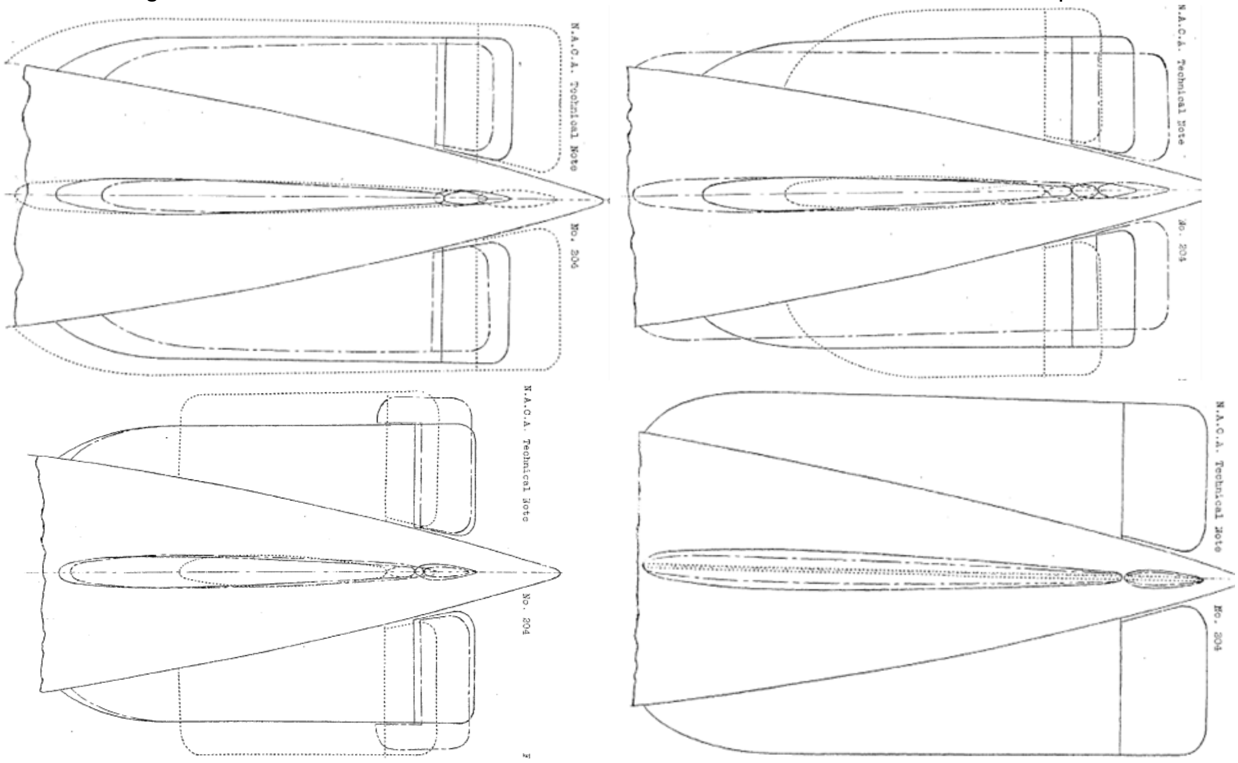

Source: Rizzo (1924).

More recently, an evaluation regarding scalability of airship design has been produced, resulting from a cooperation between the former head of Cargolifter CL-160 design and the University of Stuttgart, *Dr.-Ing. Schäfer* and *Prof. Dr.-Ing. Kröplin*, respectively. The study addresses all design areas, breaking expectations that only the "cube-cube-law" is valid by showing that several other aspects affect the design of an airship, including changing the scale relationship (SCHÄFER and KRÖPLIN, [201-?]).

Regarding aerodynamics and flight mechanics, it first discussed inertia scalability. Since the translational inertia scales with the volume (d^3) and the rotational inertia (around longitudinal or lateral axes) scales with the fifth power (d^5), an explanation of why small airships get a satisfactory behavior in rotation with only one lateral thruster (fore or aft), whereas the large ones need both (bow and stern) in order to suppress the translational movement, is given. Then, based on this conclusion, and mentioning Stinton's "response to control factor - *RCF*" (1997[21] apud Schäfer, 2015) (aerodynamics d^2 / inertia d^3), a comparison between airships and airplanes is made, bringing to light the airplanes PIO effect for small or marginally stable aircraft.

With this, the need for a huge aerodynamic force to get a small reaction is explained, comparing the LOTTE and the CL-160 airships. Comparing them both at their operational speeds, the *RCF* ratio is 16:1. However, there is a dynamic pressure difference (ratio of 1:9), which must be take into account, resulting in a final ratio of 2:1 in the response to control efficiency, respectively. It is also concluded that the CL-160 would be expected to react more markedly in a translational movement, while the LOTTE would react quicker to rotational inputs. Besides that another fraction of reduction is expected for the bigger airship because of the smaller relative control surface area.

Beyond this analysis, the classical elevator reversal effect is also discussed, since it has some scale influence as well. It occurs when the pilot applies a pitch up command, generating a downforce at the tail, in order to climb with the airship at equilibrium. At first, while this aerodynamic downforce resulting from the elevator command holds, the inert airship sinks instead of climbing, until it rotates and produces positive dynamic lift. This effect is determined by the elevator reversal

[21]STINTON, D. The design of the aeroplane. 1997, p. 571.

speed, at which the airship path will not be affected by a pitch up command as the nose-up moment balances up with the pendulum stability (restoring moment) (MOWFORTH, 1985); below this value, the resulting movement is therefore in reverse, downwards.

Figure 48 - Low-speed control reversal dynamics schematic.

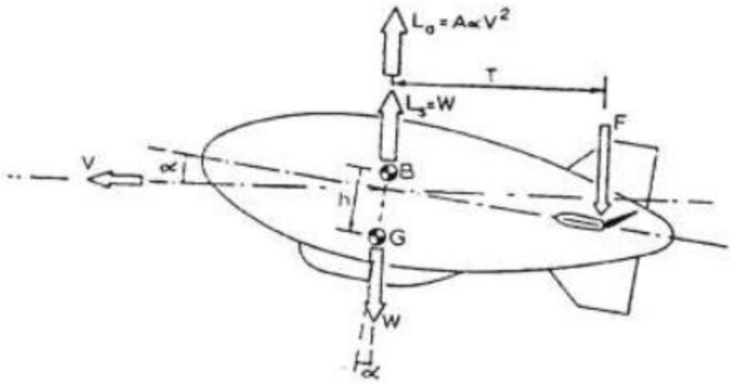

Source: Mowforth (1985).

The relationship of this effect with the properties of the ship is established considering its size, the CG-CB distance and the aerodynamic characteristics. According to the Figure 48 diagram and considering the airship to be neutral and suddenly tilted, it is possible to calculate the control reversal speed:

$$\vartheta > \sqrt{\frac{W \cdot h}{K \cdot T}}$$

Equation 28 - Control reversal speed definition.
Source: Mowforth (1985).

K in Equation 28 is a constant of a specific airship, while the other variables are depicted in Figure 48. It is also possible to investigate this condition considering the aerodynamic pitching moment and the gravitational moment as equal to each other, and applying the derivatives. After simplifications and linearizations, this approach would lead to:

$$\vartheta^2 = \frac{2 \cdot \bar{Z}_G \cdot V^{1/3}}{\frac{\partial C_{M(hull)}}{\partial \alpha} + \bar{x}_F \cdot \frac{\partial C_{L(hull)}}{\partial \alpha}}$$

Equation 29 - Control reversal speed definition.
Source: Schäfer and Kröplin ([201-?]).

, where

$\frac{\partial C_{M(hull)}}{\partial \alpha}$	= hull pitching moment derivative with AoA, [1/°]
$\frac{\partial C_{L(hull)}}{\partial \alpha}$	= hull lift coefficient derivative with AoA, [1/°]
$\bar{Z}_G$	= vertical distance (parallel to hull radius) between CB and CG, [m]
$\bar{x}_F$	= longitudinal distance between CB and tail CP, [m]

Equation 29 is derived based on Figure 49.

Figure 49 - Control reversal speed dynamics schematic.

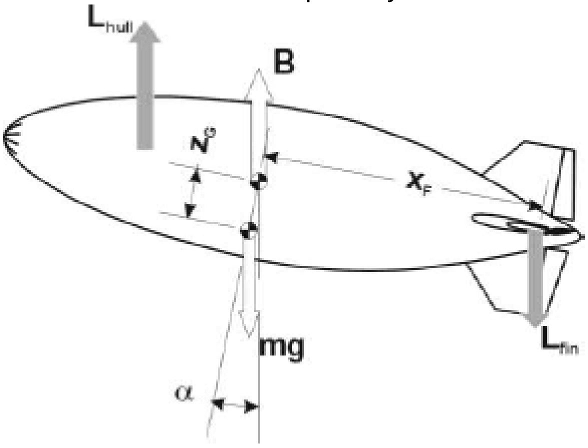

Source: Schäfer and Kröpling ([201-?]).

Deriving the reversal speed, it is possible to conclude that it scales with the square root of the size. However, curiously, it seems that this speed is not affected by tail aerodynamics, but only slightly by its position (SCHÄFER and KRÖPLING, [201-?]).

However, all of this evaluation proved once again that estabilshed configurations are usually considered, and not the development and design of a new one. According to Schäfer (2015), there is a divergence among designers about tail size and location. By comparing some designs, one can infer that, for example, on Goodyear airships the fins are well aft and smaller, in relative size, when compared to the Skyship series. It is pointed out that there are some indexes that can be used to evaluate the stability, but they are way complex and a little bit limited or too detailed. The first and simpler method depends only on geometrical aspects, despite including also the added mass coefficients, which are not very easily defined[22]. However, it does not address the airship overall length for example, which seems to weaken this estimate.

$$I_G = \frac{\left[S_1 + \frac{S_2}{2}\right] \cdot l_1}{\left[1 + \frac{\frac{2 \cdot (S_1 + S_2)}{2}}{b^2}\right] \cdot V \cdot (k_1 + k_2)}$$

Equation 30 - Geometric dynamic stability index. Source: Schäfer (2015).

, where

S_1	= exposed empennage area
S_2	= envelope are between opposite fins
l_1	= tail moment arm (CB to CP)
b	= empennage span tip to tip
V	= envelope volume
k_1	= longitudinal additional mass coefficient

[22] No details on the added mass coefficients are provided, and therefore it is not possible to determine the dimensions with accuracy.

k_2 = lateral additional mass coefficient

The second method requires the designer to have aerodynamic derivatives estimated, including also some dynamic ones, and defining different values for lateral and longitudinal movements. This last one requires a lot of iteration loops, and an intermediate to detailed knowledge of the airship characteristics. The lateral and longitudinal stability indexes are defined differently.

The longitudinal aerodynamic index is given by the following relationship:

$$I_{Along} = \frac{\partial C_M}{\partial \alpha} + \left[\frac{\frac{\partial C_L}{\partial \alpha} \cdot \frac{\partial C_M}{\partial \dot{\alpha}} - \frac{\partial C_M}{\partial \alpha} \cdot \frac{\partial C_L}{\partial \dot{\alpha}}}{2 \cdot k_x} \right]$$

Equation 31 - Longitudinal aerodynamic stability index. Source: Schäfer (2015).

, where

k_x = longitudinal virtual mass coefficient (t = 1 + k_1)

All other terms are as already defined, while α is the AoA.

For this index, satisfactory stability was found with a range of values contained between -0.32 to -0.58. The lateral aerodynamic index is given by the following relationship:

$$I_{Alat} = \frac{\partial C_n}{\partial \Psi} + \left[\frac{\frac{\partial C_Y}{\partial \Psi} \cdot \frac{\partial C_n}{\partial \dot{\Psi}} - \frac{\partial C_n}{\partial \Psi} \cdot \frac{\partial C_Y}{\partial \dot{\Psi}}}{2 \cdot k_x} \right]$$

Equation 32 - Lateral aerodynamic stability index. Source: Schäfer (2015).

, where

k_x = lateral virtual mass coefficient (t = 1 + k_1)

C_n = yawing moment coefficient

All other terms are as already defined, while ψ is the yawing angle.

For this index, satisfactory stability was found with a range of values contained between -0.332 to -0.526.

Besides that, some of those coefficients (range of results) were never tested nor had results contaminated by mistaken test campaigns. This leads to a scenario of uncertainty and non-standardization regarding design methodology, mainly when considering the rising number of airship companies in the world nowadays.

On the other hand, Burgess (2004) presents an extremely simple coefficient for preliminary design purposes regarding tail surfaces. Some designers have based their initial design on maximum airship cross section area, but coefficients based on this parameter would vary widely with different *AR*. Therefore, based on volumetric length, $V^{\frac{1}{3}}$, and changing *AR* = **L/D$_{\text{máx}}$** to *ARb* = **L/**$V^{\frac{1}{3}}$, introduced also in order to consider noncircular cross sections, a table containing the vertical (*Av*) and horizontal (*Ah*) tail surfaces areas for some airships is presented.

Table 4 contains the total fin area, including the control surfaces. Typically, the surfaces are laterally (spanwise) extended up to nearly maximum hull diameter, and the chord length of the control surfaces is equivalent to 30% of the span of such surfaces, being equivalent to less than 20% of the total fin area.

Table 4 - Burgess' (2004) database on airship tail areas.

Type	**Designation**	**Nation**	**Volume (air displaced) [ft3]**	**Length [ft]**	**Volumetric length [-]**	***Av* [ft²]**	***Ah* [ft²]**	**Fv (Mean value = 0.151)**	**Fh (Mean value = 0.172)**
Nonrigid	S.S.Z	G Britain	70000	143	3.47	230	284	0.135	0.167
	N.S.	G Britain	360000	262	3.68	742	1124	0.147	0.222
	C	USA	180000	192	3.40	424	538	0.133	0.169
	J	USA	175000	168	3.00	455	492	0.145	0.157
	Zodiac	France	328000	262	3.80	881	838	0.185	0.176
	Astra	France	340000	262	3.75	862	1293	0.177	0.265
Semi-rigid	M	Italy	441000	269	3.53	1120	647	0.193	0.112
	O	Italy	127000	177	3.52	494	263	0.196	0.104
	P.V.	Italy	176000	203	3.62	598	617	0.190	0.196
	Roma	Italy	1250000	410	3.81	1015	1446	0.087	0.125
Rigid	R-9	G Britain	930000	526	5.39	1676	2620	0.176	0.275
	R-23	G Britain	1040000	535	5.28	1880	2280	0.183	0.222
	R-31	G Britain	1610000	615	5.25	2060	2191	0.150	0.159
	R-38	G Britain	2860000	695	4.90	2617	2938	0.130	0.146
	L-33	Germany	2100000	643	5.02	1876	2505	0.114	0.153
	L-49	Germany	2100000	643	5.02	1864	2456	0.114	0.150
	ZR-1	USA	2290000	676	5.13	2335	2870	0.134	0.165
	ZR-3	USA	2760000	656	4.68	2510	2510	0.128	0.128

Source: Burgess (2004).

By plotting the individual areas divided by the volumetric length, Fv and Fh are defined as reference coefficients. The charts are plotted below, with corresponding linear trend equations, where x is *ARb*, and y is the respective coefficient.

Figure 50 - Fv (left) and Fh (right) coefficients obtained from Burgess (2004).

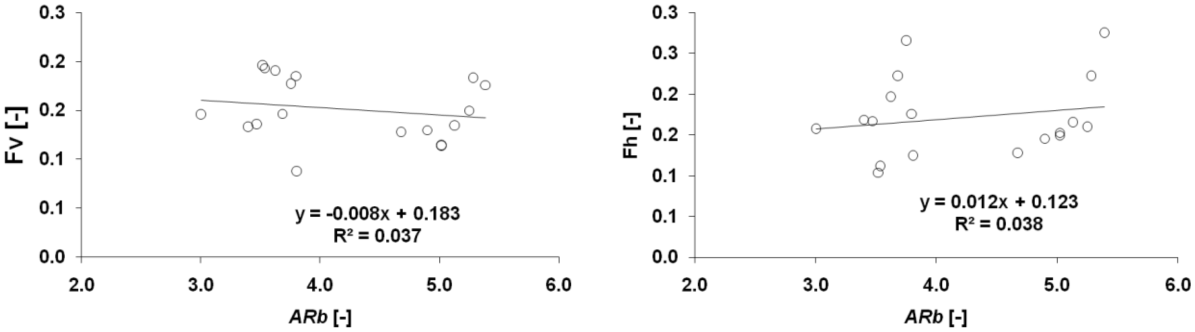

Source: Elaborated from Burgess (2004).

As depicted in Figure 50, it is rateher difficult to fit a trend to the values. Nevertheless, if one decides to consider the mean values of Fv and Fh, they are 0.151 and 0.172 respectively. Based on these coefficients, Burgess (2004) proposes that, until corrected by stability criteria derived from wind tunnel tests, it is adequate to consider the total horizontal and vertical tail individual areas as follows:

$$A = 0.13 \cdot \mathrm{V}^{\frac{2}{3}}$$

Equation 33 - Burgess' tail design criterion. Source: Burgess (2004).

, where

A	= horizontal or vertical tail planform area, [ft²]
$\mathrm{V}^{\frac{2}{3}}$	= volumetric area, [ft²]

It is important to highlight that all airships analyzed by this study had cruciform ("+") tail arrangement, which is a clear limiting design point, besides the already demonstrated scatter. Complementarily, derived from some wind tunnel tests, Burgess (2004) presents Jones' criterion of stability, named after R. Jones, of the National Physical Laboratory, from Teddington, England. Jones found that, for the British rigid airships, there was a fixed relation between the radius of turning circle, the yaw angle at the CB, in radians, and the distance from the CB to the tail surfaces center of pressure. The relation observed by Jones is as follows:

$$\frac{\mathrm{R}\psi}{\mathbf{C}} = 0.9$$

Equation 34 - Jones' relation for British rigid airships. Source: Burgess (2004).

, where

R	= radius of turning circle, [ft]
ψ	= angle of yaw at the CB, [rad]
$\mathbf{C}$	= distance from CB to center of pressure of the surfaces, [ft]

Based on the condition of a steady curve, balancing the damping and the disturbing moments, Jones obtained:

$$\frac{\mathrm{M_q} \cdot \vartheta}{\mathrm{M_\theta}} = 0.9 \cdot \mathbf{C}$$

Equation 35 - Jones' relation for a steady curve for British rigid airships. Source: Burgess (2004).

, where

M_q	= damping moment derivative with respect to angular pitching velocity, [lb.ft/ °/s]
M_θ	= disturbing moment derivative with respect to pitch angle, [lb.ft/ °]
ϑ	= forward speed, [ft/s]
$\mathbf{C}$	= distance from CB to center of pressure of the surfaces, [ft]

Based, then, on Zahm (1926) pitch stability criterion for wind tunnel models, and using Jones' criterion, the relation would be:

$$\frac{s \cdot \left(\frac{\mu}{\vartheta}\right) \cdot \vartheta^2}{M_\theta'} > 0.9 \cdot \mathbf{C}$$

Equation 36 - Jones' criterion for airship wind tunnel models stability. Source: Burgess (2004).

, where

s	= model scale factor, [-]
μ	= coefficient of damping moment in pitch for the model, [lb.ft.s/ °], according to Zahm (1926)
ϑ	= test velocity, [ft/s]
M_θ'	= model damping moment derivative with respect to pitch angle, [lb.ft/ °]
$\mathbf{C}$	= distance from CB to center of pressure of the surfaces for full scale, [ft]

One may right away notice that some confusion occurred during the presentation of the criteria. Looking at Burgess (2004), it defines Jones' criterion using ψ as the angle of yaw and R as the radius of the turning circle, but M_θ as the derivative of pitching moment with respect to pitch angle. For interpreting the wind tunnel criterion, it is assumed that M_θ' is the yawing moment derivative with yaw angle for the model.

Despite all the complexity involved in acquiring the necessary data, such as the moment derivative, this criterion is based on a very specific type of airship, i.e. conventional rigid with high *AR*, and is applicable only to the oscillation (yawing) on the lateral plane, ignoring the pitching moment. This leads to the conclusion that such rule might not apply to different aircraft, just like the previous one (Burgess' (2004) criterion).

Finally, it is still relevant to mention the work presented by Blakemore (2003). He made an investigation to determine the relation between areas and location of control surfaces for the cruciform type for nonrigid airships. ZR-1 was included for comparison purposes, although it was rigid type, because of the extensive amount of wind tunnel test data. The database (Table 5) was comprised of American airships that were known to have satisfactory control characteristics, which probably means good stability characteristics, once it is not over controllable.

Table 5 - Control surface data for nonrigid airships.

Airship	Total area [ft²] Vertical	Horizontal	Rudder	Elevator	Total	Volume [ft³]	Length [ft]	C [ft]
OB-1	228	328	48	96	556	43030	93.85	32
A-4	262	346	84	168	608	95000	162	60
J	462	492	85	122	954	174880	168	70
C	460	495	85	120	955	181000	196	77
D	460	495	85	120	955	190000	198	78
ZR-1	2401	2966	489	576	5367	2289861	680.15	290

Source: Blakemore (2003).

Based on this data, Blakemore (2003) assessed some specific coefficients against $V^{\frac{1}{3}}$:

F-Sv = $\sqrt[3]{Sv \cdot \mathbf{L}}$ Equation 37 - Blakemore's (2003) criterion for airship vertical tail.

F-Sh = $\sqrt[3]{Sh \cdot \mathbf{L}}$ Equation 38 - Blakemore's (2003) criterion for airship horizontal tail.

F-Sr = $\sqrt[3]{Sr \cdot \mathbf{L}}$ Equation 39 - Blakemore's (2003) criterion for airship rudder.

F-Se = $\sqrt[3]{Se \cdot \mathbf{L}}$ Equation 40 - Blakemore's (2003) criterion for airship elevator.

F-St = $\sqrt[3]{St \cdot \mathbf{C}}$ Equation 41 - Blakemore's (2003) criterion for airship total tail.

, where

Sv = vertical tail area, [ft²]
Sh = horizontal tail area, [ft²]
Sr = rudder area, [ft²]
Se = elevator area, [ft²]
St = total tail area, [ft²]
$\mathbf{C}$ = distance from CB to center of total area of surfaces, [ft]

Plotting F-St for convenience, aiming at total stability evaluation, one can see that the points adjust very well to a linear regression.

Figure 51 - Variation of Blakemore's criterion for total tail surface area (F-St).

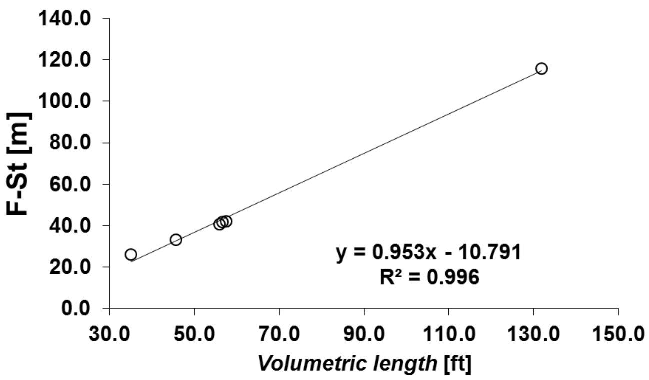

Source: Elaborated from Blakemore (2003).

By slightly modifying F-Sh and F-Sv, changing **L** for **C**, one may calculate F-Sh' and F-Sv', approximating **C** as employed for the total area calculation as having the same role for horizontal and vertical tails individually.

Figure 52 - Variation of modified Blakemore's criteria for horizontal (F-Sh') and vertical (F-Sv') tail surface areas.

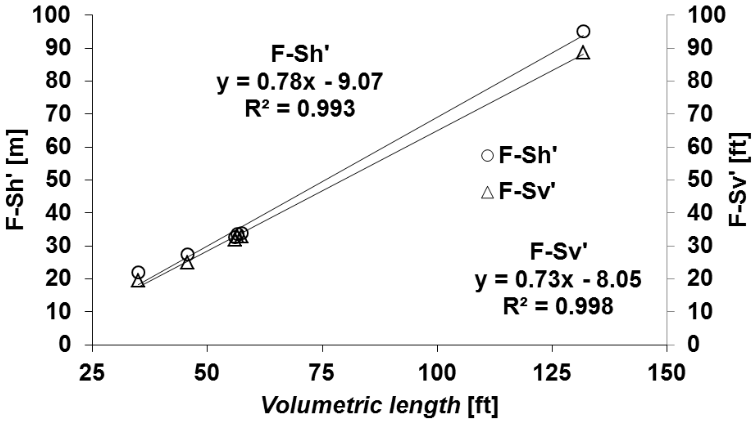

Source: Elaborated from Blakemore (2003).

This was done as it would make more sense to use the force arm length and not the ship length to individually analyze vertical and horizontal tail surfaces efficiency, in the author's opinion. The obtained curves delimitate two areas: above it the ship would be over-surfaced, whilst below, under-surfaced. Blakemore (2003) substantiated the curves by personally acquired opinions based on his LTA experience.

Nevertheless, like the two previous criteria presented, this last one is too restrictive, as it is based on very poor sampling and on a specific kind of airship, not being reliably extendable to general airship design.

3.2.2.3 The TVC concept for airships

To be clear, the main focus of this work is analyzing and providing guidance on the general aerodynamic and stability behavior of airships. Regarding stability as a design feature, it would be interesting to have as an outcome of this study a means of measuring the stability quality of airships. This would allow evaluating the influence of aerodynamic interference effects by assessing them in the real world, during wind tunnel tests. In this sense, and as a complementary portion, a parametric based index could be developed, easy to be calculated, and possible of being used during the early design process – the conceptual phase – and supported by evidence from successful operational aircraft as recorded by history.

In this section the very initial proposal is explained and characterized. The final proposal for the index and its characteristics are presented in section 5.3.7, after all results have been discussed. Developing such a tentative methodology was very convenient for this work, since along with the wind tunnel tests, the proposed index could be evaluated considering both geometry and flow conditions. The main motivation is to provide an easy workable and simple parameter that can model and describe in general terms the stability quality of conventional airships. This is very similar to what already exists for fixed wing aircraft, and is called tail-volume, and aims to be much simpler than the above presented indexes, or at least much similar to what is already typical for fixed wing aircraft.

The Tail Volume Coefficient (HALL, 2017) for fixed wing aircraft is divided in two different equations, one for the horizontal tail (Equation 42) and another for the vertical tail (Equation 43). These coefficients relate the tail area, and its distance to the aircraft CG, to wing characteristics, leading to non-dimensional numbers. Usually, aircraft whose tail volume coefficients are similar also have similar static stability characteristics. Just like it is proposed here, having those numbers in hand during the early design phases eases the process of defining an aircraft with good stability characteristics. The tail volume does not define the final aircraft, but provides guidance, reducing the detailing efforts.

$$V_H = \frac{S_H}{S_W} \cdot \frac{L_H}{MAC}$$

Equation 42 - Horizontal Tail Volume Coefficient. Source: Hall (2017).

$$V_V = \frac{S_V}{S_W} \cdot \frac{L_V}{b}$$

Equation 43 - Vertical Tail Volume Coefficient. Source: Hall (2017).

, where

S_H	= horizontal tail planform area
S_V	= vertical tail planform area
S_W	= wing planform area
L_H	= longitudinal distance from horizontal tail aerodynamic center to the aircraft CG
L_V	= longitudinal distance from vertical tail aerodynamic center to the aircraft CG
MAC	= wing mean aerodynamic chord
b	= wing span

Analyzing the standard tail volume coefficients it is noticeable right away that some of the terms would not make sense at all for conventional airships, such as wings properties. On the other hand, however, looking at areas is quite logical. Thinking about the physics of the problem, one must take into consideration that the coefficients relate the tail moment order of magnitude to the wing moment in the same direction. The simplifications include neglecting tail downwash and dynamic pressure reduction (reduced tail efficiency due to wing wake), and keeping forces directly proportional to area only.

Upon preliminary evaluation, one can conclude that basically the relevant aerodynamic characteristics for each axis, regarding the stability arrangement (tail), are compared to the lift generating arrangement (wing), in addition to keeping the same axis applicability. In other words, the wing destabilizing pitching moment is compared to horizontal tail pitching moment, for example. Drawing a parallel for airships, the lift generating surface is the hull, and the stability arrangement comprises the tail, just like for conventional aircraft. Nevertheless, disregarding the gondola presence (equivalent to not considering the fuselage for conventional aircraft), airships may be seen as very axisymmetric aircraft. Therefore, unifying horizontal and vertical coefficients into a single one seems to be reasonable.

Based on the above evaluated preliminary methodology and assumptions, the Tail Volume Coefficient (TVC) for airships is proposed as follows:

$$\mathrm{TVC} = \frac{\mathrm{S_{Tail}}}{\mathrm{V}^{\frac{2}{3}}} \cdot \frac{\mathbf{C}}{\mathbf{L}}$$

Equation 44 - Airship Tail Volume Coefficient.

, where

$\mathrm{S_{Tail}}$	= total tail area, regardless of the positioning or tail arrangement
$\mathbf{C}$	= longitudinal distance from the tail surfaces geometrical center to the airship CB

As can be seen, the proposal is to simplify the calculation as much as possible, and assess whether it is possible to infer that an airship is statically stable, regardless of the tail arrangement (“X”, “+”, “-Y” and etc.) and its precise aerodynamic center position (replaced by the geometrical center). Bearing in mind the wing parallel, the usual hull properties were applied: volumetric area and total length. The use of such parameters makes sense aerodynamically speaking (see Equation 3), and allows the TVC to become non-dimensional, as expected.

Using this proposal, along the evolution of this work a database of successful airships was developed in order to support the investigation on TVC. The database consisted of: airship name (designation), structural design philosophy (rigid, semi-rigid and blimp), envelope characteristics (volume, generatrix, total length and maximum diameter) and tail characteristics (arrangement and unit areas). By means of side and top view drawings, and knowing the envelope main dimensions, the longitudinal position of the CB and tail geometrical center were determined, besides the envelope AR. Having such information, for each aircraft, the TVC was calculated, and plotted against envelope AR.

Figure 53 - Parametric study of airships with the calculated TVC.

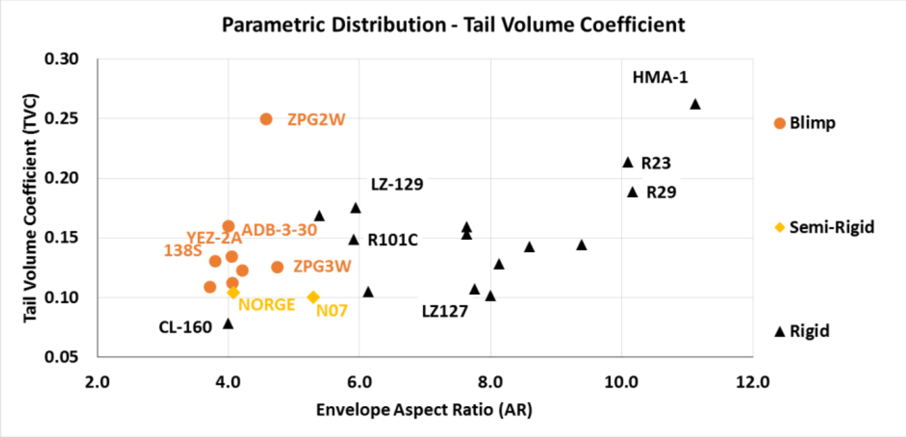

Source: Author (2018).

Among the 25 airships, whose data were trustworthy and sufficient for this work, the most relevant to airship history (well-known) were labeled. It is interesting to observe that, to a certain extent, there seems to be a higher concentration area between TVC levels 0.10 and 0.15. Although this might be questionable, this would lead to inferring that probably good stability airships would mostly present TVC values inside that range. In other words, the greater the density of airships inside a TVC range, the greater the likelihood that this range means better stability quality.

This first judgment level was established based only on research and historical data. Notwithstanding, some famous airships figure inside $0.10 < TVC < 0.15$. Among them, one can cite the Italian Norge, which travelled to the North Pole, the LZ127 (more widely known as the Graf Zeppelin), which made 590 safe journeys, including 139 transatlantic flights and an around-the-world mission. Still, the ZPG-3W, the largest non-rigid (blimp) ever flown until 2016, is inside the same range. This airship was used in dozens of marine patrolling missions until the 60s, when it was phased out. Finally, besides them, most modern airships, such as the 138S, from the 80s, and the NT-07, from the 90s, which is still flying around for sightseeing and marketing purposes, are also contained within the database. With this in mind it seems that not only a mathematical trend was found, but is supported by a reliable database of really successful aircraft. Regardless of the results, the obtained data could be put to good use for assessing stability.

The TVC concept developed and explained above, and the proposed “good stability range” ($0.10 < TVC < 0.15$) are better discussed and brought to a final proposal in section 5.3.7. After the Phase II wind tunnel campaigns (section 5.3**)** the wind tunnel model resulting stability was assessed, and the TVC concept was improved, supported by collected wind tunnel data. For those analyzes, however, some important theory regarding uncontrolled motion, which was presented above, was used.

The initial approach was essentially based on what was described in section 3.2.2.1. Assuming the inferred good TVC range, an over stable aircraft would figure above the upper limit. On the other hand, if the model tends to oscillate for a long period before reaching an equilibrium condition it may be classified as under stable, and would figure below the lower limit.

A caveat consideration is in order about a fact which took place during this work involving specifically the TVC proposal. Very close to the conclusion of this work, after all results were already processed and the initial conclusions regarding the proposed TVC were reached, the author came to know about an initial tail sizing parameter proposed by Carichner and Nicolai (2013). In their book about general aspects on airship design, two coefficients are proposed: C_{HT} and C_{VT}, which are called Horizontal and Vertical Tail Volume Coefficient, respectively. Their approach is, in practical terms, the same as was put forward by this author: a parametric study to try to identify a trend in airship tail initial sizing by means of an equivalent tail volume coefficient. C_{HT} and C_{VT} are defined as follows by Carichner and Nicolai (2013):

$$C_{HT} = \frac{S_{HT}}{\mathbf{L}} \cdot \frac{L_{HT}}{V^{\frac{2}{3}}}$$

Equation 45 - Airship Horizontal Tail Volume Coefficient. Source: Carichner and Nicolai (2013).

$$C_{VT} = \frac{S_{VT}}{\mathbf{L}} \cdot \frac{L_{VT}}{V^{\frac{2}{3}}}$$

Equation 46 - Airship Vertical Tail Volume Coefficient. Source: Carichner and Nicolai (2013).

, where

S_{HT}	= horizontal tail planform area
S_{VT}	= vertical tail planform area
L_{HT}	= longitudinal distance from the horizontal tail mean aerodynamic chord aerodynamic center to the aircraft CG (CB in the coefficient case)
L_{VT}	= longitudinal distance from the vertical tail mean aerodynamic chord aerodynamic center to the aircraft CG (CB in the coefficient case)

According to Carichner and Nicolai (2013), the proposal of such coefficients is based upon the fact that these ratios seem to be very similar for like classes of aircraft, as cited above, and airships as well. It is also emphasized that the static directional stability and control are very loose; for directional it is stated that “the airship should exhibit weather-cock stability”, whilst for longitudinal “the airship should exhibit positive static pitch stability”. For none of them, however, a degree of damping is stated to be required, and no other clear specifications, like those for typical fixed wing aircraft were provided. This may show that such proposed initial tail sizing does not aim at really providing proven stability, but only initial reference numbers for other estimates, such as weight and balance, and aerodynamics, as the tail is responsible for 10-14% of an airship empty weight, and 20% of its drag (CARICHNER and NICOLAI, 2013).

Based on an aircraft database, Carichner and Nicolai (2013) adjusted, by means of logarithmic regressions, the trend lines for each coefficient. Using the same explained assumptions and database, this author tried to reproduce the chart presented by them, obtaining (Figure 54).

Figure 54 - Horizontal and vertical tail volume coefficients trends proposed by Carichner and Nicolai (2013).

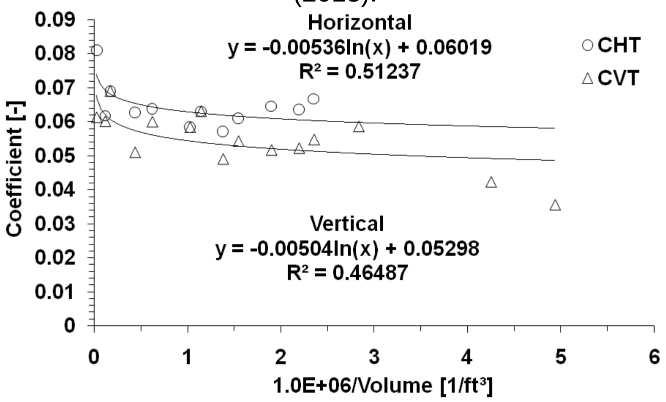

Source: Elaborated from Carichner and Nicolai (2013).

The equations obtained for the trends were very similar. Carichner and Nicolai (2013) state that the more linear trend of the horizontal tail coefficient, observed in Figure 54, is due to the fact that, for longitudinal stability, the pendulum stability and ballonet balancing are the predominant factors. In this way, these are key aspects of stability, and the tail becomes less relevant, not varying much with volume.

The author became thus very confident, given the fact that such a reliable reference work like the one published by Carichner and Nicolai (2013) was proposing essentially the same methodology developed here. However, evaluating the technical aspects of the proposal, some doubts came up. The first came from the database. Even having almost 40 aircraft configurations, Carichner and Nicolai (2013) used only 16 to obtain their trend to guide designers. When plotting all 40 aircraft, the proposed fit was far from being considered robust.

Figure 55 - Complete set of airships available from Carichner and Nicolai (2013) depicting C_{HT} (left) and C_{VT} (right).

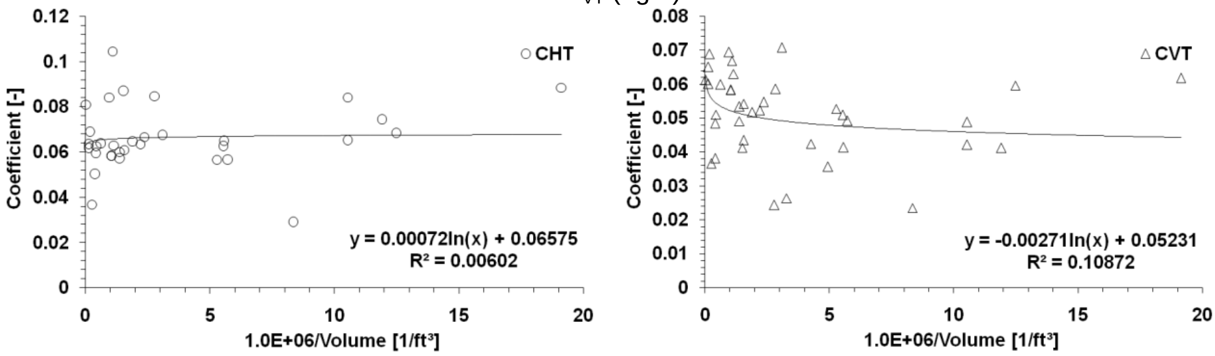

Source: Elaborated from Carichner and Nicolai (2013).

As can be seen in Figure 55, the scatter increased a lot, and the regressions became much more linear like a range of values, similar to what was originally proposed for the TVC. In addition, some relevant designs such as the YEZ-2A, the ZPG-3W, the 138S and the NT-07 were not considered, and others such as the GZ-20, the Skyship 600 and the Sentinel 1000 appeared lack data on horizontal tail areas. Nevertheless, it is interesting to note that, considering mean values, summing C_{HT} and C_{VT} for the same design leads to mean values that fall within the proposed range for the TVC.

Comparing both databases, one may reach interesting conclusions concerning tail arrangement variety. Firstly, it is clear the great majority of the aircraft had cruciform ("+") tail arrangement: more than 70% for this author and more than 80% for Carichner and Nicolai (2013). Secondly, no rigid was found to have a tail arrangement different of "+", while blimps (nonrigid) presented "X" configurations (the larger ones), and some even an inverted "Y", although very few. The CB and the arm length between tail and CB can also be compared. Very similar mean values were obtained, and are depicted below.

Figure 56 - Comparison between Author's and Carichner and Nicolai's (2013) airship databases regarding CB.

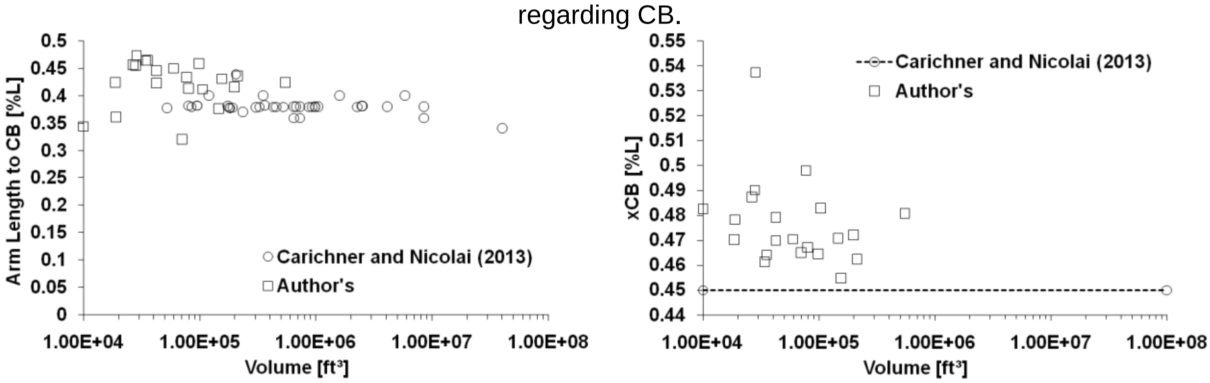

Source: Elaborated from Carichner and Nicolai (2013) and Author (2018).

Joining both databases and calculating the TVC led to a surprisingly good result: the proposed "good TVC" range was reinforced by the additional aircraft

(Figure 57). It is important to say that the two hybrid aircraft (P-791 and Aerocraft) were dropped from the database, only conventional airship configurations being considered.

Figure 57 - TVC considering Author's and Carichner and Nicolai's (2013) databases.

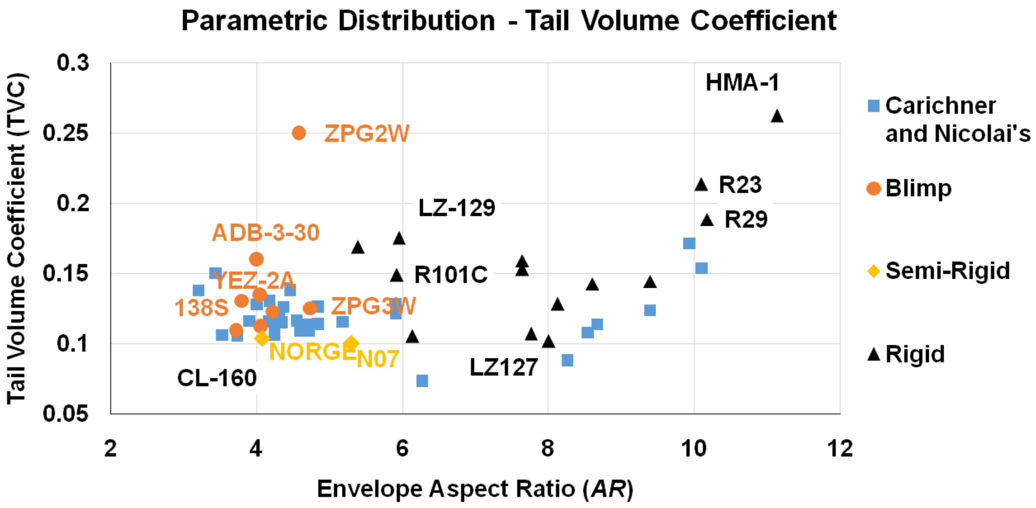

Source: Author (2018).

In any case, the proposal made by Carichner and Nicolai (2013) supports this author’s proposal regarding ensuring not only a better initial tail sizing methodology, but also to assure a certain degree of stability. The same reasoning was employed at the very end of the results discussion, where the model oscillations damping are used as a reference for the stability assessment.

4 METHODOLOGY

4 METHODOLOGY

In this chapter are described the methods applied to accomplish the experiments needed to achieve the objectives of this work. A brief discussion on the chosen methodology is made in order to clarify some choices, and guide the reader through the author's logic. First of all, the wind tunnel model and the facility itself are described, followed by a description of the instruments and their operational characteristics. Following that, the author describes some special techniques that will be used in order to have some qualitative (but important) results that should guarantee the correct interpretation of fundamental phenomena regarding the aerodynamics, stability and controllability of the studied scale model employed, and that can hopefully be applied to real airship. Besides that, the wind tunnel experiments necessary to accomplish the objectives are described, and the methodology is presented, including the similitude evaluation and the wind tunnel corrections. At the end of this chapter, an evaluation about the possible error sources and uncertainties, associated with the procedures and experiments are described and the proposed mitigation strategies are discussed. The model and the manufacturing techniques employed are presented and discussed in Appendix A.

4.1 THE AIRSHIP MODEL: PHYSICAL CHARACTERISTICS

For every experimental investigation, not only the conditions and methods are important to be described, but also the model itself. As already stated, the wind tunnel model is a scale representation of an airship prototype under study at Airship do Brasil, in São Carlos, Brazil. This model is basically that same hull structure used in the studies conducted by Cebolla (2013), with a series of modifications, mainly regarding fins fabrication and hull finishing, representing an approximately 1:116 scale model of the real aircraft. Details on model structure and fabrication can be found in Appendix A.

4.1.1 Model sizing

The model dimensions, which determine the scale factor, are derived from a sizing study developed by Cebolla (2013). Basically, as already presented, there is an impasse when defining the dimensions of a wind tunnel model: small dimensions do not represent the full-scale flow (*Re* mismatch), whilst large dimensions lead to strong interferences from tunnel walls on the results. Therefore, the challenge was to determine an intermediate point, which would be as near as possible to the desired *Re*, and would still provide acceptable results. To solve this question, relevant airship wind tunnel tests were parameterized, followed by CFD analyses of a model proposal, which led to a wind tunnel blockage ratio correction method evaluation.

From the parametric study[23], Cebolla (2013) concluded, based on a linear regression, that the mean blockage ratio among the samples was 0.0283. In other words, the maximum envelope cross section divided by the wind tunnel cross section (working section) was 0.0283 (Figure 58).

Figure 58 - Blockage ratio parametric study conducted by Cebolla (2013).

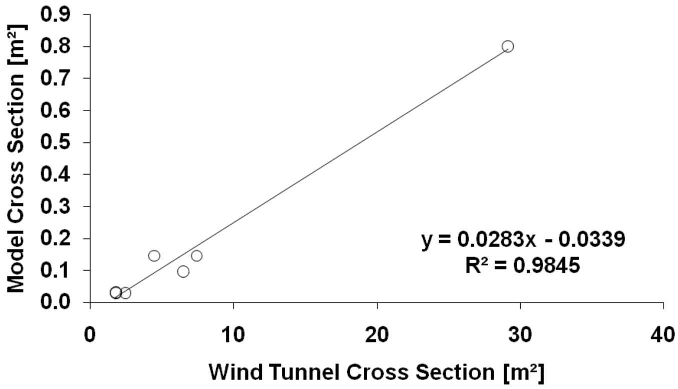

Source: Adapted from Cebolla (2013).

Following that, a CFD analysis for AoA = 0°, at 33.33m/s and local atmosphere (São Carlos, SP, Brazil), was conducted simulating 5 different blockage ratios (0.1%, 1%, 3%, 5% and 10%), plotting the envelope pressure distributions against a zero-blockage condition, i.e. farfield free flow results (no walls). A second CFD campaign was conducted for AoA = 30°, and only for three blockage ratios (0.1%, 3%, 5%), eliminating 10% (which was far too high) and 1% (worst results). By comparing the different pressure distributions, as expected, 0.1% and 3% had the best results (smaller differences), and were very similar considering the mean and mean squared errors (sum of difference between blockage ratio and farfield results).

Finally, by means of semi-empirical methods (BARLOW, RAE and POPE,1999) based on the dynamic pressure increase due to the presence of a body inside the test section, the 5 initial blockage ratios were investigated. The conclusion was that from 3% upwards, the blockage effect increases substantially, and the methods also begin to differ in their results considerably. As additional information, it

[23] The study considered the airship models used by Gomes (1990), Anderson and Flickinger (1954), Cerreta (1957), Abbott (1931), Zahm, Smith and Hill (1923) and Freeman (1932).

is usual to have blockage ratios between 1% and 10%, more typically around 5% (BARLOW, RAE and POPE,1999). However, considering that at 5% the evaluation results were already differing markedly from each other, and based on the parametric study, which led to a mean value of 0.0283, it was concluded that 3% was the acceptable figure for the LAE wind tunnel (CATALANO, 2004). Considering therefore the 3% blockage ratio, the resulting scale was 1/116*, leading to the data presented in Table 6.

Table 6 - Airship and wind tunnel model comparison.

Property	**Prototype**	**Model**[24]
Scale [-]	1/1	1/116*
Blockage ratio (***B***) [-]	-	3%
Length (**L**) [m]	135	1.157
Diameter ($\mathbf{D_{máx}}$) [m]	33.75	0.289
Slenderness ratio (*AR*) [-]	4	
Hull surface area (S_{hull}) [m²]	11537	0.8471
Volume (V) [m³]	80420	0.0506
$(\text{Volume})^{2/3}$ ($V^{2/3}$) [m²]	1863	0.1367
xCB/**L** [%]	46.7	
Top speed ($\vartheta_{máx}$) [m/s]	33.33	N/A
Re	2.98E+08**	Section 4.4

*For math purposes, scale is 1/116.7; **São Carlos region.

Source: Adapted from Cebolla (2013).

After evaluating the sizing methodology used by Cebolla (2013), and concluding that his model would suffice for the experimental needs, it was decided, for simplicity, to improve and adapt the available model, instead of fabricating a new one. The whole revision and modification process is described in Appendix A. After the preparation, the model was finally ready for starting the campaign. The surface finishing was equivalent to sandpaper 1200, very smooth and fine.

4.1.2 Model features

As described in Appendix A, the model had originally three pressure taps lanes, 90° apart from each other: Port, Upper and Starboard lanes (Figure 62); each lane has 20 taps. Besides the 60 taps on the generatrix, there are another two: bow and stern taps. These last two taps are contained in the model longitudinal axis, pointing forward and backwards respectively. With this, the model has a total of 62 pressure taps, according to the presented in Appendix B. Besides the original tapping

[24] The presented data assume that the model is perfectly identical to the virtual planned model.

distribution, more taps were produced for further investigating the flow about the stern region. Those taps are also described in Appendix B, but schematically depicted in Figure 63.

In order to have access to the HULL interior, check the pressure taps tubing and also house the acquisition system (Section 4.2.2) there are two access windows attached to the model by flush screws.

The empennage surfaces are bolted through the model stern portion, lining up the leading edges at 80%**L**. As shown in Appendix A, the stabilizers are 3D printed, and the control surfaces are carved in wood. The moving surfaces are connected to the fixed ones by means of tip screws, which act also as an axis for pivoting the surface. To set a specific deflection angle (δ), the pair of tip screws is loosened, the angle is adjusted, and the screws are tightened again. After tightening, the angle is once again checked for magnitude and tightness.

4.1.3 Model referencing

This work comprised two different parts: Phase I (steady tests) and Phase II (dynamic tests). The fixation of the model and the reference systems had important differences. The referencing to positive and negative angles will be properly presented in section 5, along with the results, while this section shows the reference systems used for each phase.

The wind tunnel testing section, as further described in section 4.2, has a parallelepipedic volume, and air flows always from left to right, to the observer, who is only capable of observing the model from a lateral window (Figure 59). This flow direction defines the longitudinal axis (x-axis), which is perpendicular to the chamber cross section, going through the section middle point. The axis direction is thus against the flow. The rectangular cross section is defined by the other two axes, which also go through the middle point and are perpendicular to first the x-axis, and to each other: lateral and vertical. The lateral axis (y-axis) points to the flow right side (where the observer stands), while the vertical, points upwards. The three axes, together with the volumetric middle point, constitute an orthogonal reference system. The axes define, in pairs, the chamber planes: longitudinal, lateral and top (Figure 59).

Figure 59 - Global reference system for working chamber and model. Support bar suppressed for clarity.

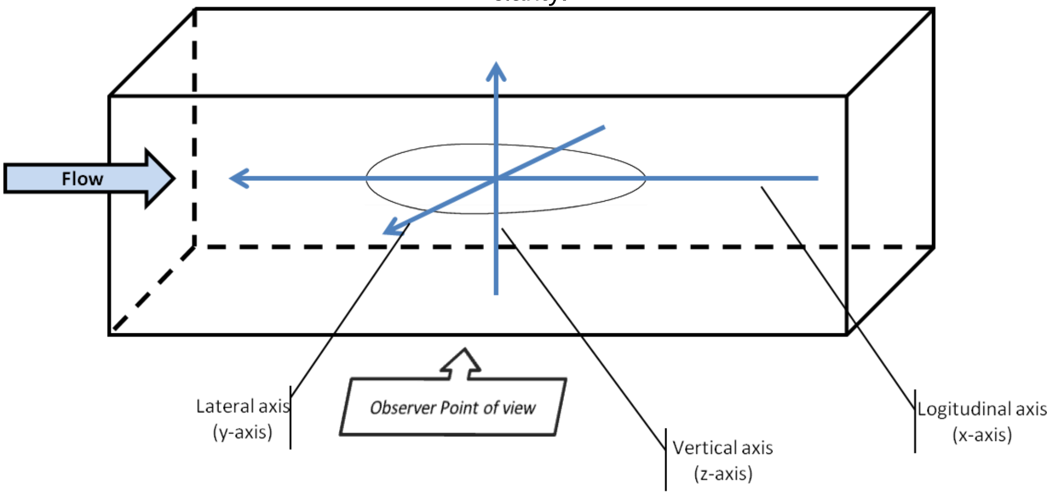

Source: Author (2018).

For Phase I (steady tests), the model support was placed collinear with the vertical axis, and its cross section was contained in the vertical plane, while the model longitudinal axis (along the HULL) concurred with the longitudinal axis. In this way, the angles were defined positive and negative so they would preserve the positive orthogonal coordinate system. Looking along the flow direction, positive angles mean nose deflection to the right (where the observer stands), while negative means to the left (Figure 60). In this case, the variable angle (around the vertical axis) was AoA, while $\beta = 0°$. During this first phase, aerodynamic forces and moments were measured. For the forces, lift and pitching moment followed the coordinate system. Drag was measured as negative for positive drag, and then converted.

Figure 60 - Working chamber top view. Support bar suppressed for clarity.

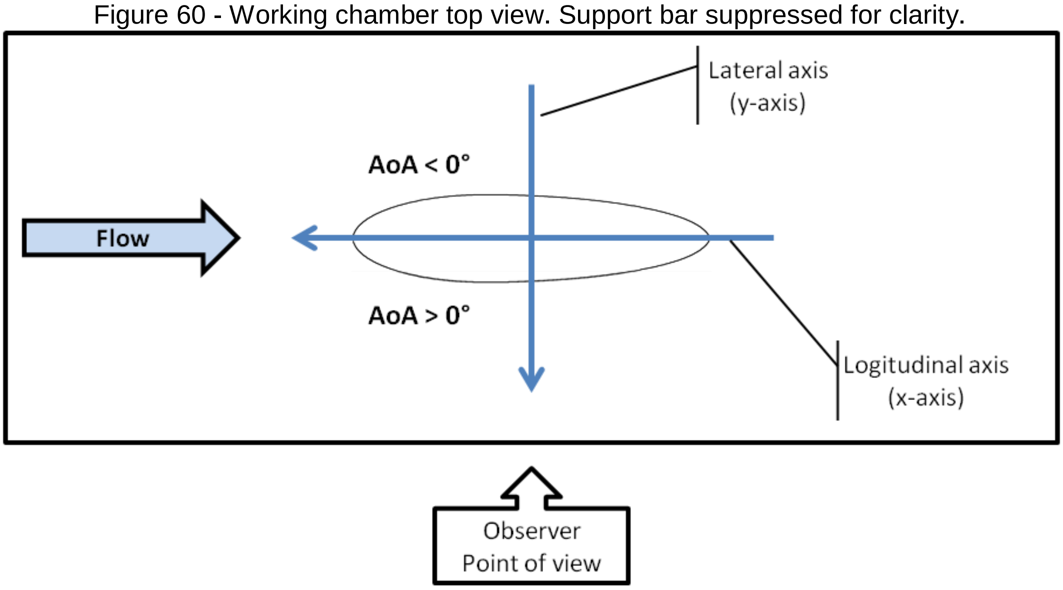

Source: Author (2018).

So, with the model in place, it is important to define model references. For Phase I, model port and starboard side as standing on the reference will be upper and lower sides, respectively. Concerning the fins, the referencing will be made according to what is easier to understand for each case, but the standard designations are shown in Figure 61, which is a view from the back of the model, towards the working chamber entrance.

Figure 61 - Working chamber back (rear) view. Support bar suppressed for clarity.

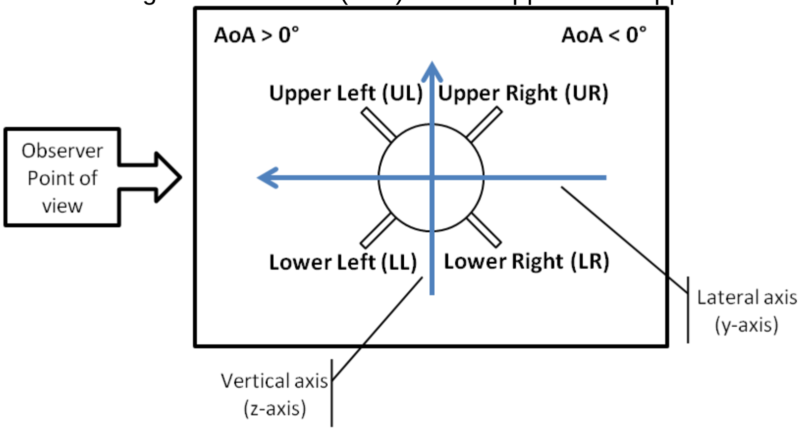

Source: Author (2018).

Still during Phase I, pressure measurements were also carried out. They were conducted at two different tap configurations. The first configuration assessed the model as a whole, and is depicted in Figure 62. The second one analyzed only the stern region, and a fin front line along the hull. Using the reference in Figure 63, the FIN pressure LINE was positioned ahead of the UL FIN, which in the forces reference corresponds to the upper starboard fin.

Figure 62 - Pressure taps (Front view).

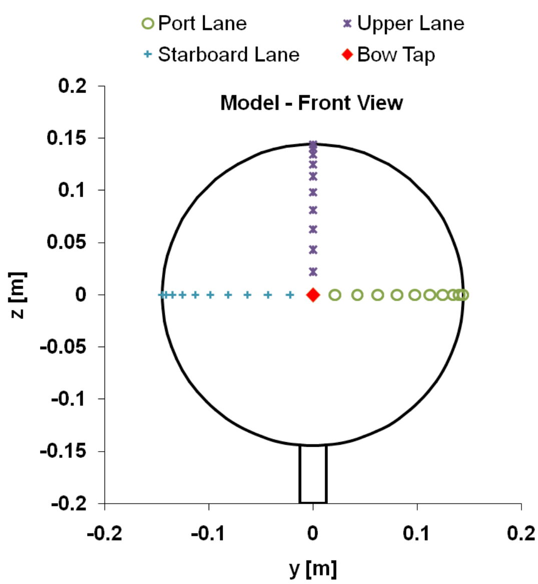

Source: Author (2018).

Figure 63 - Stern pressure taps (Rear view).

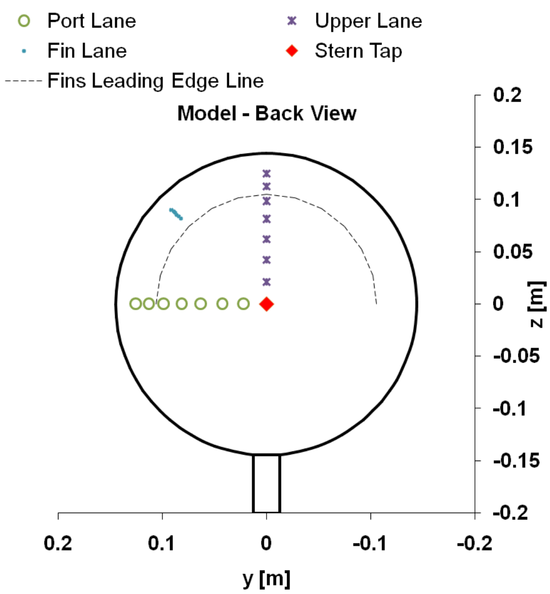

Source: Author (2018).

For Phase II, the coordinate system was kept the same, but the model reference changed. While in Phase I a turn around the vertical axis meant AoA variation, in Phase II AoA = 0°, turns around the vertical axis mean β variation, the upper side of the model matching the upper portion of the chamber. For simplicity the same sign convention was adopted. Looking from the origin, along the longitudinal axis, positive β are to the left, and negative, to right, just like was shown for AoA in Figure 61.

4.2 WIND TUNNEL FACILITY

For this work, the wind tunnel tool was chosen for several reasons, among them: availability at the university, knowledge and experience with the procedures, costs and, perhaps maybe the strangest one, the challenges. This last one is related to the similitude analysis, already mentioned and further discussed ahead, for which a solution is sought. Among the advantages, the possibility of studying various different designs just by adding or removing some pieces or parts in a very economic manner was very convenient.

Wind tunnels can be very different from each other: subsonic, transonic, hypersonic, open, closed circuit, with interchangeable chambers, etc. Each type is designed for an objective; however, some of them can be more flexible, while other can be very specific and expensive to be used (BARLOW, RAE, POPE, 1999). Due to the available items at the university, a subsonic closed circuit was competing only with other subsonic open tunnels which can provide slower velocities and, given their nature, poor control of the medium properties, such as temperature and pressure. For these reasons, the subsonic closed circuit wind tunnel was used. It has also the advantage of being very flexible, with a higher speed, a smaller turbulence level, a larger test section, more stable environmental properties. In addition, it had several types of equipment (balance, oscillations measurer, hot-wire anemometers and even microphones) prepared for a wide variety of tests.

Thus, for the practical campaign of this work, the facilities at the EESC (School of Engineering of São Carlos), University of São Paulo, in São Carlos, Brazil, were used. Specifically for the wind tunnel testing, the LAE-1 Wind Tunnel, at the Laboratory of Aerodynamics (LAE), was chosen. Designed and built by Professor Fernando Martini Catalano, PhD, and technicians of the university, the LAE-1 is a closed circuit wind tunnel, with low turbulence levels and suitable to aeroacoustics experiments as well.

Figure 64 - The LAE-1 wind tunnel.

Source: LAE-1 (2016).

Among other reasons, this wind tunnel was chosen because:

- it is a low-Mach category, which is in accordance with the velocity range of interest (Section 4.1).
- it has the largest working section available at the EESC.
- the available instrumentation for experiments are of high quality (overhead external wind tunnel balance, pressure taps real-time acquisition system, three axis hot-wire anemometer, remotely/automatic controlled angle of attack positioning, etc).
- Annex to it, there is a fully dedicated workshop/atelier, where one can design, manufacture, repair and adapt the models whenever needed, supported by high quality tooling.

To be clear, the big working section allows for a larger model, which makes it easier to achieve the aerodynamics similitude requirements, even if the speed cannot go up to higher Mach numbers, which could further help the similitude matching. Moreover, the low-speed category wind tunnels are cheaper to operate than any other high speed wind tunnel, not only because of their operational costs, but also for the costs of a stiffer and more resistant model. This makes this wind tunnel a good choice for a research that needs a large amount of test hours and the associated preparations for several experiments. The easy access to quality tooling, mainly for adaptation and reparation of the model during the campaign, and the availability of precise instrumentation for taking measurements during the experiments, with no direct costs to this research project, makes this wind tunnel, among the accessible ones, the most suitable facility for achieving the presented objectives.

4.2.1 Technical characteristics

According to Catalano (2004), the working section is rectangular, 1.29 m high and 1.67 m wide, with a length of 3 m in a constant section (Figure 64). The working compound comprises the working section chamber and the wind tunnel control room, which is insulated by a fully closed concrete walled room. This construction strategy ensures that the static pressure in the working chamber is the same as the surrounding atmospheric pressure (CATALANO, 2004).

Figure 65 - The LAE-1 wind tunnel top view.

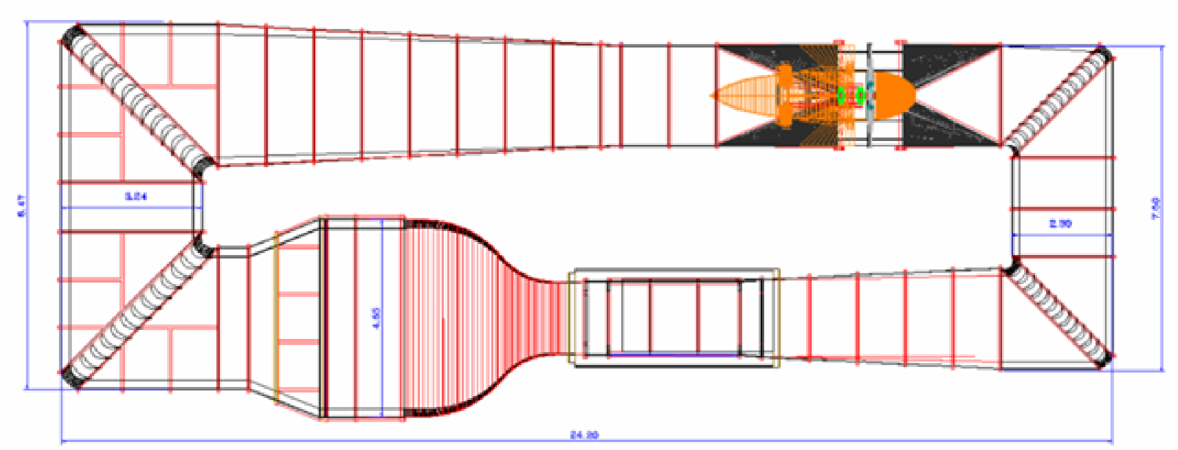

Source: LAE-1 (2016).

Around the working chamber one can find some support instrumentation, and specific sensors, like barometers and manometers, that allow the working staff to monitor the experiments in real-time. Dividing the concrete room, in order to separate the two main rooms (working chamber and control center), there is a glass wall. In addition there is a monitoring camera installed on the roof of the section, right behind the working chamber (Figure 66), this allows the staff to follow the experiment live from different points of view. It also ensures that any problem during testing can be detected right away, and one can thus interfere, stopping the wind tunnel work in case of an emergency.

Figure 66 - The LAE-1 wind tunnel camera (top) and corner vanes (back).

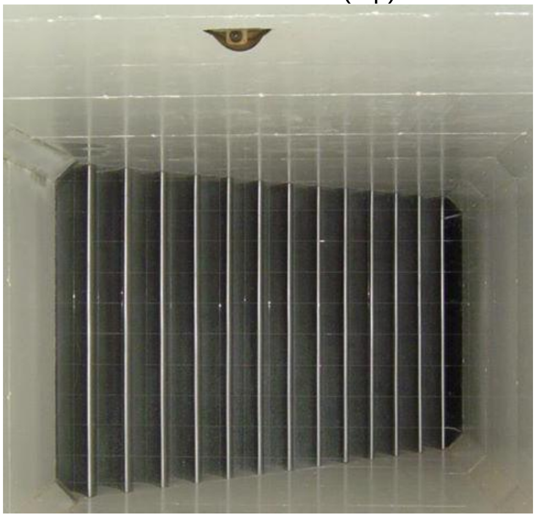

Source: LAE-1 (2016).

For the flow velocity measurement, a Pitot-static tube (Figure 67) is positioned on the wind tunnel working section left wall, right ahead the working chamber, in order to capture the air static and total pressures, so as to obtain the flow velocity, as explained in Section 4.2.2.5.

Figure 67 - The LAE-1 wind tunnel working chamber, with the Pitot tube on the left.

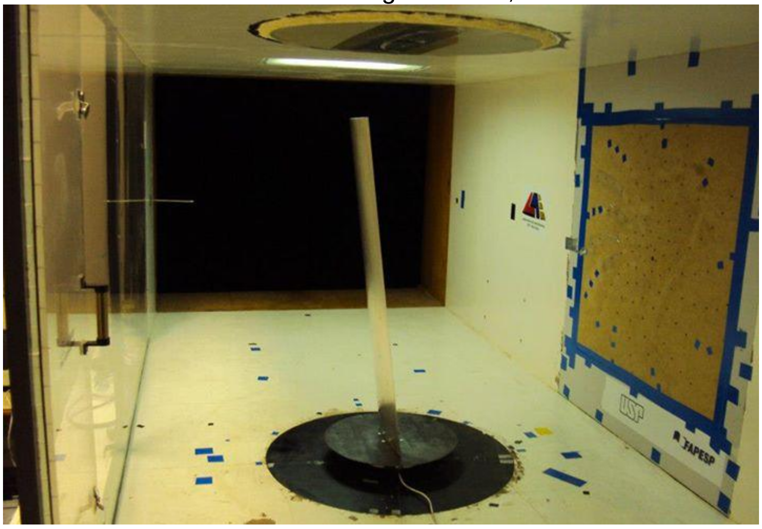

Source: LAE-1 (2016).

The physical space available for the wind tunnel limited the ratio between the working chamber and the contraction sections to 1:8. The contraction cone was designed using two cubic curves connected by an inflection point (Morel's technique) at 45% of the contraction length. This cone has the purpose of stabilizing the flow before it reaches the working chamber. In order to reduce turbulence, two 54% porosity nylon screens (nets) are mounted right before the contraction starts. It is really impressive the low turbulence level achieved, even without a honeycomb screen.

Aiming at the improvement of flow quality and minimization of the pressure losses, the four corners of the wind tunnel have corner vanes, which conduct the flow along the curve without separation and/or stagnation. Completing the shape/structural components, the LAE-1 walls have melamine foam and acoustic baffle between the corner vane sections, techniques that also help lowering the noise level.

Finally, to get the flow started, the wind tunnel has an axial fan with 8 blades (Figure 68), specially designed for high efficiency and low noise, reducing the energy consumption (low operational costs), the turbulence level and making it possible to carry out aeroacoustics studies in that facility.

Figure 68 - The LAE-1 wind tunnel powerplant.

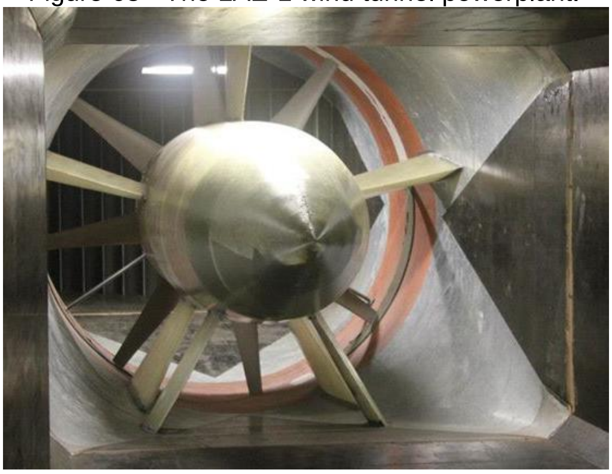

Source: LAE-1 (2016).

This fan, whose blades have a special tip treatment for noise reduction, is driven by a 150 Hp AC insulated electric motor, which is controlled by a programmable frequency inverter. With the installed powerplant, air velocity can reach 50 m/s in the working chamber, and the maximum turbulence level (Tu) is 0.21% (CATALANO, 2004).

4.2.2 Instruments: quantitative evaluation techniques

With such a facility, the instrumentation must be very accurate and precise, in order to extract the most reliable results, made possible at such well designed and built structure like the LAE-1. Every wind tunnel experiment that aims at quantitative results requires a minimum of instruments. The choice depends on what the staff wants to capture. Usually the investigated characteristics are forces and moments (lift, drag, pitching moment, etc), pressure distribution over a surface, velocity profile after a body/lifting surface, turbulent phenomena and structures, among others. For each type of variable, a different kind of instrument is needed.

In this work, in order to achieve the proposed objectives, it is necessary not only to obtain the forces and moments, but to investigate the pressure distribution over airship models as well. Beyond that, other topics included an investigation of the velocity field near the rear part of the model (the stern), where the stabilizers and control surfaces are, and even the flowfield, and vorticity, downstream from the model. In this flow investigation one must include the investigation of the hull boundary layer, and its interaction with the flow over the tail. The main reason for the last item is related to evaluating fin efficiency given boundary layer and wake separations. These last items were investigated only using qualitative techniques.

In order to support the quantitative analyses, the items of equipment employed were:

- Barometer and thermometer.
- Differential manometer.
- Wind tunnel force balance.
- Scanivalve™ (pressure transducer for model pressure taps).
- Pitot-static tube.

Clearly, these are not the only solutions to obtain the required data, but they are the instruments available at LAE EESC-USP, which can also provide the staff the required information. In the following topics, each instrument is presented and described.

4.2.2.1 Barometer, thermometer and hygrometer

The most important values to be obtained before starting a wind tunnel test are those related to the atmospheric conditions. Like explained above, due to the concrete walls around the working control room, the static pressure inside the test chamber is the same as the outside, which means the local atmospheric pressure. To capture this value, a wall integrated instrument set was used (Figure 69). Located inside the control room, very near to the working chamber, it is capable of measuring temperature, pressure, and humidity level. The barometer has a precision of ±100

Pa. The pressure was always cross-checked against a Torricelli barometer. The hygrometer has ± 1% precision regarding humidity level.

Figure 69 - Integrated instrument for atmospheric properties measurements (left), details of the barometer, the hygrometer (middle) and the external thermocouple (right).

Source: Author (2018).

With the local static pressure determined, the other important value to obtain the air density (indispensable parameter for aerodynamics), is the air temperature. For the temperature monitoring, an integrated mercury thermometer, with ±1 °C precision, was employed. It was integrated with the barometer case, and captures the air temperature outside of the working room. Both data – pressure and temperature – are read and registered manually, being necessary inputs for the software used for the test campaigns, explained ahead.It is known however that, because the wind tunnel is a closed circuit type, the air inside gets hotter and hotter along the experiment, eventually stabilizing its temperature. In order to obtain this maximum temperature, a thermocouple is used inside the wind tunnel as well. After capturing the tests maximum temperature, a sensitivity analysis is carried out in order to decide whether it is necessary to consider or not the temperature variation.

In order to obtain the air density, once temperature and pressure are known it is possible to apply the *ideal gas law* in the molar form, considering the specific gas constant $R_{specific}$ = R/M, where M is molar mass of the air, resulting in $R_{specific}$ = 287.058 J.kg^{-1}.K^{-1} for dry air, isolating the density term (Equation 47).

$$P = \rho \cdot R_{specific} \cdot T$$ Equation 47 - Ideal gas law.

, where

P	= static pressure, [Pa]
ρ	= fluid density, [kg/m³]
$R_{specific}$	= ideal gas constant, [J.kg^{-1}.K^{-1}]
T	= fluid temperature, [K]

It can be shown, using this equation, that the density variation due to temperature change is usually very small. Considering, for example, an increase of 10 °C from 25 °C, it is possible to infer that the density would decrease from 1.19 kg/m³ to 1.15 kg/m³ (around 4%), for typical pressure values at São Carlos altitude. This variation is almost negligible when considering all the other approximations (instrument reading, ideal gas consideration, etc). Moreover, since *Ma* is really small (*Ma* < 0.1), no specific results variation are obtained. For this reason, it is not necessary to take into account such temperature increase due to the air flow.

4.2.2.2 Differential manometer (micromanometer)

When working in aerodynamics, one must always think about coefficients, non-dimensionalized quantities. This is the best approach most of the time, because different shapes and velocity analyses can be thus compared and analyzed. However, during aerodynamic experiments it is seldom possible to obtain a ready-made coefficient, but rather a generic and dimensional quantity, which usually is some electrical quantity which has then to be converted to force or pressure, for example.

So in order to convert to a coefficient, one of the first values that are necessary is the dynamic pressure during the wind tunnel test. To obtain this dynamic pressure, a manometer is needed. Nevertheless it is usual to use a differential manometer, because the dynamic pressure, determined by a combination of fluid density and flow velocity (Equation 48), is obtained by means of subtracting the static pressure from the total (impact) pressure.

$$q = \frac{\rho \cdot \vartheta^2}{2}$$ Equation 48 - Dynamic pressure definition.

, where

q	= dynamic pressure, [Pa]
ρ	= fluid density, [kg/m³]
ϑ	= flow velocity, [m/s]

For this work, the 8702 DP-Calc™ Micromanometer (Figure 70) was used. Its range, which goes from -1245 Pa up to 3735 Pa, completely satisfies the intended test velocity planned for the experiments (section 4.4). Besides that, the instrument accuracy (1% of reading ± 1 Pa – the highest error would lead to a 5% change in *Re* for the largest tested value) is enough to capture with sufficient precision the values of dynamic pressure that are needed to control the flow velocity, since the air density and temperature are known.

Figure 70 - 8702 DP-Calc™ Micromanometer.

Source: Author (2018).

Figure 71 - Wind tunnel Pitot-static tube pressure hoses.

Source: Author (2018).

The chosen micromanometer is portable and a very practical instrument to use. It has two input pressure taps, to which the total and static pressure hoses are respectively connected. Before starting the measurement, the micromanoter is set to zero for the dynamic pressure, following the manual instructions. This must be done with the wind tunnel completely stopped and with no air flowing inside the tubes. It is a digital battery-run equipment, and allows the user to insert local static pressure and temperature, outputting directly the flow velocity, because it can calculate the air density with those two values. For this calculation, there is an ISA (International Standard Atmosphere) model programmed inside it. However, if the user wants to calculate the velocity by other means, he can read the dynamic pressure, instead of the calculated velocity. Another very interesting feature that is explored is the possibility of directly reading those values through an Ethernet port, supplying the data directly to the test software.

Due to its portability and simplicity, this micromanometer is used for various tasks during the experiments, being connected to a Pitot-static tube (Section 4.2.2.5), allowing the staff to collect the needed information. In this sense, from now on, during the descriptions bellow, every time this instrument is mentioned, only the word "micromanometer" is used.

4.2.2.3 Wind tunnel aerodynamic balance (aero-balance)

In order to measure the forces and moments acting on the model, an in-house wind tunnel balance was designed and built at LAE (MAUNSELL, 1977). Very similar to a traditional overhead external 6 component wind tunnel balance, it is a high precision instrument, designed for accurate measurements of the aerodynamic loads on scale models.

Figure 72 - The LAE-1 wind tunnel strain-gauge balance.

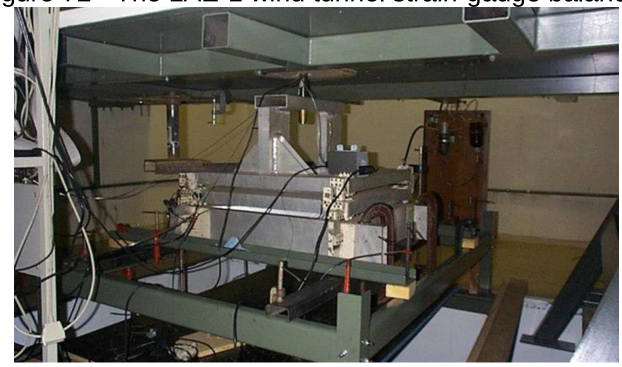

Source: LAE-1 (2016)

This balance is known as strain-gauge type, because of the nature of the magnitudes measurement. The balance converts the displacement, captured by strain-gauges, of two aluminum sheets into an electrical signal. It has a measurement precision of ± 0.7% for maximum loading (MAUNSELL, 1977). Therefore, the precision for lift, drag and pitching moment are ± 1.0 N, ± 0.19 N and ± 1.0 Nm, respectively.

The fixation angle is measured with a precision of ± 0.5 degree, and the zero angle for the model is always calibrated before starting the campaign. For this job, a protractor is used. After the results are obtained, any errors are registered and evaluated based on theory. If it is proven that, for example, the initial angle setting was phased out, the results are corrected by reprocessing the obtained data. However, in order to mitigate such problems, a calibrating technique for the reference angle was applied guaranteeing the reference position during the whole campaign. For this reason, the model was removed only a few times during all tests. In those cases, the zero reference was recalibrated, and the measurements, then, could go ahead.

All generated signals (different directions) are collected in a Wheatstone bridge circuit. These signals have a very low magnitude, milivolts order (mV) of magnitude, and for this reason they must be amplified. This procedure is carried out using the HBM (*Hottinger Baldwin Messtechnik*) MGCPlus. Afterwards, by means of

BNC-2110, from National Instruments™, a desktop and DIN rail-mountable BNC adapter, data is redirected to the embedded computer PXIe-8840, mounted in a PXIe-1082. The data acquisition (DAQ) device PXIe-6341 controls de input and output of data. The communication interface is an RS232 bus using the PXIe-8430, which also logs manometer pressure (wind tunnel dynamic pressure) and controls de AoA drive control system, explained below. The sampling frequency for measuring forces (drag and lift) and pitching moment was 1000Hz, during 10 seconds, providing 1E+04 points for each measure. The information is recorded on the PXIe-6341 computer, which is used to control and log all test data. Using the same computer, and through Matlab™ scripts, the data are processed, which means calculating mean values for each test point, estimating errors (precision) and plotting the final results in an organized way for further evaluation.

Unlike the most common arrangement, at LAE-1 the balance sits under the working chamber, mounted over a support located right below the center of the working chamber floor. In contrast with the most common 6 component balance, the LAE-1 Balance measures only three quantities: two forces in a plane (lift and drag, for example), and one orthogonal moment (pitching moment, for example). It has a fully automated system for controlling and sampling. The model is attached to a turning table, on the floor, which is connected to a shaft. Welded to this shaft there is a bar with a bushing on the other tip, which runs along a power screw. This screw is driven by a stepper motor, which is controlled by a Matlab™ script that communicates through the above described National Instruments hardware setup.

Therefore, in order to drive the model to the desired AoA, the screw is turned as many times as necessary, in the appropriate direction (clock- or counterclockwise), until the desired position is reached, as specified in the script. The path length is calculated applying the law of cosines, since the bar length and the stepper motor position are known; the number of turns is derived from the needed length to be covered divided by the screw thread pitch.

With such a system, it is possible to run a batch campaign without interaction between the model and the staff. This Matlab™ script sets the model at the desired angle, and samples the data of interest. After this sequence is completed, the screw moves again, conducting the model to the new position, until the specified sequence is finished. It is worth saying that it is always considered a transient period before sampling, so as to allow the wind tunnel flow to stabilize, and the steady condition is registered.

Finally, an important item that must never be forgotten is the balance calibration. This procedure is essential, and provides the transfer function between the measured force and the voltage signal received. For this reason, a calibration procedure is conducted using always known weights (dead-weights), and a set of pulleys and cables. In simple terms, the pulleys are positioned at the same level at the end of a strut fixed to the experiment base. Cables are fastened to the strut at its end, following the direction of measurement of the balance, and always orthogonal to each other. From there on, checking for right angles (90°), each axis is calibrated; that means for the lift calibration are added masses piece by piece, collecting the equivalent voltage signal for each mass, which are then converted into weights, which mean forces. The same procedure is carried out for the drag axis.

Figure 73 - The LAE-1 wind tunnel balance assembly scheme.

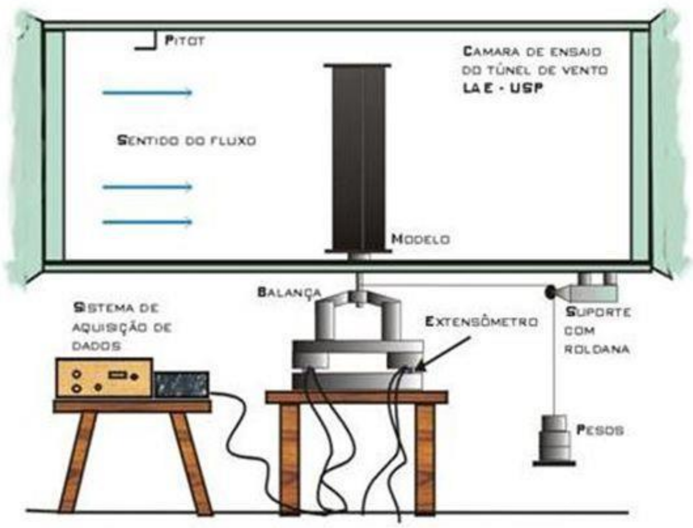

Source: LAE-1 (2016).

For the pitching moment calibration, a slightly different procedure is followed: a bar is fixed perpendicular the strut span at its end, forming a right angle. Then a cable is attached to this new end, and the procedure of adding masses and sampling the signal starts. After the measurements, and considering the length of the perpendicular “arm”, the weights are converted in moment by just multiplying the weight by the “arm” length, and the calibration is finished.

With the calibration charts, it is usually possible to interpolate the results in a linear equation, and ensure that the conversion law is correct. More details about the balance can be found in Maunsell (1977). Once the calibration process is over, the registering of the offset values, if they exist, and before each batch run, is essential. All the calibration work done for this work is registered, with the results and data collected being presented in Appendix C.

4.2.2.4 Scanivalve™ - Pressure transducer

As mentioned, among the variables of interest is the pressure distribution over a surface. In order to capture the pressure at a designated point, it is usually necessary to use a manometer that shows the value of pressure analogically or digitally. However, when doing model experiments, the need for capturing simultaneously the pressure at different locations and without interfering with the flow prevails.

In this way, normally some pressure taps are drilled into and along the surface of interest in order to map it. These pressure taps are very tiny holes made across the surface, and connected to capillary tubes (usually polymeric) that run inside the body. Due to the small diameter of the tubes, the pressure loss is very low, and one can have very accurate information on the static pressure, as wished. After all of these small hoses are ready, and all pressure taps are prepared and trimmed, the free extremity of the hoses are connected to a pressure transducer, treated in this work informally as Scanivalve™.

The Scanivalve™, model ZOC33/64 Px X1 (Figure 74), is a pressure transducer that provides pressure information via voltage signal, reading sequentially each tap on its scanning module. The device, as the force balance, provides outputs in electronic signals, which must be converted by means of a defined law to pressure values. The module is provided with calibration valving, a high speed multiplexer and signal instrumentation amplification (SCANIVALVE, 2013).

Figure 74 - The ZOC33/64 Scanivalve™ – Pressure transducer.

Source: Author (2018).

The available Scanivalve™ has 64 entries; one of them is dedicated to the instrument calibration, another one receives a derivation from the Pitot tube with the static pressure signal. Since it has these comparison ports, the results collected are already differential pressures. It is good practice to firstly collect what is called offset value, in other words, the value for each tap with zero wind.

All entries work with pneumatic inputs of up to 50 psid at a scan rate of 45 kHz; the precision, however, as typical, varies with the pressure level. The measurement is made in terms of differential pressure. The instrument used had a full scale range of ±20 inWG (4976.8 Pa).Table 7 has the accuracy according to the manufacturer's datasheet (SCANIVALVE, 2013) in terms of Full Scale.

Table 7 - Scanivalve™ - Scanning module accuracy.

Differential Pressure Level (Full Scale – FS)	Accuracy (%FS)
20 inWG	+/- 0.15

Source: Scanivalve (2013).

Besides this variation, the Scanivalve™ operation is quite simple: pressure measurements are received by the Electronic Pressure Scanning Module ZOC33/64PxX2, and are converted to high level electronic signals. The output signal is directed to the Digital Pressure Measurement DSM4000 via Ethernet connection. This last device is a data acquisition equipment that performs the unit conversions (electronic signal to differential pressure), the communication and configuration tasks for analog modules (SCANIVALVE, 2013). In sequence, the treated signal is sent to the control center computer, and is read by the DsmLinkC Software, which controls the instrumentation, and saves the pressure sample results to the designated directory. With this software, it is possible to calibrate and setup the Scanivalve™, all automatically.

With all the data compiled, and using the conversion constants, one can associate to each pressure tap, a position, and a value of pressure, so that the whole set represents the distribution over the surface in study. More detailed technical information on the equipment can be found in Scanivalve (2013).

4.2.2.5 Pitot-static tube

This kind of instrumentation is mandatory for aircraft, and is installed in almost anything that flies. Besides that wind tunnels and other facilities usually count on at least one Pitot tube in order to compare and/or calibrate results between different instruments, assuring that the read data are correct. Using this instrument is a classical technique aimed at measuring flow velocity by means of comparison between two different pressures: the total and the static pressures.

$$P_T = \frac{\rho \cdot \vartheta^2}{2} + P$$ Equation 49 - Total pressure breakdown.

, where

P_T = total pressure, [Pa]

$\frac{\rho \cdot \vartheta^2}{2}$ = dynamic pressure, [Pa]

P = static pressure, [Pa]

Figure 75 is a cut-away representation of a classical Pitot-static tube system.

Figure 75 - Pitot-static tube scheme.

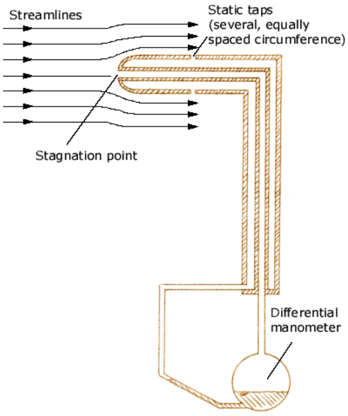

Source: eFunda (2015).

The static pressure is usually the atmospheric pressure, and is measured perpendicular to the flow by some pressure taps positioned around the tube (Figure 75). The total pressure, also called impact pressure, is measured by a tap parallel to the flow that receives the impacting flow (from there comes the designation) directly. Each tap conducts the flow through different ways to a system that compares the pressures, obtaining their difference. In the case of the static pressure, the taps (the superficial holes) must be really small. This is so in order to not affect the measurement by the incoming flow that could induce the obtainment of a smaller velocity since the flow would be partially impacting the tap, lowering the pressure difference between the taps by increasing the apparent static pressure, and consequently the estimated velocity.

Figure 76 - Wind tunnel Pitot-static tube installation.

Source: Author (2018).

After the differential pressure is obtained (Figure 75), which is designated dynamic pressure, the velocity has been indirectly already obtained (Equation 48). With the flow fluid density known, by means of a simple calculation the local velocity can be determined.

The Pitot-static tube is used for several purposes involving velocity determination by pressure measurements comparison. One of them, of high importance, is the cited measurement of the dynamic pressure inside the wind tunnel working chamber. As mentioned above, a micromanometer is connected to the Pitot-static tube inside the tunnel, ahead of the working chamber, in order to determine the dynamic pressure at each condition.

4.2.3 Visualization methods: qualitative evaluation techniques

Besides the high importance of flow characteristics and behaviors, it does not mean that they must be quantified. Sometimes it is quite acceptable and useful to determine qualitatively the flow characteristics, depending on the desired objectives.

A good example of such specific flow characterization is the vortex wake observation, or the separation region delimitation on a test model or body. While investigating a separation region, or different flow field characteristics, like the interface between boundary layer and far field, it is not required to find exactly the point where the changes really occur. Since on a real operating surface or model these positions are usually not static, but really non-stationary or non-uniform, a rough delimitation satisfies the needs. This is a fact, and when discussing about flow separation, for example, one always talks about separation “region or line”, instead of point, a terminology usually used when evaluating 2D numerical solutions.

Therefore, if there are observations to which only a qualitative evaluation is necessary, what are the instruments, or better still, the methods that can be applied to get such results? The answer to this question is given in the following paragraphs, where the wind tunnel classical visualization techniques that are applied to this work are presented and briefly explained.

4.2.3.1 Tufting visualization

The tufting visualization is a really classical and old technique applied to aerodynamic studies. The way it is carried out is so versatile, that it is used not only in wind tunnel tests, but also for flight test investigations as well. The idea is quite simple, and uses some small length fabric strings or yarns that are frayed at their ends, applied to the surface of interest, and observed, allowing the aerodynamicist to characterize the flowfield based on their behavior (NASA, 2015).

Tufts are made of popular materials such as monofilament nylon, polyester or cotton No. 60 sewing thread. It is common to coat the tufts with some kind of dye, sometimes fluorescent, in order to get better visibility and contrast. For this reason, they are relatively cheap to produce in comparison to other visualization techniques. However, some patience and time are required in order to apply the small yarns to the surface. They must be firmly attached to the surface, and for this it is usually applied glue or an adhesive tape. This is important so as to guarantee that the tufts are not blown off the surface as the test starts, and also that they affect to the minimum the flow where they are inserted. Still regarding the preparation, one must be attentive to the length, thickness and weight of the strings. They must be cut so that they are responsive to the flow, but do not alter its nature. This requires some estimation of boundary layer thickness, and more important than that, some experience in the experimental aerodynamics field.

Figure 77 - Tufts applied using adhesive tape.

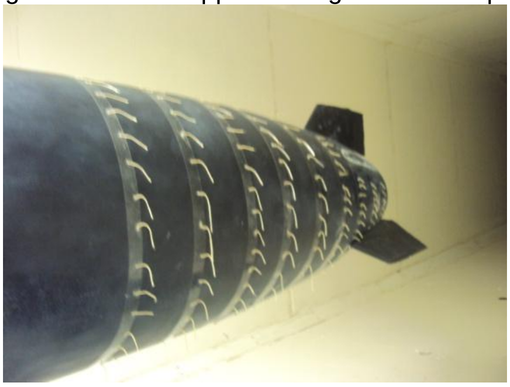

Source: Author (2018).

Figure 78 - Tufts on a real aircraft.

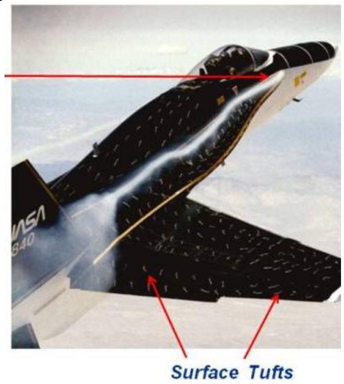

Source: NASA (2015).

The tufts functionality is very simple too. The principle is that, as the fluid flows over the body, the tufts are blown (if they were correctly designed and applied), and point downstream. This means that they represent a streamline, or the specific streamline that goes through their attachment points.

It has to be emphasized that surface tufts only provide information about the lowest region of the boundary layer, i.e. the viscous layer, and if they are fully contained within it. If not, the size of the string, mainly the diameter and weight, are overestimated, and must be corrected (NASA, 2015).

If everything is correctly dimensioned and the surface is tufted in the necessary regions, it is possible to visualize cross-flow, reverse flow and even flow separation based on the tufts direction or movement. It is even interesting to record the tufting experiment, because this makes possible to pinpoint unsteady flow regions, and some flow trends or structures in separation regions. Another interesting procedure is to deploy tufts mounted on wands which can then go in and out, or just perform some sweeps, in a specific region when looking for vortices and related structures. As the wand is moved along the specified path, and, for example, the tuft goes inside a vortex, it starts immediately to follow the local streamline as mentioned above, allowing the vortex visualization.

Nevertheless, if the intention is to visualize some patterns or behaviors off the surface, in the free stream, using only tufts is not advised, requiring special skills and experience. For such purposes, it is more indicated to combine tufts and other techniques, such as smoke or oil visualization.

4.2.3.2 Smoke visualization

To visualize the flow at a distance from the surface, a common and efficient technique is the use of smoke. With such method, one can identify and visualize vortices and separation regions. Besides this advantage of free stream flow visualization, smoke is relatively inexpensive to produce.

Figure 79 - Vortex visualization by means of smoke at LAE.

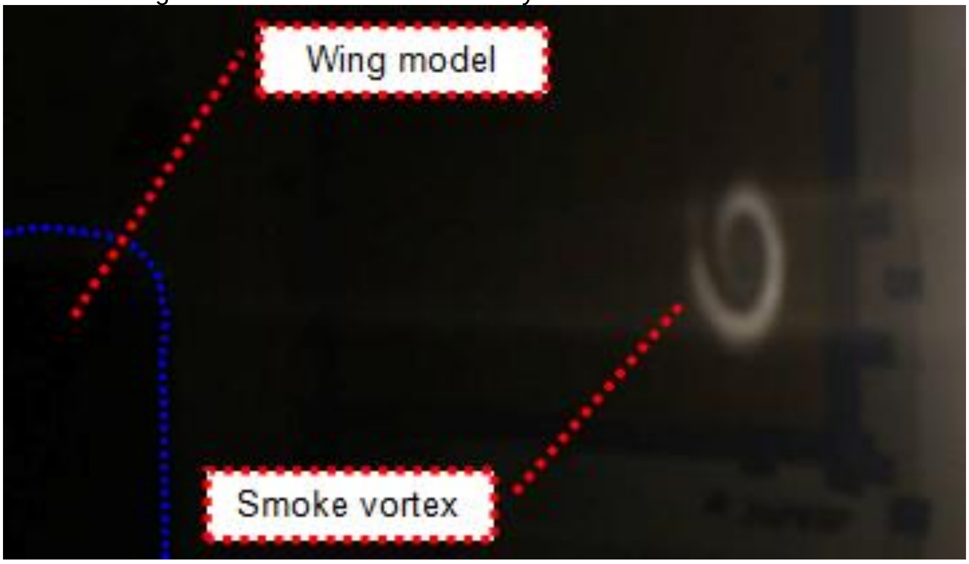

Source: LAE-1 (2016).

Among the methods for smoke generation, one of the most common employs titanium tetrachloride and tin tetrachloride which react with damp air. However it has the disadvantage that both components are corrosive. Another solution is the combination of anhydrous ammonia and hydrogen sulfide, but they produce some odors and, in contact with damp air, sulfuric acid. An alternative is the combination of steam and liquid nitrogen, producing a dense smoke with no bad effects. Another option is the burning of light oils, which produces a thin smoke, but leaves some residues.

This is an important point. The smoke must be introduced to the interest region by means of a hollow wand, free to move around the model, or through taps on the model surface. The question is that, just like for the tufts, the smoke must not alter the flow, and avoid leaving residues inside the tunnel or on the model surface. These residues must be studied, looking for toxicological effects, and be evaluated whether they alter or not the natural flow.

Another noticeable disadvantage of smoke is the limit velocity for efficient analysis, and it is also strongly dependent on proper lighting (very intense sources). Some types of smoke can work well up to around 300 mph, above that it is difficult to properly visualize flow structures. For this work, some issues were encountered, mainly regarding proper lighting and smoke density, making it difficult to visualize the flow using smoke at 35 m/s (or 80 mph). For this reason smoke tests had much lower velocities.

At LAE, an Ate-AEROTECH™ wind tunnel smoke generator was used for flow visualization by means of smoke streams. The smoke is produced by peristaltically pumping white oil (Shell Ondina EL™ – medical quality) to the tip of a probe, where a low voltage electrical coil heats the oil, converting it into a dense plume of smoke, without losses along the tubing. Oil flow rate and heater voltage are the control parameters available at the control unit. The probe is specially designed, minimizing local wake generation, allowing the generation of smooth and steady emissions of up to 5 m long smoke plumes. The probe is positioned inside the tunnel, fixed to the wind tunnel floor, ahead of the model, by some 1.5 m. Its height is adjusted so the desired flow streamline is visualized. The interference of the probe with the flow development is minimum, once it is very stiff (does not vibrate) and thin (diameter ≈ 5-6 mm for the whole assembly). In order to generate the required lighting plane, an overhead projector was used. Its light board was covered with a black opaque sticker, leaving only a thin middle light band. This band when mirrored produced a concentrated lighting plane inside the working chamber. Pictures of such assembly can be found in section 5.2.3.4.

4.2.3.3 Oil flow visualization

One special and interesting kind of visualization technique is based on an oil mixture. Especially for the visualization of separation regions, titanium dioxide, suspended in a mixture of linseed oil and paraffin, was used. Thanks to its components, the compound has a white color, which made it necessary to paint the model using black ink, in order to get the highest possible contrast. The referred solution must be applied on the surface seconds before starting the wind tunnel. This is so in order to minimize the runoff due to gravity effects, which can spoil the spread of the painting, concentrating it in specific regions, and removing it from others.

The common procedure is to apply the oil – simply called flowviz in some cases - with the tunnel stopped, leave the place and properly turn on the tunnel, setting the model to the desired condition. Then it is necessary to wait until the streaks are properly established. Once this moment is reached, the tunnel is stopped, and the results must be quickly registered, usually by means of photographs. A complementary alternative is recording the oil flow through internally installed cameras, and extract frames from the films. It is essential that the oil is applied with the adequate thickness so it can generate representative streaks (meaningful length) without pooling when the tunnel is stopped. Although it is very difficult to overcome the gravity effect, for all runs the model was painted using the same technique, with similar reaction speeds, with no unnecessary stops, resulting in useful visualization results, which can then be compared.

Figure 80 - Flow visualization by means of oil at LAE-1 wind tunnel.

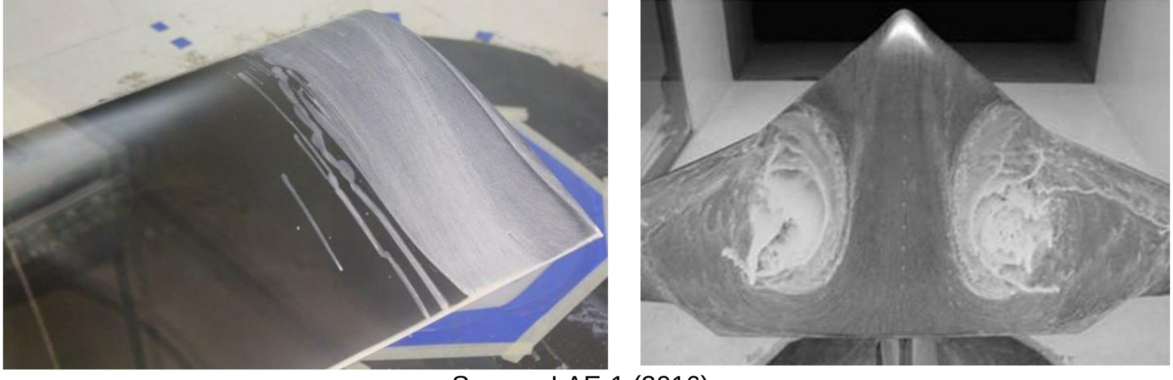

Source: LAE-1 (2016).

In a simple manner, what happens is, during the test, the oil flows over the model, carried downstream. As for the other visualization techniques, it is possible to use highlighting pigments, like fluorescents, that when illuminated with black light provide greater visibility. It is usual to see different shades over the same model (Figure 80); this is related to local the skin friction coefficient, and naturally to the boundary layer nature. Since the oil cannot penetrate the separation boundary (no flow attached to the surface), the oil patterns indicate this region. Besides that, by means of a more sensitive compound (addition of naphthalene), even transition regions can be well determined, because there is a difference between the skin friction of laminar and turbulent boundary layers. Downstream from the transition, oil will be swept away (NASA, 2016).

Once again, as for all qualitative techniques, skill and experience are required in order to adequately apply the oil, and interpret the patterns. Obviously, as already explained in the case of smoke, some clean-up is necessary between the tests and a careful evaluation of the oil influence on the nature of the flow as well.

At LAE a specific and adapted recipe is used in order to produce the “flowviz”. Titanium dioxide stays in suspension in an oleic mixture based on machine oil, oleic acid and linseed oil, with the addition of paraffin (Kerosene). Sometimes, in the case of a low speed wind tunnel, like the LAE-1, it is advisable to apply a coat of paraffin on the surface if the final mix ends up fairly thick, reducing friction with the model surface. A minimum amount of mix shall be used, and must be applied as quickly as possible, turning on the tunnel right away. Once the paraffin has evapourated and flow set, the pictures must be taken. The model cleaning is made with paraffin as well.

4.3 TESTING CONSIDERATIONS: AERODYNAMICALLY MODELING THE PROBLEM

Although the facilities are equipped with the necessary instruments, even if correctly operated, the results thus obtained are not the final numbers. For every single wind tunnel test it is necessary to make some considerations in order to firstly represent the desired condition, and afterwards bring the results to the reality outside of the tunnel or using a more technical nomenclature, to the freestream condition (usually denoted by subscript “∞”). The common approach to solve this issue is to plan the test evaluating the similitude (similarity), followed by the application of wind tunnel corrections to the results.

4.3.1 Similitude evaluation

The first step for the wind tunnel test modeling, the similitude evaluation, as already briefly discussed, aims at adjusting the wind tunnel test physical magnitudes and the model characteristics in order to have an equivalent flow influence. Usually *Re* and *Ma* are the typical values to be reproduced (Section 3.1.6.2), but some other factors are important for specific tests, like the *Fr*.

Nevertheless, sometimes, it is just impossible to achieve the same numbers, and the similitude becomes a much more complex task. In order to be representative, the test has to guarantee the same aerodynamic behavior, simulating the same flow characteristics, flowfield patterns and development. In such cases, other creative solutions must be adopted and carefully evaluated before being chosen.

Before starting the tests, the similitude must be guaranteed. It is simply not worth testing, if the results do not represent reality. As seen from the literature review (section 2), the flow for airship conditions is essentially turbulent, which may not be very well represented if smaller models at lower velocities (limitations of a wind tunnel) are used. In order to have a representative result, it must be guaranteed that the whole model (at least after its very prow region) is under a turbulent regime. Different physical strategies were experimentally evaluated. They are listed below, and detailed individually. Typical surface roughness terminology and parameters (PRECISION DEVICES, 2018) are used to characterize each roughness proposal. The mean line is the HULL surface, which for simplicity is assumed to be perfectly smooth. The roughness average (*Ra*), which will be considered the maximum profile peak above the mean line, assuming that the roughening devices are perfect, is going to be divided by the $\mathbf{r_{máx}}$, presenting the roughness size, ε, which will be used instead of *Ra*. Finally the peak density, *Pc*, will be represented by the shape of each roughening device, described and illustrated individually.

a) SMOOTH: natural flow over the smooth original model.

This case is self explaining in the sense that no intervention regarding surface roughness was made in the model, testing it with the sandpaper 1200 finished surface, according to what is explained in Appendix A.

b) FISHNET: fishnet type stocking covering the model.

This case is based on the work conducted by Gomes (1990). A nose cover was fabricated for the HULL model using a pair of fishnet type stockings, which were sewed together. The FISHNET extended from the nose up to 50%**L**. A spherical sewed portion of around 20 mm was present at the bow, and the net shape was made up of lozenges of 25 mm (height) x 10 mm (length), with a depth equivalent to 1.5 mm. Such a depth correspond to a roughness size of ε = 2.6E-03.

Figure 81 - FISHNET characteristics.

Source: Author (2018).

c) COLLANT: collant type stocking covering the model.

Derived from the previous proposal, this solution is aimed at lowering the roughness level of the FISHNET, while still fully covering the fore portion of the model. The COLLANT extended up to 45%**L**, and was fully enclosing. Nevertheless, the stocking weaving provided a roughness (between crossing yarns) equivalent to 0.5 mm in depth, which means ε = 8.7E-04. At the bow position a 5 mm spherical ending was sewed, and at around 45%**L**, there was a fabric band 1 mm high, 22 mm long. Besides this, there was a 1.5 mm high strip, forming a semi circular shape, coming from the center line underneath the model to the middle plane at the end of the stocking, beginning at around 30%**L**.

Figure 82 - COLLANT characteristics.

Source: Author (2018).

d) HEXNET: hexagonal shaped net covering the model.

Another derivation of the FISHNET, this hexagonal shaped net was placed from around 30%**L** up to 50%**L**. The hexagons were 0.5 mm deep, 4 mm wide and 6 mm high; the base of the hexagon was 2.5 mm long, while the sides were 3.5 mm in length. The net was attached to the model by means of double-sided and simple plastic tape at the ends. The roughness size here is equivalent to the COLLANT case, ε = 8.7E-04.

Figure 83 - HEXNET characteristics.

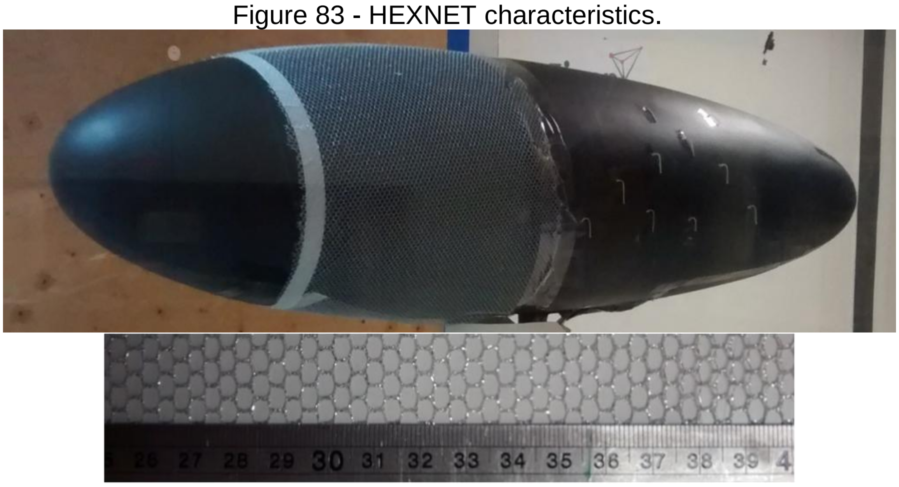

Source: Author (2018).

e) BUBBLEWRAP: bubblewrap platic covering the model.

This was the last covering technique used. The model was literally wrapped up using bubble wrap plastic up to 50%**L**. The bubbles were 4 mm high, having 10 mm, and alternately spaced 13 mm from each other's center in line. Subsequent lines were out of phase by 6.5 mm, so the junction of three bubble centers would draw an equilateral triangle. This was the most aggressive cover in terms of roughness size, resulting in ε = 6.9E-03.

Figure 84 - BUBBLEWRAP characteristics.

Source: Author (2018).

f) TRIP: tripping bands (adhesive tapes) attached to the model.

The last roughening approach used triangular tripping bands (turbulators). Made out of foam tape, the trips were bands with a straight side and a saw type side. The trip was 1 mm high and 7 mm long. Each triangle on the saw side had bases of 5 mm and height with the same dimension. This device was initially used in three different configurations. These are better detailed in section 5.2.1, but basically, trip bands were added at different positions along the model length. Although the roughness size of this configuration was ε = 1.8E-03, covering the whole fore portion of the model is completely different from tripping it, as the results showed.

Figure 85 - TRIP characteristics.

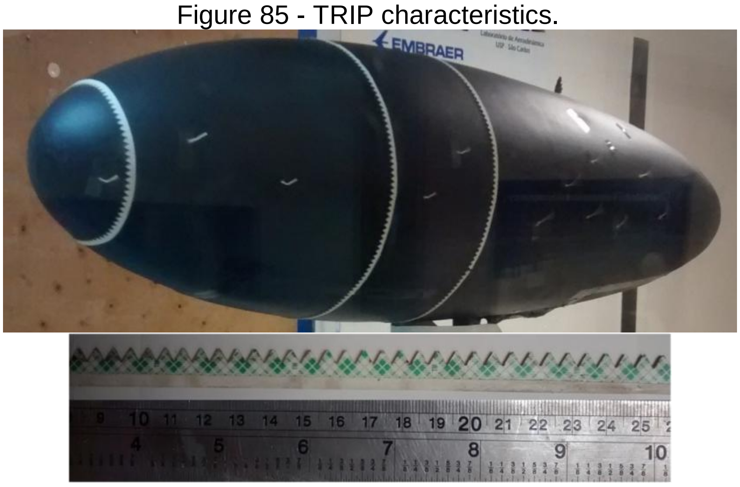

Source: Author (2018).

Table 8 contains a summary the proposed roughnesses to be assessed.

Table 8 - Summary of roughness proposals.

Roughness	Roughening characteristic	Size
SMOOTH	Surface finish	Sandpaper 1200
FISHNET	Fore half cover	ε = 2.6E-03
COLLANT	Fore half cover	ε = 8.7E-04
HEXNET	Fore half cover	ε = 8.7E-04
BUBBLEWRAP	Fore half cover	ε = 6.9E-03
TRIP	Singularity (@5%**L**;25%**L** and 40%**L**)	ε = 1.8E-03

Source: Author (2018).

Regardless of the option, in order to be acceptable, the roughening device must ensure that the model boundary layer behavior is similar to the real case and that the aerodynamic effects linked to viscosity are well reproduced. The key point is determining the sort, size and density of such “turbulators” or roughnesses.

Since the objective is to guarantee that the whole model is turbulent, like for full scale airships (DURAND, 1936), it was necessary to use flow visualization techniques (section 4.2.3). The options went through two filtering campaigns supported by numerical evaluations, basically based on drag. Once the options were filtered, before ending Phase I (section 5.2), flow visualization was carried out. By interpreting the flow patterns, turbulence was attested over the whole surface, as desired, supporting the roughness selection. As the results started to come out, care was taken assuring that the results were adequate, and that in any case no laminar reattachments occurred, ensuring full turbulent profiles, and the desired aerodynamic structures. Based on Gomes (1990), the aim was to identify the configuration that is fully turbulent, but does not completely spoil the airship aerodynamic characteristics by dramatically increasing the drag forces. Although a decision was made regarding the most adequate roughness, all the results were registered.

4.3.2 Wind tunnel corrections

The wind tunnel limitations were already discussed in section 4.2, including blockage effects and the flowfield modifications due the presence of the body. It is known that wind tunnel data require numerical corrections to a number of factors, including forces and angles, mainly because of wall effects and internal boundary layer growth. Based on Barlow, Rae and Pope (1999) for this case, a series of three-dimensional corrections for a closed test section should be applied. Those classified as applicable to this work are discussed below, but basically no corrections were conducted, although some effects were evaluated. The reason for this is the main objective of this work: characterization of airship aerodynamics and flow interferences. With such a qualitative objective, the generation of exact numerical data is not necessary, but simulating the flow in the best possible way is.

Among the applicable corrections are balance load interactions and angle mechanical calibrations, which were carried out, as explained in section 5.1. Support tares and interferences are discussed ahead, in section 5.1.2. However, still according Barlow, Rae and Pope (1999), since the runs were for comparative data, i.e. using the same support for obtaining data for comparisons, no corrections need to be applied.

The blockage corrections are comprised of two parts: solid and wake blockage. The first, given the model volume, was already assessed (section 4.1.1). The second, which regards the wakes shed from the model, depends on parasite drag. For both, no corrections were applied throughout this work. Solid blockage would be present in all cases, and again for comparative purposes, it would not be mandatory, once no exact coefficient for use in the real design was expected to be obtained. In spite of that, some evaluation on blockage is conducted in section 5.1.1. In the case of wake blockage, besides the comparison factor, as will be shown in section 5.2, once this correction is proportional to induced (parasite) drag, which is very small, it was judged that no data needed to be changed. Besides blockage, another interesting effect observed in closed sections is the increase in the thickness of the wind tunnel wall boundary layer, which leads to changes in pressure along the section, increasing real drag by an additional quantity. This effect is called buoyancy, but just as blockage, it was present for all pair to pair comparisons, being not therefore corrected.

An interesting correction is that for AoA. For an ideal wind tunnel, the flow would be parallel to the test-section boundaries, but that is not feasible. As a consequence, usually there is some up or down flow, simply called upflow, and also crossflow. With this in mind, one may consider that some upwash may appear upstream of the model in the wind tunnel section, even if the geometric AoA was precisely adjusted. This correction is especially important, because an upflow strongly affects drag measurements, while crossflow affects floor-ceiling-mounted half models. For the tests conducted, indeed some evidence of upwash was observed through oil flow visualization (section 5.2.3.4). There is a third component that induces AoA changes in the tunnel section comprised in the wall corrections compendium. This component considers finding the effective vortex span for wings with specific *AR* and taper ratios. As airship aerodynamic behavior is known to be unique, the vortices generated by the fins are not considerable in relation to the test section dimensions, it was consequently disregarded.

If the actual numeric coefficients were required, there would be corrections for forces and moments. It is interesting to highlight that all coefficients and wall corrections presented in Barlow, Rae and Pope (1999) are based on wing circulation, and therefore meant for typical aircraft. This makes their applicability questionable to airship models. Analyzing some of the wind tunnel tests conducted for airship models, it is possible to see that mostly the corrections considered airstream misalignment, buoyancy effects and support taring. McLemore (1962) cites all three corrections, but does not provide the techniques and sources. Rizzo (1924), much more simplistic, only carried pressure drop corrections, but based on specific data from the wind tunnel used, which are therefore not applicable to this case.

As a final example, it is worth looking at the work conducted by Abbott (1931) in the variable density wind tunnel. Corrections were applied regarding balance interference, which is not applicable to this work, once the balance stays underneath the tunnel floor (section 4.2.2.3). Airstream convergence corrections were considered more accurate than the conventional horizontal buoyancy correction, although mathematically similar, and were therefore applied. Nevertheless, it was only applied to drag, neglecting effects on lift, even by wall effects, once they were believed to be less than 1%. The calculated increase in drag was based on a formula for an ellipsoid with a volume and fineness ratio equal to that of the model. The proposal was to place the model in a stream converging in such a manner as to have a linear static pressure gradient. This was derived from the work of Lamb (1928) and Taylor (1928). The correction for drag (misalignment) was used at all AoA, applying the additional drag to the CB, ignoring effects on pitching moment. Also, the support corrections for any one model were assumed to be the same for all angles of pitch. It is considered however that these assumptions may have caused appreciable consistent errors.

All this evaluation demonstrates that conventional corrections need to be adapted to be properly used for testing airship models in wind tunnels. In addition, by analyzing such corrections applicability as presented in the works carried out by reference researchers, the proposal that all the mathematical work, related to them, could be dropped, based on the objectives sought for this work, is supported.

4.4 EXPERIMENTS AND TEST CAMPAIGNS DESCRIPTION AND PLANNING

To achieve the aimed objectives, test campaigns were divided in two different phases: characterization and evaluation phases. The first phase comprised all steady regime tests carried out in order to describe and characterize the airship model aerodynamics and stability for a given tail configuration: “X”. After this first campaign was completed, for the second one, six different fin configurations were installed on the model and the stability analysis was once again carried out but only using the dynamic approach – damping characteristics of free yawing osccilations (section 5.3). The main objective of the first batch of runs is to gather, evaluate and provide general but useful information about the typical aerodynamic coefficients and trends, besides presenting the flow structures and interferences present for typical airship flight conditions. For the second phase, the objective was more specific: evaluate the applicability of the proposed TVC theory (Section 3.2.2.3), and whether it is at least a good reference for very early conceptual design phases.

Qualitative techniques were used, mainly tufting and oil flow visualization. Tufts were applied to hull and fins surfaces; also oil was applied to both, but mainly on the stern region. Some runs were made with oil on the fins, in order to try capturing the different patterns due to different velocity fields. It is important to say that, during the results evaluation, a general term “surface velocity” is used. This term does not refer to the surface velocity itself, once this is assumed to be zero (no-slip condition of boundary layer classical theory). This “surface velocity” refers to the velocity of the lowest portion of the boundary layer, the viscous sublayer (*viskose Unterschicht* or *viskose Wandschicht*, according to Schlichting and Gersten, 2006). These simple techniques made it also possible to infer whether the boundary layer was in fact thin or not, with little effort. Also smoke visualization was used in order to assess the outer flow, and detached aerodynamic structures such as vortices.

All tests were carefully planned, based on the development of master tables, guaranteeing that the minimum needed amount of tests was conducted and that the results were reliable and the most accurate. The runs performed are described below, including the master table, the required instrumentation and the tests themselves, with the applied methodology. As always happens when dealing with experiments, some tests had to be re-run due to inconclusive or mistaken results. These are presented in the master tables, but were not used. The reasons which substantiate the need for re-runs are presented individually together with the tests identification. In general, the master tables are those containing all performed tests, and not just those indicated in the initial planning.

4.4.1 Phase I: Wind tunnel steady-regime tests

The basic natural flow and the aerodynamic characteristics related to the model studied had to be determined. All aerodynamic interference effects present were also evaluated for steady conditions. In other words, the typical polar curves were obtained, as well as trimming curves (polars with variable control inputs). In addition wake developments, interference effects (boundary layer interaction and vortex induction) and pressure distribution over the hull of the airship model for specific attitudes were evaluated. During this first batch of tests, the aim was to be able to characterize the general aerodynamics of a conventional airship, but with an X-tail configuration, and confirm the existence of non-linear behaviors and their intensity, tracking, identifying and describing the aerodynamic structures responsible for that.

The runs were planned based on what was expected to be tested and observed. The experimental investigations to be carried out in this first phase were compiled and entered in a specific table which gives an overview. This table, called Testing Master Table, is hereby presented for Phase I, listing for each run the control identification (ID), Reynolds number, model description (appendages and other items), date of execution and any other applicable remarks. Data like AoA range, its increment (discretization) and other flow parameters are presented together with the results, whenever it is relevant. This table should also provide a guideline on the experiments conducted, and help in organizing the results. In addition, it provides information and explanations required in order to understand other results. The presented table also contains some assessments and result recaptures conducted along the execution of the tests. This makes it easier to identify and cross relate the results to be presented on the followings pages.

Table 9 - Master Table of Wind Tunnel Tests; Phase I.

Objective	ID	*Re*	Model configuration description	Date	Remarks
First evaluation	ENV_00	1.73E+06	Bare HULL	08/09/2017	Without Fins & without fairing[25].
	ENV_01	1.74E+06	Bare HULL + 2.7mm OD Wire[26]	08/09/2017	
	ENV_02	1.06 – 2.07 E+06	ENV_01	08/09/2017	*Re* variation @fixed AoA; *Re* influence assessment.
	ENV_03	1.72E+06	ENV_01 + Root fairing[27]	08/09/2017	-
	ENV_04	1.78E+06	ENV_03 + Full-fairing[28]	09/09/2017	-
	ENV_04_R1	1.78E+06	ENV_04	09/09/2017	Repeat due to intense model vibration and irregular drag around AoA=0.
	ENV_05	1.75E+06	ENV_01 + LAE Fairing[29]	09/09/2017	-
	ENV_05_R1	1.74E+06	ENV_05 (AoA_zero = 2° + [-24;24])	09/09/2017	Repeats developed in order to assess acquisition sensibilities to different AoA ranges and increments with the LAE Fairing.
	ENV_05_R11	1.74E+06	ENV_05 (AoA_Zero =2° + [-20;20])	09/09/2017	
	ENV_05_R2	1.73E+06	ENV_05 (AoA = [-30;2;30])	09/09/2017	
	ENV_05_R12	1.37E+06	ENV_05_R11 (Frequency_WT = 20hz)	09/09/2017	
Initial model dynamics and limitations assessed – Testing parameters evaluation (all fairings removed)					
Parameters check and determination	ENV_06	1.5E+06	ENV_01	09/09/2017	Acquisition cables were symmetrically repositioned behind the support bar to reduce influence, and all fairings were removed.[30]

[25] This fairing regards structure used to cover and reduce flow influence on the support steel bar that links the model to the aerodynamic balance.

[26] This twine was twisted around the support bar in order to transition the boundary layer on the support so it would separate later, and theoretically diminish the model vibration due to separation bubbles (like von-Kàrmàn vortices).

[27] The root fairing is presented in section 5.1.2.1, and was an attempt to cover the base plate that was exposed to the flow, and could interfere severely on results.

[28] The full fairing is presented in section 5.1.2.1, and is the complete version, shielding the base plate and the bar itself (whole support structure).

[29] LAE fairing was an alternate to the first fairing in order to improve flow qualities (section 5.2.1.1).

[30] Table continues

Objective	ID	*Re*	Model configuration description	Date	Remarks
	[31]ENV_06_R1	1.5E+06	ENV_06 (AoA_0 = 3° + ΔAoA = 5°)	09/09/2017	Repeats developed in order to assess acquisition sensitivity to different AoA ranges and increments, its direction (ascending or descending), sampling rates, zeroing adjustment investigation and results verification.
	ENV_06_R2	1.5E+06	ENV_06_R1 (AoA_0 = 2°)	09/09/2017	
	ENV_06_R3	1.9E+06	ENV_06_R2 (Sampling → 2500hz for 2s)	09/09/2017	
	ENV_06_R4	1.9E+06	ENV_06_R2	09/09/2017	
	ENV_06_R5	1.9E+06	ENV_06_R2	09/09/2017	
	ENV_06_R6	1.9E+06	ENV_06_R2 (AoA = [-10;10])	09/09/2017	
	ENV_06_R7	1.7E+06	ENV_06_R2 (AoA = [10;25])	09/09/2017	
	ENV_06_R8	1.7E+06	ENV_06_R2 (AoA = [0;25])	09/09/2017	
	ENV_06_R9	1.7E+06	ENV_06_R2 (AoA = [-25;25])	09/09/2017	
Parameters assessed and determined – Surface roughness evaluation / similitude analysis					
Surface roughness assessment	ENV_07	1.71E+06	ENV_06 + COLLANT[32]	09/09/2017	-
	ENV_08	1.70E+06	ENV_07 + LAE Faring	09/09/2017	-
	ENV_08_R1	1.77E+06	ENV_08	10/09/2017	Results recapture.
	ENV_08_R2	1.76E+06	ENV_08 + Tufts	10/09/2017	Results recapture with flow visualization.
	ENV_09	1.77E+06	ENV_08 + LAE Fairing Extension	10/09/2017	Fairing extended to get closer to model; Touch identified along the negative AoAs.
	ENV_09_R1	1.76E+06	ENV_09	10/09/2017	Fairing trimmed; no problems identified.
	ENV_09_R2	1.75E+06	ENV_09	10/09/2017	Fairing re-trimmed for better symmetry
	ENV_10	1.74E+06	ENV_09_R2 (without COLLANT)	10/09/2017	-
	ENV_10_DeltaV	9.84E+05 - 2.18E+06	ENV_10	10/09/2017	*Re* variation @ AoA = 0.
	ENV_11	1.72E+06	ENV_10 + BUBBLEWRAP[33]	10/09/2017	BUBBLEWRAP loosened.

[31] Table continuation
[32] Roughness used option among others to change the flow development to full turbulent (section 4.3.1).
[33] Roughness used option among others to change the flow development to full turbulent (section 4.3.1).

Objective	ID	*Re*	Model configuration description	Date	Remarks
	[34]ENV_11_DeltaV	9.74E+05 - 2.26E+06	ENV_11	10/09/2017	*Re* variation @ AoA = 0.
	ENV_11_R1	1.70E+06	ENV_11	10/09/2017	Results recapture with fixed BUBBLEWRAP.
	ENV_12	1.70E+06	ENV_10 + HEXNET	10/09/2017	HEXNET loosened.
	ENV_12_R1	1.69E+06	ENV_12	10/09/2017	HEXNET fixed – tape tip vibration (low intensity) has evidenced non-stationary phenomena (crossflow vortex around the hull at higher AoAs).
	ENV_12_R1_DeltaV	9.65E+05 - 2.24E+06	ENV_12_R1	10/09/2017	*Re* variation @ AoA = 0°.
	ENV_12_R2	2.04E+06	ENV_12_R1	10/09/2017	Results recapture @ velocity = 30m/s.
	ENV_13	2.04E+06	ENV_10 + TRIP @25%L	10/09/2017	Trip band added.
	ENV_13_DeltaV	9.42E+05 - 2.23E+06	ENV_13	10/09/2017	*Re* variation @ AoA = 0°.
	ENV_13_R1	2.04E+06	ENV_13	10/09/2017	Results recapture.
	ENV_14	1.68E+06	ENV_13 + TRIP @40%L	10/09/2017	Trip band added; DOUBLE TRIP.
	ENV_14_R1	2.04E+06	ENV_14	10/09/2017	Results recapture @ velocity = 30m/s.
	ENV_14_DeltaV	9.66E+05 - 2.39E+06	ENV_14	10/09/2017	*Re* variation @ AoA = 0°.
	ENV_15	2.07E+06	ENV_14 + TRIP @5%L	11/09/2017	Trip band added; TRIPLE TRIP.
	ENV_15_DeltaV	9.69E+05 - 2.48E+06	ENV_15	11/09/2017	*Re* variation @ AoA = 0°.

[34] Table continuation

Objective	ID	*Re*	Model configuration description	Date	Remarks
			[35]LAE Fairing alignment check		
	ENV_15_R1	2.13E+06	ENV_15	12/09/2017	LAE Fairing alignment check to zero.
	ENV_15_R2	2.12E+06	ENV_15_R1 (AoA_0 = 4°)	12/09/2017	Zeroing assessment.
	ENV_15_R3	2.10E+06	ENV_15_R2 (AoA_{max}=29°)	12/09/2017	Maximum positioning system AoA assessment.
			LAE Fairing removed		
	ENV_16	2.11E+06	ENV_15 + Root Fairing	12/09/2017	Only base plate covered.
	ENV_17	2.10E+06	ENV_16 (Only two TRIPs, 1st and 2nd from nose)	12/09/2017	Third TRIP (@40%L) removed
	ENV_17_DeltaV	2.40E+06 - 9.40E+05	ENV_17	12/09/2017	*Re* variation @ AoA = 0°.
	ENV_18	2.07E+06	ENV_17 + COLLANNT	12/09/2017	
	ENV_18_R1	2.04E+06	ENV_18	12/09/2017	Results recapture.
	ENV_18_DeltaV	8.30E+05 - 2.39E+06	ENV_18	12/09/2017	*Re* variation @ AoA = 0°.
	ENV_19	2.04E+06	ENV_17 + HEXNET	12/09/2017	
	ENV_19_DeltaV	9.31E+05 - 2.39E+06	ENV_19	12/09/2017	*Re* variation @ AoA = 0°.
			Roughness definition complete - Fins installed (x-tail configuration)		
Stability investigation of X-tail airship configuration	ENV_20	1.69E+06	ENV_17 + δ = 0°	12/09/2017	First fins capture and assessment – δ = 0°
	ENV_20_DeltaV	9.65E+05 - 2.40E+06	ENV_20 + Velocity change	12/09/2017	*Re* variation @ AoA = 0°.
	ENV_21	2.05E+06	ENV_20 + Tufts on fins	12/09/2017	Results recapture – δ = 0° adjusted
	ENV_21_d-5	2.10E+06	ENV_21 + δ = -5°	12/09/2017	
	ENV_21_d+5	2.05E+06	ENV_21 + δ = +5°	12/09/2017	δ < 0 is convention for airship negative pitch
	ENV_21_d+10	2.05E+06	ENV_21 + δ = +10°	12/09/2017	
	ENV_21_d+15	2.04E+06	ENV_21 + δ = +15°	12/09/2017	

[35] Table continuation

Objective	ID	*Re*	Model configuration description	Date	Remarks
	[36]ENV_21_d+20	2.04E+06	ENV_21 + δ = +20°	12/09/2017	
	ENV_21_d-25	2.04E+06	ENV_21 + δ = -25°	12/09/2017	
			FISHNET installed		
	ENV_22	2.07E+06	ENV_21 + FISHNET	14/09/2017	-
	ENV_22_DeltaV	9.69E+05 - 2.49E+06	ENV_22	14/09/2017	*Re* variation @ AoA = 0°.
	ENV_22_R1	2.05E+06	ENV_22	14/09/2017	Results recapture.
	ENV_22_R2	2.11E+06	ENV_22 (AoA = [+25°; -25°])	16/09/2017	Descending AoA capture.
			DOUBLE tripped HULL and pressure measurements (FISHNET removed)		
Pressure investigation with fins and different roughnesses	ENV_23_P1	2.12E+06	ENV_21	16/09/2017	-
	ENV_23_P2	2.10E+06	ENV_23_P1 + δ = +25°	16/09/2017	-
	ENV_23_P3	2.09E+06	ENV_23_P1 + δ = -25°	16/09/2017	-
	ENV_23_P4	9.59E+05 1.61E+06 2.48E+06	ENV_23_P1	16/09/2017	*Re* variation @ AoA = 0°.
			FISHNET installed		
	ENV_24_P1	2.08E+06	ENV_23_P1 + FISHNET	16/09/2017	
	ENV_24_P4	1.77E+06 2.06E+06 2.45E+06	ENV_24_P1	16/09/2017	*Re* variation @ AoA = 0°.
			FISHNET removed – COLLANT installed		
	ENV_25_P1	2.07E+06	ENV_23_P1 + COLLANT	16/09/2017	
	ENV_25_P4	1.77E+06 2.06E+06 2.46E+06	ENV_25_P1	16/09/2017	*Re* variation @ AoA = 0°.

Pressure measurements finalized - Fins and COLLANT removed (FISHNET installed)

[36] Table continuation

Objective	ID	*Re*	Model configuration description	Date	Remarks
Roughness reverse evaluation	Env_26	2.11e+06	Env_17 + FISHNET	16/09/2017	Without fins.
	ENV_26_DeltaV	9.24E+05 - 2.39E+06	ENV_26	16/09/2017	*Re* variation @ AoA = 0°.
			Pressure transducer cables and FISHNET removed		
	ENV_27	2.21E+06	ENV_17	17/09/2017	Without cables & FISHNET.-
	ENV_27_R1	2.12E+06	ENV_27	17/09/2017	Descending AoA capture.
	ENV_27_DeltaV	9.62E+05 - 2.46E+06	ENV_27	17/09/2017	*Re* variation @ AoA = 0°.
	ENV_27_R2	2.09E+06	ENV_27	17/09/2017	Ascending AoA capture.
			Tripping bands removed – Fins installed		
FINAL FINS EVALUATION (including S1 Shorter configuration)	ENV_28	2.10E+06	BARE HULL + Fins	20/09/2017	Clean support and δ = 0°.
	ENV_29	2.04E+06	ENV_28 + Root Fairing	20/09/2017	-
	ENV_30	2.04E+06	ENV_29 + FISHNET	20/09/17	-
			Fins removed		
	ENV_31	2.04E+06	BARE HULL + FISHNET	20/09/2017	Without fins.
	ENV_32	2.04E+06	BARE HULL	20/09/2017	-
	ENV_33	2.05E+06	ENV_32 + S1 Shorter Fins	20/09/2017	δ = 0°.
	ENV_34	2.05E+06	ENV_33 + FISHNET	20/09/2017	
			FISHNET and Root Fairing removed		
	ENV_35	2.06E+06	BARE HULL + S1 Shorter Fins	20/09/2017	-
			Model removed – Support drag evaluation		
BAR DRAG	Support_00	9.82E+05 - 2.51E+06	Clean support	21/09/2017	-
	Support_01	9.82E+05 - 2.50E+06	Support_00 + Root fairing	21/09/2017	-
	Support_02	9.80E+05 - 2.50E+06	Support_01 + Twine	21/09/2017	-[37]

Source: Author (2018).

[37] Table conclusion

Table 10 - Oil flow visualization Master Table.

Objective	ID	Equivalent Configuration[38]	*Average Re* (q [Pa])	Model configuration description	Date	Remarks
Surface flow visualization	Run_00	ENV_27	2.0E+06 (520-530)	Bare HULL & TRIP AoA = 0°	08/09/2017	Flowviz
	Run_01	ENV_27		Bare HULL & TRIP AoA = 0°	08/09/2017	Flowviz adjusted and spread laterally.
	Run_02	ENV_27		Bare HULL & TRIP AoA = +10°	08/09/2017	Flowviz
	Run_03	ENV_27		Bare HULL & TRIP AoA = +20°	08/09/2017	Flowviz
	Run_04	ENV_21		Bare HULL & TRIP & S0 FINs AoA = +20°	09/09/2017	Flowviz
	Run_05	ENV_21		Bare HULL & TRIP & S0 FINs AoA = 0°	09/09/2017	Flowviz
	Run_06	ENV_22		Bare HULL & FISHNET & S0 FINs AoA = 0°	09/09/2017	Flowviz
	Run_07	ENV_21		Bare HULL & S0 FINs AoA = 0°	09/09/2017	Flowviz

Source: Author (2018).

[38] No Acquisition cables were installed for the oil flow visualization runs.

After completion of Phase I, all experiments listed were done, the properties listed above were considered as already well known, problems and behaviors were also identified, theoretically assessed, or at least sufficiently explained by detected phenomena during the experiments. Testing improvements were evaluated all along the campaign (as can be seen by the changes duly recorded in Table 9), and the magnitude of effects were assessed, including to which extent they affected other parts of the aircraft. The results are presented in section 5.2, which contains charts, pictures and conclusions regarding the investigative work as described in Table 9.

4.4.2 Phase II: Wind tunnel dynamic tests

In this work, the basic premise was that it is not only the general aerodynamics that must be investigated. Although very useful for better understanding what happens during airship flight, it was only a portion of this work. The proposed theory related to the TVC concept was investigated based on the dynamic response. To do so, during Phase I, the model, under on steady conditions, was investigated with two different tail configurations: the Standard and the Shorter (cut fins – lower *AR*), placed in the same positions. Since it is easier to change the fin size, using the same fixture, than moving them along the model, the chosen approach checked how the size affects mainly drag and moment, without assessing comparative trimming polars for simplicity. The results also provided, by testing with different roughnesses, some information on the effectiveness of the theory of variable stability (aerodynamic forces variation) efficiency due to hull boundary layer and vortex sheets interference on the tail. However, the flow changes significantly under non-stationary conditions, such as an oscillating model. It should therefore be possible to evaluate the proposal that larger surfaces provide better results, because they have more area outside of the boundary layer. Besides that, it is also possible to investigate how hull vortices influence different tail areas.

This second part, Phase II, comprises a series of dynamic (free oscillation) tests, devised in order to check whether the TVC is outside of the proposed range (Section 3.2.2.3), i.e. if the airship stability and controllability are jeopardized. The tests were conducted only in order to analyze tail damping effect under free-oscillation of the model, in an uncontrolled motion (section 3.2.2.1). The employed methodology does not aim at simulating the real dynamic behavior of the airship, but the tail aerodynamic behavior while oscillating. The used procedure was as follows.

After positioning and holding the model at a given AoA (visually large), the model is let to oscillate in a wind-off condition, dampening only by the support springs. After wind-off oscillation ceases, the model is once again held at a large AoA, and the wind tunnel flow is turned on, and the position held until the flow stabilizes. Once this condition is reached, the model is released so it can freely oscillate, tending to an equilibrium position, ideally aligned with the flow and stabilized (no remaining oscillations). There is no problem regarding not knowing the angle at all as long as it is large enough (AoA>20° - visual references available), since the interest lies on damping effects, which are observable from the curve shape, and not from absolute position values.

The angular position variation is recorded, and plotted against time. With such information, it was possible to chart the oscillations and evaluate the damping effectiveness and efficiency of each tested tail configuration. The configurations were compared based on the oscillation decay. The numerical references for the comparisons were some of the terms described in section 3.2.2.1: the exponential term (logarithmic decrement $\boldsymbol{b}$) and the damping ratio $\boldsymbol{\zeta}$. The data were interpreted as described in section 3.2.2.3.

Based on the parametric study used to propose the TVC theory. two FIN sets were available: S0 and S1 (Appendix A), representing different unit areas. Besides that, three different tail arrangements were proposed: "X" (standard configuration - Figure 254), "+" (cruciform, two rudders and two elevators – Figure 255) and "-Y" (one rudder and two ruddervators - Figure 256). The different arrangements allowed the variation of total area, and also of tail forces direction, another design challenge proposed to be solved by the TVC concept. Such variations led to denser comparison charts and more reliable conclusions. With all the information thus gathered, the efficiency of each tailplane was quantified by the configuration damping characteristics.

Still based on what is proposed in section 3.2.2.3 (TVC), hull total length and longitudinal distance between tail and CB would be the other two characteristics which could be changed. Nevertheless, none of them was changed for simplicity and time saving purposes. The main problem involved with varying the tail fixation distance would be adjusting the fins to the hull surface. As the stern region has a greater curvature profile, the fins with same area and planform would not fin forward and rearward of the standard position (longitudinal station), requiring complete new sets of them. Regarding the hull length, changing it would also not make sense considering the same hull model. In order to assess the length, a new airship configuration would then have to be developed, since L is one of the factors used in converting the TVC into a non-dimensional coefficient. In addition, changing the model length and keeping the curvature would only change *Re*. Therefore, it was decided to reduce the number of parameter variables, focusing on the characteristics of the specific airship model, the ADB-3-30.

Still for Phase II, a specific mounting system (Figure 86) named RAS (Rotary Axis Support) was used. By means of a main steel case, RAS is bolted to the working chamber floor, in the outside. The case has a rolling bearing, through which a vertical 15 mm diameter steel shaft goes inside the wind tunnel. This shaft is 450 mm long, positioning the model at level 45% in height in the working chamber. The shaft upper tip is attached to the model by a screw plug which trespasses a flange bolted to the model. The lower shaft tip has two perpendicular bars trespassing it: the springs and potentiometer arms. The upper bar holds one side of two equal (stiffness and length) tension springs, whose other side is attached to the wind tunnel frame. The lower bar has two wire actuation links. These links actuate a pair of arms connected to an axial potentiometer shaft, which is attached to the RAS case.

Figure 86 - RAS apparatus for dynamics tests (lower portion).

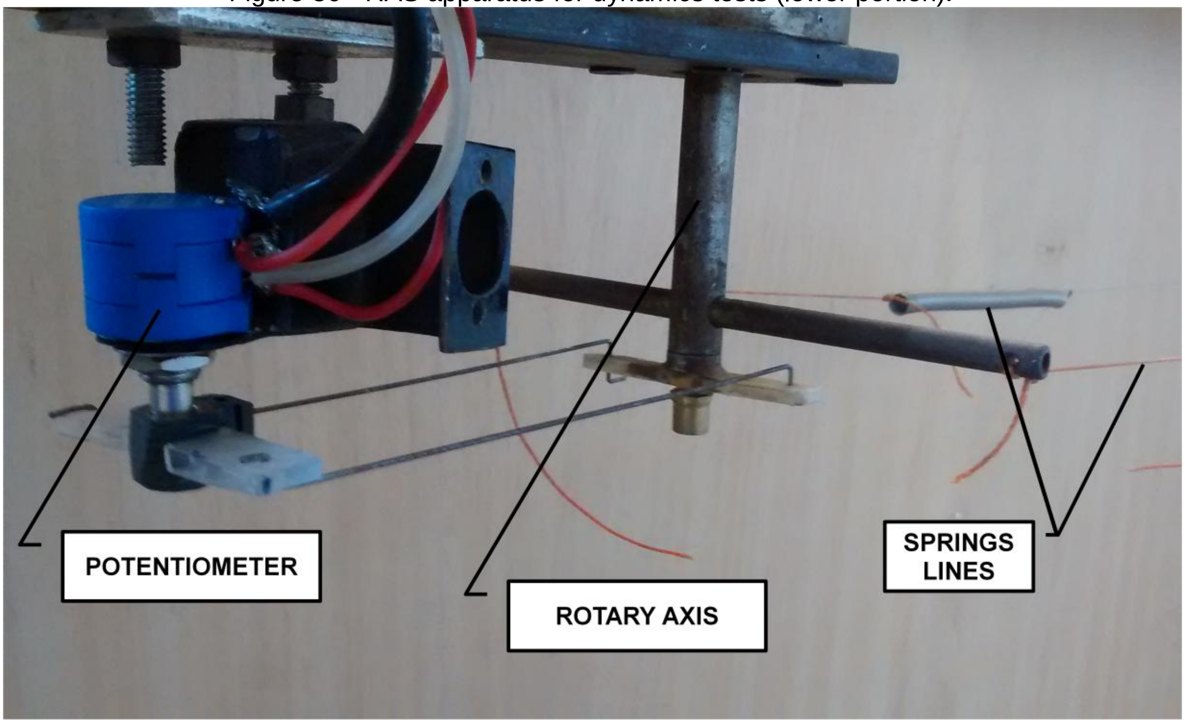

Source: Author (2018).

This way, once the model oscillates, so does the vertical shaft, in phase. This causes both lower bars to also oscillate. Each of the arms connected to the springs provide the system oscillatory properties, while the wire links change the potentiometer setting, providing a signal, which after adequate treatment, records angular position.

The springs were adjusted so the oscillations were visually adequate for the desired purposes, which means that the chosen stiffness does not reduce the oscillation to very small angles, but also does not allow the model to completely diverge (if that comes to happen for a certain condition). This ensured good tests realization, and model safety, i.e. adequate oscillatory conditions. The stiffness was not strong enough to attenuate the damping effect observation, but also not too small allowing complete inversion of the model heading in case a very bad condition developed. The damping effect can be fairly affected by system losses. Therefore, the bearings were checked to be in good conditions, and the frictions all over the system were negligible. In this way the tail damping effect could be captured with confidence.

As described, the initial positioning is made by hand and the potentiometer, a WXD-3590 Trimmer Precision Potentiometer (Figure 86), is used to track all data related to angular position. The full setup is comprised of the potentiometer feeding from a DC Digital Symmetrical Power Supply MPC-3006D, and an acquisition system, just like that one used for the aero-balance. The input voltage level was adjusted during the initial trials so noise was reduced, and oscillations were clearly identifiable through voltage measured along the variation of potentiometer resistance. The directly obtained signal, despite amplification and adequate acquisition, was very noisy, mainly due to high frequency model vibration and potentiometer sensitivity. Before being evaluated, the signal went through a detailed treatment, described in section 5.3.

As stated for Phase I, these dynamic tests were also previously planned, and all along the runs some changes and adaptations were incorporated. The resulting Testing Master Table for Phase II (Table 11) presents the identification for each run, *Re*, model description (fin set and arrangement), date of execution and applicable remarks. TVC values are calculated and presented in section 5.3.7.

Table 11 - Master Table of Wind Tunnel Tests; Phase II.

ID	*Re* (*q* [Pa})	Fin set	Tailplane configuration	Date	Remarks
DYN_000		No testing point		21/09/2017	Signal adjustment
DYN_001	Wind-off (Woff)	S1 Shorter (Low AR)	X (X-tail)	21/09/2017	-
DYN_002	Wind-off (Woff)	S1 Shorter (Low AR)	X (X-tail)	21/09/2017	-
DYN_003	4.88E+05 (30.00)	S1 Shorter (Low AR)	X (X-tail)	21/09/2017	-
DYN_004	2.82E+05 (10.10)	S1 Shorter (Low AR)	X (X-tail)	21/09/2017	-
DYN_005	7.57E+05 (72.00)	S1 Shorter (Low AR)	X (X-tail)	21/09/2017	-
DYN_006	Wind_off (Woff)	S1 Shorter (Low AR)	X (X-tail)	21/09/2017	-
DYN_007	6.03E+05 (45.80)	S1 Shorter (Low AR)	X (X-tail)	21/09/2017	-
DYN_008	9.81E+05 (121.3)	S1 Shorter (Low AR)	X (X-tail)	21/09/2017	-
DYN_011	9.54E+05 (114.8)	S1 Shorter (Low AR)	X (X-tail)	22/09/2017	-
DYN_012	Wind_off (Woff)	No tail	N/A	22/09/2017	BARE HULL
DYN_013	4.49E+05 (25.40)	No-tail	N/A	22/09/2017	BARE HULL
DYN_014	Wind-off (Woff)	S1 Shorter (Low AR)	+ (Cruciform)	22/09/2017	-
DYN_015	5.53E+05 (38.60)	S1 Shorter (Low AR)	+ (Cruciform)	22/09/2017	-
DYN_017	1.04E+06 (136.9)	S1 Shorter (Low AR)	+ (Cruciform)	22/09/2017	-
DYN_018	Wind-off (Woff)	S1 Shorter (Low AR)	-Y (Inverted Y)	22/09/2017	-
DYN_020	1.04E+06 (137.1)	S1 Shorter (Low AR)	-Y (Inverted Y)	22/09/2017	-
DYN_021	Wind-off (Woff)	S0 Standard (High AR)	X (X-tail)	22/09/2017	-
DYN_022	6.04E+05 (46.00)	S0 Standard (High AR)	X (X-tail)	22/09/2017	-
DYN_023	Wind-off (Woff)	S0 Standard (High AR)	+ (Cruciform)	22/09/2017	-
DYN_024	7.68E+05 (74.30)	S0 Standard (High AR)	+ (Cruciform)	22/09/2017	-
DYN_025	7.67E+05 (11.80)	S0 Standard (High AR)	+ (Cruciform)	22/09/2017	Results recapture
DYN_026	Wind-off (Woff)	S0 Standard (High AR)	-Y (Inverted Y)	22/09/2017	-
DYN_027	7.67E+05 (74.10)	S0 Standard (High AR)	-Y (Inverted Y)	22/09/2017	-
DYN_028	6.64E+05 (55.50)	S0 Standard (High AR)	-Y (Inverted Y)	22/09/2017	Results recapture

Source: Author (2018).

4.5 ACCURACY AND PRECISION EVALUATION – GENERAL ERRORS DISCUSSION

The numerical results of this work are going to be shown and discussed in the following chapter (Section 5). However, with each instrument chosen for a measurement, instantaneously there is a precision (random error) associated. Besides that, and related to the methodology, to the staff and to the instrumentation wear, there is a variation of the accuracy and a probable BIAS error (constant deviation) associated as well.

Every single component or set-up has an associated error, or at least an uncertainty source regarding measured values. The errors are composed by two components: bias (related to accuracy) and random variation (related to precision). Every measurement has the random variation related to repeatedly measuring the same quantity which is related to the precision of the equipment; biases, however, may also be present. Anyway, it is important to track the error propagation, and evaluate how it affects the final reliability of the measurements. Having an error linked to the measurement does not mean it is useless. Although it changes the final value obtained, for qualitative purposes or comparisons, when the error is evenly spread among the measurements, it is assumed that it is acceptable to have it thus embedded (“unknown”), i.e. if the final result accuracy is not strictly needed.

Figure 87 - Precision and accuracy illustration.

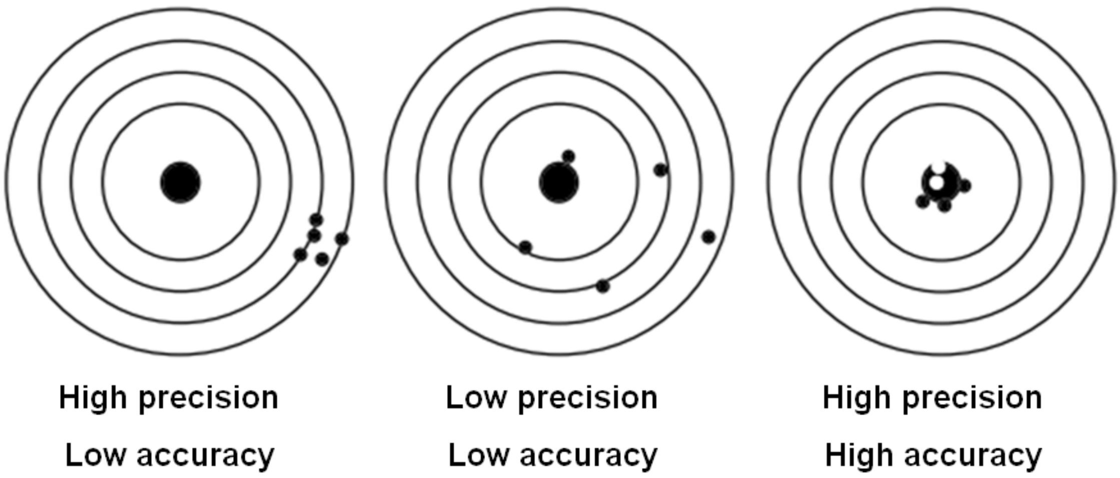

Source: Cruz et al (1997).

Nevertheless, it is interesting to have in mind that when direct measurements are combined in order to calculate (indirect measurement) a specific quantity (for example, measurement of static differential pressure and dynamic pressure to obtain

C_P) each of those associated errors propagate according to the mathematical operations carried out. In this way, a quantity *x* always has an error *Δx* associated to it. A simplified way of taking into account the error propagation during simple calculations with statically independent quantities such as addition/subtraction and multiplication/division is shown below. Suppose that, *x* and *y* are variables, with their associated errors, *Δx* and *Δy*:

$$(x \pm \Delta x) \pm (y \pm \Delta y) \pm \cdots = (x \pm y \pm \cdots) \pm \sqrt{\Delta x^2 + \Delta y^2 + \Delta \ldots^2}$$

Equation 50 - Error propagation for addition/subtraction. Source: Cruz et al (1997).

$$(x \pm \Delta x) \cdot (y \pm \Delta y) = (x \cdot y) \pm \left((x \cdot y) \cdot \sqrt{\left(\frac{\Delta x}{x}\right)^2 + \left(\frac{\Delta y}{y}\right)^2} \right)$$

Equation 51 - Error propagation for multiplication. Source: Cruz et al (1997).

$$\frac{(x \pm \Delta x)}{(y \pm \Delta y)} = \frac{x}{y} \pm \left(\left(\frac{x}{y}\right) \cdot \sqrt{\left(\frac{\Delta x}{x}\right)^2 + \left(\frac{\Delta y}{y}\right)^2} \right)$$

Equation 52 - Error propagation for division. Source: Cruz et al (1997).

It is important to highlight that this work does not aim at providing highly precise and accurate values, which would require a very deep and extensive error analysis. The objective here it to analyze interference effects and provide guidance for further precise design work, mainly at conceptual phases. Nevertheless, in order to minimize the errors of the results and values obtained, precautions were taken. Some of them were already described, and below follows possible error sources and uncertainties, with the proposed mitigation techniques for each of them. In accordance with the need of depicting how the interferences act, and their effects, it is important to guarantee that the errors are evenly spread, and also at least tracked/evaluated. This is the main reason why such topics are discussed below.

4.5.1 Dimension, format and finishing of model

In general, it is rather difficult to have a low cost accurate experimental model (in dimensions and shape). In order to balance quality and cost, and thanks to a partnership between the university and a specialized company, where the author works nowadays, the models were made out of fiber glass and covered with a rapid cure plastic compound. This surface could then be sanded until it was smooth enough (sandpaper 1200), and checked visually against a template (jig) that was laser cut with a precision of ± 0.5 mm. Appendix A presents more detailed information.

In addition, an experimental technique was applied to check the model symmetry: pressure distribution comparison. Using the three pressure taps lanes along the model, and analyzing only the model envelope, some tests were run, and the pressure distribution results were plotted. The analyses were made for AoA = 0°, for small opposite AoA (±4° and ±8°), and large opposite AoA (±20°). Results and discussions regarding the model symmetry are presented in Section 5.1.1.

According to the data thus gathered, it was possible to conclude that the model was adequate for the purposes of the work, since the geometrical errors associated with its dimensions are very close to the precision of the measurements, which is also a limitation. Moreover, when considering the experimental techniques employed, such small deviations are to be considered negligible when dealing with such low *Ma*, despite the small scale ratio of this experiment.

4.5.2 Model positioning and referencing

The positioning of a model, and its referencing, are essential to ensure that the extracted coefficient polars and derivatives are correctly based. For this reason, during the installation of the models for the tests, it was always applied more than one technique to set and check the fixation angles and positions.

Measurements were made on the model surface and on its base in order to align each pair properly. With the pairs (model + base) aligned, it was possible to align the base with the balance support. This last alignment was always carefully made considering the reference of instruments such as scales, protractors and set squares. The scale had usually a precision of +/- 1 mm. and the protractors, +/- 1°. The set squares are commonly used in the LAE wind tunnel experiments, being rigid references. In order to guarantee that the model is balanced, i.e. it is not rotated or tilted, a visual inclinometer combined with a set square was used for positioning. Finally, by means of an adapted plumbob, the model leveling was checked, ensuring that the pressure taps at the far bow and stern were at the same level from the wind tunnel working chamber floor. It is important to highlight that, once the model was moved away and again installed, all checking procedures were redone. Obviously, all positioning was subject to precision and human skills.

Finally the model (volumetric) centering in the chamber was also evaluated. Due to a construction design feature of the wind tunnel, a certain amount of off centering of the model was inevitable. Since the wind tunnel is also used for aeroacoustic investigations, there is a microphone antenna cover plate fixed to the starboard (right) wall. This plate, which is 1.5” thick, was added after the tunnel original construction, and for this reason the floor center is not the chamber center. This installation may result in changes in the measurements, such as polar curve asymmetry, higher for certain aerodynamic coefficient values (local flow acceleration), etc. Indeed such consequences were observed during the first tests, and are discussed in Section 5.

4.5.3 Instrument associated errors

Regarding the instrumentation, it was required to know the range of measurements, the precision associated, and even the calibration chart. All the commercial instruments used during this work had their calibration certificates up to date. In this list are included the micromanometer, the barometer, the thermometers and the scanivalve.

The Pitot tubes are not commercial items and therefore do not call for standard calibration procedures. Before being installed in the wind tunnel, they are tested, and compensations are made if losses are found not to be negligible. In this case, since the Pitot tubes are constantly used for all other activities, they are well known instruments, periodically checked. This allows one to consider that they work properly, the focus being on guaranteeing their precision as well. In case there was some kind of internal blockage, the Pitot tube would not let the air inside to properly reach the micromanometer. If this had happened, probably even when successively running at the same wind velocity at the same density, the indicated dynamic pressure would be different or vary. Fortunately, it was attested that there were no obstructions (no clogging), and the Pitot tube was efficient enough for the measurements. For the wind tunnel balance, the calibration procedures were already explained in section 4.2.2.3, and in Appendix C, one can find the results.

Being obvious that qualitative techniques do not require calibration procedures, it does not make sense to discuss about associated errors, as there are no numbers involved. However, since the staff depends on cameras and their correct positioning to obtain the required images, it was always attempted to take the shots/videos with some dimensional reference in the images, in order to compare different results, in case this could be needed. A common adopted solution for more difficult visualizations was the fixation of two cameras, at different specific spots.

4.5.4 General errors and uncertainties related to drag measurement

It is not the objective of this work to deeply investigate error propagation, but rather to list probable sources, and try to mitigate them as a mandatory procedure. Since the model and instrument errors were already evaluated, the missing items to be investigated were the interfaces between model and the surrounding medium. The most notable is the model support. Obviously the presence of the support, which is a cylindrical bar attached to the envelope is an error source, more precisely a bias error source. It introduces at least an additional drag force to the measured value, increasing the model final C_D.

Drag is one of the most difficult parameters to measure, among aerodynamic quantities, regarding precision, and the most sensitive to medium influence (BARLOW, RAE and POPE, 1999); this is true mainly because of the fluid mechanisms responsible for the fluid friction, which are basically the development, transition and separation of the boundary layer. The challenge involved in modeling the boundary layer is well known, and explains the complexity involved in obtaining proper drag numbers. Drag measurement precision (if errors are mitigated) is dependent on the similitude between modeling and reality, whereas sensitivity is related to flowfield perturbations which are spurious elements. This last case matches the above-mentioned case of the supports. Although essential for fastening models and transmitting their forces to the balances and measuring devices, they are classical sources of error.

As already mentioned in Section 3.1.6, there were various techniques used in previous investigations, and all of them had their own way of influencing the experiments. Aiming at the support interference mitigation, mainly on drag measurements, an incremental (methodology) evaluation of the support influence was conducted during the very first runs. The applied methodology considered a fixed dynamic pressure of 428.5 Pa (equivalent to 27 m/s), and a *Re* = 2.0E+06; the AoA was varied between -20° and +20°. Three steps (configurations), considering the model support exposure to the flow, were defined for the investigation campaign:

1. Totally exposed (Baseline) – C1.
2. Wrapped (spiral) with cotton twine – C2.
3. Isolated by an aerodynamic fairing (LAE Fairing) – C3.

Analyzing this work case, it can also be said that the support is simple enough to be modeled using analytical (or semi empirical) techniques. It may be considered an infinite cylinder, since it is shielded at both ends, having no 3D effects. That is true if we consider that the 3D interferences between model and support are negligible, a good assumption as the support has, theoretically, no relevant crossflow, nor lift generation.

This was the approach taken to analyze the results when they are obtained, serving as a good reference to cross check the values and conclude whether they are reliable or not. The expected drag reductions must be of the same order of magnitude of the drag that would be generated by the cylinder (support to the model). The obtained results for each step described above and the discussions of the associated errors are presented in Section 5.

Nevertheless, besides the “drag step” that may be added to the measurements, it is also possible that the cylinder (or any other body) presence, as already mentioned, creates some interference vortices, which may affect the flowfield, and consequently all measured parameters. This effect may be enlarged when adding the aerodynamic fairing or any other body to the medium. Complementarily, if the fairing had any sort of contact with the model, it could transfer higher forces to the tunnel aerodynamic balance. So, even after isolating the support, it is necessary to check whether the solution does not lead to a new error source. This second concern was dealt with by building a symmetric airfoil shaped fairing (LAE Fairing) attaching it to tunnel floor, and making sure it does not touch the model support. The effects on the model were then investigated, looking for abnormal behaviors originated from the fairing region. All results and discussions related to this investigation are also contained in Section 5.

During this first investigatory preparation for the main work, there was also a qualitative and preliminary analysis of some similitude and positioning uncertainties already described above. The main objective was to check such topics, and evaluate the extent of such interferences.

All results and relevant information regarding those first approaches, and the conclusions thus reached are presented and explained in the early part of the following section, as they were a basis for some final adjustments of the tests setups. The specific results of the main test campaigns, as mentioned above, are presented in Section 5 in details, followed by the pertinent analyzes and discussions.

5 RESULTS ANALYSIS AND DISCUSSION

5 RESULTS ANALYSIS AND DISCUSSION

This section contains the results that were obtained after the execution of the test campaigns listed in the previous section. Only those considered relevant to this work are presented below. They are interpreted and discussed in order to try and reach meaningful and useful conclusions. The numerical results, regressions and charts were treated using mainly Excel™ tools for simplicity and database management.

There are three main subsections in this chapter. The first one comprises the very first investigations on the model, registering the preparation and adaptation for the main campaigns. In this section, the model and its fixture are evaluated, improving the set-up, where possible, based on the obtained results. The uncertainties considered relevant are investigated, quantified and treated.

The other two sections comprise Phases I and II mentioned in Sections 4.4.1 and 4.4.2. The results are presented following the most logical (for better comprehension) sequence, which does not mean specifically the chronological sequence for all tests, since there were some iterative processes, not all detailed here. Each batch of results is evaluated, trying to extract from it the maximum amount of useful information, discussing observed effects, interactions and boundaries influences as well.

The results reliability is discussed and cross-checked against theory. This is conducted by means of qualitative analysis, comparing results to what was expected to be obtained in a general manner. The detected deviations of what was expected are analyzed, and the sources are investigated, highlighting errors or new findings.

The knowledge obtained from this work is linked to industry interests, such as enhanced performance and controllability of conventional airships. The expectation is that the results thus obtained are useful to an extent of providing new methodologies and basis for conceptual design guidance during airship project development. Besides that, suggestions for new studies and developments are also made, presenting the most likely contributions they would provide to academy and industry.

5.1 PRE-CAMPAIGN: UNCERTAINTIES AND SET-UP EVALUATION

This section deals with investigations on the model configuration, and some changes that were applied to it in order to make the future results more reliable. In short, the model support influence on the results, the wind tunnel working section configuration and also the model symmetry were focus of investigation. The conclusions after the experiments are presented here, and are to be considered for the subsequent sections, which contain the main campaigns.

5.1.1 Airship model symmetry evaluation

Ensuring that an ellipsoidal body of revolution is circumferentially symmetric along the longitudinal axis is one of the most important and relevant characteristics when modeling it. This importance comes from the fact that being asymmetrical raises the possibility of originating relevant error sources, which would disrupt the results and lead to spurious effects and results. An asymmetrical body could generate asymmetric polars, and induce unreal wakes (compared to full scale) over its own body and tail, generating force changes, besides other effects. What is certain is that the relevance and influence of these effects are unknown unless detected, and could compromise the whole study, at least by some sort of embedded bias error.

Since this is completely undesired, some verification techniques were considered: 3D mapping, surface measuring and aerodynamic characterization. Considering that the first approach is highly precise[39] to which are added some time and cost limitations, the first option was dropped. Analyzing the campaign needs, and the expected errors, it was concluded that the third approach, the aerodynamic one, would be most suitable for this work, because it would be able to show the expected problems as foreseen, and confirm or not the asymmetry issue. The sampling measurement over the model surface was conducted anyway, only in order to check some control points. The results can be found in Section 4.5.1.

Two methods of aerodynamically checking the envelope model symmetry were pursued: pressure distribution and force polar symmetry. The first approach is considered to be the most reliable, since it is more precise (instrument wise) and provide local examination (local pressure tap at a certain position), and not an integral value (force) transmitted to a balance. Nevertheless, the force curve

[39] Actually more than what is required for this work, considering that the model surface is going to go through surface changes along the tests and that the scale is very small.

approach is also relevant, and was employed, in spite of the possibility of effects from other sources, like the model support. Results from this approach are presented and discussed in Section 5.1.3.

As explained in the methodology chapter, different AoA conditions were considered for the pressure measurements (mapping): zero AoA (baseline), small and large AoA samples. Basically, keeping the dynamic pressure between 448 Pa and 443 Pa (1% variation, which may be considered negligible), the pressures at all taps were recorded for each condition and compared. The study does not aim at checking whether the values are the proper ones (only a trend is evaluated), but compare the results of opposite pressure taps lanes at opposite AoAs. In other words, it is expected that the port side result is the same of the starboard side result when the AoA is mirrored (inverted deflection side, but same absolute value), when the envelope is symmetric. In addition, it is expected that for the zero AoA configuration all three pressure lanes have the same pressure distribution profile (port, upper and starboard sides).

The first results to be obtained were those for AoA = 0° at a condition of 445.8 Pa of dynamic pressure (measured from the Scanivalve). The collected values of differential static pressures were converted into C_P, and the corresponding points were plotted (Figure 88), disregarding error propagation. The conversion process included running a reference measurement called wind-off (measurements with no airflow), which will be referred from now on simply by Woff. After the Scanivalve calibration (following the manufacturer’s built-in process), the taps measurements with no airflow were recorded, exposing the internal bias errors related to any sort of source from the instrument for each tap. The Woff values for each tap were then subtracted from the measured values, and the result divided by the dynamic pressure to obtain C_P. The results are then presented by plotting C_P against the respective pressure tap number (Section 4.1). It is interesting to observe that the pressure distribution is little different of what was seen in section 3.1. One might recall that those results were for much slender bodies, with greater *AR*, and a long almost-straight portion. Nevertheless, an overall similarity, mainly regarding adverse pressure gradient is observed. The suction peak is very discrete, and the deceleration is smooth.

Figure 88 - Pressure distribution (symmetry evaluation) for AoA = 0°.

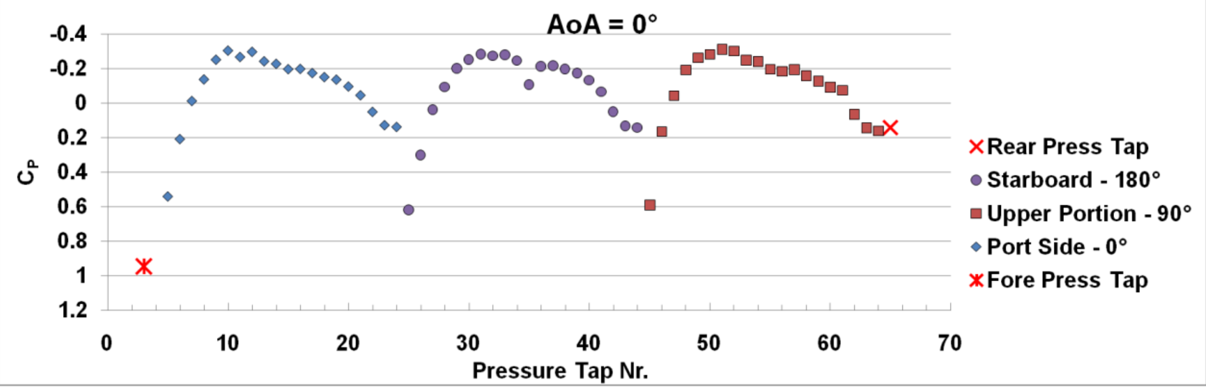

Source: Author (2018).

Analyzing the results some interesting points for consideration arose. Beginning with the bow region, the C_P for the most forward pressure tap (Tap 3) was 0.9454, and not 1 as it was theoretically expected (since the differential pressure would be the dynamic pressure). Considering only random error propagation, it can be seen that the calculated value would be 0.9454 ± 0.0395, getting much closer the aimed value of 1. Investigating the model installation, this difference can still come from some sort of bias errors related to the tap perpendicularity to the model surface and also the angle setting, which may diverge a little from AoA = 0° based on the positioning system precision and accuracy already discussed. It was however concluded that such a result would not compromise future studies, since they were not strictly dependent on this.

Going further on the results investigation it can also be seen that there is a tap (number 35) whose C_P does fit smoothly to its neighborhood trend line. This is a typical case of tap clogging or partial restriction, since the surface around the tap has no special or evident change in shape. In order to confirm that, the other runs, at different AoAs, were analyzed from this perspective as well (they are presented afterwards). Once again the same off trend behavior was indentified, and reinforcing the suspicion, for each pair of opposite AoAs, the tap showed the same values (considering the random error), being completely off trend. This tap was from there on disregarded. This decision was made since missing one tap had less impact in the results than reopening the model, and risking affecting more taps and also spoiling the delicate scanivalve set-up inside the model. Therefore and from the author's point of view, this solution presented no harm to the overall study.

Finally the attention turned to comparing the three tap lanes pressure distributions. Initially, comparing them qualitatively led to concluding that even though some points were different, they all seemed to follow the same trend, and reached similar values. This was however a first approach and not a mathematical confirmation of the expected model symmetry. In order to check that, a methodology was defined comparing the obtained C_P values with a mean C_P distribution. The mean value for each envelope station (%**L**) was calculated without taking into account the error propagation in any phase; this value was considered to be what would be the virtually expected result for all three pressure lanes. Then all error tracking was pursued, and the associated error to each tap, including even the mean calculation, was added to the respective tap mean value. The error bars would provide the limitations for the measured C_P; being within the limits would mean that the values were experimentally the same, since the only associated variation would be due to the scanivalve precision error, which is not possible to be eliminated. So the assessment was based on comparing the measured values for each tap with what would be its range around a mean value considering the associated errors. Fortunately, from the resulting chart (Figure 89), it can be seen that all C_P fell within their limits, and therefore the model itself can be assumed as being symmetrical considering the instrumentation and the test characteristics.

Figure 89 - Symmetry analysis from error propagation standpoint.

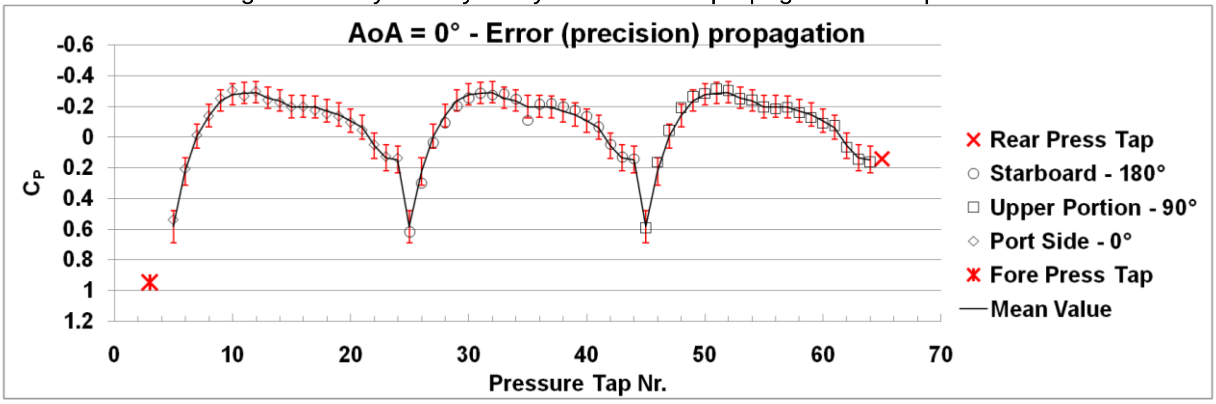

Source: Author (2018).

Although the conclusion was already reached based on AoA = 0°, as planned other AoA assessments were made. The results are presented sequentially for AoA = ±4°, ±8° and ±20°.

Figure 90 - Pressure distribution (symmetry evaluation) for AoA = ±4°.

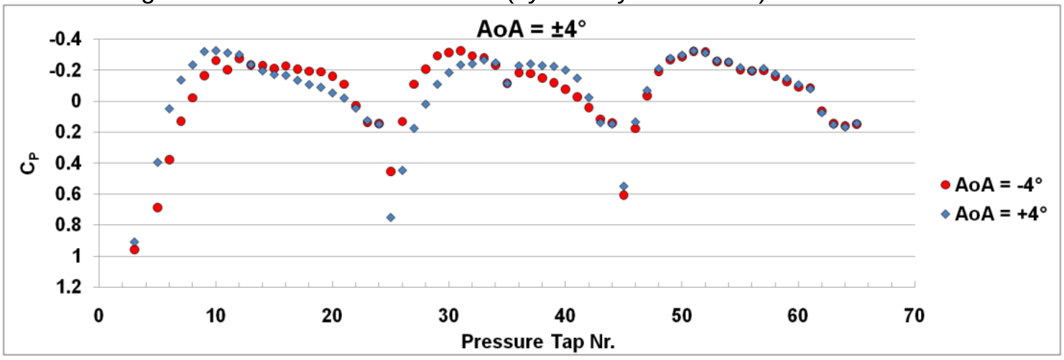

Source: Author (2018).

Figure 91 - Pressure distribution (symmetry evaluation) for AoA = ±8°.

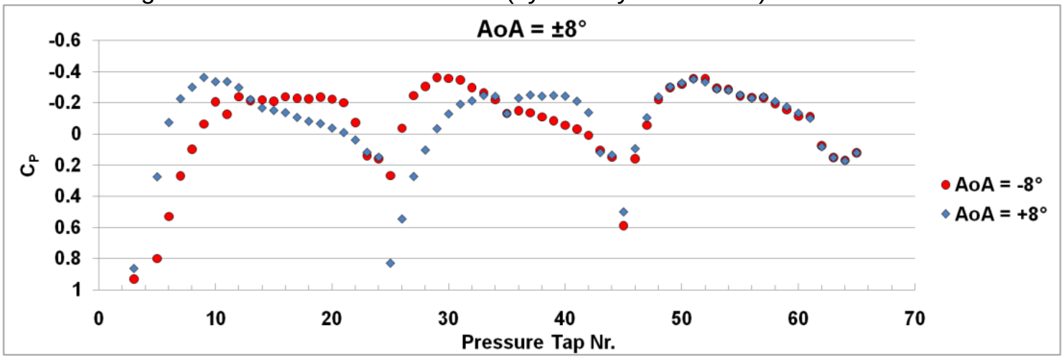

Source: Author (2018).

Comparing each opposite AoA curves, in pairs, and looking firstly only at the upper portion distribution (third pressure distribution inside each chart), it is qualitatively once again confirmed the axial symmetry. This can be stated because the upper pressure distributions were, in pairs, in a very good agreement (points over each other), showing that the top surroundings (lateral portions of the model) were very much alike. One should be cautious regarding the results for AoA = ±20°; it is seen that, although the values a very close to each other (for the same tap), there are slightly higher values when the model is on the negative AoA portion. This is, however, related to an effect which is further studied and described in the following section. It does not however invalidated the assumed hypothesis of model symmetry.

Figure 92 - Pressure distribution (symmetry evaluation) for AoA = ±20°.

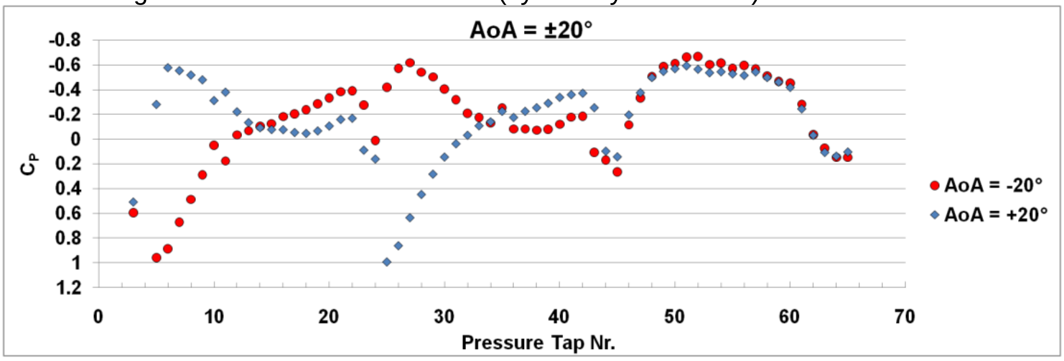

Source: Author (2018).

Finally, by comparing port and starboard pressures at opposite AoAs, one can conclude that, experimentally (including error propagation, like described before) they can be considered the same, confirming the expected symmetry. The errors were not precisely calculated for these comparisons since it would be an excessively too laborious work for reaching the same conclusion.

One last observation refers to Tap 11. It can be seen that this tap, like number 35, has an off trend behavior which is intensified as the AoA increases (it was identifiable at AoA = 0°, but very discrete). Although it does not seem to be completely clogged, since for opposite AoAs it does not present the same values, it was decided to be worth observing its results more closely during the tests campaigns, but not touching or modifying it.

5.1.2 Interferences of the model support on tests

As already discussed, in order to obtain better and more reliable results, it is better to keep the amount of additional items besides the model involved in the experiment to a minimum; this ensures the modeling is thus more precise when compared to full scale condition. However, it is necessary to have a way to connect the model to the acquisition system (the aero-balance), and also support it inside the wind tunnel. So following section 4.5.4 methodology, three main configurations were tested in order to assess how relevant the model support is in the numerical results obtained. As mentioned, only the envelope was tested, for simplicity, and avoiding other means of interference while at high AoAs.

Early on, during the first configuration (C1) test, intense vibration was witnessed during the test; the envelope was oscillating around its base, transversally to the flow direction (laterally). It was suspected that the Vortex Shedding phenomenon (BARLOW, RAE and POPE, 1999) was responsible for that behavior. Theoretically, an oscillatory flow field was developed downstream of the model support, right behind it, caused by alternating vortices detachments off the support wall. These vortices are low pressure fields, which suck the immerse body to their center; since the detachment cortices alternate left and right, the body tends to oscillate in opposite directions along the same line. Although the phenomenon was not physically visualized, its effect was evidenced in the obtained drag polar (Figure 93). Analyzing the C_D curve, it is clear that there is a plateau localized in the central region of the curve, between -10° and 10°. This *quasi* constant value may indicate that the vorticity level associated with the model vibration (transferred to the balance) was ruling (overcoming) the drag of the model itself.

The tentative theory from the first results evaluation was reinforced after the results of the second configuration (C2) were obtained. For this configuration a simple 2mm diameter cotton twine was coiled around the support. The objective was to avoid laminar flow over the tube surface, making the boundary layer to transition to turbulent flow. With this, the *Re* was increased (larger diameter) and also the flow was much more stable, ceasing with the vortex shedding. In a simple manner, the laminarity was leading to a premature boundary layer separation, directly and without any transitioning, as soon as an adverse pressure gradient was present. This premature separation caused the above-mentioned vortices to appear; once the twine is put in place, and the boundary layer is turbulent, the wake becomes uniform and stable, reducing extensively the model vibration. In such a condition, disregarding flow interactions between model and support, the only contribution should be the drag of the exposed tube (support), which is supposed to be constant at all AoA (cylinder). Then, in terms of polar, this would mean that the curve shape would be, as expected, parabolic with an upwards translation equivalent to the cylinder drag.

As expected, after the C2 results were plotted, a symmetric curve, with a global minimum around AoA = 0°, was obtained. With such a result, it seemed that the suspicion of having relevant effects of the support on the model was well founded. It is interesting to notice that the C1 and C2 curves are very close at their ends (maximum and minimum AoAs), both for values and inclination. This demonstrates once again, as suspected before, that the described effect (vortex shedding) was much more relevant at small AoAs, when the greater portion of the model drag was due to friction, a situation which is completely different from what happens when it is highly tilted (high AoAs).

Figure 93 - Model support drag polar initial evaluation.

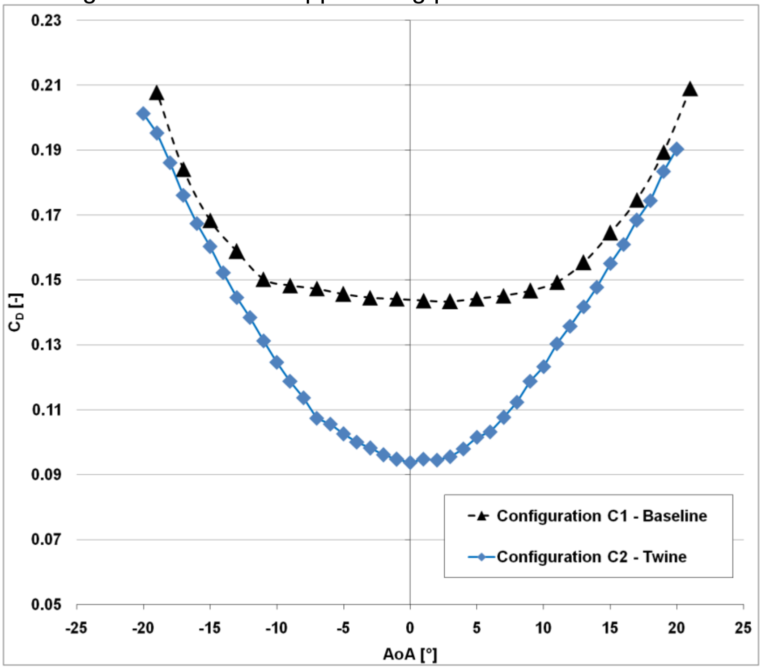

Source: Author (2018).

For the third configuration (C3), following the proposed methodology of incremental analysis, an aerodynamic fairing was added around the support. With shape based on symmetrical and low drag profiles, the fairing was made of metallic rings covered with a high density plastic sheet. The fairing was not attached to the model, but to the wind tunnel floor, at a null fixation angle; to avoid touching the model, the fairing shielded the cylinder, but its aerodynamic load was not transferred to the balance.

Figure 94 - Aerodynamic fairing for initial evaluation.

Source: Auhor (2018).

Figure 95 - Drag polars for all three support configurations.

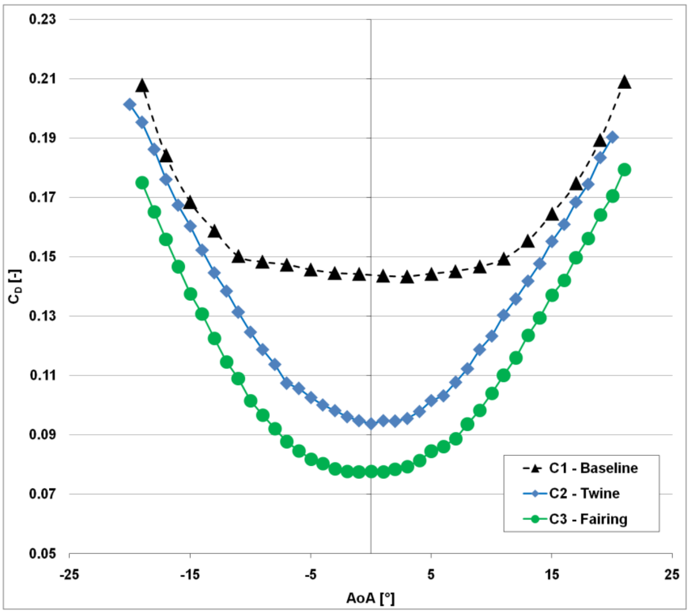

Source: Auhor (2018).

With that fairing in place, a new relevant reduction in C_D was seen and, as expected, by an almost constant value – equivalent to translating downwards the whole curve. Subtracting C3 from C2 values, a mean reduction of 0.02 (minimum of 0.016 and maximum of 0.023) was observed. Very relevant information derived from this is that the reduction is of the same order of magnitude of the model drag itself (1.0E-02). This mathematically demonstrates that some interference effects that might be underestimated are sometimes highly relevant when considering the baseline analysis (in this case an ellipsoidal low drag body – the envelope). Also important to highlight is that the attempt of not transferring any loads from the fairing to the model was successful, since the drag was reduced, whereas it could have gone up if the fairing (larger body) load was added to the calculation.

In order to crosscheck these results, and analyze whether they make sense or not, it is also possible to compare the experimental results with analytical theory. The support installation (no free ends) allows one to model it as an infinite cylinder, whose diameter is equivalent to the tube diameter (one inch) plus two twine diameters (4mm), resulting in 29.4 mm. Based on the literature (Figure 96), considering the cylinder *Re* during the test, it can be assumed that the C_D would be between 0.25 and 0.30.

Figure 96 - Variation of the drag coefficient of circular cylinders and spheres with Reynolds number.

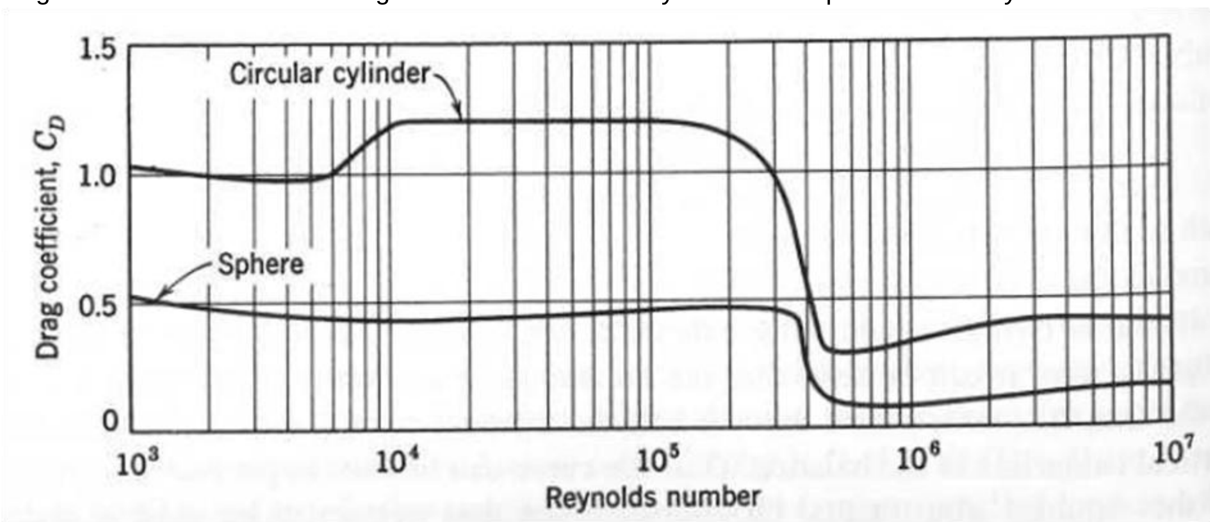

Source: Barlow, Rae and Pope (1999).

Since the fairing does not cover the whole tube (Figure 94), leaving around 100mm exposed to the flow, the reference would be 400 mm times the virtual diameter, calculated above. Then, with those figures, and considering the reference area for drag calculation as the volumetric area of the model (Table 6), one can infer that the C_D reduction (if that cylinder portion was not there) would be from 0.022 to

0.026. These analytical values are very close to the mean value obtained during the tests, which means that, if one considers, hypothetically, that the entities are isolated – i.e. no relevant interference exists, the obtained values are within the expected range. It is always important to recall that error propagation was not tracked here since the exact value was not considerd relevant; nevertheless, considering the errors, those values could be even closer.

5.1.2.1 New aerodynamic fairing

Besides the fairing described above, which was named “LAE Fairing”, a new fairing was developed in order to try to improve the shielding of the support while reducing possible interferences with the incoming flow. It is a fact that the presence of the fairing leads to changes in the streamlines, inducing even crossflow (flow along the “spanwise” direction) in some cases, such as the LAE Fairing, which is tapered and swept back.

So in order to try to mitigate the fairing interference on the model flow, a new concept was tried. Named Full Fairing, it comprises two parts: Root and Top fairings, both based on symmetrical low drag airfoil profiles. The Root has maximum thickness of 55% at 29% of the chord, which is 550 mm long; the height is 100 mm, shielding the base plate of the model support and the moment measuring module of the aero-balance. The Top is thinner (50% thickness) with a chord length of 165 mm and 350 mm in span, hiding the support bar almost completely. This Top portion is bolted to the top of the Root, and both are covered by high density cardboard, so as to preserve shapes even under the highest wind tunnel dynamic pressure used on the test campaigns.

Figure 97 - Full Fairing prototype: parts (left) and installed (left).

Source: Author (2018).

The new proposed fairing (Figure 97) was tested under some representative conditions for the test campaigns. Named Full Fairing, it was tested in portions: only the Root (ENV_03) and the complete assembly (ENV_04). Good qualitative results were obtained using only the Root Fairing, as the Full Fairing generated too much vibration on the model. This might have occurred due to the substantial change in thickness between the lower and upper portions, and a strong interaction between the flow around the fairing and vortex sheets around the hull. In addition, probably due to some fairing flow interference with the model, it was observed an increase on drag derivative along the positive portion of AoA (a steeper curve). This could have been caused by upwash effects of the Top Fairing, which virtually increased the AoA of the model for the positive portion, and decreased it for the negative AoAs. Finally, another problem observed while testing the Full Fairing was some notable irregularities (value oscillations) in drag profiles obtained around zero AoA. The explanation for those was not clear, but there is an indication they were due to increased turbulence induced on the model by the intense vibration of the Top Fairing being hit by the hull vortex sheets.

Given this situation, the use of the Full Fairing was discarded, and three possible configurations were available regarding aerodynamic exposure: clean (exposed support with twine), LAE and Root Fairing only. The first configuration counted initially on the presence of the pressure transducer acquisition cables running from model to ground behind the support bar; it was however changed, as the tests proceeded, to a very clean tube, once the pressure measurements were completed.

It is also important to highlight that the employment of fairings was strategically selected depending upon the circumstances and desired measurements. Since the full scale aerodynamic coefficients were not the objective of this work, it was somewhat acceptable not to have fairings in some cases in favor of campaign improvements, such as reducing interference on hull crossflow and vortex sheets development. The presence of fairings, when they are used, is explained when relevant together with the presentation of the results.

5.1.3 Surface roughness and wind tunnel section influence

Complementarily, taking advantage from the already prepared initial set-up, the model surface roughness was also evaluated in a very simple manner. The objective was checking in advance whether the roughness effect would be really relevant as expected. This outcome would guide the surface roughness investigation during Phase I of the main campaign. Besides that, according to the results, it would be possible to infer the boundary layer dominant flow condition, comparing smooth and rough skins.

In order to preserve the model for the next detailed tests on roughness, the technique used was tripping the boundary layer using rough (400 sandpaper equivalent) double-sided tapes attached to the model around the girth at specific lengths. Just as was done for the support, for this investigation, the methodology was incremental: two trips were fabricated, and added incrementally. Firstly, the 5 mm wide band was attached at 5%**L**, and tests were run. After that, the second band was added at 20%**L**, keeping the first one.

Figure 98 - Initial evaluation of roughness influence on drag polar.

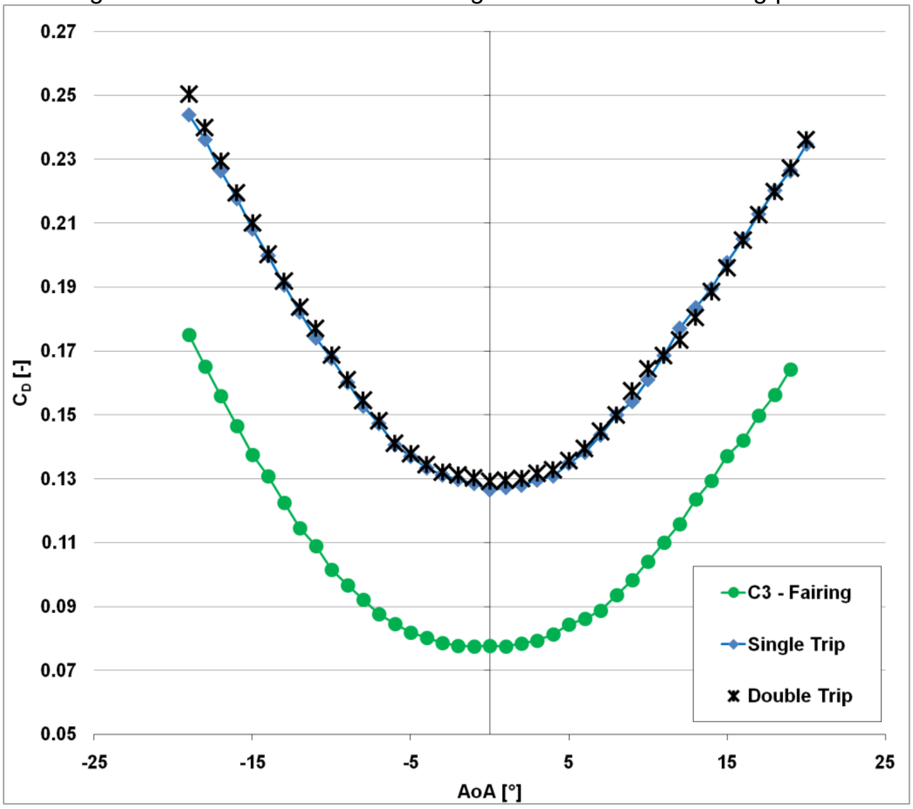

Source: Author (2018).

Analyzing the results, the first clear conclusion is that the baseline model boundary layer is essentially laminar, since the drag increase was drastic after the roughness change – a mean increase of 0.06 (maximum of 0.07 and minimum of 0.050) in C_D (Figure 98). Also, it was possible to conclude that, after transitioning to turbulent, the boundary layer does not tend to relaminarize (get back to laminar condition) as expected, considering the typical pressure gradients for conventional airship hulls. This effect may happen in some wind tunnel models when running outside of *Re* range, i.e. below it, and under a strong favourable gradient downstream of transition. This is proven by the fact that for the one trip (Single) and the two trips (Double) configurations, the C_D can be, for experimental results, considered to be virtually the same (Figure 98). In other words, if the boundary layer went turbulent after the first trip device, but got back to a laminar condition after it (a theoretical hypothesis of a roughness not forcing efficiently and effectively the transition process), the drag values for the Single trip would be lower than those for the Double trip. From the same observation, it is possible to infer that the Single Trip was capable of providing a full turbulent boundary layer alone over the full AoA range, demonstrating that, apparently, the stagnation was always contained between bow and 5%**L**. In addition, the similarity between the Single and Double Trip figures demonstrate that, once the boundary layer is turbulent, adding new trips (in this case, trips were double-sided tapes with roughness equivalent to sandpaper 400) does not increase the drag levels, a result of not increasing the turbulence level. Such results indicate that the roughness effect has to be analyzed, and properly set in order to simulate the full scale condition properly, as was planned.

The exercise of analyzing the obtained curves showed other interesting measurement characteristic. It is possible to see that as AoA increases, from around 15° in absolute values, the positive and negative portions of the drag curves tend to present considerable C_D differences. Such behavior was not expected since the model was already proven to be sufficiently symmetrical. Nevertheless, the measured values showed a difference, requiring some investigative work looking for the possible sources.

One probable source is the AoA positioning system employed. It is a kinematic system based on the Law of Cosines (Section 4.2.2.3). Its precision relies on how precise the lengths are measured, and how much play the moving parts have, because the fixation angles are calculated, and not measured. Moreover, usually this system drives models up to small AoAs, such as 10°-15°, and usually in one direction only (positive). However, in this present case, the maximum AoA is almost twice as large, and both directions are required (positive and negative). Therefore, in case of any hysteresis or approximation errors, such differences are not going to be detected in the standard tests, like those described.

Another source is the centering of the model inside the wind tunnel section with respect to the walls (Section 4.5.2). Although the model was attached to the floor surface geometrical center, aerodynamically it was not. The LAE-1 wind tunnel is also used for aeroacoustics experiments, and therefore it has a microphone antenna attached to the starboard wall, which is protected by a cover plate. This plate is 1.5 inch thick, and was longitudinally aligned with the model, along the total wall height. The presence of this plate causes the model to be off center with respect to the volume region, which leads to a slight acceleration in the working section (beyond the model volume), due to the one-sided narrowing, and also a higher acceleration at the side nearer to the wall. Those accelerations are not captured by the wind tunnel instrumentation, because its sampling region is the working chamber entrance (Figure 71). However, the local acceleration due to the model presence requires a classical correction factor – the blockage (Section 4.3.2), and would not lead to an asymmetrical drag curve. So the source for this would be the model off centering inside the chamber.

Once the model deflects in direction to the nearer wall, the air speed in that region is greater than on the other side (farther wall), because blockage is increased locally since that half portion of the section is narrower. This greater speed is responsible for a greater drag (force). When the C_D is calculated the value tends to be greater than otherwise, because the reference speed is that extracted from the wind tunnel Pitot tube (after the diffuser), which has a lower value, and not the local one. The nearer the model is to the wall, the stronger this effect is. This hypothesis is corroborated by the observed results: the negative AoAs portion has greater C_D values, and corresponds physically to the plate side.

It is again possible to estimate analytically, using the principle of mass conservation, what would be the local velocity increase. For null AoA, the narrowing due to the plate would provide a 3% increase in the local velocity, which would lead to a 4.7% greater C_D; for greater AoAs, this effect should be stronger. Then, with the objective of confirming that the plate was responsible for the asymmetry, it was removed, and the model was considered to be centered in the volume of the test section. The same test was run again, and for AoA = 0°, the C_D value decreased 6-8%, and the drag polar got much more symmetric.

Figure 99 - Drag evaluation without the microphones plate.

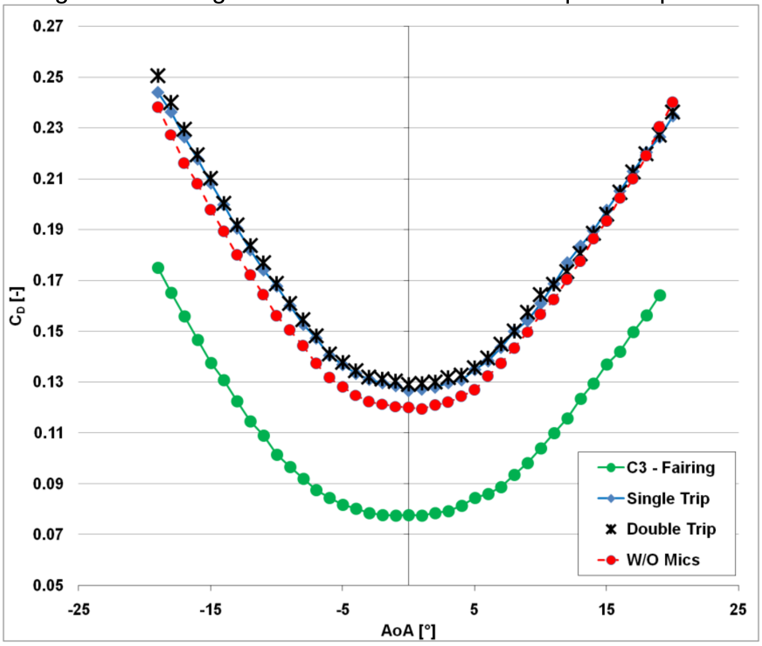

Source: Author (2018).

These conclusions on surface roughness minor changes and wind tunnel tiny asymmetry show the importance of examining each single and small parameter while planning and setting up a scale experiment in a wind tunnel. The uncertainties involved need to be at least investigated, and mitigated to their maximum, so that the results become more realistic and reliable.

5.1.4 Parameters adjustment and assessment

Some parameters needed to be set before the test campaign started. Among them were the sampling rate (frequency), sampling total time, AoA range and increment and zero AoA reference. In order to assess the parameters involved in the data capturing process and define the setup adjustments for them, a series of tests were conducted. The model was set to ENV_06 configuration, which means a simplified BARE HULL and exposed support (including the acquisition cables) – no fairings.

Three different *Re* were used: 1.5E+06, 1.7E+06 and 1.9E+06, corresponding to mean velocity values of 23.3, 26.0 and 28.3m/s respectively. The aerodynamic coefficients were also assessed using different AoA increments: [-20°; 5°; +20°], [-20°; 2°; +20°], [-25°; 1°; +25°].

During the first runs it was observed that the lift curves were shaping "low-frequency-waves-like" along a mean trend line of what would be the expected C_L curve, besides being off-centered, which means C_L = 0 occurring for AoA ≠ 0°. The drag curves were as expected for experimental results, except for the off-centering question. The zero reference was checked (the model was removed for some work after the first evaluations), and easily corrected by adjusting the model. A reference tracking mark was engraved in the tunnel instrumentation allowing quick checks during the campaigns. Solving the oscillatory shape of the curves was achieved by evaluating the sampling characteristics of the data acquisition system. The LAE-1 wind tunnel usually runs tests with less vibrating models (more rigid and/or lower velocities) and with higher C_L and C_D values than those observed for the airship model. In this way, making sure to get enough logged data, but playing with sampling rate and time, the characteristics were adjusted, capturing data for a longer period, avoiding mistaken measurements due to low frequency oscillations of the model around the desired AoA. Those oscillations might have interfered with the balance measurements, and provide bad results (for varied AoA). The setup was therefore changed from the standard LAE-1 Wind Tunnel of 1000 Hz for 5 seconds to 1000 Hz for 10 seconds, thus doubling the original 5000 samples/AoA.

The results obtained after the changes still showed oscillations, but less intense (in amplitude). Those were attributed to laminar flow separations around the support bar and the hull itself. This hypothesis was confirmed after the oscillations damped out with the tripping (roughening) devices applied to the hull surface and after the fairing was added to cover the model support, just like during the early investigations (section 5.1). The following sections provide results where this can be seen.

The first tests used the range [-20°; +20°], and an attempt was made to increase the increment, reducing testing time. However, it was observed that increments of 1° provided better trending profiles to be used during the results analysis and discussion, besides introducing smaller incremental commands to the step motor, which controls the positioning system. Moreover, based on operational limitations of flying airships, the range was increased to [-25°; +25°]. An attempt was made to increase it to [-30°; +30°], which would fit better with the operational limitations, but it was unsuccessful. This is another consequence of the usual test setups (typically wings) at the LAE-1: the aero-balance AoA positioning system produces greater deviations for greater angles, and is also mechanically limited very close to what would be 30°, since it normally goes up only to 15°-20°.

The adjusted parameters were kept throughout the campaigns for Phase I, and the results were constantly checked during the runs, in order to ensure that the outputs were adequate with respect to the adjustments.

5.2 PHASE I: AERODYNAMIC AND STABILITY CHARACTERIZATION RESULTS THROUGH STEADY TESTS

As stated above, in section 4.4.1, this first batch of runs comprised a series of steady tests with the model. By steady one must understand force and pressure measurements in static, stabilized flow conditions. Two different approaches were used: AoA and *Re* Polar, where Polar denotes a batch run varying the cited parameters (AoA or *Re*). Both methodologies were applied to the same model configurations as complementary tools, not being limited to one or another investigation. All testing campaigns for this phase were carried out between September 9th and September 21st, 2017.

The AoA Polar basically comprised varying the model AoA within the pre-defined range ([-25°; +1°; +25°]), at a fixed wind velocity inside the tunnel, and capturing Lift, Drag and Moment (around the support bar). The used reference for the forces and moment assessments were presented in section 4.1.3.

It is interesting to emphasize that since *Re* depends upon some fluid characteristics, although the velocity was kept almost constant (wind tunnel frequency to the electric motor was indeed constant), *Re* varied a little around the starting value, mainly due to temperature increases during each day, and weather changes from day to day.

For some test points through the explained batch analysis, the model pressure distribution was logged. The pressure taps position varied along the campaign, depending on what was being investigated. The model configuration varied from BARE HULL, through some different surface roughnesses, ending up with the fins installation, and trimming curves, for static stability assessments. The details regarding each roughness, the taps investigated and the obtained results are shown and discussed in the following sections.

The second test analysis methodology, the *Re* Polar, comprised fixing the model AoA at the zero reference, which means AoA = 0°, and varying the wind tunnel velocity through pre-defined steps in frequency input to the electric motor. The zero reference was chosen as the configuration for drag sensitivity to *Re* investigation in order to reduce, to its minimum, the pressure drag, and permit a better isolation and identification of the changes in friction drag due to the nature of the flow in the boundary layer, with changing roughnesses. The *Re* Polars are identified by “ENV_XX_DeltaV” in the Table 9.

This second methodology had the main objective of supporting the selection of an adequate roughness among the options which would better represent full scale flow behavior for the next investigations, such as trimming curves and drag polars development. The same remark regarding *Re* variation is applicable here. Although the frequency inputs to the motor were generally the same, despite some test envelope extrapolation conducted for evaluation purposes, the *Re* steps varied a little. Nevertheless, the objective of such polars was to investigate trends in drag variation with *Re*. Thus, whether the *Re* values are exactly the same or not should not badly affect the trend identification; indeed, it enriches the trend analysis by varying the sample points inside the same range.

However, due to geometric limitations regarding the wind tunnel facility and the model size, already explained in section 4.1.1, the *Re* was varied from approximately 9.5E+05 to 2.5E+6 only. Analyzing the obtained results, and considering the expected full scale behaviors and trends already known from the literature and research, made it possible to select an adequate curve fitting technique to extrapolate the obtained data, and take the required decision.

As complementary investigative tools, oil flow visualization and tufting techniques were applied during the runs, so that some of the phenomena could be better understood, by examining the surface flow patterns on the model. In addition, some trials of outer flow visualization using smoke were conducted. The results were very limited given the velocity characteristics and the intense lighting required. All the relevant assessments are presented in the following sections.

5.2.1 Surface roughness definition: similitude analysis

As discussed, for the results to be useful and relevant regarding model behavior, even qualitatively, the air flow should behave at least in a similar way to what happens in full scale. Considering geometry issues, the model was basically limited in this respect. So, some proposals of surface roughnesses were investigated, aiming at selecting the adequate one for further development.

The test runs for the roughness investigation were conducted with two different fairing configurations: LAE and Root (section 5.1.2). The objective, as already described, was to highlight (easier track) minor changes in drag, by reducing the overall value measured at the balance. The roughening proposals and their installation are those described in section 4.3.1. In the following sections, the results of the similitude evaluation are presented and discussed, followed by the final choice regarding the surface roughening for the airship model aerodynamic characterization.

5.2.1.1 First surface roughness evaluation – LAE Fairing

The COLLANT cover was chosen for starting the roughness evaluation, and the configuration was named ENV_07. Basically, it comprised the BARE HULL covered with the COLLANT (section 4.3.1), with no fairing hiding the support, besides the twisted twine wrapping up the support bar and the pressure transducer data acquisition cables. For the first AoA Polar, C_D values and vibration effects were high, above what was considered adequate in order to have a reliable assessment of drag sensitiveness. So, as described in section 5.2.1, the LAE Fairing was installed, and the roughness configuration kept.

Much lower drag values were obtained for the overall curve, and the symmetry quality became better as well (Figure 102). This last configuration, using LAE Fairing, named ENV_08_R2, also counted on surface flow visualization from the middle to the rear portion of the HULL using tufts. The tufting technique allowed some interesting observations, which will be addressed along this chapter according to the need and convenience.

The support however still had a portion exposed (Figure 100) and it was decided to try to decrease even more the drag level by extending the LAE Fairing up to an "almost-touching" distance. This would ensure the highest degree of shielding for the support, but could also strongly interfere with the drag polar.

Figure 100 - Original LAE Fairing.

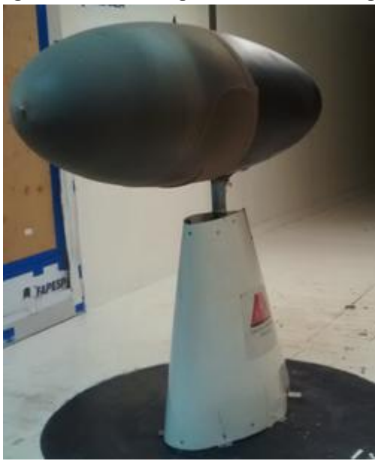

Source: Author (2018).

Figure 101 - Extended LAE Fairing.

Source: Author (2018).

After the fairing extension (Figure 101), the polars obtained for the ENV_09_R2 configuration showed once again a decrease in overall drag. The values, though, showed an intense disturbance in the vicinity of AoA = 0°, while the curve still showed good agreement in symmetry considering a second order polynomial fit.

Figure 102 - Drag polar for initial roughness assessment.

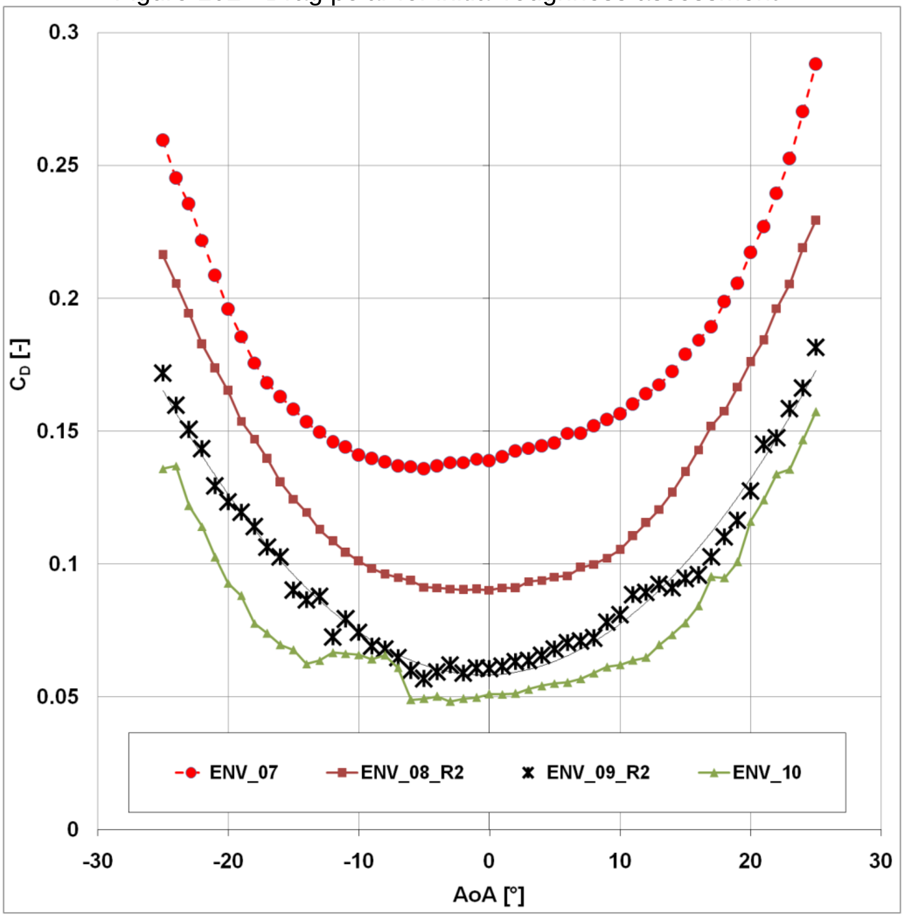

Source: Author (2018).

As previously predicted, the values oscillations were expected, since by increasing the fairing length, and therefore the proximity to the model, the aerodynamic interference level between model and fairing would rise. This was physically captured by observing the tufts behavior along the AoA variation, and comparing the configurations with and without the LAE Fairing extension. Although the gap on ENV_08_R2 could be considered small (about 100mm), observations pointed that it was large enough to allow the vortex sheet to roll up around the HULL, hitting only the support bar. The same interference effects can be seen on BARE HULL results with the extended LAE Fairing (ENV_10). It is interesting to see that the regions where the effects (disturbances) appear are quite the same for COLLANT and BARE HULL.

Figure 103 - ENV_08_R2 tufting pattern on upper side.

Source: Author (2018).

Figure 104 - ENV_09_R2 tufting pattern on upper side.

Source: Author (2018).

Comparing patterns extracted from video records of ENV_08_R2 and ENV_09_R2 around AoA = 20°, it is possible to see that the lower portion of the tufts was affected: their inclination changed from aligned downstream (Figure 103) to highly turbulent oscillatory around the longitudinal axis (Figure 104), appearing even inverted tufts, meaning separated oscillatory regions. Moreover, an intensification of non-stationary behaviors, such as model vibrations for |AoA| > 10°, was also observed along the runs.

All of those characteristics showed that, for the conclusions on roughness, it would be necessary to decrease interference, ensuring a more realistic flow, allowing aerodynamic entities, such as vortex sheets and the boundary layer itself, to develop freely. Nevertheless, the very first similitude assessment was conducted using the LAE Fairing extended configuration in order to obtain at least some guidance on selecting from the diversity of options regarding roughness. Using the extended LAE Fairing seemed to be the best approach for keeping the drag level at its lowest. Besides that, the problems observed for larger AoAs would not be an issue when assessing the C_D variation with *Re* at AoA = 0°, and the lowest portion of drag polars, which showed well behaved portions.

The similitude analysis has the objective of ensuring that the model behaves aerodynamically in a similar manner as the full scale aircraft. This means in other words that the aerodynamic structures are developing in the same manner to what they would at full scale. Testing airships in wind tunnels, as already discussed in section 3.1.6.2, is rather difficult mainly because of the similitude problems. It is necessary to make sure that vorticity patterns are similar; the boundary layer develops in a similar scalable manner and so on. This boundary layer scale factor is essential when robust aerodynamic coefficients are needed in order to supply information to flight dynamics modeling and flight testing analysis, for example.

This work, however, is not aimed at obtaining exact values, but a qualitative characterization of the ship, and of its general aerodynamic and stability nature. In that sense, ensuring that the boundary layer is turbulent all over the model, well attached to it (to the possible extent), does not relaminarize and grows steadily was deemed sufficient.

On the other hand, it is necessary to properly select the devices to force transition, as they may strongly affect drag. If the transitioning effect is too strong, it can lead to an extremely turbulent boundary layer, raising drag to unrealistic values. The focus would then be to choose a configuration which ensures a turbulent boundary layer so as to get the lowest drag level possible, not counting the clean configuration.

Complementarily, according to Curtiss, Hazen and Putman (1976[40] apud Cebolla, 2013), the testing regime of this work is the "transition regime" (Figure 35), i.e. near to a C_D curve local minimum. Based on this, although it is a well known fact that the overall C_D decreases with increasing *Re* (disregarding compressibility effects), proposing that it could rise up to a threshold value[41] upon which data extrapolation may not be unfitting; it might indeed be a good hypothesis. If one considers that the *Re* is two orders of magnitude lower than full scale, whilst flow velocity is already close to the current operating airships top speed, then the boundary layer could consequently scale up dimensionally, increasing C_D as well in the process.

---

[40] CURTISS JR., H.C.; HAZEN, D.C.; PUTMAN, W.F. LTA Aerodynamic Data Revisited. *Journal of Aircraft*, v.13, n.11, p.835-844, 1976.

[41] This is slightly different from what is stated by Curtiss, Hazen and Putman (1976, apud Cebolla, 2013), as presented in section 3.1.6.2.

Assuming this as a given for this work, it was considered important that data from *Re* Polars had to fit well onto logarithmic curves versus *Re*, which, despite the increase shown, do not rise in a very steep manner. This allows that, while reaching very high *Re*, the C_D curve is able to smoothly change its growth trend, decreasing as expected at greater *Re*, without discontinuities or abrupt changes.

As following this hypothesis could lead to wrong results, it was always put as the last evaluated characteristic. The main reason is that, according once again to Figure 35, C_D should grow, and then steadily decrease from the value reached at *Re* = 1E+07, matching the Schoenherr-von Kármán relation (Figure 36) if only skin friction is measured. In this case, for AoA = 0°, and only increasing velocity, based on section 3.1.2, it is possible to assume that the measured drag is dominantly of the skin friction type. Then, a logarithmic growth trend would represent a good transition to full scale (Figure 36). However, the expected *Re* range where it would occur is outside of that feasible for this work, meaning that it would not be observable. Such an outcome could be regarded as an error (an uncertainty would be more appropriate) if put as a restriction. Therefore, to make it clear, the log-fit is not deemed as the perfect approach to fit the curves, but the best among the simple options, and is used only for comparison purposes. Fortunately, the log-fitting worked well combined with the other analysis requirements, as shown below, and as such was able to identify the probable converging configurations.

So, following such described strategy depicted, AoA and *Re* Polars were run. A BARE HULL run was carried out (ENV_10), and each model cover was tested individually: COLLANT (ENV_09 - only drag polar without *Re* change), BUBBLEWRAP (ENV_11) and HEXNET (ENV_12). Among the covers, just the FISHNET was dropped from this first evaluation. It was introduced afterwards, on the next roughness analysis phase (section 5.2.1.2), when the results from first options were already known. This was done because the FISHNET had already been proven to be an alternative based on Gomes (1990). For the tripping options, an incremental strategy was used, generating three configurations: SINGLE TRIP at 25%**L** (ENV_13), DOUBLE TRIP at 25%**L** and 40%**L** (ENV_14) and TRIPLE TRIP at 5%**L**, 25%**L** and 40%**L** (ENV_15). The trips were all added incrementally, because it was necessary to be sure that the boundary layer as a whole was turbulent. So, if no efficient transition occurred, a new trip would be added in order to make it turbulent downstream.

After this first batch was complete, the *Re* Polars were analyzed, putting the AoA Polars as a secondary source of information since they were not fully reliable yet, given the roughness uncertainty. The plotting of the *Re* Polars (Figure 105) highlighted some important aspects, leading to quick conclusions.

Figure 105 - *Re* Polars for initial roughness assessment.

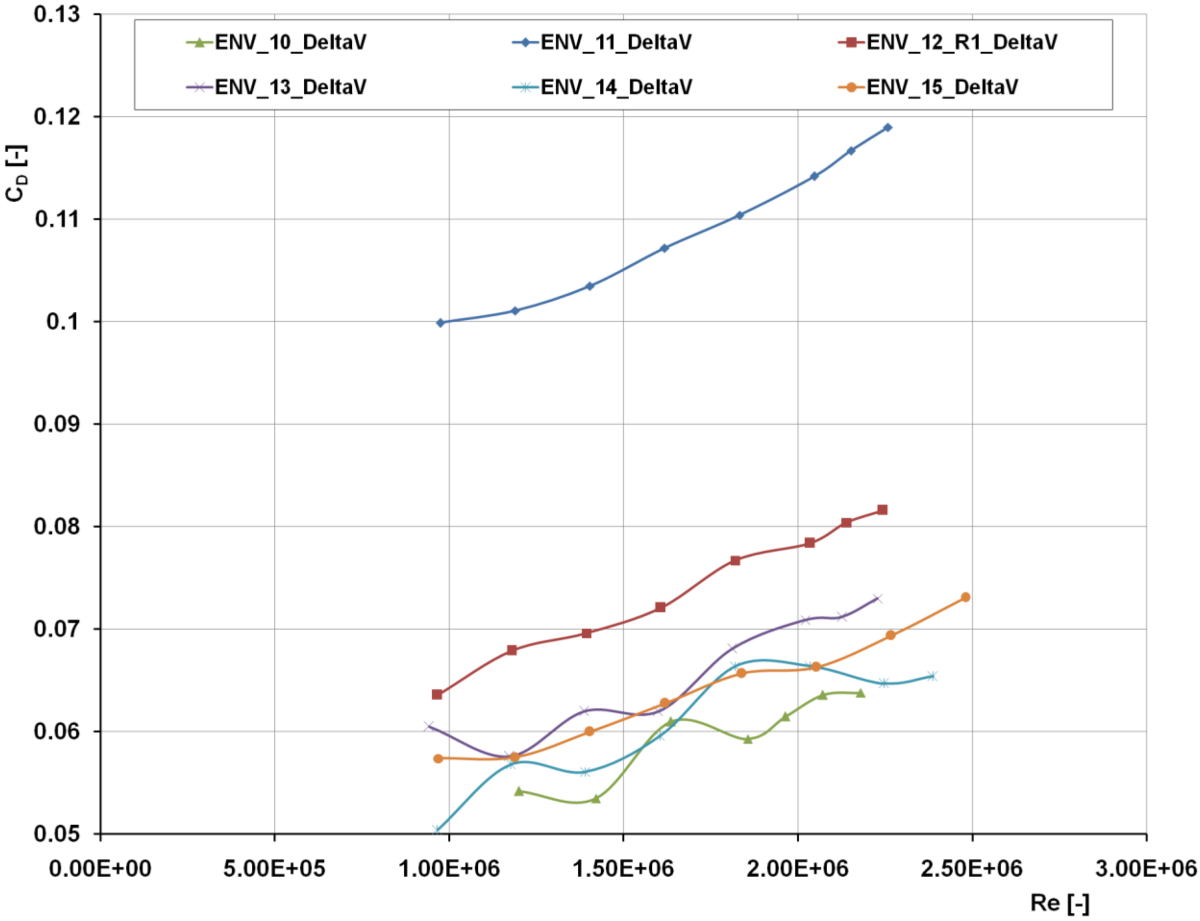

Source: Author (2018).

The BUBBLEWRAP (ENV_11) option was excluded from the subsequent runs. Its drag reached almost the double of BARE HULL (ENV_10), while the other options were in the vicinity of it. Also the HEXNET (ENV_12) was somewhat off when compared to the BARE HULL, the TRIP configuration results being some 15% higher. This, however, did not exclude them from the next runs, since it presented a very well defined trend.

Interesting results were observed for the TRIP options. Even though the three configurations returned very similar results, the C_D values for the DOUBLE TRIP (ENV_14) were lower than those for the SINGLE TRIP (ENV_13), and, further, results for the TRIPLE (ENV_15) were higher than DOUBLE (ENV_14), but lower than SINGLE (ENV_13). Although these results seem not to be intuitive, there are explanations.

For the first comparison, the presence of the SINGLE TRIP, instead of generating the transition, was probably only reducing the boundary layer stability, leading to a downstream earlier unavoidable laminar separation when compared to the BARE HULL separation line, which results of a laminar flow development naturally transitioned to turbulent, and therefore more stable than SINGLE TRIP. This should be true as the *Re* variation is small, and the boundary layer stability is not relevantly improved by the inherent flow characteristics. Adding the second TRIP behind the first one may have helped to effectively force the boundary layer to transition, improving its stability, reducing the separation region, and consequently the drag as well. For the second comparison, the addition of the third TRIP ahead of all the others, and very near to the bow (5%**L**), anticipated the boundary layer transition at low local velocities, making it possible for it to transition and steadily grow naturally. For the DOUBLE TRIP, probably the region ahead of the first TRIP (<25%**L**) had a long - if not complete - laminar flow. When the added TRIP at 5%**L** transitioned it to turbulent, the skin friction drag increased, and the obtained C_D values were larger as well. Similar results were obtained at the early stages of model investigation, described in section 5.1.3.

From these last results, the SINGLE TRIP configuration was dropped; besides causing the highest *Re* polar, it was supposedly not properly representing the desired flow. The doubt then involved DOUBLE and TRIPLE TRIP. By evaluating the results, and analyzing the overall model aerodynamics, it was concluded that the key to transitioning was the TRIP at 5%**L**. Once the bow, which has low local edge velocity, is already turbulent the boundary layer will be able to grow turbulent to the full length of the model. This is, indeed, the mechanism seen in real airships: the laminar region practically does not exist; structures and surface roughness (fabric finishing) do not allow it as well. In support of this assessment, one may recall what was obtained by Cornish, III and Boatwright (1960) regarding frictional drag decrease due to nose fairings.

The direct conclusion then would be to drop all three TRIP options, and keep only the bow TRIP, a new configuration. This would probably suffice for this work needs if the AoA was kept small. This, however, would mean having the stagnation point between the bow most fore point and the TRIP. The BARE HULL pressure distribution for AoA = -20°, shown in Figure 92, shows that the stagnation point moved from Tap Nr.3 (BOW) to Tap Nr.5 on the port side. Even though this tap is contained in the desired range (within x < 5%**L**), it shows that the stagnation point travels along the model. So in order to ensure that it would not fall off the range, resulting in the coexistence of laminar and turbulent regions on the model, it would be safer to have another TRIP. So the third TRIP (at 40%**L**) was removed, and a new double configuration was generated: trips at 5%**L** and 25%**L**.

As a result from first analysis, this last configuration, simply named TRIP, was kept for further similitude evaluations along with HEXNET, COLLANT and FISHNET options.

5.2.1.2 Final surface roughness evaluation – Root Fairing

This second part of the similitude analysis applied the same evaluation techniques described above. The Root Fairing took over the LAE Fairing place. It covered only the base of the support (base plate and balance moment acquisition module), and let the bar, with the acquisition cables, exposed. This made the C_D increase, approximately doubling that first analysis (section 5.2.1.1), an order of magnitude similar to that for the LAE Fairing without extension (ENV_08_R2).

Before starting the testing sequence with the outcome configurations from the first roughness evaluation, the TRIPLE TRIP configuration was tested with the Root Fairing (ENV_16). Then the TRIP configuration was tested (ENV_17). The resulting drag polars were compared. As previously obtained for DOUBLE and TRIPLE options, there was great similarity in values between them (ENV_16 and ENV_17), showing an almost perfect fit in values between both C_D polars (Figure 106).

Figure 106 - Drag polar comparison between TRIPLE TRIP and TRIP configurations.

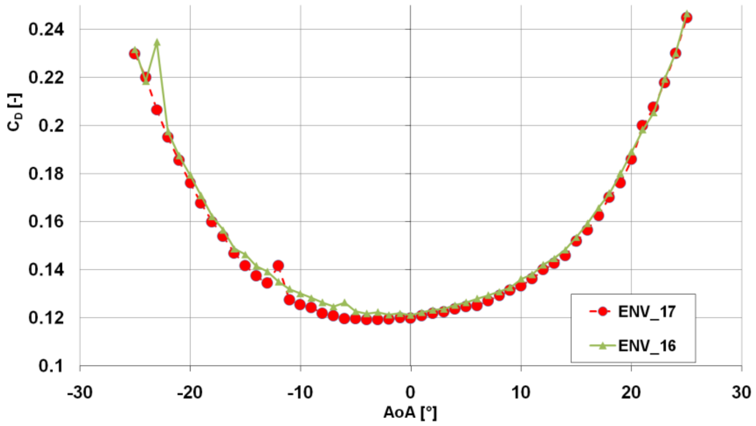

Source: Author (2018).

This made it clear that the fairing did not have a decisive influence on the C_D degree of similarity between different configurations; the results changed in magnitude, but still by similar amounts for both. It also shows that the TRIP configuration is reasonably equivalent to the TRIPLE TRIP, which supports the previous assumption by a different means.

Once the TRIP configuration therefore was cross-checked, the *Re* Polar was run, followed by the COLLANT (ENV_18), the HEXNET (ENV_19) and the FISHNET (ENV_26). The last three covers were applied to model, on top of the TRIP configuration. Although this procedure may draw some criticism, and make the evaluation questionable, the surface was checked. Recalling that the tripping bands are made out of foam and their thickness is rather small, their interference on the model surface was negligible, even when hand checked. In addition, configuration ENV_27 was assessed. It is essentially the same configuration of ENV_17 except for the support exposure. On ENV_27 the pressure transducer data acquisition cables and the external twisted twine were removed, remaining only the Root Fairing installed.

After the runs completion, analyzing the results showed again relevant information to feed the analysis. Although all surface flows were fully turbulent, there were three distinct levels regarding C_D (Figure 107). The highest (ENV_26) was approximately 50% greater than the lowest (ENV_17). Besides that, coincidently the two highest C_D values curves (ENV_26 and ENV_19) did not fit well with the adopted logarithmic curve. Instead, simple linear fitting seemed to be the most adequate when checking the "R^2" values for the fit. Known as the coefficient of determination, R^2 is calculated by Excel™ with the curve fitting, and represents how close the data are to the fitted regression line. In general, the closer to 100%, the better the model fits the data. It is also important to check the geometric adjustment in order to be sure that the trend is followed, since R^2 may be high although the fit is not good enough. This is however an issue usually observed for non-linear regressions.

Figure 107 - *Re* Polars for varied roughnesses using Root Fairing.

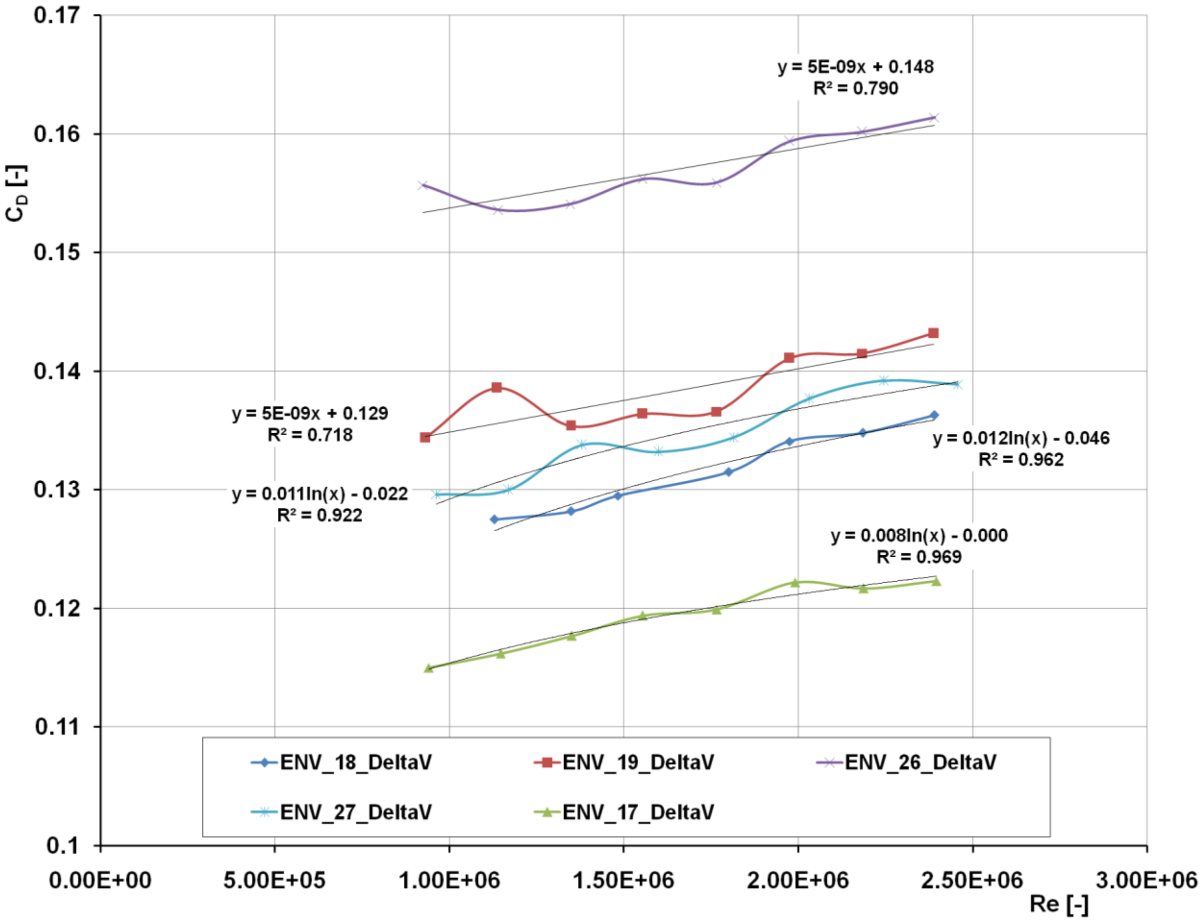

Source: Author (2018).

While high values were not in good agreement with the log-fit, the lower curves (ENV_17, ENV_27 and ENV_18) fitted well a logarithmic model with $R^2 > 90\%$. The other two configurations (ENV_19 and ENV_26) fitted simple linear ascending models. This leads to the conclusion that with increasing *Re*, for these last roughnesses, the drag value does appear to be going to converge to a limit or at least grow more slowly when going to full scale *Re*. It means, therefore, that these roughening covers (HEXNET and FISHNET) are not only transitioning the boundary layer, but are also drastically increasing skin friction drag through a high turbulence level, above what represents full scale, changing what would be the natural behavior of the airship.

Further, looking at the other three curves left, which fitted the logarithmic approach, it is interesting to observe that there is an almost 10% step in value between the lowest (ENV_17) and the other two (ENV_18 and ENV_27). By assessing the fitting quality, it is possible to infer that ENV_17 and ENV_18 fit better the log-trend (higher R^2), and one of them should be chosen.

As a quick elucidation, before concluding on roughness, it is important to mention that assessing the ENV_27 configuration was one of a series of final evaluations conducted after all experiments of Phase I were carried out. The specific objective was to recapture same interference effects identified before starting the campaigns (section 5.1), but employing a turbulent flow development (with roughness). So, it is no coincidence that ENV_27 was not selected as the configuration for generating the trimming curves, as it did not even exist at that time. The quantitative results for ENV_27 were however included so the reader could have more information regarding support interferences, as explained above. As expected according to what is explained in section 5.1.2, the ENV_27 configuration led to increases in model vibration and drag. This latter feature could be once again demonstrated not only by comparing the drag level in Figure 107**,** but also checking the C_D polar in Figure 109. The ENV_27 curve presents, very consistently, higher values in relation to ENV_17, besides some value oscillations and local value increases near smaller AoAs as well.

Figure 108 - Lift polars for varied roughnesses.

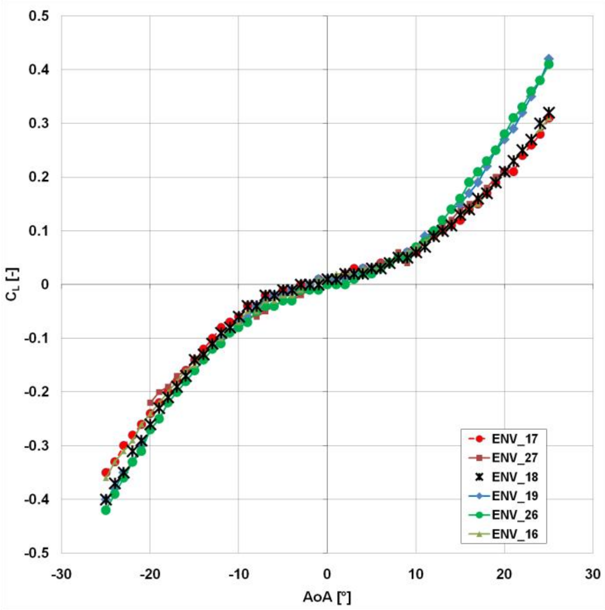

Source: Author (2018).

Figure 109 - Drag polars for varied roughnesses.

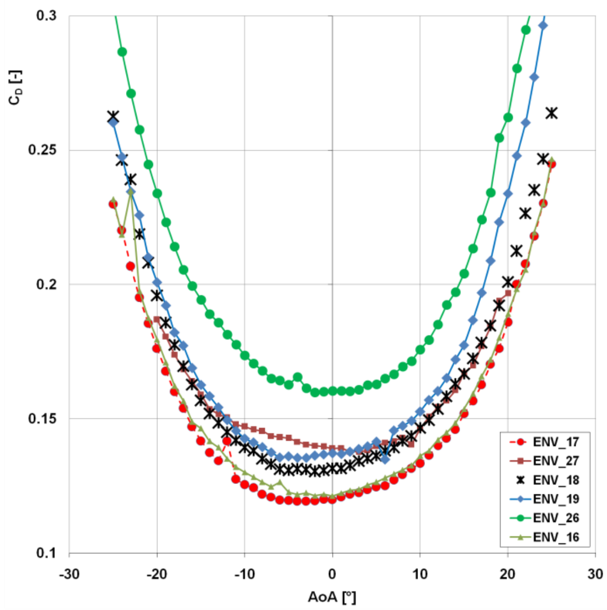

Source: Author (2018).

Analyzing the C_L results also helps to demonstrate that they are mainly affected by changes in the support aerodynamic behavior. When comparing both C_L polars, ENV_17 and ENV_27, it is clear that they fit each other very well, especially when considering a comparison of typical experimental results. Since this kind of support, steel circular bar, has negligible influence on lift, such an outcome was expected, supporting thus the initial hypothesis.

Recalling then the objective of the roughness investigation, it is essential to ensure a turbulent boundary layer, without increasing friction drag above what would be seen in a natural turbulent flow, which better represents the airship full scale aerodynamics. In other words, it is important to guarantee that drag increases by only forcing the boundary layer transition, and not by transitioning it and inserting more friction than would be seen for full scale.

In this way, after all this evaluation, the TRIP configuration (ENV_17) was selected as the surface roughness for the next runs. It transitioned the boundary layer and increased drag by the lowest amounts among the options, and had a good trend fitting. In roughness terms, the configuration was comprised by two trip bands as described in section 4.3.1(f), positioned at 5%**L** and 25%**L**. Proving the TRIP as the best solution provides other working gains, such as simplicity (materials, manufacturing and workability), low costs, renewal (replacement) and others. This may also contribute to the work of future researchers, guiding them to a quick, simple and reliable solution on roughening.

Later, after the pressure measurements were concluded, oil flow visualizations were carried out, avoiding the risk of clogging any pressure tap. In this way, ENV_17 exact configuration was not checkes. As described above, ENV_27 was chosen to represent ENV_17 on flow visualization. Since such techniques are qualitative approaches, the geometric differences between both were considered negligible. Regarding the increase in vibration, it was deemed quite acceptable that at low AoA both behaviors were also much similar, and the surface flow of ENV_17 would be well represented. One must consider that the main objective was to assess the TRIP configuration effectiveness in forcing the boundary layer to transition.

Before effectively reaching any conclusion, two attempts were made. The first used a denser pigmented oil mix. The proposal was to adjust the mix and also check the level of turbulence. It was possible to identify that the boundary layer was fully turbulent by comparing the flow patterns before and after the second TRIP (at 25%**L**). The patterns (Figure 110 and Figure 111) demonstrate that before and after the TRIP at 25%**L** the surface flow patterns are quite similar, well streamlined and the pigment, even the denser type, was well carried along the whole model surface. These are evidences that the velocity close to the model surface, indeed the momentum, was high, indicating turbulent boundary layer profiles (Figure 13).

Figure 110 - TRIP at 25%L (Top view) for ENV_27.

Source: Author (2018).

Figure 111 - TRIP at 25%L (Upper-Side view) for ENV_27.

Source: Author (2018).

However, some undesirable structures, such as swiveling flow spots, were obtained right behind the TRIP. It indicated that it was necessary to lighten the oil mix, as it was probably too heavy to be carried away where the momentum was a little weaker. The proportion of kerosene was increased, improving the pigment suspension, making it easier for the flow to carry the pigment downstream.

The new patterns showed interesting results, not observed before. Looking at the second TRIP from the side view, along the lateral axis (Figure 112), the lightened oil mix made it possible to identify better how the flow behaves very near to TRIP. As expected, upstream, there is a deceleration and some stagnation, showing a “saw wall” (pigment accumulation) pattern. However, the flow is able to overcome the trip thickness, and to reattach downstream at approximately a TRIP thickness of longitudinal distance.

Figure 112 - Side view of surface flow pattern past the TRIP at 25%**L**.

Source: Author (2018).

The detailed analysis of Figure 112 leads to a second observation: the reattachment on the upper portion of the model is a bit different of that on the side-lower portion. On the upper portion, as observed using the denser mix, the reattachment is directly turbulent, even though some reacceleration is developed (the further downstream, the better the streamlined pattern). However, on the side-lower portion, there is a laminar reattachment (much thinner, aligned and closer vestiges - hairline like region). Moreover, the direction is not only along the longitudinal axis, but inclined in the upper direction, although the incoming flow (upstream of the TRIP) is well aligned with the longitudinal axis. These inclined hairline traces pattern sustains itself only a few millimeters downstream of the TRIP, apparently entering a transition region, similar to those observed for Tollmien-Schlichting waves amplification. This is followed by a very short laminar bubble (dark scattered band), transitioning downstream to turbulent, becoming once again aligned with the longitudinal axis. This last observation may indicate that the TRIP “saw-like” geometry may have some local influence on the lateral flow. However it is deemed not relevant in the general overall result analysis.

This analysis, in spite of the local aerodynamic observations regarding the TRIP device, reveals that the boundary layer developed fully turbulent as desired, surely transitioning at its very beginning (first TRIP at 5%**L**), and that the flow was capable of maintaining itself turbulent just with the proposed TRIP (one at 5%**L** and the other at 25%**L**) configuration.

5.2.2 BARE HULL aerodynamic structures – flow visualization

Before going into the airship proper characterization by inserting tail fins and measuring forces and moments with them incorporated, it is worthwhile understanding what the main aerodynamic structures that appear just with the BARE HULL are.

First, using the ENV_27 configuration, the condition of AoA = 0° was investigated. The first impressive result came out during the wind tunnel flow stabilization period.

While velocity increased up to tunnel stabilization, it was possible to follow the formation and strengthening of the flow structures. Limiting streamlines were observed converging from top and bottom to an almost middle water level on the model. A pattern similar to a fishbone was formed.

Figure 113 - Sequential frames of Run_00 for ENV_27 in 4 seconds steps for AoA = 0°.

Source: Author (2018).

The mean line, to which all others converged, is probably a high intensity vortex attachment line. The (hull) port vortex (on the observer’s side) rotates in counterclockwise direction looking downstream at the tunnel test section. This supports the fact of lower limiting streamlines point upwards, and upper streamlines, downwards. It is also possible to see that this middle attachment line goes downwards with increasing x/**L**.

It was also interesting to see that, as expected, the flow behavior as visualized was very symmetrical, being apparently similar on both sides. Another symmetrical vortex developed on the other side, and its attachment line could be seen after the wind tunnel was turned off, and the paraffin had already evapourated, leaving the pigment attached to the surface aligned with the surface streamlines. There was not so much pigment on the lower portion, because at the very beginning of tests, only the port side of the model was designated to be observed.

Figure 114 - Rear view from starboard side of ENV_27 for AoA = 0°

Source: Author (2018).

The limiting streamlines pattern on the top of the BARE HULL were also evaluated, and revealed the symmetrical behavior very well. Looking at it, one can easily identify another fishbone type pattern, dividing the flow from the middle line to both sides. It is also possible to observe that the fishbone spread out process increases with increasing x/**L**. This behavior was observable laterally as well.

Figure 115 - Top view from behind the model at AoA = 0°.

Source: Author (2018).

Comparing those observed results with Nonweiler's theory presented by Thwaites (1960), and with the results of Han and Patel (1979) for low incidence, it can be inferred that the middle line is in fact a vortex which appears in flows past bodies of revolution at low incidences. This shows that, to a certain extent there is some deviation regarding perfect leveling and alignment of the model on the longitudinal plane. This situation might produce some upwash effect on the model and on the working chamber, influencing future tests. However, this problem seems not to be easily solvable considering the available means of fixing and adjusting the model inside the chamber. Therefore, it was left as something to be dealt with.

In order to confirm that the observed middle line is in fact an attachment of a vortex tube, as described by Thwaites (1960), a specific run with tufts was carried out.

Figure 116 - Sequential frames of Run_00 of ENV_27 for AoA = 0°; smooth surface.

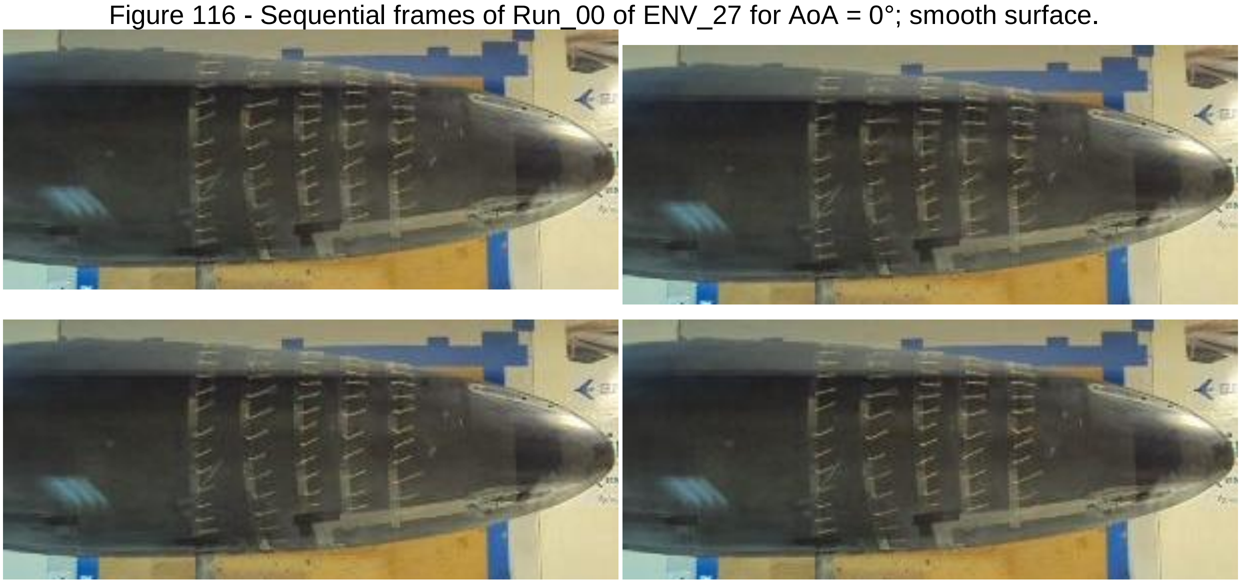

Source: Author (2018).

Analyzing the resulting frames, it is possible to see the same “fishbone converging” trend, and also that some tufts present less straight patterns than others, i.e. oscillatory tips. Watching the videos, it is possible to see that those tufts are indeed oscillating, while the others are well aligned in a defined direction. Nevertheless, both groups are attached to the surface, meaning no separation, but the condition of turbulence for the oscillating ones. Comparing the oscillating tufts position with the oilflow results attests that these tufts are in the vicinity of the supposed longitudinal vortex tube. This match in position and the oscillatory behavior lends further evidence to confirm that the middle line is indeed an open separation line producing a vortex very near to the surface (HAN and PATEL, 1979). The same tufting visualization was conducted with the FISHNET installed. The same conclusion was reached, with the strong evidence that the tufts oscillations are rather intense (Figure 117).

Figure 117 - Sequential frames of Run_00 of ENV_27 for AoA = 0° with FISHNET.

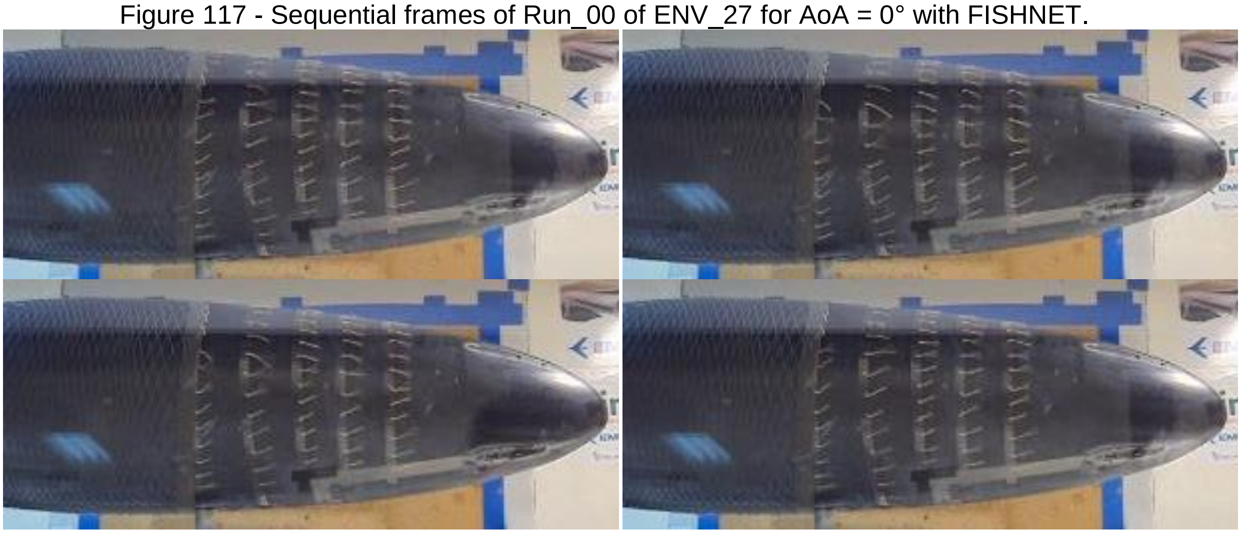

Source: Author (2018).

Complementarily, at the very end of the model, from around 95%**L** onwards, the stern region was covered by a thick white flowviz layer, which contained swiveling spots. It was so thick, that even with the high flow velocity, it was dripping, and not moving along with the fluid. These are the typical characteristics of the 3D separation type called bubble or closed separation: the pigment is not carried, detaches from the body and presents vortical flow. A second run with a little more flowviz oil on the lateral side was conducted, and the bubble separation at the stern region was more clearly observed. Also according to Thwaites (1960), the point past which the attachment line converges would be a stagnation point, with limiting streamlines ending there, and the pair of lateral vortices leaving the body (Figure 23).

Figure 118 - Detail views of BARE HULL stern region for AoA = 0°.

Source: Author (2018).

Very close observations during the runs, difficult to be shown here due to the details dimensions, showed that the support bar had some effect on the flow over the lower surface. Nevertheless, given the theory previously presented and supported by the results shown above, those effects were considered negligible, once the expected flow structures appeared clearly. Also, despite the slight incidence identified, no “owl” structures like those observed by Fairlie (1980) or predicted by Patel (1993) were visualized. It is important to highlight that the HULL is not exactly like the studied prolate spheroids, which have the maximum diameter at the middle length. Here $\mathbf{D_{máx}}$ is at around 38%**L**, which certainly influences the flow development. The results presented in section 3.1.5 are going to be used for comparison purposes, but not as strict references of what should be seen.

Once surface attached vortical structures were identified on the BARE HULL for AoA = 0°, the aim was to find out how the flow behaves for larger AoAs. The first step was an increase of 10° in AoA.

Figure 119 - Sequential frames of Run_02 for ENV_27 in 5 seconds intervals for AoA = +10°.

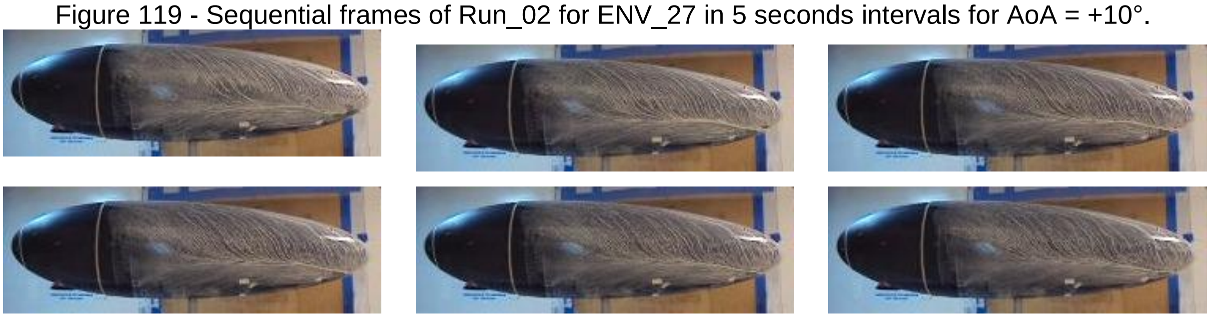

Source: Author (2018).

The test point was run, and modifications were noticed right away. Another converging line (strong white dense line) appeared, but a little bit lower than before.

However, it is important to remember that, once AoA increased, the observed lateral pictures now represent the upper side of BARE HULL (recall referencing from section 4.1.3), or the leeward side as defined in section 3.1.5. From the video frames (Figure 119), it is possible to see that the lines are converging in a much steeper manner. Nevertheless, since this is the upper portion, one should expect the white line aligned, acting as a source, emanating streamlines to lateral sides, as can be seen in Figure 119. Once the velocity was cut, pictures were taken of the model. The flowviz oil, however, was too dense, and gravity effects acted very quickly, making the oil to run downwards where its concentration was higher (between the red dashed lines – Figure 120). In any case, it was possible to observe that well streamlined regions formed on the upper and lower portions (blue solid lines), which are indeed BARE HULL starboard and port sides at AoA = +10°, respectively. Still, between both dashed red “Vees”, there is a wide region where less pigment was attached before stopping the tunnel. These two regions were probably high velocity regions, once pigment was taken away, even being dense. The upper region probably extended itself up to the lower converging line (Figure 119), like is seen for the lower, but was contaminated by the running downwards flowviz due to gravity effect.

Figure 120 - Limiting streamlines on model upper side at AoA = +10°.

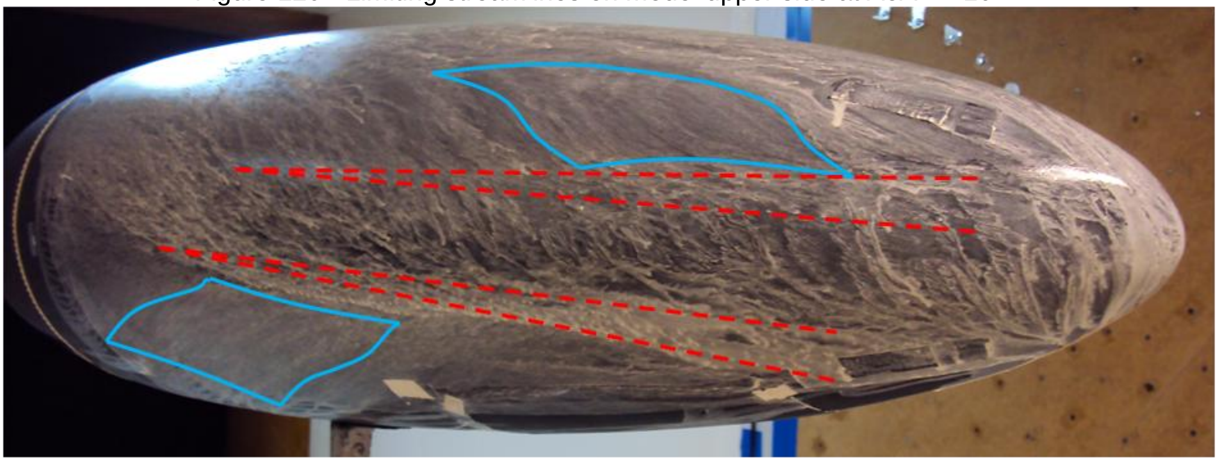

Source: Author (2018).

The presence of the support bar in the middle of the crossflow path may have a connection with the fact of the symmetry line (between red “Vees”) being little downwards (to the port side, considering the image in Figure 120 is the BARE HULL upper side). The probable upwash induced by some misplacement of the model along the longitudinal plane does not seem to be a relevant issue, as in such the flow pattern would point upwards in Figure 120 and not downwards. Starboard limiting streamlines were observed, and as expected were going from the lower to the upper side, converging to an almost horizontal trend, when reaching the leeward side.

Figure 121 - Limiting streamlines on model starboard (aerodynamic) side at AoA = +10°, rear (left) and fore (right) views.

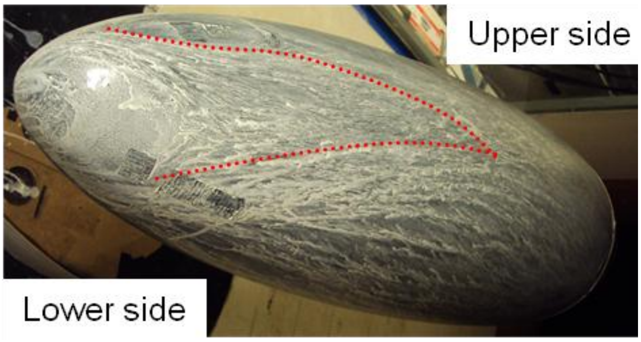

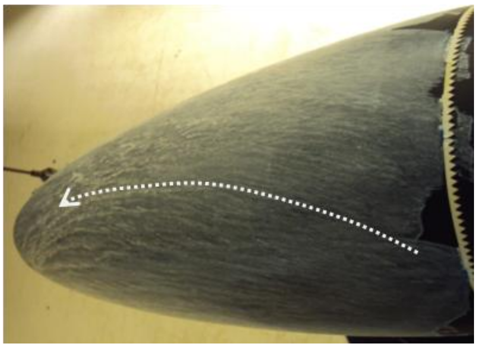

Source: Author (2018).

Observing the same side (starboard - aerodynamically wise), it is possible to observe a conical region where the streamlines are not clearly oriented and individualized, being constituted much more of white stretched dots than lines. This is probably a region where surface velocities were not very high, like a conical vortice region. Considering than that this vortex has a core proportional to the surface conical width, there must be outer flow streamlines that are overcoming these conical tubes, and reattaching on the upper side in order to have patterns such as those well streamlined regions (between solid blue lines) observed in Figure 120. Recalling the theoretical predictions presented by Thwaites (1960), it is possible to infer that external streamlines do seem to overcome the lateral vortices and go to the upper portion of the body. Since AoA = +10° may still be taken as relatively small, probably this is a good assumption. Also, the fact that a conical vortex pattern was observed, and not just a line, like before, might be linked to viscous effects. The increase in AoA imposes an increased adverse pressure gradient, causing the vortex to lose momentum, making it not strong enough to overcome the pressure gradients, enlarging its core size (reducing rotational velocity). Similar observations were made by Han and Patel (1979) and Fairlie (1980).

No relevant changes in the separation line and in the stern bubble were observed, despite the increase in AoA. The problems with the thick oil layers, and not clearly observable results, however, made it difficult to reach more conclusions. Therefore, the mix was lightened, increasing the proportion of paraffin (Kerosene). A run for AoA = +20° was conducted aiming at increasing the phenomena intensity and clarity. The obtained patterns showed an outstanding quality, and the flow was much easier to understand. Firstly, with the lighter flowviz, the limiting lines between different structures were much clearer.

Figure 122 - Sequential frames of Run_03 for ENV_27 in 5 seconds intervals for AoA = +20°.

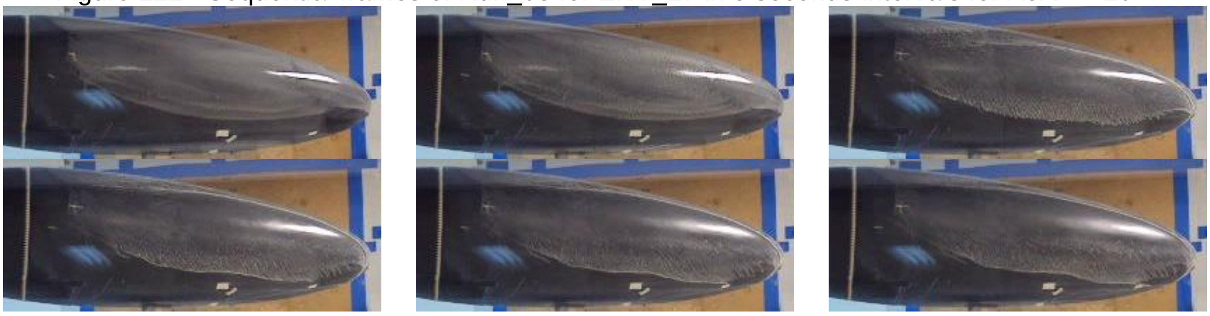

Source: Author (2018).

Observing the sequential frames (Figure 122), in contrast with the other two, a new behavior showed up: as expected, the flow at the upper (aerodynamic) portion divided itself along a mean line going to the sides symmetrically. It is possible to see, however, that, as for AoA = +10°, this middle line is not very well aligned with the model longitudinal axis, being in this case dislocated to the starboard side (aerodynamic). Also, by analyzing the lower portion of the frames (from the middle of the top to the port side – aerodynamically referencing), it is possible to infer that this is not a high velocity field, as the flowviz ran down due to gravity, even at a high wind tunnel dynamic pressure. In this sense, the surface oil would be sort of shielded from the outer flow. This is probably the same conical vortex development observed before, but this time taking place on the port side.

Figure 123 - Run_03 upper view of upper side (AoA = +20°).

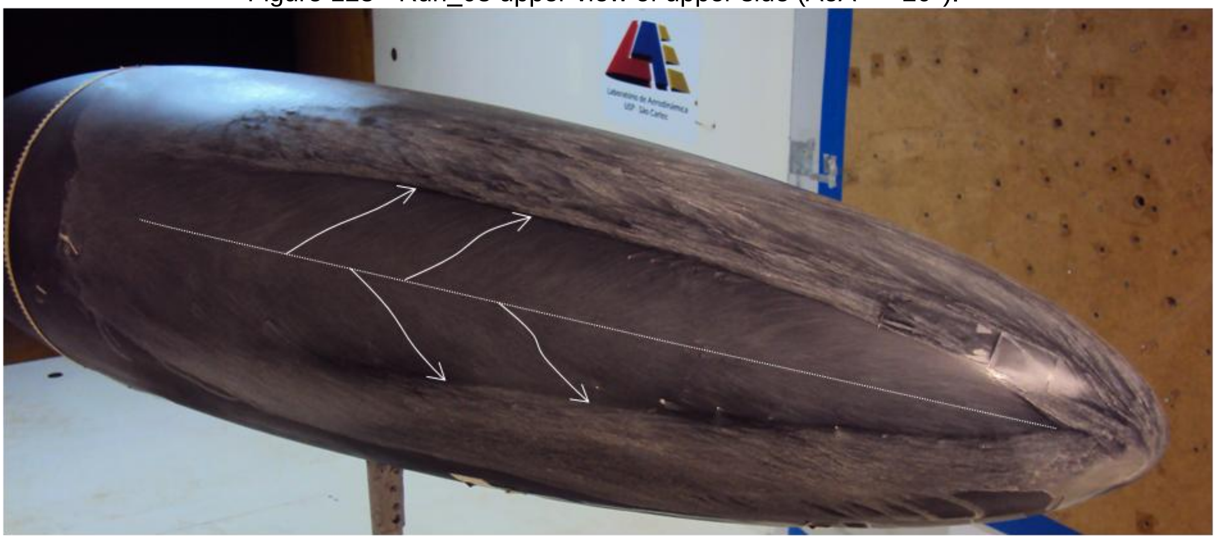

Source: Author (2018).

The observed flow tendency of running from a middle line to the sides was clearly observed. A leaf-like pattern (darker region in Figure 123) with well defined and thin limiting streamlines, hairline-like, evidences a very high surface velocity.

Figure 124 - Leaf-like pattern in detail for AoA = +20°.

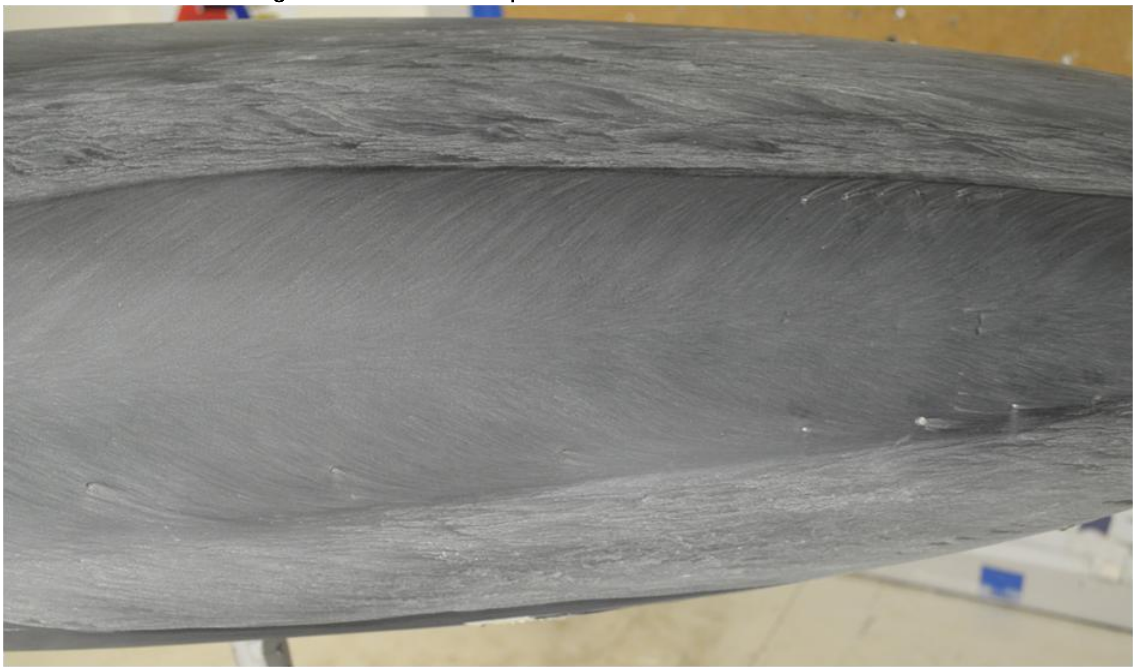

Source: Author (2018).

Figure 125 - Leaf-like pattern closer detail.

Source: Author (2018).

It is also possible to see that, in both directions, the streamlines end in thick dark lines. These dark lines are the thresholds between the upper pattern and a conical flowviz white scattered region. In addition, the dark color demonstrates that the local velocity there is rather high, as the local surface was essentially cleaned (remember that black is the model color). Still, by looking from underneath, one can see that the leaf-like pattern is in fact off-centered from the top (aerodynamic side) middle line, as mentioned above. Nevertheless, the pattern is dislocated upwards, once its middle line (origin of the streamlines on the leaf-like pattern) appears above the global middle line (red line in Figure 126), which lies right between fins fixation points (closed circuit of white lines in Figure 126). This means that for higher AoAs, the model misplacement (together with the wind tunnel section upwash) may become more relevant. The reason for that may be the increased interference between the stronger lateral vortices and the induced upflow, which may move the aerodynamic structures upwards.

Figure 126 - Run_03 lower view of upper side (AoA = +20°).

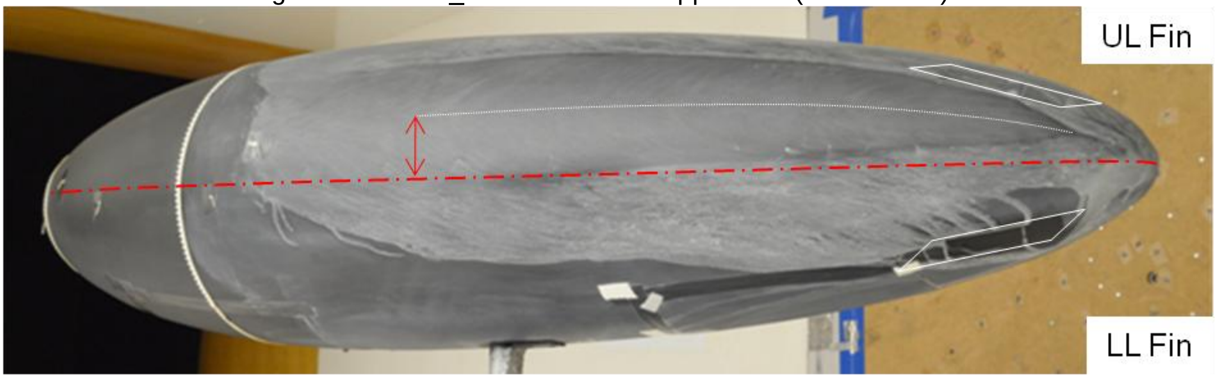

Source: Author (2018).

By evaluating the aerodynamic starboard flow, the same observed trends for AoA = +10° were seen: very steep upward limiting streamlines. All those lateral streamlines were also converging to a well defined black line, which was a limiting line with the same scattered white region cited above.

Figure 127 - Detail view of upcoming limiting streamlines on starboard side of Run_03 for AoA = +20°. It is possible to see the streamlines converging to the conical vortex separation line.

Source: Author (2018).

Analyzing the region between the starboard side and the top reveals a well defined conical region. With a white scattered pattern, this region must have a small surface velocity, as the pigment was not well transported along the flow. This conical region is symmetrical in relation to the first mentioned white region when analyzing the video frames. With very well defined borders, this region seems to be a low pressure region, once the streamlines were sucked to it.

Figure 128 - Rear view of Run_03 for AoA = +20°.

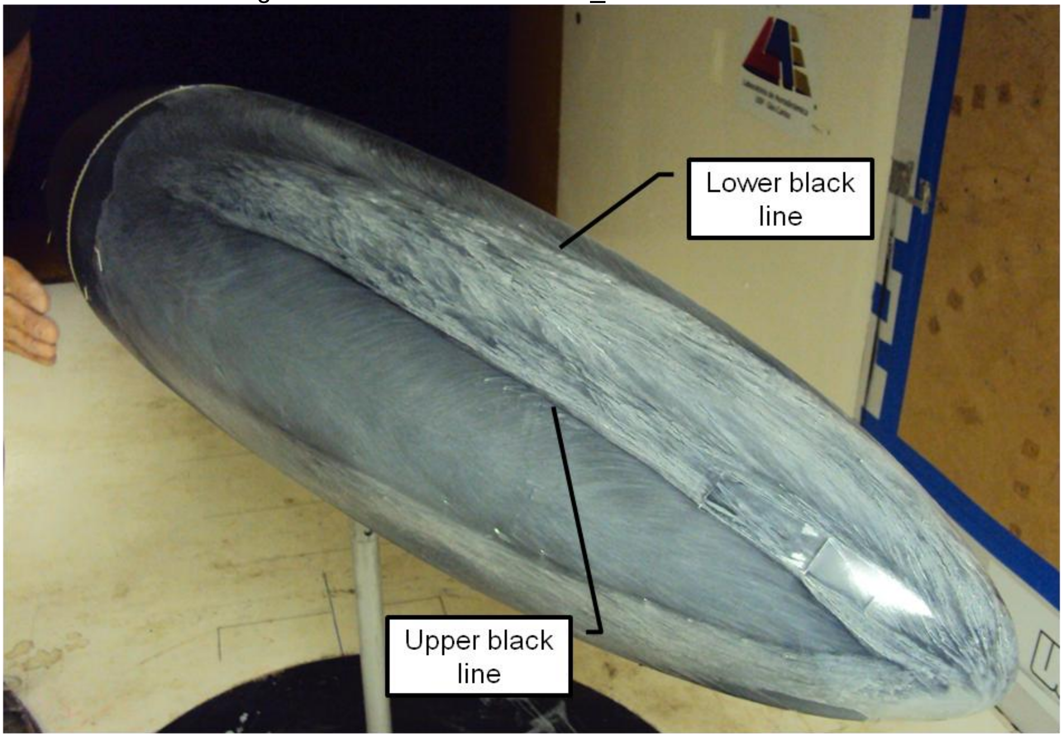

Source: Author (2018).

Figure 129 - Starboard side of Run_03 for AoA = +20°. The white region shows the BARE HULL region covered by the conical vortex.

Source: Author (2018).

Aerodynamically evaluating all patterns makes it possible to devise a probable outer flow. Firstly, the upper leaf-like pattern (Figure 124) is probably the result of a pair of counter-rotating vortices which are acting on the top of the model, with downward velocities being added on the aircraft longitudinal plane. The port vortex rotates counter-clockwise, while the starboard vortex rotates clockwise, looking downstream at the tunnel test section. This explains why a middle line is formed, and why streamlines in opposite directions come from it (i.e. emerging limiting streamlines). The middle line is an open type attachment line from both vortices. In addition, because the vorticity of both is strong, the induced crossflow velocity is also high, creating the opposite lateral limiting streamlines on the leaf-like pattern. This is very similar to the top vortices topology depicted by Fairlie (1980) (Figure 28).

The conical white regions, observed between around 30° and 60° above the aerodynamic lateral plane on both sides, are surface limiting lines of growing low-strength wakes of conical vortex or bubble-like structures. Probably, given a strong adverse pressure gradient, the streamlines layer coming from windward side detaches along the lower[42] black line (Figure 128). The separated sheet coming from the BARE HULL lower limiting black line rolls up inwards and seems to reattach on the upper black line (Figure 128). Nevertheless, analyzing the 3D separation criteria established by Maskell (1955) and also explained by Patel (1993), it would not be possible to have a reattachment on the upper line and sustain the top vortices existence as they are. Therefore, the bubble should be a double bubble of low strength counter-rotating directions. The bubbles outer limiting lines (dotted lines in Figure 130) would clash with each other at the top, and roll towards the surface, creating standing eddies (dashed lines in Figure 130). This formation is described by Maskell (1955) and treated as a mixed flow, taking place when a bubble forms in between two opposite 3D separation lines (black lines in Figure 128). As consequence, at the clash point (a singularity point), a free vortex layer appears (dash-dot line in Figure 130), which then leaves the bubble surface and rolls up in the same direction as the top vortices. This process was inferred from the leaf-like pattern shown in the previous figures.

It is interesting to observe that, despite the strong scatter (Figure 129), it is possible to observe a very discrete diverging tendency from the middle to the sides on the white (conical) region. This attests that, although being very low strength, the double-bubble standing eddies can constitute a proposal which makes sense, as they could be “pushing” the limiting streamlines to the separation lines (black lines in Figure 128). This very low intensity in vorticity also supports the fact that no clearly detectable attachment line can be observed (which might also be due to the flowviz density). Going deeper on the double-bubble cycle, one will notice that the limiting streamlines inside each bubble are going to meet the limiting streamlines outside of

[42] Lower and upper black lines are referenced aerodynamically; one must remember that the model longitudinal plane was contained in the wind tunnel section top plane.

the bubbles (black lines in Figure 128), leading to open separation lines. These separation lines will maintain the bubble separation surface (dotted lines in Figure 130), enclosing this local structure.

Figure 130 - Crossflow streamlines (general topology) schematics inferred from observed surface flow patterns, looking downstream of the flow. Not to scale

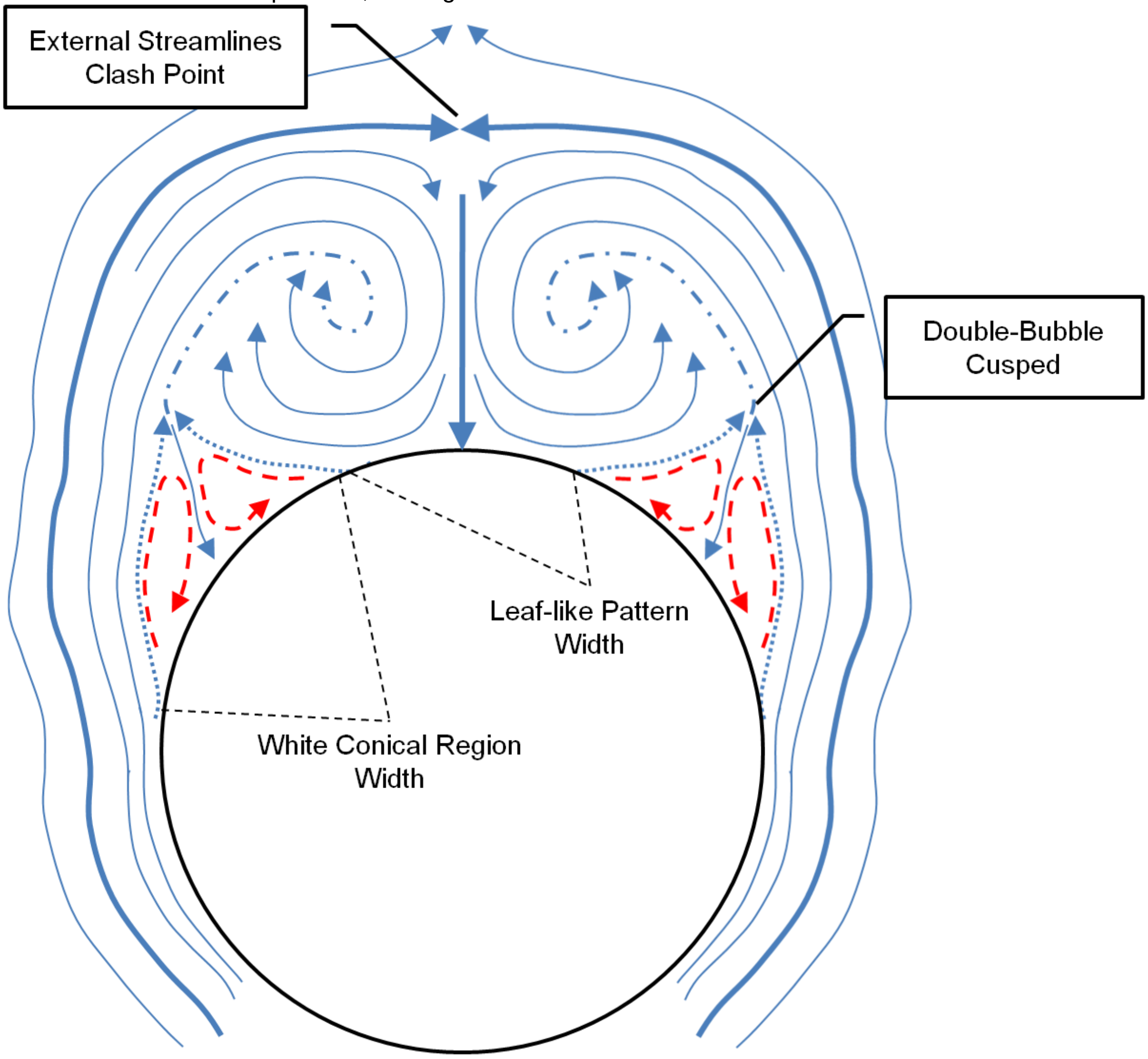

Source: Author (2018).

The proposal of the double-bubble structure also supports the increase in core size, and the scattered surface pattern (different from the hairline-like on the upper side). The separation bubbles would generate almost stagnant air regions in the crossflow direction (remember that the standing eddies are of low strength), allowing longitudinal streamlines (a sort of secondary flow) to flow along its constant pressure lines. Once those longitudinal streamlines are low in velocity, the slightly inclined scattered aspect, seen in Figure 129, makes sense, being a combination of longitudinal and crosswise flows.

Figure 131 - Schematic representation of the starboard side showing an upper view of the Double-bubble region for positive incidence (topology) resulting from the observed surface flow patterns. Not to scale.

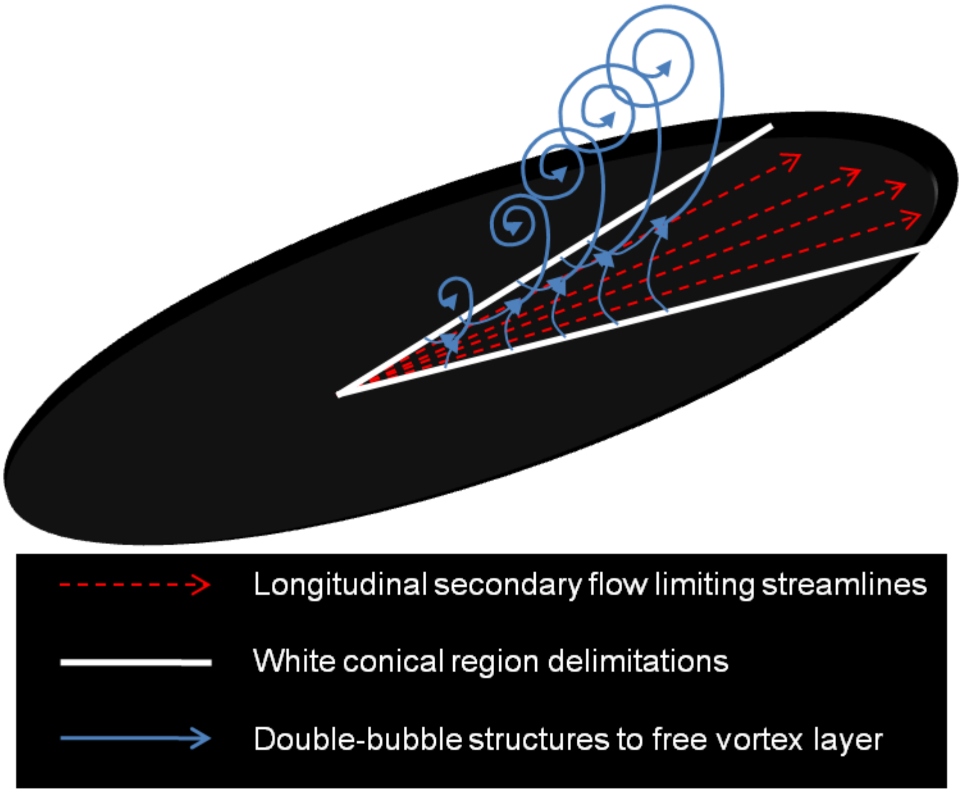

Source: Author (2018).

The top vortices are in turn impelled by the bubble separated vortex layer (coming from the cusped edge) and reinforced by the external streamlines which overcome the double-bubbles, and clash with each other over the HULL, rolling downwards. These lateral separation layers are also counter-rotating, having the same rotational directions as the top vortices in lateral pairs, i.e. both port vortices rotate in same direction, which is the opposite direction of both starboard vortices. Also, comparing this case with previous results, it is possible to see that these conical regions (bubbles regions) grow proportionally to AoA: the greater the incidence, the further upstream they begin. It seems to be a very plausible explanation: as the leaf-like region gets wider for a certain longitudinal extent, while the white conical region width (proceeding along the bubbles lengths) is relatively small, and, for some flow, overcoming it is still possible. With the bubbles increasing in length, it gets more difficult to overcome them, and reattach at the top. As a consequence, the upper pattern gets narrower, while the white conical region gets wider.

This is very similar to the physics involved in the flow past separation bubbles. The major difference is that usually downstream of a separation bubble on an airfoil, for example, reattaching is much easier than for the BARE HULL. The truth behind this lies in the fact that, since the curvature is less pronounced in the airfoil, the adverse pressure gradient is also lower than would be in the case of trying to reach the upper portion of a cylindrical cross section, like the BARE HULL.

Moreover, considering this hypothesis as true, these external lateral streamlines, which do not reattach, still have a rotational trend, since they are trying to go over the bubbles. As they do not reattach, they roll up over themselves and detach as individual vortex tubes. This would be the case when the double-bubble structure is so large that the free vortex layer originating from its cusp just rolls over itself.

This would be a similar behavior like that observed for cylinders subject to flow across the diameter, and the detaching vortices would be like von Kármán vortices. This proposal may draw support from Thwaites (1960), based on Figure 132, if the crossflow *Re* is low enough.

Figure 132 - Crossflow in planes perpendicular to a body of revolution at incidence.

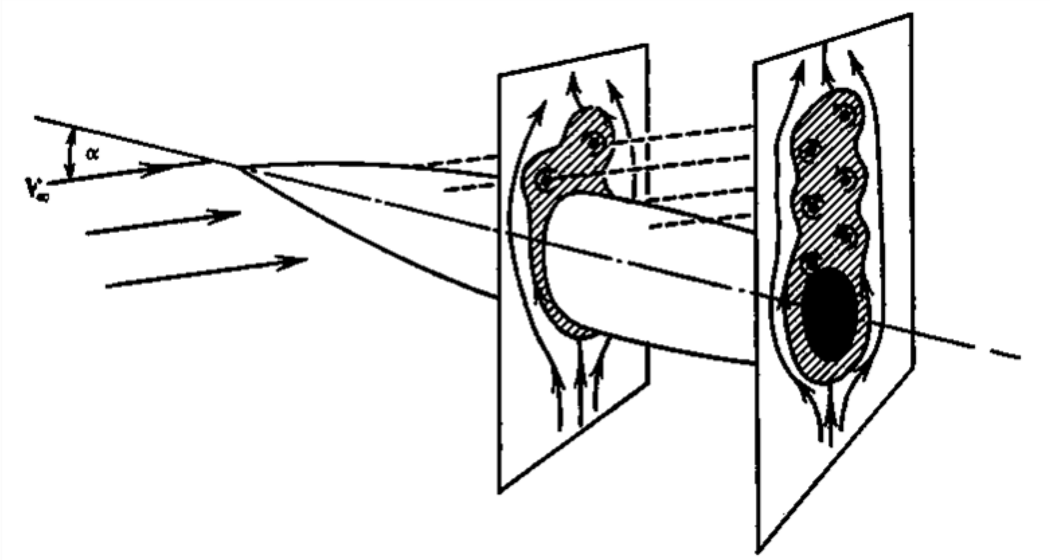

Source: Thwaites (1960), p. 411.

Although this seems to be a rather complex hypothesis, and difficult to be explained only based on surface flow observations, it matches very well the flow characteristics presented by Thwaites (1960), Fairlie (1980), Patel (1993) and also Maskell (1955).

Besides that, studying Figure 24, one can see aerodynamic structures developing in a similar manner to what is proposed above. Figure 24 is also based on experimental data for AoA = +20°, standing for moderate incidences, but also based on surface patterns. The main observed difference between the proposed explanation, and the observed patterns from Thwaites (1960), is that for this last one, there is a lateral region between the lateral vortex cores, which is represented as being rather small, and the upper vortices, where no vorticity is observed. Nevertheless, the body studied there is clearly different from the one used in this work, and so should be the surface patterns.

A similar investigation with tufts using the FISHNET, trying to potentialize the turbulence effects, was carried out. As can be observed from the sequential frames (Figure 133), the portion equivalent to what would be the port conical vortex shows turbulence despite the thick white scattered layer observed previously when using flowviz. This is another indication that it is probably a low strength large vortex.

Figure 133 - Sequential frames of Run_03 of ENV_27 for AoA = +20° with FISHNET.

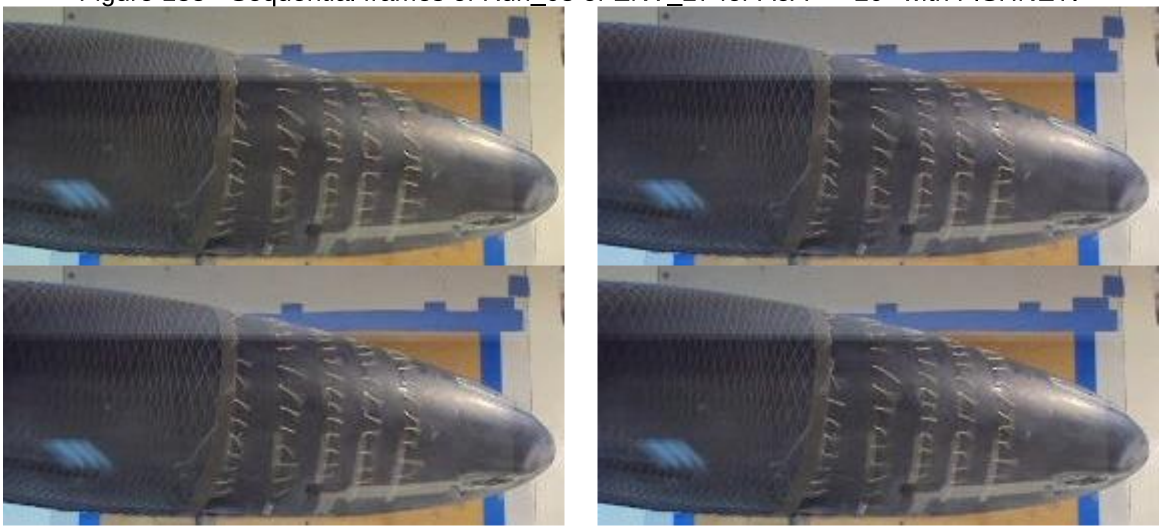

Source: Author (2018).

Another tufting investigation was made in order to assess the symmetry on the lower side, as applying oil to the whole model is very difficult without having runoff problems. Still using the FISHNET, for AoA = -20°, sequential frames were extracted from a video record. Comparing the different frames (Figure 134), which are approximately 2 seconds apart, no clear difference is observed regarding tufts alignment. This could attest that no vortical or separated flow is acting on the lower side. However, it is also possible to confirm that the boundary layer is turbulent, because the tips of the tufts show an intense oscillatory motion around a mean direction. In this way, as expected, the flow seems to be well attached, from underneath, going to the starboard and port sides originating from a mean line, almost aligned with the BARE HULL longitudinal axis. The slight misalignment is probably due to a small issue with the incidence adjustment, as pointed out by the first oil visualization exercise (Figure 113).

Figure 134 - Sequential frames of Run_03 for ENV_27 for AoA = -20° with FISHNET.

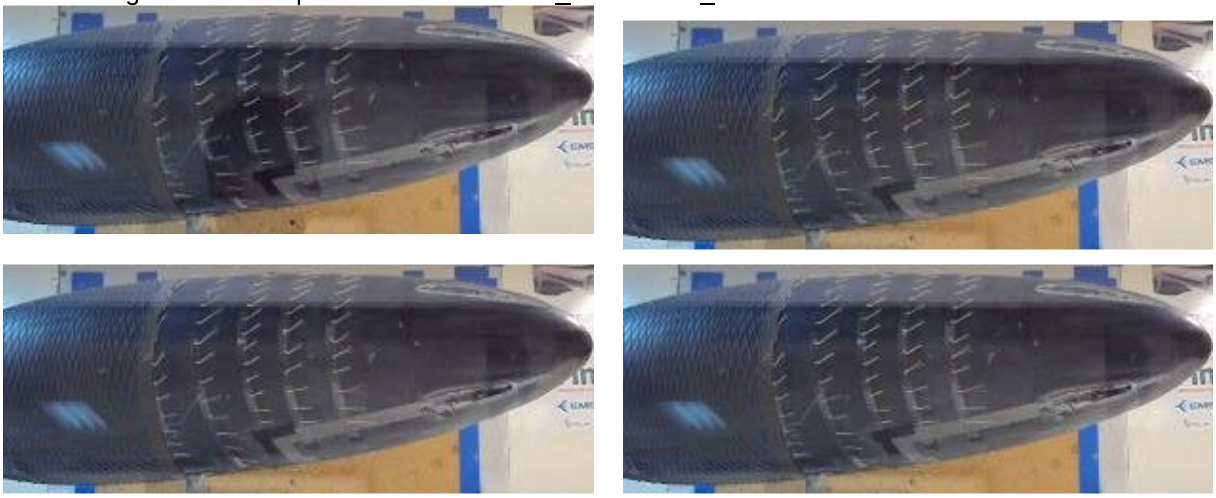

Source: Author (2018).

The same result may be observed without the FISHNET (Figure 135 and Figure 136). However, the tufts density was not that high, showing poor results regarding visualization, the same problem faced by Han and Patel (1979).

Figure 135 - Lower side of ENV_27 at AoA = -15°.

Source: Author (2018).

Figure 136 - Lower side of ENV_27 at AoA = -24°.

Source: Author (2018).

Despite all the evaluations, it is difficult to affirm that this is the exact flow structure without actually visualizing the outer flow. For this reason, some smoke visualization was conducted. But, since it was carried out with the fins installed, it is presented later, in section 5.2.3.4.

The fact is that very wide low longitudinal velocity regions exist on both sides of the BARE HULL, whilst the top has certainly a very strong vortical flow. In a whole, these surface pattern investigations attest that the flow past the BARE HULL is very complex and three-dimensional, with a strong influence of vorticity and crossflow.

5.2.3 AIRSHIP characterization – behaviors and trends

Once the most adequate roughness for flow similitude was selected, the tail fins were installed on the model. The X-tail configuration used the S0 FINs set described in Appendix A. A detailed investigation was carried out, because such FINs are scaled versions of the fins under study for the new aircraft concept at AdB (section 1.2). For this configuration, the C_D trend against *Re* was assessed, trimming curves were extracted, varying equally the control surfaces of each fin, and some pressure measurements were made along a line on the surface right upstream of one of the fins, and in between two pairs of them (Figure 63). Regarding visualization, tufts were installed around the fins on the stern portion of the HULL, and on fin surfaces as well. Complementarily, after pressure and force measurements were made, oil flow visualization was also conducted for the HULL+TAIL configuration, from now on named AIRSHIP.

It is important to highlight that even with the tail installed, it is still possible to say that AIRSHIP data are going to be C_L, C_D and C_M[43], although the aero-balance measures moment around the vertical axis. This is true because the X-tail configuration is axisymmetric, allowing to look at the AIRSHIP as pitching on the lateral (x-y) plane of the working chamber (Figure 59).

5.2.3.1 Tailplane influence on the model aerodynamics: forces and moment

The first interesting assessment to be carried out was comparing the results with and without fins. ENV_20 had the fins installed without control surface deflection, which means δ = 0°. AoA and *Re* Polars were obtained for it. However, while evaluating the first results, a strong asymmetry around AoA = 0° was observed mainly on the C_D curve, although the C_L and C_M curves also presented some off-centering for AoA = 0°. This led to some questions concerning flow separation over the fins, and probable assembly symmetry problems.

New tufts were added to the fin surfaces, and the fins positioning was checked. Unfortunately, there were some issues regarding lack of perfect symmetry among the four fins, both in longitudinal positioning (downstream/upstream) and in angular positioning (perpendicularity to the surface and local AoA - fixation angle). These latter problems were not easily solvable, and would be something to deal with along the campaign. Since the trend characterizations were the main objective, such problems were felt not to affect the expected outputs. During the fins check, the

[43] The moment was measured at around 50%**L**, where the support was fixed, and then mathematically transferred to 25%**L**. This was a standardization procedure, and will be better discussed at the end of this section and during the dynamic tests evaluation. Basically, this is a standard output provided by the acquisition software employed for the LAE-1 wind tunnel tests, and has no direct relation with airship flight mechanics, constituting a simple reference.

control surfaces were also re-adjusted to zero, making sure that no control input would affect the first run.

Figure 137 - ENV_21 configuration in the LAE-1.

Source: Author (2018).

After that, ENV_21 configuration was run. Little change was observed regarding C_L, there was only a minor improvement in symmetry for small AoAs, whilst both curves concurred very well (Figure 138). Looking at C_D results also showed almost no relevant changes for the overall curve (Figure 139).

Figure 138 - Lift polars for initial comparison between BARE HULL and AIRSHIP.

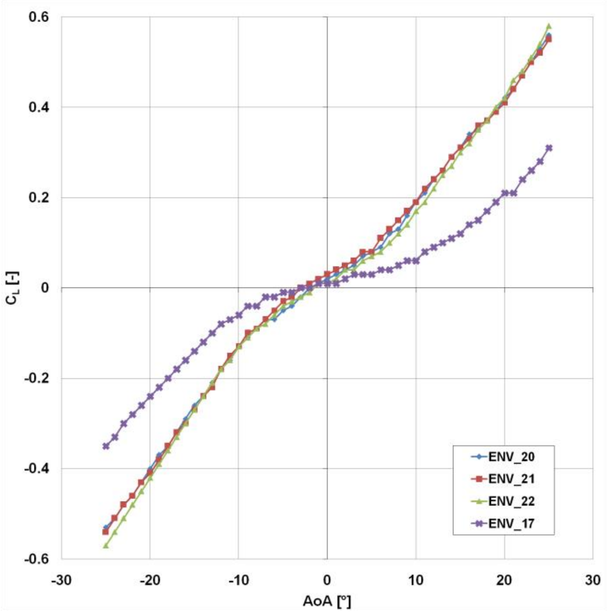

Source: Author (2018).

Figure 139 - Drag polars for initial comparison between BARE HULL and AIRSHIP.

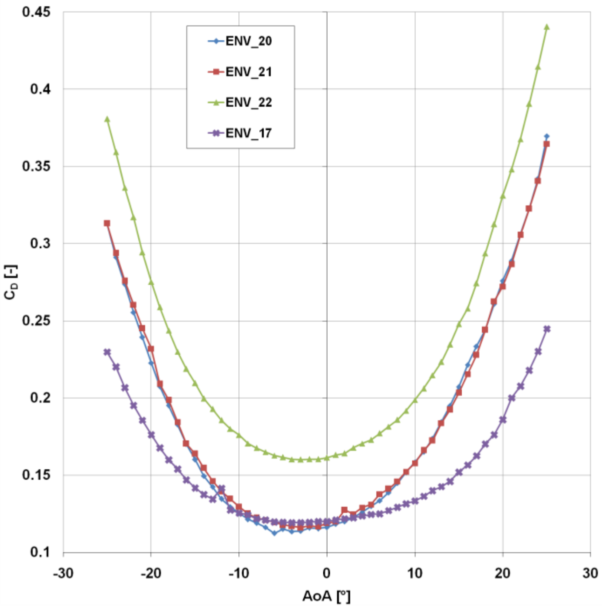

Source: Author (2018).

The C_M curve (around 25%**L**), however, showed major changes, with improved symmetry and trend. This means that the correction (zeroing) applied to the control surfaces had relevant effect on the moment acquisition, which is sensitive enough to capture any deviations.

Figure 140 - Moment polar against AoA for initial comparisons between BARE HULL and AIRSHIP.

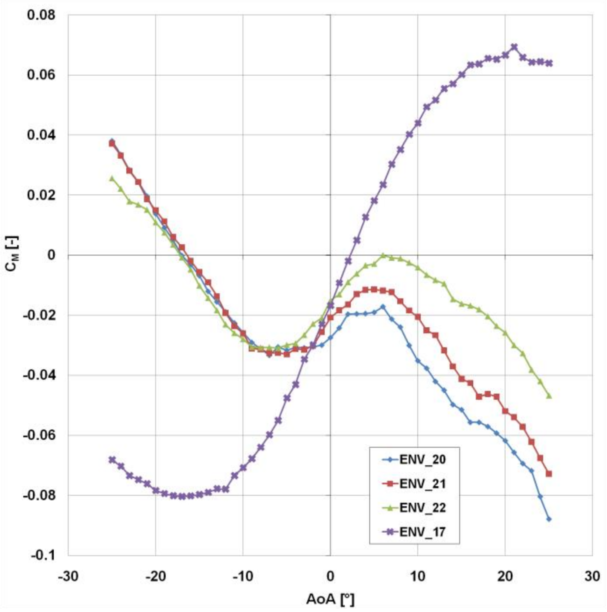

Source: Author (2018).

Figure 141 - Moment polars against lift for initial comparison between BARE HULL and AIRSHIP

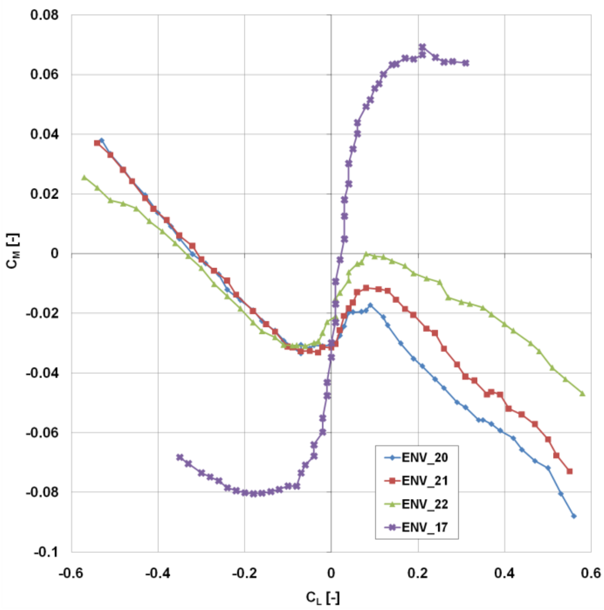

Source: Author (2018).

Nevertheless, all curves still shared the same issue: off-centering. This was probably due, to a certain extent, to the fins mispositioning. Analyzing the AoA = 0° case, supposing, for example, the FINs fixed at a slightly positive angle, then a positive lift would be generated, but a negative pitching moment, since the tail is behind the axis of reference. Both facts are observable when evaluating the obtained curves. An indication of the misplacement of the FINs may be seen in Figure 254. A schematic sequence of the physics of the supposed misplacement is shown in Figure 142; for simplification purposes, only lift was drawn. Assuming the AIRSHIP free to swivel, with increasing velocity, fins generate lift, inducing a negative pitching moment, which changes the HULL AoA. This causes the HULL to generate some lift, and the FINs to decrease theirs. The AoA magnitude ends being the one which provides a balance around the pitch axis.

Figure 142 - Sequential physical effect of FIN mispositioning.

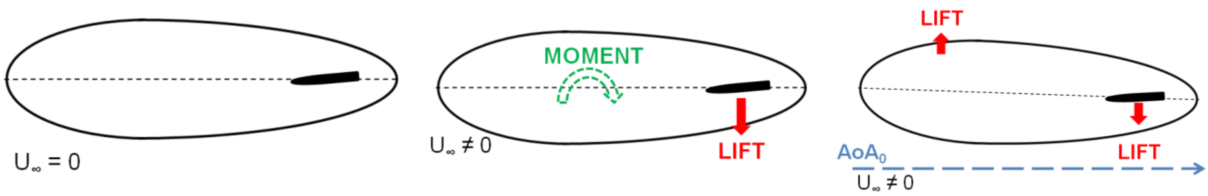

Source: Author (2018).

Also, when looking at the drag curve (Figure 139), still considering the fins positive fixation angle, one can clearly see that the curve is translated to the left, which means lower drag values at slightly negative AoAs. This is also in agreement with the supposition of fins mispositioning, mainly considering that the forces (lift and drag) are rather relevant when compared with results just for the ellipsoidal body (HULL), since they are aerodynamic surfaces, behaving as wings. Therefore, if the fixation angle is positive, and the AoA is negative, there is a decrease in the effective angle on the tail, reducing drag and lift generated.

Knowing the issues that would affect the whole testing campaign, work moved on to the next step: comparing aerodynamic characteristics with and without fins. As expected, according to section 3.1.4, with the fins installed, the curves got a much more linear trend than what was seen for the BARE HULL. Besides that, a relevant increase in C_L, mainly for high AoAs, was obtained. This increase in lift results from the combination of the FIN aerodynamic lift generation and the LCO (Lift Carry-Over) effect, mentioned in section 3.1.5, which is an increase in BARE HULL lift due to the presence of the FINs. The latter figure is very complex to be obtained, as it is necessary to calculate the lift before and after adding the tailplane by integrating the pressure distribution, and not comparing only forces, because the fin lift generation would be mistakenly included. In order to evaluate the increase in lift, for the AIRSHIP (TRIP and FISHNET), the global C_L difference, called LCO* (in reference to original LCO), is depicted in Figure 143. It is possible to fit the LCO* curves very well using second-order polynomial and linear trends as well, once the quadratic term is very small. This leads to the conclusion that the increase in lift generated by the fins is not directly linear with AoA, but is also probably ruled by some other factors, such as outer flow aerodynamic structures, and induced velocities.

Figure 143 - AIRSHIP LCO* with TRIP and FISHNET for the complete AoA range.

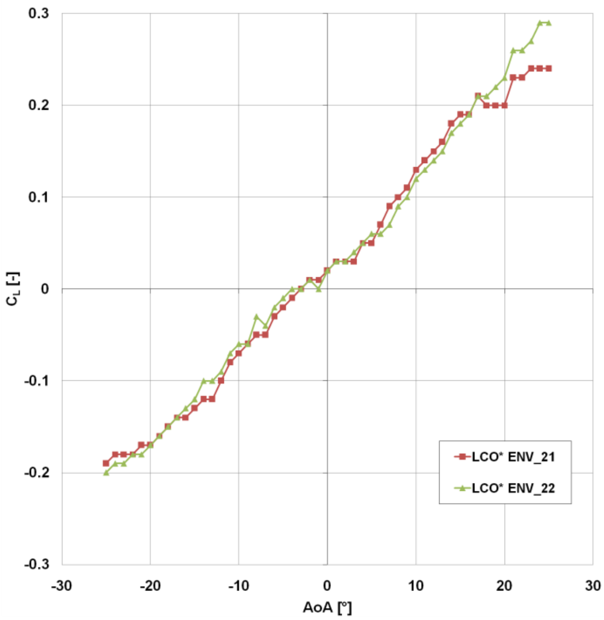

Source: Author (2018).

Figure 144 - AIRSHIP LCO* with TRIP and FISHNET for positive portion of AoA range.

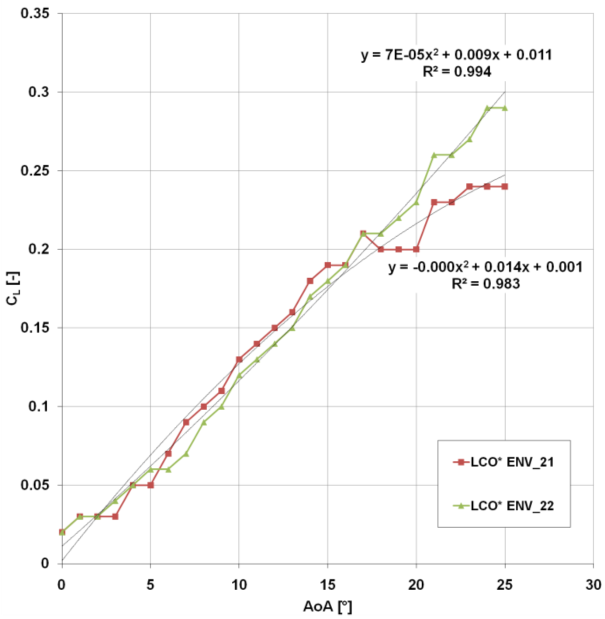

Source: Author (2018).

It is interesting to observe that around small AoAs ([-10°; 10°]), the $C_{L\alpha}$ with fins is smaller than what is seen for the rest of the AoA range. This tendency of going towards what the BARE HULL curve, providing smaller C_L and $C_{L\alpha}$, may be explained by the fact that, for small AoAs, the fins are less effective in producing lift, and the BARE HULL is still relevant in contributing to it. Remarkably, it is also interesting to highlight that, differently from other lifting surfaces, no stall (decrease in lift with increase in AoA) was identified, neither for BARE HULL nor for AIRSHIP, although the AoA went up to 25°. This shows that there is still a feasible range to increase AoA, and generate more lift, if desired.

However, when looking at C_M, for the BARE HULL configuration, some sort of absolute stabilization and further decrease in pitching moment is observed for |AoA| > 15°; the curve shape is similar to stall regions of regular lifting surfaces. This may indicate that, for such large AoAs, drag plays a relevant role in the AIRSHIP pitching moment (Figure 140). Still, while C_M for the BARE HULL is statically unstable, the C_M for AIRSHIP is overall statically stable, as expected. Nevertheless, in the range of smaller AoAs ([-10°; +10°]) there is a slight statically instability trend. In other words, while increasing AoA up to these angles the model still tends to increase AoA. However, near to the thresholds there is an inflection, and the AIRSHIP becomes statically stable, and the AoA tendency to increase starts to fall. The Inflection points of this sinusoidal region coincide with the same points where the

C_L curve changes $C_{L\alpha}$. It is possible then to confirm the assumption stated above for C_L, and say that these are AoAs where fins begin to be effective enough to overcome BARE HULL aerodynamic forces. Similar patterns were also observed by other researchers, and were shown in section 3.1.6.3.

Still with respect to C_M, an unexpected result is observed: the curves seem to be translated downwards, and $C_M \neq 0$ for $C_L = 0$ & AoA = 0°. This is contrary to what was expected for an axisymmetric model, and must still be linked to the misplacement issue noticed on fins installation, as described above. The same off-centering is observed for BARE HULL results on C_M. The explanation however probably lies on the fixation angle of the model. It is usually acceptable if the required AoA_0 = 0° is a little off. Also, as evaluated in section 3.1.6.1, although the model has an acceptable symmetry, the means used to manufacture it and the limitations of that process, may have led to some asymmetry, which becomes relevant when evaluating such small aerodynamic coefficients. However, it must be emphasized that this does not jeopardize the work, as the main objective - aerodynamic and stability characterizations - can still be achieved.

Regarding drag, once again, C_D values for small AoAs are very similar for both configurations, whereas for greater AoAs the C_D curve is narrower for the fins configuration, showing a pronounced increase in drag with fins. One can then infer that the fins skin friction drag is small compared to the BARE HULL while the AoA is small, probably because their wet area is relatively small, and the aerodynamic profiles are low drag as well. However, when AoA is increased, and the fins begin generating lift, induced drag also takes its place. This increases significantly the model total drag, as induced drag is usually an order of magnitude greater than skin friction, which is dominant for the BARE HULL. Once again, it is possible to determine what, in this work, is called Drag Carry-Over (DCO*). This is defined as the difference between AIRSHIP (TRIP and FISHNET) and BARE HULL drags, best evaluated by plotting it against C_L^2 (Figure 145 and Figure 146). Again, similarly to what was explained for LCO*, this figure comprises the increases in BARE HULL drag (due to the FINs presence) and the drag add up of FINs. It is possible to see that close to the origin, there is a region where the relation between DCO* and C_L^2 is quadratic. However, isolating the portion after this range of small AoAs, the trend becomes much more linear. This shows that the flow characteristics are indeed complex, mainly for small AoAs, when dominance of BARE HULL flow structures prevails. Then, when linearity is observed, it is with respect to the squared value of C_L, demonstrating that the DCO* is basically induced drag, which is determined by lift characteristics.

Figure 145 - AIRSHIP DCO* with TRIP and FISHNET for the complete positive AoA range.

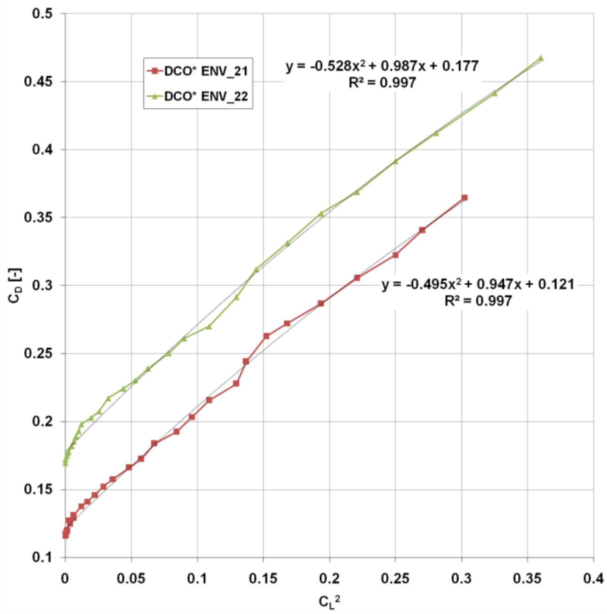

Source: Author (2018).

Figure 146 - AIRSHIP DCO* with TRIP and FISHNET for high AoAs.

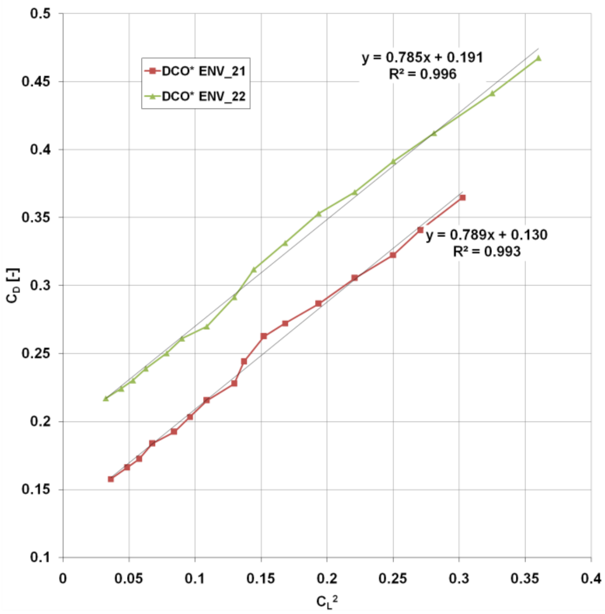

Source: Author (2018).

Finally, but before going deeper to the stability investigation, and following the last topic on roughness analysis (section 5.2.1), it is interesting to check what would happen if a stronger roughening device was chosen for the experiments. This is important in the sense that, as described in section 3.1.1.1, the fins effectiveness in airships is highly influenced by boundary layer thickness. The truth behind that lies in the fact that inside the boundary layer the mean flow velocity is lower than outside. This affects the spanwise velocity profile along the fin, especially in the root portion, reducing the aerodynamic response capacity of the FINs. To assess it, ENV_22 configuration was tested, comprising the FISHNET over the BARE HULL, in the same manner as before.

A slight, almost negligible, increase in $C_{L\alpha}$ and an improvement in the centering of the curve was observed after using the FISHNET, but no relevant changes in the overall shape of the C_L curve took place (Figure 138). From airfoil design theory, it can be suggested that the increase in $C_{L\alpha}$ might have happened because of the boundary layer thickening process (increase in δ_{99} – section 3.1.1.1), virtually enlarging the body and its maximum effective thickness, which is directly connected to lift generation. The curve centering however may be linked to a decrease in the lift generation on the fins, as introduced above. If one imagines that each fin is a series of lift generating strips, and the incoming velocity for one of the strips is reduced, the overall lift is going to decrease. This slower strip could be that one very near to the wall, where the boundary layer - or a separation wake - runs. Once the misalignment was due to FIN lift because of mispositioning, the decrease in velocity would also lead to less lift, reducing the previous observed offset (Figure 142).

This same inference may be applied to explain what happened to C_M (Figure 140 and Figure 141). There was small decrease in $C_{M\alpha}$ for negative AoAs, but a large one for the positive portion. Recalling the previous analysis, one may conclude that C_M is more sensitive than C_L to AoA, since it also depends on distances, which are relatively important considering the FINs at the stern region, and the model proportions. Assuming again that one or more fins are fixed at positive angles (i.e. misaligned), reducing their effective portion, or that larger low velocity areas (due to thicker boundary layer) have developed, leads to less lift produced, which in turn reduces the moment generated. In this way, the C_M curve would translate upwards, and also flatten. This is exactly what is observed when comparing ENV_22 and ENV_21 results.

Assessing the drag changes is much easier. With the FISHNET there is a clear increase in C_D level - almost an overall 30% increase. The curve also has an improved centering, similar to what was obtained for C_L. The reason for this may be attributed to the same above cited probable flow changes – thicker boundary layer. Also a *Re* Polar was generated for ENV_22, and compared to the ENV_20 results. The first clear difference is the drag level, which is higher than 30% in mean values. Besides that, the results for ENV_22 do not show a good regression quality using a log model, fitting much better when an ascending linear trend line is used.

Figure 147 - *Re* Polars for ENV_20 and ENV_22.

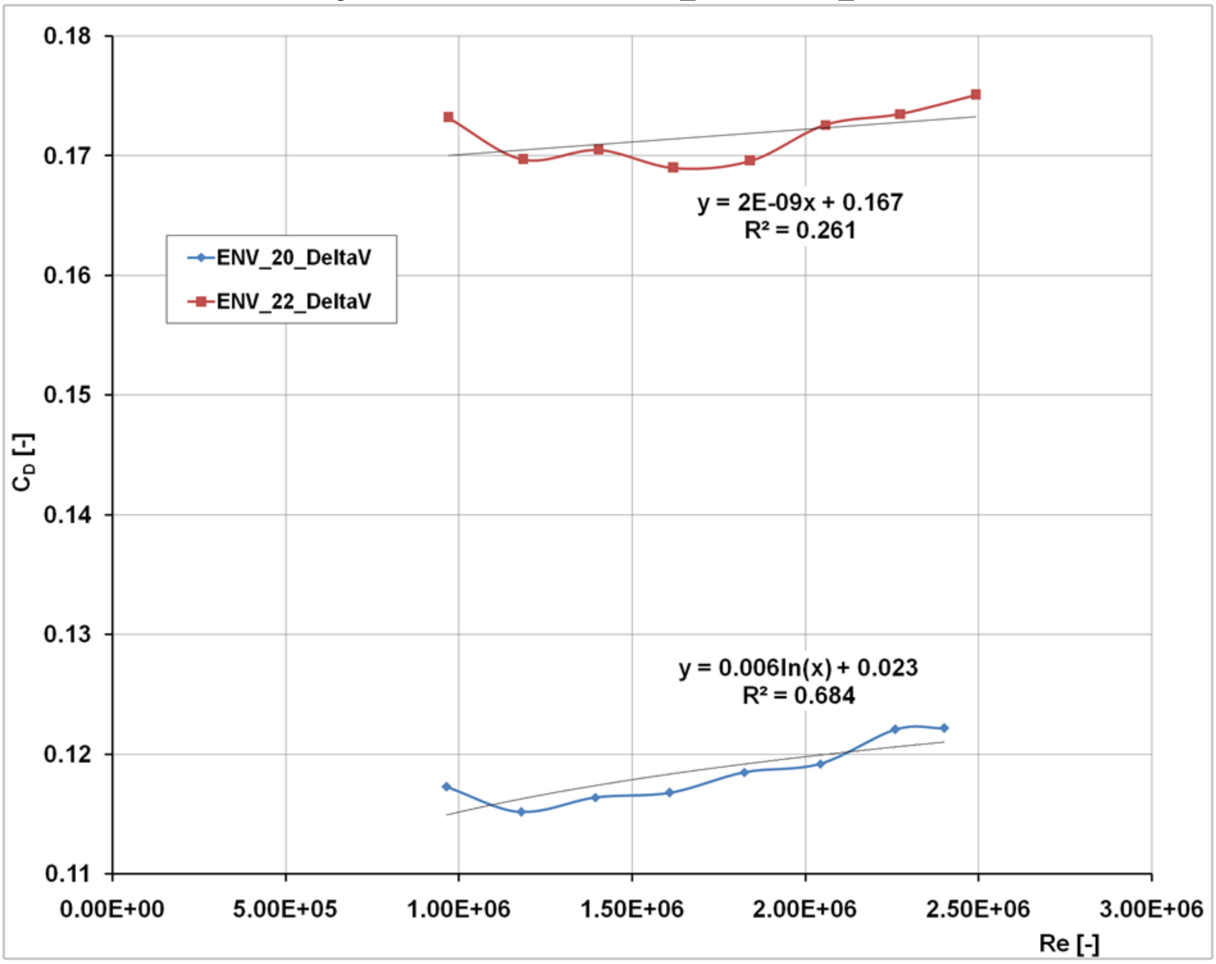

Source: Author (2018).

All the results and observations regarding ENV_22 seem to reinforce to a considerable extent the assumption that the boundary layer exerts a relevant influence on the fins aerodynamics. Dropping the FISHNET configuration in favor of the TRIP is then concluded to be a good choice, since the former was overemphasizing the level of turbulence, generating considerable influence on the FINs. However, there is also the possibility of underestimation of the boundary layer thickening using only the TRIP. This draws attention to the importance of properly addressing and evaluating the boundary layer development in quantitative terms. In this work, such research was not conducted, but suggestions for future investigations are better described in the conclusions chapter (section 6).

5.2.3.2 Pressure distribution on stern region

Complementing the force analyses, pressure measurements were conducted in order to assess the changes in the flow velocity around the AIRSHIP. Only the stern region was investigated (between 75%**L** and 100%**L**). This decision was based on the fact that the presence of the fins would not strongly affect the flow far upstream of their position. Howsoever, in order to improve the investigation a new line of pressure taps - named "F_" - was built right in front of the UL fin (Appendix B). This new pressure line is simply called FIN line. Also intermediate taps - named "__.5" - were inserted in between the pre-existent ones for port and upper taps lines, improving the discretization. Except when specified, the tests were conducted at a mean *Re* = 2.1E+6, meaning around 32.0 m/s velocity, very similar to that used along the rest of the AoA Polars. It is important to highlight that two taps, one on the upper and the other on the fin lines, showed off-trend results. The model was physically inspected for local bumps or dents, roughness or some sort of geometric irregularities that could have been causing those results, but nothing was found. The conclusion was that they were probably partially clogged, since there is no physical or aerodynamic explanation for the obtained results. However it is not possible to affirm that the tap is fully clogged, once the measured values changed along the runs. Even though these points do not change the overall results, the runs were performed but their results were ignored.

The first investigation carried out comprised comparing the effect of different roughnesses (TRIP - ENV_23_P1, FISHNET - ENV_24_P1 or COLLANT - ENV_25_P1) on the stern pressure distribution, also comparing the results with the BARE HULL configuration. Looking at the results for AoA = 0°, it is possible to conclude that the combined presence of FINs and different types of roughness, regardless of the option, increased the suction at the stern region. The fins leading edges begin around x/**L** = 80%; from there on a local acceleration would be expected, because of the throat created by the pair of FINs, considering the principle of mass conservation. This effect would only be sustainable if such local flow had enough added momentum. Having turbulent boundary layers probably assured it for the three the cases. Besides this, the increase in boundary layer thickness, because of the roughening, also probably increased outer flow velocity, consequently increasing suction, represented as a more negative C_P. It is worth remarking that the results observed for BARE HULL are for a lower *Re*. While BARE HULL *Re* is around 1.5E+06, the rest of the results is for 2.1E+06. This difference, however, as discussed below, should not be relevant in terms of the comparison required by this work.

Figure 148 - Pressure distribution at stern along port side for different roughnesses at AoA = 0°. The dashed line is the reference (not to scale) longitudinal position of FIN.

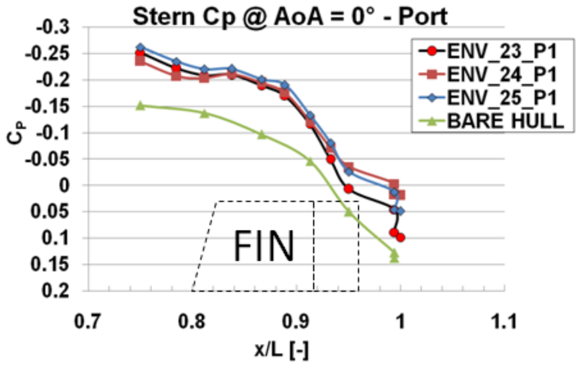

Source: Author (2018).

Figure 149 - Pressure distribution at stern along upper side for different roughnesses at AoA = 0°. The dashed line is the reference (not to scale) longitudinal position of FIN.

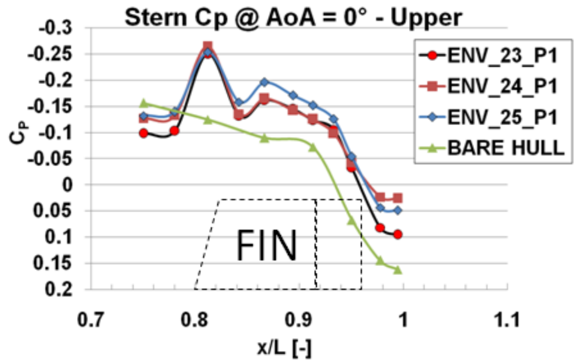

Source: Author (2018).

Focusing on the very end of the model, it is possible to see that the pressure distributions with roughness do not follow the same trend as the BARE HULL. Instead, at a certain region, the pressure gradient reduces, and the pressure values tend to stabilization, to an almost constant value. This point where the pressure gradient abruptly changes, and the pressure distribution becomes almost constant, is typically where the boundary layer separates or detaches; the pressure level after it is the pressure inside the separation wake. In other words, it is possible to see that the turbulent boundary layer separates before the body end, even though it is very close. This separation causes a separation wake (Figure 184 and Figure 185) to appear, and increases drag. An observed fact that supports this inference is the difference in C_P levels, and where it occurs for each configuration. The FISHNET configuration separates at the highest (suction or close to negative figures) C_P level, which denotes a thicker boundary layer as well, and greater drag. This once again shows that there are relevant differences among the roughening solutions, and the proper assessment of them is essential.

Evaluating the new taps, ahead the UL FIN (Figure 150), it is observed that the gradient is adverse for all configurations. This was expected, as this is an incompressible subsonic flow. The presence of bodies downstream has influence upstream, and so the flow decelerates the closer it gets to the fin leading edge (Figure 210 and Figure 211). An interesting fact to highlight is that, although the gradients are similar for all three configurations, C_P values for the TRIP are smaller. That is probably due to a thinner boundary layer as discussed above.

Figure 150 - Pressure distribution upstream of the UL FIN on the HULL surface for different roughnesses at AoA = 0°.

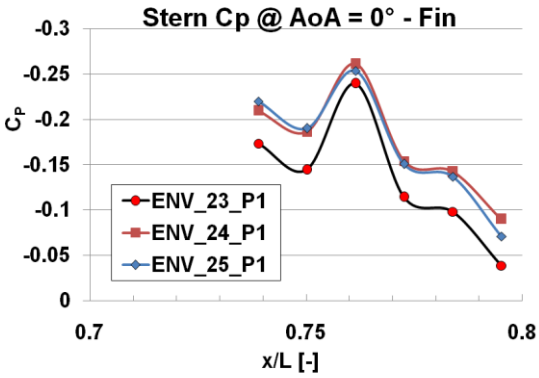

Source: Author (2018).

It is also worth observing that, even at AoA = 0°, upper and port lines ended up with considerably different pressure distributions after the FINs were added. The port line had a relevant increase in suction, whereas the increase in the upper line was smaller. This means a greater increase in local velocity along port side when compared to the upper. Without visualizing the flow it can be difficult to find explanations for that. However, using the patterns (Figure 120, for example) registered with oil visualization, and considering that the FINs change the flow around the HULL, it is possible to propose an explanation for the changes.

Before adding the fins, a well defined white line coming from the upper to the lower portion of the HULL was observed (Figure 113). It immediately indicated that the model, although carefully positioned, had some deviation regarding its effective angle of fixation on the longitudinal plane. Although considered almost negligible, there could also be some influence of the Root Fairing on generating the observed upwash. Once the FINs were installed, and since their fixation angles were not probably perfectly adjusted, the upwash effect was intensified, accelerating even more the flow around the AIRSHIP sides. This increase is then observed as an increase in suction, as captured, supporting the small, but non-negligible difference between upper and port lines (C_P). Further flow characteristics are better assessed in section 5.2.3.4 by means of visualization.

The same pressure taps were logged for AoA = -25° and AoA = +25° in order to assess the AIRSHIP flow behavior at large AoAs. Looking at the port line pressure for AoA = +25° (Figure 151) allows one to conclude that a large majority of taps are almost constant in C_P, which indicates a separated flow region. Such an observation was expected. The model port side at AoA = +25° is aerodynamically equivalent to the upper side of a pitching up ship, where the greater amount of suction will take place, including the presence of the suction peak (which occurs further upstream from the observed region). Once the pressure gradient must be strongly adverse after the suction peak for such an AoA - as a reference one can look at Figure 92, separation would probably occur, and is likely at a certain point in studied region. It is interesting to notice that this separation seems to begin at around 80%**L**, coinciding with the FINs physical beginning as well. Once separation usually leads to a thick wake, this would also be expected lower the efficiency of the fins, since the local velocities would decrease. This is very similar to what was described by Cornish, III and Boatwright (1960) and Lutz et al (1998) about leading edge separation ahead of the fins, and the interference with the HULL boundary layer. A supporting evidence for that may be seen in Figure 186 and Figure 195. Another interesting point is that apparently this phenomenon is well defined for the configurations with FISHNET and COLLANT, but appears to be lighter for the TRIP case. This last observation also makes sense. In those two former cases, the boundary layer is predictably more turbulent, and also thicker, evidencing the separation much clearly.

Figure 151 - Pressure distribution at stern along port side for different roughnesses at AoA = +25°. The dashed line is the reference (not to scale) longitudinal position of FIN.

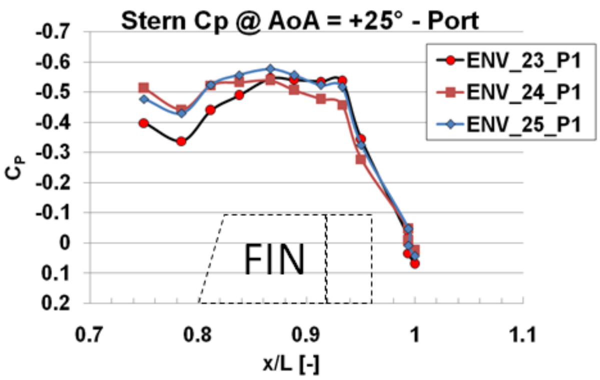

Source: Author (2018).

Figure 152 - Pressure distribution at stern along upper side for different roughnesses at AoA = +25°. The dashed line is the reference (not to scale) longitudinal position of FIN.

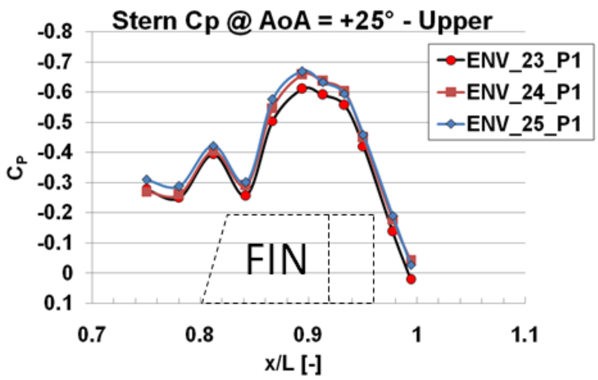

Source: Author (2018).

Looking at the upper distribution, which corresponds to the lateral starboard side of the ship, one can identify a fairly constant C_P (despite the problematic tap), which is followed by a sudden acceleration downstream of it. Such behavior would indicate the probable existence of a separated flow area, after which the flow is able to reattach to the surface, and even accelerate. Once again, looking at the flow patterns (Figure 212 and Figure 213) one can see separated regions (scattered stretched patterns) followed by streamlined oil traces, which helps to support the proposal above. The same pressure pattern is observed for AoA = -25° on the upper line (Figure 154). This demonstrates the good symmetry quality of the model, as the crossflow behavior in both pitch directions is very similar.

Figure 153 - Pressure distribution at stern along port side for different roughnesses at AoA = -25°. The dashed line is the reference (not to scale) longitudinal position of FIN.

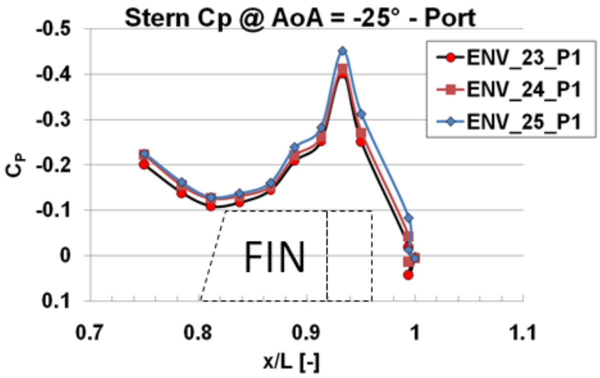

Source: Author (2018).

Figure 154 - Pressure distribution at stern along upper side for different roughnesses at AoA = -25°. The dashed line is the reference (not to scale) longitudinal position of FIN.

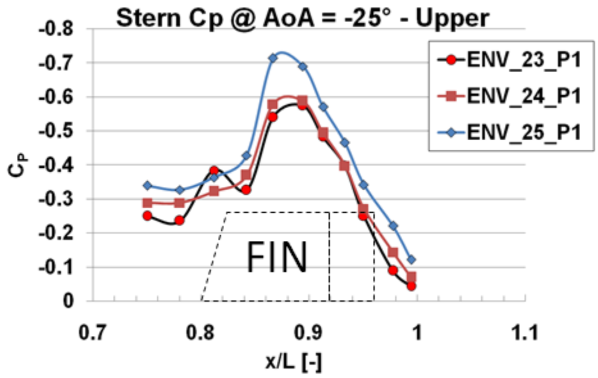

Source: Author (2018).

A remarkable difference is observed however for the port line for AoA = -25° (Figure 153). In this case, the AIRSHIP port side is the lower side of the lifting body. Usually, in such cases, the gradient should be favorable for a longer extent, and the adverse gradient should be much lighter, resulting in a smoother curve. As such, up to 80%**L**, C_P decreases at a very moderate rate. However, once the flow reaches the region between fins, there is a sudden local acceleration, reaching a peak, after which a second strong adverse gradient appears, preserving the due proportions. It is very interesting to physically notice that the presence of fins does accelerate the flow. Although it happens in a slight manner, considering the overall C_P values, the acceleration is detectable, as has been supposed.

Going further with the investigation, the FIN pressure line is in between the lateral (upper line) and upper/lower (port line) sides of the AIRSHIP (Figure 63), but dislocated in the direction to port line. As such, it could be expected to see more negative C_P for negative AoAs, as in this case the flow would be accelerating to overcome the curvature and reach the region between fins (UL and UR) in a favorable gradient. For positive AoAs, the C_P should reduce in magnitude, as in this case the pressure line would be in a region that, being near to the upper side, still is also near to low velocity areas dominated by vortex sheets separating from the HULL, and as such probably subject to an adverse pressure gradient. These expected results are much in agreement with what was obtained for the FIN line.

Figure 155 - Pressure distribution upstream of the UL FIN on the HULL surface for different roughnesses at AoA = -25°.

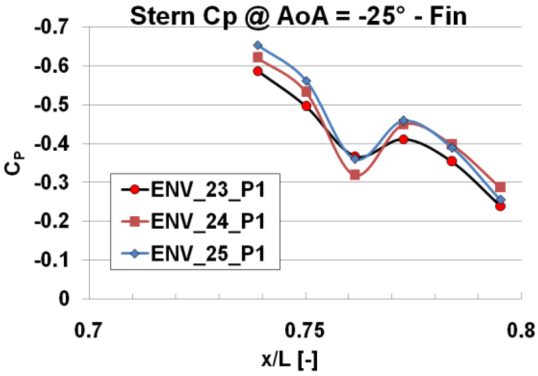

Source: Author (2018).

Figure 156 - Pressure distribution upstream of the UL FIN on the HULL surface for different roughnesses at AoA = +25°.

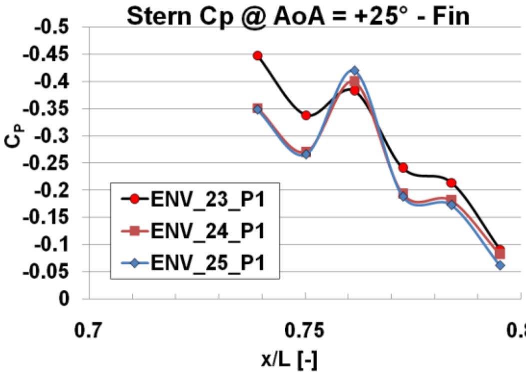

Source: Author (2018).

However, still looking at the FIN line results, while for AoA = -25° the curves fit close together, for AoA = +25°, the adverse gradient for the TRIP configuration is stronger than for the other two configurations. This may be explained once again by boundary layer characteristics.

The investigated region, at high positive AoAs is strongly dominated by a three-dimensional vortical flow, as depicted in Figure 28. Also, the measured pressure line is very close to one of the vortex attachment lines, i.e. the secondary line (Figure 24). For the TRIP configuration, the boundary layer is probably thinner and the edge velocity fairly smaller as well. A thinner boundary layer would be capable of “carrying” less momentum (less turbulence) in order to help it overcome the adverse gradient. In this way, the vortex would detach sooner from the HULL, and its core could be wider, covering a wider region (wider white region in Figure 212).

Once vortex cores are low pressure areas, considering the core could cover a portion of the taps line, in this configuration (TRIP) the C_P would be more negative. This would be true if the taps were nearer to the vortex limit, or contained by its core, in contrast with the other two configurations. By what is observed using surface flow visualization, the vortex reattaches to the surface, probably forming a strong narrow vortex tubing (black line in Figure 209 or separation line in Figure 210).

In any case, the presence of the FIN still requires the flow to decelerate upstream of the surface. For these reasons, all C_P distributions should tend to the same final value, right ahead of the fin leading edge. This last characteristic is very clear when examining the results (Figure 155 and Figure 156). Concluding the reasoning, as in the case of the TRIP configuration the flow was coming from a stronger suction region, upon reaching the FIN, it should decelerate quicker than for the other configurations, showing a stronger adverse gradient. The FISHNET and COLLANT configurations seem to generate very similar turbulence levels when in the vicinity of the vortical region, given their very similar Cp distributions in this case. It is important to highlight that such reasoning is somewhat complex for this case, because it comprises a three-dimensional flow, strongly influenced by crossflow (consequently a much more complex boundary development). I takes place in the vicinity of a vortical flow region (probably a recirculating flow region inside a separation bubble) and right upstream of a lifting surface (fin).

In addition a *Re* Polar was run for the ENV_23 configuration, in order to assess how the pressure distribution changes in the stern portion of the AIRSHIP with changing velocity. The runs were conducted for TRIP - ENV_23_P4, at three different *Re*: 9.6E+05, 1.6E+06 and 2.5E+06. It is possible to see from the results that the further downstream, the more similar the pressure distributions and Cp levels get.

Figure 157 - Pressure distribution along port side with varied Re for TRIP at AoA = 0°. The dashed line is the reference (not to scale) longitudinal position of FIN.

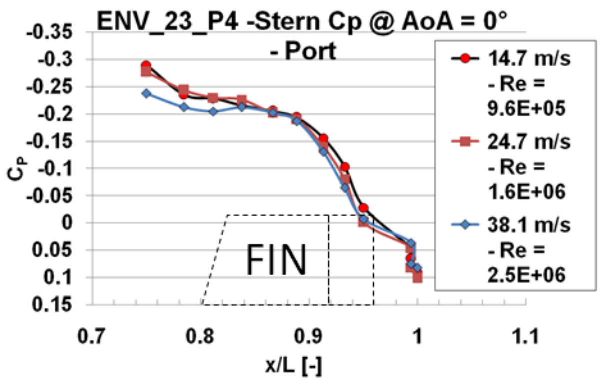

Source: Author (2018).

Figure 158 - Pressure distribution along upper side with varied Re for TRIP at AoA = 0°. The dashed line is the reference (not to scale) longitudinal position of FIN.

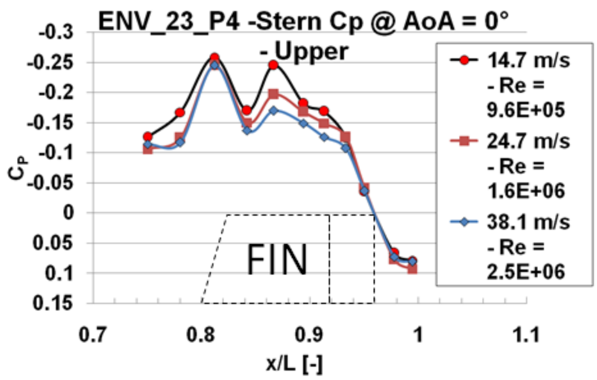

Source: Author (2018).

The fact that, independently of *Re*, all flows are separating at the very end may be a good explanation for greater differences upstream, i.e. away from separation. Given this, considering all boundary layers fully turbulent and the separation region dominated by vortical flows, the increase in instability effects leading to the separation phenomenon begin around the same location for all three: where the pressure gradient gets more “aggressive” - adverse. As vortices carry a lot of momentum and induce mixing from the outer flow to the inner flow (from outside to inside of the boundary layer), and assuming that the differences in *R*e are not large enough to overcome that, vorticity ends up dictating how the flow behaves locally.

Nevertheless, although the captured differences are very discrete, some particularities do exist, mainly up to around 90%**L**. The main reason for that may be attributed to the differences in boundary layer thicknesses for different *Re*. As Re increases, it is typical that the boundary layer thickness will decrease, considering it is already in a turbulent regime. This effect is clearly observable with significant changes in fluid velocity, considering the same geometric conditions and subsonic flow. In the case of this work, unfortunately, it was not possible to produce relevant changes in *Re*. In spite of that, when analyzing Figure 157 and Figure 158, it is possible to see that with increasing *Re*, suction reduces, meaning smaller boundary layer edge velocities. This effect is easily observable when assessing upper and fin lines pressure distributions.

Also, looking at the fin line distribution (Figure 159), one can easily identify a decrease in suction with increasing velocity. This reinforces the fact that the greater differences among the configurations take place upstream of the FINs. This should happen especially upstream of the stern separation region, where its influence is smaller, and the natural behavior, as a function of *Re*, is dominant on the flow.

Figure 159 - Pressure distribution upstream the UL FIN on the HULL surface with varied *Re* for TRIP at AoA = 0°.

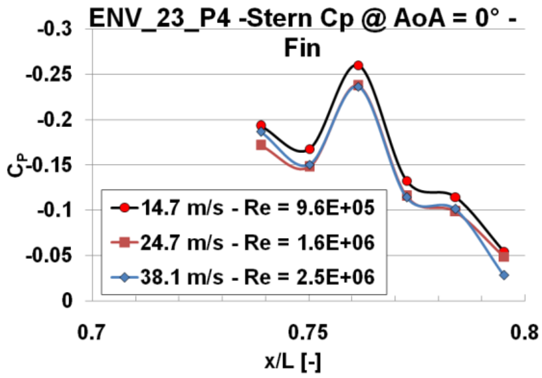

Source: Author (2018).

Looking at the fin line also calls attention to another interesting effect: the differences between the first and second steps in *Re* are greater than between the second and third. This possibly indicates that there must be a converging trend to threshold values regarding boundary layer thickness with increasing *Re*. In other words, increasing *R*e will produce a thinner the boundary layer, but there will be a limit. This limit will be a converging value to which the thickness will come, and significant changes in pressure distribution will no longer appear, as the displacement thickness will not relevantly change anymore. This should be true considering that only changes in *R*e due to velocity changes, at subsonic conditions, will occur, i.e. geometry, compressibility, etc are not changing.

5.2.3.3 Static stability and aerodynamic evaluation with control inputs

Once the first evaluation, with FINs installed, was completed, and the main aerodynamic differences and interferences associated with their presence at the HULL were already assessed, the study went deeper regarding stability questions. Although stability was checked and confirmed by the negative overall derivative of the C_M curve, only one trim point was identified. Considering the literature (section 3.1.4), three different points were advanced for AoA = 0°. This was however impossible because of the curve offset due to the mispositioning issue affecting the tailplane.

All those previous analyses had the control surfaces set to zero deflection. The proposal was then to vary the control surface deflection angle (δ), in order to observe how the aerodynamic coefficient curves would behave. It was decided to vary δ by 5°. It was established as convention that positive deflections would pitch the AIRSHIP up. δ was adjusted mathematically using the Law of Cosines, calculating the dimensions which would guarantee the desired angle. Although this approach is not very precise, it was considered sufficient assuming that, given the model scale factor and the focus being more on qualitative than quantitative data, the behavior would still be well reproduced, and captured. The selected deflections were: -25°, -5°, +5°, +10°, +15°, +20°. The proposal was to save testing time, but also cover a wide range of deflections, assessing opposite angles as well. The range [+5°; +5°; +20°] allowed to track trends, -5° and +5° test points allowed a symmetry comparison and -25° represented large deflections.

Starting with the drag polar (Figure 160), it is possible to conclude that while δ is held to small values, up to 5°, C_D values are very much similar, and the variation is very small, in the vicinity of small AoAs. With increasing AoAs, the curves get apart and lose symmetry. A remark is relevant here. Comparing the zero deflection with δ = +5° supports once again the explanation already presented regarding the misplacement of the tailplane. The symmetry for the curve with δ = +5° is better than that for δ = 0°. It is possible then to infer that the control surface deflection in the same direction of the misfixation of the fin itself is exerting a “cancelling” aerodynamic effect on it, adjusting the aircraft to what should have been the standard configuration. From δ = +10° on, the curves proportionally translate upwards and to the right, for positive deflections. A symmetric behavior regarding lateral displacement is observed for negative deflections, being obvious that in both cases drag increases with increasing |δ|. It is also relevant to highlight that the deflection curves superimpose on each other for high AoAs opposite in signal to the deflection. As an example, for positive deflections, the curves superimpose on each other at the high positive AoA portion, while relevant drag increases are seen on the negative AoA portion. This shows that the increase in drag due to the deflection is more related to increase in lift generation than in form drag, since such increase is seen on the AoA portion that increases the effective AoA on the surface in favor of the deflection.

Figure 160 - AIRSHIP drag polars with varying control surface input.

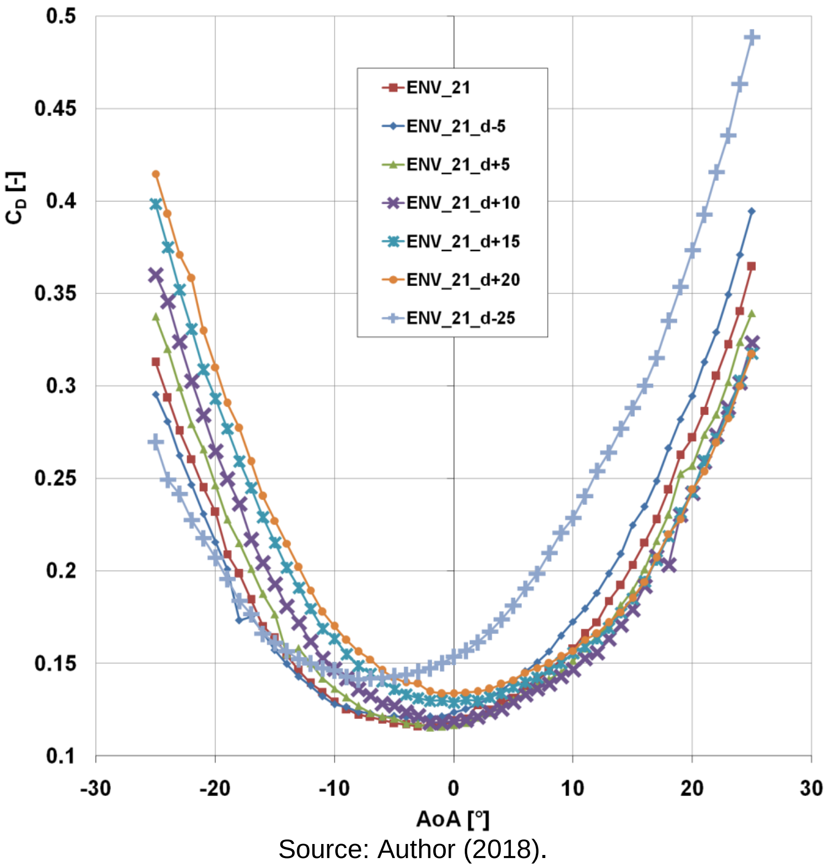

Source: Author (2018).

Another interesting observation regarding this specific configuration is that, apparently, 25° deflection is in the vicinity of - or already above - the maximum surface efficiency. This was inferred based on the C_D curve for δ = -25°. Compared to the others, and mirroring the results for δ = +20° as a reference, there is a relevant increase in drag, much above the stepwise behavior observed along the gradual increase. This may indicate that the surface is reaching a stalled or near-stall condition, as great increases in drag usually indicate stalls (or partial separation regions). This is quite acceptable, although no stall was observed before, since the three-dimensional vortical structures formed around the HULL are also capable of generating lift. Then, even if the tail fins are reaching their limit in lift generation, the HULL may still generate some more lift, similarly to how a delta wing would do, but on a small magnitude, if compared to fins capacity.

Changing attention to the C_L curve, it is interesting to observe that deflection variation only translates the curves along the vertical direction, going upwards for negative deflections, and downwards for positive deflections (Figure 161). This behavior is quite similar to the trailing edge flap effect on conventional wings: an increase in lift for the same AoA with flap deflection downwards. This shows that the lift generate by the fins is dominant in the whole aerodynamic arrangement, once the HULL contribution is almost undetectable with deflected surfaces. An interesting phenomenon, discussed in section134, might probably be felt while flying an airship similar to this model, for such a *Re*: reversal of command. As already explained, it is exactly what is seen on the curve. If one applies positive deflection aiming to go up, there might be a relevant decrease in lift, which could be capable of impelling the ship downwards instead of upwards, even if it pitches up. Nevertheless, one must not forget that airships do not fly only on aerodynamic lift, but mostly on buoyancy. If however the net lift without control surfaces deflection is very close to zero, which means equilibrium, the reverse of command can be really relevant.

Figure 161 - AIRSHIP lift polars with varying control surface input.

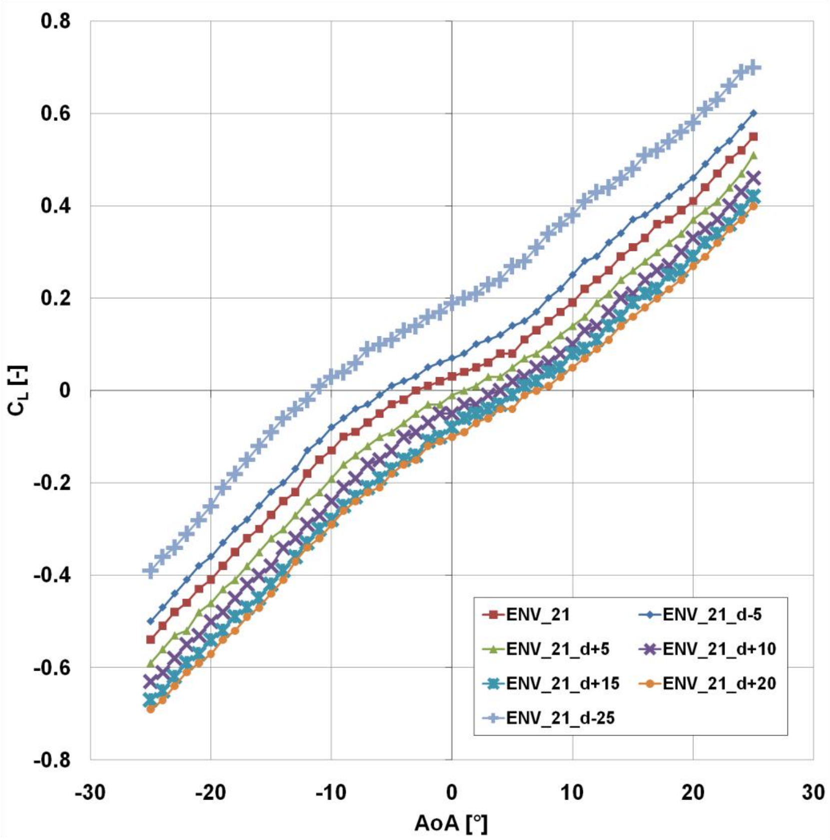

Source: Author (2018).

The C_L variation steps between deflections seem to be very much similar in value up to the transition from +15° to +20°, when such step variation becomes smaller. It is also possible to see that, considering the trend and mean values, the absolute difference in lift between δ = +20° and δ = -25° is almost negligible. The curve shapes are very similar, indicating that the flow mechanisms are still the same. It is possible then to infer that the near-stall condition (for the tailplane), proposed above on the drag evaluation, is very adequate. The increase in lift, although existent, is rather small, and also not proportional to other steps observed from zero up to δ = +15°. At least some sort of lift plateau (maximum C_L region) is being reached, once the absolute increase in C_L is almost irrelevant along the whole AoA range, even with 5° more deflection.

During the runs, this similarity in values (off trend in steps) was right away noticed, and the deflection angle was checked once test run ENV_21_d+20 was over. It was confirmed that the deflection was set at the correct position, i.e. δ = +20°. The stiffness of the angle lock was also confirmed to be good, eliminating the possibility of relative movement during the run. This last assessment also supports the results cited about drag for high deflections. Looking at the flow visualization results, it is possible to see that a vast portion of the FINS is already separated at this AoA, what might impair control effectiveness.

The moment results referenced to the center line point located at 25%**L** have very similar trends to those assessed while analyzing C_L (Figure 162). There is a very well defined stepwise increase between different deflections, with the increment changing more drastically once again between $\delta = +15°$ and $\delta = +20°$. Also it is interesting to highlight that the expected three trim points, as described above ($C_M = 0$ for AoA = 0° & $C_L = 0$) is obtained for $\delta = +5°$. This reinforces the proposed explanation already provided about the deviations when comparing theory and actual results. In ths way, at the same deflection for which C_L and C_D would have to behave as the standard $\delta = 0°$, C_M also confirms this estimate. In the case of C_M, it is even possible to see, due to its higher sensitiveness, that the perfect adjustment to obtain a representation of standard configuration ($\delta = 0°$) would be just a little lower than $\delta = +5°$.

Figure 162 - AIRSHIP moment polars against AoA with varying control surface input.

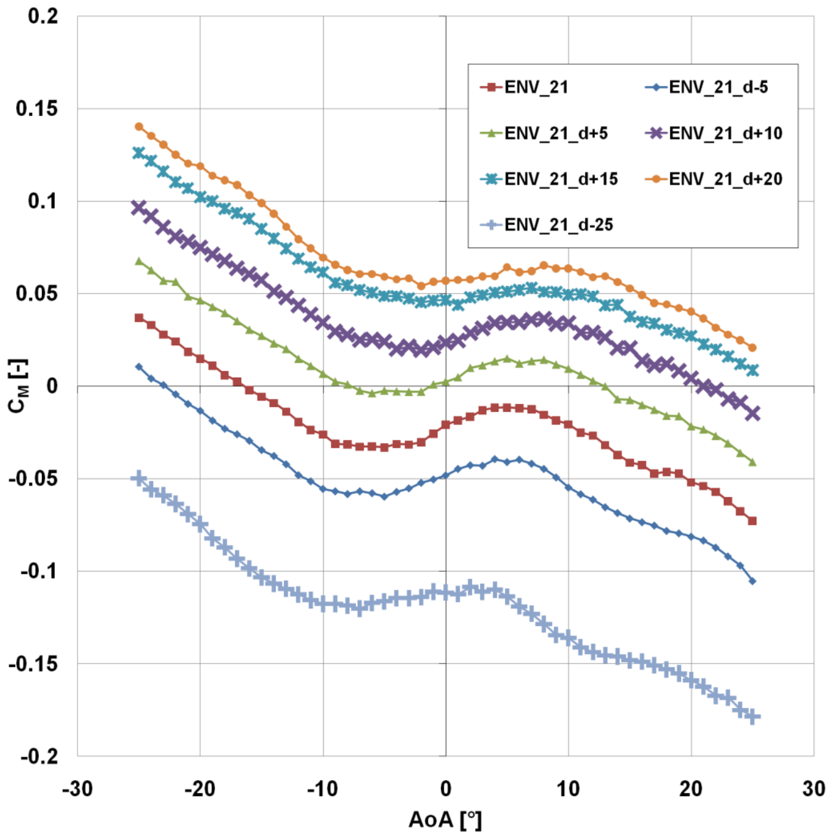

Source: Author (2018).

Another conclusion that can be extracted from the C_M results regards the stability evolution with increasing δ through the AoAs range. Although all curves attest that the AIRSHIP is stable ($C_{M\alpha}$ is negative) through the appraised range, it is interesting to observe that the shape of the curves change slightly from one to another step in δ. The middle portion of the curves, which has a sinusoidal shape, tends to flatten with increasing δ. This points that, when at high deflections, there will be an AoA range in which the C_M variation will be small when compared to the rest of the curve, and the AIRSHIP will have a range of apparently statically neutral stability. In other words, if it suffers an external input, which is not strong enough to put the ship out of this cited AoA range, it will keep the induced attitude, provided the controls are not touched. Considering the theoretical framework and stability as a whole, including also the dynamic stability characteristics, one must consider that the pendulum mode is the major contributor to airship longitudinal stability, despite the static characteristics.

Besides this flattening tendency, which is not very prominent, but just a trend when checking the results for larger δ, a vertical translation effect is much clearer and obvious. With increasing values of positive deflection, the curve shifts upwards aligned with the AoA grid, while with increasing values of negative deflection, it goes downwards in the same reference. When looking at C_M in relation to C_L (Figure 163), this shift occurs along the upper left diagonal. In other words, with increasing positive deflections, the C_M curve shifts upwards and to the left. This means that the more negative the C_L value, the greater will be the pitching up moment. Although it seems not to be intuitive, the truth behind this behavior lies with playing with aerodynamic angles. If $\delta > 0°$ at AoA = 0°, it will pitch up the aircraft. If the AoA goes then to a negative value (producing negative lift for a certain range, depending on the δ value), the resulting angle on the taiplane will become higher, and the pitch up moment will also increase. This is clear for this type of aircraft, because the aerodynamic forces generated by the tail are relevant in the overall resulting force, when compared to just the HULL forces. This also brings back the reversal of command effect, but keeping the buoyancy and flight speed discussion in mind.

Figure 163 - AIRSHIP moment polars against lift with varying control surface input.

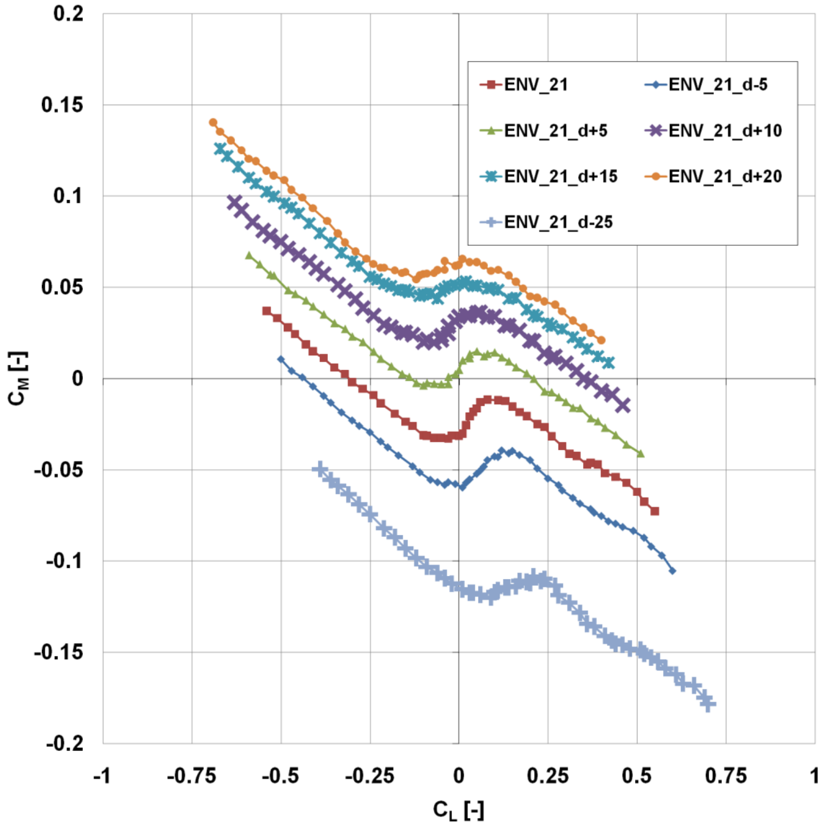

Source: Author (2018).

Given the relevant influence of the fins identified for the stern flow, described in section 5.2.3.1, another pressure distribution investigation, more focused on that, was made. The TRIP configuration was assessed at AoA = 0°, but with δ = -25° and δ = +25° (Figure 164). The proposal was to identify how fin geometry affects the flow around them. The first results to analyse are the FIN line Cps. While δ = 0° and δ = +25° concur almost perfectly with each other, for δ = -25°, the Cp curve shifts upwards, pointing to some local acceleration.

Figure 164 - AIRSHIP pressure distribution upstream of the UL FIN on HULL surface for varied control surface inputs.

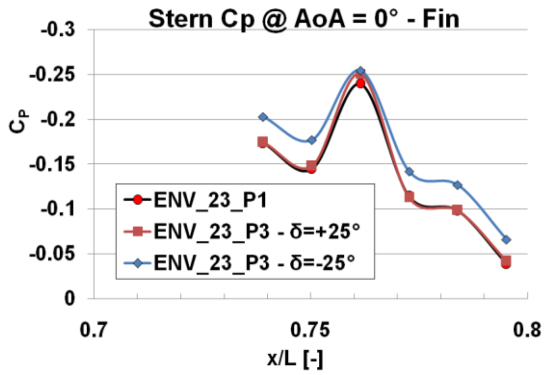

Source: Author (2018).

Besides that, the curves for the upper line (Figure 166) seem very similar to each other, although the δ = -25° sustains a discrete acceleration up to around

94%**L**, while the other two are decelerating since around 84%**L**. Finally, looking at the Port line, a much more challenging result was obtained. For δ = -25°, matching the beginning of the fins, some flow acceleration is captured up to around 92%**L**, which is very near to the FINs trailing edge (at approximately 95%**L**). Also, when comparing δ = +25° to δ = 0°, a deceleration of the local flow is seen, identifiable by the smaller absolute values of C_P along the line.

Figure 165 - AIRSHIP pressure distribution along port side for varied control surface inputs.

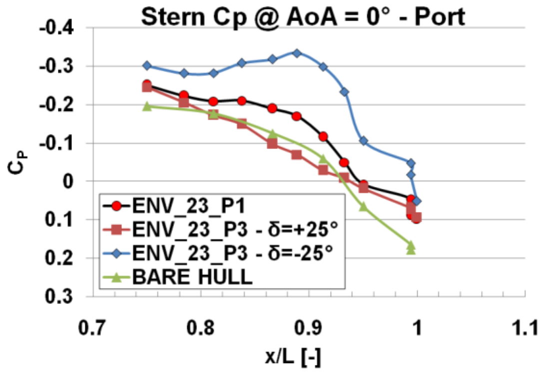

Source: Author (2018).

Figure 166 - AIRSHIP pressure distribution along upper side for varied control surface inputs.

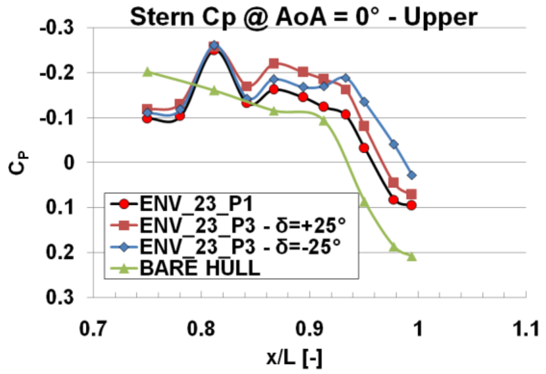

Source: Author (2018).

Such a result seems to be very odd, and questionable, since for symmetric deflections one would expect also symmetric results. However, paying attention to the tail configuration helps understanding this last result, as well as the others.

Considering the X-tail configuration, when all control surfaces are deflected to δ = -25°, all trailing edges will deflect to the right (looking upstream inside the wind tunnel test section). In this configuration, and assuming that the FINs are generating lift, there will be an increase in circulation around each of them, and also some upwash effects upstream of the FINs, inducing velocity to the left (also looking forward). Both effects are typical of all lifting surfaces. The increase in circulation on the left FINs, next to the port line, accelerates the flow, since both FINs on the left are accelerating the flow in between them (both have what would be the wing upper side pointing innerwards - Figure 167).

Figure 167 - Schematics of tail surfaces circulation on port side with δ = -25°.

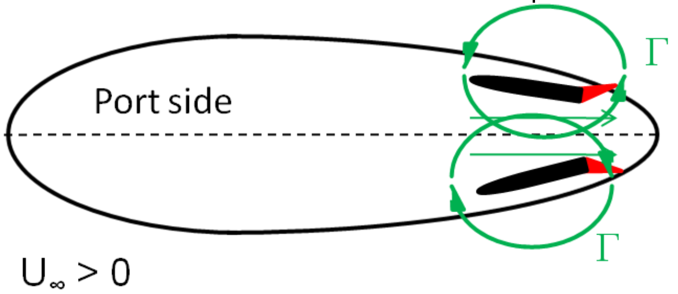

Source: Author (2018).

This explains the results for more negative C_P along the port line for δ = -25°. When looking at the upper side line (Figure 168), while the left fin decelerates the flow (wing lower side), the right fin accelerates it (wing upper side). This concurrence leads to an almost cancelling result, causing the results for δ = -25° to be similar to δ = 0°.

Figure 168 - Schematics of tail surfaces circulation on upper side with δ = -25°.

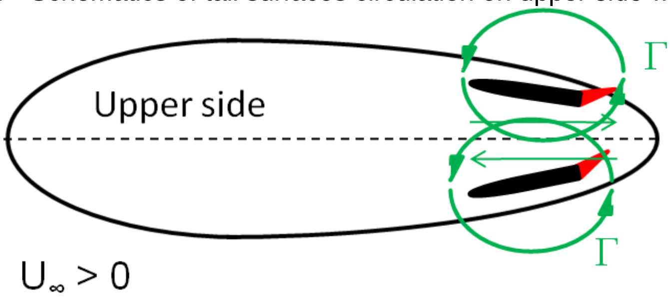

Source: Author (2018).

The small acceleration observed is probably linked to a combination of upwash and downwash effects, of both top FINs, on the upper side line, since there is upwash up to center of pressure, and downwash downstream of it. This is another way of interpreting the circulation effect, which should be easier to understand than more elaborated flow sums and subtractions. A combination of them, with the result out of the acceleration/deceleration concurrence explained, will result in the pressure measured along the line. One must recall that the pressure sensed is non-directional, which means that it does not matter the flow direction, but its intensity.

Figure 169 - Schematics of tail surfaces upwash on upper side with δ = -25°.

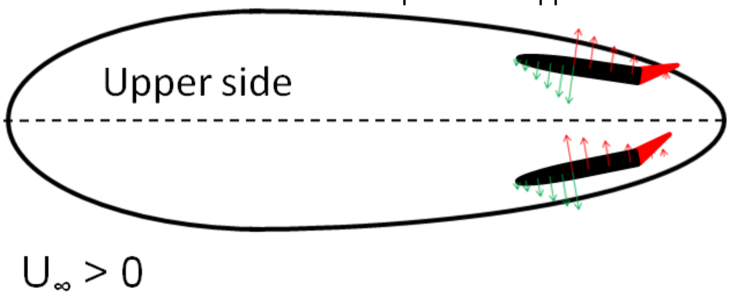

Source: Author (2018).

Using the same approach for δ = +25°, both fins on the left would decelerate the flow between them (decreasing C_P absolute values), while some aerodynamic combination of top fins would lead to a very discrete change on the upper line. It is important to remark that the results along the upper line may also be somewhat different due to the misplacement problem with the fins, and probable asymmetries.

The same circulation theory proposal can support what was observed for the FIN line (Figure 164). Since the FIN line is influenced by the accelerated flow region between both left fins, and also by upwash effects of the UL fin, observing an increase in suction for δ = -25°, as captured, would be the expected result. All this discussion and the way it appears to support the observed results, reinforces the explanation and lends credence to it.

5.2.3.4 AIRSHIP aerodynamic flow structures – flow visualization

With the addition of the FINs it has already been shown that a number of changes occurred. Obviously lift and drag increased, and the pitching moment changed as well. For sure, as already discussed above, based on the figures obtained, the changes were not direct sums of the individual behavior of each of the bodies: HULL and FINs. The resultant characteristics must be a result of a combination of them, with one interfering on each other's flow.

In this section, the most relevant results regarding flow visualization are presented, and registered in order to support some of the proposals presented for explaining observed numerical trends and results.

Along the runs conducted for forces and moments, tufts were also employed. They were the first visualization tool applied for the AIRSHIP configuration. Using them, it was possible to investigate the flow over the HULL, and also on the FIN surfaces. The tufts were applied on the port side of the AIRSHIP (left side looking upstream of the tunnel test section).

The first investigations used ENV_21. Some pictures were taken in order to assess FIN flow separations, while the AoA increased. Observing the patterns for AoA = -5° (Figure 170), it was possible to see a strong attachment of the tufts to the surface, as would be expected, and an upward converging tendency for those tufts attached to HULL. This was the expected pattern, as the observed region is the "lower side" of the flow. However, something interesting is seen for the tufts on the fins. Despite all of them being also well attached to the surface, the outer they were in the spanwise direction, the better aligned with the wind tunnel flow they seemed to be. This shows that some sort of velocity profile exists along the fins spanwise direction. The tufts which were closer to HULL also showed slightly more vibration, even similar to the more external ones. This is caused by turbulence in the flow, and means for the inner tufts, that the interaction between HULL and FIN boundary layers was markedly turbulent, as expected.

Figure 170 - Tufts visualization of ENV_21 “lower side”, stern region, at AoA = -5°.

Source: Author (2018).

With increasing positive AoA (Figure 171 and Figure 172), the tufts on the fins increased in vibration (unsteady oscillatory motion) as a whole, probably due to an increasing local turbulence. The alignment also improved a little, also meaning greater velocity, as expected for the “upper side”. No separation was observed for any AoA within the range. However, the tufts positioned nearest to the FIN tips showed much more oscillation; this was probably linked to tip vortex being generated while the surfaces generated lift.

Figure 171 - Tufts visualization of ENV_21 “upper side”, stern region, at AoA = +5°.

Source: Author (2018).

Figure 172 - Tufts visualization of ENV_21 “upper side”, stern region, at AoA = +14°.

Source: Author (2018).

The same tufting visualization was kept during variation of control surface deflections, while obtaining the trimming curves. The main objective was to observe whether any evident separation would occur once the deflections, and as consequence de local camber, were changed.

Figure 173 - Tufts visualization of ENV_21 “port side”, stern region, at AoA = 0° & δ = +5°.

Source: Author (2018).

Figure 174 - Tufts visualization of ENV_21 “port side”, stern region, at AoA = 0° & δ = +10°.

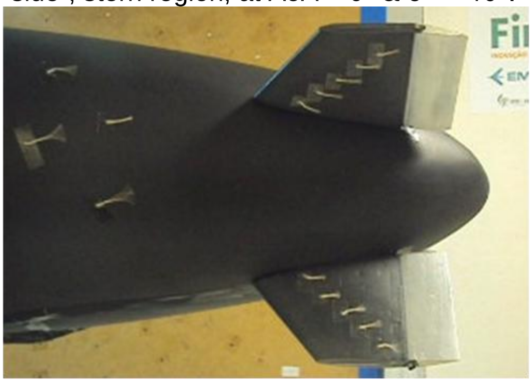

Source: Author (2018).

Figure 175 - Tufts visualization of ENV_21 “upper side”, stern region, at AoA = +5° & δ = +15°.

Source: Author (2018).

It is possible to infer that, for small AoAs, the flow on HULL does not change significantly upstream of the fins, at least regarding direction. Also, there still seems to be that an almost middle converging line formed along the HULL side (tufts point to each other), with a slight upwash in relation to the FINs. Analyzing the tufts on the FINs shows an interesting trend: with increasing deflection, turbulence increases significantly, mainly on the LL FIN. Also some relevant spanwise flow is observed, as the tufts increase their deflection towards the stabilizer tip.

However, despite the observable increase in turbulence on the lower (aerodynamic) side of UL and LL FINs, no separation was seem; tufts remained attached. Then, for the next step, AoA and deflection were increased. With δ = +20° & AoA = ±25° new pictures were taken (Figure 176 and Figure 177).

Figure 176 - Tufts visualization of ENV_21 “lower side”, stern region, at AoA = -25° & δ = +20°.

Source: Author (2018).

Figure 177 - Tufts visualization of ENV_21 “upper side”, stern region, at AoA = +25° & δ = +20°.

Source: Author (2018).

As expected, for the negative AoA, all tufts presented a much lower degree of turbulence. The tufts on the HULL pointed upwards, indicating that the streamlines, as seen before, still tend to go over the sides of the AIRSHIP. Even middle tufts still pointed a little upwards, which may indicate that the FINs are inducing some sort of upwash on the HULL. Looking at the pictures for positive AoA shows that the turbulence on the HULL is high, demonstrated by very oscillatory tufts. These tufts appear to point in opposite directions, going from the middle to both sides (recalling the leaf-like pattern for BARE HULL). The degree of turbulence on the FINs increased significantly, but still no separation seemed to have occurred, although the LL FIN main flow direction seems to be a crossflow (spanwise). This led to a relevant decrease in lift for this specific surface. Also, separation might not have occurred, because the deflections contribute to decrease the surface equivalent camber, reducing suction and the adverse pressure gradient.

The control surface was then deflected in the opposite direction, i.e. δ = -25° (Figure 178 and Figure 179). In this case, for both observed FINs, the tufts were on upper side surfaces. It is possible to see that, differently from what happened for negative deflections, velocity clearly increased in between the UL and LL FINs. The HULL tufts were still turbulent, but showed less misalignment with respect to previous observations, and the tufts on the tail pointed much inwards, demonstrating that the streamlines were converging to the middle portion of the AIRSHIP. This indicates that the greater the tail lift, the greater the suction between them. Nevertheless, the inner tufts not seemed to change their behavior significantly. From the videos, it is possible to see that the oscillation frequency for them is much lower, indicating that they are subjected to lower speed streamlines.

Figure 178 - Tufts visualization of ENV_21 “upper side”, stern region, at AoA = +5° & δ = -25°.

Source: Author (2018).

Figure 179 - Tufts visualization of ENV_21 “upper side”, stern region, at AoA = +21° & δ = -25°.

Source: Author (2018).

Using the FISHNET to increase turbulence in the model leads to noticeable change in the inner tufts behavior (Figure 180 and Figure 181). Despite an overall increase in turbulence, the oscillatory frequency of the inner tufts increased substantially, even for smaller angles. Along the video for AoA = +20°, it is also possible to observe that inner ones present sometimes a separation behavior, such as inversion of flow direction, but later restore their original setting, alternately. This might be a consequence of interactions between HULL and FINs boundary layers, generating leading edge separations, for example.

Figure 180 - Tufts visualization of ENV_22 “upper side”, stern region, at AoA = +5°.

Source: Author (2018).

Figure 181 - Tufts visualization of ENV_22 “upper side”, stern region, at AoA = +20°.

Source: Author (2018).

In general, however, tuft density was not large enough to sense changes on the velocity profile along the FINs, and would not also be capable of providing details on surface flow. These tufts, can even, to some extent, interfere in the results for the FINs, as their dimensions may be considerable when working with such a small scale model like the one used in this work.

Therefore, like for the BARE HULL, once the pressure measurements were completed, oil flow visualization was conducted. Four runs were carried out: Run_04 (TRIP & AoA = +20°), Run_05 (TRIP & AoA = 0°), Run_06 (FISHNET & AoA = 0°) and Run_07 (Smooth & AoA = 0°).

Starting with Run_05 (Figure 182), the first observation is that the same converging line, indicated by the tufts, is formed. With the FINs, however, the curve shows a much steeper ending, converging to separation a little earlier than for the BARE HULL. This increase in steepness may be attributed to FINs influence on the flow.

Figure 182 - Sequential frames for Run_05 oil flow visualization.

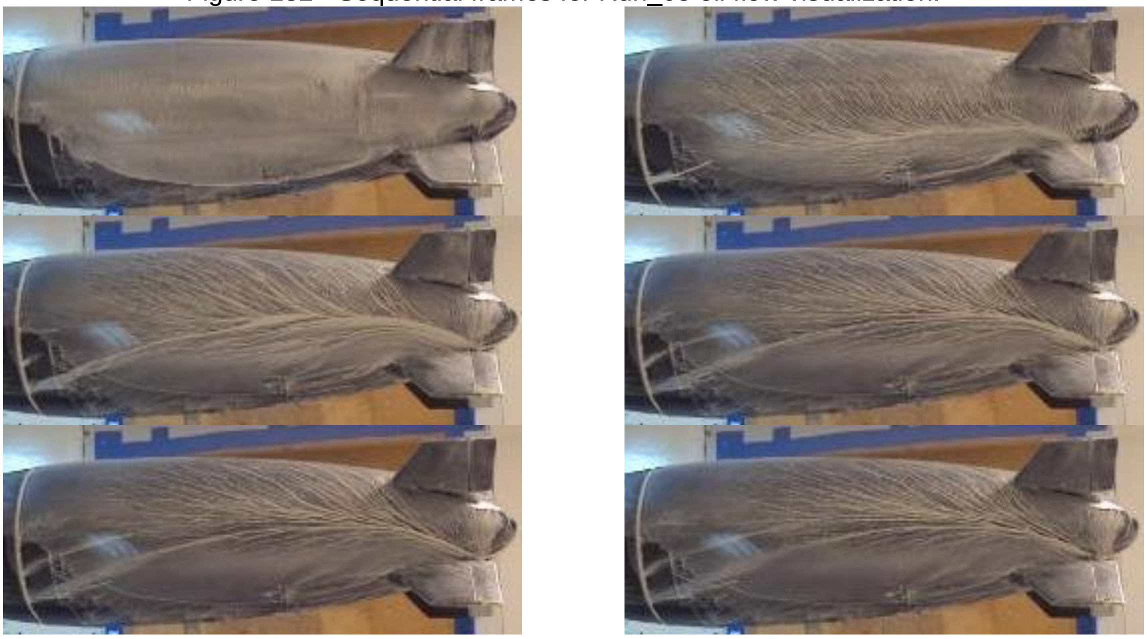

Source: Author (2018).

Comparing the converging limiting streamlines, it is possible to see that the lower ones have greater velocities, as their pigment pattern is much thinner. Watching the videos, it is possible to see that they also converge much quicker to the attachment line with the upper streamlines, which have thicker oil patterns.

The upper limiting streamlines gently adapt themselves to the UL FIN presence, changing relevantly their pattern once they get nearer to the tail. Also an accumulation of pigment is observed ahead of the fins, showing a thicker white line. This is the leading edge stagnation region, also detected by pressure measurements, around which the incoming streamlines go, changing their direction, in order to overcome the obstacle (FIN). However, no special effect from FINs is clearly observable on HULL, despite the change in streamlines direction.

Figure 183 - Detail of Run_05 stern region oil flow visualization.

Source: Author (2018).

Recalling the fact that the lateral middle line is in fact a vortex attachment line, it is expected then that the inner trailing edge of the lower FINs will be immersed in a vortical turbulent flow, as each lateral line goes past each one of them respectively. Looking closer at the tail pattern, one may clearly see that there are two areas of high oil concentration: the stern cone and the inner trailing edge of the LL FIN.

Figure 184 - Stern region, port side of Run_05 oil flow visualization.

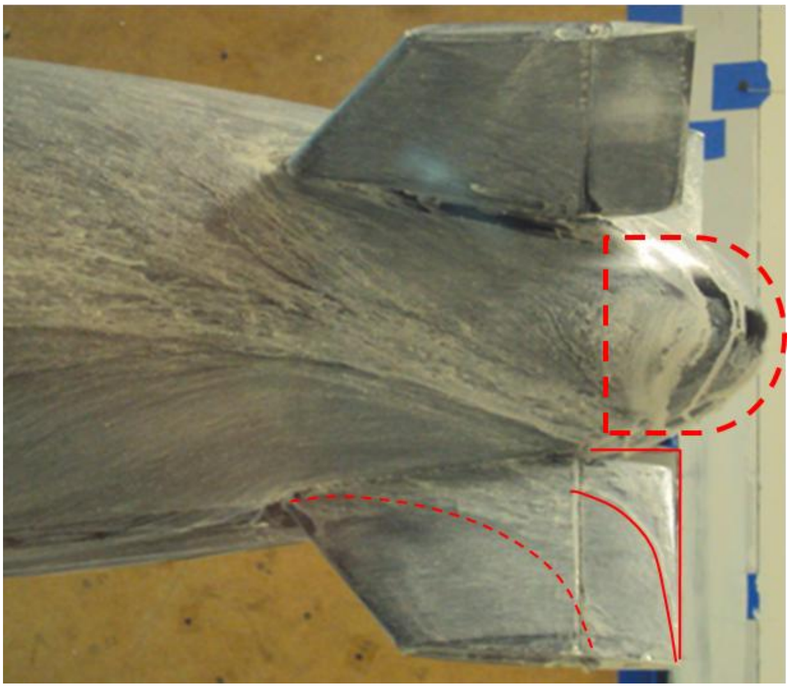

Source: Author (2018).

Figure 185 – Detail of stern region, port side of Run_05.

Source: Author (2018).

These two regions constitute separated flow portions of the AIRSHIP. Besides this, looking specifically at the LL FIN, it is possible to identify a clear limiting line (dashed line) across which the surface friction reduces. This is attested by the steady increase in white pigment attached to the surface. This may be a transition region between vortex perturbed and unperturbed flow, as it culminates at the extensive trailing edge separation. This trailing edge separation was so clear that a portion of oil ran down, concentrating on the control surface tip, and then dripping from there (Figure 185). In addition, looking closer at it, one may recall the patters described by Cornish, III and Boatwright (1960). The detected separation frontlines obtained by them in full scale for a very similar shaped hull were very similar in position to these obtained here in a small scale. This reinforces the view that the chosen roughness (TRIP) is adequately simulating the desired flow conditions.

Examining the upper flow brings new information as well. From the FIN leading edges, downstream, the concentration of white pigment increased, demonstrating a decrease in velocity (Figure 186). The mechanism seems to occur from the middle to the sides (dotted red line). As a consequence, the FIN roots are largely affected by that, having their local velocity also relevantly decreased in relation to the outer flow (color comparison – dashed red line). This was also observed by Cornish, III and Boatwright (1960), who described it as an interference between hull and fins boundary layers, leading to separation wakes (Figure 6). The affected area is very similar to that proposed by Hoerner (1960) depicted in Figure 9. However, bearing in mind the visualization, Equation 7 would point to a slightly thicker boundary layer. Nonetheless, for initial conceptual evaluation purposes, this seems to be a good approximation, since it is close enough in magnitude and shape.

Figure 186 - Rear view of Run_05 upper side oil flow visualization.

Source: Author (2018).

Also the upper FINs had extensive trailing separation as depicted by the dash-dot ("**- . -**") red lines. It is difficult to advance the reason why it happened, but it might be linked to the HULL-FIN boundary layer separation at the root. A reinforcing clue is that the UL FIN showed a less intense separation, and the same occurred at its root, in comparison with the UR. Recalling the observed flow patterns for a low *AR* wing intersecting a surface, shown in section 3.1.5, one might remember that near-to-wall vortices buildup near to the root region and near to the trailing edge as well. The strength of such vortices, influenced by the HULL boundary layer, might be related to the extent of this trailing edge separation.

Still inspecting the FINs, a typical flow pattern was repeated in all of them. For all four the boundary layer began laminar, and transitioned to turbulent before separating. This can be seen in the pictures below.

Figure 187 - Limiting streamlines on UL FIN, lower side for Run_05.

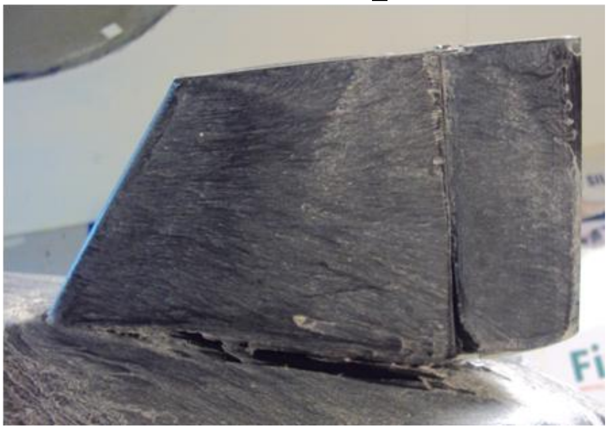

Source: Author (2018).

Figure 188 - Limiting streamlines on UR FIN, upper side for Run_05.

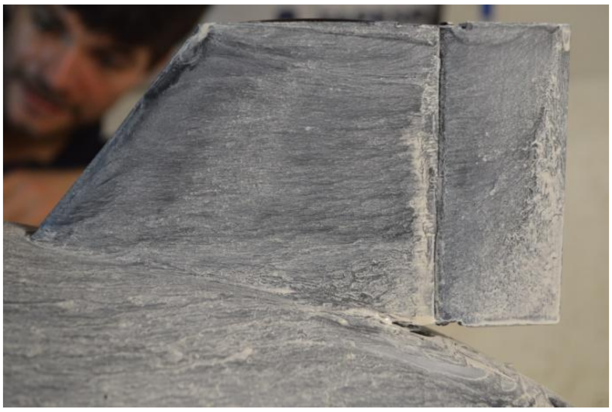

Source: Author (2018).

Figure 189 - Limiting streamlines on LL FIN, upper side for Run_05.

Source: Author (2018).

Figure 190 - Limiting streamlines on LR FIN, lower side for Run_05.

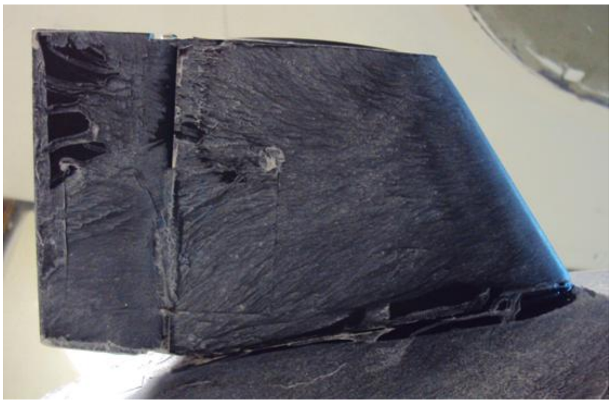

Source: Author (2018).

At the leading edge the limiting streamlines are very well aligned and hairline-like. After a short length, after overcoming the leading edge curvature, a scattered pattern is observed, followed by a thin black band (for some of the FINs this is not so clear cut, and can be observed only at some spanwise positions), where probably Tollmien-Schlichting waves are being amplified. After that, a denser white scatter is seen, which reveals an increase in local vorticity. Downstream of this portion, which is very short in this case, the limiting streamlines improve alignment once again, and the flow is fully turbulent until HULL interference effects reach the tail, changing once again the flow characteristics. Figure 191 is a closer picture of UL FIN leading edge, showing in detail the hairline-like limiting streamlines of the very early laminar boundary layer. Figure 192 is a general representation of the explained separation process, mainly for low *Re* flows over airfoils. It is interesting to see the that middle portion, where the separation bubble exists, is not observable on the fins, showing that their transition occurs directly from laminar to turbulent without any special (singular) flow structure.

It is interesting to see that some differences appear here when compared to the results presented by Patel (1993). The observed trailing edge separation does not decrease near a wall, and no spiral nodes are detected, at least with this flowviz, on the FINs surface. This is probably due to the HULL boundary layer dominance over the root flow near the FINs. The same do not appear to have occurred for tests discussed by Patel (1993), as the base flat plate employed was rather short, having a much simpler flow than the HULL.

Figure 191 - UL FIN leading edge oil flow visualization for Run_05.

Source: Author (2018).

Figure 192 - Schematics of separation-induced transition process on a NACA2415 airfoil using oil-flow visualization.

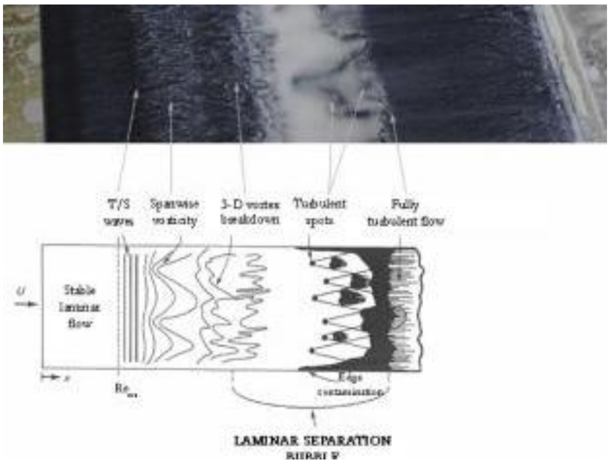

Source: Genç (2016).

Once the model was examined using the adequate roughness chosen, i.e. the TRIP configuration, the FISHNET was installed to assess the flow changes given the expected increase in turbulence. Run_06 was conducted at the same mean flow conditions as the rest of the campaign; however, a greater level of vibration was observed, probably due to the increase in turbulence (Figure 193).

Figure 193 - Sequential frames for Run_06 oil flow visualization.

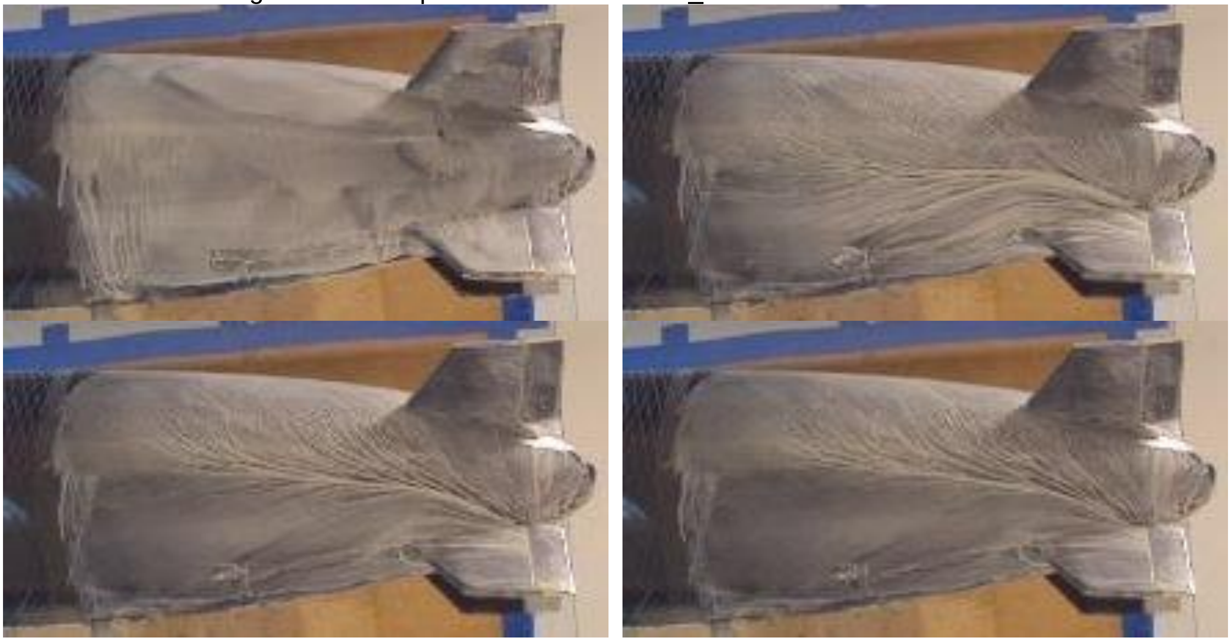

Source: Author (2018).

The first clear difference to be observed is that the streamlines became thinner than before, mainly for the upper portion, which means greater near-wall velocities. Besides that, the lateral attachment line presented less curvature, shorter straight length, in favor of a linear downward limiting line. Also, the end of the attachment line was a little upstream; whereas for the TRIP (Run_05) it ended near the control surface leading edge, here it ends at the stabilizer root.

Figure 194 - Rear view of Run_06 port side oil flow visualization.

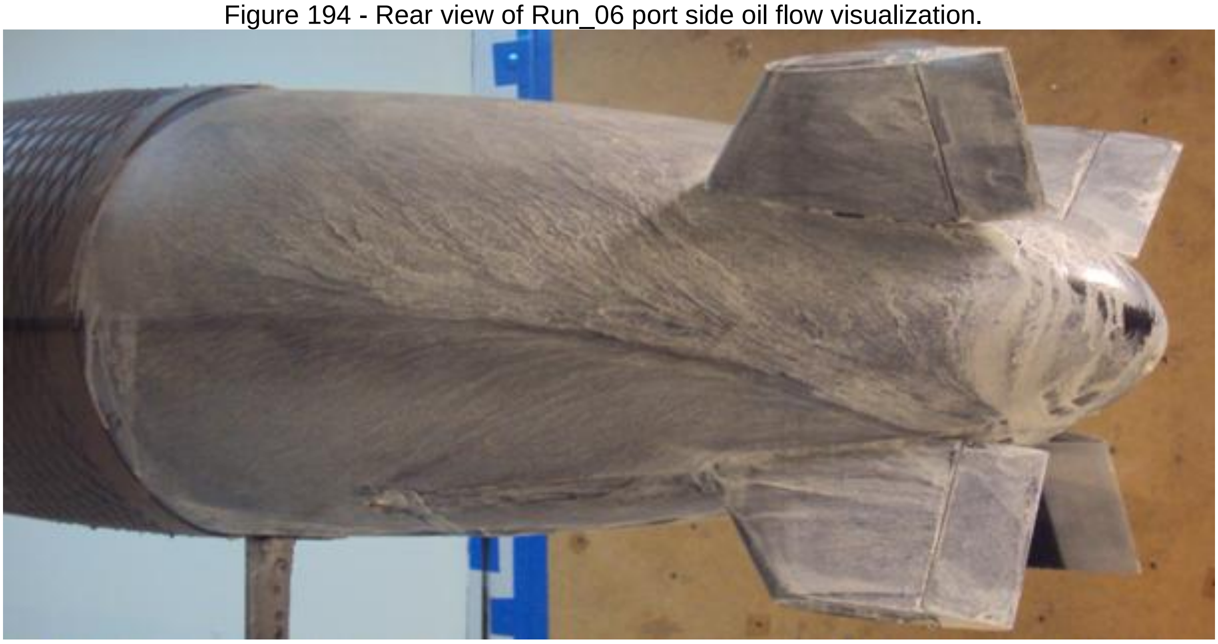

Source: Author (2018).

Similarly, the HULL separated region also increased. The separation line, travelled upstream, almost reaching the FIN roots in some cases. A good explanation for the fact that although the near-wall velocity seemed to be larger separation occurred earlier is the boundary layer thickness. It probably went thicker given the FISHNET, and was not able to easily overcome the generated adverse pressure gradient.

Figure 195 - Rear view of Run_06 upper side oil flow visualization.

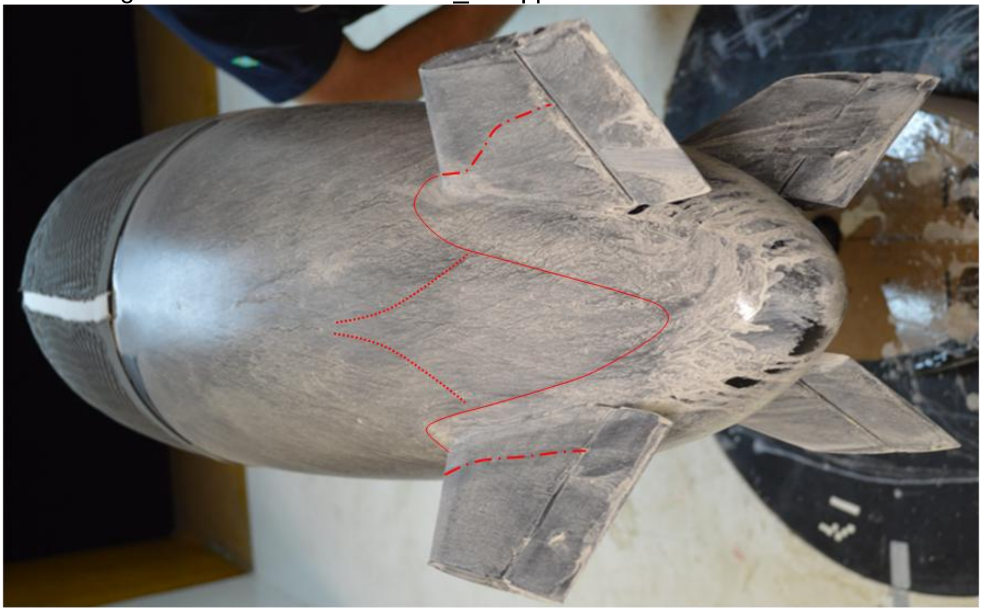

Source: Author (2018).

Assessing the upper side, other evidences of increase in boundary layer thickness are seen. Horseshoe-like patterns appear around the FIN roots (Figure 195). These wider white layers surrounding the FINs demonstrate lower velocity regions, with an increased degree of turbulence. These might be physical evidence of the leading edge separation wakes mentioned by Cornish, III and Boatwright (1960), which extend downstream, reaching the HULL separation region, and joining it as a “Vee” pattern. It is also possible to observe that the FINs have wider white layers near to the root, attesting that the flow velocity for the root region is lower than before (TRIP configuration), leading to less efficient surfaces as well. All these changes demonstrate that the interference between HULL and FIN boundary layers are more than relevant, and scalability should be a key factor to properly model the aircraft in the wind tunnel. Examples of thresholds between low and high velocity regions on the FINs are shown below (Figure 196 and Figure 197).

Figure 196 - Limiting streamlines on LL FIN upper side for Run_06.

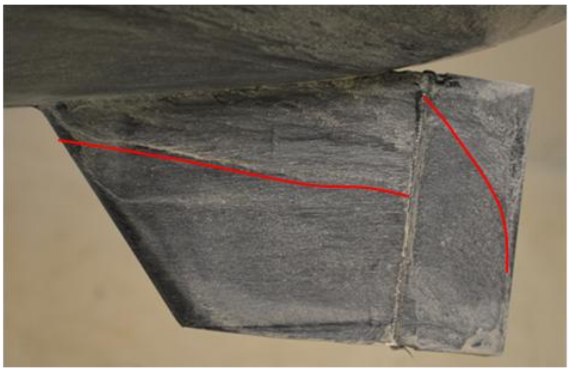

Source: Author (2018).

Figure 197 - Limiting streamlines on UR FIN upper side for Run_06.

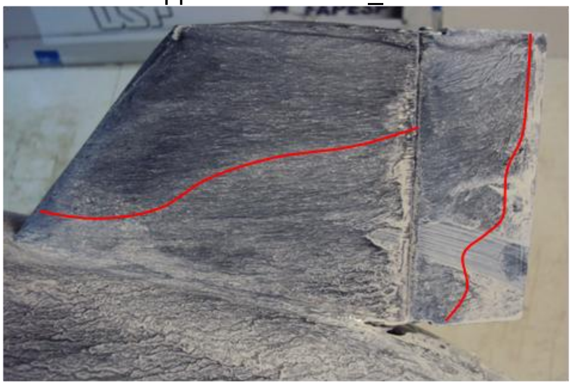

Source: Author (2018).

Regarding the boundary layer development along the HULL middle portion, well defined regions were observed. Inspecting the flow right downstream of the FISHNET, on the starboard side, one can see the evolution of the surface level of turbulence. A first thick white layer (Figure 198 - #01) shows that the flow was still reattaching to the HULL after leaving the FISHNET level. Once it attaches, the dots start stretching (Figure 198 - #02), streamlining downstream to what would be a fully developed turbulent flow (Figure 198 - #03), and reducing in density. Nevertheless, after some length, the streamlines redirect themselves downward, in thicker limiting lines (Figure 198 - #04). This last region is where vortical structures begin exerting stronger influence over the ship, decreasing the longitudinal velocity, and inducing the flow downwards, towards the lateral attachment line.

Figure 198 - Run_06 turbulence level evolution along starboard side.

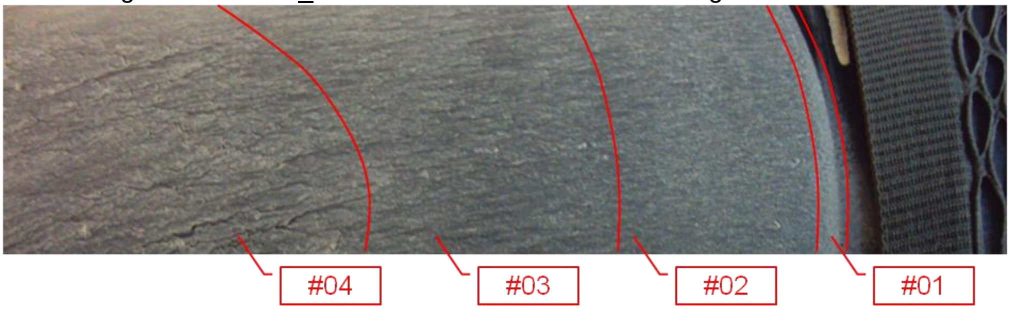

Source: Author (2018).

Figure 199 - Detail of flow downstream the FISHNET on Run_06 upper side.

Source: Author (2018).

The last assessed configuration for AoA = 0° was the Smooth. With no roughnening device, and with the polished BARE HULL (Appendix A), Run_07 was conducted under the same flow constraints.

Figure 200 - Sequential frames for Run_07 oil flow visualization.

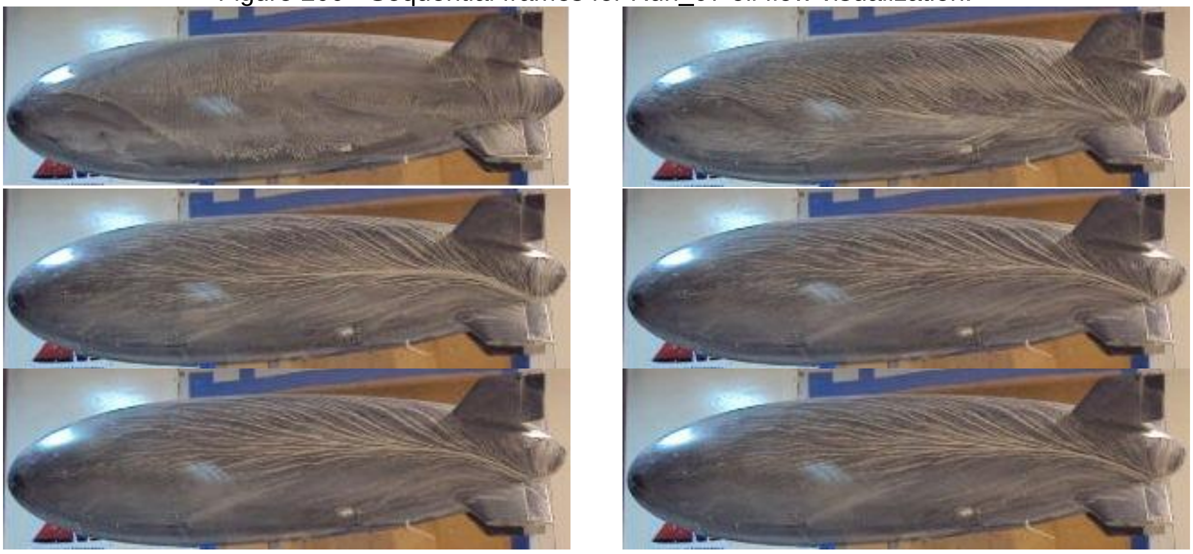

Source: Author (2018).

As an overall result, all limiting streamlines ended up thicker, even the lower ones (Figure 200). The end of the lateral attachment line converged to almost the same position as in the TRIP case, but a little upstream (earlier). Also, the middle portion of the attachment line was much straighter than for FISHNET (Run_06), even when compared to TRIP (Run_05). This shows that the nature of the boundary layer has influence on the development of the lateral vortex, which is responsible for the attachment line. As a general conclusion, it can be said that the less the turbulence, the smaller the attachment line curvature. Analyzing the AIRSHIP upper portion (Figure 201), the limiting streamlines are much thicker, attesting lower velocities. Also, it is possible to say that the flow, besides going down as the others, runs down in a less steep gradient. This matches the straightening observed for the attachment line. Interestingly, the region in between the fins does not show the apparent reduction in velocity observed for the other two roughening configurations. This shows that, with the expected laminar development, the interferences between HULL and FINs are much smaller. As confirmation of that, it is possible to observe that the limiting streamlines around the FIN leading edges are less preeminent, and the flow deviation is smaller.

Figure 201 - Rear view of Run_07 upper side oil flow visualization.

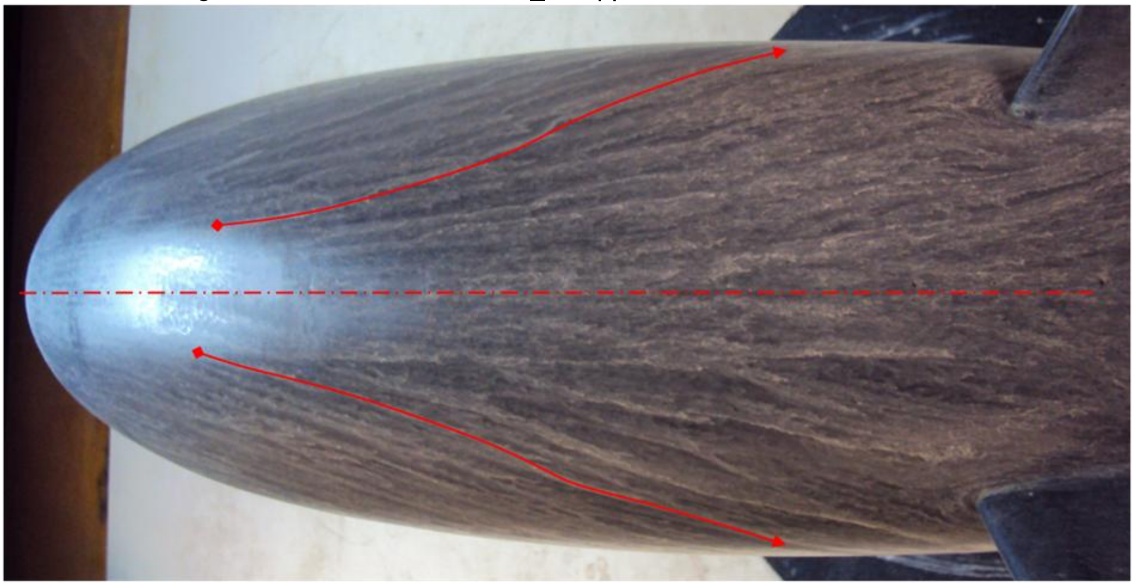

Source: Author (2018).

By inspecting the upper FIN patterns (Figure 202 and Figure 203), it is possible to confirm that the interference level has in fact decreased. Lower velocity regions near the root were diminished, in some cases being restricted to far downstream. The pattern of HULL separation also appears further downstream on the upper side, and with a more circular threshold defining it, different from what was observed for the other previous two cases (horseshoe- or “Vee”-like).

In addition, almost no trailing edge separation is observed for the upper FINs, supporting the proposal that this phenomenon was also a consequence of the interaction between HULL and FINs flows. Besides that, longer regions of laminar flow are observable on the FINs, followed by well defined transition bands, leading to turbulent attached flow along the remaining chord length. Separations were detected only at the very end, where rough sharp edges appeared (control surface cowl).

Figure 202 - Limiting streamlines on UL FIN upper side for Run_07.

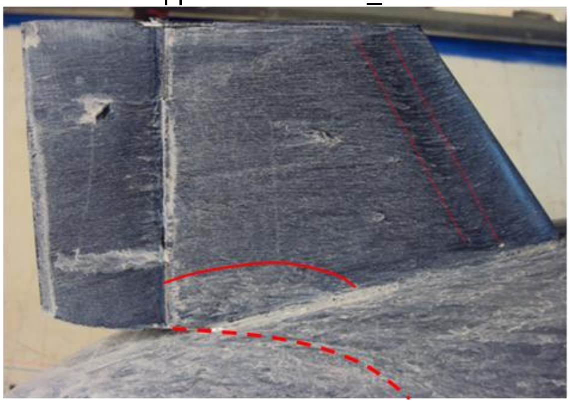

Source: Author (2018).

Figure 203 - Limiting streamlines on UR FIN upper side for Run_07.

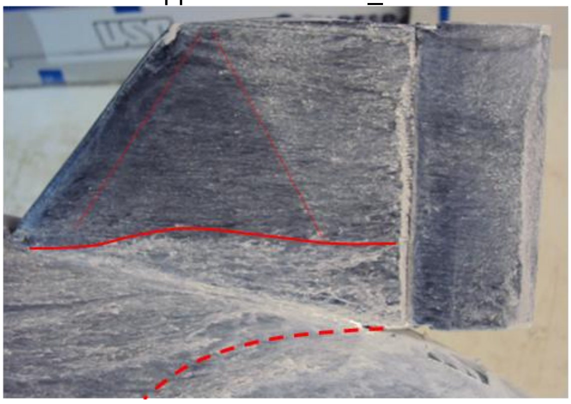

Source: Author (2018).

Laterally, as explained, the rear stagnation point is very similar to TRIP, but the region between the UL and LL FINs shows much more run-off problems (gravity effect). One may infer that separation is already beginning at the region, at least laterally. The stern region (Figure 204) is fully covered by flowviz oil, just like for the others, but consistently linked to the lateral region between FINs. The separated region on the LL FIN control surface is also visible, confirming that it has much more to do with the lateral vortex, than with the boundary layers interaction.

Figure 204 - Detail of Run_07 stern region (port side).

Source: Author (2018).

Still, the FINs show wider laminar flow bands, and a smaller vortical turbulent extent. This may be seen by the change in the white regions, whose scatter is much lighter: smaller dots, a thinner layer and better aligned streamlines (less sinuous).

Observing the upper side of both lower FINs (Figure 205 and Figure 206), it is possible to still see low velocity regions near to the root. Those, however, constitute a combination of the HULL boundary layer and the separation of upcoming outer streamlines, which are converging to the lateral open separation lines.

Figure 205 - Starboard side of Run_08 oil flow visualization.

Source: Author (2018).

Figure 206 - Port side of Run_08 oil flow visualization.

Source: Author (2018).

This assessment can be supported by the fact that the longer separation regions are closer to the HULL, decreasing with increasing spanwise position (triangular pattern). The nearer the streamlines are to the HULL, the stronger they are influenced by the lateral vortex. That greater influence means greater upwash effect, i.e. higher induced local AoAs, and earlier separations. The same effect was observed for the other two configurations, and could now be clarified.

Obviously, local protuberances have strong influence on the flow, and under such flow conditions (low *Re*) may lead to separation. Sources like these may be loose tape tips, hard spots/bumps on the model surface, geometrical roughness and adjustments, etc. Nevertheless, such unconformities do not compromise the results, once they are easily observable, and can then be disregarded.

After the symmetrical evaluation using different roughnesses was completed, the nature of the aerodynamic interferences between HULL and FINs were determined, as well as their sensitivities to flow conditions (laminarity and turbulence). The final step was to assess how the flow would behave with the tail installed but at a higher AoA. Case Run_04 comprised flow investigations for a configuration equivalent to ENV_21 at AoA = +20°, under the same mean velocities (*Re* ≈ 2.1E+06) (Figure 207).

Figure 207 - Sequential frames for Run_04 oil flow visualization.

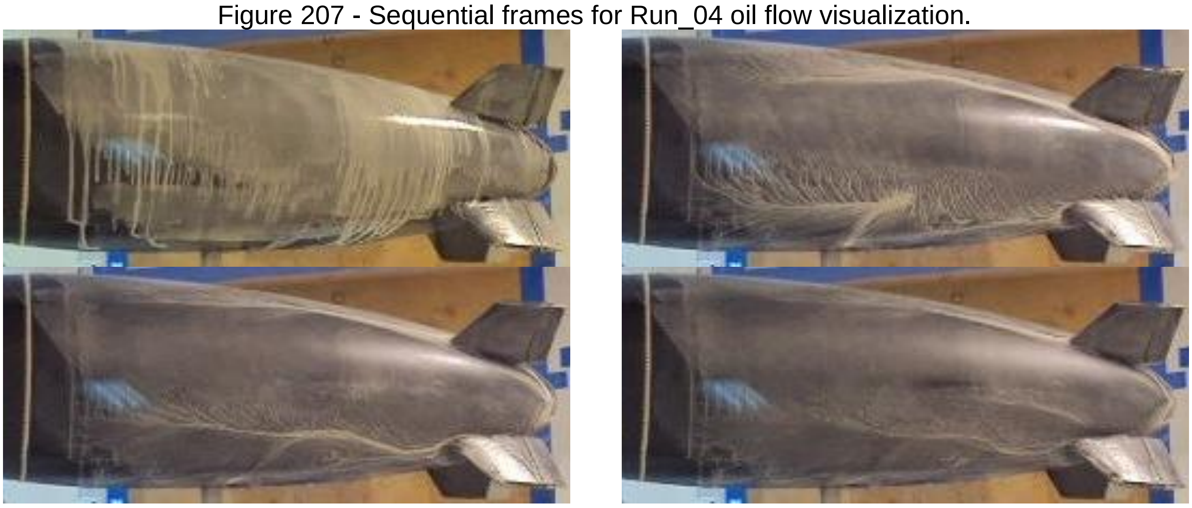

Source: Author (2018).

Similarly to what was seen for the BARE HULL, the upper (aerodynamic) side of the AIRSHIP showed a leaf-like pattern. Interestingly, its limiting lines were veering forward the FINs (UL and LL) leading edge lines. Watching the video record, it is very curious to observe how the lower white line is moved along the HULL upwards, and how it still flows (swiveling) inside (around) itself without dripping. The flowviz line could have been held up by an attached high vortical tube, which appeared to slowly feed the LL FIN root with oil. The observed behavior resembles an aqueduct with swiveling water in it.

Nevertheless, it was probably the separation line of the streamlines layer which detaches forming the lateral conical region (separation bubble). Like was observed for the BARE HULL, the model is a little off regarding incidence, and therefore the aerodynamic structures are not quite symmetric. The swiveling effect along the white limiting line occurs, because probably on one side the separating streamlines apply, through shear, a torque to the outer portion of the fluid. This torque decreases across the fluid line radius, rotating it upwards, and letting gravity pulls the other side of the fluid tube downwards. In a simple manner, it would be like rolling up a long modeling clay strip, where the clay is the flowviz oil. The oil quickly flows downstream, in the direction of the LL FIN, given the low resistance inside the separated region (Figure 207).

Comparing upper and lower limiting lines, it is also possible to see that the support bar had strong influence over the outer flow. The lower limiting line is sinuous, and along the video it is possible to see the middle portion of oil on the HULL run down for a while before being held up, while upstream and downstream of it the line was already forming at same level. This attests that during the lateral separation bubble formation - section 5.2.2, the support bar was breaking up the upcoming streamlines, which were not strong enough yet. Also, after stabilization, it is possible to see that the later portion of the lower limiting line presents a curved shape, like a curve belly. The expected trend would be a constant narrowing process of the leaf-like pattern along **L**, like what was observed before for the BARE HULL. Observing the surface flow pattern one can also infer that the “belly” is off-trend. Probably, the reattaching streamlines which were reaching that point were less “strong” (had less momentum), reattaching sooner, and therefore showing the “belly pattern”. This decrease in momentum has the support bar as the source.

Looking closer at the upper (aerodynamic) side, an unexpected pattern is seen. The leaf-like pattern was, like for the BARE HULL, misaligned in relation to the longitudinal axis. However, while getting closer to the tail, it redirects to the region in between UL and LL FINs. The lower limiting streamlines (shorter white arrows - Figure 208) got stretched, and were sort of sucked towards the LL FIN (long white arrows - Figure 208). Also, a scattered region was formed between the lower limiting line (red arrows) and the leaf-like pattern lower border (dotted red line). This is probably the conical separation bubble formed on the port (aerodynamic) side. The presence of this region at such place supports the explanation that the “flowviz aqueduct” was right above the HULL port (aerodynamic) side separation line.

Figure 208 - Run_04 stern (port view) oil flow visualization.

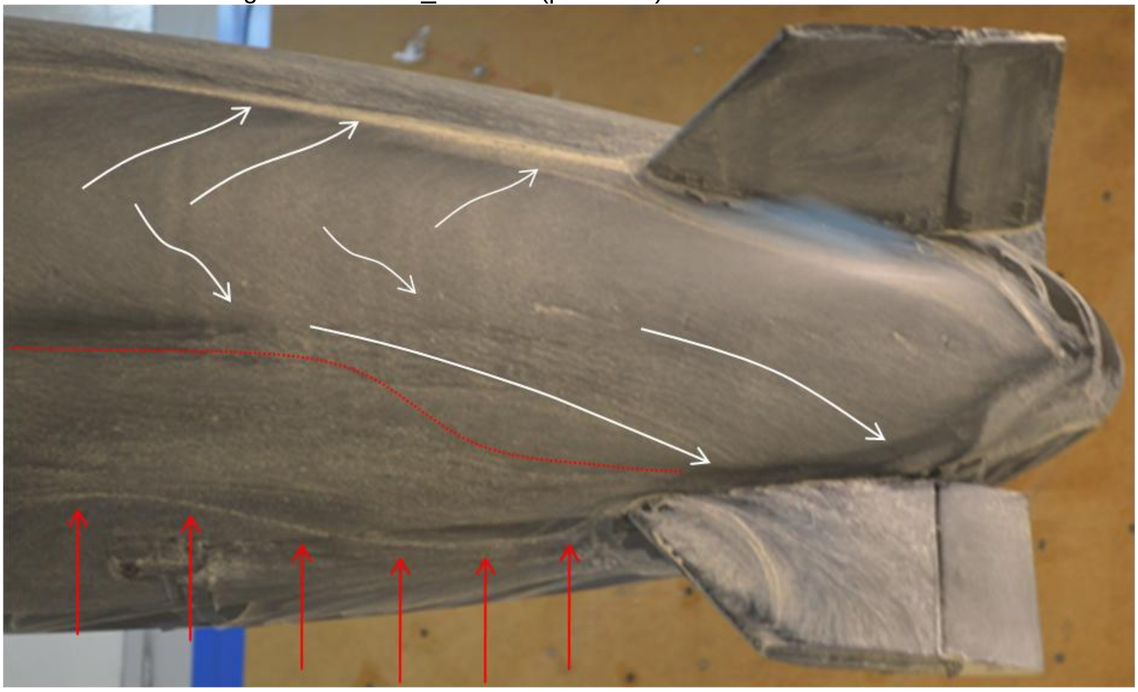

Source: Author (2018).

By analyzing the video, it is possible to see that a very strong swiveling flow is formed on the top of LL FIN. Not only the upper streamlines were sucked, but also the white scattered region seems to drain to the LL FIN (Figure 208). Comparing the surface pattern with that of Figure 31 shows a high degree of similarity.

Figure 209 - Detail view of LL FIN upper side oil flow visualization for Run_04.

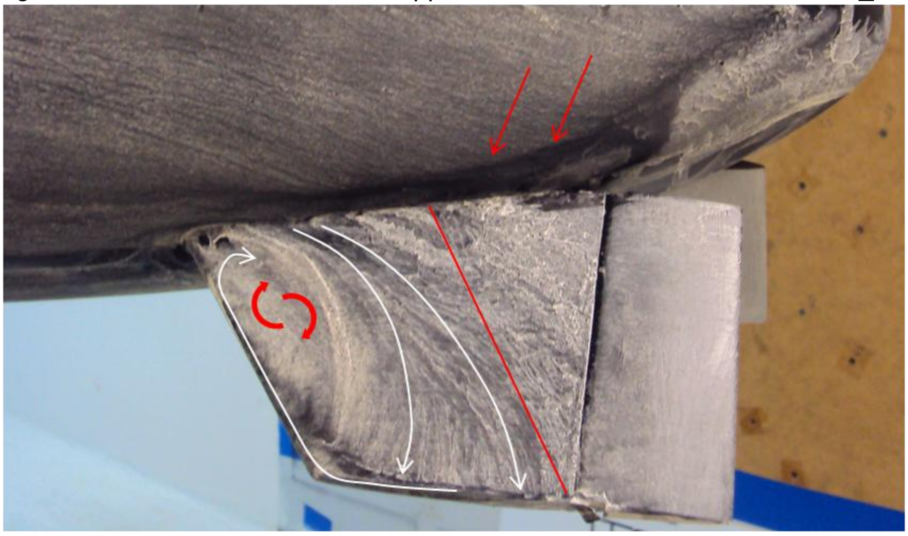

Source: Author (2018).

Analyzing in detail the surface (Figure 209), it is easy to identify a white thick parabolic line connecting root to tip. The records show that flowviz oil was swiveling inside the region delimited by this line and the leading edge. The vorticity was so strong, that oil was flowing to the tip and being sucked to the leading edge. The same effect (crossflow – spanwise flow) was detected using tufts if one can recall, which was previously shown. Differently from what was shown by Patel (1993), the flow on the LL FIN upper side was highly influenced by the intersected surface flow (HULL), and therefore the bifurcation (Figure 31) does not take place in this case

This a typical case of leading edge separation, which occurs when extremely high AoAs are set and/or the surface has a sharp leading edge geometry. The whole flow at the edge is separated, and this is probably due to the outer streamlines overcoming the lateral conical separation bubble. The incidence is almost 90° if a tangential path is assumed along the HULL curvature. The high AIRSHIP AoA probably led to a thick lateral vortex. When the outer streamlines tried to overcome it in order to join, over the upper surface, the flow from the exposed side (remember that AoA = +20°), they hit the fin almost perpendicularly, leading to a direct separation. Not clashing on the top side, the outer streamlines do not sustain the leaf-like pair of counter-rotating vortices. This supports the stretching of the limiting streamlines. From this point of view, the stretching would then accommodate a straightening of them with the axial flow, once vorticity was jeopardized.

Figure 210 - Detail of HULL and UL FIN interference effects for Run_04 oil flow visualization.

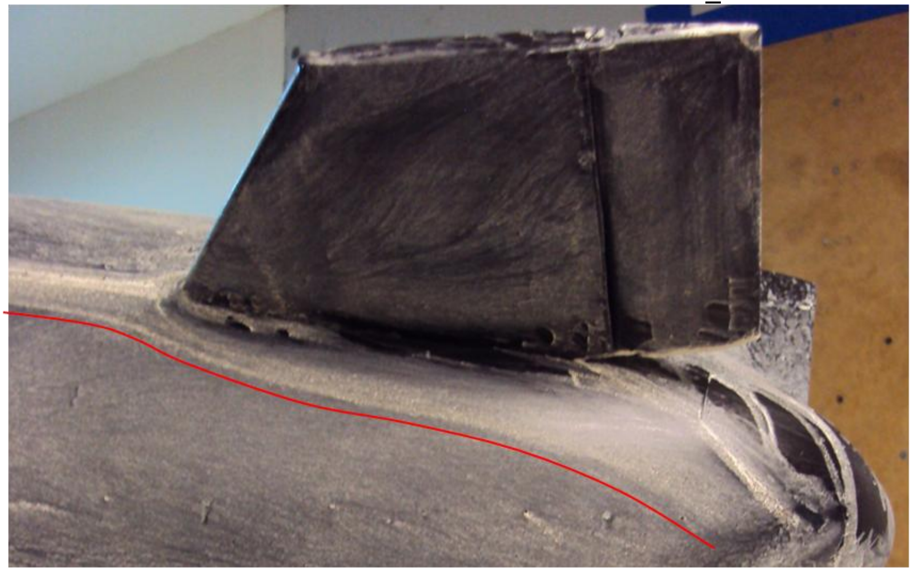

Source: Author (2018).

Complementarily, observing the FIN root (Figure 210), there is a thick black band. This denotes the previous “aqueduct” track. Probably, some tube vortex, originated at the leading edge, was formed. Its high intensity together with the local low pressure (separation), helped to suck the upper streamlines, feeding the swivel on the top of the FIN. Obviously, downstream of the spanwise flow (solid red line –

Figure 210) the FIN surface was white. Another contributing effect that could help to stretch the upper streamlines is the lift generated by the UL FIN. The circulation produced by it would induce some flow acceleration in the region between the UL and the LL FINS. Nevertheless, considering the strength of the swiveling structure as whole, this could be, in this case negligible.

Changing topic, but still focusing on the AIRSHIP upper (aerodynamic) side, one might have noticed the thick white limiting line at the top (Figure 208). This line, like for the BARE HULL comprised the convergence between a conical lateral separation bubble, and leaf-like streamlines. In this case, however, it is thick and white, meaning that the longitudinal velocity is really low, if it exists. Also, the further downstream, the thicker it gets. With FINs installed this line is exactly the geometrical line leading to the UL FIN. Along this line, due to the flow stagnation at the FIN leading edge, the longitudinal velocity decreases up to a stagnation point. Nevertheless, since it is fed by both described structures, more pigment tends to accumulate along it. This pigment does drain longitudinally, like for the BARE HULL, because the streamlines, which already have lower velocities (stagnation being reached), are also forced to deviate from the FIN in order to keep flowing downstream. This is the typical behavior of subsonic flow, and was also identified for the UL Fin through pressure taps.

Figure 211 - Detail of UL FIN upstream stagnation line for Run_04.

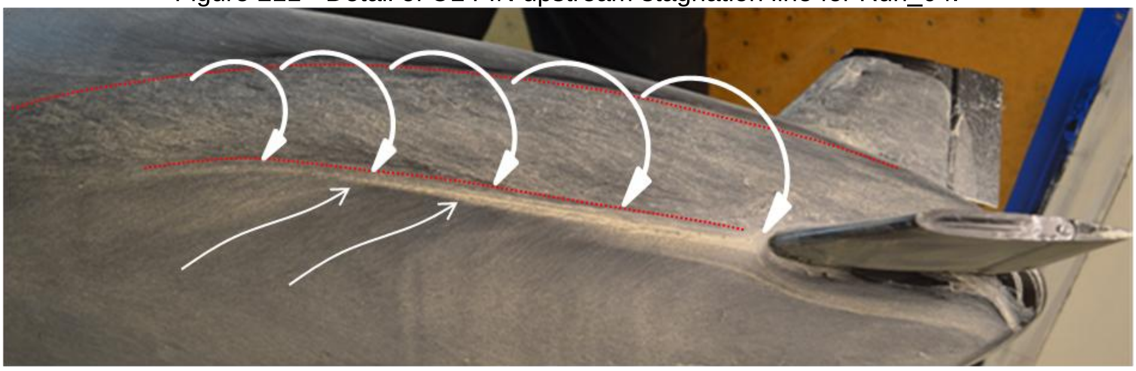

Source: Author (2018).

Figure 211 shows in detail the stagnation line for UL FIN. At the top of the picture, it is possible to see the first separation line (solid black line), where the curved arrows come from. The stagnation line, as explained is fed by the conical lateral bubble from the starboard (aerodynamic) side through the leaf-like upper streamlines. Around the root of UL FIN a thick white band is formed, denoting a large region of low velocity, resulting from the interaction between HULL and FIN flows.

Concluding this case, one FIN (UL) is immersed in the double-bubble separation wake, and the other shows no streamlined flow given the leading edge separation. It is important to remember that the aerodynamic structures are off-centered given the slightly positive fixation angle (section 5.2.2), and the support bar weakening effect on one of the side bubbles. Nevertheless, this may represent a momentary lateral gust, far from being an improbable situation. Centering the structures, would probably lead to an equally bad situation. The leaf-like pattern would align at the top, then both upper fins would be immersed inside the conical lateral separation bubbles wake, becoming ineffective from an aerodynamic point of view.

Inspecting the upper side of the model (starboard aerodynamic side) shows, rather surprisingly, interferences between HULL and FINs. Another large swiveling region was identified. Generated from another leading edge separation, but this time from the UR FIN, this structure was formed on the HULL surface, inside the conical vortex (Figure 212 and Figure 213).

Figure 212 - Rear view of Run_04 starboard side oil flow visualization.

Source: Author (2018).

Figure 213 - Detail of UR FIN leading edge separation inducing vorticity on HULL surface.

Source: Author (2018).

The separation was a result of upcoming streamlines hitting the fin leading edge, and not being able to keep the flow from there on. The separation generated a low pressure region, which was accelerated by upstream lateral streamlines and by the low longitudinal velocity flow (starboard separation bubble region) on its outer portion, creating a vortical region. Looking from another stand point allows one to see that the sink-like structure is shaped mainly against the lateral upcoming streamlines, whose limiting streamlines are seen on the HULL surface. The vorticity level may also be rather strong, as there is a clear and well defined black band around the white core.

The UR FIN is then, similarly to those on the left, quite impaired in effectiveness. The accumulation of oil at the root was so high, that it did not dry even after almost 4 minutes of running the tunnel. Looking at the surface pattern, the UR FIN presents scattered white dots, but no streamlines. This means that no streamlined flow is present.

On a final assessment of the starboard (aerodynamic) side, the upper side of the UL FIN reveals important information regarding the lateral vortices. Near to its root, it is possible to see a clean black line apparently aligned with the HULL curvature. As is known, when the surface is as shown, high near-wall velocities are developing. Therefore, if the lateral vorticity was a large conical vortex only, that clean cut line would not appear. In this way, the proposal of a wake, similar to a separation bubble, seems to be more adequate (Double-bubble).

Remembering that the bubble would appear along the lateral upcoming flow, and that two separation lines occur (double-bubble), a thin intense dark line would be formed along the separations. These patterns would be aligned with the outer flow direction, and would be perpendicular to the upcoming streamlines. This would lead to a well defined line along the HULL. Such pattern was seen for the BARE HULL, but is shaded by the UL FIN stagnation line here. Inside this bubble there would be stagnated air, with very little vorticity, induced by inner standing eddies, resulting from outer bubble streamlines clashing. This characteristic is seen on the HULL surface. Along the conical white region large scattered white dots are observed. Nevertheless, once the bubble is formed orthogonally to the outer flow direction, there will still be some longitudinal velocity across it, as shown in Figure 131.

With the surface flow visualizations it was also possible to demonstrate that, for large AoAs, an X-tail aircraft like this would have tail surfaces with very low effective, practically inoperative in some cases. This does not seems to match what is seen on the C_L curves, which show increasing lift up to |AoA| = 25°. Probably other sorts of lift generation may arise with increasing AoA, counting on the HULL. Those vortex-based lift generation effects, like for delta wings and lifting bodies, are pretty possible in this case with such a complex and eddy flow. One must also have in mind that, for ENV_21 (TRIP configuration), from AoA = +15° on, the LCO gradient starts decreasing (Figure 144) This may be a result of the observed impairing characteristics to which the FINs are subject for large AoAs.

Also, by observable interference phenomena between HULL and FINs, the numerical results obtained for different roughnesses were supported. Based on the obtained patterns, it was possible to validate the choice of the TRIP configuration, which provided turbulence over the whole model without overemphasizing it, besides allowing for the development of all relevant flow structures and interferences.

As a complementary technique aimed at trying to better attest the complex vortical structures described, some outer flow visualization was tried by means of smoke. Using the apparatus described in section 4.2.3.2**,** the smoke was generated and released as a plume inside the working chamber upstream of the model.

Figure 214 - Detail of smoke probe.

Source: Author (2018).

Figure 215 - AIRSHIP model and smoke probe in the wind tunnel.

Source: Author (2018).

Before actually using smoke to inspect the flow around the model, a long string was attached to the smoke probe in order to assess the possible slightly positive fixation of the model. The string was attached below the HULL longitudinal axis, and the model adjusted to AoA = 0°.

Figure 216 - Sequential frames of upwash string (white twine) patterns.

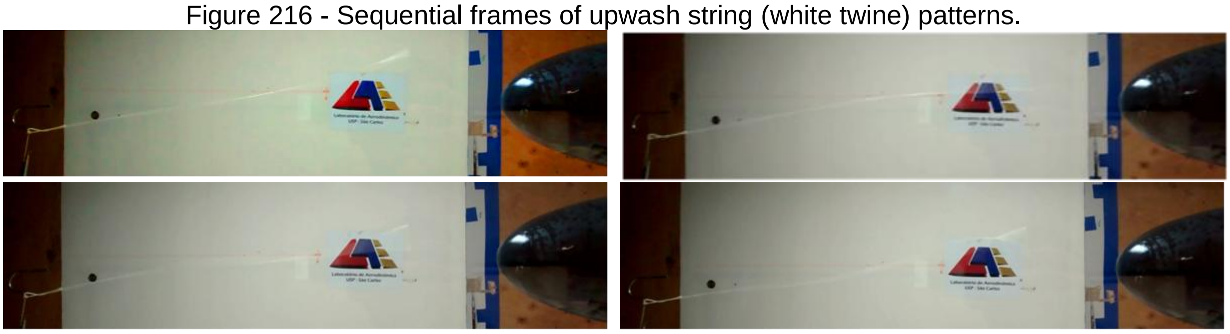

Source: Author (2018).

Analyzing the video frames and the string shapes makes it possible to say that there was indeed an induced upwash in the section. The string always pointed upwards, towards the model upper side. Even when oscillating, it never went below the lateral plane level height. Besides the possibility of being a problem induced by some positive fixation angle of the model, according to Barlow, Rae and Pope (1999), this might also be an upflow issue at the working chamber entrance, like what was described in section 4.3.2. However, since it was a known and confirmed effect, and no impeditive consequence was generated for the desired purposes, the tests were continued regardless of the upwash.

In order to achieve a minimally observable smoke trail, wind tunnel velocity had to be substantially reduced. The final *Re* was around 5.0E+05, an order of magnitude smaller than those used for the rest of the tests. With this, it was already expected to see enlarged vortical structures. Nevertheless, the objective was to check their existence, rotational direction and average position. In this way, the campaign was continued. The model had the tripping bands removed, and was set to AoA = +20°. The roughness was removed so the increase in velocity about the model could be smaller, facilitating the visualization as well.

A first evaluation, with lights on, was made in order to confirm the existence of vortex shedding over the upper (aerodynamic) side, as proposed in section 5.2.2. The smoke plume was released, and as expected it went over the lateral side, without touching it, still being a moderate thin plume. After flowing downstream and past the body, the plume became a dense white blur with a shape changing in time (Figure 217).

Figure 217 - Flow over the AIRSHIP at AoA = +20°. Wake vortex shown by smoke.

Source: Author (2018).

The changing shape characteristics are typical of detaching vortices. The size of the blurs varied between small and large, alternately. This is a characteristic of detaching vortex pairs, like von Kármán vortices, confirming the proposal advanced during the BARE HULL investigation. Vortices changing shapes are shown below, in steps of 1 second, extracted from videos.

Figure 218 - Sequential frames showing vortices wake revealed by smoke past AIRSHIP at AoA = +20°.

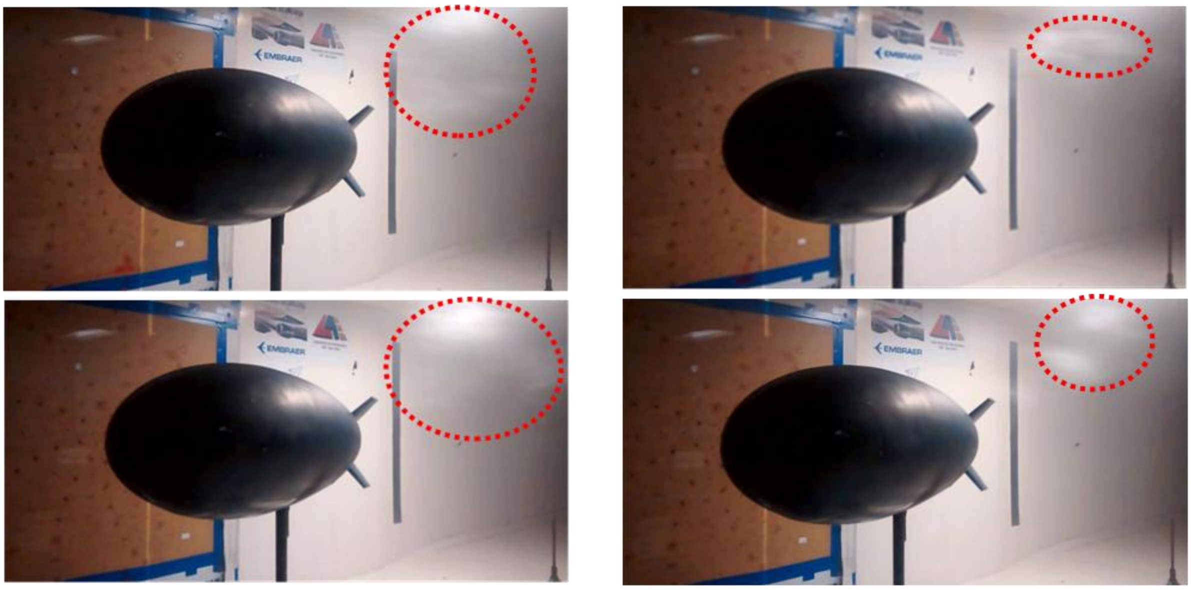

Source: Author (2018).

The blur probably constitutes the visualization of an alternating detaching vortices wake, and its size/density is directly linked to the vortex strength: the denser the blur, the stronger the vortex. This should be true since the higher the vorticity level, the weaker the vortex fading will be with the outer flow velocity. It is important to highlight that only one side of the wake is being visualized. This is the reason why some weaker vortices are seen; their presence corresponds to stronger vortices on the other side of the wake.

For the next step, the objective was to visualize the outer flow nearer to the HULL. Background lights were turned off, and the plane light was intensified. By intensifying this light source, only the highly contrasting flow structures are observed. For this reason, what is observed is the direction of denser smoke – preferential flow. Looking at around 70%**L**, it was possible to track upcoming outer streamlines flowing over the starboard (aerodynamic) side. The farther it is from the HULL, the less dense the smoke. Near to the region where the leaf-like pattern was obtained, the smoke plume reaches a peak, and is redirected to the HULL surface. When it touches the HULL, the plume reveals a wide attached vortex, whose rotation direction is clockwise looking downstream at the tunnel test section, as was predicted during the oil flow results discussion. Sequential frames of the tail, taken from at the observer’s side, were organized and are shown below, depicting the phenomenon (Figure 219).

Figure 219 - Sequential frames depicting outer flow going over the AIRSHIP side and rolling into a vortex on the upper side at AoA = +20°.

Source: Author (2018).

The observed phenomenon is a positive contribution to the proposed interpretation of the oil flow patterns obtained. The smoke trails allow one to observe the upcoming streamlines, and the generation of the top vortex. Physically, with the instrumentation available, it is difficult to precisely measure and determine its position. Nevertheless, such qualitative confirmation appears sufficient for the desired purposes.

In order to assess the vortex development along the flow, the plane light was moved downstream while images were recorded. Sequential frames of incremental positions along **L** are shown below (Figure 220). The dotted red lines denote the UL FIN position. It was not possible to keep the camera static, because of lighting and perspective issues. For this reason, the reference points for the frames change a little.

Figure 220 - Sequential frames along **L** showing the development of a top staboard vortex at AoA = +20°.

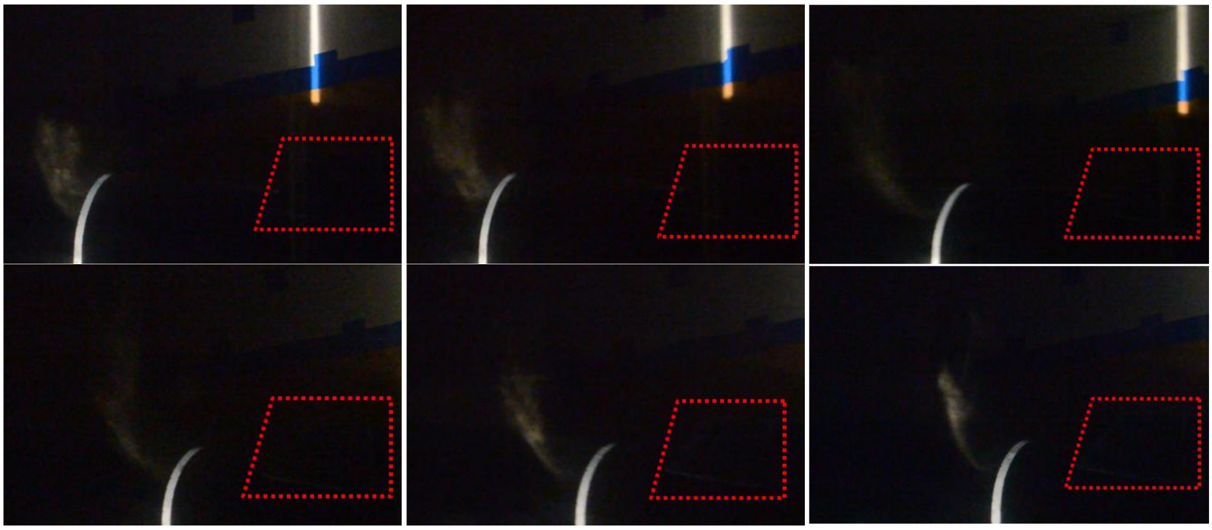

Source: Author (2018).

It is possible to see that the vortical structures grow along **L**, and gradatively separate from the AIRSHIP, constituting an eddy wake. This detachment can be inferred from the decrease in the contact area (touch width) between HULL and smoke pattern. Near to the tail station, already completely detached vortices were also visualized.

Figure 221 - Sequential frames highlighting the detached eddy wake at the tail region at AoA = +20°.

Source: Author (2018).

Also downstream of the FINs some visualization was possible along the AIRSHIP wake. With the plane light, however, it was not possible to capture the lighter blurs, as shown in Figure 222.

Figure 222 - Sequential frames highlighting the detached eddy wake past the AIRSHIP at AoA = +20°.

Source: Author (2018).

These sequential observations of detached vortices qualitatively match those conducted with lights on, shown before (Figure 217). Moreover, these observations, by two different lighting techniques, support the proposed vortex shedding effect across the HULL, explained in section 5.2.2. In other words, the wake past the AIRSHIP may be assumed as a pair of alternating vortices detachment layers (Figure 132).

Unfortunately, there was only one smoke probe available, and visualizing both sides was not possible. The visual observation of the aerodynamic flow structures was much better with unaided eyes, although the lighting and velocity issues were not completely solved given the instrumentation availability. These factors made capturing pictures with good definition rather difficult, a situation made even more challenging by the wind tunnel acrylic wall reflections.

Nevertheless, all the evidence captured using the flow visualization techniques, comprising sections 5.2.2 and 5.2.3.4**,** and the observations arising from them, physically demonstrate how complex the flow about an airship can be. As expected the interferences are really relevant, and the bodies definitely cannot be modeled as single aerodynamic entities.

5.2.4 Airship static stability: fin size evaluation

Before going to wind tunnel campaign Phase II, a last investigation was conducted using aerodynamic steady flow tests. A second set of tail fins was fabricated, as described in Appendix A. The second fins were shorter than the previous ones. For this reason, in order to facilitate the differentiation between both configurations, the original set was called Standard **-** S0 and the new one, Shorter **-** S1. The objective of this investigation was to quickly compare both configurations, mainly regarding drag and stability characteristics, and provide an assessment on how fin size affects airship aerodynamics.

Figure 223 - S0 and S1 FIN sets schematic comparison.

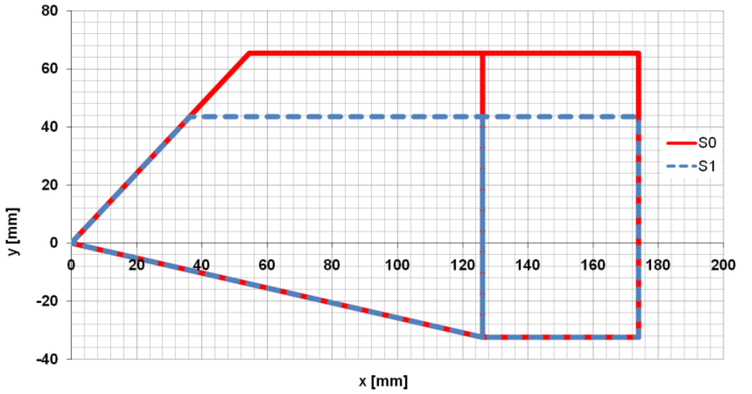

Source: Author (2018).

In order to do so, the TRIP roughness configuration was undone, and the HULL was converted back to the original smooth surface. Also the Root Fairing was removed (the acquisition cables had already been removed for oil flow visualization). In this way, each set of fins was tested in three different incremental configurations: "w/o Fairing", "Smooth" (Root Fairing included) and "Fishnet" (Root Fairing included). The proposal was to assess FIN effectiveness under boundary layer extremes, where the Smooth would have a partial laminar flow, with eventual separation further downstream, and Fishnet would generate a fully "exaggerated" turbulent flow. The objective of removing the Root Fairing was generating a base line, mainly regarding questions involving upwash effects. For both roughness configurations, though, the Root Fairing was on. It is also worth saying that some results for TRIP were recalled for comparison purposes. The *Re* was kept to the same mean value of 2.1E+06 used for the whole campaign.

Beginning with the C_D evaluation, the first clear result is that the Root Fairing has a relevant effect on drag reduction. This was, however, already shown before in section 5.1. Nevertheless, the fairing was removed here, not because of C_D evaluations, but for C_L and C_M assessments. Another obvious and already consolidated result is that the FISHNET largely increases drag, by almost 50% for small AoAs, such drag being even greater than that without the Root Fairing.

Figure 224 - Drag polars for S0 FINs set with different roughnesses.

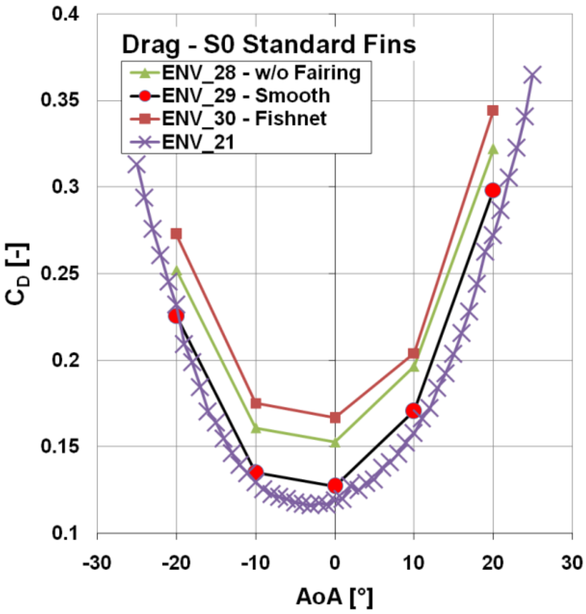

Source: Author (2018).

Figure 225 - Drag polars for S1 FINs set with different roughnesses.

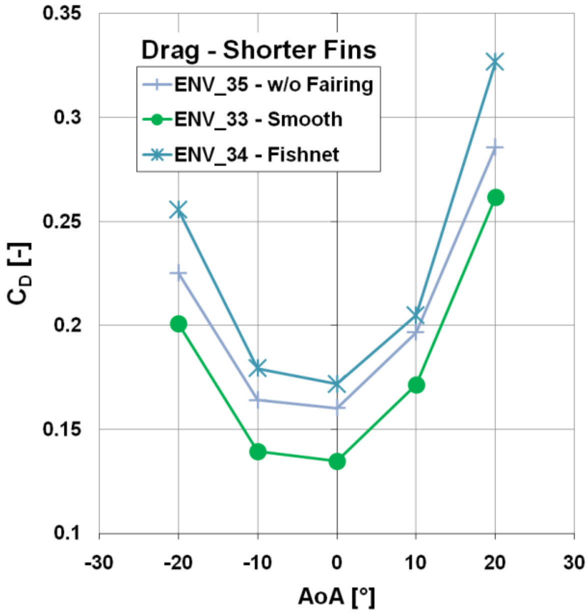

Source: Author (2018).

Despite this, the main objective was to assess how drag changes comparing both FIN sets. For small AoAs, C_D values are almost the same for both configurations. It is interesting to observe that in fact, after a closer look (Figure 226), the Shorter configuration presents indeed some higher C_D values. With increasing AoAs, however, as expected, the Standard configuration has greater C_D. This behavior occurs for both types of roughnesses.

Figure 226 - Drag polars comparing S0 and S1 FINs configurations.

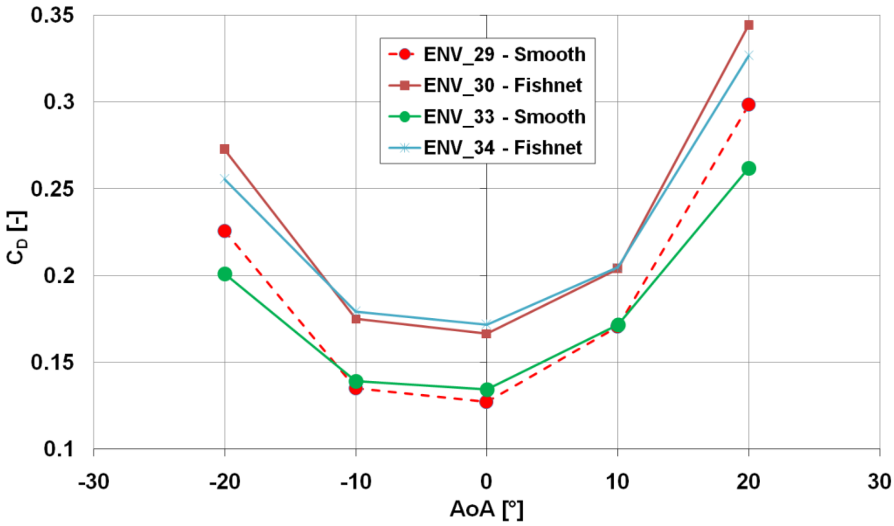

Source: Author (2018).

This demonstrates that these differences among configurations are probably dominated by the induced drag on the tail. This is a plausible explanation, once, as already discussed, FIN skin friction drag is probably negligible compared to HULL skin friction drag. Since Shorter has a smaller *AR*, its C_{Di} would be greater for the same C_L (Equation 9). However, with increasing AoA, Standard (S0) configuration produces enough more lift, and its C_{Di} overcomes Shorter's (recall that C_L is squared - Equation 9). Trying to support this supposition, C_D x C_L was plotted.

Figure 227 - Drag polars against lift comparing S0 and S1 FINs configurations.

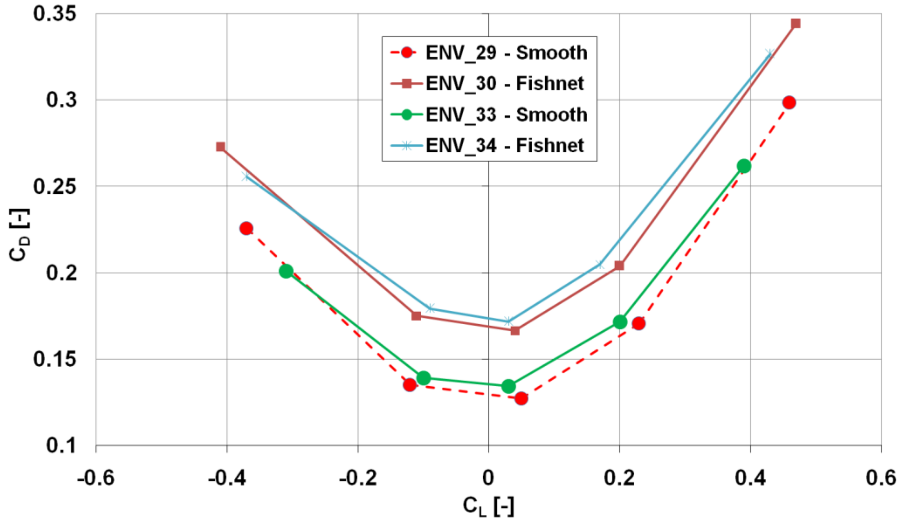

Source: Author (2018).

It is possible to see that the relation described above really begins inverting when C_L increases expressively (Figure 227). In other words, for the same produced C_L, C_D for the Shorter configuration is still greater for small AoAs. This supports the hypothesis that its C_{Di} level is greater. An obvious reason would be the "worse" (smaller) *AR*. Nevertheless, the crossing point (where the relation inverts) stands for rather high C_L values, demonstrating that the balance among all C_{Di} properties (Equation 9) is not very straight forward.

It is important to make it clear that, although C_D was greater for small AoAs using the Shorter configuration, the difference is very small (around 2% for the roughness case, and 3-4% for the smooth surface). For higher AoAs, the Shorter configuration decreases 5-6% for the rough surface, and 10-12% for the smooth, in comparison with Standard. Nevertheless, conventional airships fly very seldom at such high AoAs, and for the short period while they stay there, this increase in drag would not be operationally significant.

Looking at C_L, an overall reduction in the lift generation capacity was identified when using the Shorter FINS. This was expected according to what was concluded in section 5.2.3.1: the fins are responsible for a relevant portion of the lift generated by the AIRSHIP. Figure 228 and Figure 229 show the percentage decrease in C_L for each AoA, considering the Standard FIN values as the reference.

Figure 228 - Lift polars comparing S0 and S1 results for Smooth surface.

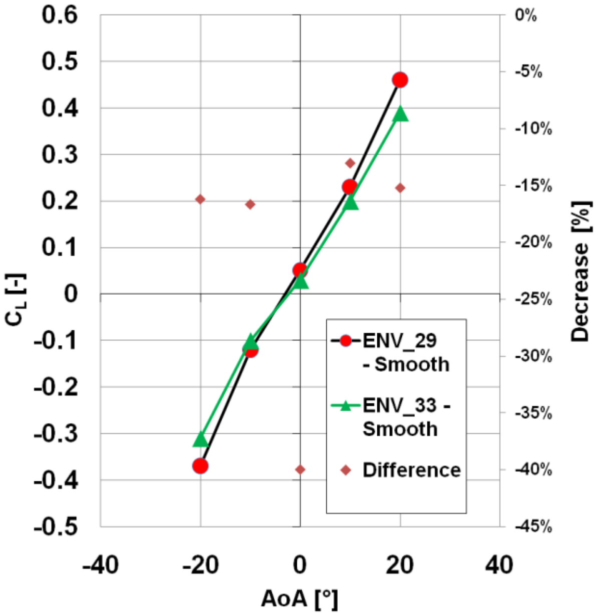

Source: Author (2018).

Figure 229 - Lift polars comparing S0 and S1 results for Fishnet surface.

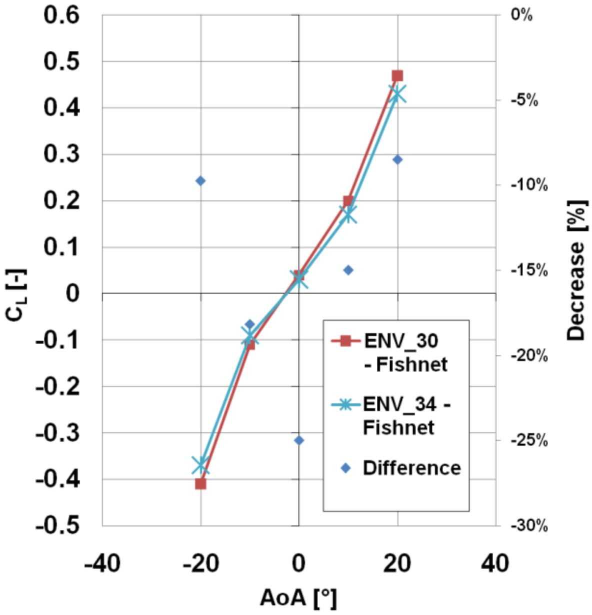

Source: Author (2018).

In general, except for AoA = 0°, the decrease is about 10-15%. The difference in values for AoA = 0° are higher since the C_L reference values are rather small, and even negligible changes lead to great percentage differences. The mean decrease in C_L may be compared to the decrease in area between both tail configurations. The Shorter configuration is equivalent to 79% of the Standard in area. Also, its *AR* is 56.5% of the original set. This reduces even more the lift generation, since the lift distribution is deteriorated. Also, resembling the induced drag discussion, this difference in *AR* increases C_{Di} by 77%, based on Equation 9.

Still looking at C_L, but then at each configuration separately, considering the different roughnesses, also provide interesting results. The first conclusion is that the presence of the Root Fairing has apparently almost no effect on lift. However, when roughness is increased by using the FISHNET, an unexpected behavior is observed. The C_L curve becomes apparently less linear. This cannot be affirmed unconditionally as the amount of data points is small. Even though, the $C_{L\alpha}$ for small AoAs is smaller than it is for |AoAs| > 10°. In other words, for smaller AoAs, the lift generated by the rough configuration is smaller than that generated by the smooth one. This phenomenon inverts with increasing AoA. The results obtained for ENV_21 were added to Figure 230 in order to have the results for the TRIP configuration.

Figure 230 - Lift polars for S0 FINs for different roughnesses.

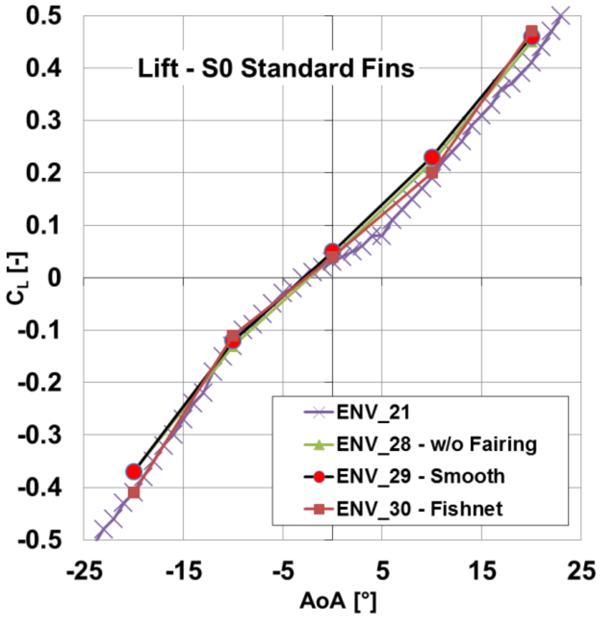

Source: Author (2018).

Figure 231 - Lift polars for S1 FINs for different roughnesses.

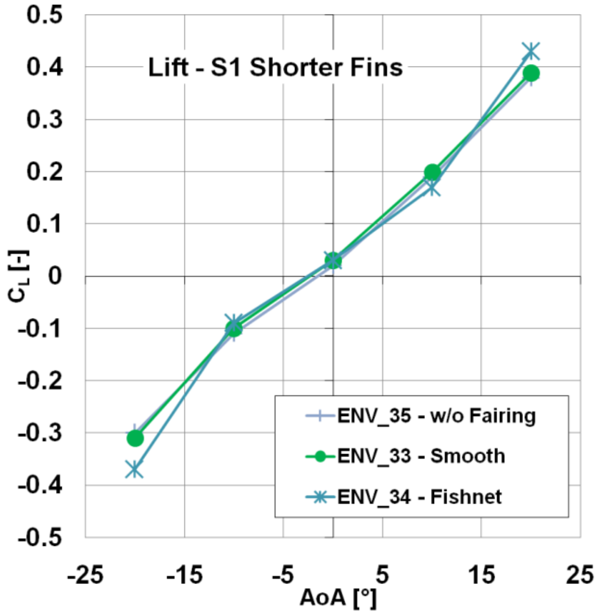

Source: Author (2018).

Although such result seems not to be intuitive, it may be explained based once again on boundary layer development. For the Smooth configuration, while attached to the body, the boundary layer is thinner, and the transition to turbulent flow occurs further downstream. In this way, the fins are affected by smaller low velocity regions, producing more useful lift than with the FISHNET. This configuration produces a fully turbulent boundary layer, which ends up thicker near the fins. Simplifying it, considering that the growth rate for turbulent flow is greater than for laminar, and the thickness is proportional to x/**L**, one may imagine how thick the layer will end up being. The longer the turbulent region, the thicker the layer will be at the end.

However, with increasing AoA, the Smooth configuration, due to its laminar portion, has earlier separation lines, generating thicker lateral vortical wakes, which reduce the dynamic pressure on a larger portion of the fins. The FISHNET configuration, due to its turbulent boundary layer separates further downstream, sustaining greater increases in AoA with thinner low velocity layers and regions than the Smooth. Then, given the turbulent boundary layer, the AIRSHIP can go up to higher AoAs producing thinner low velocity regions compared to separation or vortical wakes. This allows the FINs to be more effective, since large portions of them are immersed in the outer flow (greater dynamic pressure), and this appears at last as an increase in C_L.

For C_M a direct reflex consequence of the last described phenomenon with C_L can be seen. For smaller AoAs, with rough surface, the fins seem to be less effective, and consequently more unstable when compared to the smooth surface case (Figure 232 and Figure 233). Nevertheless, differently from what was expected, for greater AoAs, the rough configuration also appears to be less stable.

Figure 232 - Moment polars for S0 FINs with different roughnesses.

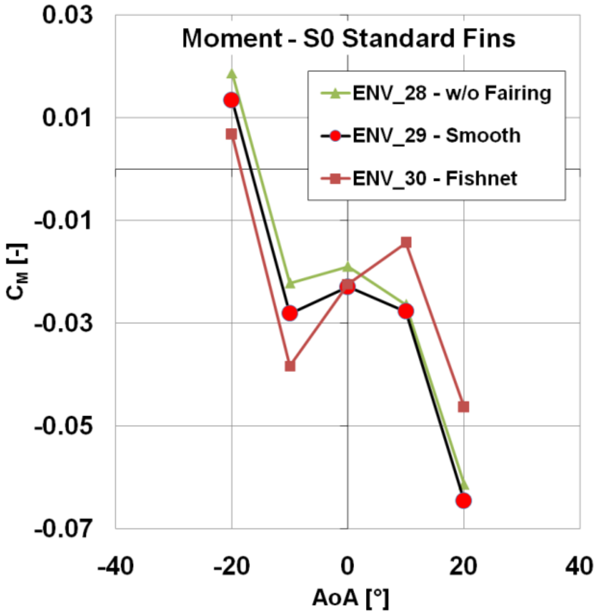

Source: Author (2018).

Figure 233 - Moment polars for S1 FINs with different roughnesses.

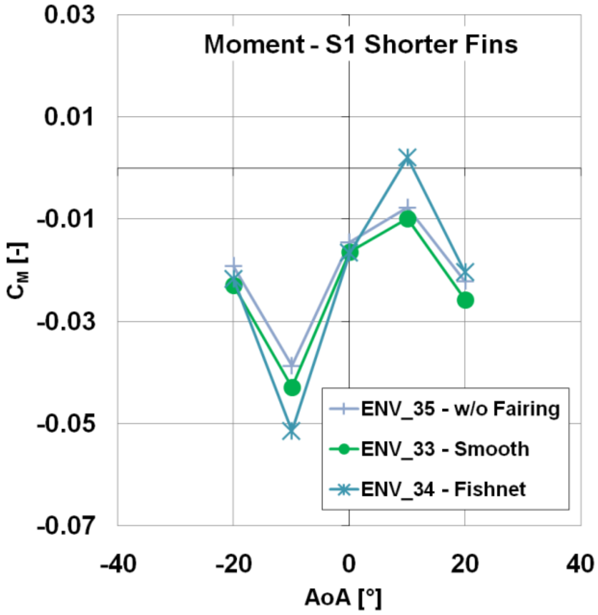

Source: Author (2018).

Apparently, although there was an increase in the lift produced by the fins (Figure 228 and Figure 229), it seems it was not enough to assure the required restoring pitching moment. This may indicate that drag plays a significant role in C_M estimation, differently from what is usually considered for conventional aircraft, given, in the latter case, the small arm lengths to the CG, and the smaller force values as well.

In order to assess this, xCP was calculated (estimated) using C_D, C_L and the original C_M (at 50%**L** - i.e. value directly measured by the balance). The schematics describing the procedure are shown in Figure 234, where Lift will be "L", Drag will be "D" and Moment, "M".

Figure 234 - Schematics of xCP estimate procedure.

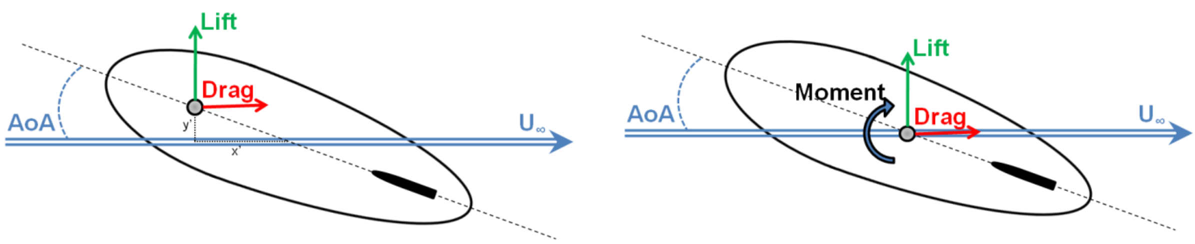

Source: Author (2018).

Based on the diagram, xCP would be calculated as follows, by balancing moments:

$$M_{@50\%\mathbf{L}} = L \cdot x' + D \cdot y' = L \cdot x \cdot \cos AoA + D \cdot x \cdot \sin AoA$$

Equation 53 - Balancing moments equations for wind tunnel model.

Assuming that AoA is small enough so that the length along the body is equal to its projection on the axis, xCP is:

$$xCP = \frac{M_{@50\%\mathbf{L}}}{L \cdot \cos AoA + D \cdot \sin AoA} = \left(\frac{C_M}{C_L \cdot \cos AoA + C_D \cdot \sin AoA}\right) \cdot \mathbf{L}$$

$$\frac{xCP}{\mathbf{L}} = \left(\frac{C_M}{C_L \cdot \cos AoA + C_D \cdot \sin AoA}\right)$$

Equation 54 - Estimate of xCP nondimensional position from axis position.

Assuming that x_{axis} is the nondimensional position of the model axis (pivot or support bar) along **L**, then the nondimensional xCP from nose will be:

$$\overline{xCP} = x_{axis} - \frac{xCP}{\mathbf{L}} = x_{axis} - \left(\frac{C_M}{C_L \cdot \cos AoA + C_D \cdot \sin AoA}\right)$$

Equation 55 - Estimate of xCP nondimensional position from nose.

By comparing C_D and C_L, one can easily observe that, besides being of the same order of magnitude, with increasing AoA, the values also get very close to each other in terms of magnitude. In this way, it is important to verify how relevant the arm length for drag is in comparison to lift. Given that the drag arm is a function of the AoA (Equation 53), the greater the AoA, the greater the arm as well. Also, if CP is ahead of the reference axis (xCP < 50%**L**), the drag will always contribute as a destabilizing force (i.e. in favor of |AoA| increase). For the evaluated AoA, assuming the worst condition, where CD ≈ CL, drag moment could be up to 40% of the lift moment. In this way, it makes sense that a configuration with greater drag provides also greater destabilization for a certain condition.

Figure 235 - Moment polars around 50%**L** for S0 FINs with different roughnesses showing the respective xCP for each AoA.

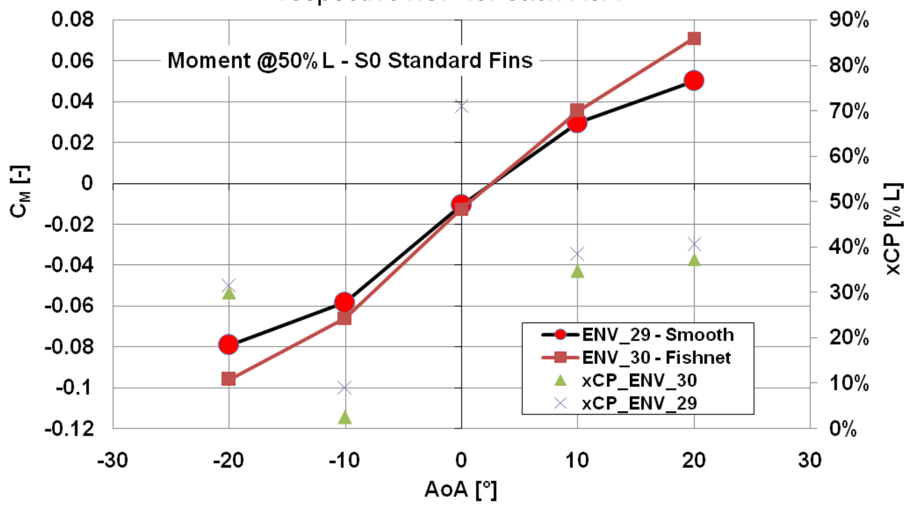

Source: Author (2018).

By analyzing the C_M at 50%**L**, for Smooth and Fishnet configurations with Standard (S0) FINs, one can easily see that the Fishnet is always less stabilizing than the Smooth. This has a direct relation with xCP. It is a fact that the CP travels forward with increasing AoA (the suction peak moves forward, unbalancing the pressure distribution towards the leading edge). However, once separation begins to be relevant, and stall conditions appear, the CP moves backwards again (Figure 236).

Figure 236 - CP travel for a typical airfoil with AoA.

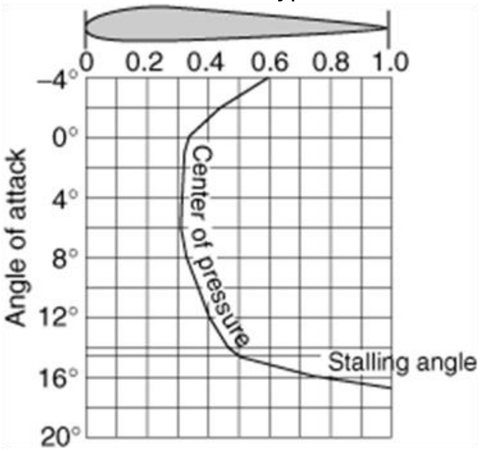

Source: Aviation dictionary (2018).

In this sense, assuming that the Smooth configuration has an anticipated separation in relation to Fishnet, the xCP for this later configuration will always be much forward. Even if separation is negligible for comparison purposes, the more turbulent boundary layer (thicker) shifts xCP forward, for any given AoA, as the suction is higher due to greater edge velocity. In this way, since the most forward xCP is, the more unstable the configuration will be for the same forces, the results from Figure 235 seem adequate. This all supports the proposed explanation, and also matches the estimated xCP for each case. In the studied range, all calculated xCP were ahead of the reference axis (support bar at 50%**L**), indicating unstable curves for both configurations.

As conclusions from this, there are two worthy remarks; the first is that, if it is desired to easily assess standardized stability it is important to conduct the tests around the model CB. This point, which is usually vertically aligned with CG, may be assumed for airships – flying near to equilibrium condition - as equivalent to the neutral point for conventional aircraft (section 3.2) - or the aerodynamic center for airfoils, and therefore drag and lift forces would not need to be transported. If it is not done this way, both forces must be transported as explained above (Figure 234), meaning that drag may not be neglected.

The second remark is specific for this X-tail aircraft configuration (Figure 137 – the ADB-3-30, AdB's project described in section 1.2). Considering that the CB is at 46.7%**L**, both fins configurations, Standard and Shorter, show static unstable characteristics around the CB. This means that either some sort of feedback assisted control must be implemented, or the surfaces must be redesigned, considering only static stability results. However, it is important to once again emphasize that, for airship, longitudinal stability is essentially ensured by the pendulum mode stability (relative positive between CG and CB), and for the analysis carried out here, this point (dynamic stability) is missing. It is always interesting to recall that stability is related to a certain reference point; for conventional airships, usually the CB-CG station is the reference, and those two points are usually vertically aligned to improve longitudinal stability, through the above mentioned pendulum mode (section 3.2).

At last, still for C_M, when comparing Standard (S0) and Shorter (S1) configurations, however, an expected result shows up: larger surfaces provide better stability characteristics. Indeed, the Shorter configuration is relevantly more unstable for small AoAs than the Standard (Figure 237). Besides that, the fins effectiveness for the Shorter was already shown to be much smaller as well (Figure 228 and Figure 229).

Figure 237 - Moment polars comparing S0 and S1 FINs sets with differente roughnesses.

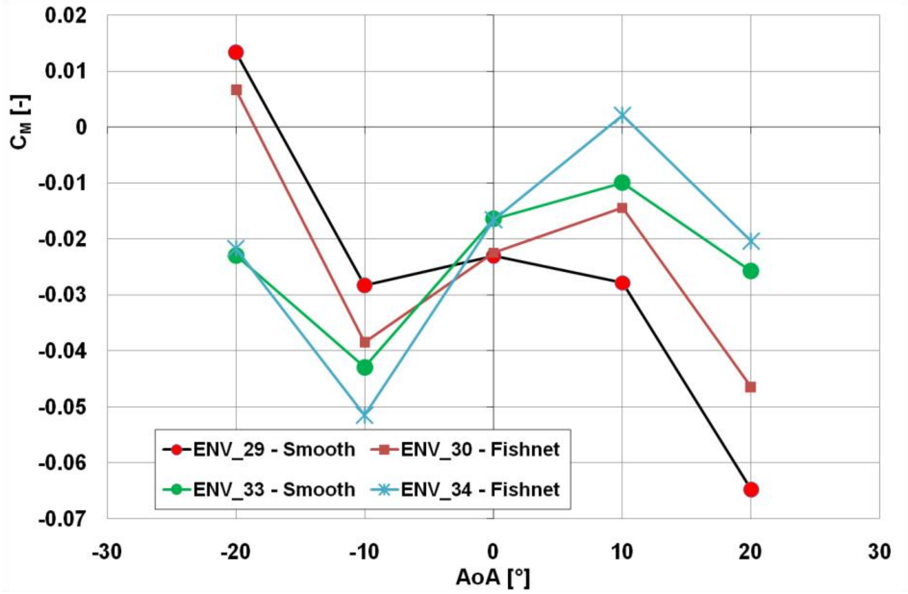

Source: Author (2018).

For the same AoAs, and above |AoA| = 10° – region where the configuration gets locally stable in relation to 25%**L** (Figure 237), the Standard configuration reaches more than 200% of C_M values for S1. Also, looking at $C_{M\alpha}$ as a whole, by means of a linear regression, it is possible to see that curve derivative can be slightly neutral to positive for the Shorter configuration (Figure 237). This attests an overall unstable tendency. Although some short stable regions exist, they converge to unstable regions again considering dynamic changes of AoA. With such a behavior the configuration would have issues with dynamic stability, even considering pilot inputs.

Almost all previously studied C_M curves had 25%**L** as reference. In order to assess how the moment would behave considering different references, C_M was mathematically transported to different hull stations, considering only C_L for transportation (Equation 56), disregarding C_D for simplicity.

$$C_{M@x1} = C_{M@x0} + C_L \cdot (x1 - x0)$$ Equation 56 - Moment transportation.

, where

$x1$ = desired longitudinal position of moment reference divided by **L**, [-]
$x1$ = original longitudinal position of moment reference divided by **L**, [-]
$C_{M@x0}$ = C_M at original position, [-]
$C_{M@x1}$ = C_M at desired position, [-]

Five positions along **L** were chosen for comparison: 0%**L** (nose), 10%**L**, 25%**L** (standard results plot), 50%**L** (axis/support bar position) and 75%**L**. The results are plotted in Figure 238 and Figure 239.

Figure 238 - Moment polars around different longitudinal positions for S0 FINs.

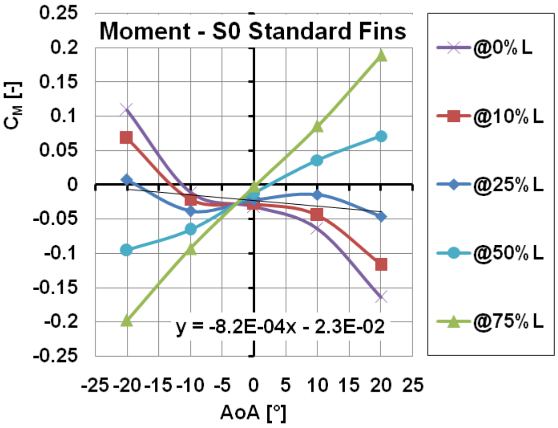

Source: Author (2018).

Figure 239 - Moment polars aorund differnet longitudinal positions for S1 FINs.

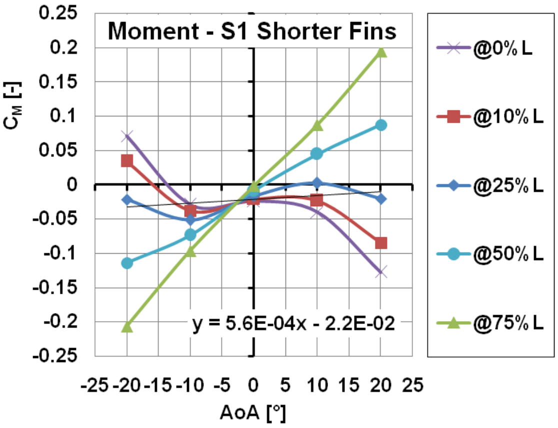

Source: Author (2018).

This analysis shows that the axis position for static stable characteristics would be far forward, between 10%**L** and 25%**L**, for both configurations; obviously more forward for S1 than for S0. By comparing the overall $C_{M\alpha}$ to the one corresponding to where all bodies would be stable, i.e. bow (0%**L**), based on the trend lines, it is possible to conclude that Shorter FINs provide around 70% of the Standard configuration stability – derivatives, this comparison being based on a linear regression of the whole curve. Nevertheless, S0 is clearly statically stable throughout the whole range, which is not true for S1. The Shorter FINS present an almost neutral middle region (small AoAs), even around the bow.

Figure 240 - Moment polars around nose for S0 and S1 using Fishnet.

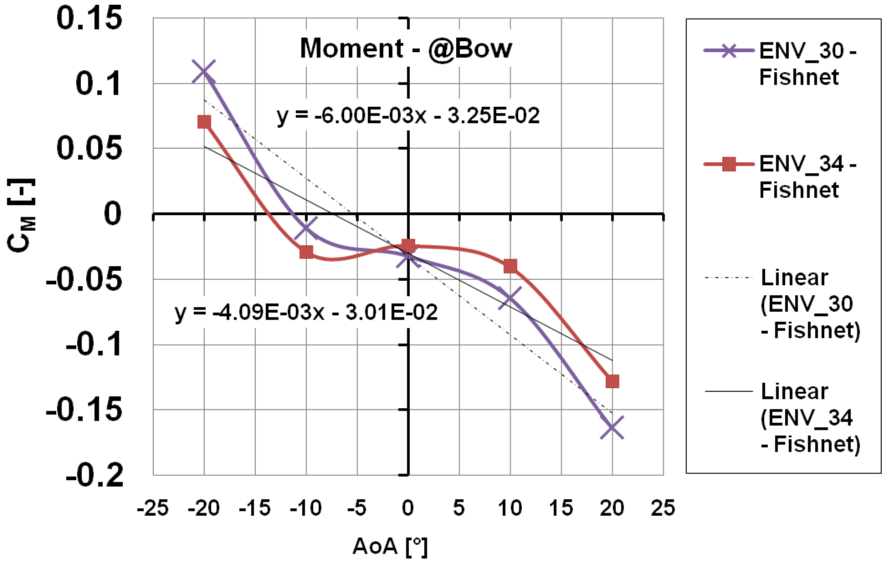

Source: Author (2018).

This (Figure 240) shows some relation between areas, stability quality and generated lift, at least for this fin planform, recalling that S1 has 79% of the S0 FIN area. It is important to remember, however, that this C_M is referenced to the bow. Doing the same proportion calculation, but using results from around 50%**L**, one obtains that S1 is 25% less stable than S0, i.e. both are qualitatively similar. However, trying the same exercise for 25%**L** leads to failure, since S0 is slightly stable, whereas S1 is unstable, by similar order of magnitude. Despite the difference, the ratio between the magnitudes is 68%, although no direct reason was found. Moreover, inspecting the relation between both, S0 and S1, around 75%**L**, results in an even more surprising information: both show the same instability regarding $C_{M\alpha}$. Apart from the fact that the estimate transportation of C_M disregarded drag, it seems to be difficult to link directly FIN area with $C_{M\alpha}$. However, as a mental note, for the CB and bow regions, the ratio seems to fit reasonably.

As an overall conclusion, the comparisons of different FIN sets definitely showed that, although boundary layer and vortices exert strong influence on the tail, there might be some trend or possible "rule of thumb" that could be established to conceptually predict airship stability quality. The expected relations between FIN area and stability were qualitatively observed, although the configurations were shown to be, as a whole, statically unstable for pitching moment around the CB.

For this “rule of thumb”, this work proposes the TVC method, which is presented and described in section 3.2.2.3. The calculated TVC for both configurations, S0 and S1, would be 0.16 and 0.13 respectively. Compared to the reference values (0.10 < TVC < 0.15 from section 3.2.2.3) and assuming them as correct, the values would indicate them as stable. This leads to the conclusion that some further investigation must be carried out in order to assess how to adjust the TVC parameter, so that it reflects not only an initial tail sizing, but stability characteristics as well.

5.3 PHASE II: STABILITY CHARACTERIZATION RESULTS THROUGH DYNAMIC TESTS

To better generalize the results regarding stability quality, it was decided to assess TVC mainly by means of free oscillation tests, which would simulate an uncontrolled motion of the airship, referenced around the support fixation. The oscillation will simulate yaw free oscillation, close to what would be the yaw subsidence mode (section 3.2.1) if the dynamic properties and flight condition (degrees of freedom) were well simulated. It is important to highlight that, although the results here led to interesting observations and trends, essential terms, such as the virtual mass and inertia obviously did not play here the same role they would in full scale. The model mass is around 4.0 kg, while the estimated buoyancy is 0.054 kg (≈1.4%). They are therefore out by the same order of magnitude, and this excludes their relevance on the dynamics (KHOURY, 2012). In this way, it is important to make it clear that the dynamic tests carried out are essentially free oscillations aerodynamic damping evaluation, and are not meant to simulate the dynamics of the airship flight.

5.3.1 Parameters adjustments

For the dynamic tests, based on the results obtained previously regarding longitudinal stability references (section 5.2.4), the axis was moved to 38-40%**L**[44] for the directional oscillation. Besides that, the support bar was changed for a much thinner one, with no base plate, making it possible to attach the model directly to the

[44]Measuring with precision the exact position of the axis was unviable given the model curvature; 2% difference is equivalent to around 20 mm. The position is assumed as 40%**L**.

RAS. This thinner bar, however, had a lower stiffness, which gave the model some longitudinal oscillation freedom. The tests were carried out anyway, always being attentive to the results, and physical observations.

All runs were video recorded, so interesting frames could be extracted later on. The model was moved a little downstream in the working chamber, avoiding the "turntable", since it required a rigid fixture. It also went down by a few centimeters given the length of the new support. None of the cited changes were considered relevant for the final results, as the model blockage ratio was still approximately the same (3% for AoA = 0°).

A series of test runs was conducted in order to adjust the model to the test requirements and assess how the instrumentation outputs should be so as to better sample them. This was necessary as dynamic testing is not usually as straightforward as steady tests. The results were logged at a sampling rate of 1000 Hz, for time lengths varying between 10 s to 40 s, depending on model damping. Almost all comparison charts are plots of only the first 20 s of oscillation. This provided between 40000 and 10000 test points for each test run.

After the first evaluations, a problem linked to the support bar (axis) was noticed right away: given the lower stiffness, the velocities could not go up to the previous test runs (Phase I), and no other stiffening system could be easily adapted to the RAS. As a consequence, velocities went up only to around 12 m/s for S0 and 16 m/s for S1. The corresponding *Re* were 8.0E+05 and 1.1E+06. This ensured that longitudinal oscillations kept to a minimum, avoiding combined effects. In any case, even allowing for lower velocities, the results were worth obtaining, and their interpretation led to relevant conclusions, as shown below.

5.3.2 Results processing methodology

It is important to mention the topic of data processing as for this Phase II this process was much more complex. While in Phase I forces were quickly converted to coefficients, in Phase II a much more complex mathematical work was carried out in data reduction, i.e. in converting raw data into readable results. Briefly, as described in section 4.4.2, the tests carried out by holding the model at a sufficiently (visually) large β, turning on the wind tunnel, waiting until flow stabilization and then releasing the model, letting it to free oscillate. The oscillation was tracked by a potentiometer, whose voltage level with time was comparable to β variation.

Once the resulting voltage data (as explained in section 4.4.2) was obtained, although clear trends did show up, it was decided that the noise level was too high to make practicable comparisons of results. In this way, each data set went through a first frequency filtering process, so noise in signal could be suppressed, and the damping curve could be better identified as a result.

By using Matlab™ built-in functions, the Savitzky-Golay FIR smoothing filter (function "sgolayfilt") (MATHWORKS, 2017) was applied to each obtained data set. This filter was chosen, because among the quick filtering options available, this one provided the best results regarding visual curve trend preservation. A fifth-order model was chosen, considering a frame length = 1001. The filter parameters were also adjusted visually, using well behaved curves such as free oscillations at wind-off conditions. Figure 241 is an example of data before and after filtering technique application. The data points were connected through lines without dots, although the results are experimental, in order to clarify the trends. With markers, the data scatter would end up being too thick, making it difficult to properly visualize it.

Figure 241 - Raw and filtered output example using “sgolayfilt” function.

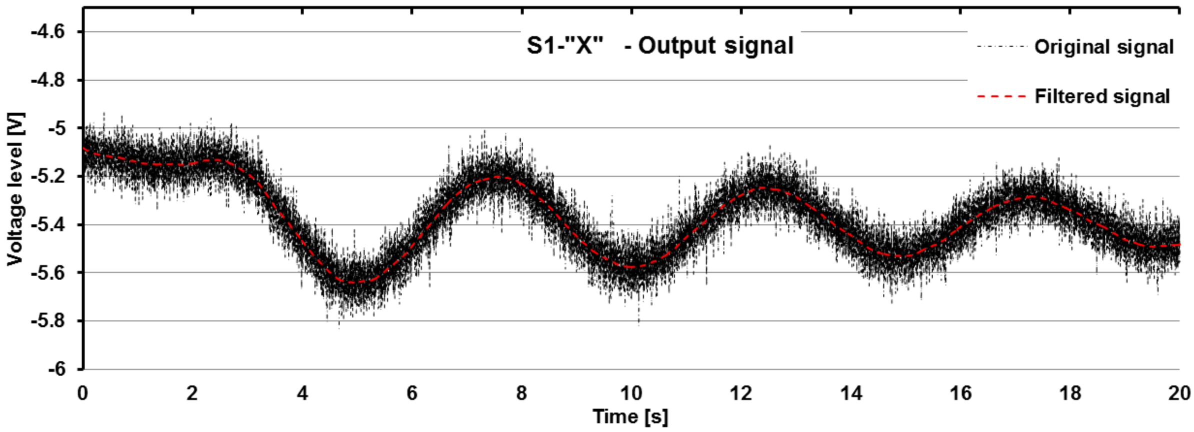

Source: Author (2018).

With all results filtered, the resulting curves were much better defined for the subsequent mathematical work. As expected, they all showed an exponential sinusoidal decay trend, typical of damped oscillation cases. Based on this, a non-linear regression technique was applied. The proposal was to fit all curves using a general equation (Equation 25) so they could be compared in terms of numbers (quantities), and not only visually.

The mathematical approach was comprised of two steps. Firstly, using this time Excel™, for each test run, the parameters of Equation 25 were set by hand to values that, through visual comparison, provided shapes very similar to the filtered curve. Then and secondly, the curve adjustment was improved by means of a nonlinear optimization algorithm.

The previous step was very important, since it provided good starting points for the iterative model to improve the fitting. A “GRG nonlinear” solver (FRONTLINESOLVERS, 2017) was selected, and all parameters of Equation 25 were set as variables. The process was controlled by minimizing the squared difference between function results and filtered results (“sgolay” output). The convergence criterion was set as 1.0E-04. Although such optimization algorithms usually provide locally optimal solutions, since the starting point was good and all results were visually checked against the original data, it was assumed that the mathematical models were adequate for the desired purposes.

Figure 242 - Examples of proposed curve fitting results for real oscillations obtained for configuration S1-"X" at different velocities.

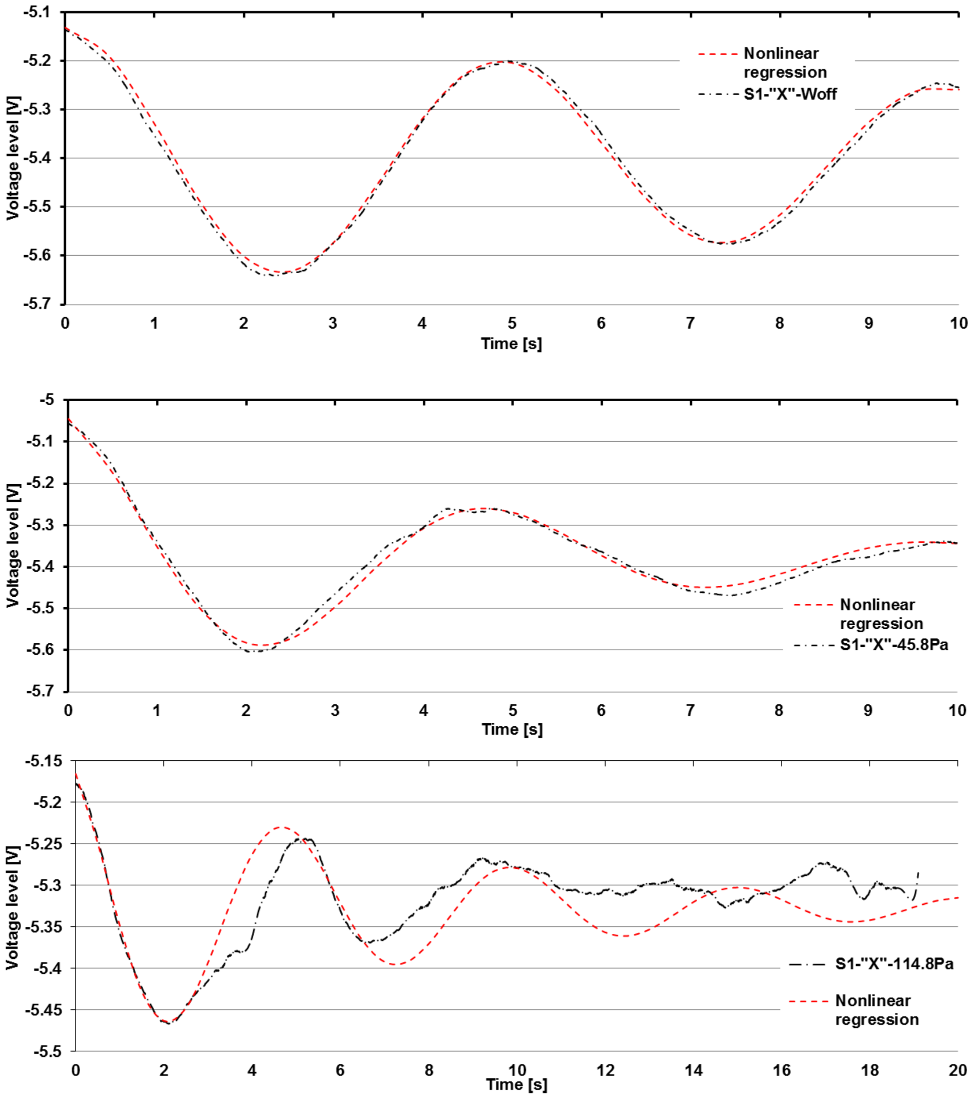

Source: Author (2018).

Figure 242 presents three different examples of curves obtained through the described procedure. It is possible to see that some fit better than others, but this has much more to do with the tests physics then with the math models. In other words, improving the math models would not improve the regression much, because the captured oscillations were somewhat problematic. Besides that, using mathematical models very different from those from oscillatory motion theory would not allow an easy comparison, as is expected. Specific observed issues regarding measured data are discussed ahead.

As already explained, the main objective was to compare the damping characteristics, i.e. the outer envelope decay curve (Figure 46). The adjusted curves were all shifted to the zero voltage signal level, because the oscillations occurred around the power supply level input, i.e. around approximately 5V. Nevertheless, after the results of interest were selected, for clarity purposes, the curves were shifted to the zero voltage level, considering a vertical translation of the regression results obtained using Equation 25, for each of them.

All results were also normalized by dividing the original voltage by the obtained fit function amplitude (“A” of Equation 25). Some of the curves do not start at |V|=1, because of the issues described in section 5.3.3.

Using results for the configuration S1-"X", all steps of the mathematical procedure are depicted. Figure 243 is the filtered data, followed by Figure 244, which is the nonlinear regression obtained through Excel™.

Figure 243 - Filtered outputs for S1-"X" configuration.

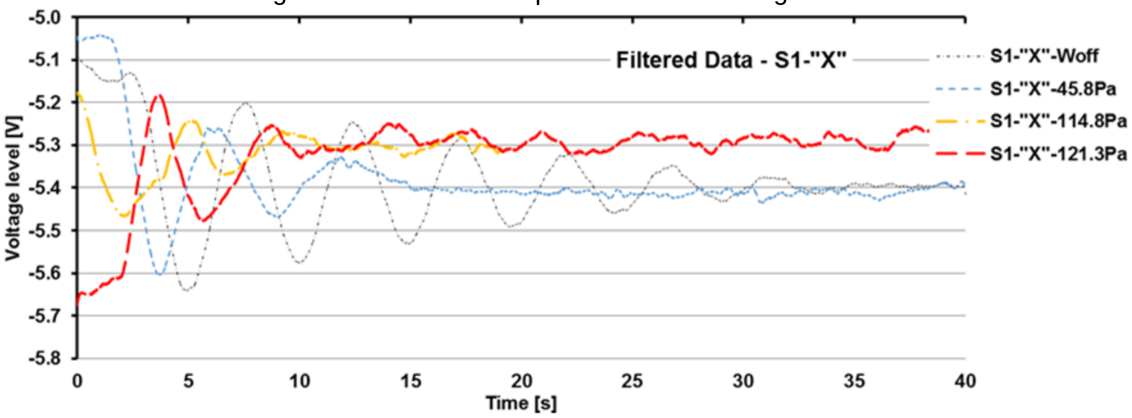

Source: Author (2018).

Figure 244 - Nonlinear regressions used for S1-"X" configuration.

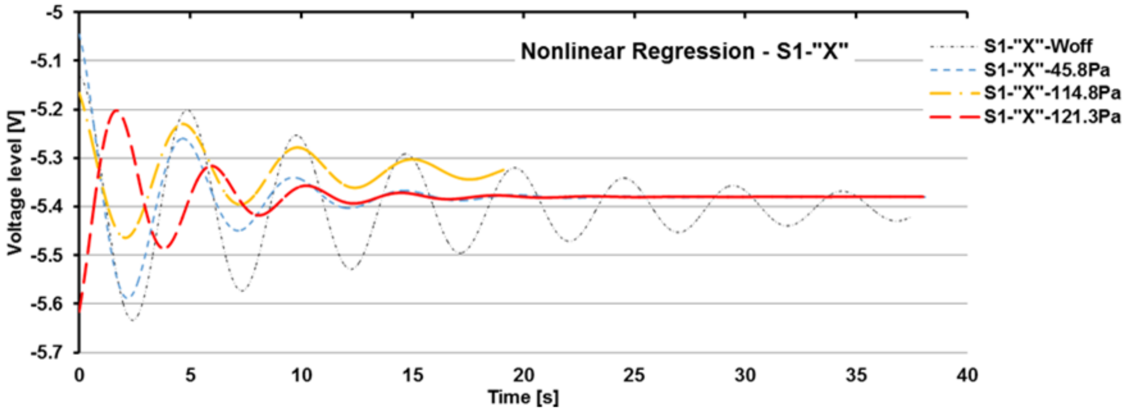

Source: Author (2018).

It is important to explain that, in Figure 243, the almost straight voltage levels before oscillations correspond to the signal level while the model was held tilted. Once it is released, the level immediately decays, and the oscillations begin. Those levels were mathematically eliminated before doing the regressions. As described, the curve fittings were normalized and shifted to the reference zero level to facilitate comparison (Figure 245), and the exponential decay envelope was plotted (Figure 246), providing an easier way to compare stability levels (damping ratio).

Figure 245 - Normalized and translated nonlinear regressions for S2-"X" configuration.

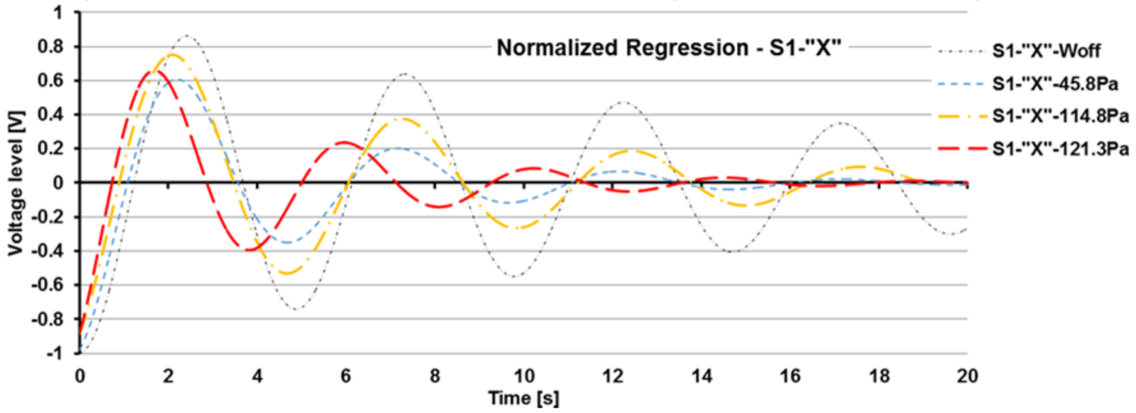

Source: Author (2018).

Figure 246 - Exponential decays obtained for S1-"X" configuration.

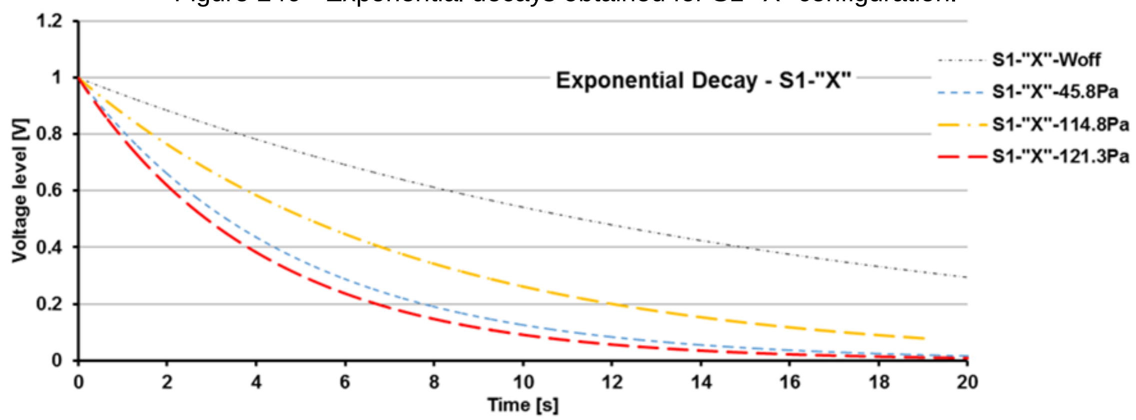

Source: Author (2018).

After all this mathematical work was carried out, it was finally possible to compare results, and assess stability quality

5.3.3 Early results assessment

These S1-“X” results were selected as examples to start with in order to highlight a phenomenon observed during the dynamic test runs, which was clearly observed then. With increasing velocity, the stabilization level diverges from the voltage reference (around -5.3V for Figure 243). This supports what was proposed in section 5.2.3, i.e. that there is some sort of asymmetry in the model, probably related to fins mispositioning. One may conclude that, because with increasing velocity fins efficiency improves, and the generated lift increases as well. This situation induces the AIRSHIP to stabilize under a negative β. It is important to remember that, during Phase II, AoA becomes β, because the AIRSHIP is now oscillating around its vertical axis for all tail configurations.

Recalling section 5.2.3, it was concluded that the fins were misplaced positively, this being reason why the curves had offsets to the negative side of AoA. Here the same effect is seen, and the explanation should be exactly the same. Figure 247 shows the model stabilized at a negative β for the wind-on condition. By observing the tufts, it is possible to confirm that the observed side is the lower side.

Figure 247 - Sequential frames for the model stabilized at negative β; wind-on condition.

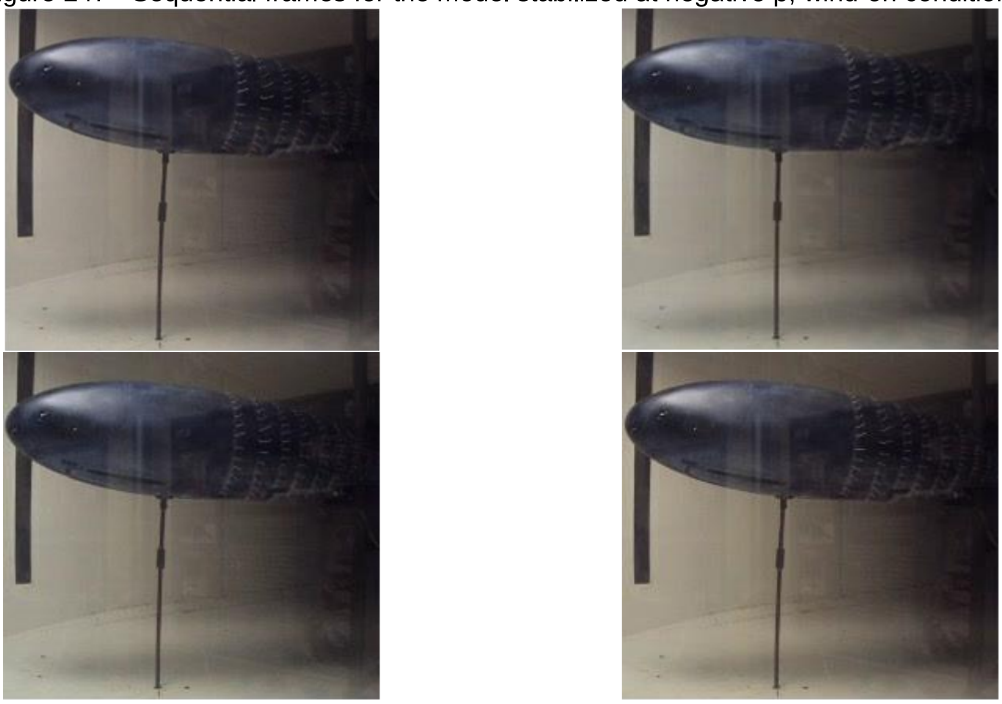

Source: Author (2018).

The sequential frames (Figure 247), taken at intervals of 1 second, also allow one to observe the model oscillation given the low axis stiffness. The frames were cut using the same reference. It is possible to see that the hull varies its attitude and the axis bends, with variable deflections.

Another interesting result are the effects of the initial perturbation (amplitude and position). Although results for 121.3 Pa and 114.8 Pa were obtained at almost the same velocity, the oscillation input was made around different references. For the 121.3 Pa case, the standard procedure was followed, the AIRSHIP model being held until flow stabilization. In the second case (114.8 Pa), the model was let stabilize with the flow, and then was disturbed around this physical zero (effectively a negative β), but with a smaller input. For this second case, the normalized exponential decay is fairly smoother. For the 121.3 Pa case, however, the exponential decay is stronger at the very beginning until the model reaches the offset position. From there on, the decay reduces drastically, and the model oscillates, while reducing amplitude, still for some period around the new reference (Figure 248).

Figure 248 - Filtered and Nonlinear regression oscillation outputs for S1-"X"-121.3Pa.

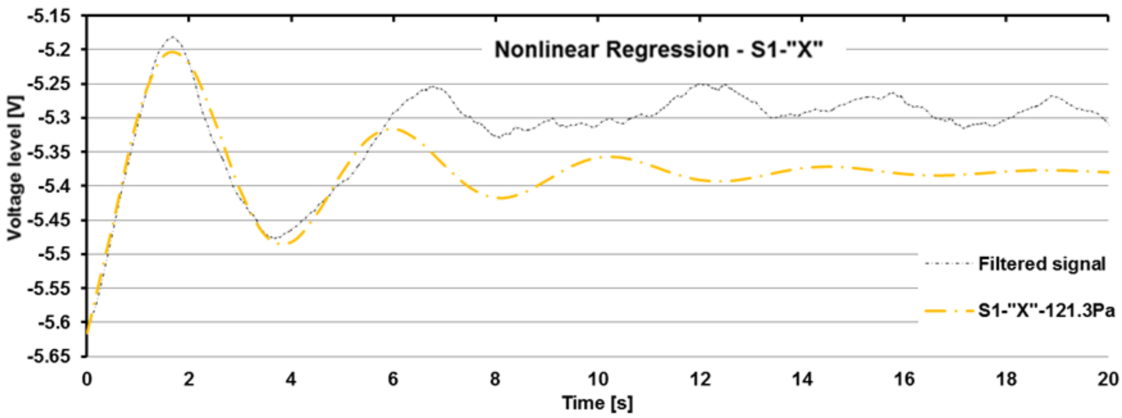

Source: Author (2018).

This is a direct materialization of what was seen for C_M in Phase I. For high AoAs (which here are β), the model presents a stronger stable behavior (higher negative derivative value - $C_{M\alpha}$), while at small AoAs the stable region is much reduced, being even unstable in some cases (Figure 240).

It is interesting to analyze what this means physically. If an unstable region is reached, it leads to an increase in AoA. However, at increased AoA the AIRSHIP becomes stable again, decreasing AoA until it reaches the unstable region again. This cyclic behavior keeps indefinitely until enough oscillation energy is lost in the RAS or some control input is made, in the case of a real aircraft, so as to subside such oscillation. This is somewhat similar to the pendulum mode stability with due proportions, and considering the lack of full representation of the dynamic characterizes of the model.

This phenomenon is the reason why the later portion of the filtered data decays, but very slowly (Figure 248 is an example). For such portions, however, the mathematical model provides a constant mean value level. Technically it is the same sort of result that would be captured if the model had indeed converged and stabilized. It is important to highlight that, if the above interpretation is correct, the transition region between stable and unstable (or less stable in most cases) is very short, when it exists, because no global divergence is observed, only local perturbations. This conclusion may be confirmed by checking the $C_{M\alpha} = 0$ extent in the results (section 5.2.4). It is clear that the corresponding AoA range is rather small, therefore indicating that the assumption/explanation just made is quite credible.

Despite this change in oscillation reference, the results were considered adequate, since the damping effect was properly addressed, i.e. typical decay curve and logarithmic decrement (***b***) were obtained. Those residual small oscillations do not strongly affect the calculated damping ratio, and were present in almost all results (except for those highly damped). Furthermore, such oscillatory movement is a consequence of the actual dynamic stability behavior of the AIRSHIP explained above, but does not represent the initial damping, which was considered more relevant.

A final remark during this early assessment is that, when fitting the curves, care must be taken in order to make sure that the important portion is well fitted. For both cases discussed above (121.3 Pa and 114.8 Pa - Figure 246), the exponential decays could end up being very similar. This would make sense, if focusing the fitting on the final portion, once the final damping is similar for both. However, it is not the final damping behavior that is being prioritized, but the initial. This shows that the way the filtered data is treated in the fitting was a key process. It may become somewhat difficult in cases where local oscillations take place, like in the two discussed. For this reason, during the calculation of the error for the regression convergence, a feature was implemented so specific portions of the signal could be better fitted than others.

Discussing about the physics, these final small oscillations may be easily treated by the pilot on a real flight, or be acceptable in some cases, not being the best way of representing AIRSHIP stability. It is also possible to say that the final residual oscillations have something to do with turbulence, model degrees of freedom (support stiffness) and noisy results, besides the actual physical characteristics. This reinforces the decision to focus on the initial portion of the oscillation.

In order to better illustrate this question, the result for DYN_015 was fitted in two portions. Two different regions were delimited: one representing high β, and the other representing small β. The resulting fittings (oscillations and decay envelopes) are plotted on the top of filtered data (Figure 249).

Figure 249 - Filtered output for S1-"+"-38.6Pa configuration, showing different damping characteristics over time.

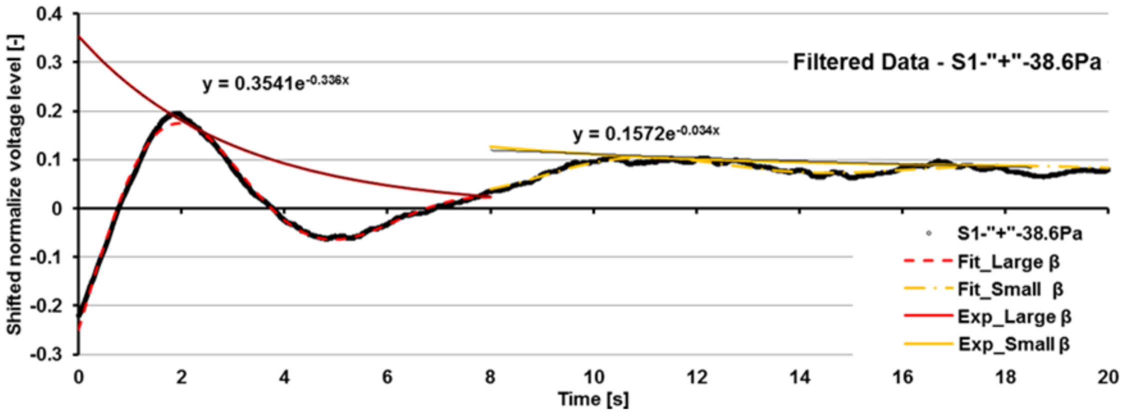

Source: Author (2018).

Then, in general, the fittings were applied to the first portion of the filtered signals obtained, capturing the initial and stronger damping effects of each configuration. The final portion, where oscillations are reduced (lower amplitude), were considered to be a good fit if the period and decay matched fairly between the dislocated portion and the proposed regression (Figure 248). As a consequence, the reference offset shown in Figure 249 was translated, but the behavior of the oscillatory motion was made equivalent.

With the results processing cleared, and the main phenomena pointed and explained, it is then possible to investigate the actual results in fact. Using the described theory from section 3.2.2.1, the values for natural frequency, damped frequency and damping ratio were determined for all cases, as discussed below.

5.3.4 Results for S0

The results for the Standard configuration (S0) showed underdamped oscillations, i.e. $\zeta < 1$. This means that at least some oscillation occurred for all cases before the model could reach the equilibrium position. It is important to recall that the runs for S0 had a mean *Re* = 8.0E+05 (Table 11 - Master Table of Wind Tunnel

Tests; Phase II.). Although that is much lower than what would be expected for a robust simulation, it is important to say that in terms of comparison, it is still in the same range as those used for the Shorter (S1) configuration (*Re* ≈ 75%, and within the same order of magnitude). It was thus possible to provide a qualitatively comparison assessment between FIN sizes and among tail configurations. All normalized oscillations resulting from the nonlinear regression process are presented in Appendix D.

Looking firstly at the wind-off conditions, all results presented a highly underdamped behavior. However, differently from what was expected, the exponential decay for “-Y” was smoother than for the other two cases, which were very similar (Figure 250). Since the wind-off case is more influenced by geometrical and inertia factors of the model and the RAS (springs, friction, etc) than by the model aerodynamic and stability characteristics, this was considered very odd. As the changes in tail configuration were, in terms of inertia (mass) and damping (cross section), almost negligible, the variation expected would be similar to that between “X” and “+”.

Figure 250 - Exponential decays for S0, with different tail arrangements at wind-off condition.

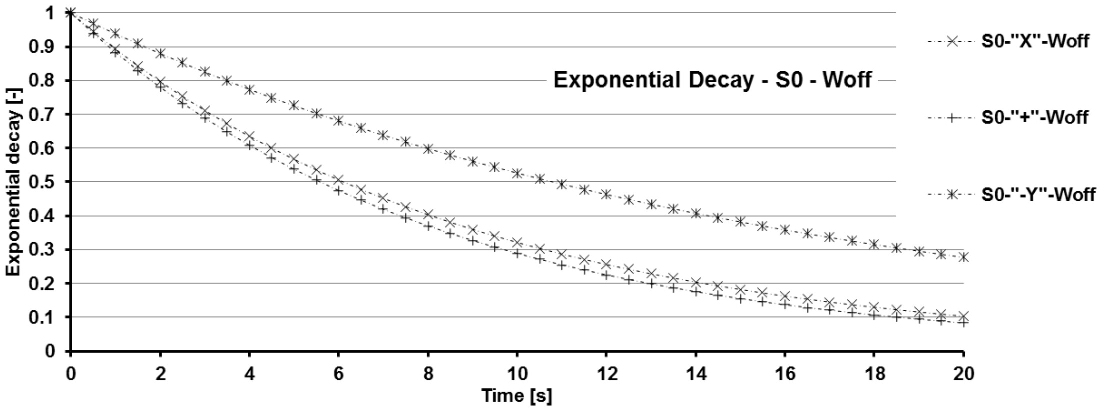

Source: Author (2018).

Setup and results were checked, and a probable explanation for that would be linked to some data acquisition issue. As will be shown ahead, the “-Y” arrangement generated very consistent results, when compared to the other types of tail. Therefore, although such difference was not expected, after checking the wind-on conditions it was concluded that no re-runs were necessary.

Once the flow velocity was different from zero, the expected dynamics appeared, and the results showed relevant changes in the model behavior. The first clear observation, made already during the runs, was that the damping ratios had increased. This is shown by the greater decays, i.e. less time to reach the equilibrium (zero level) position (Figure 251). However, the damping effect was not equal for all configurations.

Figure 251 - Comparison between wind-on and wind-off exponential decays for S0, with different tail arrangements.

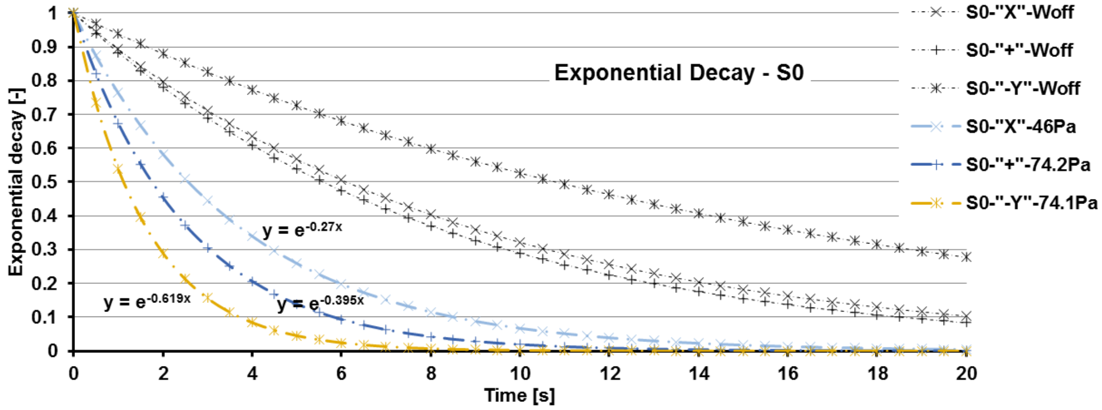

Source: Author (2018).

The three tail configurations ("-Y", "+" and "X") showed well spaced results, and the "-Y" type had the most damped result (230% higher than the lowest case). The "X" configuration, however, differently from what was seen for the wind-off situations, showed the smoothest results, and its ***b*** was 53% of the mean value of "-Y" and "+". Despite the larger tail area (total and projected), which leads to a greater TVC (according to section 3.2.2.3), the velocity for "X" was around 80% as that of the other two cases. Considering a simplistic aerodynamic model, one could expect that the resulting unit forces (force per unit area) on the tail would also be 80%, i.e. 20% lower than that for the "-Y" and "+" configurations.

As a comparison example, and already anticipating some results, for a 15% difference in flow velocities (around 32% difference in dynamic pressure) for the "-Y" (Figure 252), it is possible to see that a 36% difference in decay is observed. Nevertheless, on the other hand, by looking at S1-"X" (Figure 253), a 165% difference in dynamic pressure (around 130% difference in flow velocity) provides an increase of only around 9% in decay.

Although the decay results depend strongly on the curve fitting process quality, which could be considered as responsible for the differences, all cases were assumed as equivalent fitted (Appendix D), by applying the techniques already described. So, based on the results obtained, no linear or simple proportional explanation, based on the flow velocity or tail size, seems to be right away adequate. This shows that probably aerodynamic interference effects play, as expected for such a complicated flow structure, a significant role also in stability characteristics.

Figure 252 - Exponential decays for S0-"-Y" at different velocities.

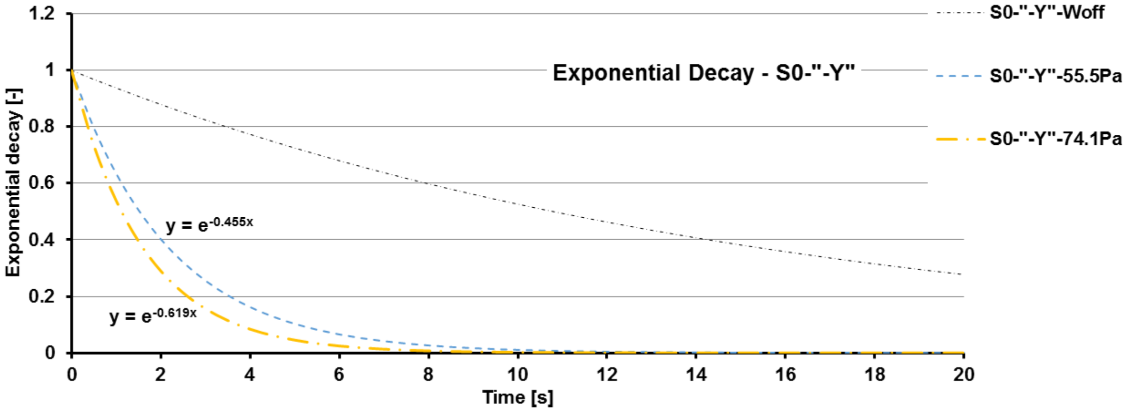

Source: Author (2018).

Figure 253 - Exponential decays for S1-"X" at different velocities.

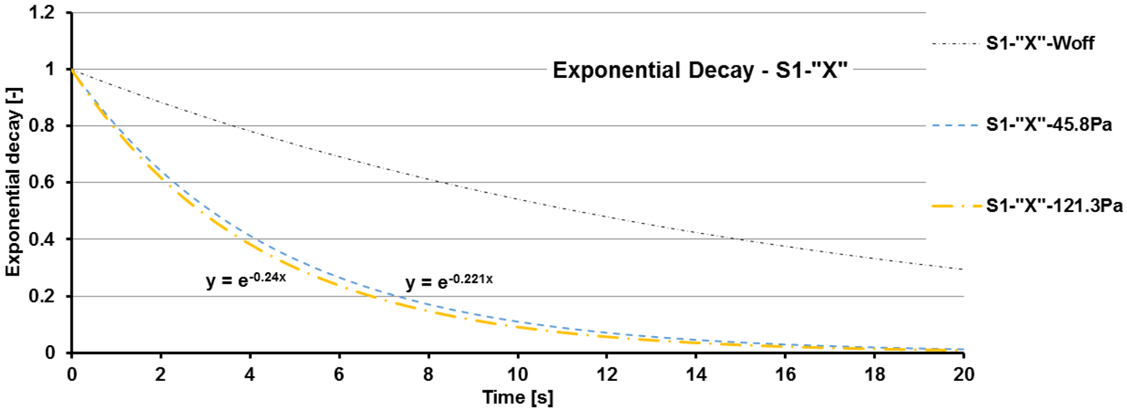

Source: Author (2018).

Proceeding with the investigation on the possible causes, and considering the proposed TVC concept, the three configuration geometries were compared. Adapting the TVC concept, and changing the assumption that the tail arrangement would not be really relevant, the areas projected on the longitudinal plane were calculated for each model.

The calculation results pointed out that, if projecting areas is purely by itself acceptable, neglecting any external influences from aerodynamic flow structures, such as crossflows and vortices, the damping for “X” should be even stronger than the others, because its summed projected area is the largest among the options.

Assuming then that this projection proposal as valid, the model itself was assessed. Through photographs from behind[45], the real projection angle of each fin for each configuration was calculated. It is also important to recall that marking and fabricating the different holes for attaching the tailplane configurations was a very

[45] One must consider that this was a reference method. It is well known that taking reliable pictures, well aligned and positioned is extremely difficult. However, this was a comparative evaluation, and all configurations were subject to the same issues regarding camera positioning, leveling, etc.

difficult task to be conducted with precision. This is because the HULL surface is curved, and referencing the ready-made model (finished HULL) is also complicated, mainly using manual methods (the way it was done in this work). The obtained results for projection angles are registered below, along with the respective pictures.

Figure 254 - Projection angles assessment for "X" tailplane.

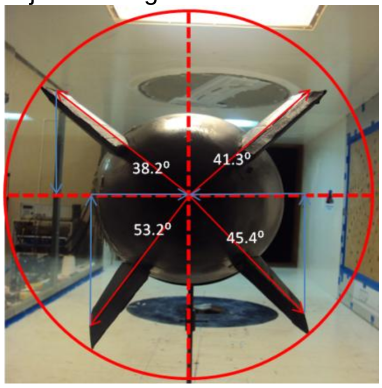

Source: Author (2018).

Table 12 - Projections for "X" tailplane.

"X"	UL	UR	LL	LR	Ideal Projection Factor [-]	Full Projection Factor (FPF) [-]	Deviation
Projection angle [°]	51,8	48,7	36,8	44,6	2,83	2,79	-1%
Projection ratio [-]	0,62	0,66	0,80	0,71			

Source: Author (2018).

Figure 255 - Projection angles assessment for "+" tailplane.

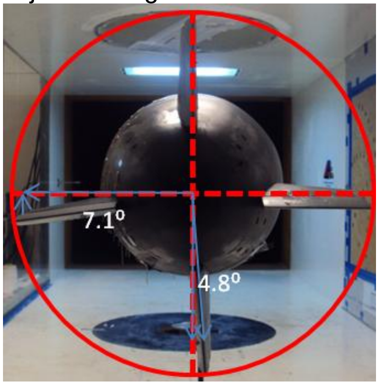

Source: Author (2018).

Table 13 - Projections for "+" tailplane.

"+"	Port	Upper	Lower	Stbd.	Ideal Projection Factor [-]	Full Projection Factor (FPF) [-]	Deviation
Projection angle [°]	-7,1	0,0	-4,8	0,0	2,00	2,12	6%
Projection ratio	0,12	1,00	1,00	0,00			

Source: Author (2018).

Figure 256 - Projection angles assessment for "-Y" tailplane.

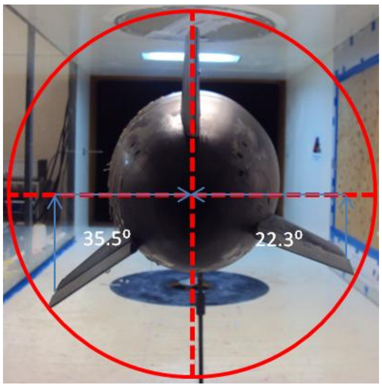

Source: Author (2018).

Table 14 - Projections for "-Y" tailplane.

"-Y"	Port	Upper	Stbd.	-	Ideal Projection Factor [-]	Full Projection Factor (FPF) [-]	Deviation
Projection angle [°]	35,5	0,0	22,3	-	2,00	1,98	-1%
Projection ratio	0,58	1,00	0,40	-			

Source: Author (2018).

Before continuing, while inspecting the FINs for such calculations, other problems were identified, attesting the real complexity involved in precisely adjusting wind tunnel models. The ”+” and “-Y” configurations also had positioning issues. For the “+” case (Figure 257), the upper rudder had a slightly positive fixation misalignment, while the port ruddervator of “-Y” had small positive incidence. Both nonconformities had the same effect: stabilizing the AIRSHIP with a negative β. Only the “-Y” was capable of being fixed considering the available materials, and the model constraints.

Figure 257 - Examples of observed FINs mispositioning for “+” (left) and “-Y” (right) configurations.

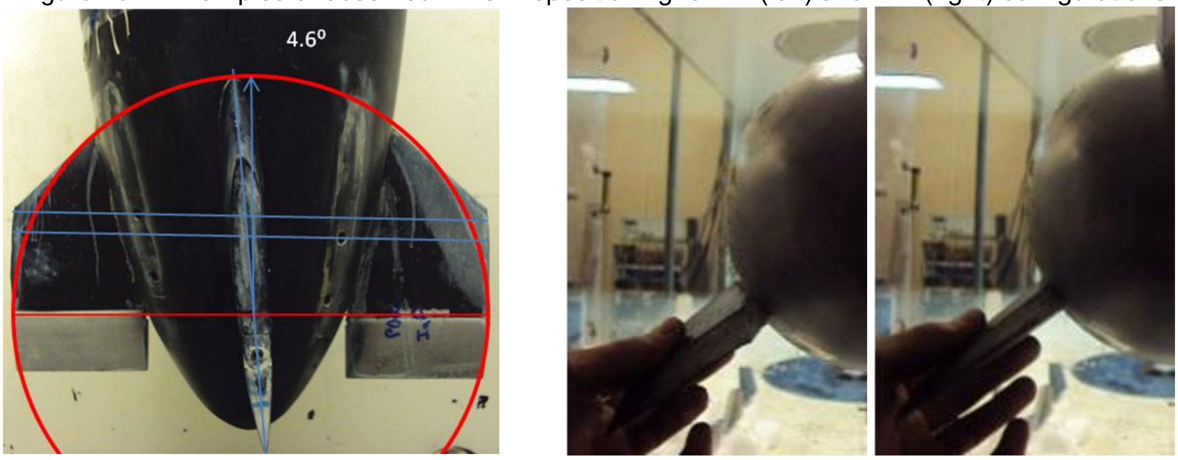

Source: Author (2108).

Continuing with the projection investigation, even considering the errors in misplacement, the “X” configuration achieves the largest projected area. So, considering the proposal that only the projected area is sufficient for a good initial stability estimate, the results for the X-tail should be the best. However, as already shown, they appeared indeed to be the worst regarding damping.

The reason for this must then lie in the complexity of the outer flow characteristics. Recalling the results observed in section 5.2.3.4 at high AoAs, the upper fins on the X-tail configuration are almost completely immersed in the pair of vortexes[46] originated from the vortex layer detachment from the HULL (Figure 128). This effect, which is clearly observable on the BARE HULL, also takes place with the fins in place (Figure 211 and Figure 212).

Given the fact that the “X” configuration has the same aerodynamic behavior in pitch and yaw, if no gondola is present (it would be in a real airship), the same aerodynamic interferences take place irrespectively of the axes. In the case of the dynamic tests, the difference is that some variation occurs with changing sides and intensity, given the oscillatory motion around the vertical axis, i.e. with varying β. This means that the pair of vortexes appears nearer to the starboard side when $\beta < 0$, and to the port side for $\beta > 0$, both on the upper and lower portions of the model (see pattern results in sections 5.2.2 and 5.2.3.4)

Considering this information, and the well-known fact that vortex cores have lower longitudinal velocities than the outer flow, since “linear kinetic energy” is converted into “rotary kinetic energy”, the dynamic pressure on the affected fins decreases. As a consequence of this fact, the lift generated by the surface also decreases, reducing the overall damping effect.

Still, it is important to highlight that these fins are very near to the separation line, on the upper portion of the model (Figure 208). Also, it is relevant to say that the fins on one side may affect the fins on the other. Changes in the flow, such as separations (Figure 213) and corner vortices resultant from the interaction between HULL and FINs boundary layer, as described by Cornish, III and Boatwright (1960) and Lutz et al (2005), and inferred from the oil flow visualization runs, lead to reduced efficiency on the already vortex affected side. This last shading effect is especially relevant in the X-tail configuration, since fins are, to a certain extent, on each other’s wake at high AoAs.

[46] Individually, i.e. one on each side, port and starboard of the model aerodynamic reference.

However, for this explanation to make sense, the other two configurations must be assessed from the outer flow point of view as well, and the resulting behavior must be supported by similar insights. In order to do so, some assumptions need to be made, since the “+” and “-Y” configurations were not steady tested or had their flow footprints visualized. Therefore, BARE HULL patterns and aerodynamic behavior will be combined with the X-tail results in order to predict how the flow would behave for the other two arrangements. Obviously, this approach was conducted considering due proportions and predictable effects, also based on the theoretical framework developed by other researchers (section 3.1).

Evaluating the “+” configuration firstly, based on what is shown in Figure 212, the first conclusion is that the upper and lower fins (rudders) would be out of the pair of vortex wakes. This can be assumed as true by bringing to mind the results predicted by Lutz et al (2005), which show the vortex layer rolling up over the suction side of the fin, but not shading it. In the worst case, they would be partially immersed in it, in a way that the separation line would almost match the stagnation streamline. In this last case, the upper side (suction) of the fins would be on a lower rotary velocity region, while the lower side (pressure) would be on the higher outer flow velocity region. Nevertheless, both fins would be subject to some downwash effect besides the increase in differential pressure. This downwash would be a result of the lateral limiting streamlines converging to the vortex layer separation line (Figure 212). In this way, despite the increase in suction due to the flow, the rudder AoA (in fact, the resulting β) would be a few degrees lower than the AIRSHIP β. Anyway, both surfaces would be preserved, generating lift, and not being shaded, is a much better situation than that for the X-tail.

For the “-Y” configuration, the outer flow is probably a combination of the other two described. The upper fin (rudder) would probably be immersed in some flow very similar to the upper fin for the “+” configuration. This means a surface not shaded, fully functional, with a probable increase in suction, in despite of a smaller β. However, the lower surfaces would be in a similar situation to that discussed for “X”, but with considerable improvements. The first fact related to the geometry is that, while “X” has fins apart by 90°, for “-Y” they are apart by 120°. This makes the shading effect less strong; not irrelevant, but almost. Secondly, the much upper positioning of the fins put them completely out of the predictable vortex wake, making them much more efficient than the “X” fins. Also, considering the inclination of the limiting streamlines which converge to the vortex sheet separation line, one may infer that the left fin (starboard fin) would even have an increase in local AoA (Figure 211). This would increase its lift and drag in favor of stabilizing the AIRHSIP.

As a conclusion, it is possible to say that, from this developed point of view, qualitatively, “+” and “-Y” do seem to be able to provide better damping results, confirming the measurements for the S0. Similar trends were also observed for the S1 configuration as follows on the next section. As a final assessment of Phase II results, these observed interference characteristics were translated in terms of efficiency for the tail. This topic is discussed later, in section 5.3.7.

5.3.5 Results for S1

For S1, the obtained results had a similar trend as observed for S0. All decay curves had $\zeta<1$, characterizing underdamped oscillations. As for S0, all normalized nonlinear regressions are registered in Appendix D. A difference was observed regarding wind-off results when compared to S0. This time, the curves all concurred very well, as is normally expected. Looking closer, it is even possible to see that, even though they are very close to each other, “X” damps better than “+”, which is in turn better than “-Y”.

Figure 258 - Exponential decays for S1 configurations at wind-off condition.

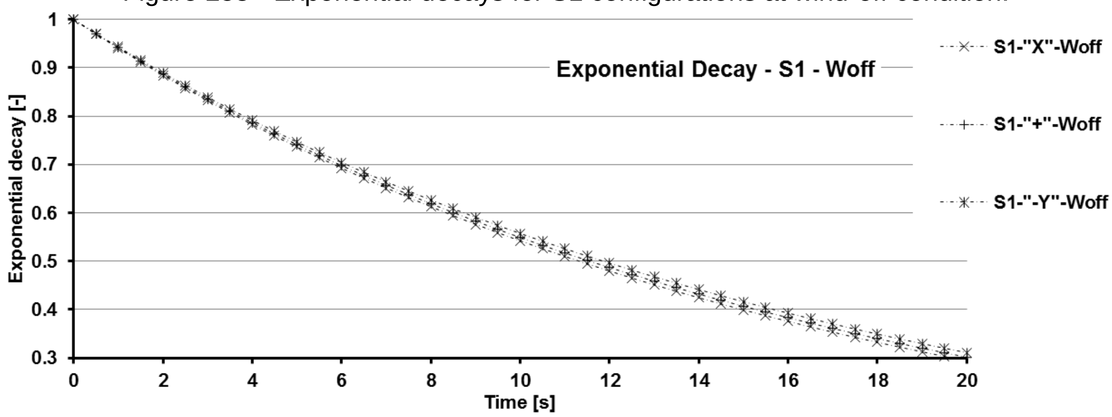

Source: Author (2018).

This result makes sense when assessing the damping characteristics without the proper aerodynamic behavior of the fins, as larger values of area and inertia tend to provide better damping. This should be true, because the drag generated by the FIN surfaces is the main damping factor, when the wind is off.

For wind-on conditions, the same effectiveness observed for S0 was observed for S1, i.e. the “-Y” configuration provided the greater damping effect, while the X-tail was the one with the least damping. The “+” configuration stayed in between the other two tailplane arrangements. It is worth saying that, once again the results for the “X” were obtained under a slightly lower velocity, though in this case being a much closer figure, i.e. around 95% of the other two.

Figure 259 - Exponential decays for S1 configurations comparing wind-on and wind-off conditions.

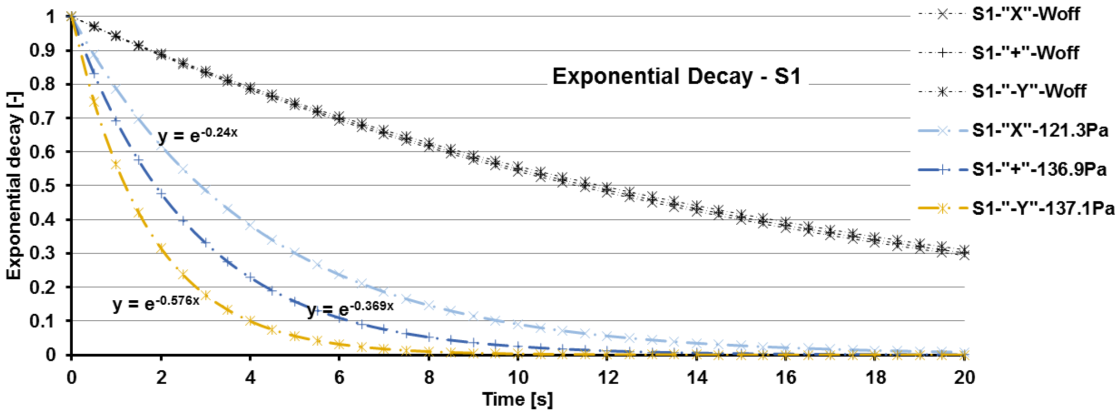

Source: Author (2018).

For this case, however, the curves were much apart from each other. With increasing time, as also observed for S0, “-Y” and “+” get closer to each other before “X” does that. This shows that, despite the wider spread of the curves, the “-Y” and “+” results were still closer, and their mean result is still better than for the “X” configuration.

The results obtained for the S1 set support the proposals presented for explaining the obtained results for S0. The damping efficiencies for different tail arrangements were qualitatively the same. Such an observation shows a trend that can therefore be used to support a refinement of the TVC concept.

5.3.6 S0 and S1 comparisons

Once S0 and S1 were individually analyzed, and that a pattern was identified, as was hoped for, it is relevant then to compare results for S0 and S1. The proposal is assessing how the different individual areas change the results. As shown in Appendix A, one must keep in mind that the S1 individual FIN areas are 79% of the corresponding S0. It was identified that, for the same individual area, there is a well-defined sequence of preferential tail arrangements in terms of efficiency. In this section, the objective is to try and attest that greater areas necessarily increase the damping effect.

Disregarding the observed issue with the wind-off result of S0 - “-Y” configuration, the damping effect increased with increased area as was expected.

Figure 260 - Exponential decays for S0 and S1 at wind-off conditions.

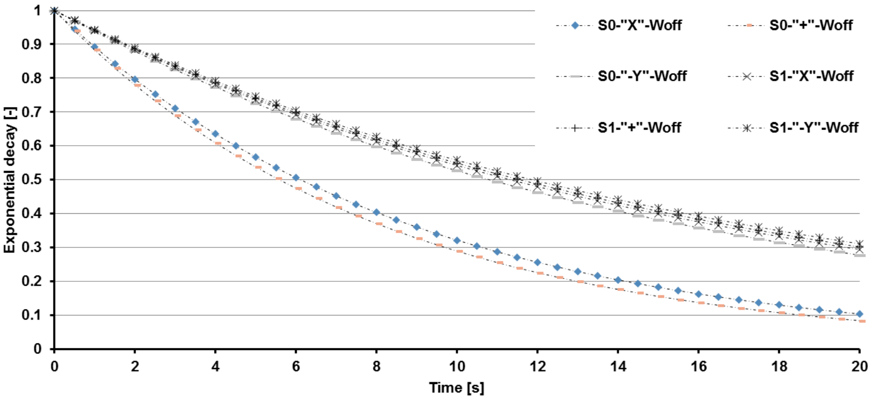

Source: Author (2018).

Although the increases are relevant, no direct connection to the increase in area is observed. The logarithmic decrements for each case are shown in Table 15.

Table 15 - Logarithmic decrements for S0 and S1 at Woff.

FIN set	Tailplane arrangement	Logarithmic decrement - *b*	
		Wind-off	Increase*
S0	"X"	0.113	53%
	"+"	0.124	107%
	"-Y"	0.064	10%
S1	"X"	0.074	N/A
	"+"	0.060	N/A
	"-Y"	0.058	N/A

* Percentage increase is calculated with respect to the equivalent tail arrangement for S1 FIN set.

Source: Author (2018).

The obtained results for wind-on conditions came out as expected. With increased individual area, the damping factors also increased regardless of the tailplane configuration (Table 16). Nevertheless, the identified increase was not as high as expected.

Table 16 - Logarithmic decrement for S0 and S1 at wind-on.

FIN set	Tailplane arrangement	Logarithmic decrement - *b*	
		Wind-on	Increase*
S0	"X"	0.270	12.5%
	"+"	0.395	6.97%
	"-Y"	0.619	7.41%
S1	"X"	0.240	N/A
	"+"	0.369	N/A
	"-Y"	0.576	N/A

* Percentage increase is calculated with respect to the equivalent tail arrangement for S1 FIN set.

Source: Author (2018).

The decay envelopes remained very close to each other for the same configuration (“X”, “+” and “-Y”), as shown in Figure 261.

Figure 261 - Exponential decays for S0 and S1 at wind-on conditions.

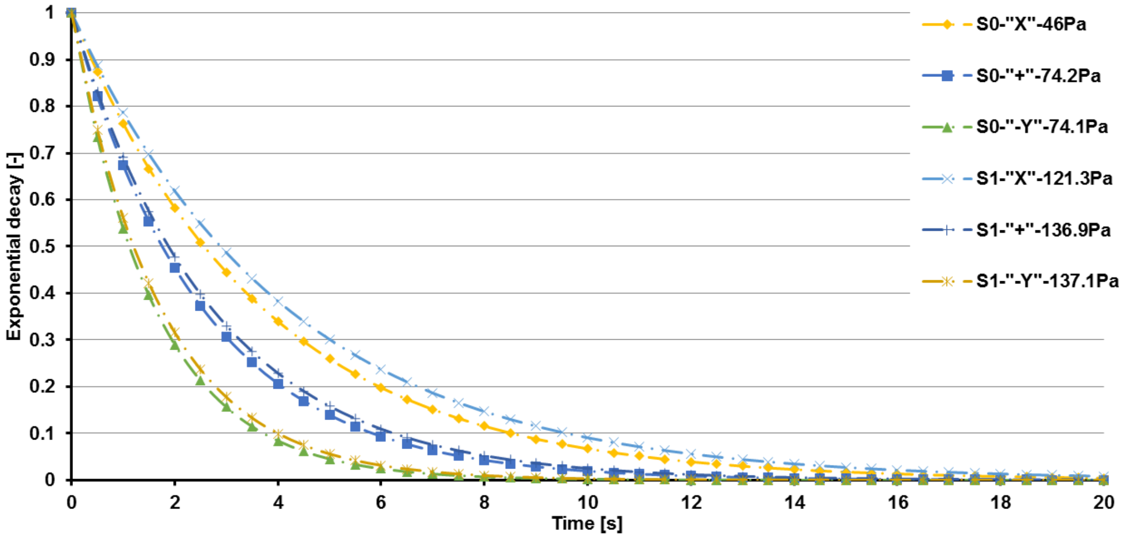

Source: Author (2018).

Closely analyzing the curves, and comparing the logarithmic decrements for all curves, it is possible to see that the increase in damping ratio from S1 to S0 for each tail type is smaller than that for wind-off conditions. Such increases appear to be similar for the respective “-Y” and “+” curves, while being a little greater for the “X” curves. This same similarity in behavior between “-Y” and “+” was already observed individually, i.e. for the same individual area, when comparing the curves spreads among all three tailplane options.

A possible explanation for the smaller increases in damping ration for wind-on conditions may be attributed to flow interferences once again. Assuming that flow developments are similar for both, S0 and S1, and that the root region of both configurations is the same (changing therefore just FIN area and *AR* from one configuration to another), for wind-on conditions the boundary layer develops along the HULL, and shades a relevant portion of the fins roots (section 5.2.3.4). This shading of the region where most fin area is concentrated, means the actual increase in area is significant only toward the tips. Complementarily, the region of increased area between S1 and S0, i.e. the tip, also constitutes a low efficiency lift generating spanwise position (due to smaller chords and the stronger influence of tip vortices). Besides that, the external vortex layers may affect more the longer fins (S0) than the shorter fins (S1), since those flow structures grow as they detach from the HULL (section 5.2.3.4).

This last proposal may seem to contradict what was shown by Rizzo (1924). However, none of his configurations were like this one tested: the fin roots were kept the same and area growth took place along the leading and trailing edges following the sweep angles (Figure 223). When he changed *AR*, he also reduced the area influenced by the boundary layer (reduced chord length), whereas for the increased area, the increase in the spanwise direction was very small, due to the large root chord (Figure 47). Finally, Rizzo (1924) did not assess the non-stationary effects that may be produced by oscillations. In other words, the strong crossflow, with changing direction and magnitude, induced in the boundary layer, and the changing vorticity generated on the outer flow, were not present, since his experiments were steady-state (static). On the other hand, observing such flow structures was not possible in this work, because of equipment limitations. Visualizing outer flow under oscillatory conditions would require very efficient cameras, imagery treatment and quick responding visualization techniques, which were not available for this study.

Besides looking at the decay envelope, it is also interesting to observe the oscillation itself for each case. The amount of complete oscillations during the converging motion is related to system frequencies, both natural and damped. These frequencies are defined as described in section 3.2.2.1 and Equation 26.

The number of oscillations and the parameters of the oscillatory decays for each configuration are shown in Table 17. Two figures for oscillations are presented for each case, and they are respectively the number of oscillations observed up to the stabilized portion for the actual signal and for the obtained nonlinear regression. The oscillations occurring along the converging portion of the curves, as described above in section 5.3.3, were not counted.

Table 17 - Damped oscillation parameters (Equation 25) for S0 and S1 tail arrangements.

Characteristics		A* [V]	***b*** [rad/s]	ω [rad/s]	**ζ** [-]	ω_0 [rad/s]	Φ [rad]	Nr. of Osc.
S0	**"X"**	0,338	0,270	1,53	0,174	1,56	3,177	3/3
	"+"	-0,366	0,395	1,74	0,221	1,78	0,008	1/2
	"-Y"	-0,452	0,619	1,75	0,333	1,86	-0,394	2/2
S1	**"X"**	0,269	0,240	1,47	0,161	1,49	3,644	2/3
	"+"	-0,157	0,369	2,29	0,159	2,32	-0,925	1/2
	"-Y"	-0,286	0,576	2,68	0,210	2,74	-2,194	2/1

* The unity for amplitude is given in Volts, and not in degrees or radians, as the data measured was voltage; the voltage level was compared and interpreted as a reference to angular position.
Source: Author (2018).

As already pointed out in this section, damping ratios **ζ** for S1 were smaller than those for S0. It is also interesting to observe that as the damping increased, so did the natural and damping frequencies, i.e. they were more cycles in the same period. However, looking at the number of oscillations it seems that the "+" type was the least oscillatory, whereas "X" was the most. The frequency values for "+" and "-Y" are however, and once again, too close in value to differentiate them clearly in this case. An interesting observation shows that for S1 the damping factor **ζ** for "X" and "+" may be considered as being virtually the same since their difference in value is approximately 1%. This reinforces the observed trend that the "-Y" seems to be the best configuration with increasing area and velocity regarding yawing moment damping.

5.3.7 TVC EVALUATION

As presented in section 3.2.2.3**,** TVC was initially introduced by Equation 44 - Airship Tail Volume Coefficient. The proposal is to produce a simple index rule that could provide designers, at a very early stage of an airship project, valuable guidance on stability. Using derivatives and other approaches, such as the one proposed by Schäfer (2015), seems to be adequate, but would require much more aerodynamic work than a simple "rule of thumb", which could help during the conceptual design evaluation at the very beginning. On the other hand, using proposals like those made by Burgess (2004) and Blakemore (2003) does not ensure stability, as they provide guidance only for initial sizing, besides having come from a very limited airship data source, with very specific tail arrangements and envelope shapes.

The initial idea tried to generalize the concept as much as possible. In other words, just add up all areas, regardless of the fixation radial angle, meaning that, for example, the "+" and "X" types would provide the same stability characteristics if each fin was identical. This was quickly revealed to be wrong when analyzing the results of the dynamic tests (Phase II). In the sequence, a second and potentially much better oriented approach, aimed at taking into account the projected area on the plane of interest was considered, e.g. for directional stability the projected area on the longitudinal plane should be the basic parameter. This should make more sense, assuming the simplistic approach represented by the incoming air on a lifting surface[47]. Nevertheless, even this approach also did not provide good results against captured data.

On the other hand, investigating the outer flow and the interference effects between HULL and FINs provided relevant information on the how the air flow develops over the tailplane, and what the main structures and their spatial ranges are. The conclusions pointed to the fact that, depending on the tail disposition, one must apply individual attenuation factors for each configuration, incorporating those issues in order to predict the effective damping area at the tail. This approach is very similar to what is done in general for fixed-wing aircraft spin prediction. Depending on the tail arrangement, the shading effect of the wake on the stabilizer is calculated, and the effective tail damping area is reduced by that amount.

In order therefore to better adjust the TVC proposal, a similar approach to that applied to spins was developed. However, the adjustments were based on the observed physical results (aerodynamic interferences). Four effect factors were defined: vortex, leading edge separations, streamlining and upwash. Using the data provided in Table 17, and considering the effects as explained in section 5.2.3.4, these mathematical factors were applied to all tailplane configurations. Each effect factor was mathematically applied to the projection factor of each fin according to the effect applicability. This means that, for example, the vortex factor multiplied the area projection of both port fins (UL and LL) of the "X" configuration, and so on, considering the above explained outer flow characteristics.

After the factors for each applicable fin were defined, an iterative method was applied in order to match the proportions between the Full Projection Factor (FPF) for different tailplane arrangements and two physical characteristics: logarithmic decrement ($\boldsymbol{b}$) and damping ratio ($\boldsymbol{\zeta}$). In other words, in an ascending order, $\boldsymbol{b}$ and $\boldsymbol{\zeta}$ were divided by the smallest of them among configurations, but within same area configurations, i.e. a sequence was built for S0 and another for S1.

Then, with the proportional increases obtained, the effect factors were varied, until the resulting Corrected Projection Factor (CPF - sum of each fin area multiplied by the applicable effect factor) was obtained and matched the same proportional increase for each tail arrangement. By dividing CPF per FPF, and multiplying the

[47] It is important to recall that, although such projections are used for raw estimates in fixed wing aircraft, it is proven that more accurate methods are necessary for predicting the actual aerodynamic coefficients, once inclined (dihedral) swept surfaces are strongly subject to three-dimensional flow.

result by the ratio between the ideally projected area and the real projected area (shown in Table 12, Table 13 and Table 14), the so called Projected Attenuation Factor (PAF) was obtained for each configuration, using the ***b*** and **ζ** approaches. Also the Full Attenuation Factor (FAF) was determined by dividing CPF by the number of surfaces, in a more generalized approach.

With such attenuation factors it was possible to investigate how the proposed TVC concept would change. An interesting fact is that using this approach, TVC can be as easily calculated as in Equation 44, and just corrected by the applicable Attenuation Factor according to the chosen tail configuration. The obtained Attenuation Factors are registered in Table 18.

Table 18 - TVC attenuation factors.

Tailplane	**Based on ζ**		**Based on *b***		**Mean Value**	
	PAF	**FAF**	**PAF**	**FAF**	**PAF**	**FAF**
“X”	0.29	0.20	0.29	0.20	0.29	0.20
“+”	0.45	0.26	0.50	0.28	0.475	0.27
“-Y”	0.78	0.51	0.90	0.58	0.84	0.55

Source: Author (2018).

Analyzing the obtained values, it is interesting to see that, despite the used factors, ***b*** or **ζ**, being of a different nature, the final obtained results are very close, showing that the system frequency has very small effect on the quality of directional dynamic stability.

Continuing with the TVC evaluation, Figure 262 was plotted again considering the projected area on the longitudinal plane, instead of the total area. This leads to a proposal, like for conventional aircraft, of different TVCs for pitch and yaw. In this case, as a means of differentiation, it is going to be called TVC_Y (Tail Volume Coefficient – Yawing).

Figure 262 - Tail Volume Coefficient for Yawing characteristic; parametric distribution.

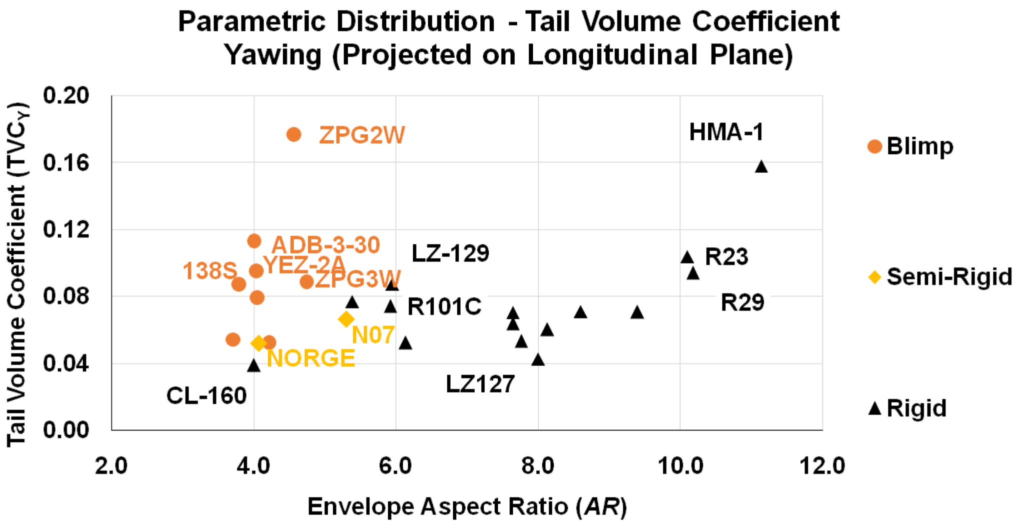

Source: Author (2018).

Such a proposal also matches what was derived by Carichner and Nicolai (2013), who also distinguished between the vertical and horizontal tail volume coefficients. As described in section 3.2.2.3, their data were added to the charts after all work was already carried out, in order to provide a degree of comparison and allow the author to evaluate their proposal applicability.

Figure 263 - Tail Volume Coefficient for Yawing characteristic; parametric distribution including Carichner and Nicolai's (2013) database.

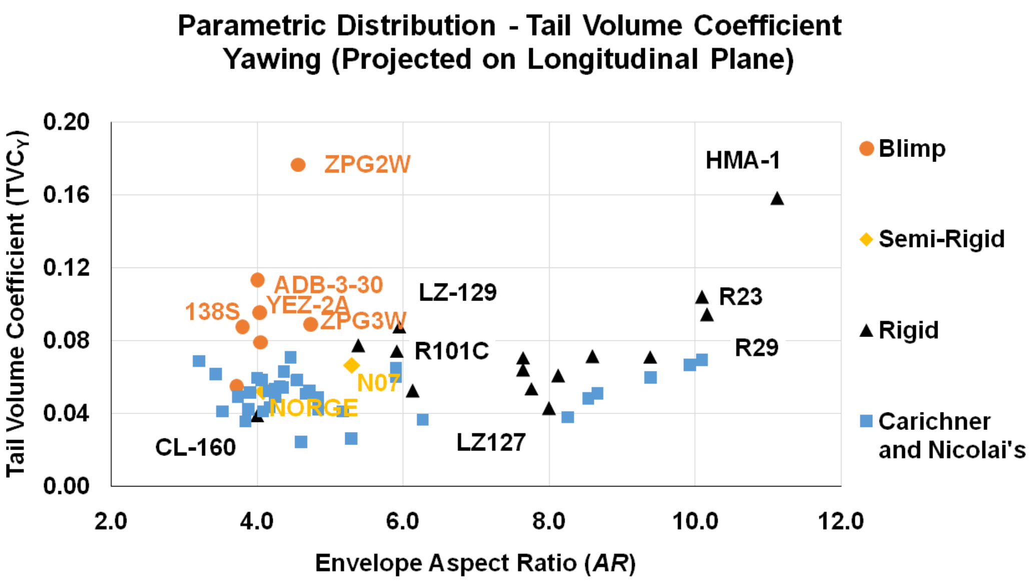

Source: Author (2018).

The data from Carichner and Nicolai (2013) contained a wide variety of rigid and nonrigid airships, but they were plotted all for highlighting purposes. It is very interesting to see that, increasing the database helped even more defining a certain region for TVC_Y, as a function of envelope *AR*, and which is situated where a significant amount of real airships are placed. It is very difficult to establish that a trend curve exists using this parameter, but one can clearly see that there appears to be a preference for having TVC_Y within 0.04 and 0.08, regardless of the airship structural construction and *AR*. Therefore, it is possible to say that, as a reference for initial tail sizing, at least for the vertical tail, a good approach would be to calculate the necessary projected area to be within the above limits, and then mathematically find the actual area based on the desired tail arrangement. Nevertheless, one must remember that this means no stability assurance.

Using the same trend approach applied by Carichner and Nicolai (2013), the complete airship database was used to have the TVC_Y calculated, and it was then plotted against the inverse of each envelope volume (1.0E+06/Volume) in cubic feet (ft^3) (Figure 264).

Figure 264 - TVC_Y calculated for the whole database, including Carichner and Nicolai's (2013), against the inverse of the volume of each airship.

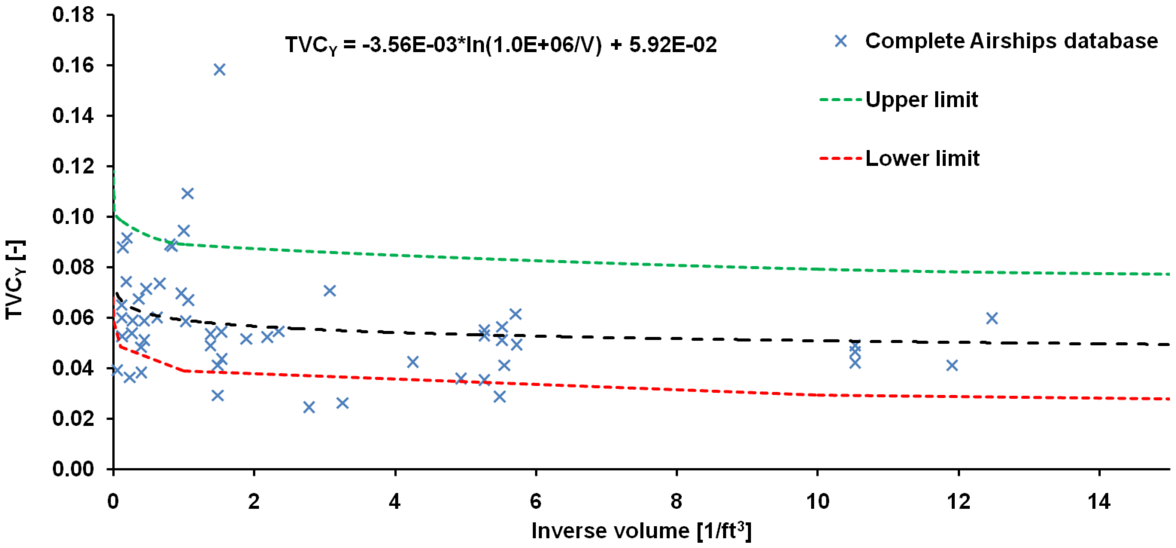

Source: Author (2018).

It is possible to observe that same logarithmic trend may be applicable, but, like before, it would not be in fact a good fit. Again it seems more reasonable to identify a region (band) instead of a trend line. Upper and lower limits are 0.025 apart from the proposed middle trend line. Once the volume here is inverted, it is important to highlight that the largest aircraft are those where the data points concentration is greater.

Just as discussed above, this is only an initial tail sizing reference, offering no actual stability information. In order to try to quantify the degree of stability, both raw TVC approaches (projected and not projected) had their values corrected according to tailplane configuration considering PAF and FAF, for ***b***, **ζ** and mean values between both parameters[48]. The charts are available in Appendix E.

Analyzing the results, the first conclusion is that the new dominating range is between 0.02 and 0.06 for all six corrected factors, regardless of the TVC type (projected or not) and the correction factor. This is indeed a good outcome, as it demonstrates that an actual trend exists, even with the applied changes, based on the results of this work. Finding a trend that comes from real aircraft demonstrates that the conclusions obtained so far appear to make sense in real life. It is important to say that the way the tests and mathematically modeling were conducted, FAF is a mathematical modeling result of the observed phenomenon for PAF.

Given the similarity among the results thus obtained and aiming at the maximum simplification, it would make sense to choose TVC corrected by FAF. However, recalling that the outer flow, and consequently the vortical and wake structures, are dominated by the hull oscillatory plane, it would not make sense to predict longitudinal and lateral stabilities for the “-Y” with the same factor. Differently from the “+” and “X” types, the “-Y” is not symmetric with respect to both longitudinal and lateral planes. Moreover, none of the configurations would be, considering the presence of a gondola attached to the envelope. Balancing all those aspects, and considering that the projected area calculation is also easy enough to be carried out, TVC_Y corrected for PAF was chosen, and named as just TVC_Y.

Evaluating in more details the TVC_Y chart (Figure 265), it is possible to see that the “-Y” configurations (138S and NT-07) underwent a considerable increase regarding their previous positions, as a consequence of the latter formulation. The other blimp aircraft got much closer to each other, despite the fact that they share almost equally “X” and “+” tailplane arrangements among the samples. The rigid aircraft, all “+” tail types, kept their scatter very similar through the adjustments.

The chart was reorganized, and the data points were plotted regarding their tail arrangement, and not the structural construction technique. The equivalent TVC_Y.for the tested “X-”configurations (S0 and S1) were also inserted. The models were included considering the CB at the correct place (46.7%**L**) and at the place where RAS was attached (40%**L**). This was done because, around the actual CB, the

[48] As explained, Carichner and Nicolai’s (2013) database was not available before the very end of the results discussion, and therefore is not presented in all charts.

configuration was found to be statically and dynamically unstable, whereas for 40%**L**, they were at least dynamically stable.

Figure 265 - TVC_Y corrected by PAF mean value from author's database.

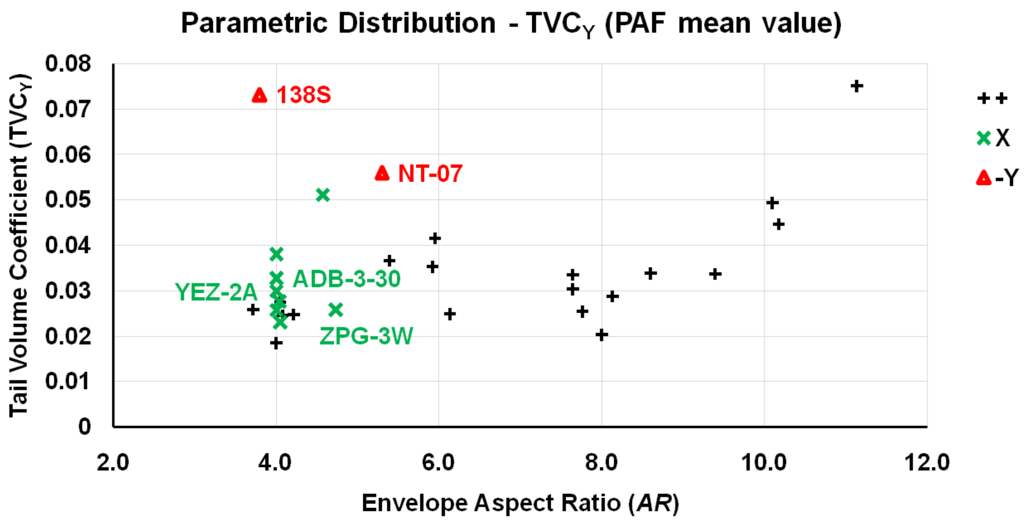

Source: Author (2018).

The greater concentration of airships is seen within the 0.02 to the 0.04 range, which could indicate a probable good degree of stability within this range. Nevertheless, the models used in this work with the axis position for oscillations going through the CB, also figure inside this range, and those configurations are known to be unstable, at least under the wind tunnel testing conditions. This may indicate that probably no clear-cut line is possible to be defined for a simple stability law, or the wind tunnel tests were not sensitive enough to really simulate the differences. It is important to recall that the wind tunnel campaigns were run at relatively low flow velocities and, for the BARE HULL finishing, only for ease of comparison purposes. These conditions, besides being from far from matching the desired similitude, seemed to provide meaningful results anyway.

While some unstable configurations are within the supposed good range, on the other hand, the most modern operating[49] aircraft, which are “-Y”, figure at the top, above 0.05. Based on facts, these last apparent discrepancies were analyzed. The 138S had a similar model built at Airship do Brasil, the ADB-3-X01, identical to the 138S regarding flight dynamics. The prototype went through some flight testing campaigns[50], and it was found to be really stable regarding yawing moments. With engines at idle, at low wind speeds (below 10 knots), the aircraft was capable of

[49] CL160 and ADB-3-30 are not operational.

[50] The author himself was a flight test engineer during almost all official testing flights of the ADB-3-X01.

efficiently aligning itself with the flow direction, when positioned almost perpendicularly to gusts. The NT-07 also shown to be very stable, apparently required the use of some maneuvering motors to improve its maneuvering capability[51]. The 138S configuration, however, also provides very good maneuverability, proven by flight testing, which makes the statement about the NT-07 doubtful, considering this latter type has a smaller TVC_Y.

Recalling Burgess' (2004) comments on *AR* and referencing to volumetric length instead of diameter, the TVC_Y was multiplied by *ARb* (section 3.2.2.2), trying to better model the concept. The TVC_Y-*ARb* would then be simply: projected area multiplied by its arm length to the CB, divided by the hull volume. Blakemore's (2003) data were included in the chart for reference. The output was a much spread out chart along the *ARb* axis, and obviously an increase in magnitude. The inferior threshold appeared at around 0.075, and 138S and NT-07 got nearer to each other. Nevertheless, as before, probable unstable configurations according to wind tunnel testing, such as the ADB-3-30, were at the same level or even above probable stable ones, such as the ZPG-3W and YEZ-2A.

Figure 266 - TVC_Y-*ARb* against *ARb* including Blakemore's (2003) database.

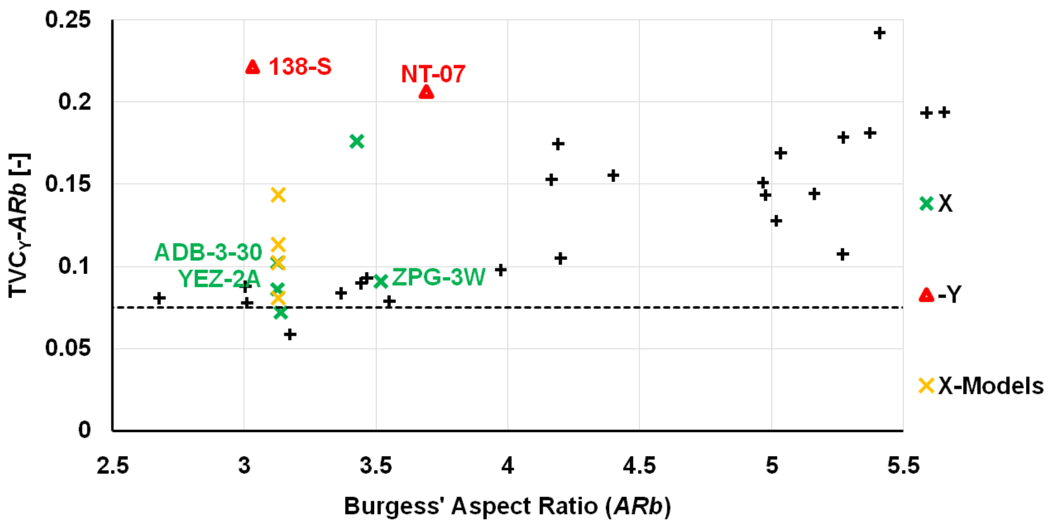

Source: Author (2018).

It is a fact that, despite all this discussion, it is contradictory to have safe operational aircraft at the same level of verified unstable configurations, when defining a stability coefficient. This demonstrates that either the proposed TVC approach is too simplistic, and does not properly address the dynamics involved, or the dynamic tests conducted do not well represent the in-flight free-oscillation motion.

[51] Information based on discussions with people working in lighter-than-air technology.

There is still another possibility: the existence of a transition region, between 0.075 and 0.1, where near-to-extreme controllable and stable aircraft might concur. One must remember that, in his conclusions, Gomes (1990) affirms that all modes were stables, but “continuous bobbling” response was found for the aircraft, i.e. slow frequency response to external disturbances, increasing the likelihood of over controlling by the pilot. Also, no specific data regarding ZPG-3W stability was found. On the other hand the ADB-3-30 scale models proved anyway to be unstable, keeping the question.

As explained, adding the database provided by Carichner and Nicolai (2013) at the final phase of the results evaluation and discussion led to an enriched chart. The wind tunnel models (“X”, “+” and “-Y”) with the modified CB were also included (Figure 267).

Figure 267 - TVC_Y-*ARb* against *ARb* for the whole airships database available: author’s, Blakemore’s (2003) and Carichner and Nicolai’s (2013).

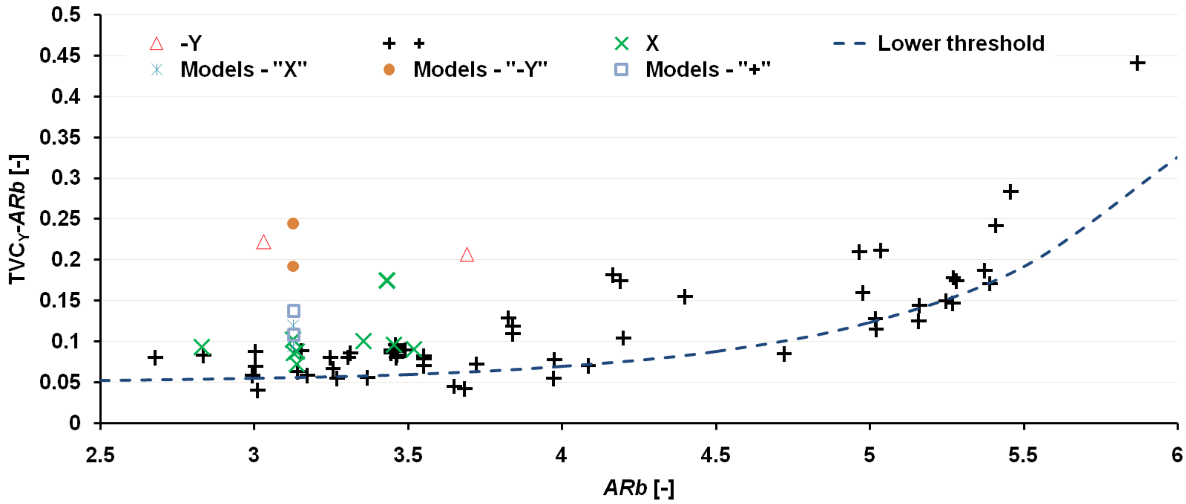

Source: Author (2018).

The previous observed trends were reinforced by the newly added data. For small *ARb* there seems to be a denser concentration of aircraft around the lower threshold (0.075), independently of any “X” or “+” tail arrangement. With increasing *ARb*, the TVC_Y–*ARb* also increases. Differently from Figure 266, given the increased number of data points, it seems they could fit some exponential curve. The proposed lower threshold (dashed curve) is defined by the following equation:

$$\mathrm{TVC_Y} - ARb = 0.05 + 0.0001 \cdot \mathrm{e}^{1.32 \cdot ARb}$$ Equation 57 - TVC_Y-ARb lower threshold.

Also, if the TVC_Y–*ARb* may be assumed as a measuring reference, although the “-Y” configurations seem to be overestimated in terms of stability, the ADB-3-30 modified “-Y” models presented similar coefficient values when compared to real aircraft of the same type of tail, which minimizes this doubt. Complementarily, airships with an “X” tail arrangement presented greater TVC_Y-*ARb*. This probable greater stability could be attributed to larger tail areas when compared to other similar envelopes with a “+” tail, once the former showed to be less effective (smallest PAF). The problem of having apparently unstable wind tunnel models at supposedly stable levels persists however.

Using the newly compiled data, the previous TVC_Y was plotted against typical *AR* as well, in order to compare both approaches.

Figure 268 - TVC_Y against *AR* for complete airships database: author’s, Blakemore’s (2003) and Carichner and Nicolai’s (2013).

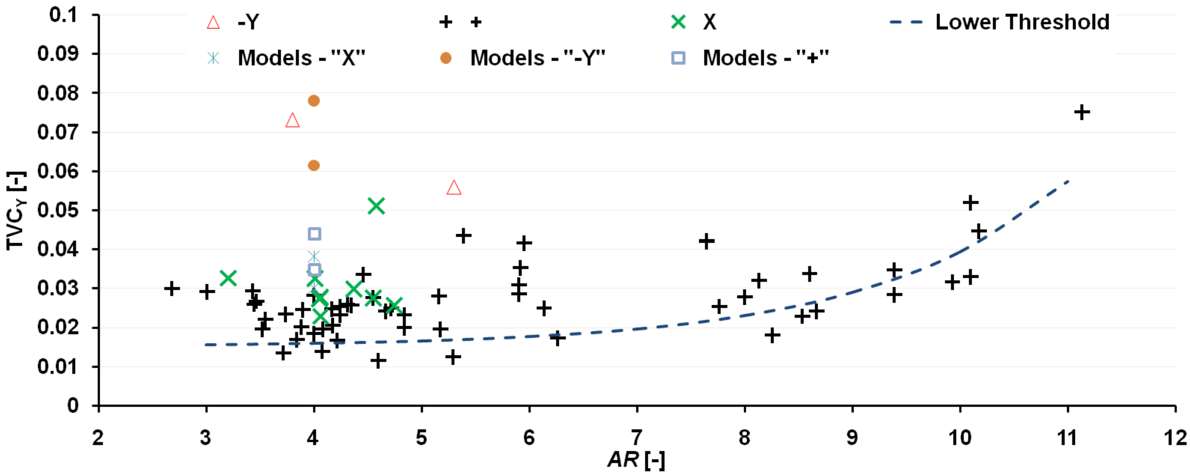

Source: Author (2018).

Analyzing the obtained chart (Figure 268), the same conclusions stated above can be reached. The lower threshold in this case is defined by:

$$\mathrm{TVC_Y} = 0.015 + 0.0001 \cdot \mathrm{e}^{0.55 \cdot AR}$$ Equation 58 - TVC_Y lower threshold.

It is possible to see that the chart “stretched” in both the vertical and horizontal directions when compared to Figure 267. This “stretching” makes a qualitative definition much more sensitive to small changes, and less precise, within due proportions. This leads to the conclusion that, for the aimed purposes, it is better to focus on the TVC_Y-*ARb*, which is also simpler, being defined as:

$$\mathrm{TVC_Y} - ARb = \frac{\mathrm{L_{CB-CA}} \cdot \mathrm{S_{VT-Proj}}}{\mathrm{V}} \cdot \mathrm{PAF}$$ Equation 59 - TVC_Y definition.

, where

$\mathrm{L_{CB-CA}}$	= longitudinal distance between aircraft CB and the geometrical center of the projected vertical tail
$\mathrm{S_{VT-Proj}}$	= projected vertical tail area on longitudinal plane
V	= envelope volume
PAF	= Projection Attenuation Factor (Table 18)

As a conclusion, in order to conduct an initial tail sizing estimate with a minimum degree of directional stability, the proposal is to use Equation 59, in order to establish the lowest acceptable TVC_Y-*ARb* given the *ARb* parameter. Then, with this value and knowing the applicable PAF mean value based on Table 18**,** iterate between projected area and arm length to the CB, obtaining the initial tail arrangement.

Even considering the questions regarding the unstable wind tunnel models which came out at the same level of real and stable aircraft, the parametric study, as whole pointed out some important extra information which may be extracted, and are worth mentioning. It is possible to observe that the “+” type dominance occurs for the whole range of *ARb*, but are the only one which were used for *ARb* > 6. The more modern airships, besides having smaller *ARb* (between 3 and 4), are more varied regarding tail arrangements. Curiously, among the sampled data, only two aircraft were identified as “-Y”, despite the apparently identified better stability. An interesting fact from the database is that while comparing similar aircraft, the “-Y” tail ones have the smallest added up areas, followed by the “+” and “X” types respectively. This matches in some manner the observed damping trends obtained as a result of the dynamic tests of Phase II. Unfortunately, however, the reliable airship sources regarding tail areas and envelope characteristics were scarce. Even though not really new trends are foreseen, once conventional airships are very similar in shape to those investigated in this work, mainly nowadays, this made the database relatively small in scope, and the study less embracing than it could have been otherwise.

6 CONCLUSIONS

6 CONCLUSION

Supported by previous published works in the LTA field, and based on a specific airship configuration, the ADB-3-30, it was possible to successfully assess specific and general aerodynamic and stability characteristics for this type of aircraft. By means of steady tests, a relevant investigation on adequate roughness for airship wind tunnel testing similitude purposes was conducted, leading to a very simple and practical solution: a saw-like simple tripping band. The typical aerodynamic curves were obtained, confirming some expected general trends for lift and drag. Worrisome characteristics concerning static stability for this specific X-tail configuration were identified. Also dynamic stability evaluations showed the need for further improvements on the stability characteristics of the design of ADB-3-30, as the results indicated stable behavior only around unfeasible reference points for a realistic airship arrangement. Nevertheless, the results also provided some good advice regarding tail configuration efficiency, pointing the “-Y” tail as the most efficient for damping yawing oscillations when compared to the “X” and “+” types.

All the studies were complemented and supported by extensive surface and outer flow investigations. Using qualitative techniques, it was possible to establish a significant number of aerodynamic flow structures and their behaviors with changing attitude. A high degree of interference between hull and tail fins was found, as expected, being all explained. The interference sensitivity to different kinds of hull surface roughness, which meant different flow developments, was also evaluated. The flow was confirmed to be rather complex, dominated by longitudinal vortical structures, affecting differently each type of tailplane arrangement. Some relevant differences, when compared to previous prolate spheroids studies, were identified as singularities of this specific hull shape.

In spite of the careful evaluation and studies carried out in order to advance a simple coefficient for tail design, it was not possible to show a clear and direct agreement between the proposed TVC and the results obtained. The wind tunnel dynamic tests, which led to the numerical data for the TVC study, did not seem to reasonably scale up the aircraft dynamic characteristics. Not all geometric and inertial characteristics of a real in-flight aircraft could be present in the wind tunnel, highlighting among them virtual mass and CG precise positioning. This makes these results somewhat questionable in numbers. Anyway, the obtained data shows interesting trends, which were also observed in reality (using a real aircraft database) regarding tail design. Moreover, in terms of a qualitative comparison, the results are rather interesting, and the TVC_Y-*ARb* was proposed as an initial vertical tail sizing and stability assessment based on parametric studies. This all enriches the available knowledge on the topic, and can also lay the ground work for future research work.

A very relevant conclusion regarding general aspects is that testing airships in wind tunnels is quite a complex task. Besides the typical scalability issue, some other tough obstacles were faced. The strongly three-dimensional flow is dominated by large eddy structures (attached and detached, leading to non-linear behaviors), interacting with each other, comprising a very complex balance. This complexity leads to very sensitive aerodynamic flow arrangements, which may be easily disturbed by vibration, low model attachment stiffness, construction, positioning and adjustment details (here scale plays an important role again) and so on. Also, the actually measured forces are rather small when compared to typical airfoils, and minor errors and geometric deviations may lead to relevant inconsistencies when dealing with the resulting numerical data. During the work development, although care was taken with every single action, some nonconformity was inevitable. This however did not appear to compromise the desired investigations.

The work objectives, mostly qualitative, were achieved. The aircraft and its aerodynamic and stability characteristics were comprehensively described. The results should be useful, considering both academic and industrial purposes. Based on them, design considerations may be better constructed. Also some flight characteristics might also be better explained and understood.

As for next and further studies, it would be interesting to map the airship outer flow, inserting some quantitative measurements. Also the wake past the aircraft could be better visualized by means of hot-wire anemometry or multi-holes Pitot tubes. It would also be useful to try a larger extent visualization of the model surface, and at larger AoAs, something which was not possible to be done along this work due to instruments limitations.

For the specific X-tail configuration, as stated, some deeper investigations must be conducted. Mainly tail size and positioning must be reevaluated, since large interferences were observed, leading to low efficiency, and unstable characteristics of both natures, static and dynamic. Next steps would be including the gondola in the studies, which will surely affect stability and flow development, and also map the center of pressure travel along the tests. Both changes would provide substantial fundamental information for changes aimed at better design. If possible, trying larger scales for the wind tunnel models or using towing tanks, with smaller blockage effects (maybe an open section wind tunnel) would also help to support and confirm the results pointed out in this work, regarding boundary layer and aerodynamic behavior similitude. It would also be a worthwhile approach to test models whose flight test data is available, like the ZS2G-1, in order to compare the wind tunnel results with full scale, increasing the rougheness proposal reliability.

For the parametric tail design generalization, it would be interesting to improve the model representativeness regarding inertias, but also include oscillations in the longitudinal plane for the “-Y” configuration. Another relevant task would be to conduct the same tests with different envelope shapes, tail fin positions and sizes along the hull. This would improve the data variability, probably facilitating the observation of trends and numerical relations. Including some oscillatory analyzes for different combinations of attitudes (pitch and yaw simultaneously) would be interesting as well, for better simulating real flight events, like gusts and updrafts. Also, oscillations with control actuation would provide interesting information on controllability as well, making it possible to compare and balance stability and controllability, which can be opposites for the same configuration.

As discussed, a long journey is ahead in order to get to the final and most generalized results on the proposed topics. Nevertheless, this work for sure contributes with some steps towards the desired aim.

REFERENCES

ABBOTT, Ira H. *Airship Model Tests in the Variable Density Wind Tunnel.* Langley Memorial Aeronautical Laboratory, National Advisory Committee for Aeronautics, Langley Field, Washington, January 27, 1931. REPORT No. 394.

AEROS. *Aeroscraft Corporation in Brief* [online]. [cited 12 march 2016]. Available from: http://aeroscraft.com/about-us/4583940322.

AIRSHIP DO BRASIL. *Time Line* [online]. [cited 12 March 2016]. Available from: http://www.adb.ind.br/linhaTempo.jsp.

ALLEN, H.J. and PERKINS, E.W. *A Study of Effects of Viscosity on Flow over Slender Inclined Bodies of Revolution*. Moffett Field, CA, August 1951. NACA TR-1048.

ANDERSON, A.W. and FLICKINGER JR., S.J. *Wind-Tunnel Tests of a 1/48-Scale Model of the ZXS2-1 Airship with Various Tail Configurations*. Washington D.C., Navy Department, TMB AD-3110, 1954.

ATMANI, R., BRIMA, A. and ASKOVIC, R. Study of Three-Dimensional Separation of Boundary Layer over Blunt Bodies. *Journal of Hydrodynamics*. v. 21, n.1, p.100-107, 2009.

AVIATION DICTIONARY. *Center-of-pressure travel* [online]. [cited 16 january 2018]. Available from: http://aviation_dictionary.enacademic.com/1291/center-of-pressure_travel.

BAILEY, D.B. *Patrol Airship Concept Evaluation (PACE)*. Warminster, Pa, March 1985. Final Report, NADC-85019-60.

Balloon No. 6 [online]. [cited 12 march 2016]. Available from: http://www.earlyaviators.com/edumon3.htm.

BARLOW, J.B.; RAE JR., W.H.; POPE, A. *Low-Speed Wind Tunnel Testing*. 3rd ed. United States of America: Jhon Wiley & Sons, 1999. 713 p.

BLAKEMORE, T.L. and PAGON, W.W. *Pressure Airships*. University Press of the Pacific, 2003. 356 p.

BURGESS, Charles P. *Airship Design*. Reprinted from the 1927 edition. Honolulu, Hawaii: University Press of the Pacific, 2004. 340 p.

CARICHNER, G.E. and NICOLAI, L.M. *Fundamentals of Aircraft and Airship Design: Volume 2 – Airship Design and Case Studies*. American Institute of Aeronautics and Astronautics, Inc. Reston, Virginia. 2013. 945 p.

CATALANO, F.M. *The New Closed Circuit Wind Tunnel of the Aircraft Laboratory of University of São Paulo, Brazil*. In: 24th INTERNATIONAL CONGRESS OF THE AERONAUTICAL SCIENCES, 2004.

CEBOLLA, I.H. *Wind Tunnel Testing for New Airship Configuration* [Graduation final work]. São Carlos: University of São Paulo, 2013.

CERRETA, P.A. *Wind-Tunnel Investigation of the Drag of a Proposed Boundary-Layer-Controlled Airship.* Washington D.C., U.S. Navy, 1957. TMB Aero Report 914.

CREMA, L.B. and CASTELLANI, A. *Some Trends in Airship Technology Developments*. Advisory group for Aerospace Research and Development, North Atlantic Treaty Organization, August, 1983. AGARD Report No. 717.

COOK, M.V., LIPSCOMBE, J.M. and GOINEAU, F. Analysis of the Stability Modes of the Non-rigid Airship. *The Aeronautical Journal*. June 2000, Vol. 104, No. 1036. p. 279-290.

CORNISH III, J.J. and BOATWRIGHT, D.W. *Application of Full Scale Boundary Layer Measurements to Drag Reduction of Airships.* Conducted for Office Naval Research by the Aero physics Department of Mississippi State University, 18 January 1960. Research Report #28.

CRUZ, C.H.B., et al*. Guia para Física Experimental Caderno de Laboratório, Gráficos e Erros Instituto de Física*. IFGW, Unicamp, 1997.

DURAND, W.F., ed. *Aerodynamic Theory: A General Review of Progress*. New York Dover Publications, v. 6, 1936.

EFUNDA, INC. *Pitot tubes theory* [online] [cited 14 July 2015]. Available from: http://www.efunda.com/designstandards/sensors/pitot_tubes/pitot_tubes_theory.cfm.

EL OMARI, K., et al. *Turbulence Modeling Challenges in Airship CFD Studies*. In: SEMINARIO MATEMÁTICO GARCÍA DE GALDEANO, No. 31, 2004. p. 545-554.

ELFES, A., et al. Project AURORA: Development of an Autonomous Unmanned Remote Monitoring Robotic Airship. *Journal of the Brazilian Computer Society* [online], 1998, vol. 4, n° 3. [cited 12 March 2016]. Available from: http://www.scielo.br/scielo.php?script=sci_arttext&pid=S0104-65001998000100009&lng=en&nrm=iso.

ESCHER, R. *Airship Manufacturer Database* [online]. [cited 12 March 2016]. Available from: http://www.myairship.com/database/index.html.

ETKIN, B. and REID, L.D. *Dynamics of flight: stability and control.* 3rd ed. John wiley & Sons, Inc. 1996. 400 p.

FAIRLIE, B.D. *Flow Separation on Bodies of Revolution at Incidence* [online]. In: 7TH AUSTRALASIAN HYDRAULICS AND FLUID MECHANICS CONFERENCE, Brisbane, 18-22 August, 1980. p. 338-341. Available from: http://people.eng.unimelb.edu.au/imarusic/proceedings/7/Fairlie.pdf.

FITZPATRICK, R. *Damped Harmonic Oscillation* [online]. [cited January 2018]. Available from: http://farside.ph.utexas.edu/teaching/315/Waves/node10.html.

FREEMAN, H.B. *Force Measurements on a 1/40-Scale Model of the U.S. Airship "Akron".* Langley Memorial Aeronautical Laboratory, National Advisory Committee for Aeronautics (N.A.C.A.), 1932. Report No. 432.

FREEMAN, H.B. *Measurements of Flow in the Boundary Layer of a 1/40-Scale Model of the U.S. Airship 'Akron'*. Langley Field, VA, April 1932. NACA TR-430.

FREEMAN, H.B. *Pressure Distribution Measurements on Hull and Fins of a 1/40 Scale Model of the U.S. Airship 'Akron'*. Langley Field, VA, April 1936. NACA TR-443.

FRONTLINESOLVERS®. *Excel Solver - Grg Nonlinear Solving Method Stopping Conditions*. [online] [cited December 2017]. Available from: https://www.solver.com/excel-solver-grg-nonlinear-solving-method-stopping-conditions.

FUNK, P., et al. *Experiments on the Flowfield of an Inclined Airship Body*. Stuttgart: Institut für Aerodynamik und Gasdynamik, Universität Stuttgart, Germany. 1998.

GENÇ, M.S. et al. Acoustic Control of Flow over NACA 2415 Airfoil at Low Reynolds Numbers. *Journal of Aerospace Engineering*. 29. 2016.

GOMES, S.B.V. *An Investigation of the Flight Dynamics of Airships with Application to the YEZ-2A* [PhD. Thesis]. Cranfield: Cranfield Institute of Technology, 1990.

GOMES, S.B.V. *Airships in Brazil - The past, present and prospects for the future.* In: 12th LIGHTER-THAN-AIR SYSTEMS TECHNOLOGY CONFERENCE, LIGHTER-THAN-AIR CONFERENCES, San Francisco, CA, U.S.A., 1997. San Francisco: American Institute of Aeronautics and Astronautics, Inc, 1997. AIAA-97-1432.

GOODYEAR. *Goodyear Blimp* [online]. [cited 12 March 2016]. Available from: http://www.goodyearblimp.com/relive-history/#page/70.

GOOGLE. *Project Loon: Loon for all* [online]. [cited 12 March 2016]. Available from: http://www.google.com/loon/.

HALL, S. *How Big the Tail* [online]. EAA Chapter 62. [cited December 2017]. Available from http://www.eaa62.org/technotes/tail.htm.

HAN, T. and PATEL, V.C. Flow Separation on a Spheroid at Incidence. *Journal of Fluid Mechanics*, vol. 92, part 4, 1979. p. 643-657.

HIGGINS, G.J. *Tests of the N.P.L. Airship Models in the Variable Density Wind Tunnel.* Langley Memorial Aeronautical Laboratory, National Advisory Committee for Aeronautics, Langley Field, Washington, September, 1927. TECHNICAL NOTES No. 264.

HOERNER, S.F. *Fluid-Dynamic Drag: theoretical, experimental and statistical information*. New Jersey: Published by the author, 1965.

HOPKINS, E.J. *A Semi-Empirical Method for Calculating the Pitching Moment of Bodies of Revolution at Low Mach Numbers*. Moffett Field, CA, May 1951. NACA RM-A51C14.

JEX, H.R., and GELHAUSEN, P. *Pre- and Post-Flight-Test Models Versus Measured Skyship-500 Control Responses.* In: 7TH AIAA LIGHTER-THAN-AIR TECHNOLOGY CONFERENCE, Monterey, CA, August 1987.

JONES, R., and BELL, A.H. *Experiments on a Model of the Airship R.101*. HIS MAJESTY'S STATIONERY OFFICE, London, 1926. ARC RM-1168.

JONES, R., WILLIAMS, D.H., and BELL, A.H. *Experiments on a Model of the Airship R.29*. HIS MAJESTY'S STATIONERY OFFICE, London, 1920. ARC RM-714.

JONES, S.P., and DELAURIER, J.D. Aerodynamic Estimation Techniques for Aerostats and Airships. *Journal of Aircraft*, Vol. 20, No. 2, 1983. p. 120-126.

KHOURY, G.A., ed. *Airship Technology*. 2nd ed. Cambridge: Cambridge University Press, 2012. 768 p.

KLINE, S.J., *Similitude and Approximation Theory*. Springer-Verlag, New York, 1986.

KORNIENKO, A. *System Identification Approach for Determining Flight Dynamical Characteristics of an Airship from Flight Data* [PhD Thesis]. Stuttgart: University of Stuttgart, Germany, 2006.

KUZMIN, D. *Dimensionless form of equations* [online]. [cited 27 May 2016]. Available from: http://www.mathematik.uni-dortmund.de/~kuzmin/cfdintro/lecture3.pdf.

LAE-1, *Wind tunnel* [online]. [cited 12 March 2016] . Available from: https://www.facebook.com/TunelDeVentoDoSaalaeeescUsp.

LAMB, H. *Notes on the Forces Experienced by Ellipsoidal Bodies Placed Unsymmetrically in a Converging or Diverging Stream*. British A.R.C. R&M No. 1164, 1928.

LAMB, H. *The Inertia-Coefficients of an Ellipsoid Moving in a Fluid*. October, 1918. Reports and Memoranda, No. 623.

LEE, H.C. Analysis of the Static and Dynamic Stability Properties of the Unmaned Airship. *KSAS International Journal*, Vol. 2, No. 2, November 2001. p. 82-94.

LUTZ, Th., and FUNK, P. Aerodynamic Interference Effects of Airships. In: SECOND INTERNATIONAL SYMPOSIUM ON TRANSDISCIPLINARY FLUID INTEGRATION, TFI-2005, Hyuga, Miyazaki, October 26-27, 2005.

LUTZ, Th., et al.. Aerodynamic Investigations on Inclined Airship Bodies. In: 2ND INTERNATIONAL AIRSHIP CONVENTION AND EXHIBITION, Bedford, Great Britain, 1998.

LUTZ, Th., et al.. Summary of Aerodynamics Studies on the LOTTE Airship. In: 4TH INTERNATIONAL AIRSHIP CONVENTION AND EXHIBITION, Cambridge, England, 2002.

MASKELL, E.C. *Flow Separation in Three Dimensions*. Royal Aircraft Establishment, Farnborough, November, 1955. Report No. AERO.2565.

MATHWORKS®. *R2017b Documentation: sgolayfilt (Savitzky-Golay filtering)* [online]. [cited December 2017]. Available from: https://www.mathworks.com/help/signal/ref/sgolayfilt.html.

MAUNSELL, M.G. *Desenvolvimento, construção e ensaios de uma balança aerodinâmica* [Master's Thesis]. São Carlos: Escola de Engenharia de São Carlos, Universidade de São Paulo, 1977.

MCHUGH, J.G. *Pressure-Distribution Measurements at Large Angles of Pitch on Fins of Different Span Chord Ratio on a 1/40-Scale Model of the U.S. Airship 'Akron'*. Langley Field, VA, April 1937. NACA TR-604.

MCLEMORE, H.C. *Wind-Tunnel Tests of a 1/20-scale Airship Model with Stern Propellers*. National Aeronautics and Space Administration, Washington. January 1962. Technical Note D-1026.

MCLEOD, M. *Return of the Airship* [online]. Design Engineering, March 8, 2012. [cited 12 March 2016]. Available from: http://www.design-engineering.com/features/return-of-the-airship/.

MEI, C. C. *Notes on 1.63 Advanced Environmental Fluid Mechanics* [online]. 2009. [cited 27 May 2016]. Available from: http://web.mit.edu/fluids-modules/www/basic_laws/1-9Sca-sim.pdf.

MERZKIRCH, W. *Techniques of Flow Visualization.* 1987, AGARD No. 302.

MOWFORTH, E. *An Introduction to the Airship*. The Airship Association, 1985. p. 32-33.

MUNK, M.M. *The Aerodynamic Forces on Airship Hulls*. Springfield, VA, January 1924. NACA TR-184.

NASA. *Tufting and smoke visualization* [online]. [cited 10 July 2015]. Available from: https://www.grc.nasa.gov/www/K-12/airplane/tunvsmoke.html.

NASA. *Surface oil flow* [online]. [cited 22 May 2016]. Available from: https://www.grc.nasa.gov/www/k-12/airplane/tunvoil.html.

CIMBALA, J.M. *Nondimensionalization of the Navier-Stokes Equations* [online]. [cited 27 May 2016]. Available from: http://www.mne.psu.edu/cimbala/me320web_Spring_2015/pdf/Nondimensionalization_of_NS_equation.pdf.

PANNELL, J.R., and BELL, A.H. *Experiments on Rigid Airship R.29*. Langley Field, VA, January, 1920. ARC RM-675.

PANNELL, J.R., and FRAZER, R.A. *Account of Some Experiments on Rigid Airship R.26*. Langley Field, VA, January, 1920. ARC RM-674.

PANNELL, J.R., and FRAZER, R.A. *Experiments on Rigid Airship R.33*. Langley Field, VA, 1919. ARC RM-668.

PANNELL, J.R., and JONES, R. *Experiments on a Model of the German Rigid Airship L33*. HIS MAJESTY'S STATIONERY OFFICE, London, 1917. ARC RM-361.

PATEL, V.C. Three-dimensional Flow Separation. *Sadhana*, vol. 18, issue 3-4, 1993. p. 553-574.

PRECISION DEVICES, INC. *Surface Roughness Terminology and Parameters* [online]. [cited January 2018]. Available from: http://www.predev.com/pdffiles/surface_roughness_terminology_and_parameters.pdf

PRENTICE, B. and ADAMAN, M. Economics of Cargo Airship for Food Transport to Remote Northern Communities. *Research in Transpotation Business & Management*. Vol. 25, 2017. p. 87-98.

RIZZO, F. *A Study of Static Stability of Airships.* Langley Memorial Aeronautical Laboratory. September, 1924. NACA TN-204.

SAGAUT, P. *Large Eddy Simulation for Incompressible Flows*. 3rd ed. Springer, 2005. 585 p.

SCANIVALVE. *Data Sheet No. G480:* Electronic Pressure Scanning Module ZOC 33. Liberty Lake, 2013.

SCHLICHTING, H. and GERSTEN, K. *Grenzschicht-Theorie*. 10 aufl. Springer-Verlag Berlin Heidelberg 2006.

SCHÄFER, I. *Summary of Information Received from Norman Mayer to WG Tail Questions*. São Carlos, 2015. Document Number JS xx.

SCHÄFER, I., and KRÖPLIN, B. *Scaling Effects on Airships*. Stuttgart: University of Stuttgart. [201-?].

STOCKBRIDGE, C., CERUTI, A. and MARZOCCA, P. Airship Research and Development in the Areas of Design, Structures, Dynamics and Energy Systems. *International Journal of Aeronautical and Space Sciences*, 2012, Vol. 13, No. 2, p 170-182.

TAYLOR, G.I. *The Force Acting on a Body Placed in a Curved and Converging Stream of Fluid*. British A.R.C. R&M No. 1166, 1928.

JERSEY. *The Air Navigation (Jersey) Order 2008* [online]. [cited 12 march 2016]. Available from: https://www.jerseylaw.je/laws/superseded/PDFs/2009/03.105.pdf.

THE AIRSHIP ASSOCIATION. *Introduction* [online]. [cited 12 March 2016]. Available from: http://www.airship-association.org.

THWAITES, B., ed. *Incompressible Aerodynamics*: *an Account of the Theory and Observation of the Steady Flow of Incompressible Fluid past Aerofoils, Wings and Other Bodies*. United States: Dover Publications, 1960. 636p.

TUCKERMAN, L.B. *Inertia Factors of Ellipsoids for use in Airship Design*. 1926. NACA REPORT, No. 210.

TUCKERMAN, L.B. *Notes on Aerodynamic Forces on Airship Hulls*. 1923. NACA REPORT, No.129.

UNITED STATES WAR DEPARTMENT. *Technical Manual of Airship Aerodynamics*. War Department, Washington, 1941. 80 p. TM No. 1-320.

VIANNA, I.O.A. *Metodologia do Trabalho Científico:* um enfoque didático da produção científica. EPU, 2001, p. 304.

WANG, X., et al. Experimental Investigations on Aerodynamic Characteristics of the ZHIYUAN-1 Airship. *Journal of Aircraft*, July-August 2010, Vol. 47, No. 4, p. 1463-1468.

WANG, X., MA, Y., and SHAN, X. Modeling of Stratosphere Airship. *Advances in Theoretical and Applied Mechanics*, 2009, Vol. 2, No. 3, p. 123-142.

WATERHOUSE, James R. *Estudo de Viabilidade de Dirigíveis de Carga.* São Carlos, 2011. Report Rev. 2.

YOUNG, A.D. *The calculations of the total and skin friction drags of bodies of revolution at zero incidence.* London, HMSO: ARC R&M, 1939.

ZAHM, A.F. *Stability Equations for Airship Hulls*. Navy Department, 1926. Report No. 212.

ZAHM, A.F.; SMITH, R.H.; HILL, G.C. *The Drag of C Class airship Hull with Varying Length of Cylindrical Midships.* Bureau of Construction and Repair, Navy Department, 1923. Report No. 138.

WESTCOTT, R. *World's longest aircraft is unveiled in UK.* [online]. BBC News, 2014. [cited 12 March 2016]. Available from: http://www.bbc.com/news/business-26337673.

Appendix A

This appendix presents the main wind tunnel model manufacturing details and procedures, so the same model can be reproduced by other researchers if desired. The base model was manufactured by another colleague from AdB, Isaac Heras Cebolla (2013), who started studying AdB's airships using the wind tunnel. The model was completely disassembled and cleaned. After that it was remanufactured, having a new coating, fixation system, internal tubing and completely new tail fins. The following topics describe the original manufacturing procedure, but also the new manufacturing techniques applied by the author with the support of technicians from LAE.

Wind tunnel model

This work aims at better understanding the aerodynamic and its influence on the stability of an X-tail conventional airship, besides looking at the specific aerodynamic interference effects involved in the operation of such a vehicle. With this in mind, the wind tunnel model was chosen to be a scale model of a prototype under studies at AdB. The main purpose is to study a concept which is considered to be a good candidate for industry, and in some sort of way diminish the challenges involved in funding for this research. Since this work has AdB's support, it is worthy to study a concept based on its researches, and at the same time an aircraft with which the author is familiarized and works directly on. The following topics contain information regarding the whole manufacture of the model: plug-in, mold and the model itself manufacturing, describing the peculiarities of each process.

Brief description

As already stated in Section 4.1, the experiment model was designed in order to minimize the wind tunnel test section blockage, and consequent walls interference in the study, converging to a 1/116 scale mode. Responding to needs for investigating the pressure distribution over the airship, it also had to have pressure taps, which led to a hollow model, housing all related equipment (Scanivalve™ and pressure taps tubing, for example). The model three view and dimensions can be seen in Section 4.1, where they are also compared to the original airship prototype under study.

Plug-in manufacturing

With the dimensions defined, the construction of the model was planned to be made from a positive plug-in, passing to a negative mold manufacture, ending in the hollow model. The plug-in existence comes from the need for an internal compartment in order to house equipments related to the investigation of the pressure distribution.

In order to lower the costs, easy the manufacturing and reduce the weight, the structure of the plug-in is a combination of 3mm thick wood discus and Expanded Polystyrene (EPS); the firsts provide stiffness and patterning, while the second, the desired shape. The model crude structure is shown in Figure 269.

Figure 269 - Plug in (EPS and MDF).

Source: Cebolla (2013).

The foam thickness varies, trying to explore the advantage of hull slightly diameter variations. In other words, where the diameter has a smaller gradient, the EPS discus is thicker. This eases the construction, decreasing the number of parts and assemblies. For example, in the middle, the EPS discus has 80 mm, while in the prow and stern, only 20 mm.

The discs were aligned so their centers were coincident, and by means of a 1 inch diameter steel bar, all of them were crossed and joined. With the structure base joined and aligned, the steps were filled with joint compound, and after that, covered with fiberglass woven and epoxy resin, giving uniformity and a first shape approach.

Figure 270 - Plug in covering with fiberglass.

Source: Cebolla (2013).

After that first shape was reached, it was necessary to guarantee that the correct scale hull was being achieved. To check the plug-in conformity, a steel template of the hull generatrix was made. The steel sheet was marked and laser cut, being manufactured in two pieces, joined afterwards in middle, and containing bearings (similar to washers) in the terminations, which fit to the steel tube in the center. With this system, it was possible to turn the model and use the template as a manual lathe. This procedure counted on adding progressively joint compound and fast drying finishing compound until the desired shape was obtained, removing the excess using the steel sheet (template). To illustrate the process, some picture of the model before applying the compounds and trimming using the template were taken, highlighting the gap between the pattern and the plug-in under development.

Figure 271 - Plug in surface trimming.

Source: Cebolla (2013).

This simple system was very efficient and helpful, and led to an almost finished plug-in. When the template shape level was reached, the pattern was removed, and the surface was hand finished. This last procedure was made applying fast drying finishing compound and sanding the surface. After that, the steel bar had its terminations cut off, and the prow and stern holes were covered with joint compound and hand finished with sandpaper also.

Before laminating the mold, the plug-in in a whole was finished by sprinkling thinned fast drying finishing compound with a spray gun, and sanding the surface with a sequential sandpaper roughness: 500, 800 and 1200. This assured a very well finished surface, as shown in Figure 272.

Figure 272 - Plug in final surface.

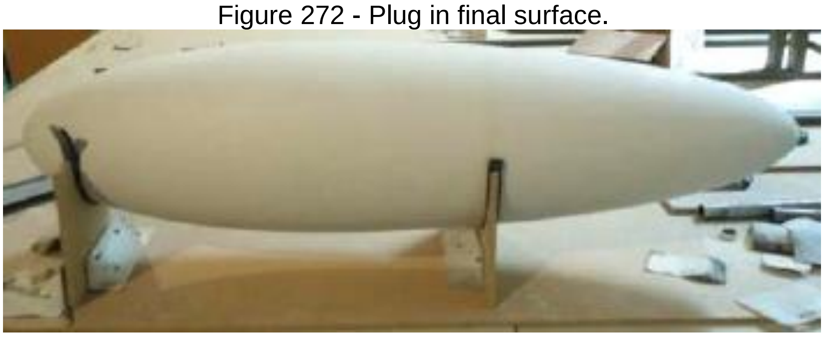

Source: Cebolla (2013).

Mold manufacturing

The next step was to have the mold, which would be used to manufacture the wind tunnel model (the shell – hollow model). Firstly, to protect the plug-in and easily release the mold after laminating, the plug-in was covered with many hands of mold release and Carnauba wax. Also some Medium Density Fiberboard (MDF) wood cut with the plug-in shape was made to provide the mold flanges and be used as a surface for laminating. The chosen material for the mold was Chopped Strand Mat (CSM) fiberglass and polyester resin.

The process to obtain the desired mold was more troublesome. The first tryout, aiming at producing a four-part mold, had the objective of manufacturing the final model in two parts: forward and rear. Before applying the CSM fiberglass, a layer of gel coat was applied in order to provide a smoother surface for the final model laminate. However, during the cure process something went wrong, and some problems showed up. The mold parts had adhesion problems to the fiberglass due to excessive cure of the gel coat and possible contamination. Besides that, after the complete cure under the sun light, some void was identified. Bubbles caused by unreacted or under-cure, solvent, water, oil or air pockets appeared on the surface.

These problems required a recover of the plug-in, removing remaining resin and gel coat. The mold philosophy was changed, and it was chosen to be a two-part mold: port and starboard. Avoiding additional failures maybe caused by the gel coat, this component was removed from the list, and additional care was put in the process. In order to seal the joint between flange and plug-in, body filler was applied to the gap. This second concept led to a very successful mold, which was used to manufacture the final model shell.

Figure 273 - Final mold for model manufacturing.

Source: Cebolla (2013).

Wind tunnel model manufacturing

With the finished mold, it was possible to laminate the final hull structure. Using fiber glass and polyester resin, each half shell was manufactured, and released from the mold. The thickness of each half is about 2 mm, grating stiffness to the model and enough resistance to bearing stresses due to fixations. Since the model contains internal components, it must also have some access to it. This access is guaranteed by two windows; fiberglass panels were cut off from one half, and the lids were manufactured separately and fitted to the model. The aft lid contains an oblong slot making it possible to conduct out the internal systems cable, below the wind tunnel, collecting the data.

Figure 274 - Model halves next to its mold.

Source: Cebolla (2013).

Before closing the model (joining the half shells), the original pressure tapping were installed. Three longitudinal arcs were defined on the surface, obviously not along the windows, and going in between the tail fins. Each pressure line has twenty 20 taps, totalizing 62 taps when summing the prow and stern orthogonal taps. Still before the junction, an internal reinforcement was installed. An annulus was manufactured with a 9 mm thick MDF wood and glued to the shells internally so a steel tube could be attached to the hull and be the link between the model and wind tunnel balance. Initially, it was made by means of only using internal fixation solutions (kneading tube extremity, bolting it to the internal annulus, etc). Finally, the model was assembled. The parts were joined with fiberglass cloth bands and polyester resin, and surface finished, so they were crispy (turbulence induction).

Modifications and remanufacturing

The model was not in proper conditions to be used by this author, and needed some treatment to be done. Firstly the whole model was dissembled; the painting cover was completely removed, by means of sanding, up to the fiber glass structure.

Figure 275 - Crude model ready for recover (pressure tapping tags evidenced).

Source: Author (2018).

After that, the pressure taps positioning was maintained for the second trial of this model (now recovered and manufactured by this author) .The taps distribution along the arcs was defined by means projecting the angular positions equally spaced on a semi circumference with the diameter equals to the length of the model, and projecting the points into a line along the center of the model, and orthogonally project the resulting points into the model surface arc. The taps distribution and nomenclature is present in Appendix B. The tubes used for the taps are 0.4 mm walls thickness, and 1 mm internal diameter, made of polyurethane. Each tube was passed across a hole made normal to the surface, and glued to the hull by means of cyanoacrylate, trimmed to the surface level (Figure 276), and double checked with compressed air, guaranteeing that they were not obstructed.

Figure 276 - Pressure tapping tubes trimming.

Source: Author (2108).

Since the model was not surface finished (sanded and painted) yet, all taps were covered by thin pins, which were added and removed as necessary. Each of them has an identification number which helps the installation procedure on the transducer, and the mapping of the results.

Figure 277 - First surface covering (pressure taps blocked).

Source: Author (2018).

Afterwards, during some structural integrity evaluation with the model, an alternate solution for the fixation was used. A steel plate was cut and folded in an “L-shape”, being the connection between the tube and the belly of the hull. It was riveted to the hull (using a steel sheet inside as shield) and to the tube, to which it was also welded, assuring stiffness and safety. The upper fixation, inside the hull, where the bar was smashed, had a riveted joint also, joining the steel tube and the composite reinforcement.

Figure 278 - L-shaped reinforcement.

Source: Author (2108).

Figure 279 - Internal fixation reinforcement.

Source: Author (2108).

The free extremity of the tube was welded to a 2 mm thick steel disc perpendicular to it, which fit to the wind tunnel balance fitting.

The raw surface was finished by applying fast drying finishing compound and sanding it with sandpaper 220, 320 and 400 sequentially. In the sequence, the final surface finishing began. Firstly, a mixture of fast drying finishing compound and solvent (thinner) was wrinkled over the surface, covering the joining and the whole composite structure, after the remaining powder of the sanding was blown away. The surface was then sanded with sandpaper 400 and 600. Some defects, like small holes and areas where there were not enough resin in the laminate, were found; the compound was manually added and sanded again. The surface was very smooth already at this stage – even ready for wind tunnel testing, but not prepared for receiving the painting yet.

Figure 280 - Lacquer covering.

Source: Author (2108).

Figure 281 - Final painting.

Source: Author (2108).

Since the painting was necessary in order to preserve the model and also allow the flow visualization techniques to be applied, the surface received a sealing lacquer layer typically used for wood and fast drying compound. After the layer was dry, two layers of matte black automotive enamel were sprayed. This color guarantees enough contrast with the white color of the flow visualization oil. Meanwhile the fixation steel tube was also painted with a silver spray, similar to aluminum color, in order to clearly differentiate both structures: airship and steel tube.

After the painting was ready, the model was sanded with 400, 600, 800 and 1200 grades of sandpaper, removing some creepy painting, making it smoother. After this, the surface was cleaned spraying oil with nano- spheres – exclusive of the LAE facilities – on the surface and polishing it with cloth.

Figure 282 - Hull model finished.

Source: Author (2108).

Tail fins manufacturing

As stated, this work studies the stability of an X-tail conventional airship, and the model here is based on an AdB's prototype. Using the same characteristics of this project, and scaling it, the fins of this model have a NACA 0012 as the airfoil.

Each fin is divided in two parts: stabilizer and control surface (a.k.a. ruddervator). Aiming at investigating the behavior and aerodynamic characteristics for different tail arrangements, and even analyzing the aircraft trimming, the fins simulate the real ones, counting on movable surfaces. The stabilizers were manufactured at AdB, using a FDM 3D printer, the RoBo 3D R1™, a low-cost, open source and easy to use device. It is sold fully assembled, and is equipped with a heated bed (glass) for printing with both ABS and PLA filaments. The stabilizers were printed using 1.75mm PLA filament, divided in two pieces, so the precision could be better. Several trials were made before the acceptable result was achieved.

Figure 283 - One of the final prototypes standing on the 3D printer table.

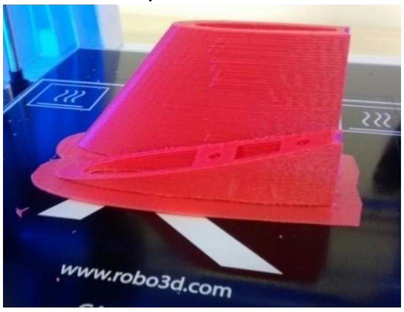

Source: Author (2108).

Figure 284 - S0 Fin stabilizer ready for surface finishing.

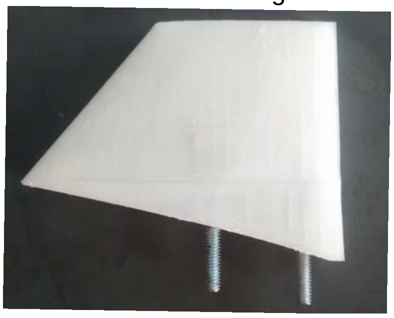

Source: Author (2108).

The final printing configuration has the stabilizer divided right at the end of the line of contact with the hull. This made it possible to join them by two flat faces, preserving the curve agreement. It was made by gluing and using joint compound. With the final piece assembled, the surface finish was not very smooth. A thin layer of mass of added to it, and the assembled stabilizer was sanded, trimming the surface imperfections, achieving a better quality, essential for wind tunnel testing. Also the surface was painted in black, allowing future oilflow visualization. In order to fix the stabilizer to the hull, two 6 mm diameter threaded rods internally glued to the stabilizers are used. Internally, nuts and washers are used to retain the fin to the hull.

Figure 285 - S0 and S1 Fins finalized.

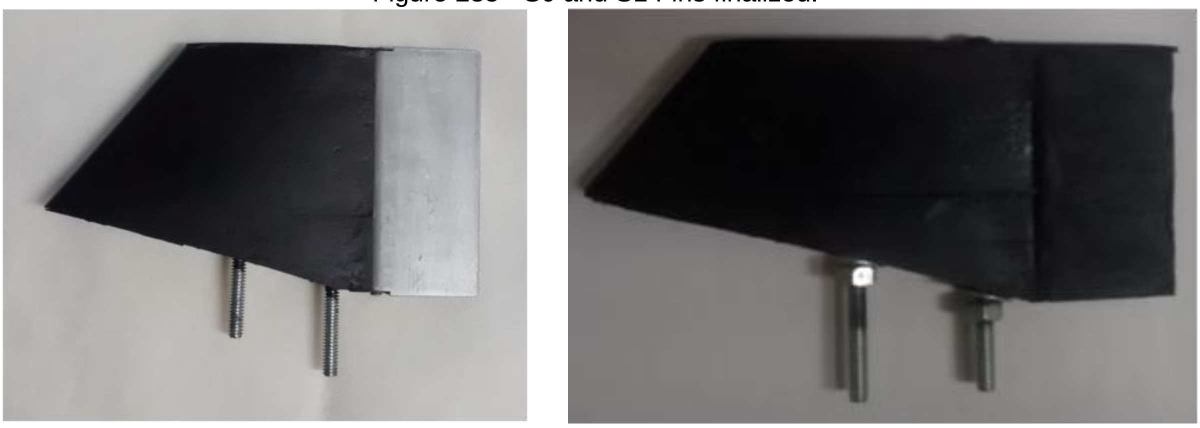

Source: Author (2108).

The control surfaces were manufactured from solid wood, and simplified, disregarding tapering, since, for this scale, it became too small. In order to attach the control surface to the stabilizer, its tip and root rear portion were carved, and fin aluminium terminations were glued to them. The control surfaces had same carving process so they could be adjusted to the holding terminals. Finally, by means of wood screws, the control surfaces were attached in between the aluminium plates along their axis. This way, besides attaching and holding the control surface position (depending on tightness), the screws act as rotating axis for deflection adjustment.

Two different sets of fins were manufactured: S0 (Standard) and S1 (Shorter). All manufacturing and mounting features are the same for both sets. The difference stands on span. S1 has the upper portion length equivalent to 2/3 of S0. The final dimensional properties of each fin set are registered in Table 19.

Table 19 - Fin sets (S0 and S1) dimensions.

Property	S0	S1
Chord[1] [mm]	174	174
Control Chord [%]	27.5%	
Span[2] [mm]	65.4	43.6
Area[3] [mm^2]	13200	10400
AR[4] [-]	0.324	0.183

[1]Maximum chord along the straight line.
[2]Upper portion span.
[3]Surface total area, disregarding envelope curvature.
[4]Aspect ratio assuming upper portion spanwise only.

Source: Author (2018).

Figure 286 and Figure 287 are drawings of S0 and S1 FINs planforms.

Figure 286 - S0 Fin planform dimensions

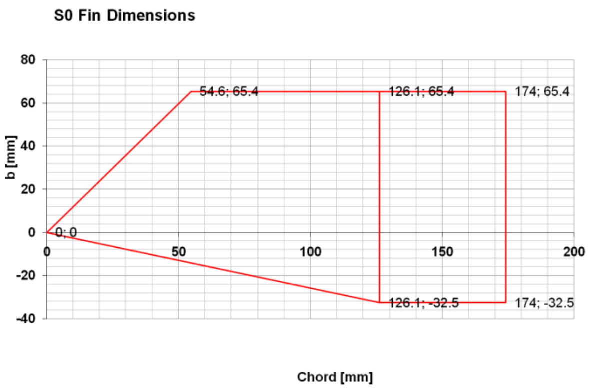

Source: Author (2108).

Figure 287 - S1 Fin planform dimensions

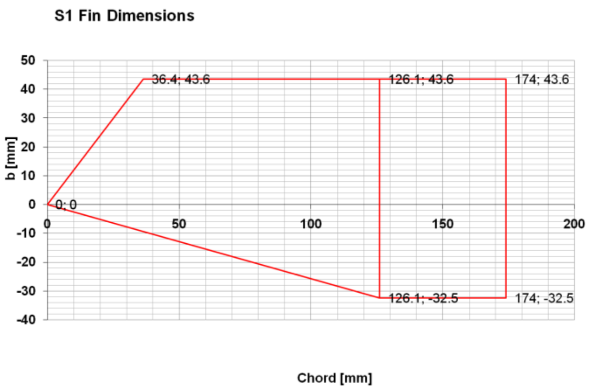

Source: Author (2108).

Appendix B

The original model fabricated by Cebolla (2013) had provisions for 62 pressure taps. Two of them were called bow and stern taps, since they are located in the longitudinal axis at the positions they are named after. The other 60 taps are distributed along three lanes. Each lane has its designation based on the side where it stands on the model, according to the reference presented in Figure 61. So, the 20 taps distributed on the upper portion are called Top line, those to left are called Port line and finally, those to the right, Starboard line. All of those taps were recovered or remade, as described in Appendix A.

This original tapping distribution derives from the projection of a semi-circumference (180°) divided in 21 equal pieces on the hull longitudinal axis. In other words, a normalized semi-circumference (180°) was divided in equal angle increments, and the intersection between the circumference and the radius corresponding to each incremental angle was projected on the horizontal axis (Figure 288).

Figure 288 - Pressure tapping definition on normalized circumference.

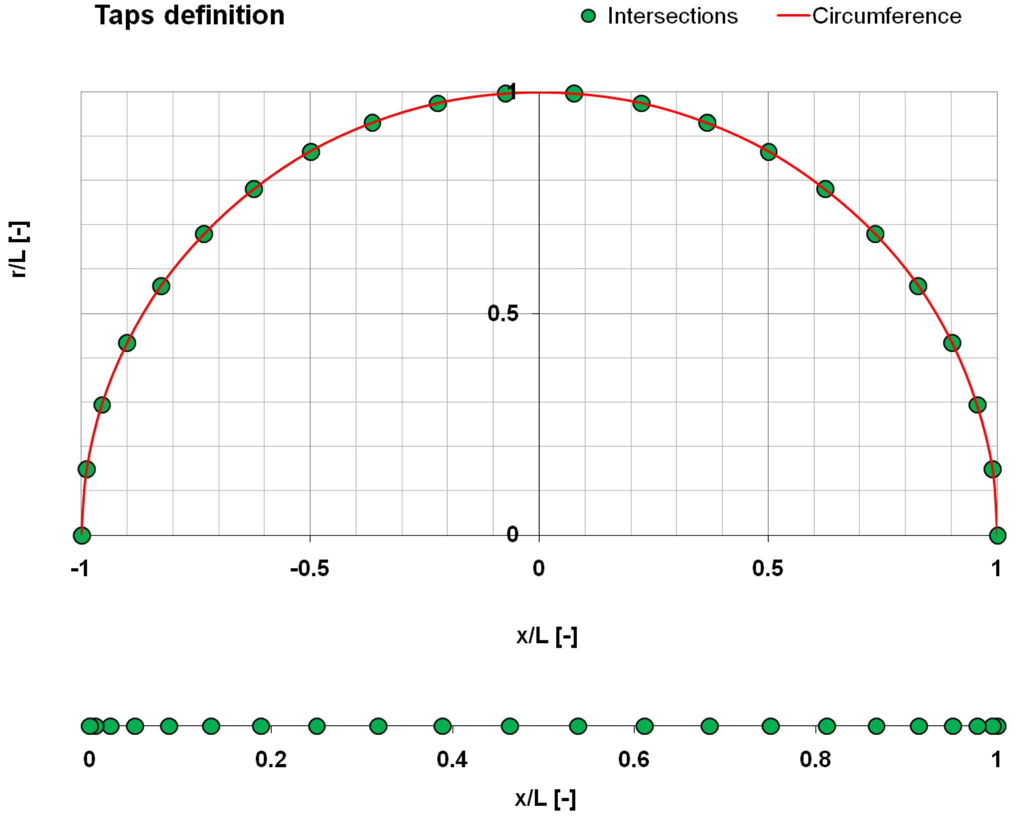

Source: Author (2018).

These normalized coordinates were then scaled to the model hull length, and projected back onto the model surface considering its generatrix (Figure 289).

Figure 289 - Normalized HULL semi cross section with pressure tapping distribution.

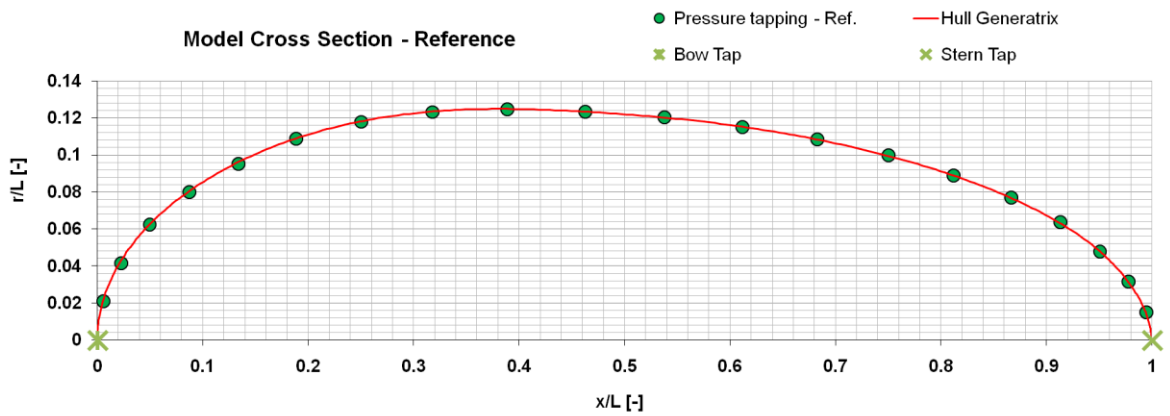

Source: Author (2018).

In order to improve the flow investigation about the airship model stern region some more taps were manufactured. Firstly, four taps were added to Port and Top lines between subsequent existing taps. Complementarily, a lane of taps was added right ahead the Upper Left (UL) fin. These taps were much closer to each other, and were not aligned with the existing taps. Their objective was to capture the flow stagnation upstream the fin. The described additional taps were placed as follows:

Figure 290 - Additional taps.

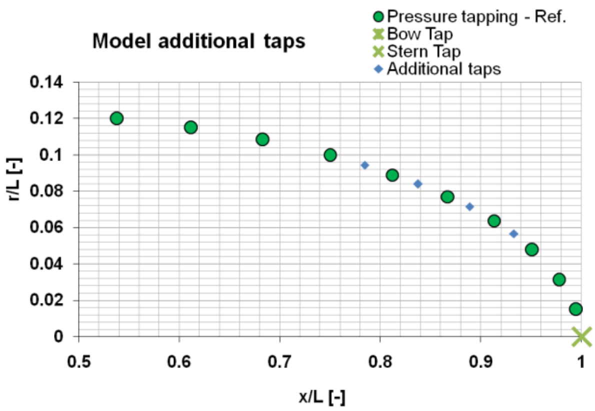

Source: Author (2018).

Figure 291 - Fin line taps.

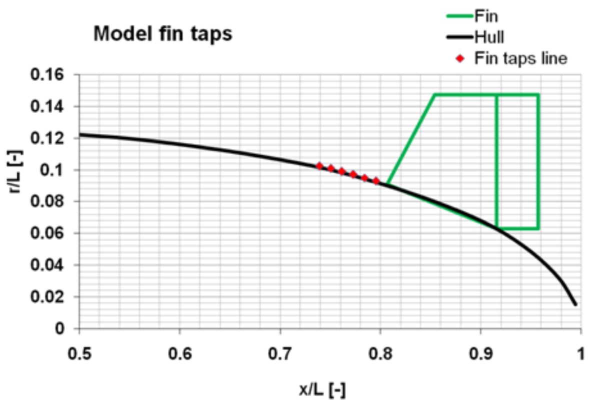

Source: Author (2018).

The pressure taps mapping for the first measurements (before additional taps) is presented below, in Table 20. The table contains the longitudinal and vertical position, and the adopted nomenclatures for each tap. It is important to highlight that those are the theoretical positions.

Table 20 - Pressure Transducer (Scanivalve™) Taps – Mapping.

Taps Ref. Nr.[1]	Port	Stbd.	Upper	x/L [-]	r/L [-]
1	5	25	45	0.006	0.021
2	6	26	46	0.022	0.042
3	7	27	47	0.050	0.062
4	8	28	48	0.087	0.080
5	9	29	49	0.133	0.095
6	10	30	50	0.188	0.109
7	11	31	51	0.250	0.118
8	12	32	52	0.317	0.123
9	13	33	53	0.389	0.125
10	14	34	54	0.463	0.123
11	15	35	55	0.537	0.120
12	16	36	56	0.611	0.115
13	17	37	57	0.683	0.109
14	18	38	58	0.750	0.100
15	19	39	59	0.812	0.089
16	20	40	60	0.867	0.077
17	21	41	61	0.913	0.064
18	22	42	62	0.950	0.048
19	23	43	63	0.978	0.032
20	23	44	64	0.994	0.015

[1]Consider Figure 289, counting from left to right.
Taps 1 and 2 were used for scanivalve, and 3 and 4 were Bow and Stern taps respectively.

Source: Author (2018).

For the second pressure measurement phase, when specifically the stern investigation took place, a different transducer mapping was used, once the taps to be measured were different too. Once again, those are the theoretical positions, and all the fabrication referencing was made in place, by measuring along the generatrix, and mathematically converting it to longitudinal position.

Table 21 - Pressure Transducer (Scanivalve™) Additional Taps – Mapping.

Ref. Name	Port	Ref. Name	Upper	x/L [-]	r/L [-]
18	2	58	14	0.750	0.100
18,5	3	58.5	15	0.785	0.094
19	4	59	32	0.812	0.089
19.5	5	59.5	33	0.838	0.084
20	6	60	34	0.867	0.077
20.5	7	60.5	35	0.889	0.072
21	8	61	36	0.913	0.064
21.5	9	61.5	37	0.933	0.057
22	10	62	38	0.950	0.048
23	11	63	39	0.994	0.032
24	12	64	40	0.994	0.015

The scanivalve tap Nr. 1 was used for dynamic pressure and Nr. 13, for Stern tap.

Source: Author (2018).

Table 22 - Pressure Transducer (Scanivalve™) UL FIN Taps – Mapping

Ref. Name	Fin line	x/L [-]	r/L [-]
F1	41	0.739	0.102
F2	42	0.750	0.100
F3	43	0.761	0.098
F4	44	0.773	0.097
F5	45	0.784	0.095
F6	46	0.795	0.092

Source: Author (2018).

Appendix C

The calibration of the outputs of the aerodynamic balance followed the process described in section 4.2.2.3. This appendix contains the table and charts, along with the linear regressions, which led to the factors used to convert voltage into force (lift and drag). The moment calibration was obtained from a previous experiment. This does not compromise the results, once the main objective was comparing results, and not obtaining the accurate results. The final used conversion factors are presented below (Table 23), followed by the specific data.

Table 23 - Aerodynamic balance conversion factors.

Property	Conversion factor
Drag [N/V]	8.724
Lift [N/V]	5.510
Moment [N.m/V]	-61.94

Source: Author (2018) and Catalano [52](2017).

Drag calibration

Table 24 - Drag calibration data.

Drag dead weight [N]	Drag voltage output [V]
0.00	0.00
8.42	0.90
17.09	1.85
26.06	2.86
35.24	3.89
44.52	4.99
53.88	6.12
63.24	7.24
73.50	8.48
84.11	9.82

Source: Author (2018).

Figure 292 - Drag calibration chart.

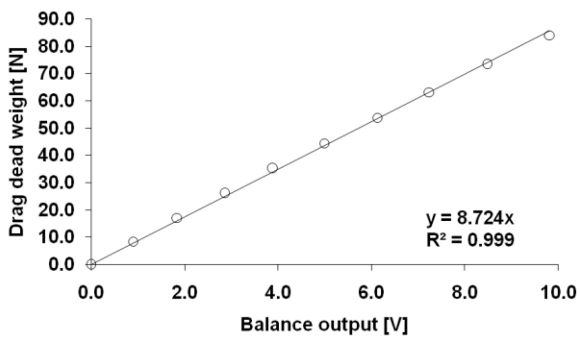

Source: Author (2018).

[52] Moment calibration acquired from LAE database developed for previous testing.

Lift Calibration

Table 25 - Lift calibration data.

Lift dead weigh [N]	Lift voltage output [V]
0.00	0.00
8.42	1.59
17.09	3.20
26.06	4.81
35.24	6.43
44.52	8.05
53.88	9.70

Source: Author (2018).

Figure 293 - Lift calibration chart.

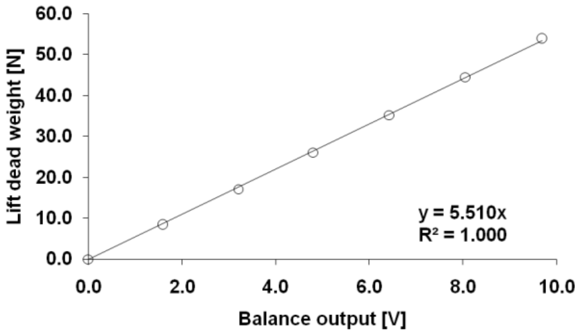

Source: Author (2018).

Appendix D

This appendix contains the final used results deriving from the obtained data during Phase II wind tunnel campaign, regarding the dynamic tests of FINs configurations S0 (Standard) and S1 (Shorter). The results are presented showing the obtained curves after signal processing, following what is described in section 5.3.2. Therefore, the plots of the normalized nonlinear regressions considered for extracting the decay envelopes used along the evaluations for each case are shown below.

The main objective is to allow the reader to check how the signals ended up before being used. For S1, two special cases - “+” and “-Y” - are presented along with their respective filtered outputs. These cases were the most troublesome regarding curve fitting, and therefore not only the regression, but the signal itself are depicted, so the reader can assess and compare the fitting quality. Despite the limitations involved, the regressions were all considered very well succeeded, and results, reliable.

S0 (Standard) FINs Results

Figure 294 - Normalized signal for S0-“X”.

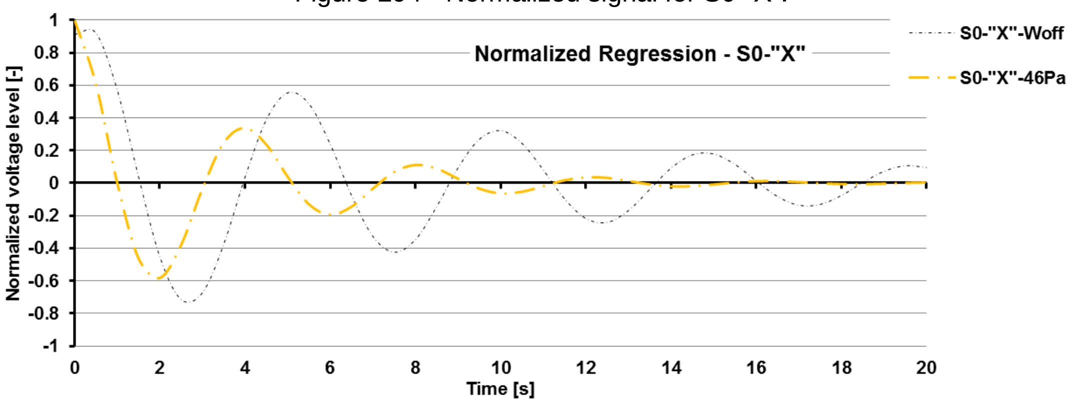

Source: Author (2018).

Figure 295 - Normalized signal for S0-“+”.

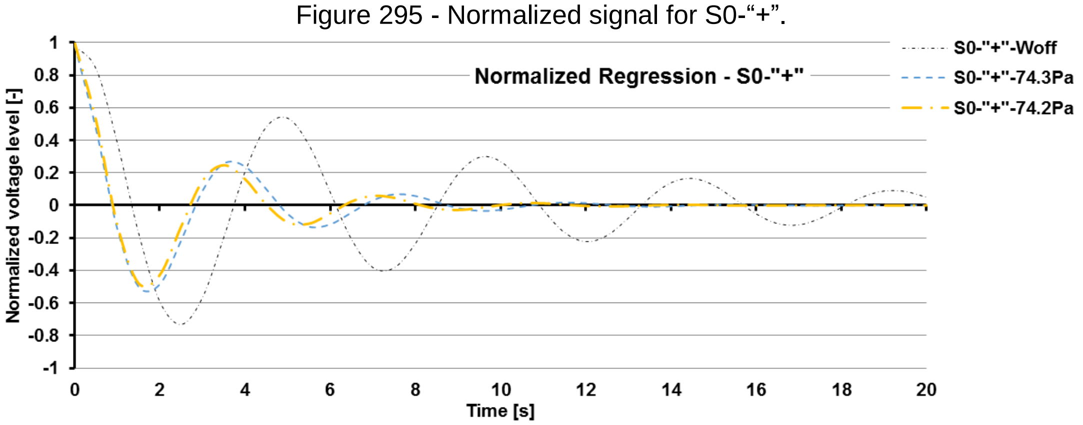

Source: Author (2018).

Figure 296 - Normalized signal for S0-“-Y”.

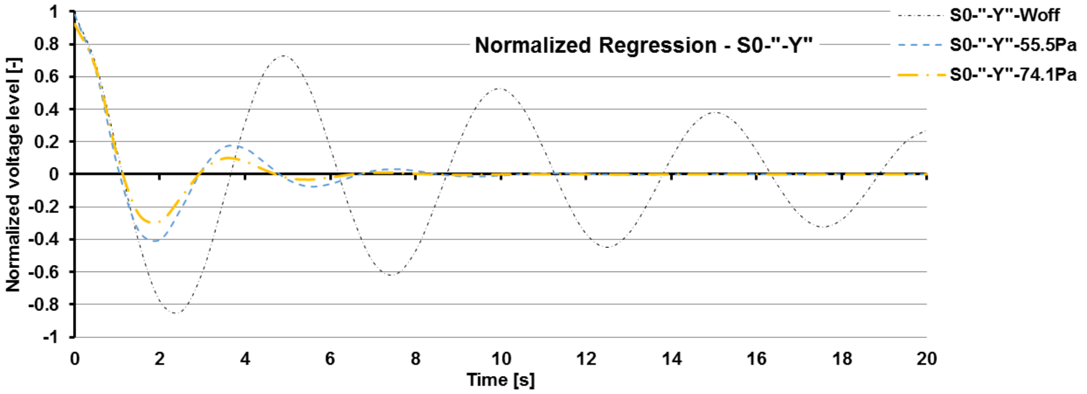

Source: Author (2018).

S1 (Shorter) FINs Results

Figure 297 - Normalized signal for S1-“X”.

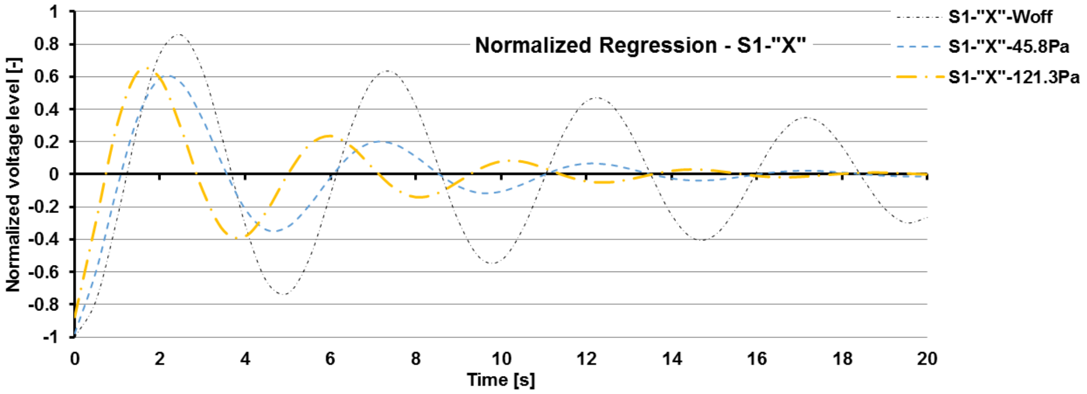

Source: Author (2018).

Figure 298 - Normalized signal for S1-“+”.

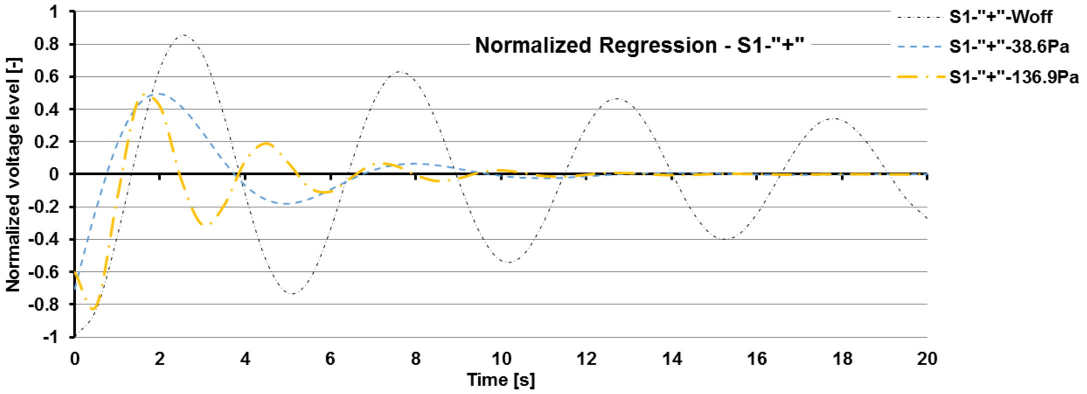

Source: Author (2018).

Figure 299 - Nonlinear regression for S1-"+"-136.9Pa.

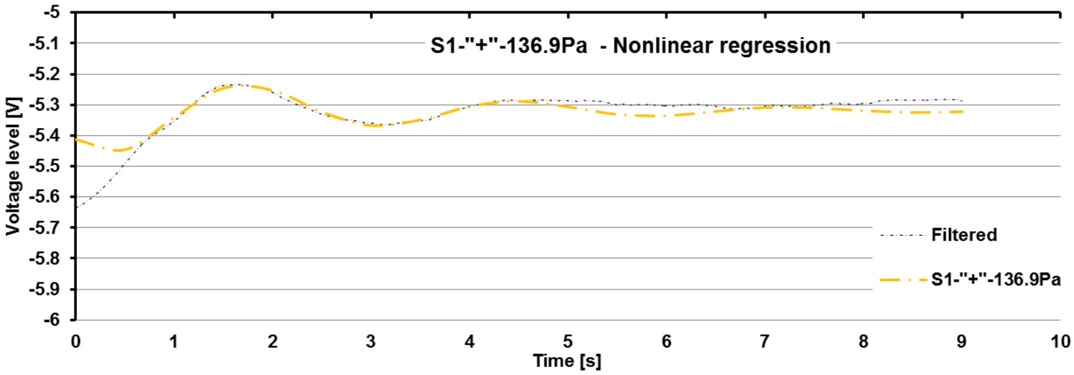

Source: Author (2018).

Figure 300 - Normalized signal for S1-“-Y”.

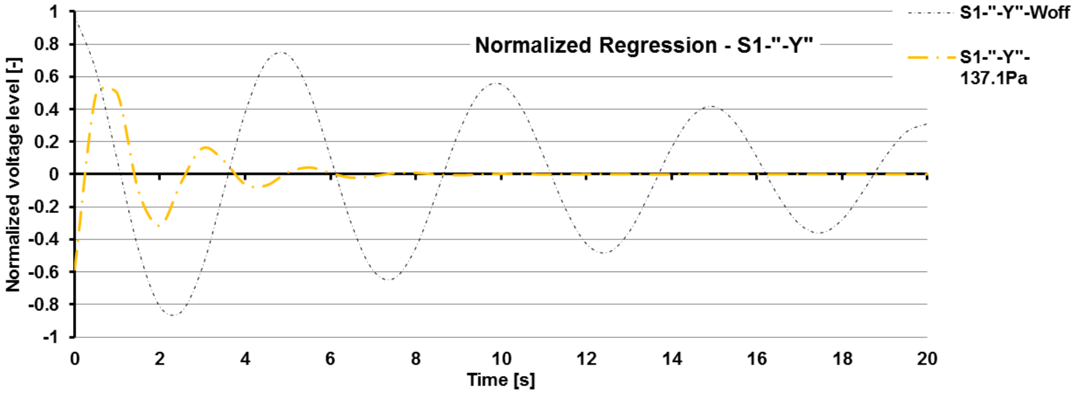

Source: Author (2018).

Figure 301 - Nonlinear regression for S1-"-Y"-137.1Pa.

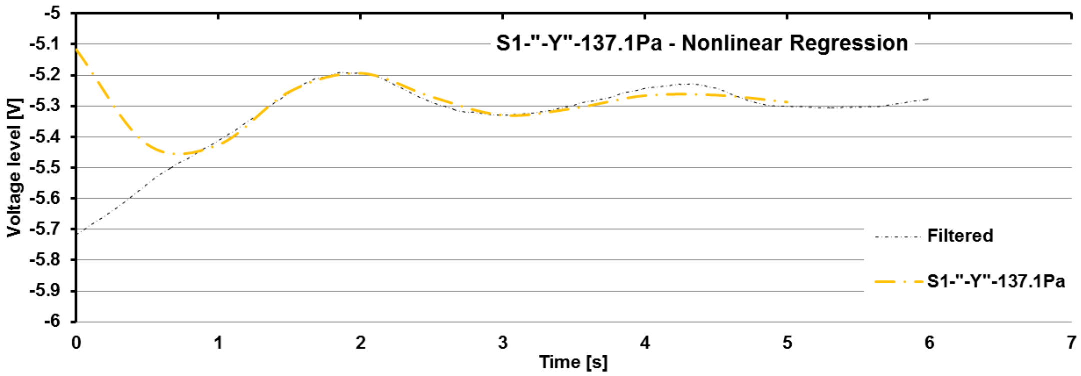

Source: Author (2018).

Appendix E

This appendix contains the calculated TVC using the different approaches cited in section 5.3.7.

Figure 302 - TVC calculated for Author's database using FAF based on damping ratio.

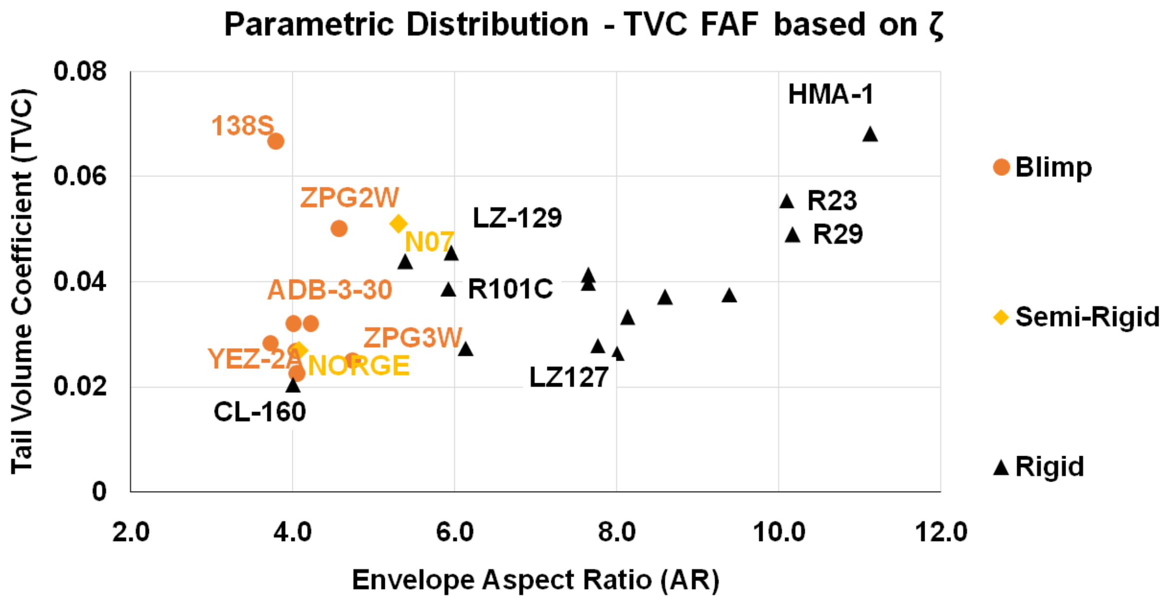

Source: Author (2018).

Figure 303 - TVC calculated for Author's database using FAF based on logarithmic decrement.

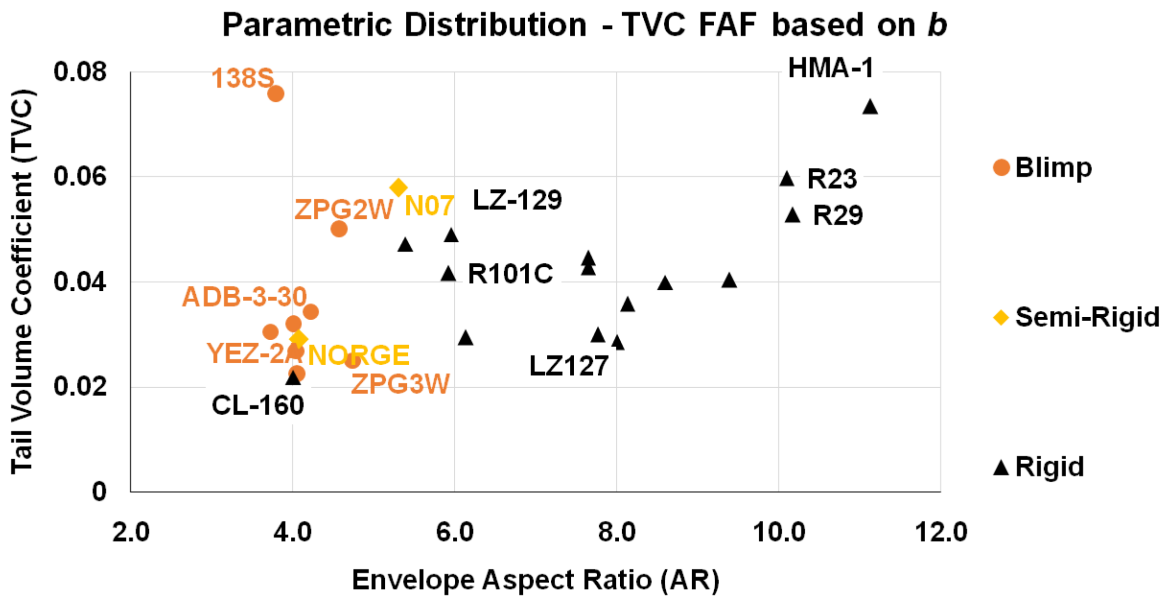

Source: Author (2018).

Figure 304 - TVC calculated for Author's database using FAF mean value.

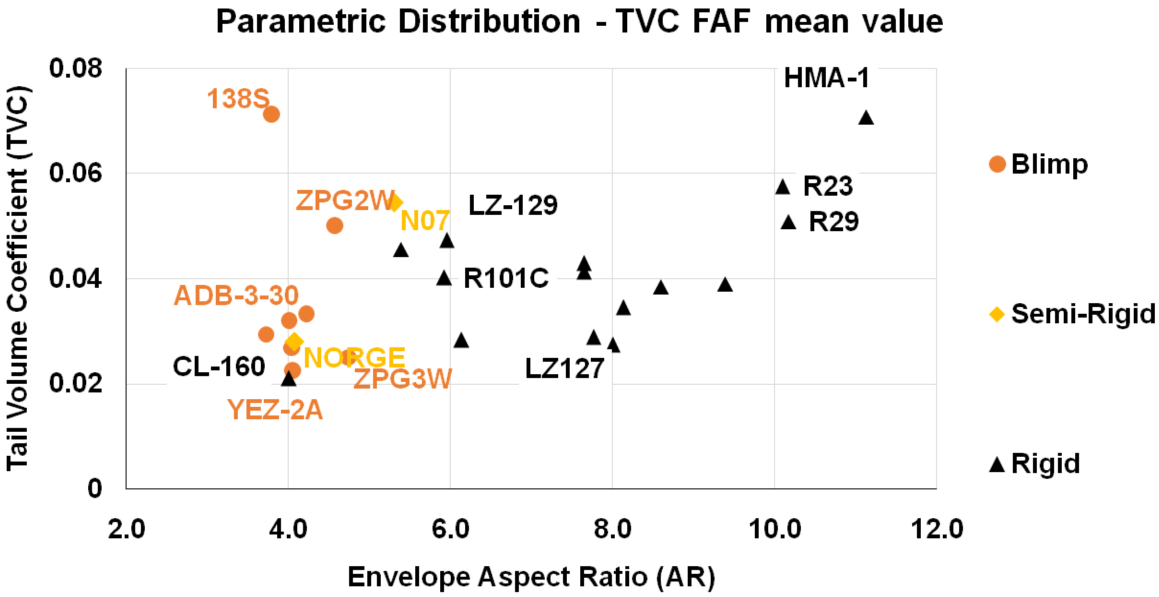

Source: Author (2018).

Figure 305 - TVC_Y calculated for Author's database using PAF based on damping ratio.

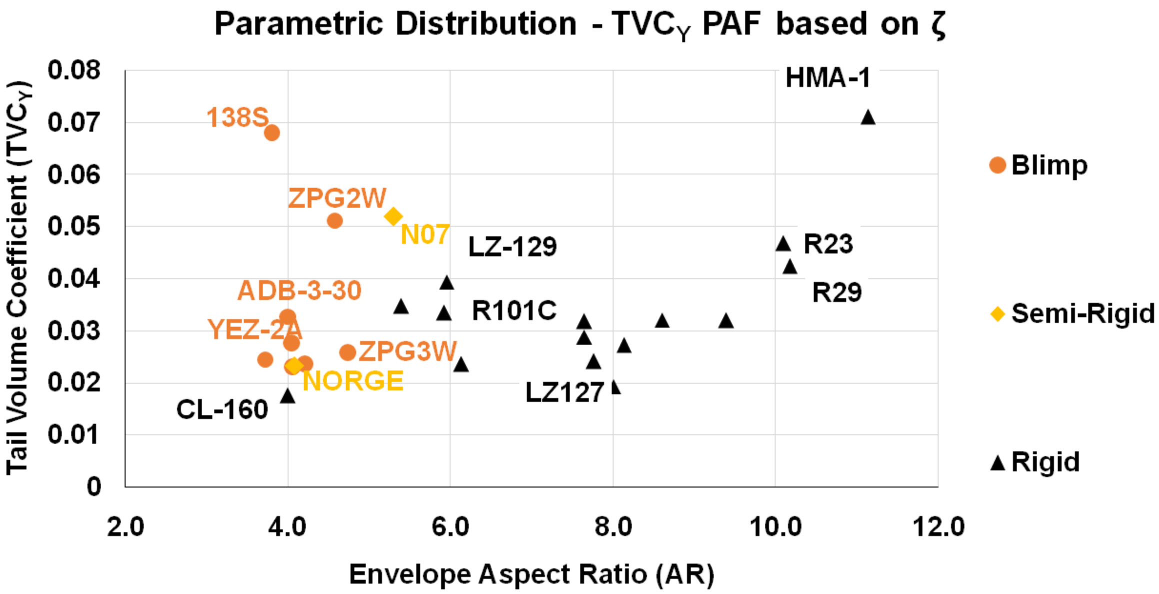

Source: Author (2018).

Figure 306 - TVC_Y calculated for Author's database using PAF based on logarithmic decrement.

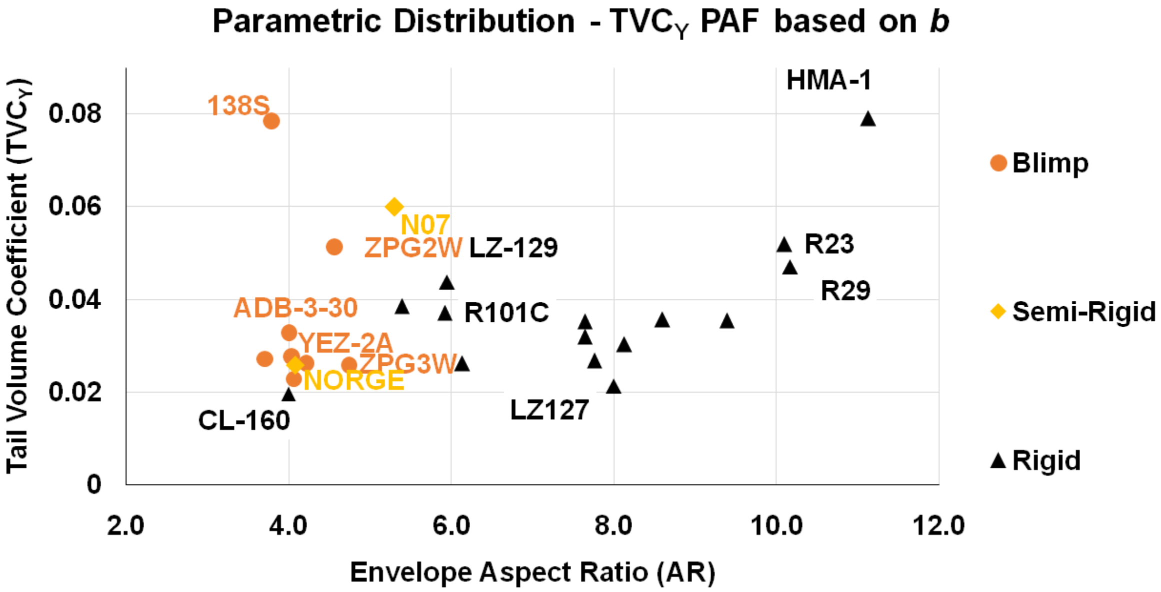

Source: Author (2018).

Figure 307 - TVC_Y calculated for Author's database using PAF mean value.

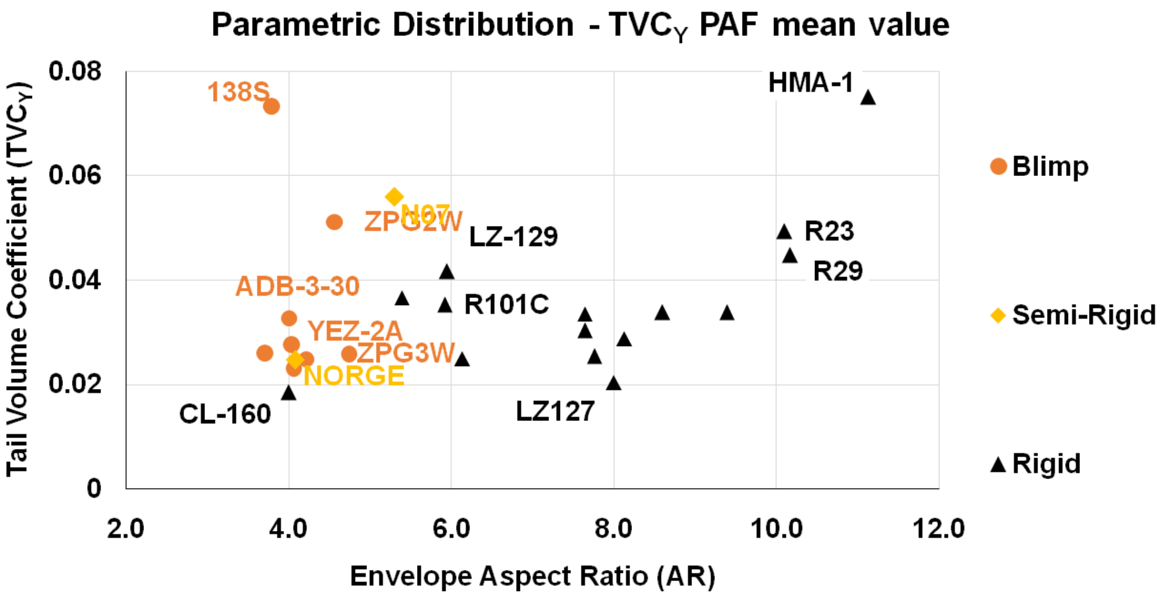

Source: Author (2018).